Physics of Atomic Nuclei, Vol. 63, No. 9, 2000, pp. 1489–1496. Translated from Yadernaya Fizika, Vol. 63, No. 9, 2000, pp. 1573–1579.

NUCLEI
Experiment

Investigation of αγ Angular Correlations in the Reaction ^{15}N(p, αγ)^{12}C Induced by 7.5-MeV Protons

A. V. Ignatenko, V. M. Lebedev, N. V. Orlova, and A. V. Spassky

Institute of Nuclear Physics, Moscow State University, Vorob'evy gory, 119899 Russia

Received July 8, 1999; in final form, September 23, 1999

Abstract—The double-differential cross sections for the reaction ^{15}N(p, αγ)^{12}C induced by 7.5-MeV protons are measured for alpha-particle emission angles from 20° to 160°. All even spin–tensor components of the density matrix for the 2^+ state (4.44 MeV) of the final nucleus are reconstructed by a model-independent method. For the same state of the carbon nucleus, the populations of magnetic sublevels and the components of the angular-momentum-orientation tensor are analyzed as functions of the alpha-particle emission angle. Our experimental data are compared with theoretical predictions based on the triton-cluster-pickup mechanism treated within the coupled-channel method. It is shown that correlation features are sensitive to the reaction mechanism and to structural characteristics of the nuclei involved. The role of sequential processes is emphasized. © *2000 MAIK "Nauka/Interperiodica".*

1. INTRODUCTION

The present article reports on a continuation of our investigations into angular correlations between photons and massive particles in nuclear reactions involving light nuclei and leading to the formation of ^{12}C nuclei in the 2_1^+ state. Our previous studies of elastic alpha-particle and ^{3}He scattering on ^{12}C nuclei [1, 2] and of the formation of the state in question in reactions featuring the transfer of one nucleon or two nucleons [3–5] revealed that, in some cases, angular correlations are more sensitive to the reaction mechanism than angular dependences of the relevant differential cross sections.

The reaction ^{15}N(p, α)^{12}C has been studied rather well. In particular, the angular and differential dependences of the differential cross sections for the formation of the ground and the lowest excited state of the final nucleus were measured over a broad energy range extending to 45 MeV [6]. However, these measurements could not be uniquely interpreted in terms of the simplest direct transitions (such as the pickup of a cluster and the DWBA), compound-nucleus formation, and preequilibrium processes.

At the same time, correlation measurements provide a clue to reaction dynamics and allow a verification of the model assumptions used to interpret all existing data on this reaction. In addition, such measurements are sensitive to the structural properties of the initial and final nuclei. In particular, the rotational origin of the lowest 0_1^+–2_1^+ states of the ^{12}C nucleus, which has a sizable quadrupole deformation ($\beta_2 \sim -0.5$ [7, 8]), is expected to affect all the aforementioned reactions. This feature of the ^{12}C nucleus dictates the use of the coupled-channels method (CCM) in analyzing experimental data, whereby the eventual theoretical results may differ significantly from the predictions of a conventional DWBA analysis.

Here, we report on the first measurements of αγ angular correlations in the three-nucleon-transfer reaction ^{15}N(p, αγ)^{12}C. The data from these measurements are sufficiently vast to allow a reconstruction of all even spin–tensor components of the density matrix for the 2_1^+ state of the final nucleus.

The reaction is assumed to proceed via the triton-cluster-pickup mechanism analyzed on the basis of the CCM.

2. EXPERIMENTAL PROCEDURE AND DATA ANALYSIS

Incident protons with a kinetic energy of 7.5 MeV were delivered by the 120-cm cyclotron installed at the Institute of Nuclear Physics (Moscow State University). The proton energy was determined by comparing the energy that beam protons scattered in a thin gold target (0.22 mg/cm^2) lose in a silicon detector with the energy loss of alpha particles from the standard ^{226}Ra source OSAI-1. The incident energy was tuned by moderating protons in thin aluminum foils, and the beam spot on a target was formed by focusing magnetic quadrupole lenses (see [9] and references therein). The energy spread of the proton beam amounted to some 70 and 150 keV at E_p = 7.5 and 3.5 MeV, respectively.

The detection of the reaction products and their time and energy analysis were performed with the aid of a data-acquisition system that was characterized by a distributed architecture and which provided several stages of data processing [10]. The first stage, which was identical to that in our previous studies [11] and which

relied on CAMAC modules and on a 131A processor, consisted in sorting out the analog signals from spectrometric devices. At the second stage, these signals were digitized by a minicontroller driven by a Siemens CS167 processor. Finally, the accumulated data were filtered and processed by a local network of two IBM PCs.

In measuring double-differential cross sections, charged secondaries were detected by an array of four surface-barrier semiconductor counters 100 μm thick that were made from silicon and which had an angular resolution of ±2.5°. The angular and energy dependences of the differential cross section were measured by a single detector with an angular resolution of ±1°. These detectors were attached to a table that was arranged in the scattering chamber in such a way that its angle of inclination with respect to the horizontal plane could be changed within an angle of π/2.

Secondary photons were detected by an array of four scintillation counters based on NaI(TI) crystals with an angular resolution of ±12°. Photons of energies between 2.0 and 4.5 MeV, which are characteristic of the radiative transition of the 2^+ excited state (4.44 MeV) of ^{12}C to the ground state, were analyzed for coincidence with product alpha particles.

A layer of melamine powder enriched in ^{15}N to 99% and precipitated from a spirit suspension onto a thin gold substrate was used as a target. The thickness of the target estimated by comparing the yields of elastically scattered alpha particles from the target under study and from a Dacron film of known thickness was found to be close to 1 mg/cm^2. The amount of ^{15}N in the target was also estimated by irradiating it with 28-MeV alpha particles and comparing the resulting angular dependence with that measured in [12]. The reported measurement of the cross section for the reaction ^{15}N(p, α)^{12}C(g.s.) at E_p = 7.5 MeV proved to be consistent with the data from [13] on the cross section for the inverse reaction ^{12}C(α, p)^{15}N(g.s.) at E_α = 16.3 MeV.

A model-independent method for reconstructing the spin–tensor components $A_{k\kappa}(\theta_\alpha)$ of the density matrix on the basis of the measured double-differential cross sections for the reaction, $W(\theta_\gamma, \varphi_\gamma; \theta_\alpha)$, was described comprehensively elsewhere [14]. It consists in solving, by the method of least squares, the following overdetermined set of linear equations for nine components:

$$d^2\sigma/d\Omega_\alpha d\Omega_\gamma \equiv W(\theta_\gamma, \varphi_\gamma; \theta_\alpha)$$

$$= \frac{1}{4\pi}\sum_{k,\kappa} A_{k\kappa}(\theta_\alpha)\bar{P}_k^\kappa(\cos\theta_\gamma)\sqrt{\frac{2}{2k+1}}\cos\kappa\varphi_\gamma.$$

Here, the angles θ_α, θ_γ, and φ_γ specify the directions of alpha-particle and photon emission in the system of spherical coordinates with the z axis aligned with the proton-beam direction and the xz plane taken to be coincident with the reaction plane, while $\bar{P}_k^\kappa$ are associated Legendre polynomials. The overall normalizaion of the spin–tensor components is fixed by the condition $A_{00}(\theta_\alpha) \equiv d\sigma/d\Omega(\theta_\alpha)$. The values of k are determined by the relations $\mathbf{k} = \mathbf{J}_f + \mathbf{J}_f$ and $\mathbf{k} = \mathbf{L} + \mathbf{L}$, where J_f is the spin of the excited state and L is the multipole order of the radiative transition, while κ may assume integral values between $-k$ and k.

The double-differential cross sections measured in three planes (with respect to the reaction plane) made it possible to reconstruct all nine even spin–tensor components $A_{k\kappa}(\theta_\alpha)$ of the density matrix for the 2^+ state (4.44 MeV) of the ^{12}C nucleus. For the same state of ^{12}C, we were also able to estimate the population of magnetic sublevels, $P_{\pm M}$, and the components of the angular-momentum-orientation tensor, $t_{k\kappa}$, as functions of θ_α [14]. In deducing the values of $A_{k\kappa}(\theta_\alpha)$ from the measured cross sections, we took into account the finite dimensions of the scintillation counters [14]. The quantities $A_{k\kappa}(\theta_\alpha)$ were largely reconstructed at confidence levels in excess of 0.1.

3. RESULTS AND DISCUSSION THEREOF

The measured cross sections for the formation of the ground state of the ^{12}C nucleus and of its first excited state (2_1^+) in the reaction ^{15}N(p, α)^{12}C are illustrated in Figs. 1*a* and 1*b*, respectively, as functions of θ_α in the range 20°–160° (in the laboratory frame). These dependences are typical of direct processes, although the θ_α distribution for the formation of the 2_1^+ state tends to be symmetric with respect to θ_α = 90°.

For alpha-particle emission angles of 45°, 60°, and 120°, the measured cross sections are depicted in Fig. 1*c* as functions of the incident energy E_p (varied between 3.5 and 7.5 MeV). The data for the formation of the ground state of ^{12}C are consistent with excitation functions for the inverse reaction from [13], where these data overlap. The excitation functions for the formation of the 2_1^+ state of ^{12}C are quite regular and tend to decrease toward higher E_p. At the same time, the excitation function for the formation of the ground state of ^{12}C shows oscillatory behavior at all values of alpha-particle emission angles.

The double-differential cross sections for the reaction ^{15}N(p, αγ)^{12}C were measured for 18 values of θ_α between 20° and 160° (in the laboratory frame), five to nine values of θ_γ, and three values of the azimuthal angle φ_γ (180°, 225°, and 270°). The density-matrix elements $A_{k\kappa}(\theta_\alpha)$ for k = 2 and 4 as extracted from the measured cross sections are illustrated in Fig. 2 as functions of θ_α. For the same 2_1^+ state of ^{12}C, the θ_α dependences of the populations of magnetic sublevels and of the components of the quadrupole- and hexadecapole-moment-orientation tensors as inferred from the values of $A_{k\kappa}(\theta_\alpha)$ are plotted in Figs. 3 and 4, respectively.

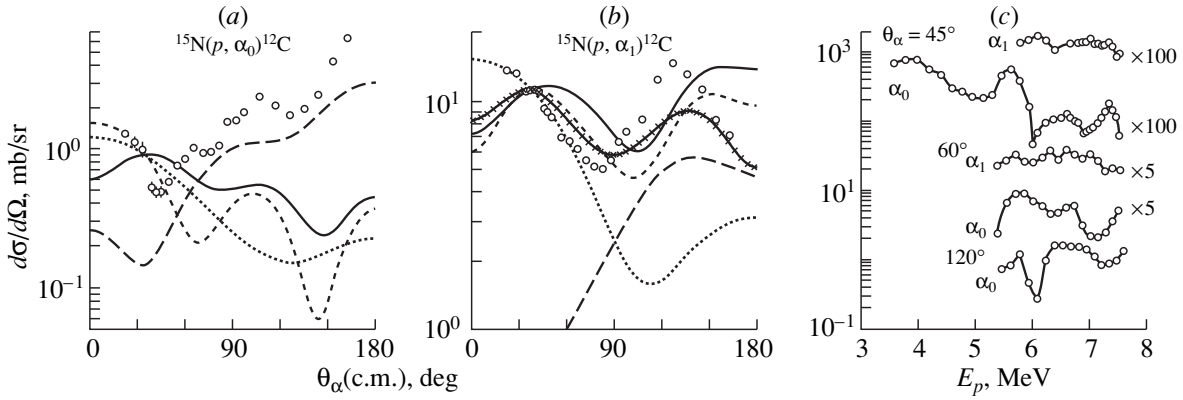

Fig. 1. Differential cross sections for the formation of (*a*) the ground and (*b*) the first excited (2_1^+) state of the ^{12}C nucleus in the reaction ^{15}N(*p*, α)^{12}C at E_p = 7.5 MeV as functions of the alpha-particle emission angle. Points represent our experimental data. The solid curve, short dashes, the dotted curves, and the solid curves with crosses illustrate the results of the calculations assuming the triton-cluster-pickup mechanism treated on the basis of the CCM with the parameter sets no. 1, 2, 3, and 5 from Table 1, respectively. Long dashes show the prediction for the heavy-stripping-particle mechanism. (*c*) Energy dependences of the differential cross sections for the above reaction leading to the transition to (α_0) the ground and (α_1) the first excited state of the ^{12}C nucleus for three different values of the angle θ_α (in the laboratory frame). The curves connecting the data points are drawn to guide the eye. The coefficients by which the experimental data are multiplied are shown by the curves. In this figure and in those that follow, the error bars on data points represent statistical uncertainties.

On the whole, the above quantities show complex oscillatory dependences on θ_α, and the maximum values of all components of the tensors of various ranks prove to be comparable. In particular, the quantities $t_{k\kappa}$ show θ_α dependences suggesting a significant rearrangement of the nucleus. Relatively strong oscillations of these components indicate that the nuclear surface has considerable dynamical deformations in various modes. The multipole moments of an excited ^{12}C nucleus are not collinear with its symmetry axis, and a significant precession of the total angular momentum is observed at all values of the light-particle emission angle. To summarize, the angular dependences of the measured dynamical characteristics of the reaction ^{15}N(*p*, α)^{12}C indicate that its underlying mechanism is fairly intricate.

The data are compared with the predictions that are based on the assumption of the cluster-pickup mechanism and which were obtained by using the CHUCK computer code [15], which takes into account the coupling of channels in the initial and in the final state. The quantities associated with correlations were computed with the aid of some ancillary codes. Our computational scheme is illustrated in Fig. 5. Channel coupling had to be taken into account both in the initial and in the final state, since the ^{15}N nucleus possesses a significant quadrupole deformation [16]. The $3/2^-$ state (6.32 MeV), which fully relaxes to the ground state via an *M*1*E*2 transition [8], was chosen for a level in the rotational band.

The values assumed for the CCM parameters are listed in Table 1, while the parameters of the Woods–Saxon optical potentials are quoted in Table 2. For the real part of the final-state optical potential *A*1, we take the form from [18], where it was obtained by fitting the real generalized potential calculated theoretically within the approximation of the four-body problem (alpha-particle scattering on a bound system of three alpha particles). The depth of the imaginary part of this potential was found here from the best fit to all components $A_{k\kappa}(\theta_\alpha)$; the parameters r_W and a_W were set to the values from [19], where the optical potential in ques-

Table 1. Parameter values used in the calculations by the coupled-channel method

Option number	$\beta_2(^{15}N)$	$\beta_2(^{12}C)$	Potential*	k_0^{**}	k_1^{**}
1	0.3	−0.5	*A*1	0.5	4.0
2	0.0	−0.5	*A*1	0.5	4.0
3	0.3	−0.5	*A*2	0.25	1.7
4	0.0	−0.1	*A*1	0.4	4.0
5	−0.3	−0.5	*A*1	0.4	2.6
6	0.3	−0.5	*A*3	15.0	8.0
7	0.1	−0.5	*A*1	0.5	5.3
8	0.2	−0.5	*A*1	0.6	5.0
9	0.4	−0.5	*A*1	0.5	3.5
10	0.5	−0.5	*A*1	0.45	2.0

* The values of the optical-potential parameters are presented in Table 2.

** The normalization factors *k* in the angular distributions of alpha particles from transitions to the ground and the first excited state of the final nucleus are labeled with the subscripts 0 and 1, respectively.

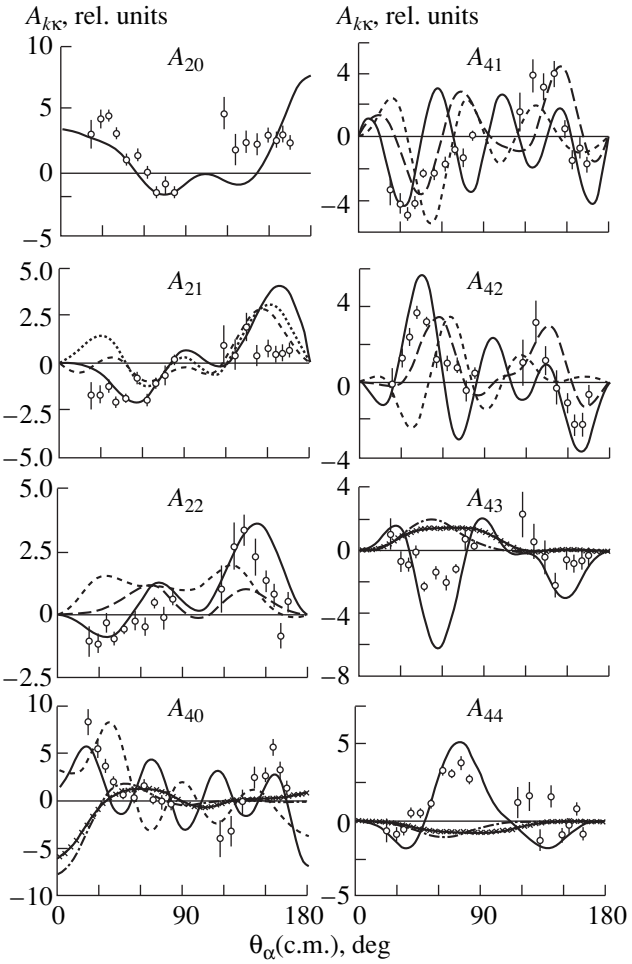

Fig. 2. Reconstructed spin–tensor components $A_{k\kappa}$ of the density matrix for the 2_1^+ state of the ^{12}C nucleus according to data on the reaction ^{15}N(p, $\alpha\gamma$)^{12}C at E_p = 7.5 MeV versus the alpha-particle emission angle θ_α (points). The ordinate scale is chosen in such a way that the component $A_{00} \equiv d\sigma/d\Omega$ is expressed in mb/sr units. The solid curves, the dotted curves, the dash-dotted curves, long dashes, short dashes, and the solid curves with crosses represent the results of the calculations assuming the triton-cluster-pickup mechanism treated on the basis of the CCM with parameter sets no. 1, 2, 3, 4, 5, and 6 from Table 1, respectively.

tion was used to describe elastic alpha-particle scattering on ^{12}C nuclei at E_α = 18.5–25.0 MeV. The standard values of r_V = 1.25 fm and a_V = 0.65 fm were assumed for the parameters of the Woods–Saxon potentials for the bound states, while the depth parameter of the spin–orbit term in the potential was assigned the value of $\hat{\lambda}$ = 25.

In alpha-particle-induced transitions between light nuclei, the use of the optical model for constructing distorted waves is known to lead to results that are very sensitive to the parameters of optical potentials. In view of this, we tried here not only the potential $A1$ but also a few alternative assignments sometimes used for the

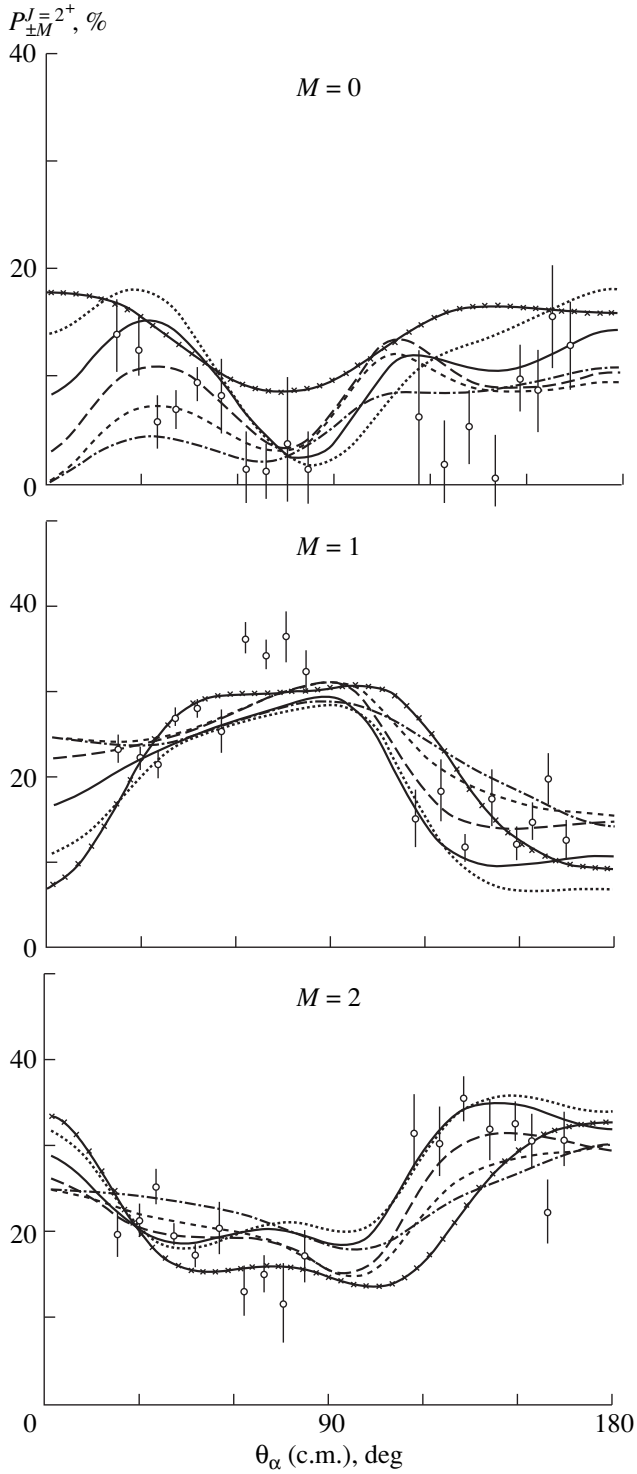

Fig. 3. Reconstructed populations of the magnetic sublevels of the 2_1^+ state of the ^{12}C nucleus in the reaction ^{15}N(p, $\alpha\gamma$)^{12}C versus the alpha-particle emission angle θ_α (points). The solid curves, the dash-dotted curves, short dashes, long dashes, the dotted curves, and the solid curves with crosses represent the results of the CCM calculations with the $\beta_2(^{15}\text{N})$ values from the parameter sets no. 1, 2, 7, 8, 9, and 10 from Table 1, respectively.

optical-potential parameters in the energy range $E_\alpha \approx$ 9–16 MeV (see Table 2). However, we found that the angular dependences of the majority of the spin–tensor components $A_{k\kappa}(\theta_\alpha)$ could not be adequately reproduced with any alternative form of the final-state potential.

The spectroscopic amplitudes computed with the wave functions from [20] are displayed in Table 3. In the CCM calculations, we used the normalization factor of $D_0^2 = 46 \times 10^4$ MeV^2 fm^3 [21]. Additional normalizations of the reaction cross section and of other components $A_{k\kappa}(\theta_\alpha)$ were performed by fitting the computed values of $A_{00}(\theta_\alpha)$ to the measured cross section at small values of the alpha-particle emission angle. The relevant normalization factors for the various sets of the parameters are listed in Table 1. From this table, we can see that the CCM calculations with the potentials *A*1 and *A*2 tend to underestimate the ratio of the cross sections for the formation of the 2_1^+ state of ^{12}C and its ground state. On the contrary, the use of the potential *A*3 results in overestimating the above ratio. As soon as the final-state potential is chosen to be *A*1, the normalization factors prove to be fairly insensitive to varying the parameter of ^{15}N deformation between 0 and 0.4.

From Figs. 1*a* and 1*b*, it can be seen that the CHUCK calculations fail to reproduce the observed angular distributions of alpha particles, especially for transitions to the ground state. This disagreement may be caused by various factors, including that which is associated with a ^{16}O resonance whose manifestations may be traced in the energy dependence of the cross section for ground-state formation (see Fig. 1*c*). However, the shape of the angular distributions, which is peculiar to direct processes, suggests that this is not the only reason behind the above disagreement: a poor description of the angular distributions may be associated with other direct mechanisms, of which the foremost consists in heavy-particle stripping (HPS).

For the HPS mechanism, the angular distributions were calculated by the method of distorted waves as implemented for finite-range interaction and codified in the OLYMP-3 package [22]. The parameters of the optical potentials for the initial and for the final state were taken to be identical to those in the CCM calculations. The parameters of the potentials for bound states are listed in Table 2. The widths with respect to the decays $^{15}\mathrm{N} \longrightarrow {}^{11}\mathrm{B} + \alpha$ and $^{12}\mathrm{C} \longrightarrow {}^{11}\mathrm{B} + p$ were computed by using the SHIRINA package [23], which takes into account the excited states of the ^{11}B nucleus. The wave functions of the nuclei involved were borrowed from [20]. The calculated contributions of the HPS mechanism to the angular distributions of alpha particles are depicted in Fig. 1 without extra normalizations. We can see from this figure that, for the production of the ground state, the inclusion of the HPS contribution improves considerably the agreement between the measured and the calculated angular distributions of alpha

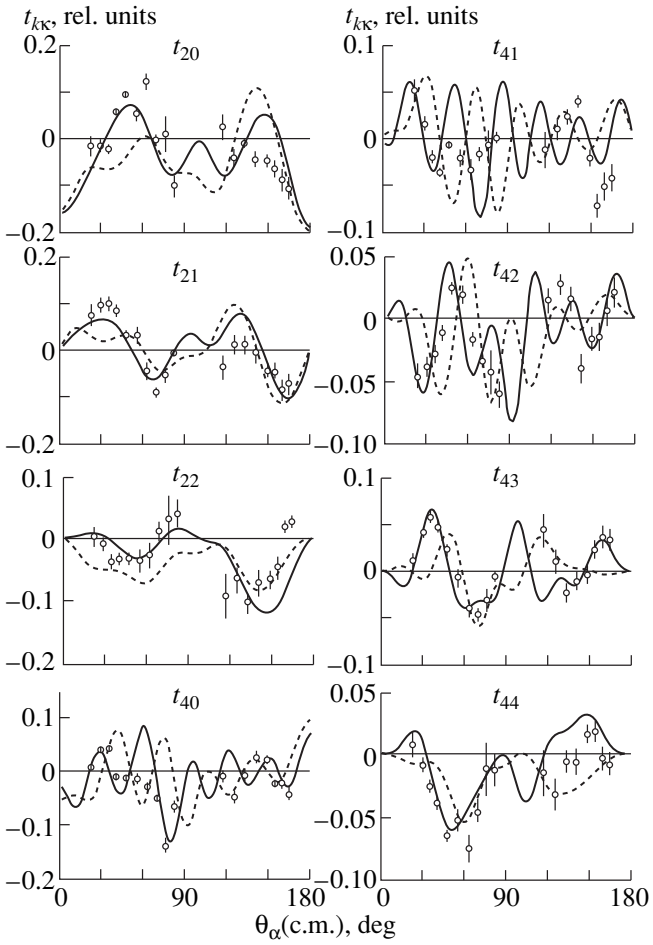

Fig. 4. Reconstructed $k = 2$ and 4 components of the angular-momentum-orientation tensor for the 2^+ state (4.44 MeV) of the ^{12}C nucleus according to data on the reaction $^{15}\mathrm{N}(p, \alpha\gamma)^{12}\mathrm{C}$ at $E_p = 7.5$ MeV versus the alpha-particle emission angle θ_α (points). The solid and dashed curves represent the results of the CCM calculations with the parameter sets no. 1 and 5 from Table 1, respectively.

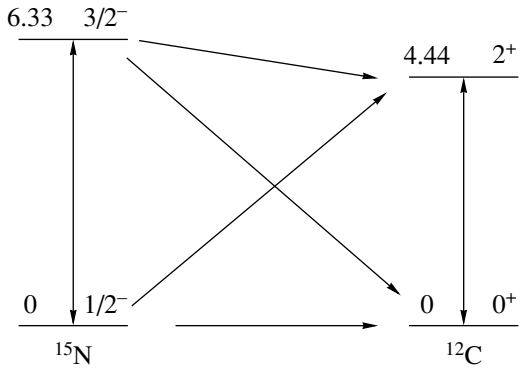

Fig. 5. Scheme of the CCM calculations. Double-sided arrows show the couplings between the nuclear levels involved, while simple arrows correspond to transitions featuring particle transfer. Also quoted in the figure are the excitation energies of the levels (in MeV) and their spin–parities.

Table 2. Values of the optical-potential parameters

Channel	Potential	V, MeV*	r_V, fm	a_V, fm	W, MeV	r_W, fm	a_W, fm	V_{so}, MeV	r_{so}, fm	a_{so}, fm	r_c, fm	References
$^{15}N + p$	$P1$	49.84	1.205	0.605	1.61**	1.03	0.53	5.32	1.205	0.605	1.25	[17]
$^{12}C + \alpha$	$A1$	161.0	0.85	0.770	5.0	1.5	0.6				1.4	[18]
	$A2$	125.0	1.97	0.5	1.5**	1.97	0.5				1.4	[17]
	$A3$	200.0	1.97	0.6	4.0**	1.87	0.3				1.4	[17]
$^{15}N \longrightarrow {}^{11}B + \alpha$		–	1.2	0.5								
$^{12}C(2^+) \longrightarrow {}^{11}B + p$		–	1.6	0.6								
$^{12}C \longrightarrow {}^{11}B + p$		–	1.2	0.5								

* The depths of the potentials for bound states were derived from the corresponding values of the binding energy.

** The surface potential was taken in the Woods–Saxon form.

particles; moreover, this contribution proves to be dominant everywhere with the exception of the region of the smallest angles. For the transition to the first excited state, the HPS contribution is significant only in the region of the largest angles. On this basis, we can conjecture that the HPS mechanism but weakly affects angular correlations in the $\alpha\gamma$ system.

Our estimates for the compound-nucleus-formation mechanism (these results are not presented here) that rely on the CNCOR package [24] indicate that its contribution to the angular distribution for the formation of the ground state is sizable only at small values of the angle θ_α; for the production of the first excited state, however, the compound-nucleus-formation mechanism leads to a nearly isotropic distribution, in a glaring disagreement with experimental data. For the components $A_{k\kappa}(\theta_\alpha)$, this mechanism likewise predicts fairly structureless angular dependences symmetric with respect to 90°, which are at odds with the experimental data. In view of all the above, we can conclude that the reaction $^{15}N(p, \alpha\gamma)^{12}C$ is not strongly affected by the formation of a compound nucleus.

In the ensuing analysis of correlation features, we therefore assume the mechanism of light-particle pickup. In Fig. 2, the reconstructed components $A_{k\kappa}$ as functions of θ_α are compared with model predictions. In this figure and in those that follow, the best fits to the data are depicted by solid curves.

Table 3. Spectroscopic amplitudes A_{lj}

$J_A \longrightarrow J_B$ transition	l	j	A_{lj}
$1/2^- \longrightarrow 0^+$ (g.s.)	1	1/2	–0.334
$1/2^- \longrightarrow 2^+$ (4.44 MeV)	1	3/2	–0.575
	3	5/2	–0.448
$3/2^-$ (6.33 MeV) $\longrightarrow 0^+$ (g.s.)	1	3/2	–0.172
$3/2^-$ (6.33 MeV) $\longrightarrow 2^+$ (4.44 MeV)	1	1/2	0.308
		3/2	–0.244
	3	5/2	0.117
		7/2	–0.189

Since the adopted model involves a comparatively large number of parameters, it is important to check the sensitivity of the predictions to variations in the key model parameters.

The deformations of the initial and final nuclei are considered first. Only the quadrupole deformation was taken into account here, since effects due to higher modes are known to be small [2]. The deformation parameters β_2 for the ^{12}C and ^{15}N nuclei were chosen in such a way as to obtain the best overall fit to the reconstructed components $A_{k\kappa}(\theta_\alpha)$.

The highest sensitivity of the prediction to β_2 variations is observed in the region $\theta_\alpha \le 20°$, where there are no experimental data. Off this angular region, the β_2 dependence proved to be less pronounced; still, the data there permit drawing some conclusions on the deformation parameters. By varying the values of β_2 within the ranges $0.1 < |\beta_2(^{12}C)| < 0.7$ and $0 < |\beta_2(^{15}N)| < 0.5$, we have found that deformations of both the initial and the final nucleus must be taken into account in order to describe the data on the $\alpha\gamma$ correlation. By way of example, we indicate that, irrespective of β_2 (^{12}C) values, the assumption of $\beta_2(^{15}N) = 0$ proves to be incompatible with the reconstructed angular dependences of the components A_{21}, A_{22}, A_{41}, and A_{42} [at the same time, the description of the angular dependences of the differential cross sections is somewhat better here than at nonzero $\beta_2(^{15}N)$]. In the ensuing calculations, we therefore took the conventional value of $\beta_2 = -0.5$ for the ^{12}C nucleus and further adjusted the magnitude and sign of $\beta_2(^{15}N)$.

It turned out that the description of all dynamical quantities under analysis, $A_{k\kappa}(\theta_\alpha)$, $P_{\pm M}(\theta_\alpha)$, and $t_{k\kappa}(\theta_\alpha)$, was considerably improved upon taking into account the deformation of the ^{15}N nucleus. As to the optimum

value of the relevant deformation parameter, it was found to be somewhat different for the different dynamical quantities. The majority of the spin–tensor components $A_{k\kappa}(\theta_\alpha)$ suggest the value of $\beta_2 = 0.3$; the components of the angular-momentum-orientation tensor $t_{k\kappa}(\theta_\alpha)$ are better described at $\beta_2 = 0.3$–0.4; and the populations of the magnetic sublevels, $P_{\pm M}(\theta_\alpha)$, are compatible with $\beta_2 = 0.2$–0.4. Thus, the value of $\beta_2 = 0.3$ provides the best simultaneous fit to all the above quantities. For the populations of the magnetic sublevels, the predictions that assume $\beta_2 = -0.5$ for the ^{12}C nucleus and various values of β_2 for the ^{15}N nucleus are illustrated in Fig. 3.

Negative values of β_2 for the ^{15}N nucleus were also tried in our calculations, but none of these proved to be compatible with the functional forms of the components $A_{k\kappa}(\theta_\alpha)$. For example, the choice of $\beta_2 = -0.3$ effectively results in that the components A_{21}, A_{22}, A_{40}, A_{41}, and A_{42} for θ_α values in the forward hemisphere appear to be in antiphase with the experimental dependences (see Fig. 2), although the corresponding changes in the angular dependence of the differential cross section are not so pronounced (see Fig. 1*b*). Figure 4 shows the $t_{k\kappa}(\theta_\alpha)$ values calculated with the values deformation differing only in sign ($\beta_2 = +3$ and -0.3). It can be seen that the positive value of β_2 provides a better description of the data in this case as well. Thus, the sign of β_2 for the ^{15}N nucleus is reliably fixed by analyzing the correlation features.

Fixing the value of $\beta_2(^{15}\mathrm{N})$ at 0.3 and varying $\beta_2(^{12}\mathrm{C})$, we find that the data favors negative values of the latter parameter in the range $|\beta_2| \cong 0.4$–0.5.

We proceed to probe the uncertainties associated with the choice of optical potentials. The results of the calculations prove to be particularly sensitive to variations in the parameters of the optical potential for the $^{12}\mathrm{C} + \alpha$ final state. Indeed, the use of this potential in the alternative forms *A*2 and *A*3 leads to significant variations in the results for the components A_{40}, A_{43}, and A_{44} (see Fig. 2); moreover, the calculation of the differential cross section with the potential *A*2 shows similar trends (see Fig. 1). Even relatively small (within 10%) variations in the parameters of the final-state optical potential affect the results sizably.

To conclude, we have measured angular correlations in the reaction $^{15}\mathrm{N}(p, \alpha\gamma)^{12}\mathrm{C}(2_1^+)$ at $E_p = 7.5$ MeV. The results of our measurements suggest that this reaction largely proceeds via the pickup of a triton cluster from the target nucleus. The measured correlations are significantly affected by sequential processes associated with a collective origin of the nuclear states involved in the above reaction. As might have been expected, the dynamical characteristics inferred from data on αγ correlations show higher sensitivity to variations in the model parameters than the angular distributions of alpha particles.

That the description of some components $A_{k\kappa}(\theta_\alpha)$ on the basis of the triton-pickup mechanism is not fully consistent with the data suggests possible contributions from subtler mechanisms that may involve retarded interactions. Since the inclusion of such additional mechanisms in the computational scheme requires an involved analysis, we will address this problem in our future investigations.

ACKNOWLEDGMENTS

This work was supported in part by the Russian Foundation for Basic Research (project no. 97-02-16329) and by the foundation Russian Universities: Fundamental Research (grant no. 53-56).

REFERENCES

1. A. V. Ignatenko *et al.*, Yad. Fiz. **57**, 195 (1994) [Phys. At. Nucl. **57**, 181 (1994)].
2. V. M. Lebedev *et al.*, Izv. Ross. Akad. Nauk, Ser. Fiz. **63**, 70 (1999).
3. A. V. Ignatenko *et al.*, Izv. Ross. Akad. Nauk, Ser. Fiz. **63**, 1037 (1999).
4. V. M. Lebedev *et al.*, Yad. Fiz. **62**, 1546 (1999) [Phys. At. Nucl. **62**, 1455 (1999)].
5. V. M. Lebedev *et al.*, Izv. Akad. Nauk, Ser. Fiz. **64** (2000) (in press).
6. F. Ajzenberg-Selove, Nucl. Phys. A **449**, 1 (1986).
7. M. Yasue *et al.*, Nucl. Phys. A **394**, 29 (1983).
8. É. V. Lan'ko *et al.*, *Probabilities of Electromagnetic Transitions in Z = 1–30 Nuclei* (Nauka, Moscow, 1972).
9. I. B. Teplov *et al.*, Prib. Tekh. Éksp., No. 6, 45 (1965).
10. A. V. Ignatenko *et al.*, in *Proceedings of the 49th Conference on Nuclear Spectroscopy and Structure of Atomic Nuclei, St. Petersburg, 1999*, p. 156.
11. A. V. Ignatenko *et al.*, Preprint No. 89-13/90, NIIYaF MGU (Institute of Nuclear Physics, Moscow State University, Moscow, 1989).
12. H. Oeshler *et al.*, Nucl. Phys. A **202**, 518 (1973).
13. I. B. Teplov *et al.*, Zh. Éksp. Teor. Fiz. **48**, 385 (1965) [Sov. Phys. JETP **21**, 253 (1965)]; N. S. Zelenskaya *et al.*, Izv. Akad. Nauk SSSR, Ser. Fiz. **35**, 193 (1971).
14. N. S. Zelenskaya and I. B. Teplov, Fiz. Élem. Chastits At. Yadra **18**, 1283 (1987) [Sov. J. Part. Nucl. **18**, 546 (1987)]; *Properties of Excited Nuclear States and Angular Correlations in Nuclear Reactions* (Énergoatomizdat, Moscow, 1995).
15. P. D. Kunz and J. Cejpek, The Niels Bohr Institute, Computer Program Library, Computer Code CHUCK, 1977.
16. E. Fabrici *et al.*, Phys. Rev. C **21**, 844 (1980); B. J. Harvey *et al.*, Phys. Rev. **146**, 712 (1966).
17. C. M. Perey and F. G. Perey, At. Data Nucl. Data Tables **17**, 1 (1976).
18. N. S. Zelenskaya and I. B. Teplov, *Exchange Processes in Nuclear Reactions* (Mosk. Gos. Univ., Moscow, 1985).

19. A. V. Ignatenko *et al.*, Preprint No. 90-25/171, NIIYaF MGU (Institute of Nuclear Physics, Moscow State University, Moscow, 1990).

20. A. N. Boyarkina, *Structure of 1p-Shell Nuclei* (Mosk. Gos. Univ., Moscow, 1973).

21. C. R. Bingham and M. L. Halbert, Phys. Rev. **158**, 1085 (1967).

22. O. Yu. Balashova *et al.*, in *Brief Description of Software Facilities for the Computers of the Institute of Nuclear Physics of Moscow State University* (Mosk. Gos. Univ., Moscow, 1978), p. 97.

23. N. S. Zelenskaya *et al.*, in *Brief Description of Software Facilities for the Computers of the Institute of Nuclear Physics of Moscow State University* (Mosk. Gos. Univ., Moscow, 1978), p. 47.

24. T. L. Belyaewa *et al.*, Comput. Phys. Commun. **73**, 161 (1992).

Translated by A. Asratyan

Physics of Atomic Nuclei, Vol. 63, No. 9, 2000, pp. 1497–1503. Translated from Yadernaya Fizika, Vol. 63, No. 9, 2000, pp. 1581–1587.

NUCLEI
Experiment

Radiative Strength Functions for Dipole Transitions in $^{57, 59}$Co

S. S. Ratkevich, I. D. Fedorets*, B. A. Nemashkalo[1)], and V. E. Storizhko[2)]

Kharkov State University, pl. Svobody, Kharkov, 310077 Ukraine

Received January 13, 1999; in final form, April 12, 1999

Abstract—Data on the (p, γ) reactions on $^{56, 58}$Fe that were taken at proton energies of E_p = 1.5–3.0 MeV and which were averaged over resonances are used to determine the absolute values of the radiative strength function at energies below 10 MeV. The results obtained in this way are compared with the results of the calculations that rely on the statistical approach and which take into account the temperature of the nucleus and its shell structure. Good agreement with experimental data is achieved without any variation of parameters. © *2000 MAIK "Nauka/Interperiodica".*

1. INTRODUCTION

Experimental and theoretical investigations of the energy dependence of radiative strength functions for nuclei whose shells are filled almost completely or completely revealed that, if the Lorentz distributions that describe well the electric giant dipole resonances excited in such nuclei are extrapolated to the region of low energies, the resulting curve complies with experimental data neither in absolute value nor in shape. For example, an extrapolation of a Lorentzian curve to the region of low energies of gamma rays yields radiative-strength-function values that are eight times as great as the corresponding experimental values obtained in [1] for the ^{59}Co nucleus, which has a nearly filled proton shell (Z = 27). Attempts undertaken in [1] to change the absolute values of the radiative strength function by varying parameters used in determining this function proved to be futile; therefore, its behavior was considered to be anomalous. On the other hand, the same authors [2] obtained data on the radiative strength function for the ^{65}Cu nucleus that were in good agreement with the extrapolation of the corresponding Lorentzian form. A deviation of the radiative strength function from the Lorentzian behavior is at odds with the well-known Brink hypothesis. In accordance with this hypothesis, primary $E1$ transitions that are observed in radiative nucleon capture are associated with the same processes as giant dipole resonances approximated by a Lorentzian form; moreover, giant resonances built on the ground state and on excited states of the final nucleus are described in terms of the same parameters. The above deviations may suggest the nuclear-structure dependence of the radiative strength function.

The objective of the present study is to determine the absolute values of the radiative strength functions for the electric dipole transitions in $^{57, 59}$Co nuclei near the nucleon binding energy and to analyze their energy dependence. We determine here the relevant radiative strength functions from the averaged intensities of primary gamma transitions that proceed to individual low-lying states of the nuclei being investigated and which are excited in the (p, γ) reactions on $^{56, 58}$Fe nuclei at incident-proton energies between 1.5 and 3.0 MeV. The energy Q of the (p, γ_0) reactions on these target nuclei is 6.02 MeV for ^{56}Fe and 7.37 MeV for ^{58}Fe. These values of Q are sufficiently large for the densities of states in compound nuclei to satisfy the requirements that ensure the applicability of the statistical description. The thresholds for the (p, n) reactions on ^{56}Fe and ^{58}Fe nuclei exceed 5 and 3 MeV, respectively. Owing to this, investigations could be performed over a wide range of incident-proton energies below the neutron threshold.

2. EXPERIMENTAL RESULTS AND THEIR ANALYSIS

Following [1], we determined the radiative strength functions in question by the method of averaging over the resonances of a compound nucleus formed upon incident-proton capture by the target nucleus. This averaging, which is necessary for effectively suppressing Porter–Thomas fluctuations [3] and for achieving a satisfactory statistical accuracy, was ensured by an optimal choice of target thicknesses and by a successive addition of gamma-ray spectra measured at different energies with a step equivalent to the target thickness. In taking an average over an interval of width 180 keV for ^{57}Co and an average over an interval of width 220 keV for ^{59}Co, the scatter of data that is associated with Porter–Thomas fluctuations did not exceed the statistical uncertainty of measurements, which was within 20%.

We used targets manufactured by electrolytically precipitating, onto a gold substrate, ^{56}Fe (the degree of enrichment was 99.9%) in order to obtain 849-μg/cm^2-

* e-mail: Ivan.D.Fedorets@univer.kharkov.ua

1) Kharkov Institute for Physics and Technology, Akademicheskaya ul. 1, Kharkov, 310108 Ukraine.

2) Institute for Applied Physics, National Academy of Sciences of Ukraine, Sumy, Ukraine.

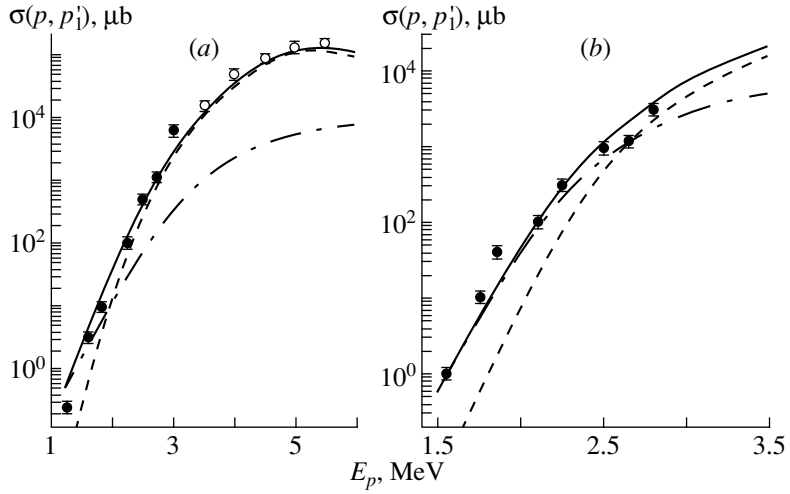

Fig. 1. Cross sections for inelastic proton scattering on (*a*) ^{56}Fe and (*b*) ^{58}Fe target nuclei (experimental points and calculated curves): (closed and open circles) experimental data from [11] and [12], respectively; (dash-dotted and dashed curves) contributions to the calculated cross sections from, respectively, Coulomb and nuclear scattering; and (solid curve) the sum of the Coulomb and nuclear contributions.

and 1.729-mg/cm^2-thick samples or ^{58}Fe (the degree of enrichment was 90.7%) in order to obtain 849-μg/cm^2-thick samples. The measurements were performed by using protons accelerated by an electrostatic accelerator to energies in the range 1.5–3.0 MeV, which was scanned with a variable step equal to proton-energy losses in the target. The spectra of gamma rays corresponding to primary transitions were measured by a pair spectrometer arranged at an angle of 55° to the proton-beam direction. The yields of gamma rays corresponding to direct transitions to the ground states of ^{57}Co and ^{59}Co were also measured with the aid of a NaI(Tl) detector of dimensions 200 × 200 mm^2. The strategy of our experiment and the procedure that we used for specific measurements were described in detail elsewhere [4].

As in [1], radiative strength functions were determined here by using the fact that the radiative-strength function $S_{\lambda f}(E_\gamma)$ for electric dipole transitions can be related to the proton-capture cross section $\sigma(p, \gamma_f)$. With the aid of the Hauser–Feshbach formula, the relation in question can be reduced to the form

$$\bar{\sigma}_{p,\gamma_f} = \frac{\pi\lambda_p^2}{2(2I+1)}\sum_{I_c j_p l_p}(2I_c+1) \times \frac{T_{l_p j_p}\times 2\pi E_\gamma^3 S_{\lambda f}(E_\gamma)}{\sum_{j_{p'} l_{p'}} T_{l_{p'} j_{p'}} + \sum_{j'}\int_0^{E_\lambda} 2\pi\rho_{j'}(E_\lambda - E_\gamma)E_\gamma^3 S_{\lambda f}(E_\gamma)dE_\gamma}, \quad (1)$$

where λ_p is the incident-proton wavelength; I is the spin of the target nucleus; I_c is the spin of the compound nucleus; j_p and l_p are, respectively, the spin and the orbital angular momentum in the input channel; $j_{p'}$ and $l_{p'}$ are the corresponding quantities in the output channel involving proton emission; $S_{\lambda f}(E_\gamma) = S_{\lambda f}^{E1}(E_\gamma) + S_{\lambda f}^{M1}(E_\gamma)$ is the sum of $E1$ and $M1$ radiative strength functions for transitions from the group λ of compound-nucleus states at energy E_λ to the state of energy E_f; $T_{l_p j_p}$ and $T_{l_{p'} j_{p'}}$ are the penetrability factors for protons in the input and the output channel, respectively; and $\rho_{j'}(E_\lambda - E_\gamma)$ is the density of levels characterized by a spin j' and an excitation energy $E = E_\lambda - E_\gamma$. In our calculations, we took into account the correction for cross-section fluctuations of the Ericson type, which arise because of a small number of open channels, since such a correction may prove to be of importance at low energies [5]. It was assumed in [1] that, for $E1$ transitions, the dependence of the radiative strength function on the energy E_γ has the form

$$S_{\lambda f}(E_\gamma) = a\frac{10^{-14}}{2\pi}A^{8/3}E_\gamma^{k-3}\ (\mathrm{MeV}^{-3}), \quad (2)$$

where a and k are parameters, whose values are fixed in fitting expression (2) to experimental data. The value of $k = 4.7$ was obtained in [1] by extrapolating the Lorentzian form that describes the giant dipole resonance in ^{59}Co to the energy region under study. For the case of a direct γ_0 transition to the ground state of the ^{59}Co nucleus, a least squares fit of the theoretical cross section $\sigma(p, \gamma_0)$ to its experimental value yielded $a = 1.5$ [1]. The radiative strength function as determined by using the above values of the parameters a and k reproduces the slope of the Lorentzian curve, but the absolute values of this function differ from that which would be expected on the basis of extrapolation by a factor of 8 [1].

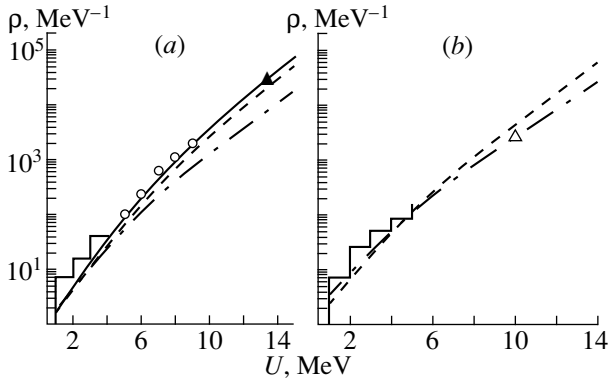

Fig. 2. Level densities in the (*a*) ^{57}Co and (*b*) ^{59}Co nuclei versus excitation energy: (broken lines) discrete levels established in [14, 15], (open circles) experimental data from [17], (closed triangle) experimental result from [18], (open triangle) experimental result from [19], (dash-dotted curve) results of the calculation within the back-shifted Fermi gas model with the parameter values from [20] and the nuclear moment of inertia set to half the rigid-body value, (dashed curve) results of the calculation within the back-shifted Fermi gas model with the parameter values from [20] and the nuclear moment of inertia set to the rigid-body value, and (solid curve) results of the calculation with the parameter values adopted in the present study.

In the present study, the radiative strength function appearing in the denominator on the right-hand side of (1) was parametrized either in a Lorentzian form or in that form which was obtained in the approach developed in [6, 7] on the basis of Fermi liquid theory. The quantity $S_{\lambda f}(E_\gamma)$ in the numerator was chosen in such a way as to reproduce the absolute values of the partial cross section that were obtained experimentally. The penetrability factors for protons were calculated with allowance for the results reported in [8–10]. The parameters of the optical potential were determined from the best fit to the experimental cross section for the reactions ^{56,58}Fe(p, $p'\gamma$) (Fig. 1), ^{56,58}Fe(p, γ), and ^{58}Fe(p, n) in the region of incident-proton energies below 4 MeV. The experimental cross-section values presented in Fig. 1 were borrowed from [11, 12] for inelastic proton scattering on ^{56}Fe nuclei and from [13] for inelastic proton scattering on ^{58}Fe nuclei. For the geometric parameters of the real part of the optical potential, we chose the values

$$r_r = 1.17 \text{ fm}, \quad r_s = 1.32 \text{ fm},$$

$$a_r = 0.70 \text{ fm}, \quad a_s = 0.58 \text{ fm}.$$

With the exception of the diffuseness parameter set to a value less than that in [8], all the above values are identical to those from that study. For the real part of the potential, we took the values

$$V_r(E) = 59.34 - 0.37E \text{ for } ^{56}\text{Fe},$$

$$V_r(E) = 58.0 - 0.32E \text{ for } ^{58}\text{Fe};$$

for the imaginary part of the surface potential, we set

$$W_s(E) = 3.85 + 0.72E \text{ for } ^{56}\text{Fe},$$

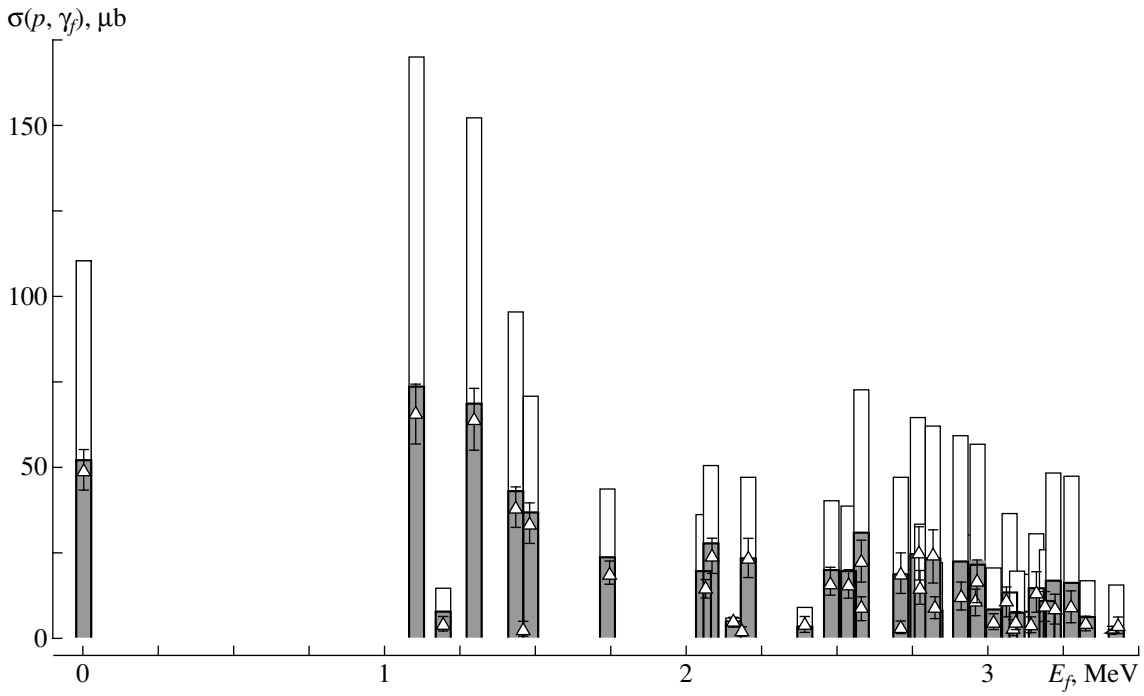

Fig. 3. (p, γ_f) partial cross sections for ^{58}Fe targets: (shaded areas of the histogram) cross sections calculated with the radiative strength functions as obtained within the statistical approach [6, 7] allowing for shell effects and for the nuclear temperature, (unshaded sections of the histogram) cross sections calculated with the radiative strength functions in a Lorentzian form, and (open triangles) experimental cross sections.

Table 1. (p, γ_f) partial cross sections for ^{56}Fe targets

E_f, MeV	J^π	σ^{expt}, μb, E_p = 2.84 MeV, ΔE_p = 180 keV	σ_1^{calc}, μb	σ_2^{calc}, μb	σ_3^{calc}, μb
0.0	$7/2^-$	23.0 ± 4.4	37.53	19.57	26.55
1.224	$9/2^-$	5.6 ± 1.5	3.44	2.96	4.50
1.378	$3/2^-$	24.9 ± 4.7	50.63	14.74	23.15
1.505	$1/2^-$	16.4 ± 6.3	33.42	8.97	13.58
1.690	$11/2^-$	1.1 ± 0.5	1.56	0.93	1.21
1.758	$3/2^-$	18.5 ± 4.2	40.15	11.16	16.00
1.897	$7/2^-$	7.2 ± 1.8	12.86	5.22	6.55
1.920	$5/2^-$	11.3 ± 3.1	19.49	6.77	8.79
2.133	$5/2^{-}$*	14.4 ± 4.4	38.32	8.43	13.36
2.311	$7/2^-$				
2.479	$3/2^{-}$*	4.9 ± 2.0	18.02	5.52	5.85
2.485	$9/2^-$				
2.514	$7/2^-$	3.0 ± 1.5	19.02	4.15	4.51
2.523	$13/2^-$				
2.560	$9/2^-$				
2.611	$7/2^-$	3.3 ± 1.6	24.54	6.69	7.31
2.615	$9/2^{-}$*				
2.723	$9/2^{-}$*	12.0 ± 4.1	30.10	7.13	9.89
2.731	$3/2^-$				
2.743	$11/2^-$				
2.804	$5/2^-$	9.2 ± 3.5	30.20	8.41	8.65
2.879	$3/2^-$				
2.981	$1/2^+$	8.0 ± 3.0	22.36	5.05	8.63
2.982	$5/2^{-}$*				

Note: The superscripts "expt" and "calc" label, respectively, the experimental and calculated cross-section values; the subscripts "1", "2", and "3" on the latter label the theoretical values corresponding, respectively, to the radiative strength functions in a Lorentzian form, to the radiative strength functions calculated with allowance for only the nuclear temperature, and to the radiative strength functions calculated with allowance for nuclear temperature and shell effects. Asterisks indicate spin–parity assignments chosen in the present study.

$$W_s(E) = 5.6 - 0.25E \quad \text{for} \quad {}^{58}\text{Fe}.$$

In these expressions and in those that precede them, all values are given in MeV.

The parameters of the real part of the optical potential differ only slightly from the global parameter set that is presented in [8] and which was derived on the basis of data on the scattering of protons with energies in excess of 9 MeV; however, the parameters of the imaginary part of the same potential differ from those in the global set more pronouncedly. At the same time, our parameters comply well with the results reported in [10], where an optical-model version that takes into account the dispersion relation between the imaginary and the real part of the potential underlies the description of proton scattering on ^{56}Fe target nuclei at incident-proton energies between 4.08 and 7.74 MeV.

The level densities in the ^{57}Co and ^{59}Co nuclei were calculated on the basis of the back-shifted Fermi gas model, with the parameters being set to a = 6.4 MeV^{-1} and Δ = –0.02 MeV for the former and to a = 5.5 MeV^{-1} and Δ = –0.77 MeV for the latter. In these calculations, we used the rigid-body value for the ^{57}Co moment of inertia and half of it for the ^{59}Co moment of inertia. These parameter sets ensure the best agreement of the computed values of the level densities (see Fig. 2) with data from [14, 15] on the discrete section of the energy-level diagram for the nuclei being investigated and with data obtained from an analysis of the experimental spectra of neutrons from (p, n) reactions in the proton-

Table 2. (p, γ_f) partial cross sections for ^{58}Fe targets

E_f, MeV	J^π	σ^{expt}, μb E_p = 2.8 MeV, ΔE_p = 220 keV	σ_1^{calc}, μb	σ_2^{calc}, μb	σ_3^{calc}, μb
0.0	$7/2^-$	49.0 ± 3.9	110.80	51.38	52.15
1.099	$3/2^-$	68.6 ± 6.4	170.62	57.71	74.10
1.190	$9/2^-$	8.5 ± 5.0	17.72	6.96	7.72
1.292	$3/2^-$	64.3 ± 9.7	153.47	51.65	68.93
1.434	$1/2^-$	65.8 ± 15	172.14	61.78	68.74
1.460	$11/2^-$				
1.482	$5/2^-$				
1.745	$7/2^-$	19.5 ± 4.3	43.93	16.33	23.73
2.062	$7/2^-$	29.5 ± 8.3	87.56	32.41	46.41
2.087	$5/2^-$				
2.154	$9/2^-$	9.5 ± 2.3	12.17	6.42	8.03
2.184	$11/2^-$				
2.205	$5/2^-$	23.7 ± 7.4	47.52	17.05	24.78
2.395	$9/2^-$	4.4 ± 2.0	9.44	3.68	4.48
2.479	$5/2^-$	19.3 ± 4.4	40.50	14.48	20.32
2.540	$5/2^-$	68.1 ± 17	123.86	46.65	64.52
2.582	$3/2^-$				
2.586	$7/2^-$				
2.713	$1/2^+$	99.9 ± 25	148.38	58.73	89.18
2.722	$9/2^-$				
2.770	$3/2^-$				
2.782	$5/2^-$				
2.817	$3/2^-$	32.9 ± 8.7	86.43	24.47	35.45
2.826	$7/2^-$				
2.912	$3/2^-$	30.6 ± 17	147.37	42.74	54.93
2.958	$5/2^-$				
2.966	$3/2^-$				
3.015	$7/2^-$	4.7 ± 2.2	20.35	7.33	9.09
3.063	$1/2^-$	16.7 ± 6.4	30.33	19.78	21.47
3.082	$9/2^-$				
3.09	$7/2^-$				
3.141	$7/2^-$	4.2 ± 1.8	19.36	6.72	8.06
3.160	$3/2^+$	23.4 ± 12	56.89	21.90	25.50
3.194	$5/2^-$				
3.220	$3/2^-$	38.4 ± 8.6	96.21	32.46	43.27
3.276	$3/2^-$				
3.323	$7/2^-$	4.8 ± 1.4	17.16	5.94	6.80

energy range E_p = 6–10 MeV [16, 17], as well as with data deduced from an analysis of Ericson fluctuations at U = 14 MeV for ^{57}Co [18].

The scheme used here to compute radiative strength functions [6] takes into account the dependence of the spread width of the giant dipole resonance on the energy E_γ, the effect of the nuclear temperature, and the role of shell corrections and of the Pauli exclusion principle. Within this approach, the $E1$ strength function for

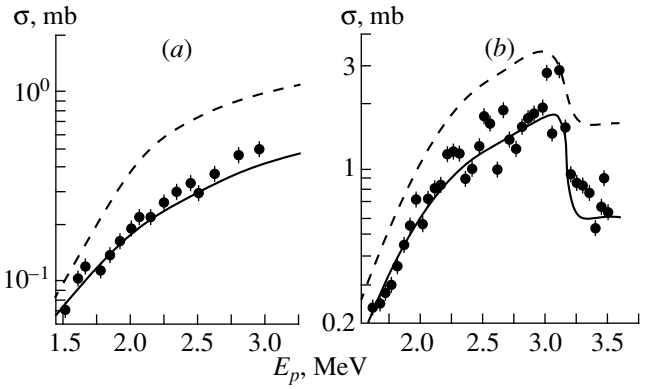

Fig. 4. Total cross sections for the (p, γ) reactions on (*a*) ^{56}Fe and (*b*) ^{58}Fe target nuclei: (closed circles in Fig. 4*a*) experimental cross-section values derived from the estimates of the results presented in [11, 12], (closed circles in Fig. 4*b*) experimental cross-section values from [13], (dashed curves) cross sections computed with the radiative strength functions in a Lorentzian form, and (solid curves) cross sections computed with the radiative strength functions as obtained within the statistical approach developed in [6, 7].

the case of a double-peaked giant dipole resonance can be represented in the form

$$S_\gamma^{E1} = 8.67 \times 10^{-8} \times 2\pi[1 + \exp(-E_\gamma/T)]^{-1} \times \sum_{i=1}^{2} \frac{\sigma_i E_i^2 \Gamma_{R(i)}(E_\gamma)}{(E_\gamma^2 - E_i^2)^2 + E_i \Gamma_{R(i)}(E_\gamma)}, \quad (3)$$

where

$$\Gamma_{R(i)}(E_\gamma) = \Gamma_i \rho_{2p-2h}(E_\gamma, T)/\rho_{2p-2h}(E_i, T).$$

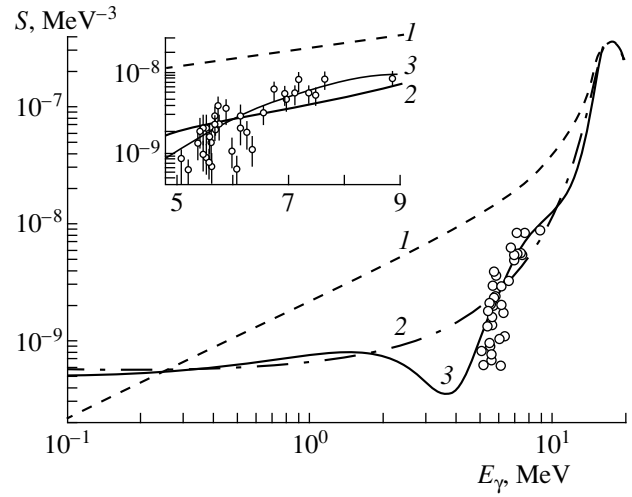

Fig. 5. Experimental and theoretical values of the radiative strength functions for primary gamma transitions in ^{57}Co: (open circles) radiative-strength-function values at E_p = 2.84 MeV, (curve *1*) Lorentzian dependence, (curve *2*) results of the calculations within the statistical approach with allowance for only nuclear temperature, and (curve *3*) results of the calculations within the statistical approach with allowance for the nuclear temperature and shell effects.

In these expressions, σ_i, E_i, and Γ_i are, respectively, the cross sections at the maxima, the positions of the components of the giant dipole resonance, and their widths. The values of these parameters are chosen in such a way as to ensure the best fit of the resulting Lorentzian shape to experimental data that Alvarez *et al.* [21] present for the (γ, n) reaction on ^{59}Co. In calculating the level density $\rho_{2p-2h}(E_\gamma, T)$, we took into account the shell structure of the spectrum of single-particle levels and the effect of the nuclear temperature on the occupation numbers for these nuclei.

In order to calculate the *M*1 strength function, we made use of the relation [7]

$$S_\gamma^{E1}/S_\gamma^{M1} = 0.03A(E_\gamma^2 + (\pi T)^2)/B_n^2, \quad (4)$$

where B_n is the neutron binding energy.

Tables 1 and 2 display the measured values of (p, γ_f) partial cross sections for ^{56}Fe and ^{58}Fe target nuclei and the values calculated for these cross sections by formula (1) with various radiative strength functions. In order to visualize these results more clearly, the experimental and the calculated values of the (p, γ_f) partial cross sections for direct gamma transitions to ^{59}Co states are shown in Fig. 3 as a histogram. The shaded areas of the histogram correspond to the cross sections computed with the radiative strength functions found within the statistical approach [6, 7] with allowance for the shell structure and nuclear temperature, while the unshaded areas represent cross sections evaluated with the radiative strength functions having a Lorentzian form. In Fig. 4, the theoretical values of the total cross sections for the (p, γ) reactions on ^{56}Fe and ^{58}Fe nuclei are contrasted against relevant experimental data.

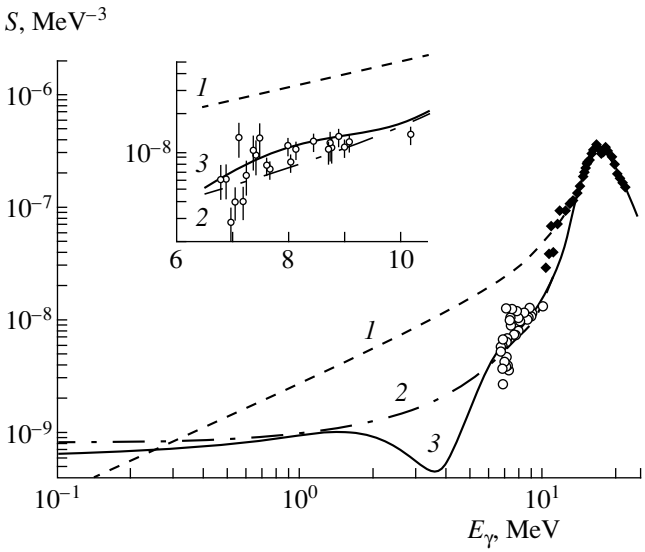

Fig. 6. As in Fig. 5, but for ^{59}Co. Open circles represent the radiative-strength-function values at E_p = 2.82 MeV. Closed diamonds illustrate data from [21]. The notation for the curves is identical to that in Fig. 5.

The radiative-strength-function values obtained in the present study from an analysis of the (p, γ) reactions on ^{56}Fe and ^{58}Fe nuclei are displayed in Figs. 5 and 6. The curves in these figures represent theoretical estimates of the radiative strength function that correspond to a Lorentzian form (curve *1*), to the results of the calculations that are based on expression (3) and which allow for only temperature (curve *2*), and to the results of analogous calculations including both temperature and shell effects (curve *3*). The contribution of $M1$ transitions, which is not shown in the figures, does not exceed 15% for various states of ^{57}Co and ^{59}Co. That the known values of the giant-dipole-resonance parameters for ^{59}Co were used throughout for want of experimental data on the giant dipole resonance in ^{57}Co obviously had an adverse effect on the degree of agreement between the results of our calculations and the experimental values of the radiative strength functions for ^{57}Co.

3. CONCLUSION

Our results indicate that, in the gamma-transition-energy range under study, the absolute values of the radiative strength functions for ^{57}Co and ^{59}Co fall significantly short of values on the Lorentzian curves that describe the corresponding giant dipole resonances. At the same time, the radiative strength functions as calculated within the approach developed in [6, 7]—this approach relies on Fermi liquid theory and takes into account nuclear temperature and shell effects—agree with experimental data without the use of adjustable parameters. This is at odds with the Brink hypothesis, according to which the radiative strength function for dipole transitions must not depend on the properties of the final nuclear state.

REFERENCES

1. K. Nilson, B. Erlandsson, and A. Marcinkowski, Nucl. Phys. A **391**, 61 (1982).
2. B. Erlandsson, K. Nilson, and A. Marcinkowski, Z. Phys. A **293**, 43 (1979).
3. C. E. Porter and R. G. Thomas, Phys. Rev. **104**, 483 (1956).
4. B. A. Nemashkalo, V. E. Storizhko, and K. V. Shebeko, Yad. Fiz. **36**, 1083 (1982) [Sov. J. Nucl. Phys. **36**, 633 (1982)].
5. J. W. Tepel *et al.*, Phys. Lett. B **49**, 1 (1974).
6. V. K. Sirotkin, Yad. Fiz. **43**, 570 (1986) [Sov. J. Nucl. Phys. **43**, 362 (1986)].
7. V. K. Sirotkin and D. F. Zaretskiĭ, Izv. Akad. Nauk SSSR, Ser. Fiz. **52**, 984 (1988).
8. F. D. Becchetti and G. W. Greenlees, Phys. Rev. **182**, 1190 (1969).
9. S. Kailas and M. K. Mehta, in *Proceedings of the 2nd Indo–US Symposium on Nucl. Phys. Cyclotron and Intermediate Energy, Bombay, 1982*, Vol. 1, p. 505.
10. N. Boukhorouba *et al.*, Phys. Rev. C **46**, 2375 (1992).
11. G. A. Krivonosov *et al.*, Yad. Fiz. **24**, 40 (1976) [Sov. J. Nucl. Phys. **24**, 239 (1976)].
12. D. B. Nichols, R. G. Arns, H. J. Hausman, *et al.*, Phys. Rev. **183**, 945 (1969).
13. S. G. Times *et al.*, Nucl. Phys. A **563**, 473 (1993).
14. M. R. Bhat, Nucl. Data Sheets **67**, 195 (1992).
15. C. M. Baglin, Nucl. Data Sheets **69**, 733 (1993).
16. V. Mishra *et al.*, Phys. Rev. C **49**, 750 (1994).
17. M. I. Svirin and G. N. Smirenkin, Yad. Fiz. **48**, 682 (1988) [Sov. J. Nucl. Phys. **48**, 437 (1988)].
18. T. Ericson *et al.*, Annu. Rev. Nucl. Sci. **16**, 183 (1966).
19. M. Kicinska-Habior *et al.*, Phys. Rev. C **36**, 612 (1987).
20. W. Dilg *et al.*, Nucl. Phys. A **217**, 269 (1973).
21. R. A. Álvarez *et al.*, Phys. Rev. C **20**, 128 (1979).

Translated by A. Isaakyan

Physics of Atomic Nuclei, Vol. 63, No. 9, 2000, pp. 1504–1510. Translated from Yadernaya Fizika, Vol. 63, No. 9, 2000, pp. 1588–1595.

NUCLEI
Experiment

Measurement of Cross Sections for the Reactions ^{241}Am(n, 2n) and ^{241}Am(n, 3n)

A. A. Filatenkov and S. V. Chuvaev

Research and Production Association Khlopin Radium Institute, St. Petersburg, 194021 Russia

Received February 24, 1999; in final form, September 20, 1999

Abstract—The cross sections for the reactions ^{241}Am(n, 2n)^{240}Am and ^{241}Am(n, 3n)^{239}Am are measured for several neutron-energy values in the range 13.42–14.86 MeV. An upper limit on the cross section for the reaction ^{241}Am(n, α)^{238}Np is also obtained. © *2000 MAIK "Nauka/Interperiodica".*

1. INTRODUCTION

Conversion and utilization of long-lived radioactive products of the nuclear industry are among the most important problems being solved presently in this realm. Here, problems associated with the transmutation of actinide elements are worthy of special note. Difficulties are numerous in dealing with these nuclear species, partly because experimental data on the cross sections for nuclear reactions proceeding on them are scanty or often nonexistent. The smallest amount of information has been obtained for the relevant (n, 2n), (n, 3n), (n, p), and (n, α) reactions, which are extremely difficult from the experimental point of view. Since reliable and maximally comprehensive information about the cross sections for reactions induced in radioactive nuclei would contribute substantially to developing efficient technologies for the transmutation of nuclear wastes and to reducing the costs of such technologies, it is desirable to extend investigations in these realms.

This article reports on the first ever experiment devoted to measuring the cross sections for the reactions ^{241}Am(n, 2n)^{240}Am and ^{241}Am(n, 3n)^{239}Am, which has been recently performed at the Khlopin Radium Institute (St. Petersburg, Russia). Additionally, the experiment has enabled us to set an upper limit on the cross section for the reaction ^{241}Am(n, α)^{238}Np. In passing, the experiment has also determined cumulative yields of more than 20 fragments of ^{241}Am fission, but these data will be published elsewhere.

2. EXPERIMENTAL PROCEDURE

The experiment was performed at the NG-400 neutron generator that is installed at the Khlopin Radium Institute and which produces quasimonochromatic neutrons via (d, T) reactions. Containers with irradiated samples were arranged at various angles with respect to a solid Ti–T target, whereby it became possible to cover the neutron-energy range between 13.42 and 14.86 MeV. Induced gamma activity was measured with Ge(Li) and HPGe detectors equipped with metal screens, which significantly attenuated intense gamma radiation from the products of the natural radioactive ^{241}Am decay. The gamma-ray spectra were measured continuously for a few days after the exposure; this enabled us to identify reliably γ peaks in the spectrum by additionally using data on the half-lives of reaction products.

The measurements consisted of a few individual runs, where we used various container designs, various geometric arrangements of exposures, various detectors and γ-radiation absorbers, and various procedures for determining the sample masses. In view of this, the results from individual experimental runs could be considered to be independent to a great extent. Table 1 quotes the experimental parameters of the measurements.

Below, the individual steps of the experiment are considered in more detail.

2.1. Exposures

A total of six exposures of nine freshly prepared americium samples were performed, the samples being arranged at different angles with respect to the accelerator beam at distances of 1.5 to 3.6 cm from the target. The exposure duration was varied from 1 to 17.5 h, with the samples accumulating neutron fluences in the range $(0.4–10.7) \times 10^{13}$ neutron/cm^2.

The total neutron fluence received by the sample was determined with two niobium foils fixed at the front and back surfaces of the container with americium. The cross section for the reaction ^{93}Nb(n, 2n)^{92m}Nb was used as a reference; precision data on this cross section were obtained earlier [1]. In the course of irradiation, the neutron-flux variations were measured by two independent scintillation detectors; of these, one oscillated about the target between –120° and +160° along the arc of radius 1 m, while the other was rigidly fixed at an angle of 15° at a distance of 2.1 m

1063-7788/00/6309-1504$20.00

Table 1. Basic features of the experiment

Number of sample	Sample type	Sample mass, mg	Number of exposure	Exposure time, h	Neutron energy, MeV	Fluence $\times 10^{13}$, neutron/cm^2	Detector of gamma radiation	Absorber
1	Solution	2.58	I	12.7	14.69	1.63	Ge(Li)	Pb
2	Solution	2.58	I	12.7	14.21	1.36	Ge(Li)	Pb
3	Solution	2.59	I	12.7	13.56	1.06	Ge(Li)	Pb
4	Solution	0.54	II	17.0	14.84	2.98	Ge(Li)	Cd
5	Solution	0.61	II	17.0	14.09	3.27	Ge(Li)	Cd
6	Solution	1.13	II	17.0	13.48	0.55	Ge(Li)	Cd
7	Solution	2.01	III	17.5	14.73	10.7	Ge(Li)	Cd
8	Salt	3.10	IV	1.02	13.42	0.55	HPGe	Cd
8	Salt	3.10	V	15.02	14.84	6.48	HPGe	Cd
9	Salt	1.62	VI	3.13	14.86	0.44	HPGe	Cd

from the target. Electronic modules servicing the detectors were coupled, through CAMAC controllers, to a PC that accumulated information about the properties of the neutron flux that were measured in the course of irradiation.

The spectral distribution of neutrons that interacted with the sample nuclei was calculated on the basis of a code that took into account actual experimental conditions, such as the sample diameter and thickness, its position with respect to the neutron-producing target, deuteron-beam diameter and position at the target, total thickness of the tritium-containing layer and the tritium distribution in it, and variations in the angular and energy parameters of the deuteron beam during its moderation [1]. Figure 1 shows the integrated spectral properties of neutrons in the samples as calculated by this method for each exposure.

The mean relative values of the neutron fluences received by the sample and by the niobium foils were calculated by the same procedure allowing for the details of actual geometry. In order to go over to the absolute values, the geometric mean of the fluences calculated for two reference niobium foils was normalized to the corresponding value measured experimentally.

2.2. Samples

The samples were prepared from an aqueous solution or from americium nitrate. Since the samples had sizable activities (about 10^8 Bq), they were packed thoroughly into containers that ensured their repeated and reliable sealing. The design of the containers provided for their subsequent disassembly in order that their expensive material could be used again after a radiochemical purification of irradiated americium.

The dimensions of the volume filled with the solution or americium nitrate varied between 8 and 16 mm in diameter and between 1 and 3.5 mm in height. Two niobium foils of diameter 14 mm and thickness 0.1 mm, used to determine the neutron fluence, were fastened to the front and to the back surface of the inner container.

The samples were of high purity. According to the certificate, the total concentration of alien fissile elements in the samples did not exceed 0.1%. However,

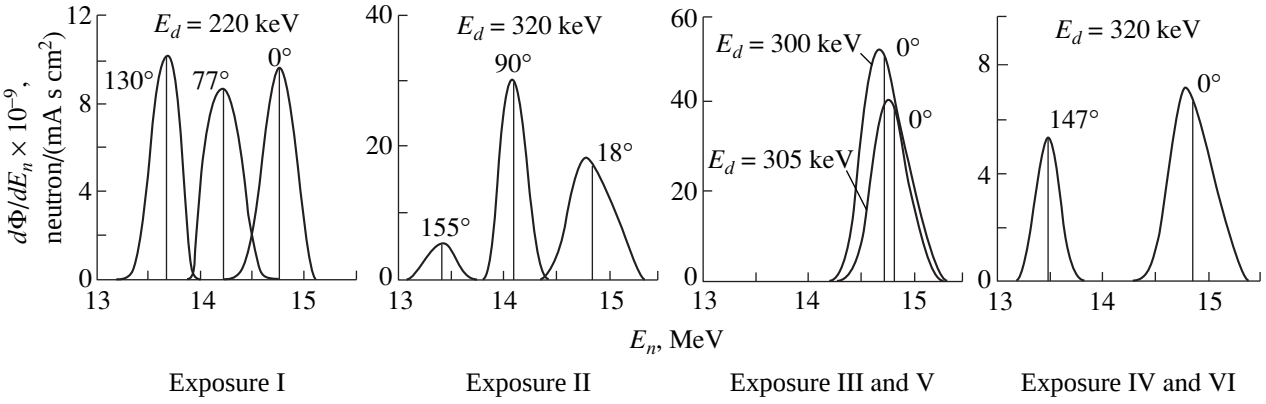

Fig. 1. Calculated energy distributions of neutrons within the irradiated samples for the actual geometric arrangement.

Table 2. Properties of gamma radiation from the products of the (n, 2n), (n, 3n), and (n, α) reactions on ^{241}Am nuclei

Reaction	Reaction product	$T_{1/2}$, h	Decay product	E_γ, keV	Y_γ, %
^{241}Am(n, 2n)	^{240}Am	50.8(3)	^{240}Pu	888.80(5)	25.1(4)
				987.76(6)	73.2(10)
^{241}Am(n, 3n)	^{239}Am	11.9(1)	^{239}Pu	226.378(8)	3.30(20)
				228.183(1)	11.3(6)
				277.599(1)	15.0(7)
^{241}Am(n, α)	^{238}Np	50.81(5)	^{238}Pu	984.45(2)	27.8
				1025.87(2)	9.6(5)
				1028.54(2)	20.3(8)

the requirements on the isotopic purity of the samples were much more severe in this experiment. Especially severe requirements were imposed on the possible admixtures of other americium isotopes, ^{242m}Am and ^{243}Am, because the products of their spontaneous fission emit photons of the same energy as the products of the reactions ^{241}Am(n, 3n)^{239}Am and ^{241}Am(n, α)^{238}Np. The upper limit on the possible admixture of other americium isotopes is determined by the conditions prevalent in a given experiment of the type being discussed (primarily, neutron flux, exposure time, and duration of photon counting), and it was required that this limit not exceed 10^{-7} g/g. In order to verify whether the samples satisfy these requirements, we performed long-term measurements of the gamma-ray spectra of the samples prior to exposures. In processing the spectra, we did not reveal any traces of americium isotopes other than the main isotope ^{241}Am. An upper limit on the possible content of ^{242m}Am and ^{243}Am in the samples used was estimated to be below 10^{-8} g/g.

2.3. Measurement of Gamma-Ray Spectra

As was mentioned above, the samples originally had an activity on the order of 10^8 Bq, about half of the decays of the initial nuclei being accompanied by the emission of 59.5-keV photons and photons of lower energies. It was necessary to suppress this intense gamma radiation in order to provide favorable conditions for measuring rather weak gamma radiation from the reaction products in the energy range 226–1029 keV, its activity being approximately between 1 and 100 Bq. Basic features of this gamma radiation that were borrowed from [2–4] are quoted in Table 2.

In measuring the pursued gamma-ray spectra, various absorbers were used to suppress soft intrinsic gamma radiation from ^{241}Am. After the first exposure, the samples were placed into a lead container that had walls 5 mm thick and which completely absorbed basic gamma radiation from ^{241}Am with energies below 60 keV. Concurrently, 987.8-keV gamma rays emitted by ^{240}Am nuclei from the relevant (n, 2n) reaction suffered a 34% attenuation.

In order to determine the absolute efficiency of photon detection in the above nonstandard geometric arrangement, an irradiated niobium foil containing the ^{92m}Nb isomer whose activity was measured separately was placed at the geometric center of the americium sample in the aforementioned lead container. Since photons emitted in ^{92m}Nb decay are of energy 934.2 keV, which is close to the energy of 987.8 keV corresponding to ^{240}Am decay, only minor corrections for nonidentity of the americium and niobium samples were needed. Under such conditions, the absorption of 934.2-keV photons (Nb) by the container bottom differed from that of 987.8-keV photons (Am) by 1.8%; the difference of the recording efficiency without container due to the energy difference was –5.3%; and the difference of the recording efficiency due to variations in the shape of the samples and their photon self-absorptions was –0.6%. In total, the difference in efficiencies of recording the 934.2- and the 987.8-keV photons (Nb and Am, respectively) was –4.0%.

In subsequent measurements, a set of disk plates from metal cadmium was used as absorbers, whereby a sharper variation in gamma-radiation absorption was ensured in the energy range between 60 and 200 keV with the result that there arose more favorable conditions for determining the cross section for the reaction ^{241}Am(n, 3n)^{239}Am, where it was necessary to measure the induced activity of the samples emitting 227- and 277-keV photons. Figure 2 illustrates the typical geometry of such measurements.

Under the above conditions, the gamma-radiation attenuation as a function of the absorber thickness was measured with a set of three standard gamma-ray sources from ^{241}Am, ^{152}Eu, and ^{109}Cd that were placed at the position of the container shown in Fig. 2. The attenuation values obtained experimentally for gamma radiation of various energies were compared with the results of the calculations relying on the tabular attenuation-factor values from [5]. It can be seen from Fig. 3 that, over the entire range of the energies considered here, the actual absorption is consistent with the attenuation factor determined according to the relation $C = e^{-\mu d}$. A rise in the experimentally measured absorption at energies below 200 keV, which were not used in deter-

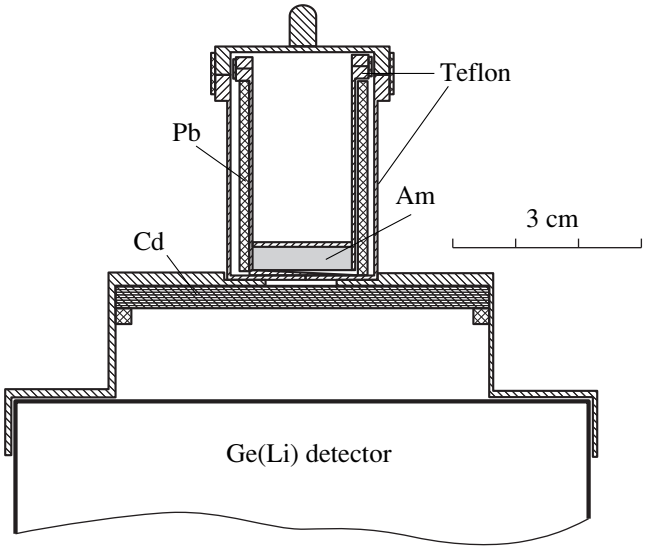

Fig. 2. Geometry of measurements of gamma-ray spectra.

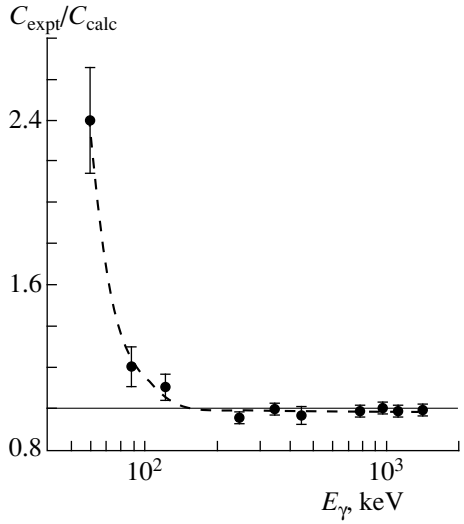

Fig. 3. Ratio of the measured and the calculated photon absorption as a function of energy. The cadmium absorber is 3.5 mm thick.

mining the cross sections, seems to be due to an increase in the contribution of inclined photon tracks, which were ignored in the above attenuation law.

That gamma-radiation absorption in the geometric arrangement illustrated in Fig. 2 was estimated correctly was additionally confirmed by the results obtained by measuring gamma-ray spectra of unirradiated ^{241}Am, which feature a few γ lines associated with spontaneous radioactive decay of ^{241}Am and characterized by energies above 100 keV and yields on the order of 10^{-6} per decay event [6]. These data are also shown in Fig. 3.

In measuring the gamma-ray spectra of americium-containing samples, the cadmium-absorber thickness was chosen to be 3.5 mm, which ensured a more than 10^8 attenuation of 59.5-keV gamma radiation without noticeable absorption of 228- to 988-keV photons, for which the attenuation changed by a factor of 1.89 to 1.18.

The gamma-ray spectra of the irradiated samples were measured repeatedly for 3 to 5 days. The spectra were then processes with the aid of the SAMPO code [7]. For each spectrum, we determined approximately 200 γ peaks. The majority of these were associated with gamma radiation from the fission fragments, but a small number of the peaks belonged to the spectra of the products originating from the relevant (n, 2n) and (n, 3n) reactions. In order to render the identification of the γ peaks more reliable, the decay curves were plotted for each of them. Even in the intricate cases where gamma radiations from different sources overlapped, this enabled us to determine correctly the intensity of the components having expected half-lives.

2.4. Determination of Sample Masses

Three methods were used to determine the number of ^{241}Am nuclei in the sample: (i) measurement of the absolute α activity of a representative portion of the corresponding sample; (ii) measurement of the intensity of the basic 59.5-keV gamma-radiation line with a yield of 0.395 per decay event for an irradiated ^{241}Am sample with respect to the same line of the standard ^{241}Am γ source from the OSGI set; (iii) measurement of the absolute intensities of other γ lines occurring at energies above 100 keV and accompanying the alpha-decay of ^{241}Am. These lines, characterized by very low yields, about 10^{-6} per decay event, were nevertheless dominant in the gamma-ray spectra measured with an absorber. The properties of the corresponding γ lines were taken from the compilation presented in [6]. Their energies and yields are the following: 146.55 keV and 4.61×10^{-6}, 169.56 keV and 1.73×10^{-6}, 322.52 keV and 1.52×10^{-6}, 376.65 keV and 1.38×10^{-6}, 662.40 keV and 3.64×10^{-6}, and 722.01 keV and 1.96×10^{-6}. The last method appeared to produce the most precise results. Eventually, the mass of a given sample was determined as a weighted mean of individual measurements.

2.5. Calculation of the Cross Sections

The reaction cross sections σ_{AB} were calculated by the well-known formula

$$\sigma_{AB} = \frac{N_{B0}}{N_A \Phi_n}. \quad (1)$$

We determined the number of nuclei of the reaction product, N_{B0}, using the induced activity of the sample and taking into consideration the decay of the product

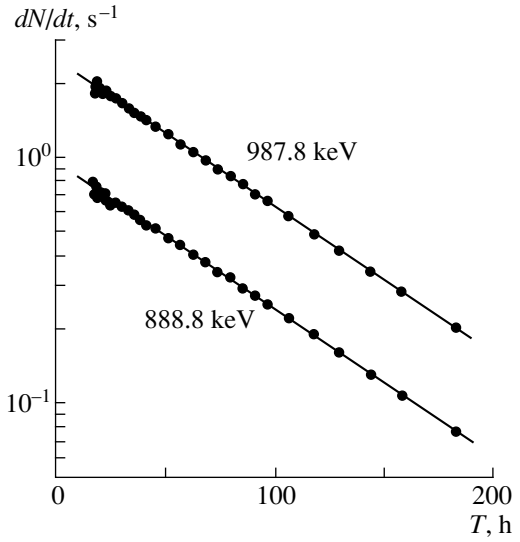

Fig. 4. Decay curves measured after exposure V for γ radiation from the products of the reaction ^{241}Am(n, $2n$)^{240}Am. The solid lines correspond to the ^{240}Am half-life of 50.8 h.

nuclide over the exposure time and the time interval within which we measured the γ-ray spectrum:

$$N_{B0} = \frac{S}{\lambda_B(t_2^c - t_1^c)\varepsilon_\gamma Y_\gamma}\left(\int_{t_1^c}^{t_2^c} dt^c \frac{\int_{t_1^i}^{t_2^i} F_n(t^i)e^{-\lambda_B(t^c - t^i)}dt^i}{\int_{t_1^i}^{t_2^i} F_n(t^i)dt^i}\right)^{-1}. \quad (2)$$

Here, S_γ is the γ-line area; λ_B is the decay constant; ε_γ is the absolute efficiency of the γ spectrometer used; Y_γ is the quantum yield of the corresponding γ line; $F_n(t^i)$ is the instantaneous value of the neutron flux; and t^i and t^c are instants within, respectively, the exposure time and the time over which we measured the gamma-ray spectra. The number of initial nuclei, N_A, is related by simple equations to the mass or the activity of the ^{241}Am sample used, these masses and activities being determined as is described above. The neutron fluence Φ_n received by the sample over the exposure time was calculated by integrating, over the volume, the neutron-flux values determined at discrete points on the basis of a code for computing the neutron field. The absolute value of the neutron flux was normalized to reference data obtained with the niobium foils as was described above.

Table 3. Measured cross sections for the reactions induced by neutrons of energy about 14 MeV incident on ^{241}Am nuclei

Neutron energy, MeV	Reaction cross section, mb	
	^{241}Am(n, $2n$)^{240}Am	^{241}Am(n, $3n$)^{239}Am
13.42	253(24)	
13.48	247(20)	
13.56	239(25)	
14.09	207(22)	
14.21	229(25)	
14.69	199(22)	
14.73		3(2)
14.84	193(22)	12(3)
14.86	215(15)	

Note: The cross section for the reaction ^{241}Am(n, α)^{238}Np at 14.84 MeV does not exceed 1.5 mb.

The errors in the reaction cross sections received the greatest contributions from the uncertainties in the neutron-fluence estimate (3–6%), the sample-mass measurement (3–8%), the determination of the γ-peak areas (0.3–30%), the γ-line yields used (3–10%), and the efficiency of γ-radiation detection (2–4%). The total contribution to the error from other sources did not exceed 3%. Hence, the total error in determining the reaction cross sections amounted to 8–15% for the bulk of the results.

3. RESULTS AND DISCUSSION

3.1. Cross Section for the Reaction ^{241}Am(n, $2n$)^{240}Am

The (n, $2n$) cross section at a neutron energy of about 14 MeV is expected to be a few hundred millibarns. It is of paramount importance to know it precisely, because the long-lived isotope ^{240}Pu appears to be a product of ^{240}Am decay. Despite this, there have been no experimental data until recently that could be used to determine the cross section for the reaction ^{241}Am(n, $2n$)^{240}Am. This is the reason why estimates taken from different libraries differ significantly. In particular, upper and the lower bounds on the ^{241}Am(n, $2n$)^{240}Am cross section at a neutron energy of 14.0 MeV from different national libraries differ by a factor greater than 2.3.

In our experiment, the 888.8- and 987.8-keV peaks accompanying the β^+ decay of ^{240}Am were distinctly seen in the gamma-ray spectra of the irradiated ^{241}Am samples. Variations in the intensities of these γ peaks with time reckoned from the completion of one of the exposures are illustrated in Fig. 4. As can be seen from the figure, the experimental decay curves for the 888.8- and 987.8-keV γ lines correspond to the known ^{240}Am half-life of 50.8 h. The relative intensities of these γ peaks also agree well with the values of 0.251 and 0.732 per decay event, respectively, which are presented in handbooks. This suggests that gamma radiation from ^{240}Am was correctly identified and that no disregarded source of gamma radiation contributes significantly in the close vicinity of the above two γ peaks.

The cross section for the reaction ^{241}Am(n, $2n$)^{240}Am was determined by means of the procedure described above. The resulting numerical values are quoted in Table 3, along with the corresponding errors.

In Fig. 5, the experimental data are compared with the estimates from various libraries (JENDL-3 [8], ENDF/B-VI [9], JEF-2 [10], BROND-2 [11], and CENDL-2 [12]). Despite a considerable scatter of the estimates, the results of the present experiment are in reasonable agreement with them, falling within the intervals of the predicted values. The JEF-2 and JENDL-3 estimates appeared to be the closest to the experimental results in the neutron-energy range 13.42–14.86 MeV.

3.2. Cross Section for the Reaction $^{241}Am(n, 3n)^{239}Am$

The reaction ^{241}Am(n, $3n$)^{239}Am leads to the production of ^{239}Pu nuclei upon the β^+ decay of ^{239}Am nuclei with a half-life of 11.9 h. As in the preceding case, there have not hitherto been experimental data on this reaction. The scatter of the estimates for the reaction cross sections was still wider than that for (n, $2n$). By way of example, we indicate that, at the neutron energy of 14.0 MeV, the lower and the upper bound on the cross section for the reaction ^{241}Am(n, $3n$)^{239}Am are, respectively, 0.52 (ENDF/B-VI) and 46.7 mb (JENDL-3).

Experimental problems in measuring the ^{241}Am(n, $3n$)^{239}Am cross section were still more serious than those in measuring the (n, $2n$) cross section. This was due to a number of factors complicating these measurements (a smaller cross-section value, a smaller gamma-radiation yield further attenuated by the absorber, a higher background level in this region of the γ-ray spectrum, and so on). A special difficulty is associated with the gamma radiation of the fission fragments. Since the fission cross section is two orders of magnitude larger than the (n, $3n$) cross section in the neutron-energy region studied here, we cannot rule out the possibility that gamma radiation from some fission fragments will mask the weak radiation from ^{239}Am. Unfortunately, this is indeed the case. A preliminary analysis of the experimental conditions revealed that 226.4- and 228.2-keV gamma transitions cannot be used to determine the number of product ^{239}Am nuclei, because they nearly coincide with the much more intense (by more than two orders of magnitudes) gamma radiation from ^{132}Te nuclei (E_γ = 228.2 keV, $T_{1/2}$ = 3.204 d), which are produced in ^{241}Am fission. However, the 277.6-keV γ line can be used for this purpose. This line features three components of nearly coincident energies, but their half-lives are markedly different. Owing to this, the dominant contribution from ^{239}Am decay could be observed within a few hours after the exposure, with the exception of the first two hours, when the γ-line intensity is sizably affected by the decay of the short-lived fission fragment ^{134}Te (E_γ = 277.9 keV, $T_{1/2}$ = 42 min).

One of the experimental decay curves constructed for the 277-keV γ line and used to determine the cross section for the reaction ^{241}Am(n, $3n$)^{239}Am is displayed in Fig. 6, where we can clearly see three components. In order to isolate more reliably the component associated with ^{239}Am decay, a special procedure was developed that employed consistently a priori known information about the relevant half-lives, whereby uncertainties in the final results could be reduced somewhat. The resulting numerical values of the cross sections for the reaction ^{241}Am(n, $3n$)^{239}Am are quoted in Table 3. By comparing them with known estimates (see Fig. 7), we can see that our experimental data agree best with the BROND-2 and CENDL-2 estimates.

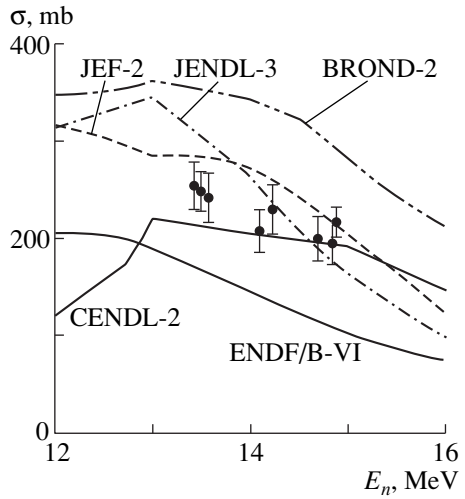

Fig. 5. Cross section for the reaction ^{241}Am(n, $2n$)^{240}Am.

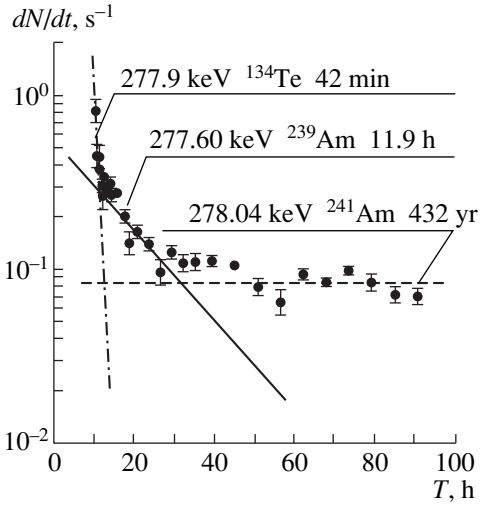

Fig. 6. Decay curve for the 277-keV γ line used to determine the cross section for the reaction ^{241}Am(n, $3n$)^{239}Am.

3.3. Cross Section for the Reaction $^{241}Am(n, \alpha)^{238}Np$

The expected cross section for the reaction ^{241}Am(n, α)^{238}Np is very small. At the neutron energy of 14.0 MeV, FENDL/A-2.0 estimates it at 0.367 mb. This explains the total absence of experimental data on this reaction. Nevertheless, it is necessary to know the ^{241}Am(n, α)^{238}Np cross section both for the sake of

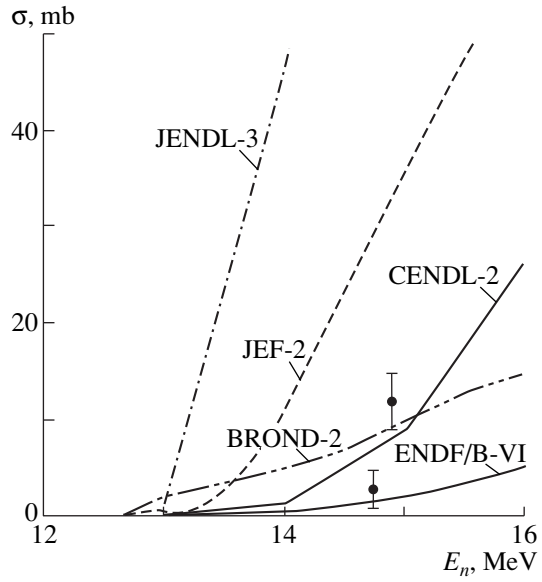

Fig. 7. Cross section for the reaction ^{241}Am(n, 3n)^{239}Am.

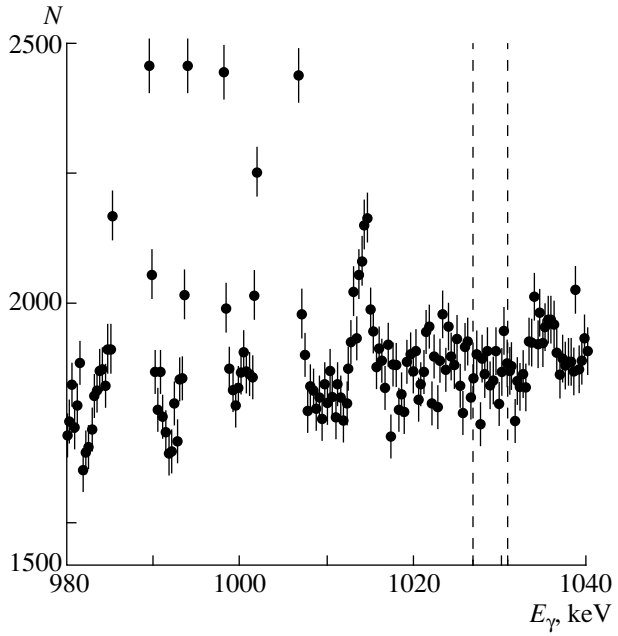

Fig. 8. Section of the gamma-ray spectrum in the energy region where the E_γ = 1028.5 keV line associated with the decay of ^{238}Np nuclei produced in the reaction ^{241}Am(n, α) was expected to occur.

completeness and for the purposes of a satisfactory systematization in this range of nuclei. There is yet another incentive to develop relevant experiments: since a calculation of small cross sections for reactions associated with the emission of charged particles is a rather involved problem, experiments would furnish important information enabling one to optimize the parameters of the theoretical models and to improve their predictive power.

The experimental conditions for measuring so small a cross section against the background of the others exceeding the (n, α) cross section by two or three orders of magnitude were the least favorable. Figure 8 shows a section of the γ-ray spectrum, where the γ peaks accompanying ^{238}Np decay were expected to occur. It took 100 h to obtain this spectrum the time interval between the completion of irradiation and the beginning of measurements being 60 h. The sample mass was 3.1 mg, and the total neutron fluence received by the sample used amounted to 6.48×10^{13} neutron/cm^2. No statistically significant peaks corresponding to ^{238}Np decay were revealed in the spectrum. Assuming that the area of the sought peaks is smaller than the three standard deviations from the background in this region, we were able to set an upper limit of 1.5 mb on the ^{241}Am(n, α)^{238}Np cross section.

4. CONCLUSION

We have reported the ^{241}Am(n, 2n)^{240}Am and ^{241}Am(n, 3n)^{239}Am cross sections measured for the first time at several neutron-energy values in the range 13.42–14.86 MeV. That there were no relevant experimental data until recently had an adverse effect on the quality of cross-section estimates that differed considerably in various national libraries. We hope that our experiment will be a useful supplement to intensively developing theoretical investigations into the physics of processes associated with the production and transmutation of radioactive wastes.

REFERENCES

1. A. A. Filatenkov, S. V. Chuvaev, V. N. Aksenov, *et al.*, IAEA Report INDC(CCP)-402 (1997).
2. E. N. Shurshikov, Nucl. Data Sheets **53**, 601 (1988).
3. M. R. Schmorak, Nucl. Data Sheets **66**, 839 (1992).
4. E. N. Shurshikov and N. V. Timofeeva, Nucl. Data Sheets **59**, 947 (1990).
5. O. F. Nemets and Yu. V. Gofman, *Nuclear Physics: A Handbook* (Naukova Dumka, Kiev, 1975).
6. Y. A. Akovali, Nucl. Data Sheets **72**, 191 (1994).
7. M. J. Koskelo, P. A. Aarnio, and J. T. Routti, Nucl. Instrum. Methods **190**, 89 (1981).
8. K. Shibata, T. Nakagawa, T. Asami, *et al.*, JAERI-1319 (1990).
9. P. F. Rose, BNL-NCS-17541 (1991).
10. C. Nordborg and M. Salvatores, in *Proceedings of the International Conference on Nuclear Data for Science and Technology, Gatlinburg, Tennessee, 1994*, Vol. 2, p. 680.
11. H. D. Lemmel and P. K. McLaughlin, IAEA-NDS-90, Rev. 7 (1993).
12. Liang Qichang and H. D. Lemel, IAEA-NDS-61, Rev. 4 (1996).

Translated by E. Kozlovskiĭ

Physics of Atomic Nuclei, Vol. 63, No. 9, 2000, pp. 1511–1517. Translated from Yadernaya Fizika, Vol. 63, No. 9, 2000, pp. 1596–1602.

NUCLEI
Experiment

Generation of Circularly Polarized Photons by Relativistic Electrons Moving in a Crystal

N. N. Nasonov[1)], G. P. Pokhil, and A. F. Tulinov

Institute of Nuclear Physics, Moscow State University, Vorob'evy gory, Moscow, 119899 Russia

Received February 26, 1999; in final form, September 23, 1999

Abstract—The relativistic-electron (relativistic-positron) acceleration arising in its scattering on the potential of a crystal atomic string is highly anisotropic, which causes polarization of accompanying radiation. The possibility of developing an efficient source of circularly polarized photons by using electrons or positrons of energies attainable at many operating accelerators is demonstrated and analyzed. © *2000 MAIK "Nauka/Interperiodica".*

1. INTRODUCTION

For a long time, coherent bremsstrahlung from relativistic electrons in oriented crystals [1] has been successfully employed to obtain quasimonochromatic linearly polarized photons of high energy, which are extensively used in elementary-particle physics and in the physics of photonuclear reactions [2].

Circularly polarized gamma radiation is of no less interest; however, no efficient sources of such radiations have been developed so far. Previously, the birefringence of photons in an oriented crystal was proposed as a means for transforming a linear polarization into a circular polarization [3] (advances in these realms are surveyed in [4]). Unfortunately, this means is sufficiently efficient only in the region of quite high photon energies (on the order of 10^2 GeV or higher).

In order to generate circularly polarized radiation, Lapko *et al.* [5] proposed using a high degree of circular polarization of the electron acceleration—that is, the rotation that the vector of the electron acceleration executes in the transverse plane as an electron is scattered on the potential of an atomic string in a crystal. The directions of the circular polarization of the acceleration (as well as the direction of the circular polarization of emitted photons) are different for particles moving on the right and the left of the atomic-string axis. The contributions to the yield of radiation from these particle groups can be separated under the conditions of nondipole radiation. Bearing this in mind, the authors of [5] proposed separating photons of specific circular-polarization direction by collimating radiation at an angle with respect to the incidence plane preset by the string axis and the primary-particle momentum. An important modification of the method was proposed in [6] on the basis of the coherent interference of radiation generated by a particle on different strings lying in the same atomic plane in a crystal of finite thickness. This modification allows one to reduce sharply the width of the emitted-photon spectrum.

The method proposed in [5, 6] requires high energies of emitting particles (a few tens of GeV or even higher) and a collimation of the radiation, but the latter presents a technical problem at such energies.

The generation of circularly polarized photons by a relativistic-positron flux reflected from a crystal surface (a crystal surface represents a plane of atomic strings on which the radiation is produced) was considered in [7]. The approach proposed in [7] is advantageous in that it provides the possibility of using positrons of moderately low energy (on the order of 10^2 MeV). A significant drawback of the method is that it requires crystals with an atomically pure surface of an area about a few tens of square centimeters: such surfaces can hardly be obtained at present.

In this article, we analyze the possibility of generating circularly polarized photons as the result of dipole radiation from electrons and positrons in a thin crystal. Interest in this problem is provoked primarily by the following two circumstances:

(i) Electron and positron beams of energies on the order of 10^2 MeV, which can be achieved at many operating accelerators, can be used for this.

(ii) As in the approach proposed in [5], it is possible to obtain a high degree of circular polarization of the radiation.

In our calculations, we use the system of units where $\hbar = c = 1$.

2. GENERAL RELATIONS

Let us consider coherent radiation from relativistic particles entering a crystal with an incident momentum parallel to the atomic planes at a small angle with respect to the axis of atomic strings lying in these planes. Our analysis will be based on the general semi-

[1)] National Research Center Kharkov Institute for Physics and Technology, Akademicheskaya ul. 1, Kharkov, 310108 Ukraine, and Belgorod State University, Belgorod, Russia.

1063-7788/00/6309-1511$20.00

classical expression [8] for the polarization matrix of the spectral density of radiation from a particle in an external field:

$$\frac{dE_{jk}}{d\omega dO} = \frac{e^2\omega^2}{4\pi^2}\int dt_1 dt_2 L_{jk} \times \exp\{i\omega'[t_1 - t_2 - \mathbf{n}\cdot(\mathbf{r}_1 - \mathbf{r}_2)]\}, \quad (1)$$

$$L_{jk} = \frac{(\varepsilon+\varepsilon')^2}{4(\varepsilon')^2}(\mathbf{e}_j\cdot\mathbf{v}_1)(\mathbf{e}_k\cdot\mathbf{v}_2) - \frac{\omega^2}{4(\varepsilon')^2}[(\mathbf{e}_j\cdot\mathbf{v}_2)(\mathbf{e}_k\cdot\mathbf{v}_1) - (\mathbf{v}_1\cdot\mathbf{v}_2) + v^2].$$

Here, $\mathbf{r}_{1,2} = \mathbf{r}(t_{1,2})$ is the trajectory of the radiating particle, $\mathbf{v} = d\mathbf{r}/dt$, $\mathbf{e}_{j,k}$ are the polarization vectors, ε is the particle energy, ω is the photon energy, $\varepsilon' = \varepsilon - \omega$, $\varepsilon'\omega' = \varepsilon\omega$, and $\mathbf{n}$ is a unit vector in the direction of the radiation.

In the case of dipole radiation considered here, the angle of particle scattering on the crystal must be smaller than the specific radiation angle m/ε, where m is the electron mass. Performing integration by parts in expression (1) and setting the particle velocity to $\mathbf{v}(t) \approx \mathbf{v} = \text{const}$ in the resulting expression, we then arrive at

$$\frac{dE_{jk}}{d\omega dO} = \frac{e^2}{4\pi^2(1-\mathbf{n}\cdot\mathbf{v})^2} \times \int_0^T dt \int d\tau G_{jk}\exp\{i\omega'(1-\mathbf{n}\cdot\mathbf{v})\tau\}, \quad (2)$$

$$G_{jk} = \frac{(\varepsilon+\varepsilon')^2}{4(\varepsilon')^2}(\mathbf{e}_j\cdot\mathbf{b}(t+\tau/2))(\mathbf{e}_k\cdot\mathbf{b}(t-\tau/2)) - \frac{\omega^2}{4(\varepsilon')^2}(\mathbf{e}_j\cdot\mathbf{b}(t-\tau/2))(\mathbf{e}_k\cdot\mathbf{b}(t+\tau/2)) + \frac{\omega^2}{4(\varepsilon')^2}\mathbf{w}(t+\tau/2)\cdot\mathbf{w}(t-\tau/2),$$

$$\mathbf{b} = \mathbf{w} + \frac{\mathbf{v}}{1-\mathbf{n}\cdot\mathbf{v}}\mathbf{n}\cdot\mathbf{w},$$

where T is the target thickness, while the particle acceleration $\mathbf{w}$ can be expressed, in accordance with the relativistic equation of motion, in terms of the crystal potential $\varphi(\mathbf{r})$ as

$$\mathbf{w} = -\frac{e}{\varepsilon}(\nabla - \mathbf{v}(\mathbf{v}\cdot\nabla))\varphi(\mathbf{r}). \quad (3)$$

In the case being considered, the potential $\varphi(\mathbf{r})$ can be represented as

$$\varphi(\mathbf{r}) = \bar{\varphi}(x) + \sum_{l\geq 1}\varphi_l(x)\cos(g_l y), \quad (4)$$

where $\bar{\varphi}(x)$ is the averaged potential of the atomic planes; the two-dimensional oscillating component is generated by atomic strings lying in these planes, the string axes being aligned with $\mathbf{e}_z$; and $g_l = 2\pi l/a$, a being the distance between the neighboring strings. The explicit expressions for $\bar{\varphi}(x)$ and $\varphi_l(x)$ are different for radiating positrons and electrons and will be presented below in performing specific calculations.

According to Eqs. (3) and (4), the trajectory of the radiating particle represents a superposition of a smooth trajectory of the motion in the averaged potential $\bar{\varphi}(x)$ of the atomic planes and small-scale oscillations caused by periodic irregularities of the potential of a plane that are induced by the atomic strings. The characteristic radiation frequencies associated with these two types of motion belong to different ranges. The high-frequency radiation component of interest is due to the scattering of a fast particle on the atomic strings; therefore, only the quickly oscillating component of the acceleration, $\tilde{\mathbf{w}}(t)$, which is controlled by the potential $\sum_l \varphi_l(x)\cos(g_l y)$, must be substituted into the integrand on the right-hand side of (2). Let us specify the initial particle velocity by the expression

$$\mathbf{v} = \mathbf{e}_z\left(1 - \frac{1}{2}\gamma^{-2} - \frac{1}{2}\boldsymbol{\psi}^2\right) + \boldsymbol{\psi}, \quad \mathbf{e}_z\cdot\boldsymbol{\psi} = 0,$$

$$\varepsilon = m\gamma.$$

The quantity $\tilde{\mathbf{w}}(t+\tau)$ can then be represented as

$$\tilde{\mathbf{w}}(t+\tau) = \sum_{l\geq 1}(\tilde{\mathbf{w}}_l[x(t+\tau)]\exp[ig_l\psi_y(t+\tau)] + \text{c.c.}), \quad (5)$$

where the coefficients can easily be determined from Eqs. (3) and (4). Since the trajectory $x(t+\tau)$ is a smooth function against the quickly oscillating exponential, it can be assumed that $\tilde{\mathbf{w}}_l[x(t+\tau)] \approx \tilde{\mathbf{w}}_l[x(t)]$ when we substitute (5) into (2). After some simple algebra, Eqs. (2)–(5) yield the expression

$$\frac{dE}{d\omega} = \frac{e^4\eta}{8\varepsilon\psi_y^2(1-\eta)}\sum_{l\geq 1}\frac{1}{g_l^2}\left\{1 + (1-\eta)^2 - 4\frac{\eta}{\eta_l}\left(1 - \frac{\eta}{(1-\eta)\eta_l}\right)\right\}\left\langle\int_0^T dt\left[\left(\frac{d\varphi_l}{dx}\right)^2 + g_l^2\varphi_l^2\right]\right\rangle\sigma\left(\frac{\eta_l}{1-\eta_l} - \eta\right) \quad (6)$$

for the radiation spectrum and the relation

$$\frac{dE}{d\omega}\xi_2 = \frac{e^4\eta[1+(1-\eta)^2]}{4\varepsilon\psi_y^2(1-\eta)}\sum_{l\geq 1}\frac{1}{g_l^2}\left(1 - \frac{2\eta}{(1-\eta)\eta_l}\right) \times\left\langle\int_0^T dt\varphi_l\frac{d\varphi_l}{dx}\right\rangle\sigma\left(\frac{\eta_l}{1+\eta_l} - \eta\right) \quad (7)$$

for the second Stokes coefficient ξ_2, which characterizes the degree of circular polarization of emitted photons.

In (6) and (7), $\eta = \omega/\varepsilon$; $\eta_l = 2\varepsilon g_l \psi_y/m^2$ is the ratio of a characteristic energy in the radiation of the lth harmonic to the radiating-particle energy ε; $\sigma(x)$ is the Heaviside function; and angular brackets denote averaging over the trajectories of the particle flux, which are determined by the point x_0 at which the particles enter the crystal and their angles of incidence, ψ_x. In deriving formulas (6) and (7), we have used the following representations of unit vector $\mathbf{n}$ and the polarization vectors $\mathbf{e}_j$:

$$\mathbf{n} = \mathbf{e}_z\left(1-\frac{1}{2}\boldsymbol{\Theta}^2\right)+\boldsymbol{\Theta}, \quad \mathbf{e}_z\cdot\boldsymbol{\Theta} = 0, \quad dO = d^2\Theta,$$

$$\mathbf{e}_1 \approx [\mathbf{n}\times\mathbf{e}_x] \approx \mathbf{e}_y - \Theta_y\mathbf{e}_z,$$

$$\mathbf{e}_2 \approx [\mathbf{n}\times\mathbf{e}_1] \approx -\mathbf{e}_x + \Theta_x\mathbf{e}_z.$$

Expressions (6) and (7) form the basis for the ensuing analysis of the spectral and polarization properties of the radiation from the positron (electron) flux in the crystal of small thickness T.

3. RADIATION FROM RELATIVISTIC POSITRONS

The averaged potential of a plane for positrons, $\bar{\varphi}(x)$, is close to a parabolic potential with the well center occurring in the middle between the neighboring atomic planes. The functions $\bar{\varphi}(x)$ and $\varphi_l(x)$ appearing in the total potential (4) are given by

$$\bar{\varphi}(x) = \varphi^{(0)}\left(\frac{2x}{c}\right)^2,$$

$$\varphi^{(0)} = \frac{2\pi ZeR}{ba}\exp\left(\frac{u^2}{2R^2}\right)\left[1-\Phi\left(\frac{u}{\sqrt{2}R}\right)\right], \qquad (8)$$

$$\varphi_l(x) = \varphi_l^{(0)}\exp\left(-\kappa_l\frac{c}{2}\right)\cosh(\kappa_l x), \quad \varphi_l^{(0)} = \frac{8\pi Ze}{\kappa_l ba},$$

where $\kappa_l^2 = g_l^2 + R^{-2}$, R is the radius of the electron screening of an atom (we use here the simplest statistical atomic model with exponential screening), c is the distance between the neighboring atomic planes, b is the distance between string atoms, u is the root-mean-square amplitude of thermal vibrations of the atoms, and $\Phi(x)$ is the error function.

Considering the fundamental aspect of the problem, we neglect the angular spread of radiating positrons of the beam. In this case, the equation of motion for particles entering the region of the averaged crystal potential (8) with a momentum parallel to the atomic planes has the simple solution

$$x(t) = x_0\cos(\omega_0 t), \qquad (9)$$

where x_0 is the coordinate of the point at which a positron enters the crystal ($-c/2 \le x_0 \le c/2$) and $\omega_0^2 = 8e\varphi_l^{(0)}/\varepsilon c^2$.

Let us now proceed to analyze the coefficient $F_l = \left\langle \int_0^T dt\,\varphi_l \frac{d\varphi_l}{dx}\right\rangle$ from (7) (the answer to the question of whether it is possible in principle to obtain circularly polarized photons by the method being considered depends crucially on this coefficient). From the expression

$$F_l = \frac{1}{2}\kappa_l\varphi_l^{(0)^2}e^{-\kappa_l c}\left\langle\int_0^T dt\sinh(2\kappa_l x_0)\cos\omega_0 t\right\rangle, \qquad (10)$$

it follows that $F_l(-x_0) = -F(x_0)$, whence we can see that positrons moving along trajectories that are symmetric with respect to the center of the planar channel emit photons whose circular polarizations have opposite directions (at each instant, these particles have accelerations whose circular components are of equal magnitudes, but they are of opposite signs). Moreover, it follows from (10) that, for a fixed trajectory, the sign of the coefficient F_l is conserved only within the time interval that does not exceed a quarter of the period of positron oscillations in the channel. Therefore, the required crystal thickness T is determined by the condition

$$T = \pi/2\omega_0, \qquad (11)$$

whence it follows that the sign of the coefficient F_l depends on the sign of the impact parameter x_0 exclusively and that the sign of x_0 determines unambiguously the direction of positron scattering on the potential of a plane (for instance, a particle is deflected to the left of the channel plane when $x_0 > 0$).

Owing to these two important circumstances, a coincidence scheme simultaneously recording a radiated photon and the direction in which the positron that has emitted this photon leaves the crystal makes it possible to single out the contribution to the radiation yield from positrons having trajectories characterized by a fixed sign of x_0. Since experiments studying radiation from relativistic particles in crystals are usually conducted in the single-particle mode, the application of a coincidence scheme is not expected to require much more complex experimental facilities.

In practice, a system determining the direction of positron escape from the crystal can be implemented by using two thin semiconductor plates (Fig. 1) that are transparent to hard photons, but which detect positrons by ionization losses.

In calculating the integral in (10) with respect to t, we must take into account a fast (exponential) decrease of the potential harmonics $\varphi_l(x)$ with increasing distance from the atomic planes. It is reasonable to perform averaging over x_0 separately for the intervals

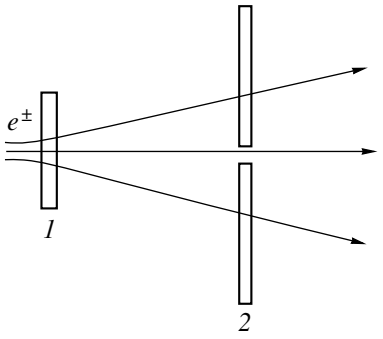

Fig. 1. Coincidence scheme: (*1*) crystal target and (*2*) semiconductor plates.

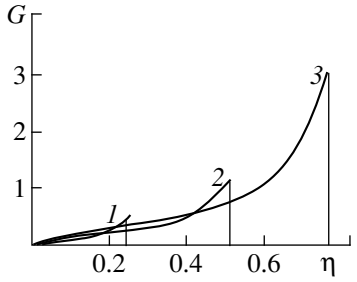

Fig. 2. Universal spectrum of radiation: η_1 = (*1*) 0.3, (*2*) 1, and (*3*) 3.

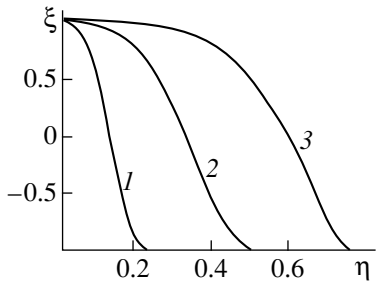

Fig. 3. Degree of radiation polarization as a function of the relative photon energy: η_1 = (*1*) 0.3, (*2*) 1, and (*3*) 3.

$0 < x_0 < c/2$ and $-c/2 < x_0 < 0$. After some simple algebra, we obtain

$$F_l \approx \pm\frac{\varphi_l^{(0)^2}}{4\omega_0 c}\sqrt{\frac{\pi}{2\kappa_l c}}, \qquad (12)$$

where, for example, the plus sign corresponds to particles from the interval $0 < x_0 < c/2$.

Since the coefficients F_l decrease fast with increasing number l of a harmonic ($F_l \approx l^{-5/2}$), we can restrict our consideration to the first harmonic. For the radiation spectrum and the degree of circular polarization, the eventual analytic expressions following from (6) and (7) are given by

$$\frac{dE^{(p)}}{d\eta} = A^{(p)}G(\eta)\sigma\left(\frac{\eta_1}{1+\eta_1}-\eta\right),$$

$$A^{(p)} = \frac{\sqrt{\pi}e^2(e\varphi_1^{(0)})^2}{16\varphi_1^2\omega_0}\frac{g_1^2+\kappa_1^2}{g_1^2}\frac{1}{(2\kappa_1 c)^{3/2}},$$

$$G = \frac{\eta}{1-\eta}\left\{1+(1-\eta)^2-4\frac{\eta}{\eta_1}\left[1-\frac{\eta}{(1-\eta)\eta_1}\right]\right\}, \qquad (13)$$

$$\xi_2^{(p)} = \pm\xi(\eta)\sigma\left(\frac{\eta_1}{1+\eta_1}-\eta\right),$$

$$\xi = \frac{2g_1\kappa_1}{g_1^2+\kappa_1^2}\frac{(1+(1-\eta)^2)\left(1-\frac{2\eta}{(1-\eta)\eta_1}\right)}{1+(1-\eta)^2-4\frac{\eta}{\eta_1}\left(1-\frac{\eta}{(1-\eta)\eta_1}\right)}.$$

Since $2g_1\kappa_1/(g_1^2+\kappa_1^2) \approx 1$, the dependences of G and ξ_2 on the emitted-photon energy ω are characterized by single parameter η_1. Figure 2 shows the curves representing the spectral dependence $G(\eta)$ at various values of η_1. The corresponding curves for $\xi(\eta)$ in Fig. 3 demonstrate the possibility of obtaining quasimonochromatic photons with a high degree of circular polarization within the approach being discussed.

To conclude this section, we present an expression for estimating the total number of radiated photons:

$$N^{(p)} \cong \frac{e^2}{8m\sqrt{Rc}}\left(\frac{\pi Ze^2}{abg_1\kappa_1\psi_y}\right)^{3/2}\frac{g_1^2+\kappa_1^2}{\kappa_1^2}Q(\eta_1), \qquad (14)$$

$$Q(\eta_1) = \frac{1}{\sqrt{\eta_1}}\left[\frac{8}{\eta_1}+\frac{\eta_1(2+\eta_1)}{2(1+\eta_1)^2}+\left(1-\frac{4}{\eta_1}-\frac{8}{\eta_1^2}\right)\ln(1+\eta_1)\right].$$

As can be seen from (14), the energy dependence of $N^{(p)}(\varepsilon)$ is absorbed in the function $Q(\eta_1)$. The coefficient of this function in (14) is determined exclusively by the parameters of the crystal and by the angle ψ_y specifying the orientation of the positron velocity with respect to the atomic strings. By way of example, we indicate that, for positrons radiating photons in a silicon crystal, $N^{(p)} \approx 10^{-5}Q(\eta_1)$. It should be emphasized that $Q(\eta_1)$ is a nonmonotonic function of η_1: $Q(\eta_1) \approx 4\sqrt{\eta_1}/3$ for $\eta_1 \ll 1$ and $Q(\eta_1) \approx (\ln\eta_1)/\sqrt{\eta_1}$ for $\eta_1 \gg 1$. It can easily be shown that an increase in the number of emitted photons with increasing positron energy in the low-η_1 region, where the effect of quantum recoil is immaterial in radiation, is associated with the increase in the crystal thickness T determined from (11). A decrease in $N^{(p)}$ with increasing positron energy at high values of η_1 is due to the suppression of the radiation yield by the quantum-recoil effect. Figure 4 shows the dependence $Q(\eta_1)$, which permits choosing optimum values for the positron energy and for the orientation angle ψ_y.

4. RADIATION FROM RELATIVISTIC ELECTRONS

An analysis of the possibility of using electron beams to generate circularly polarized photons by the proposed method is of the greatest practical interest. In the case of emitting electrons, the atomic strings are located at the center of the planar channel at the bottom of the potential well. The properties of the potential (4) are then determined by the formulas

$$\bar{\varphi}(x) = \varphi^{(0)}\left(1-\frac{2|x|}{c}\right)^2, \quad \varphi_l(x) = \varphi_l^{(0)}e^{-\kappa_l|x|}, \quad (15)$$

where the coefficients $\varphi^{(0)}$ and $\varphi_l^{(0)}$ coincide with those given in (8) for $|x| \le c/2$.

Taking into account the sign of the electron charge, we conclude that the potential $\bar{\varphi}(x)$ (15) is essentially anharmonic for channeling electrons; as a result, the period of electron oscillations in the channel depends sharply on the impact parameter x_0. In the case of positron channeling in a crystal of thickness T given by (11), the sign of x_0 determines unambiguously both the direction of positron escape from the crystal and the sign of circular polarization of the emitted photon, while, in the case being considered, these features depend on the sign and on the absolute value of x_0 in a rather complicated way at a preset crystal thickness T.

In the case being discussed, the shape of the spectrum and the photon-energy dependence of the degree of the circular polarization of emitted photons are given by the expressions

$$\frac{dE^{(2)}}{d\eta} = \frac{e^2(e\varphi^{(1)})^2T}{8\psi_y^2}\,\frac{g_1^2+\kappa_1^2}{\kappa_1^2}G(\eta)\sigma\left(\frac{\eta_1}{1+\eta_1}-\eta\right)f_1(T),$$
$$\xi_2^2 = \pm\xi(\eta)\sigma\left(\frac{\eta_1}{1+\eta_1}-\eta\right)f_2(T), \quad (16)$$

which are similar to (13). The ± signs in (16) correspond to the directions of electron escape from the crystal. The functions $f_1(T)$ and $f_2(T)$, which determine the crystal-thickness dependence of the radiation yield and of the degree of circular polarization, can be represented as

$$f_1 = \frac{1}{Tc}\int\limits_{S^\pm} dx_0 \int\limits_0^T dt e^{-2\kappa_1|x(t,x_0)|},$$
$$f_2 = \frac{1}{Tc}\int\limits_{S^\pm} dx_0 \int\limits_0^T dt\,\mathrm{sgn}[x(t,x_0)]e^{-2\kappa_1|x(t,x_0)|}/f_1. \quad (17)$$

Integration in (17) with respect to x_0 is performed within the regions $S^\pm$ corresponding to a certain direction of electron escape from the crystal and consisting of a set of bands of x_0 values, which can easily be inferred from the trajectory of electron motion in the channel. From (3) and (15), it follows that this trajectory is given by

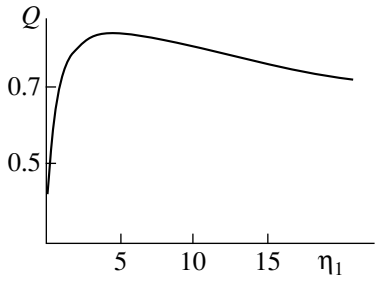

Fig. 4. Radiation yield as a function of the parameter η_1, which is proportional to the particle energy.

$$x(t,x_0) = (-1)^n\frac{c}{2}\left\{1-\left[1-\frac{2x_0}{c}\right]\cosh(\omega_0(t-2nT_0))\right\},$$
$$(2n-1)T_0 \le t \le (2n+1)T_0, \quad (18)$$
$$T_0 = \frac{1}{\omega_0}\mathrm{arccosh}\left(\frac{1}{1-2x_0/c}\right).$$

The function $x(t, x_0)$ is presented for electrons entering the crystal within the impact-parameter range $0 \le x_0 \le c/2$. For $x_0 < 0$, the trajectory is determined from the symmetry conditions, the quantity ω_0 in (18) being coincident with the analogous quantity in (9).

For the functions $f_2(T)$ and $f_1(T)$, expressions convenient for a numerical analysis can be derived from (17) and (18). They can be represented as

$$f_2(T') = \frac{1}{2T'}\sum_{l=0,2}\sum_{k\ge 0}\left\{\int\limits_{y_{l+4k}}^{y_{l+4k}} dy\int\limits_{z_1}^{y} dz g(z,y)\right.$$
$$\left.+\int\limits_{y_{l+2+4k}}^{y_{l+1+4k}} dy\int\limits_{z_2}^{y} dz g(z,y)\right\} f_1^{-1}(T'),$$

$$g(z,y) = \frac{e^{-kz}}{\sqrt{(1-z)^2-(1-y)^2}},$$

$$f_1(T') = \frac{1}{2T'}\sum_{k\ge 0}\left\{k\int\limits_{y_{1+k}}^{y_k} dy\int\limits_0^y dz g(z,y)\right.$$
$$\left.+\int\limits_{y_{1+2k}}^{y_{2k}} dy\int\limits_{z_3}^{y} dz g(z,y)+\int\limits_{y_{2+2k}}^{y_{1+2k}} dy\int\limits_0^{z_4} dz g(z,y)\right\},$$

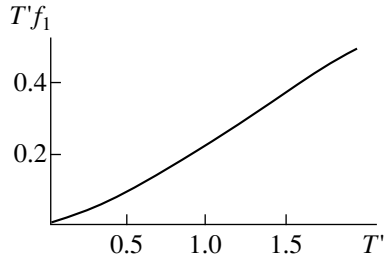

Fig. 5. Yield of radiation from electrons as a function of the parameter $T' = \omega_0 T$, which is proportional to the crystal thickness.

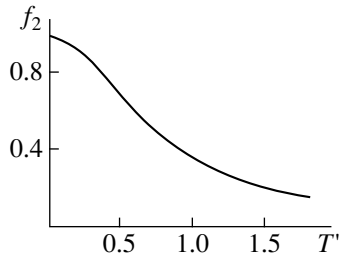

Fig. 6. Degree of circular photon polarization as a function of the parameter $T' = \omega_0 T$, which is proportional to the crystal thickness.

where

$$T' = \omega_0 T, \quad y_m = 1 - \frac{1}{\cosh(T'/m)}, \quad T'_0 = \omega_0 T_0,$$

$$z_1 = z(T' - (l + 4k)T'_0, y),$$

$$z_2 = z((l + 2 + 4k)T'_0 - T', y),$$

$$z_3 = z(T' - 2kT'_0, y),$$

$$\kappa = c\kappa_1, \quad z_4 = z((2 + 2k)T'_0 - T', y),$$

$$z(t', y) = 1 - (1 - y)\cosh t'.$$

Figure 5 displays the function $f_1(T')$ illustrating a nearly linear dependence of the radiation yield on the crystal thickness. As the crystal thickness is increased, the emitting particles are spread fast over the phase space with the result that the degree of radiation polarization decreases monotonically. Figure 6 shows the dependence $f_2(T')$.

Thus, a high degree of circular polarization of photons produced by the proposed method can be expected only in the case of very thin crystals (of thickness $T \leq 1/2\omega_0$). We will now consider the example of how the proposed scheme can be implemented by using an extracted electron beam from the Pakhra synchrotron of the Lebedev Institute of Physics (Russian Academy of Sciences), where the energy of accelerated particles is about 600 MeV and where the angular spread of their beam is about 10^{-4}. With a thin silicon crystal used as a radiator and oriented along the (100) plane, the critical angle of planar channeling is about 2.5×10^{-4}, which exceeds considerably the angular spread of the beam, so that the total phase space of the beam can be used. At an angle of the particle-velocity orientation with respect to the crystal axis, ψ_y, about 10^{-2}, the proposed method makes it possible to obtain a quasimonochromatic flux of photons with an energy of about 150 MeV at the maximum. At the crystal thickness of about 0.5 μm, the spectral density of radiation, $dE/d\omega$, is about 2×10^{-4} in the region of maximum (this is nearly 20 times as great as the radiation density of ordinary bremsstrahlung), the degree of circular polarization of the radiation being about 0.4 at the maximum.

5. CONCLUSIONS

The above analysis of the possibility of generating circularly polarized photons by relativistic charged particles in an oriented crystal leads to the following conclusions:

(i) Owing to an unambiguous relation between the sign of the circular polarization of a photon emitted in the scattering of a relativistic particle on atomic strings lying in a crystal atomic plane and the direction of emitting-particle scattering by this plane, the use of a coincidence scheme would permit separating the yields of radiation having left- and right-hand circular polarization.

(ii) The proposed scheme makes it possible to generate circularly polarized photons with a quasimonochromatic spectrum by using either electrons or positrons moving in the planar-channeling mode in a thin crystal.

(iii) The radiation in question is of a dipole character, so that one can employ particle beams of energy about 10^2 MeV, which can be achieved at many operating accelerators.

(iv) Numerical examples constructed on the basis of the formulas that have been obtained in the present study and which provide a complete quantitative description of the spectral–angular and polarization features of the radiation demonstrate a high efficiency of the proposed method.

(v) Under the conditions of interference, the spectral–angular distribution of the radiation undergoes a significant rearrangement, which depends on the sign of the emitting-particle charge. As a result, the radiation may become much more intense.

(vi) The interference changes sharply the angular dependence of polarization of the resulting radiation.

ACKNOWLEDGMENTS

This work was supported in part by the Russian Foundation for Basic Research (project no. 98-02-17238) and the STCU Foundation (grant no. 285).

REFERENCES

1. M. L. Ter-Mikaelyan, *Medium Effect on High-Energy Electromagnetic Processes* (Akad. Nauk Arm. SSR, Yerevan, 1969).
2. A. P. Potylitsyn, *Polarized Photon Beams of High Energies* (Énergoatomizdat, Moscow, 1989).
3. N. Cabibbo, G. da Plato, J. de Franceschi, and U. Mosco, Nuovo Cimento **27**, 979 (1963).
4. V. G. Baryshevskiĭ and V. V. Tikhomirov, Usp. Fiz. Nauk **159**, 529 (1989) [Sov. Phys. Usp. **32**, 1013 (1989)].
5. V. P. Lapko, N. N. Nasonov, and V. M. Sanin, Yad. Fiz. **55**, 3183 (1992) [Sov. J. Nucl. Phys. **55**, 1774 (1992)].
6. V. Lapko and N. Nasonov, Phys. Lett. A **195**, 97 (1994).
7. V. V. Tikhomirov, Zh. Éksp. Teor. Fiz. **109**, 1188 (1996) [JETP **82**, 639 (1996)].
8. V. N. Baĭer, V. M. Katkov, and V. M. Strakhovenko, *High-Energy Electromagnetic Processes in Oriented Crystals* (Nauka, Novosibirsk, 1989).

Translated by E. Kozlovskiĭ

Physics of Atomic Nuclei, Vol. 63, No. 9, 2000, pp. 1518–1526. From Yadernaya Fizika, Vol. 63, No. 9, 2000, pp. 1603–1611.

NUCLEI
Theory

Observation of an α-Cluster Structure in ^{36}Ar*

V. Z. Goldberg, G. V. Rogachev, M. Brenner[1)], K.-M. Källman[1)], T. Lönnroth[1)], M. V. Rozhkov, S. Torilov[2)], W. H. Trzaska[3)], and R. Wolski[4)]

Russian Research Centre Kurchatov Institute, pl. Kurchatova 1, Moscow, 123182 Russia

Received November 16, 1999; in final form, March 20, 2000

Abstract—Excitation functions for ^{32}S + α elastic scattering are measured by a new method based on inverse kinematics and a thick gas target. Data corresponding to the ^{36}Ar excitation range 12–16 MeV are treated within the *R*-matrix approach. Spin–parity assignments are given for over 40 new levels. © *2000 MAIK "Nauka/Interperiodica".*

1. INTRODUCTION

It is well known that α-cluster structures manifest themselves in atomic nuclei. In [1, 2], it was shown that such a structure persists at high excitation energies (20–30 MeV).

The authors of [3–5] studied the α-cluster states of ^{32}S in the resonance scattering of alpha particles on a ^{28}Si target. They treated data in a broad excitation region (10–20 MeV) within the single-level approximation of *R*-matrix theory and found a succession of levels of different spins with negative and positive parities. The states of the same spin were fragmented into sharp peaks occupying about 2 MeV of the excitation region (Lorentz distribution). It was claimed that the density of these states is much lower than the density of statistical levels in ^{32}S. In lighter nuclei, like ^{16}O or ^{20}Ne, if a few levels of the same spin happened to be nearby, they were assigned to different rotational or cluster bands (see [6] and references therein). A heavier nucleus, ^{44}Ti, was investigated by Frekers *et al.* [7] in a high-precision study, where α-cluster states were identified mainly after averaging over many compound-nucleus levels. After proper averaging, α-cluster states were observed as single bumps of a definite spin with drastically different appearance as compared to α-cluster structure observed in the ^{16}O nucleus.

Such radical changes were not observed in our review study of this structure for nuclei ranging from ^{16}O to ^{24}Mg [8]. Also, very fruitful investigations of α-transfer reactions induced by ^{6}Li [9–11] stressed similarities rather than differences between the α-cluster structures in ^{20}Ne, ^{40}Ca, and ^{44}Ti, at least for the excitation region up to 11 MeV.

The ^{36}Ar nucleus was not thoroughly studied earlier, probably because of difficulties associated with the use of sulfur targets. A measurement of elastic alpha-particle scattering by ^{32}S in the bombarding-energy range 10.0–17.5 MeV, at 100-keV intervals, was carried out by the Florida group [12]. The aim of that work was to fix the optical-potential parameters, but no spin assignments were made there. A study in the energy range 4.0–8.9 MeV at 50-keV intervals was reported by Coban *et al.* [13], who gave tentative assignments for three levels. Spin assignments for some levels were also proposed by Artemov *et al.* [14], who made very difficult correlation measurements.

To fill the existing gap in the mapping of α-cluster structure for nuclei in the range between ^{32}S and ^{44}Ti, we have decided to obtain new information about the ^{36}Ar nucleus. For this purpose, we have measured the excitation function for the elastic scattering of ^{32}S on helium at excitation energies of the compound system ^{36}Ar between 11.5 and 22 MeV. Our recently perfected method [15, 16] allowed us to obtain the excitation function in a truly continuous way instead of the traditional step-by-step approach. Here, we present the results of our analysis for the region from 11.5 to 16 MeV. The spin–parity assignments are made for 44 levels in ^{36}Ar.

2. EXPERIMENT

The experiment was carried out at the K-130 cyclotron at the Physics Department of the University of Jyväskylä, Finland, with a 160-MeV ^{32}S beam. The beam entered a 1.3-m scattering chamber via 3-μm thick window made from a Havar foil. In order to monitor the beam intensity, we used ^{32}S ions backscattered from this foil. The chamber was filled with a helium gas. Recoiling alpha particles (which result from the interaction of sulfur ions with helium) were detected by an array of silicon detectors positioned in the chamber (in the gas) in the forward direction and also directly at

* This article was submitted by the authors in English.

1) Department of Physics, Åbo Akademi University, Porthansgatan 3, FIN-20500 Åbo (Turku), Finland.
2) St. Petersburg State University, St. Petersburg, Russia.
3) Department of Physics, University of Jyväskylä, PO Box 35, FIN-40351 Jyväskylä, Finland.
4) Cracow Institute of Nuclear Physics, Poland.

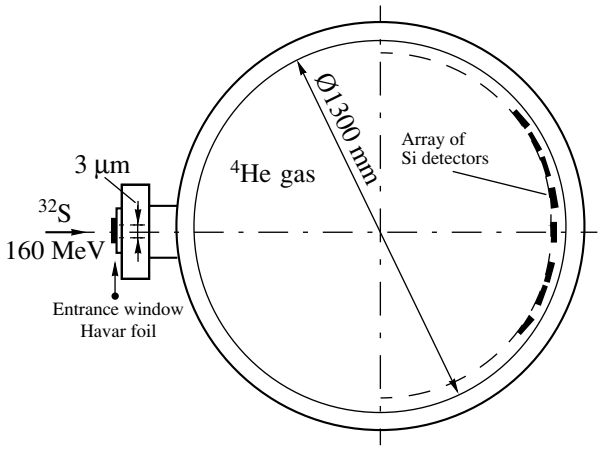

Fig. 1. Experimental setup. Scattering chamber was filled with a ^{4}He gas acting as a target and as a beam absorber. The pressure was 350 mbar. An array of Si detectors recorded recoil alpha particles (result of interaction between sulfur ions and nuclei of helium atoms).

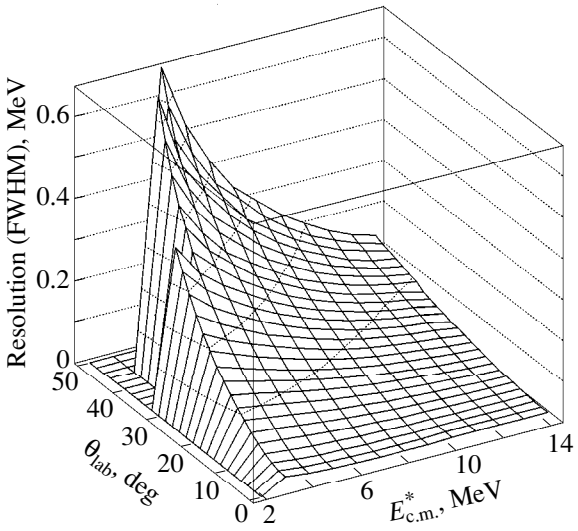

Fig. 2. Monte Carlo simulation of the experimental resolution at various detection angles and excitation energies.

zero degree. The gas pressure was adjusted in such a way as to stop the ^{32}S beam before the zero-degree detector at a sufficient distance in order to reduce the flux of low-energy recoils originating from Coulomb scattering. This inverted-kinematics approach allowed us to measure continuously a large excitation region of ^{36}Ar in a single run. The experimental setup is sketched in Fig. 1.

Since ^{32}S ions lose about a fifth of their energy (32 MeV) in the entrance foil, one might expect a serious degradation of the resolution, mostly due to straggling. In fact, the straggling will contribute less than 0.4 MeV to the beam spread, and the total beam spread upon passing the foil will be about 1.2 MeV, which includes the initial beam spread of 0.5%. The observed beam spread in the chamber after the window was higher, about 3 MeV, largely because of the nonhomogeneity of the foil. This spread increases with penetration depth. Typically, a sharp resonance occurring around the center of the chamber will have position spread of about 4 cm. Fortunately, this spread does not seriously affect the energy resolution for alpha particles detected at zero degree. The alpha-particle energy in the laboratory frame is

$$E_{\rm lab}(\alpha) = 4E_{\rm HI}\frac{mM}{(m+M)^2}(\cos\theta_{\rm lab})^2, \qquad (1)$$

where $m = 4$, $M = 32$, and $E_{\rm HI}$ is the heavy-ion energy just prior to the collision. The sharp resonance selects (in accordance with its width) the interaction energy; hence, the energy of the recoiling alpha particle is also fixed. The energy lost by recoiling alpha particles over a 4-cm passage in helium will be about 200 times less than that lost by heavy ions, as follows from the expression [the well-known Bethe–Bloch formula and expression (1) were used to obtain it]

$$\frac{dE/dx(^{32}{\rm S})}{dE/dx(\alpha)} \approx \frac{4Z^2_{^{32}{\rm S}}M^2}{Z^2_\alpha(M+m)^2} \approx 200. \qquad (2)$$

Therefore, the final resolution as recorded by the zero-degree detector is quite good. A computer simulation of the experimental resolution is illustrated in Fig. 2. The experimental excitation function measured at zero degree (zero degree corresponds to 180° in the c.m. frame) is displayed in Fig. 3. With increasing detection angle, the energy resolution deteriorates, as can be seen in Fig. 2. The main reason for this deterioration is detection-angle broadening associated with a resonance spread along the beam path. In our experiment, the largest laboratory angle relative to the chamber center was 26°. It is worth noting that, because each detector "sees" recoils emerging from the whole path in the gas, resonances with different excitation energies are observed at different laboratory angles by the same detector placed at any angle different from zero degree. Highly excited states populated by resonance scattering near the entrance window are observed at smaller angles than low excitations. Necessary transformations into the c.m. frame are made by means of a computer code that takes into account all relevant experimental conditions.

Unfortunately, we did not find a simple and reliable way to make precision measurements of absolute cross sections. Taking into account uncertainties in external monitoring, we estimate that absolute cross sections are obtained with a precision higher than 30%. A possible error in absolute values of the excitation energy is less than 50 keV, and the relative values are obtained with a precision higher than 10 keV.

Figure 3 makes it possible to compare our measurement at zero degree, which corresponds to 180° for a

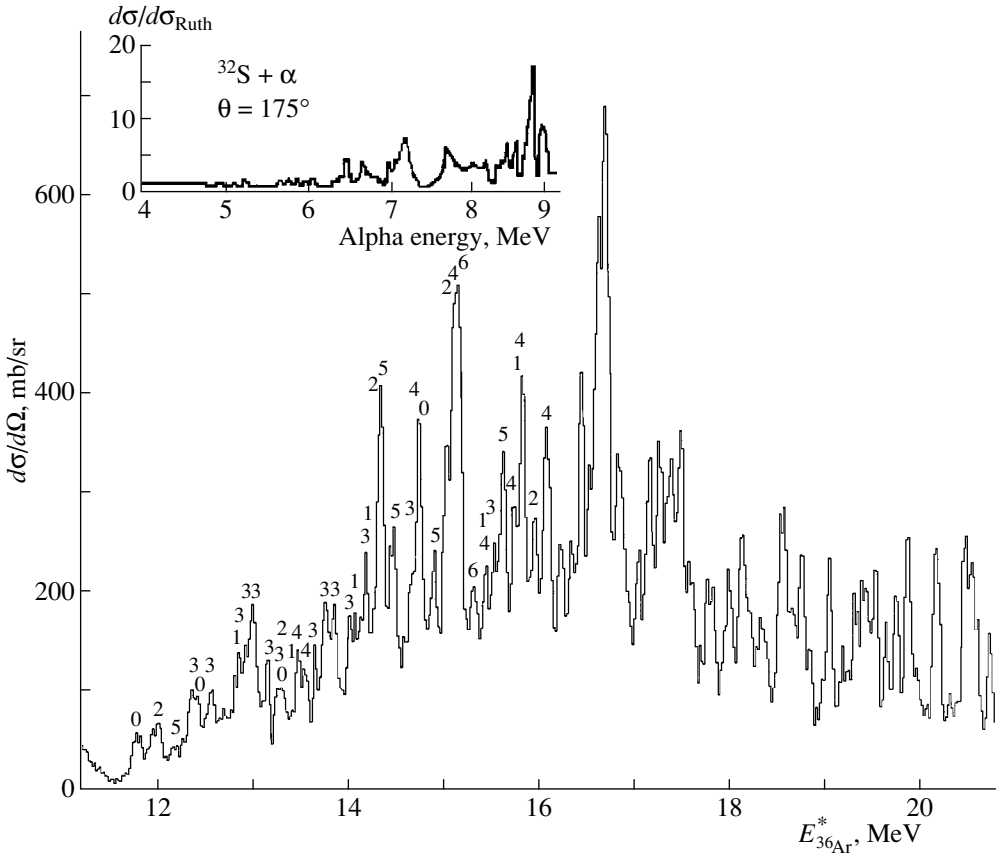

Fig. 3. Excitation function for elastic alpha-particle scattering on ^{32}S at 180° in the c.m. frame. Numbers above the peaks show the spins for corresponding resonances. Inset displays the α spectrum for elastic alpha-particle scattering on ^{32}S at 175° from [13]. An alpha-particle energy of 7 MeV in the inset corresponds to an excitation energy of 12.86 MeV in ^{36}Ar.

traditional setup, with that from a recent tandetron study [13] (the results of the latter are shown in the inset). The spectrum in the inset was obtained at 175° with a resolution of 25 keV and with 50-keV steps. The inset displays the values of absolute cross sections as ratios to the cross section for Rutherford scattering. A proper comparison shows that our cross sections are smaller by about 20%.

3. RESULTS

Figure 4 presents excitation functions measured at various laboratory angles of the detectors. (Approximately half of measured data are displayed.) For each specific curve, we show border values of c.m. angles for the low–high energy borders.

3.1. Treatment of Excitation Functions

The excitation functions were analyzed within the *R*-matrix approach [17]. Following the procedure outlined in [18] and successfully used by the Wisconsin group (see [6] and references therein), we partitioned the scattering amplitude into a nonresonance term and the sum of resonance partial waves.

For spinless particles, the scattering amplitude can be written as

$$f(\theta) = \rho(\theta)\exp(i\chi) - \frac{i}{2k}\sum_m (2l_m+1)\frac{\Gamma_{l_m}}{\Gamma} \times [\exp(2i\beta_{l_m}) - 1]\exp(2i\phi_{l_m})P_{l_m}(\cos\theta), \quad (3)$$

where ρ and χ are the background amplitude and the background phase shift, respectively; β_l is the resonance phase shift; and ϕ_l is the relative background phase shift. The cross section then takes the form

$$\frac{d\sigma}{d\Omega} = |f(\theta)|^2. \quad (4)$$

The resonance phase shift is given by

$$\beta_{l_m} = \arctan\left(\frac{\Gamma}{2(E_{\mathrm{res}_m} - E)}\right). \quad (5)$$

The background amplitude ρ was assumed to be a smooth function of energy and was interpolated by the lines connecting the set of energy points (five points for a 5-MeV excitation interval). In order to reduce the number of free parameters, the background phase shift

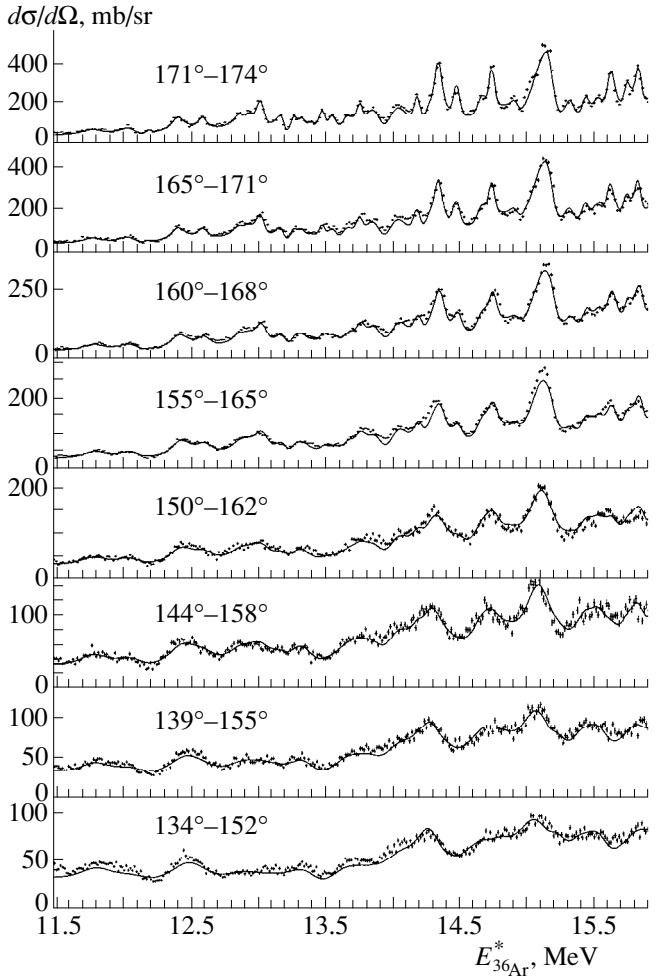

Fig. 4. Excitation functions at various angles. Solid curves represent an *R*-matrix fit convoluted with the experimental resolution.

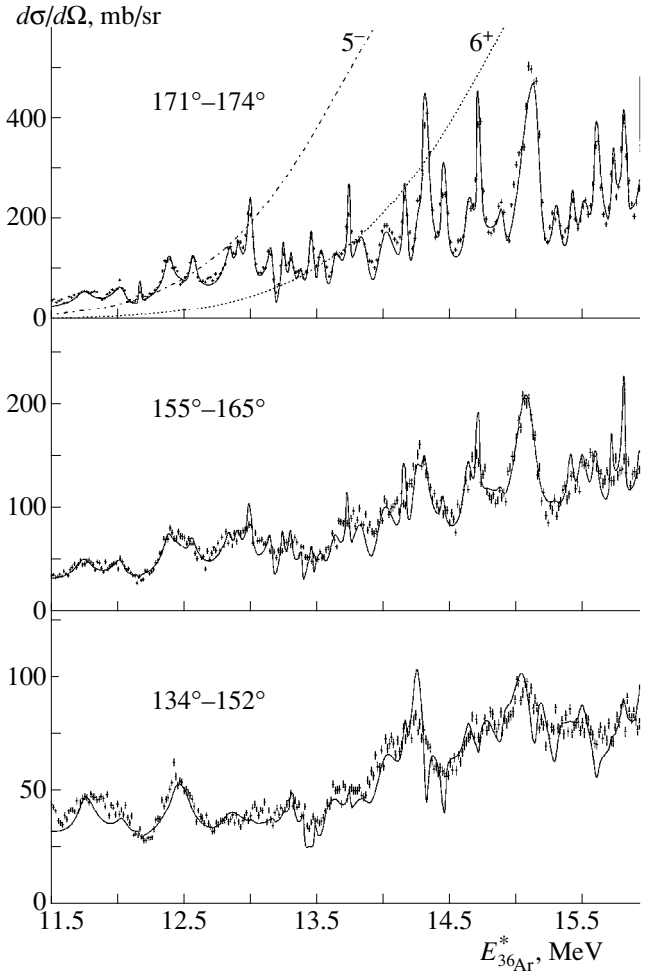

Fig. 5. Excitation functions at various angles for $^{32}S + \alpha$ elastic scattering with nonconvoluted theoretical curves obtained from an *R*-matrix fit. The dotted and dash-dotted curves in the figure for angles 171°–174° represent the energy dependence of the maximum cross-section value that could be observed in the present experiment for, respectively, spin-6 and spin-5 resonances.

χ was considered to be zero. The phase shifts ϕ_{l_m} were fixed for each resonance and were not varied with energy and angle. As was said above, the different parts of the excitation functions obtained by each detector placed at a certain position in the chamber correspond to different solid angles and different laboratory angles (apart from the zero-degree detector) and are measured with somewhat different resolutions. A transformation of the actual experimental conditions into calculated distributions convoluted with the actual experimental resolution was performed with a dedicated Monte Carlo code. A separate fitting code enabled us to compare the "ideal" calculated curves with the convoluted ones. Some "ideal" curves are presented in Fig. 5.

In our analysis, the fitting procedure was shown to consume the greatest part of time. We were unable to find a good searching procedure for regions populated by many interfering resonances. Therefore, a manual fit was made first, and a final computer fit with a routine χ^2 procedure followed. The values of each spin were checked at least twice for each resonance. The main idea of the fit was to identify resonances with "substantial" α widths. Our moderate energy resolution and a limited angular region did not allow identification of all possible states. However, a better overall fit provided more confidence in basic results. Also, weak resonances that were missed in the first approach were included in this second fit. Such weak, uncertain resonances were added only if their presence affected the distributions in the expected way.

The parameters of the extracted resonances were accumulated in the table. Some of the assigned widths are much less than the experimental resolution. This is possible owing to interference effects that are manifested up to three widths apart from the resonance. The widths of many resonances are close to the experimental resolution. In majority of such cases, the widths

Summary of resonance parameters

N	E_x, MeV	J^π	$\Gamma_{c.m.}$, keV	$\Gamma_\alpha/\Gamma_{tot}$, %	γ_α^2, keV	$\gamma_\alpha^2/\gamma_{WL}^2$, %	Ratio (9)
1	11.770	0^+	159	60	691	97	0.53
2	12.050	2^+	109	17	232	32	0.35
3	12.180	5^-	9	10	560	78	0.55
4	12.405	3^-	70	15	190	26	0.37
5	12.460	0^+	250	100	605	85	0.33
6	12.575	3^-	59	18	146	20	0.35
7	12.840	1^-	200	18	72	10	1.2
8	12.865	3^-	50	11	51	7	0.62
9	12.920	3^-	50	14	55	7	0.55
10	13.016	3^-	48	36	119	16	0.22
11	13.182	3^-	39	34	76	10	0.25
12	13.260	0^+	300	30	88	12	1.2
13	13.263	3^-	29	25	37	5	0.36
14	13.320	2^+	35	25	17	2	0.51
15	13.410	1^-	19	34	7	1	0.70
16	13.483	4^+	17	34	67	9	0.21
17	13.560	4^+	90	30	282	39	0.24
18	13.650	3^-	100	25	80	11	0.39
19	13.750	3^-	19	34	19	2	0.29
20	13.875	3^-	159	54	209	29	0.19
21	14.010	3^-	200	50	215	30	0.21
22	14.060	1^-	300	50	99	13	0.49
23	14.175	3^-	37	44	30	4	0.24
24	14.210	1^-	159	64	61	8	0.37
25	14.250	2^+	79	23	15	2	0.65
26	14.325	5^-	45	37	252	35	0.17
27	14.460	5^-	35	30	134	18	0.21
28	14.650	3^-	79	30	28	4	0.37
29	14.722	4^+	25	46	31	4	0.17
30	14.780	0^+	200	89	64	9	0.39
31	14.904	5^-	50	11	46	6	0.51
32	15.071	2^+	201	66	67	9	0.22
33	15.117	4^+	106	12	25	3	0.61
34	15.160	6^+	74	24	462	64	0.23
35	15.300	6^+	70	17	255	35	0.32
36	15.415	4^+	50	23	18	2	0.31
37	15.420	1^-	600	85	161	22	0.25
38	15.495	3^-	79	23	12	1	0.44
39	15.595	5^-	50	31	61	8	0.18
40	15.715	4^+	25	25	7	1	0.29
41	15.800	1^-	150	30	12	1	0.64
42	15.813	4^+	19	37	8	1	0.19
43	15.940	2^+	39	34	4	1	0.38
44	16.065	4^+	100	38	37	5	0.18

could not be defined to a high precision. There is a dilemma to make a peak either narrower and higher or broader and lower. We have noticed a tendency of experimentalists to create a nonconvoluted spectrum closer to the observed one. This is the reason why, in many cases, the widths presented for sharp resonances in fact represent an upper limit on the width. Data on the absolute values of α widths are much more reliable (their precision is higher than 15%), because these are defined by the product of the width and of the peak height.

A much broader excitation-energy region was covered in the analysis. Therefore, the effect of far-away resonances on the high-energy border of the displayed data is taken into account.

The table also quotes the reduced α widths in units of the Wigner limit. As usual, $\Gamma_\alpha = 2P_l\gamma_\alpha^2$, and the Wigner limit, γ_{WL}^2, is equal to $3\hbar^2/2\mu R^2$. The channel radius R used to calculate the Wigner limit and the penetrability factors P_l was chosen to be 5 fm. In all, we have obtained data on more than forty new quasistationary states in the ^{36}Ar nucleus.

In order to interpret our results appropriately, it is necessary to know the main experimental restrictions that limit our observation of states characterized by large α widths. The low-energy limit of the present measurements is close to the value of the Coulomb barrier. High-spin levels must be very narrow because of penetrability factors; being convoluted with the experimental resolution, they can be unobservable against the background of Coulomb scattering and lower spin states. It is expected that the total width of high-spin states is controlled primarily by the alpha-particle partial widths because the penetrability factors favor alpha decay. Figure 5 displays the evaluated cross sections convoluted with the experimental resolution for spin-5 and spin-6 resonances near the low-energy edge. The curves give the highest limit on cross sections that is reached when the total width of a resonance is equal to its α width. The maximum widths of resonances were evaluated on the basis of a potential model, but the result is in fact governed by the penetrabilities. From Fig. 5, we can see that, by means of our technique, it is hardly possible to observe spin-6 resonances within the excitation region around 12 MeV; spin-5 resonances are still observable, but they can manifest themselves as rather small peaks. On the other hand, low-spin resonances could be very broad at higher energy; because of the factor $(2J + 1)$, they must be weak in relation to high-spin ones. An analysis revealed that spin-zero resonances of width $\Gamma_\alpha \geq 0.3\Gamma_{tot}$ could be observed by the interference picture.

3.2. Does the Observed Structure Represent Statistical Fluctuations?

A general picture of rather broad well-separated structures having widths in the range 20–200 keV and a regular appearance at different scattering angles deviates considerably from the picture of simple Ericson fluctuations [19]. Estimates based on the expressions given in [20] show that the density of states in the excitation region being investigated increases by one order of magnitude from a few hundred units per MeV at the low-energy border, the average total width of a statistical state being changed from a few keV to 20 keV. It is obvious that general features of the excitation function (averaged over experimental resolution) are stable even to some drastic changes in the statistical background. It should also be noted that a regular change in the interference picture in response to sign reversal is incompatible with the fluctuation picture. Sign reversals are obvious in the analysis and can be seen in Fig. 5 at 13.5 and 14.5 MeV, where spin-4 and spin-5 resonances are present. Figure 6 illustrates a formal analysis of the angular correlation function for the excitation region around 12 MeV, where we found two 3^- levels and a broader 0^+ level. The dashed curve shows the expected behavior of the angular correlation function for the pure case of a compound nucleus (Ericson fluctuations), while the solid curve represents the experimental result. Figure 6 shows that these two curves are very different, especially in view of the fact that the experimental curve has a maximum at 145°. At this angle, any angular correlations of Ericson fluctuations are expected to be broken. Differences in absolute value are generally related to a contribution of direct processes (experimental curve), which always allow correlations.

As a first step, one can try to estimate compound-nucleus absorption within simple statistical models. Neglecting direct contributions, we can decompose the total resonance width as

$$\Gamma_J^{\text{tot}} = \Gamma_J^{\alpha} + \Gamma_J^{\downarrow}, \tag{6}$$

where Γ_J^{α} is the entrance-channel width, while $\Gamma_J^{\downarrow}$ is the compound-nucleus-spreading width of the resonance. The total spreading width of the spin-J resonance can be broken down into the elastic α width and the sum over all other decay widths:

$$\Gamma_J^{\text{tot}\downarrow} = \Gamma_J^{\text{CN}\to\alpha} + \sum_i \Gamma_J^{\text{CN}\to i}. \tag{7}$$

In the case of an idealized compound nucleus, we have $\Gamma_J^{\alpha} = \Gamma_J^{\text{CN}\to\alpha}$ and

$$\frac{\Gamma^{\text{tot}\downarrow}}{\Gamma_J^{\text{CN}\to\alpha}} = \frac{P_{J\alpha} + \sum_i P_{J_i}}{P_{J\alpha}}, \tag{8}$$

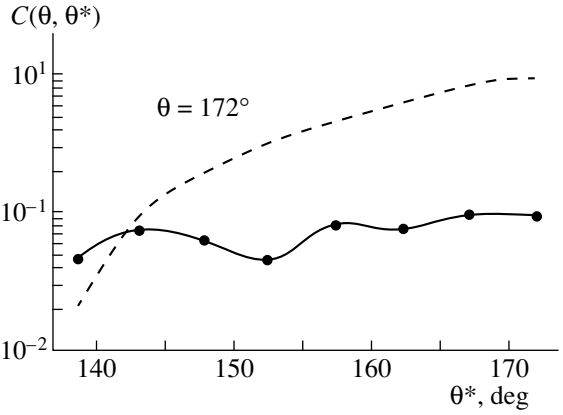

Fig. 6. Experimental angular correlation function averaged over 400 keV at an excitation energy of 12.4 MeV (solid curve) and expected behavior of the angular correlation function for a pure compound-nucleus Ericson fluctuation (dashed curve).

where P_J are penetrabilities. For purely statistical resonances, we therefore have

$$\frac{\Gamma^{\text{tot}\downarrow}}{\Gamma_J^{\text{CN}\to\alpha}} \frac{P_{J\alpha}}{P_{J\alpha} + \sum_i P_{J_i}} = 1. \tag{9}$$

Using Eq. (9), one can now estimate the contribution of compound-nucleus formation to the resonance width. If the ratio on the right-hand side of (9) is close to unity, then it is the compound nucleus that makes a dominant contribution. The lower the ratio, the smaller the compound-nucleus contribution. The values of this ratio are quoted in the table for all resonances observed in the present study. As can be seen from the table, the average experimental ratio is about 0.3. This value must be treated as an upper limit (because of the "human" factors mentioned above). This fact only highlights the unusually large α width of each observed resonance.

3.3. General Review of the Results

Spin-zero levels. The broad and strong levels near 12 MeV are obvious in the entire angular region of the present measurements and are dominant at the largest angles. Their summed α width is about 200% of the Wigner limit. The other two, much weaker 0^+ levels at higher energies, were included largely because of interference effects.

Spin-1 levels. As a rule, spin-1 levels were obvious in the entire energy region. Tentative assignments are given for the weak levels nos. 7, 15, and 41. Indeed, level no. 7 was included after the study reported in [13], where a tentative 1^- assignment was given to a broad structure in this region. The inclusion of this level improved the agreement with data at the largest angles. There is no single 1^- level with a dominant reduced α

width. The sum of the reduced widths of the observed 1^- levels is about 40% of the Wigner limit.

Spin-2 levels. Five spin-2 levels have been found in the region investigated here. The most intense spin-2 level (no. 32) is not reliable, because several other intense levels overlap it. The sum of the reduced widths of the observed 2^+ levels is about 50% of the Wigner limit.

Spin-3 levels. Fourteen 3^- levels have been found in the region. The authors of [13] reported a spin-3 resonance as the result of the Regge pole analysis of the angular distributions for the elastic scattering of 7.7-MeV alpha particles on a ^{32}S target. This energy obviously corresponds to the group at 13.5 MeV in our measurements, where two 4^+ and two 3^- states could have contributed to their data. Unfortunately, a more straightforward comparison with data from [13] is not possible. The sum of the reduced widths of the observed 3^- levels is 170% of the Wigner limit.

Spin-4 levels. Eight 4^+ levels have been found in the region investigated here. Their total width is about 60% of the Wigner limit. A dominant contribution to the sum comes from two nearby levels in the vicinity of 13.5 MeV.

Spin-5 levels. Five 5^- states have been found in the region being discussed. Evidence for a 5^- state at 12.2 MeV with a "large" reduced width was reported in [14]. It was found from a measurement of (d, α) angular correlations in the reaction ^{32}S(^{6}Li, d)^{36}Ar(α). As was shown above, observation of high-spin states at low excitation energies is restricted by our experimental resolution. Let us consider this level as a specific example. If we take the Wigner limit to estimate the width of the state, its natural width will be 2 keV. A few other decay channels are possible for this state, but, because of poor penetrability factors, we may take into consideration only the protonic decay to the ground state in ^{35}Cl. The penetrability factor for this protonic decay could be ten times as great as (with the lowest possible orbital angular momentum) that for alpha decay. Therefore, a 20-keV width can be considered as a good estimate for an upper limit on the width of the state in question. A small anomaly at 12.18 MeV is seen in our spectra obtained in measurements near zero degree. The anomaly, which actually manifests itself as a spin of 5 in the angular distribution, can be described as a spin-5 resonance with $\Gamma_\alpha \le 0.1\Gamma_{tot}$, Γ_{tot} being equal to 9 keV. The agreement between the excitation energy obtained in the two studies seems too good if we take into account a 500-keV energy resolution in [14] and difficulties in observing a level characterized by so small a ratio of $\Gamma_\alpha/\Gamma_{tot}$ in the $d\alpha$ coincidence measurements. We can easily obtain the same description of the anomaly if we increase $\Gamma_\alpha/\Gamma_{tot}$ up to 0.25 and simultaneously decrease the width of the resonance down to 1.4 keV. Our experimental resolution gives no way to distinguish between the two cases. (However, it is worth noting that the reduced width increases only by 15% in the second case.) In principle, the width of this 5^- level can be obtained in a very high-resolution study of alpha-particle scattering. Another way is to make $d\alpha$ coincidence measurements in a (^{6}Li, d) reaction with an energy resolution commensurate with that in [10, 11] to determine the ratio $\Gamma_\alpha/\Gamma_{tot}$. Knowing this ratio, we can fix Γ_{tot}. Also, it is important to note that, if we move the 5^- level by a few hundred keV to the low-energy border of our measurements, it becomes too narrow to be observed by resonance scattering. However, the reduced α width (spectroscopic factor) is not changed, and it is still large, allowing observation of this level in a stripping reaction. The above considerations show how resonance-scattering studies and investigations of direct reactions supplement each other. The sum of the reduced widths of the observed 5^- levels is about 150% of the Wigner limit.

Spin-6 levels. Two nearby 6^+ levels have been found in the present study. The sum of their reduced widths is close to the Wigner limit. Artemov *et al.* [14] found a 6^+ state at 15.4 MeV with a "large" reduced width. The agreement within 100 keV between the results of the two groups seems very good (see comments to spin-5 levels). Obviously, they should have observed two 6^+ levels as a single group.

4. DISCUSSION

Clearly, our investigation is far from complete. Therefore, it is too early to analyze level distributions and their group assignments to specific bands. For this purpose, it would be very important to obtain data in the low-excitation region in ^{36}Ar, as was done in [10, 11] for the neighboring nuclei. Nevertheless, even our present results allow a few general conclusions.

It is clear that an α-cluster structure distinctly manifests itself in the ^{36}Ar excitation region investigated here. This follows from the fact that the reduced width of a few levels with a well-defined spin saturates a significant fraction of the Wigner limit. It is important to recall that the majority of microscopic models select shell-model states that contribute to α-structure configurations, along with the *SU*(3) classification of levels. For the majority of cluster states in light nuclei, the *SU*(3) classification [21, 22] provides a good approximation for the relevant wave function. Beyond the mass of 28, spin–orbit forces become too strong and ruin the symmetry underlying the model.

The α-cluster structure fragments into several states with the same spin. For example, thirteen 3^- states occupy an excitation region of about 2 MeV. The compound-nucleus density of 3^- states was estimated according to the expressions from [20]. The estimate (about 100 compound-nucleus 3^- states per 1 MeV at the excitation energy of 14.5 MeV in ^{36}Ar) shows that the density of statistical states is only ten times as high as the observed one and increases threefold along the interval of 2 MeV. The majority of the levels are broad-

ened because of decay modes other than alpha decay. Only a few decay modes can compete with alpha decay because of small penetrability factors. It is obvious that protonic decay to the lowest states in ^{35}Cl must play an important role in the broadening of the observed states and that the reduced widths for protonic decays are also large. All in all, it seems that our experimental data give a good basis for specific interpretations, and it appears to be promising to seek a description of the observed picture within the doorway-state approach with particle–hole states as states "of the lowest complexity" [23].

Our data show that there are no relatively broad regions (about 500 keV) where levels with the same spin value would be absolutely dominant. There are excitation regions spanning 2 to 3 MeV and containing levels of the same spin, but they are interlaced with levels of other spins in between. Frekers *et al.* [7] found quite a different picture in the ^{44}Ti nucleus at approximately the same excitation energy. They observed a few separated intermediate resonances of widths between 0.2 and 0.5 MeV with different spins. It looked like each group was created by sharp fine-structure resonances of the same spin. The reason for this difference between ^{36}Ar and ^{44}Ti is not clear to us.

We could not find experimental information to relate the present data with the α-cluster structure at lower excitation energies in ^{36}Ar. However, there is convincing evidence that the α-cluster structure manifests itself from the lightest nuclei (like ^{6}Li) up to at least ^{44}Ti. The success of local-potential models (see [24, 25] and references therein) highlights this common feature of nuclear structure. Assuming that the local α–nucleus potential is basically the same for the alpha-particle interactions with ^{32}S, ^{36}Ar, and ^{40}Ca, we will try to employ data of Yamaya *et al.* [10, 11] in the present discussion. In their study of (^{6}Li, *d*) reactions, those authors could follow the α-cluster structure from the ground states of ^{40}Ca and ^{44}Ti up to excitation energies about 11 MeV. Figure 7 presents the data on the positions and on the spectroscopic factors of the 3^- and 5^- α-cluster states in ^{44}Ti and ^{40}Ca (as given in [10, 11]), along with our data for the ^{36}Ar nucleus. As can be seen from Fig. 6, a straight extrapolation from the data reported in [10, 11] leads to the middle of distributions of 3^- and 5^- states found in the present study. However, one should be very careful in extrapolating data obtained for different nuclei along the excitation energy values. Indeed, the $A^{2/3}$ dependence of the relative level positions in nuclei with different mass numbers A is inherent in local-potential models. Changes in the averaged excitation energies of the levels with the same spin in ^{44}Ti and ^{40}Ca are too large (about 2 MeV) to be explained by 6% changes in the $A^{2/3}$ factor. Also, it is well known that, as a rule, the ground states of nuclei are not coupled to α-cluster degrees of freedom. It is more natural to consider the excitation energies of α-cluster states relative to the threshold for alpha decay. In this case, the excitation energies of the ^{44}Ti and ^{40}Ca levels in question agree very well, as can be seen from

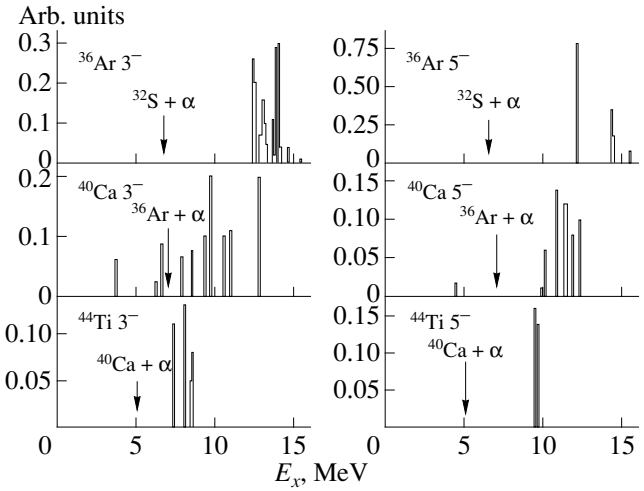

Fig. 7. Comparison of 3^- and 5^- levels in ^{36}Ar, ^{40}Ca, and ^{44}Ti. Data for ^{40}Ca and ^{44}Ti were taken from [10, 11].

Fig. 7. An extrapolation from ^{44}Ti through ^{40}Ca to ^{36}Ar leads to positions of 5^- states exactly at the excitation energy of 12.2 MeV in ^{36}Ar, where the 5^- state at 12.18 MeV was found, while the extrapolated positions for 3^- states are about 2 MeV lower than the low-energy border of the present measurements. On this basis, we expect some mixture of 3^- and 1^- states with large α widths in the excitation region 9–11 MeV in ^{36}Ar, the 3^- states and the 1^- states being, respectively, relatives of the states observed in ^{40}Ca and the members of a new band seen in the present measurements. The same arguments provide a very good correspondence between the 10.86-MeV 0^+ state in ^{44}Ti, which is believed to be a candidate for the bandhead of a higher nodal state (N = 14) [10, 11, 26], and the block of the 0^+ states found in the present study near 12 MeV.

5. SUMMARY AND CONCLUSIONS

The α-cluster structure of atomic nuclei has been investigated for a long time. However, new and important experimental results in the region from the ^{32}S to the ^{44}Ti nucleus [4, 10, 11, 14], as well as a flow of recent theoretical studies (see [24, 25, 27, 28] and references therein), show that interest in this realm has been rekindled. We hope that the present work, which has provided the first detailed investigation of a broad excitation energy region in ^{36}Ar, will contribute to a fast accumulation of new data.

We believe that this interest is related not only to the fact that α-cluster degrees of freedom is important for a broad region of nuclear mass numbers but also to the new features observed in extensive regions of excitation energies. Probably, at high excitation energies, the α-cluster structure gives rise to a doorway picture, bringing some order in the chaos assumed there. This article also provides an example of a detailed treatment of data obtained by our thick-target inverse-kinematics

method. Our results (over 40 new level assignments) are expected to give impetus to further applications and improvements of the method itself. Finally, we would like to emphasize the importance of a combined investigation of the α-cluster structure in both resonance and direct reactions.

ACKNOWLEDGMENTS

We gratefully acknowledge the support of the Academy of Finland. The work of the Russian physicists was supported by the Russian Foundation for Basic Research (project no. 97-02-17113).

REFERENCES

1. A. H. Wuosmaa, R. R. Betts, M. Freer, and B. R. Fulton, Annu. Rev. Nucl. Part. Sci. **45**, 89 (1995).
2. P. A. Butler and W. Nazarewicz, Rev. Mod. Phys. **68**, 349 (1996).
3. P. Manngård, Z. Phys. A **349**, 335 (1994).
4. M. Brenner, Z. Phys. A **349**, 233 (1994).
5. K.-M. Källman, Z. Phys. A **356**, 287 (1996).
6. C. A. Davis and R. Abegg, Nucl. Phys. A **571**, 265 (1994).
7. D. Frekers, R. Santo, and K. Langanke, Nucl. Phys. A **394**, 189 (1983).
8. V. Z. Goldberg *et al.*, Yad. Fiz. **60**, 1186 (1997) [Phys. At. Nucl. **60**, 1061 (1997)].
9. T. Yamaya *et al.*, Phys. Rev. C **42**, 1935 (1990).
10. T. Yamaya *et al.*, Nucl. Phys. A **573**, 154 (1994).
11. T. Yamaya *et al.*, Phys. Rev. C **53**, 131 (1996).
12. J. P. Aldridge, G. E. Crawford, and R. H. Davis, Phys. Rev. **167**, 1053 (1968).
13. A. Coban *et al.*, Nucl. Phys. A **645**, 3 (1999).
14. K. P. Artemov, M. S. Golovkov, V. V. Pankratov, and V. P. Rudakov, Yad. Fiz. **61**, 13 (1998) [Phys. At. Nucl. **61**, 9 (1998)].
15. K. P. Artemov *et al.*, Yad. Fiz. **52**, 634 (1990) [Sov. J. Nucl. Phys. **52**, 408 (1990)].
16. V. Z. Goldberg and A. E. Pakhomov, Yad. Fiz. **56** (9), 31 (1993) [Phys. At. Nucl. **56**, 1167 (1993)].
17. A. M. Lane and R. G. Thomas, Rev. Mod. Phys. **30**, 257 (1958).
18. S. R. Riedhauser, Phys. Rev. C **29**, 1961 (1984).
19. T. Ericson, Phys. Lett. **4**, 258 (1963).
20. A. Gilbert and A. G. W. Cameron, Can. J. Phys. **43**, 1446 (1965).
21. M. Harvey, Adv. Nucl. Phys. **1**, 67 (1968).
22. J. P. Elliot, Proc. R. Soc. London, Ser. A **245**, 128 (1958).
23. C. Mahaux and H. A. Weidenmueller, *Shell-Model Approach to Nuclear Reactions* (North-Holland, Amsterdam, 1969).
24. J. Zhang, A. C. Merchant, and W. D. Rae, Nucl. Phys. A **613**, 14 (1997).
25. F. Michel, S. Okhubo, and G. Reidemeister, Prog. Theor. Phys. **132**, 7 (1998).
26. S. Okhubo and K. Umehara, Prog. Theor. Phys. **80**, 598 (1988).
27. U. Abbondanno, N. Cindro, and P. M. Milazzo, Nuovo Cimento A **110**, 955 (1997).
28. A. S. B. Tariq, A. F. M. M. Rahman, S. K. Das, *et al.*, Phys. Rev. C **59**, 2558 (1999).

Physics of Atomic Nuclei, Vol. 63, No. 9, 2000, pp. 1527–1532. Translated from Yadernaya Fizika, Vol. 63, No. 9, 2000, pp. 1612–1617.

NUCLEI
Theory

α^8Be Cluster Model for the 0_2^+ Resonance in the ^{12}C Nucleus

I. N. Filikhin

Institute of Physics (Petrodvorets Branch), St. Petersburg State University, Ul'yanovskaya ul. 1, Petrodvorets, 198904 Russia

Received April 27, 1999

Abstract—The 0_2^+ resonance in the ^{12}C nucleus is treated on the basis of the $\alpha + {}^8$Be two-cluster model. An equation for the function describing the relative motion of the clusters is derived by using the *s*-wave differential Faddeev equations for the 3α system and by relying on the simplest version of the resonating-group method. A phenomenological potential is taken to simulate the pair $\alpha\alpha$ interaction. A three-body potential binding three alpha particles together gives rise to a resonance in two-cluster $\alpha + {}^8$Be scattering. The calculated resonance features and the calculated parameters of the wave function of the system are compared with the results obtained by other authors. © *2000 MAIK "Nauka/Interperiodica".*

1. INTRODUCTION

The 0_2^+ resonance in the ^{12}C nucleus plays a crucial role in the stellar production of carbon, since carbon nuclei are generated in reactions involving three alpha particles. In order to explain carbon abundances, it is necessary to assume that there exists some intermediate state through which this reaction proceeds [1]. It is agreed that the 0_2^+ resonance of the ^{12}C nucleus plays the role of this intermediate state. The experimental values of the parameters of this resonance are E_r = 0.3796 MeV and Γ = 8.5 eV [2].

Low-lying resonance states of the ^{12}C nucleus, including the 0_2^+ resonance, were analyzed in a number of studies. The structure of a resonance state was determined either within the $\alpha\alpha\alpha$ three-particle model or within the α^8Be two-particle model. A microscopic approach based on the resonating-group method (RGM) was used in [3–5]. Within the 3α cluster model for the ^{12}C nucleus, Hiyama *et al.* [6] solved the Schrödinger equation via an expansion in the basis of Gaussian functions. The $\alpha\alpha$ potential used in [6] leads to an excessively high binding energy for the 3α system. A correct value of the ^{12}C binding energy was obtained in [6] by additionally including a three-body potential that increases Coulomb repulsion between the alpha-particle clusters. Fedorov and Jensen [7] considered the system of three structureless alpha particles on the basis of the differential Faddeev equations, which they solved at positive energies by the adiabatic-expansion method. By adjusting the parameters of the three-body attractive interaction added to the pair $\alpha\alpha$ potential, those authors were able to reproduce the experimental values of the energy and the width of the 0_2^+ resonance in the ^{12}C nucleus. However, their model overestimates the ground-state energy of the ^{12}C nucleus. In contrast to the pair potential, the three-body interaction used in [7] does not depend on the angular variables specifying the orientation in subsystems. It was found [8] that the amplitude for the breakup of systems similar to that considered here has some special features that are due to resonances in the two-body subsystems, but which have nothing to do with three-body resonances. In view of this circumstance, which was disregarded by Fedorov and Jensen [7], their results cannot be considered as unambiguous evidence for the truly three-body character of the 0_2^+ resonance in the ^{12}C nucleus. A relativistic approach to studying the 3α cluster system was employed in the recent qualitative analysis of Hong and Lee [9], who relied on effective-potential theory.

In the present study, the 0_2^+ state of the ^{12}C nucleus is treated as a resonance of α^8Be two-cluster scattering in the $\alpha\alpha\alpha$ system. Our model hinges upon the following premise: the decay of the 0_2^+ resonance in ^{12}C nucleus proceeds through the process $^8\text{Be} + \alpha \longrightarrow \alpha + \alpha + \alpha$. According to experimental data, this channel is much more probable than the mode of direct decay into three alpha particles [10]. The contribution of the three-body-breakup amplitude to the total amplitude for the decay of the 0_2^+ resonance amounts to 4%. In order to derive effective equations describing the relative motion of the clusters in the $\alpha + {}^8$Be system, we make use of the differential Faddeev equations [11], which are reduced by taking into account the two-particle clustering of the 0_2^+ resonance in the ^{12}C nucleus—in other words, we invoke a method analogous to the RGM. As to the breakup and rescattering amplitudes, they are neglected in this approach. The short-range interaction between two alpha particles is simulated by the phenomenological potential from [12]. Of particu-

1063-7788/00/6309-1527$20.00 © 2000 MAIK "Nauka/Interperiodica"

lar interest are the three-body α-cluster-interaction potentials that were proposed in [13] for ^{12}C and in [14] for $^{12}_{\Lambda}$C, these nuclear species being treated on the basis of, respectively, the 3α and the Λααα cluster model. In [13], the parameters of the three-body potential were chosen in such a way as to reproduce the known values of the binding energy, the root-mean-square radius, and the charge form factor for the ^{12}C nucleus. The parameters of the resonance in the ^{8}Be + α system are calculated by using the energy dependence of the relevant phase shift. The resonance obtained in this way is interpreted as the 0_2^+ resonance in the ^{12}C nucleus.

The ensuing exposition is organized as follows. In Section 2, we give an account of our model and formulate the boundary-value problem for the function describing the relative motion of the clusters in the ^{8}Be + α system. In Section 3, we present the results of our calculations for the ^{8}Be ground state, which corresponds to the 0^+ resonance in alpha-particle scattering by an alpha particle; we also consider ^{8}Be + α two-cluster scattering at energies above the three-particle threshold and calculate relevant phase shifts and the parameters of the 0_2^+ resonance.

2. DESCRIPTION OF THE MODEL

Let us consider a system of three identical charged spinless particles having no internal structure. This system can be described by the differential Faddeev equations modified in such a way that the Coulomb interaction potential is included in the unperturbed Hamiltonian [11]. For systems of identical particles, the Faddeev equations take the simplest form (previously, rich experience was gained in applying these equations to such systems—see [15, 16]) and reduce to an equation for the component U of the total wave function:

$$(H_0 + V^{\mathrm{Coul}} + V_3 + V - E)U = -V(P^+ + P^-)U.$$

Here, H_0 is the kinetic-energy operator; the operators $P^{\pm}$ execute cyclic permutations of the particles in the system; V is the potential simulating the short-range two-body interactions of the particles; V^{Coul} is the Coulomb potential represented as $V^{\mathrm{Coul}} = V_{12}^{\mathrm{Coul}} + V_{13}^{\mathrm{Coul}} + V_{23}^{\mathrm{Coul}}$, where V_{ik}^{Coul} is the potential of the Coulomb interaction between particles i and k; and V_3 is the three-body-interaction potential in the system under study. The potential V_3 depends on the positions of the particles with respect to the center of mass of the system as $V_3 = V_3(\rho)$, where $\rho^2 = \sum_{i=1}^{i=3}\mathbf{r}_i^2$, $\mathbf{r}_i$ being the radius vectors of the particles.

The system of three alpha particles will be considered here in the s-wave approximation—that is, the total orbital angular momentum of the system and the individual orbital angular momenta of all subsystems are set to zero. The Faddeev component U is a function of the relative coordinates

$$\mathbf{x} = \mathbf{r}_2 - \mathbf{r}_1, \quad \mathbf{y} = \frac{1}{2}(\mathbf{r}_2 + \mathbf{r}_1) - \mathbf{r}_3.$$

The s-wave Faddeev equation is an equation for the coordinate part $\mathcal{U}(x, y)$ of the Faddeev component U. Its specific form is

$$(h_0 + V^{\mathrm{Coul}}(x, y) + V_3(\rho) + V_{\alpha\alpha}(x) - \varepsilon)\mathcal{U}(x, y) = -V_{\alpha\alpha}(x)\int_{-1}^{1} d\mu \frac{xy}{x'y'}\mathcal{U}(x', y'), \quad (1)$$

where $x = |\mathbf{x}|$, $y = |\mathbf{y}|$, and $h_0 = -\frac{3}{4}\partial_y^2 - \partial_x^2$ is the kinetic-energy operator as expressed in terms of the relative coordinates, and

$$x' = \left[\frac{x^2}{4} + y^2 - xy\mu\right]^{1/2},$$

$$y' = \left[\left(\frac{3x}{4}\right)^2 + \frac{y^2}{4} + \frac{3}{4}xy\mu\right]^{1/2}.$$

The Coulomb potential $V^{\mathrm{Coul}}(x, y)$ is given by

$$V^{\mathrm{Coul}}(x, y) = n/x + 2\frac{n}{r_>},$$

where $r_> = \max\{x/2, y\}$ and $n = 4m_\alpha e^2/\hbar^2$ ($n = 0.556$ fm^{-1}). The short-range pair interaction between the alpha particles is simulated by the s-wave component of the Ali–Bodmer potential [10]; that is, we set

$$V_{\alpha\alpha}(r) = (V_1 \exp(-(r/b_1)^2) + V_2 \exp(-(r/b_2)^2))\frac{m_\alpha}{\hbar^2},$$

where $V_1 = 125$ MeV, $b_1 = 1.53$ fm, $V_2 = -30.18$ MeV, $b_2 = 2.85$ fm, and $\hbar^2/m_\alpha = 10.44$ MeV fm^2. The three-body potential $V_3(\rho)$ is taken in the form

$$V_3(\rho) = V_0 \exp(-(\rho/\beta)^2)\frac{m_\alpha}{\hbar^2}, \quad (2)$$

where $\rho^2 = (2/3)y^2 + (1/4)x^2$, $V_0 = -24.32$ MeV, and $\beta = 3.795$ fm. These values were obtained in [13] by simultaneously fitting the binding energy, the root-mean-square radius, and the charge form factor for the ^{12}C nucleus within the 3α cluster model based on the differential Faddeev equations. The relevant boundary-value problem reduces to equation (1) with zero boundary conditions for $x, y \longrightarrow \infty$. In the present study, equation (1) is used to describe the system of three alpha particles at energies above the three-particle threshold. The 0_2^+ state is treated as a resonance of α^8Be two-cluster scattering in the 3α system. Alpha-particle scattering

by a ^{8}Be nucleus corresponds to the following asymptotic representation of the function $^0\mathcal{U}(x, y)$ for $y \longrightarrow \infty$:

$$^0\mathcal{U}(x, y) \sim \chi_0(x)(F_0(\eta, py) - a(p)G_0(\eta, py)). \quad (3)$$

Here, $(3/4)p^2 = \varepsilon - \varepsilon_0$; $\eta = (4/3)n/p$; and $F_0(\eta, \rho)$ and $G_0(\eta, \rho)$ are, respectively, the regular and the irregular Coulomb function. The energy ε_0 of the quasistationary state in the $\alpha\alpha$ system (^{8}Be nucleus) exceeds the two-particle threshold. This state is described by a function $\chi_0(x)$ specified below. The phase shift δ_0 is related to the amplitude $a(p)$ by the equation $a(p) = \tan(\delta_0)$. It should be noted that terms associated with breakup and rescattering are ignored in equation (3) [11].

The solution $^0\mathcal{U}(x, y)$ to equation (1) is represented as the product of the function $\chi_0(x)$ describing the two-body cluster and the function $f(y)$ describing the relative motion of the clusters:

$$^0\mathcal{U}(x, y) = \chi_0(x) f(y). \quad (4)$$

The function $\chi_0(x)$ is determined by the solution to the following boundary-value problem for the Hamiltonian of the two-body subsystem: this function must obey the equation

$$(-\partial_x^2 + V_{\alpha\alpha}(x) + n/x)\chi_0(x) = \varepsilon_0\chi_0(x) \quad (5)$$

and zero boundary condition at the origin, $\chi_0(0) = 0$, and its asymptotic behavior for $x \longrightarrow \infty$ must be

$$\chi_0(x) \sim F_0(\eta_0, p_0x) - a_0(p_0)G_0(\eta_0, p_0x),$$

where $p_0^2 = \varepsilon_0$ and $\eta_0 = (1/2)n/p_0$. The function $\chi_0(x)$ is normalized to unity over a sufficiently large domain of size R_x:

$$\int_0^{R_x} \chi_0^2(x)dx = 1.$$

A projection procedure reduces equation (1) to an integro-differential equation for the function $f(y)$ describing the relative motion of the clusters. Specifically, we have

$$\left(-\frac{3}{4}\partial_y^2 + V_{\text{eff}}^3 + V_{\text{eff}}^{\text{Coul}} - \frac{3}{4}p^2\right)f(y) + (V_{\text{eff}}f)(y) = 0, \quad (6)$$

where

$$V_{\text{eff}}^3(y) = \int_0^{R_x} V_3(\rho)\chi_0^2(x)dx,$$

$$V_{\text{eff}}^{\text{Coul}}(y) = \int_0^{R_x} \frac{2n}{r_>}\chi_0^2(x)dx,$$

$$(V_{\text{eff}}f)(y) = \int_0^{R_x} dx \int_{-1}^{1} d\mu\chi_0(x)V_{\alpha\alpha}(x)\frac{xy}{x'y'}\chi_0(x')f(y').$$

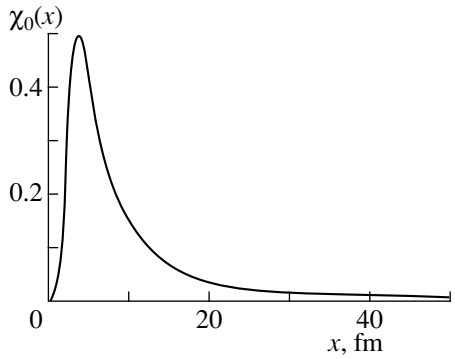

Fig. 1. Function $\chi_0(x)$ for the 0^+ resonance of $\alpha\alpha$ scattering at $\varepsilon_0 = 0.095$ MeV.

The asymptotic boundary conditions for the function $f(y)$ in the limit $y \longrightarrow \infty$ are derived from formula (3) by applying the projecting procedure. The result is

$$f(y) \sim F_0(\eta, py) - a(p)G_0(\eta, py).$$

3. RESULTS OF THE CALCULATIONS

In this section, we present the results obtained by numerically solving the effective equation (6) for the function $f(y)$ describing the relative motion of the clusters. The function $\chi_0(x)$ appearing to be a normalized solution to the boundary-value problem (5) was calculated preliminarily. The parameter R_x specifying the asymptotic domain in the variable x was taken to be 50 fm. The function $\chi_0(x)$ is plotted in Fig. 1. The parameters of the resonance state in the $\alpha\alpha$ system were derived from the energy dependence of the s-wave phase shifts for $\alpha\alpha$ scattering in the vicinity of the two-particle threshold. The results of our calculation comply with experimental data. The values obtained in the present study for the resonance energy and the resonance width are $E_r = 0.095$ MeV ($E_r^{\text{expt}} = 0.092$ MeV) and $\Gamma = 10$ eV ($\Gamma^{\text{expt}} = 6.8$ eV).

Equation (6) for the function $f(y)$ was discretized in y on a uniform grid. The asymptotic domain was defined by the parameter $R_y = 50$ fm. It is worth noting that variations in the parameters R_x and R_y in the vicinity of the values chosen for them do not affect the results of our calculations. By numerically solving the equation for the function $f(y)$, we determined the phase shifts for α^8Be scattering at energies above the 3α threshold. The phase shifts for α^8Be scattering are shown in Fig. 2, where the energy of relative motion in the c.m. frame is reckoned from the threshold for the formation of a quasistationary state in the $\alpha\alpha$ two-body system. The results of our calculations are represented by the solid curve. Also shown in Fig. 2 for the sake of comparison are the phase shifts calculated without regard for the three-body potential V_3 (long dashes) and the results obtained in [14] on the basis of the RGM

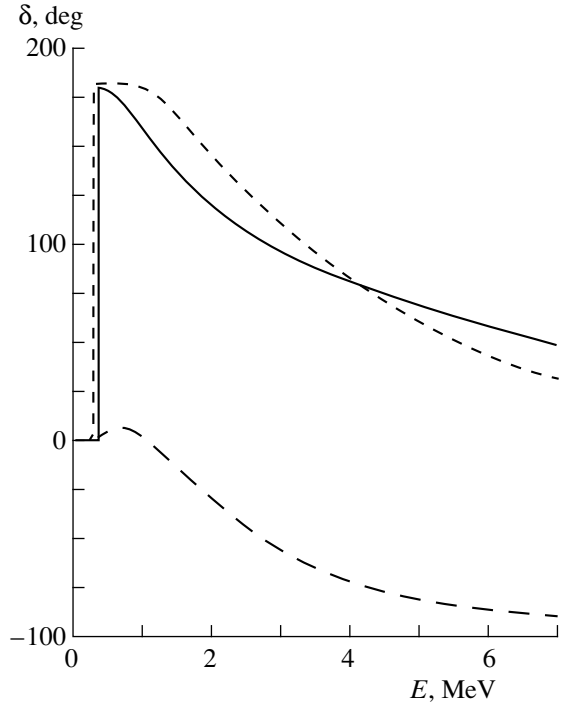

Fig. 2. *s*-wave phase shifts for alpha-particle scattering on a ^{8}Be nucleus: (solid curve) results of the present calculations, (long dashes) results of the calculation taking no account of the three-body potential V_3, and (short dashes) results obtained in [4].

within the $\alpha + {}^8$Be two-cluster model (short dashes). Experimental data suggest the presence of yet two more 0^+ quasistationary states of the ^{12}C nucleus near the three-particle threshold [5]. Their energies are 3.0(±03) and 10.49(±0.02) MeV. However, no other low-lying 0^+ resonances in the ^{12}C nucleus could be reproduced within the model adopted here. This implies that they are truly three-particle states, whose parameters must be calculated by using an exact three-body asymptotic behavior. The values obtained here for the parameters of the 0_2^+ resonance comply well with the results of the microscopic RGM calculations for the resonances of the ^{12}C nucleus within the α-cluster model [3–6]. The results of the calculations for the 0_2^+ resonance are quoted in the table.

Binding energy E_B and root-mean-square radius R of the ^{12}C nucleus (results of the calculations performed in [13, 14] within the 3α cluster model on the basis of the differential Faddeev equations with the same potentials as in the present study) and energy E_r and width Γ of its 0_2^+ resonance (the energy is reckoned from the three-particle threshold)

	E_B, MeV	R, fm	E_r, MeV	Γ, MeV
Our study	–7.26	2.47	0.47	0.0013
[5]	–5.27	–	0.71	0.031
[6]	–7.27	–	0.86	–
[3]	–7.27	2.53	0.47	–
Experimental data [2]	–7.27	2.47	0.3796 ± 0.0002	$(8.5 \pm 1.0) \times 10^{-6}$

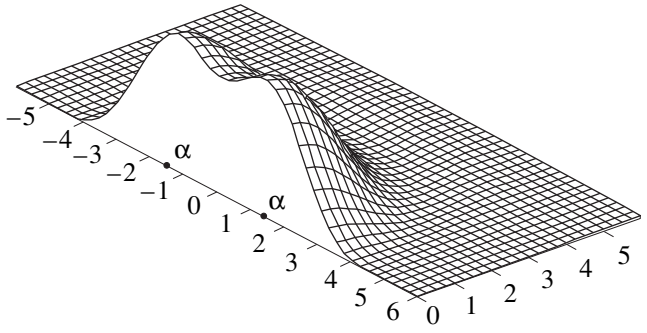

Fig. 3. Function $\Psi^2(x, y, \mu)$ plotted against the coordinates $y\mu$ and $y\sqrt{1-\mu^2}$, the distance x between the α clusters being fixed at $x = 2.8$ fm. The closed circles show the positions of the centers of mass for a chosen pairs of the particles.

In order to continue comparing the results presented here and in [14] with the results obtained by other authors, we now proceed to analyze the wave function of the 3α system. The wave function in question, $\Psi(x, y, \mu)$, depends on three variables. These are the absolute values of the vectors **x** and **y** and the cosine of the angle between them, $\mu = (\mathbf{x}, \mathbf{y})/xy$. Using equations (1) and (4), we compute the wave function by the formula [11]

$$\Psi(x, y, \mu) = \frac{\chi_0(x) f(y)}{xy} + \frac{\chi_0(x') f(y')}{x'y'} + \frac{\chi_0(x'') f(y'')}{x''y''},$$

where x' and y' were defined above, while x'' and y'' are given by

$$x'' = \left[\frac{x^2}{4} + y^2 + xy\mu\right]^{1/2},$$

$$y'' = \left[\left(\frac{3x}{4}\right)^2 + \frac{y^2}{4} - \frac{3}{4}xy\mu\right]^{1/2}.$$

Once the wave function of the system has been constructed, it is of interest to explore the relative positions of the alpha-particle clusters in the system. The most probable configuration of the particles is determined by the coordinates of the maximum of its wave function squared. Our calculations yield $x = 2.8$ fm, $y = 0$ fm, and $\mu = 0$ (for the ground state of the 3α system, the analogous results from [13, 14] are $x = 2.9$ fm, $y = 2.5$ fm, and $\mu = 0$). The relative positions of the alpha-particle clusters are illustrated in Fig. 3, which displays the square of the wave function $\Psi(x, y, \mu)$. The distance between two alpha particles is fixed at $x = 2.8$ fm, and

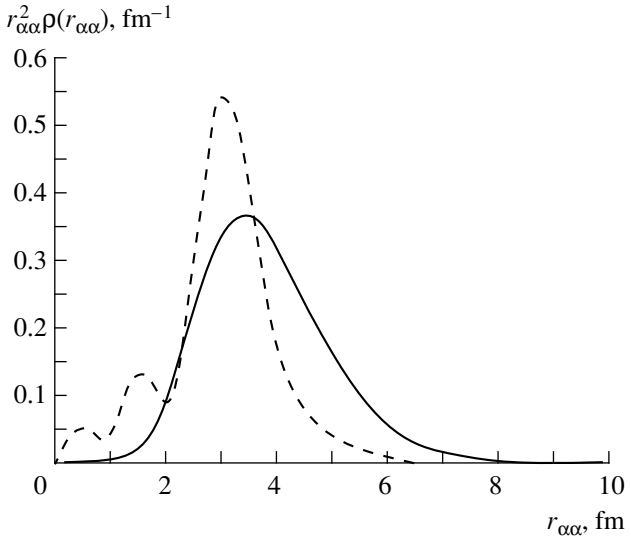

Fig. 4. Function $r^2_{\alpha\alpha}\rho(r_{\alpha\alpha})$ for the ground state of the ^{12}C nucleus: (solid curve) results of the present calculation (based on the data from [13, 14]) and (dashed curve) results obtained in [6].

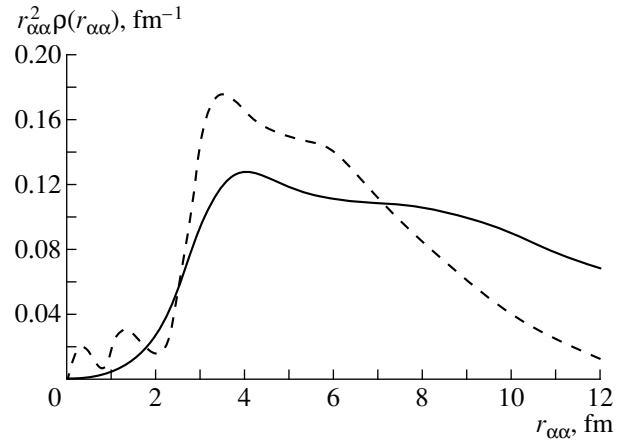

Fig. 5. Function $r^2_{\alpha\alpha}\rho(r_{\alpha\alpha})$ for the 0^+_2 resonance in the ^{12}C nucleus: (solid curve) results of the present calculation and (dashed curve) results obtained in [6].

the function under consideration is plotted against the coordinates $y\mu$ and $y\sqrt{1-\mu^2}$. Thus, we can see that the arrangement of the alpha-particle clusters in the 0^+_2 resonance differs from that in the ground state of the ^{12}C nucleus. In the former case, the centers of mass of the alpha-particle clusters form an equilateral triangle with a side of 2.9 fm, whereas, in the latter case, they form a linear chain rather than a triangle. Our result is similar to that of Hong and Lee [9], who considered a linear chain of clusters with a spacing of 2.8 fm between the neighboring clusters. We now determine the probability density $\rho(r_{\alpha\alpha})$ for finding two alpha-particle clusters at a distance $r_{\alpha\alpha}$. Figures 4 and 5 display the function $r^2_{\alpha\alpha}\rho(r_{\alpha\alpha})$ for, respectively, the ground state of the ^{12}C nucleus (according to the results obtained in [13, 14]) and its 0^+_2 resonance. The dashed curves in these figures represent the results obtained in [6], which are in qualitative agreement with our results.

4. CONCLUSIONS

A model has been proposed where the 0^+_2 resonance in the ^{12}C nucleus is treated as a resonance of α^8Be two-cluster scattering in the 3α three-body system. Effective equations describing the relative motion of the clusters in the α^8Be system have been derived from the differential Faddeev equations. A three-body interaction between α particles ensures the existence of the *s*-wave 0^+_2 resonance. The relevant 3α potential was proposed in [13] to describe the ground state of the ^{12}C nucleus. The results of the present calculations can be summarized as follows:

(i) A three-body potential of α-cluster interaction makes it possible to describe simultaneously the ground state and the 0^+_2 resonance of the ^{12}C nucleus within the *s*-wave potential model of the 3α system.

(ii) The 0^+_2 resonance in the ^{12}C nucleus can be interpreted as a two-particle resonance of α^8Be scattering.

(iii) The arrangement of the clusters in the 0^+_2 state of the 3α system is most adequately described by a linear configuration differing, however, from a regular linear cluster chain considered in [9].

ACKNOWLEDGMENTS

I am grateful to S.L. Yakovlev and V.M. Suslov for a discussion on the results presented here.

This work was supported in part by the Contest Center at the Ministry for Higher Education of the Russian Federation (grant no. 97-0-14.3-23).

REFERENCES

1. C. E. Rolfs and W. S. Rodny, *Canldrons in the Cosmos* (Univ. of Chicago Press, Chicago, 1988).
2. F. Ajzenberg-Selove, Nucl. Phys. A **490**, 1 (1988).
3. M. Kamimura, Nucl. Phys. A **351**, 456 (1981).
4. P. Descouvermont and D. Baye, Phys. Rev. C **36**, 54 (1987).
5. R. Pichter, H. Oberhummer, A. Csótó, and S. A. Moszkowski, Nucl. Phys. A **618**, 55 (1997).
6. E. Hiyama, M. Kamimura, T. Motoba, *et al.*, Prog. Theor. Phys. **97**, 881 (1997).

7. D. V. Fedorov and A. S. Jensen, Phys. Lett. B **389**, 631 (1996).
8. A. I. Baz' and S. P. Merkur'ev, Teor. Mat. Fiz. **27**, 67 (1976).
9. S. H. Hong and S. J. Lee, nucl-th/9903001.
10. M. Freer *et al.*, Phys. Rev. C **49**, R1751 (1994).
11. S. P. Merkuriev and L. D. Faddeev, *Quantum Scattering Theory for Few-Body Systems* (Nauka, Moscow, 1985).
12. S. Ali and A. R. Bodmer, Nucl. Phys. **88**, 99 (1966).
13. I. N. Filikhin and S. L. Yakovlev, Yad. Fiz. **63**, 409 (2000) [Phys. At. Nucl. **63**, 336 (2000)].
14. I. N. Filikhin, Yad. Fiz. **63**, 830 (2000) [Phys. At. Nucl. **63**, 760 (2000)].
15. A. A. Kvitsinskiĭ, Yu. A. Kuperin, *et al.*, Fiz. Élem. Chastits At. Yadra **17**, 267 (1986) [Sov. J. Part. Nucl. **17**, 113 (1986)].
16. S. L. Yakovlev and I. N. Filikhin, Yad. Fiz. **56** (12), 98 (1993) [Phys. At. Nucl. **56**, 1676 (1993)]; Vestn. S.-Peterb. Univ., Ser. 4: Fiz., Khim., No. 3, 24 (1992).

Translated by R. Rogalyov

Physics of Atomic Nuclei, Vol. 63, No. 9, 2000, pp. 1533–1545. Translated from Yadernaya Fizika, Vol. 63, No. 9, 2000, pp. 1618–1630.

NUCLEI
Theory

Triplet Cooper Pairing in Nuclear Matter and Rotational States of Superdeformed Nuclei

I. S. Shapiro†, V. A. Khangulyan[1)], and R. A. Barankov[2)]

Lebedev Institute of Physics, Russian Academy of Sciences, Leninskiĭ pr. 53, Moscow, 117924 Russia

Received June 3, 1999; in final form, September 10, 1999

Abstract—One hundred and sixty-one rotational bands of superdeformed states in nuclei are considered on the basis of a model that admits triplet Cooper pairing in superfluid nuclear matter. The behavior of the dynamical moment of inertia for such states is investigated within this model, which is shown to comply well with available experimental data and to describe successfully the rotational spectra of superdeformed states. © *2000 MAIK "Nauka/Interperiodica".*

1. INTRODUCTION

The rotational band of a superdeformed state of the ^{152}Dy nucleus was observed for the first time in 1986 [1]. This state of ^{152}Dy has the highest spin in the $60\hbar$ band, the corresponding excitation energy being about 30 MeV, which is close to the height of the fission barrier. At such excitations, the density of ordinary thermal levels is about 10^6 eV^{-1}; nonetheless, approximately 30% of all transitions are $60^+ \longrightarrow 58^+$ transitions proceeding via the emission of an $\hbar\omega = 1449$ MeV $E2$ gamma ray. Moreover, all 100% of transitions that involve levels lying between 52^+ and 24^+ or 22^+ are necessarily accompanied by the emission of $E2$ gamma rays. The rotational band is terminated at the 24^+ or the 22^+ level.

In subsequent years, more than 150 rotational bands of superdeformed states were discovered in various nuclei [2–50]. These bands are concentrated in four mass regions: in the region around $A \sim 190$, 62 bands were found in the Bi, Pb, Tl, Hg, and Au nuclei [2–18] (in all, 21 isotopes from this region feature such bands); in the region around $A \sim 150$, experiments revealed 61 bands in the isotopes of Ho, Er, Dy, Tb, Gd, Eu, and Sm [10, 19–39] (in all, there are again 21 isotopes where such bands exist) and three hyperdeformed bands in Dy [40] and Gd [41]; in the region around $A \sim 130$, 27 bands were discovered in the Pm, Nd, Pr, Ce, and La nuclei [10, 42–48] (in all, 13 isotopes of these nuclei exhibit such bands); and, finally, in the region around $A \sim 80$, 70, four bands in the ^{81}Sr nucleus [49] and four bands in ^{87}Nb [50] had been reported by the middle of 1997.

By convention, we will refer to a band as a rotational one if the excitation energy of a nucleus is given by[3)]

$$E(I) = \frac{\hbar^2 I(I+1)}{2J(I)},$$

where the moment of inertia $J(I)$ must be either a constant or a slowly changing function of the spin I. The probabilities of intraband electromagnetic transitions are much greater than those for transitions into other states and exceed single-particle estimates by nearly two orders of magnitude.

Experiments measure a cascade of $E2$ photons, which sometimes involves more than 20 transitions. The photon energy $E_\gamma(I)$ is given by

$$E_\gamma(I) = E(I+2) - E(I) = \frac{2I+3}{J^{(1)}(I)}, \qquad (1)$$

where $J^{(1)}(I)$ is the static moment of inertia of a rotational band.[4)] It is related to the excitation energy by the equation [51]

$$J^{(1)}(I) = \frac{1}{2}\left(\frac{dE}{d\mathbf{I}^2}\right)^{-1}, \qquad (2)$$

where $\mathbf{I}^2 = I(I+1)$. If, for example, $J(I) = J(I)$, then $J^{(1)}(I) = J(I)$, in which case the cascade energy appears to be a linear function of I.

From the expression for the photon energy, one can see that it involves, in addition to the static moment of inertia, the spin of the level being considered. For the rotational band of a superdeformed state, it is rather difficult to determine this spin independently. By using the dynamical moment of inertia [51], it is possible to elim-

† Deceased.

1) Moscow State Engineering Physics Institute (Technical University), Kashirskoe sh. 31, Moscow, 115409 Russia.

2) Russian Research Centre Kurchatov Institute, pl. Kurchatova 1, Moscow, 123182 Russia.

3) In the following, we set $\hbar = 1$ in all equations.

4) In some cases (see, for example, [10]), the static moment of inertia is determined by the relation $J^{(1)}(I) = (2I-1)/E_\gamma(I)$ with $E_\gamma(I) = E(I) - E(I-2)$.

1063-7788/00/6309-1533$20.00

inate the spin of the level from experimental data. For this purpose, it is convenient to introduce the quantity

$$\Delta E_\gamma = E_\gamma(I+2) - E_\gamma(I) = \frac{4}{J^{(2)}(I)}, \qquad (3)$$

where $J^{(2)}(I)$ is the so-called dynamical moment of inertia, which can be expressed in terms of the excitation energy of the nucleus as [51]

$$J^{(2)}(I) = \left(\frac{d^2E(I)}{d(\sqrt{\mathbf{I}^2})^2}\right)^{-1}. \qquad (4)$$

This quantity no longer depends on the spin of the level; if the moment of inertia of the nucleus is constant, we have $J^{(2)}(I) = J(I)$.

Depending on the spin I, the moment of inertia as determined experimentally can exhibit four types of behavior: (i) $J^{(2)}(I)$ is a growing function. (ii) $J^{(2)}(I)$ is a constant. (iii) $J^{(2)}(I)$ is a decreasing function. (iv) $J^{(2)}(I)$ is a nonmonotonic function.

The main objective of any theoretical model for describing the rotational spectrum of a superdeformed nuclear state is to reproduce qualitatively the behavior of the dynamical momentum of inertia.

By using expression (3), we can determine $J^{(2)}(I)$ from experimental data. Further assuming that $J^{(2)}(I) \approx J^{(1)}(I)$ and employing relation (1), we can estimate, on the basis of experimental data, the spin of the level to within one to two $\hbar$ units.

As a rule, a theoretical description of superdeformed nuclear states is based either on the cranking model [52] or on the model of a variable momentum of inertia. Here, we present a different approach to describing rotational states of superdeformed nuclei. In 1986, Fal'ko and Shapiro [53] put forth the idea that nuclear matter can undergo a transition to a superfluid state characterized by triplet Cooper pairing. In 1990, Shapiro [54] assumed that, since the nucleon spins have the same direction in the case of triplet pairing and since the energy of spin–rotation interaction is proportional to $(\mathbf{S}\cdot\mathbf{\Omega})$ (where $\mathbf{\Omega}$ is the angular-velocity vector), the triplet pairing of nucleons may arise at high angular momenta. As a result, nuclear matter undergoes a transition to a superfluid state, and this phase transition is interpreted as the formation of a superdeformed nuclear state.

In the present study, experimental data on the rotational states of superdeformed nuclei are considered within the model of superfluidity characterized by triplet pairing. The ensuing exposition is organized as follows. In Section 2, we present basic results obtained within this model. Section 3 is devoted to an investigation of all known rotational bands in superdeformed nuclei.

2. MODEL OF NUCLEAR-MATTER SUPERFLUIDITY INDUCED BY TRIPLET PAIRING

For the first time, the idea that nuclear matter can occur in the superfluid state was put forth in [55–57]. It was assumed in those studies, however, that Cooper pairs have zero total spin ($S = 0$) and zero orbital angular momentum ($L = 0$); that is, they have no internal degrees of freedom. In the case of ^{3}He [58–60], which also exhibits the superfluidity property, Cooper pairs occur in the $S = 1$ triplet state. Moreover, the orbital angular momentum L of a pair must be odd—in particular, $L = 1$—because of antisymmetry of the wave function of Cooper pairs. Considering that spin–orbit coupling is weak for ^{3}He, we then find that the total symmetry group is

$$SO(3)_L \otimes SO(3)_S \otimes U(1).$$

In 1986, Fal'ko and Shapiro [53] assumed that nucleons of nuclear matter form Cooper pairs in the $S = 1$, $L = 1$ triplet state. In this case, we have to deal with strong spin–orbit coupling; accordingly, the total symmetry group is

$$SO(3) \otimes U(1).$$

In the case of strong spin–orbit coupling, the total spin of a Cooper pair, $S = 1$, and its orbital angular momentum of relative motion, $L = 1$, are combined vectorially to give the total angular momentum $\mathbf{J} = \mathbf{L} + \mathbf{S}$ with $J = 0, 1, 2$.

A superfluid liquid is a Bose condensate of identical particles, where different phases correspond to different values of J. Moreover, several phases can exist even at a fixed nonzero value of J, since the state of each phase is characterized by the total-angular-momentum projection $M = J, J-1, \ldots, -J$ as well. It should be borne in mind here that the values of $M = \pm K$ ($K = 0, \ldots, J$) correspond to the same phase, since complex-conjugate wave functions are associated with angular-momentum projections having the identical absolute values and opposite signs. Therefore, there are six different phases: three at $J = 2$ ($M = 2, 1, 0$), two at $J = 1$ ($M = 1, 0$) and one at $J = 0$ ($M = 0$). The $M \neq 0$ and $M = 0$ phases are referred to, respectively, as nonunitary and as unitary ones.

The wave function of a Cooper pair is determined as the matrix element

$$\langle N|\hat{\Psi}_\alpha(\mathbf{r}_1)\hat{\Psi}_\beta(\mathbf{r}_2)|N+2\rangle = f_{\alpha\beta}(\mathbf{r},\mathbf{R}),$$

where N is the number of identical fermions and $\hat{\Psi}_\alpha(\mathbf{x})$ ($\alpha = 1, 2$) is the operator annihilating a fermion at the point $\mathbf{x}$. The variables $\mathbf{r}$ and $\mathbf{R}$ are given by

$$\mathbf{r} = \mathbf{r}_1 - \mathbf{r}_2, \quad \mathbf{R} = \frac{\mathbf{r}_1 + \mathbf{r}_2}{2}.$$

Since the direct product of two spinors involves a scalar, $S = 0$ and a vector, $S = 1$, we can rewrite the matrix $f_{\alpha\beta}$ in the form

$$f(\mathbf{r}, \mathbf{R}) = a(\mathbf{r}, \mathbf{R})i\sigma_2 + b_j(\mathbf{r}, \mathbf{R})i\sigma_2\sigma_j,$$

where $a(\mathbf{r}, \mathbf{R})$ is the wave function of a singlet Cooper pair, $\mathbf{b}(\mathbf{r}, \mathbf{R})$ is the wave function of a triplet Cooper pair, and σ_j ($j = 1, 2, 3$) are the Pauli matrices; hereafter, summation over dummy indices is implied. It is more convenient to use the wave function in the momentum representation, $b_i(\mathbf{k}, \mathbf{R})$, $i = 1, 2, 3$. Since $L = 1$, $b_i(\mathbf{k}, \mathbf{R})$ can be represented in the form

$$b_i^{JM}(\mathbf{k}, \mathbf{R}) = k_j B_{ij}^{JM}(\mathbf{k}, \mathbf{R}).$$

The complex tensor B_{ij}^{JM} is the order parameter for the JM phase.

All superfluid phases of nuclear matter, as well as their order parameters and degeneracy spaces, were determined in [53, 54] (see Table 1).

In the case of homogeneous nuclear matter, the quantity B_{ij} is independent of the center-of-mass position of a pair (that is, on $\mathbf{R}$). Under rotations about the quantization axis $\mathbf{z}$, the order parameter transforms as $B^{JM} \longrightarrow e^{iM\Phi}B^{JM}$, where Φ is the rotation angle. It follows that, for the unitary phases ($M = 0$), the order parameter is invariant under rotations about the quantization axis $\mathbf{z}$. In this case, it is meaningful to consider rotations of the spontaneous anisotropy axis $\mathbf{z}$ only about some axis orthogonal to $\mathbf{z}$. For the nonunitary phases ($M \neq 0$), rotation about the $\mathbf{z}$ axis has actual physical meaning since the axial symmetry of the superfluid condensate is broken in this case. This distinction between the unitary and nonunitary phases is of crucial importance for the origin of rotational bands in superdeformed nuclei.

The energy of the system in question is a functional of the order parameter:

$$E = F[B].$$

That the $J \neq 0$ phases of a superfluid liquid are anisotropic may generate collective excitations that correspond to rotations of the system as a discrete unit, whereby the system develops a rotational spectrum. It should be borne in mind in this connection that volume textures of the quantized-vortex type cannot arise in our systems because nuclear sizes are much smaller than the correlation length. The energy of a rotating nucleus with angular momentum $\mathbf{I}$ can be represented in the form

$$E_{JM}(\mathbf{I}) = E_{JM}(\mathbf{\Omega}) + \mathbf{I} \cdot \mathbf{\Omega}, \tag{5}$$

where $\mathbf{\Omega}$ is the angular-velocity vector and $E_{JM}(\mathbf{\Omega})$ is the energy in the reference frame rotating with the nucleus. The quantity $E_{JM}(\mathbf{\Omega})$ can be expressed in terms of scalars involving the order parameters and angular-velocity vector. In specifying the forms of such scalars, we must consider that, for the nonunitary phases ($M \neq 0$), there exists the nonvanishing vector $\epsilon_{ijk}B_{jl}B_{kl}^*$, so that we can construct a scalar linear in the angular velocity; that is,

$$\Omega_i\epsilon_{ijk}B_{jl}B_{kl}^* = i(\mathbf{\Omega} \cdot \mathbf{z})\mathrm{tr}[BB^+].$$

For the unitary phases, we have $\epsilon_{ijk}B_{jl}B_{kl}^* = 0$; hence, the angular-velocity vector must appear quadratically in $E_{JM}(\mathbf{\Omega})$. For another scalar constructed from the order parameter, we can take

$$A^2 = \mathrm{tr}[BB^+].$$

In the Ginzburg–Landau approximation, where the energy functional is approximated by a polynomial of fourth degree in the order parameter, the energy of a homogeneous nucleus in the rotating reference frame can be represented as

$$E_{JM}(\mathbf{\Omega}) = \epsilon + (-\alpha + \beta\mathbf{\Omega} \cdot \mathbf{z})A^2 + \gamma A^4 \tag{6}$$

for a nonunitary phase and as

$$E_{JM}(\mathbf{\Omega}) = \epsilon + (-\alpha + \beta\mathbf{\Omega}^2)A^2 + \gamma A^4 \tag{7}$$

for a unitary phase.

In expressions (6) and (7), α, β, and γ are unknown real parameters, while ϵ is the energy of a normal phase. Without loss of generality, we can assume that $\beta > 0$.

The conditions under which the energy functional is minimized are given by

$$\frac{\delta E}{\delta A^2} = 0, \quad \frac{\delta^2 E}{\delta (A^2)^2} \geq 0. \tag{8}$$

Table 1. Tensor structure of the order parameter

J	$\lvert M\rvert$	$B_{ij}^{J\lvert M\rvert}$	G/H
0	0	$\frac{1}{\sqrt{3}}\delta_{ij}e^{i\Phi}$	S^1
1	0	$\frac{1}{\sqrt{2}}\epsilon_{ijk}z_k e^{i\Phi}$	$(S^1 \otimes S^2)/Z_2$
2	0	$\frac{1}{\sqrt{6}}(3z_i z_j - \delta_{ij})e^{i\Phi}$	$P^2 \otimes S^1$
1	1	$\frac{1}{\sqrt{2}}\epsilon_{ijk}v_k$	P^3
2	1	$\frac{1}{\sqrt{2}}(z_i v_j + z_j v_i)$	P^3
2	2	$v_i v_j$	P^3/Z_2

Note: Here, we use the following notation: $\mathbf{x}^2 = \mathbf{y}^2 = \mathbf{z}^2 = 1$, $\mathbf{x} \perp \mathbf{y} \perp \mathbf{z}$, and $\mathbf{v} = (1/\sqrt{2})(\mathbf{x} + i\mathbf{y})$; Φ is an arbitrary complex number.

Considering that

$$\mathbf{I} = -\frac{\partial E_{JM}(\mathbf{\Omega})}{\partial \mathbf{\Omega}} \quad (9)$$

and using expression (5), we find the rotational spectrum [53, 54]. For a nonunitary phase, we obtain

$$E_{JM}(I) - E_{JM}(0) = \frac{1}{2J_0}(\sqrt{I(I+1)} - I_0)^2, \quad (10)$$

where

$$E_{JM}(0) = -\frac{\alpha^2}{4\gamma} < 0, \quad J_0 = \frac{\beta^2}{2\gamma}, \quad I_0 = \frac{\alpha\beta}{2\gamma}.$$

For the free-energy functional to have a minimum [this is ensured by fulfillment of inequality (8)], it is necessary that $\gamma > 0$. We note that conditions (8) lead to the relations

$$\frac{\mathbf{\Omega}\cdot\mathbf{z}}{\Omega} = -1, \quad (11)$$

$$A^2(\Omega) = \frac{1}{2}(\alpha + \beta\Omega) > 0. \quad (12)$$

The equality in (11) means that the nucleus being considered rotates about the quantization axis **z**. Such a rotation is unusual for collective motions in a nucleus [51]. From inequality (12), it follows that, for $\alpha < 0$, the conditions

$$\Omega > \Omega_{\rm cr} = \frac{|\alpha|}{\beta}, \quad I > I_{\rm cr} = J\frac{|\alpha|}{\beta}, \quad (13)$$

where J is the moment of inertia of the nucleus with respect to the **z** axis, must be satisfied.

Thus, we conclude that, in contrast to singlet pairing, triplet pairing is not destroyed by a fast rotation (high nuclear spin). Moreover, it follows from relation (13) that nonunitary phases, which arise only in the case of a sufficiently fast rotation, can exist. The situation here is analogous to that which is prevalent in ^{3}He, which can be in the A_1 phase only in a magnetic field.

By using relations (4) and (10), we can easily derive expressions for the dynamical moment of inertia. For the nonunitary phase, we have

$$J^{(2)}(I) = J_0 = \text{const}. \quad (14)$$

There are 32 rotational bands for which the dynamical moment of inertia can be assumed to be independent of the spin of a level in the band.

In the case of unitary phases ($M = 0$), the minimization of the Ginzburg–Landau functional leads to the expression

$$E_{JM}(\Omega) = -\frac{(\alpha + \beta\Omega^2)^2}{4\gamma},$$

whence we find the relation between the angular velocity and the spin by using (9). With the aid of the substitution $x = \Omega^2 + (2/3)(\alpha/\beta)$, we transform this equation to the standard form

$$x^3 - 3px + 2q = 0,$$

where

$$p = -\frac{2^{10}}{3^8}\left(\frac{E_{J0}^2(0)}{I_c^2}\right)^2 < 0,$$

$$q = -\frac{2^{15}}{3^{12}}\left(\frac{E_{J0}^2(0)}{I_c^2}\right)^3\left[1 + \frac{I(I+1)}{I_c^2}\right],$$

$$E_{J0}(0) = -\frac{\alpha^2}{4\gamma}, \quad I_c^2 = \frac{2}{27}\frac{\alpha^3\beta}{\gamma^2}.$$

From the condition under which the Ginzburg–Landau functional is minimized, it follows that $\gamma > 0$ [that is, $E_{J0}(0) < 0$]. The parameter α can assume both negative and positive values, so that the sign of I_c^2 is not defined unambiguously. It should be noted that the quantity I_c^2 is a parameter that has nothing to do with the spin in the rotational band. By using (5), we find that the rotational spectrum of a unitary phase can be represented as

$$E_{J0}(I) - E_{J0}(0) = -\frac{1}{3}E_{J0}(0)[H_1^2(I) - 1], \quad (15)$$

where

$$H_1(I) = \begin{cases} 2\cosh(\phi/3) - 1, & 0 < I_c^2 \\ -2\cosh(\phi/3) - 1, & -(1/2)I(I+1) < I_c^2 < 0 \\ -2\cos(\phi/3) - 1, & \\ & -I(I+1) < I_c^2 < -(1/2)I(I+1) \\ 2\cos(\phi/3) - 1, & I_c^2 < -I(I+1). \end{cases}$$

Here, we have introduced the auxiliary quantity ϕ defined as

$$\cosh(\phi) = I(I+1)/I_c^2 + 1, \quad 0 < I_c^2;$$

$$\cosh(\phi) = -(I(I+1)/I_c^2 + 1), \; -(1/2)I(I+1) < I_c^2 < 0;$$

$$\cos(\phi) = -(I(I+1)/I_c^2 + 1),$$

$$-I(I+1) < I_c^2 < -(1/2)I(I+1);$$

$$\cos(\phi) = I(I+1)/I_c^2 + 1, \quad I_c^2 < -I(I+1).$$

For $I_c^2 > 0$, expression (15) reduces to the expression for the rotational spectrum of a unitary phase from [53, 54] {formula (3.11) in [54]}. In the case of unitary phases, the connections of $E_{J0}(I)$ for $I_c^2 > 0$ with the cranking model and with the model featuring a variable moment of inertia were discussed in [61].

By using (15), we can easily show that the dynamical moment of inertia of a rotational band based on a unitary phase has the form

$$J^{(2)}(I) = -\frac{9}{4}\frac{I_c^2}{E_{J0}(0)} \times \left[H_1H_2 + \frac{2}{3}\frac{I(I+1)}{I_c^2}H_2^2 - \frac{4}{3}\frac{I(I+1)}{I_c^2}H_1H_3\right]^{-1}, \quad (16)$$

so that it grows with spin. Here, the quantities $H_2(I)$ and $H_3(I)$ are given by

$$H_2(I) = \begin{cases} 2\sinh(\phi/3)/\sinh(\phi), & 0 < I_c^2 \\ 2\sinh(5\phi/3)/\sinh(\phi), & -(1/2)I(I+1)I_c^2 < 0 \\ 2\sin(5\phi/3)/\sin(\phi), & \\ & -I(I+1) < I_c^2 < -(1/2)I(I+1) \\ 2\sin(\phi/3)/\sin(\phi), & I_c^2 < -I(I+1), \end{cases}$$

$$H_3(I) = \begin{cases} 4(-\cosh^2(\phi)\sinh(2\phi/3) + \sinh(8\phi/3)/4)/\sinh^3(\phi), & \\ & 0 < I_c^2 \\ 4(\cosh^2(\phi)\sinh(2\phi/3) - \sinh(8\phi/3)/4)/\sinh^3(\phi), & \\ & -(1/2)I(I+1) < I_c^2 < 0 \\ 4(-\cos^2(\phi)\sin(2\phi/3) & \\ + \sin(8\phi/3)/4)/\sin^3(\phi), & \\ & -I(I+1) < I_c^2 < -(1/2)I(I+1) \\ 4(\cos^2(\phi)\sin(2\phi/3) - \sin(8\phi/3)/4)/\sin^3(\phi), & \\ I_c^2 < -I(I+1). & \end{cases}$$

Thus, the model of triplet pairing in superfluid nuclear matter provides a natural explanation of the behavior of the dynamical moment of inertia in cases (i) and (ii) (see the Introduction), but it fails to describe its behavior in cases (iii) and (iv) under the assumption of homogeneous nuclear matter.

In this model of superfluid nuclear matter, there can exist phases that possess natural anisotropy. In such phases, axial symmetry is broken, so that there are no connections between the rotational states associated with them and conventional cranking models for states that are nonspherical, but which are axisymmetric.

We note that, in expressions (10) and (15) for the energy of rotational-band levels, the spin I changes by unity. Therefore, $\Delta I = 1$ and $\Delta I = 2$ transitions are allowed in such a band. However, $\Delta I = 1$ transitions are strongly suppressed for high-spin states: such $E2$ transitions are suppressed by kinematical factors, while $M1$ transitions are suppressed because of a slow rotation of the charges. Thus, there are $\Delta I = 2$ $E2$ transitions in each rotational band, so that two rotational bands characterized by identical moments of inertia and by spin values differing by unity—that is, two overlapping bands with weak signature splitting [62]—correspond in experiments to the rotational spectrum based on each phase. Joice *et al.* [63] were able to observe experimentally $M1$ transitions between such bands.

To conclude this section, we note that two adjustable parameters correspond to each phase. These are $E_{J0}(0)$ and I_c^2 for unitary phases and J_0 and I_0 for nonunitary phases. In applying the model under discussion to nuclei, it is necessary to consider that they are finite. There then arises the question of which facet of these objects—the properties of nuclear matter (that is, a phase transition to a superfluid state) or spatial quantization (effects of finiteness)—is of crucial importance for superdeformed nuclear states. If the aforementioned parameters change weakly from one nucleus to another, the phenomenon of superdeformation in nuclei is a feature inherent in nuclear matter.

3. DESCRIPTION OF EXPERIMENTAL DATA ON ROTATIONAL STATES OF SUPERDEFORMED NUCLEI

The present study heavily relies on the assumption that, upon heavy-ion collisions, which excite high-lying rotational states in the nuclei involved, triplet Cooper pairing arises in nuclear matter, so that the nuclear system formed appears to be in a superfluid state upon a phase transition. Therefore, a superdeformed state of nuclei, which is characterized by high spins, (60–70)$\hbar$, is a superfluid state of nuclear matter. In order to test this model, we analyze here more than 150 rotational bands for a broad range of nuclei.

For a basic criterion of our fits, we consider the behavior of the dynamical moment of inertia as a function of the spin of the level or as a function of the frequency of rotation, the relation between the former and the latter being given by

$$\omega = \frac{1}{4}[E_\gamma(I) + E_\gamma(I+2)]. \quad (17)$$

If the dynamical moment of inertia grows with increasing frequency of rotation, the rotational band must be associated with a unitary superfluid phase, so that the energy the cascade photons must be described by expression (15). But if the dynamical moment of inertia is constant, our fit is based on expression (10). No other behavior of the dynamical moment of inertia can be described within our approach. As was indicated above, each of the two expressions involves two adjustable parameters. For the overwhelming majority of the bands, the spins of the levels cannot be determined from experimental data directly. In view of this, it is necessary to invoke a new parameter—the spin of the

Table 2. Results of fitting rotational bands of superdeformed nuclei

	Number of nucleons		
	81, 87, 129–137	142–154	189–198
Number of nuclei with different Z	7	7	5
		19	
Number of isotopes	15	21	21
		57	
Number of rotational bands in super- and hyperdeformed nuclei	35	61 + 3HD	62
		158 + 3HD	
Number of unitary bands	6	6	49
		61	
Number of nonunitary bands	3	24	5
		32	
Number of bands that can be described in two ways	0	9 + 3HD	5
		14 + 3HD	
Number of bands that elude description	26	22	3
		51	

lowest state in the band, $I_{\min}$. For unitary phases, no difficulties arise in determining this parameter from a fit because of high sensitivity of expression (15) to the choice of spin. But for nonunitary phases, consistent variations in $I_{\min}$ and I_0 lead to the same expressions in the high-spin limit; therefore, the spin is determined, in this case, by the method described in the Introduction.

Our fit was performed in terms of the root-mean-square deviation

$$\chi = \sqrt{\frac{1}{N}\sum_{i=1}^{N}(E_i^{\text{theor}} - E_i^{\text{expt}})^2}. \qquad (18)$$

The quality of the fit was taken to be good if $\chi \le 5$ keV. To explain this, we remind the reader that, according to our strategy outlined above, any viable model must describe the behavior of the dynamical moment of inertia $J^{(2)}$, which is determined from ΔE_γ [see equation (3)]. Since the values of ΔE_γ for different bands vary between 50 and 100 keV, the criterion $\chi \le 5$ keV corresponds to precision higher than 10% in a fit to ΔE_γ.

As the result of describing all 161 rotational bands known to us from [2–50] (158 bands of superdeformed nuclei and three bands of hyperdeformed nuclei), we were able to single out four groups of bands (see Table 2).

The first group contains the rotational bands compatible with expression (15)—that is, of unitary bands. The second group consists of rotational bands described by expression (10)—that is, of nonunitary bands. Figures 1 and 2 display both theoretical and experimental results for the dynamical moment of inertia of, respectively, the ^{194}Hg(2) band (unitary case) and the ^{195}Pb(2) band (nonunitary case) versus the nuclear spin I. For these descriptions of the data, we obtained $\chi = 0.5$ keV in first case and $\chi = 0.6$ keV in the second case.

There are a number of rotational bands for which the behavior of the dynamical moment of inertia could not be determined on the basis of experimental data. These

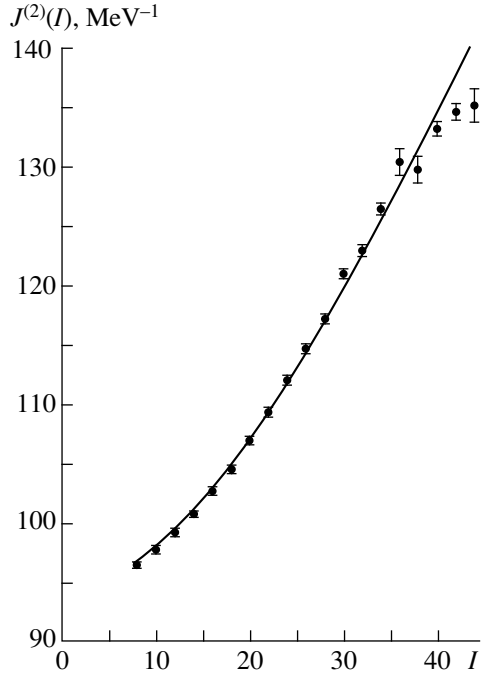

Fig. 1. Dynamical moment of inertia as a function of the nuclear spin for the ^{194}Hg(2) rotational band. The solid curve corresponds to the best fit in terms of expression (16) for the unitary phase.

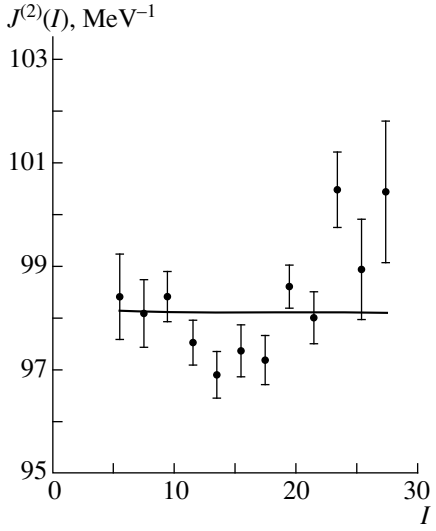

Fig. 2. Dynamical moment of inertia as a function of the nuclear spin for the ^{195}Pb(2) rotational band. The solid curve corresponds to the best fit in terms of expression (14) for the nonunitary phase.

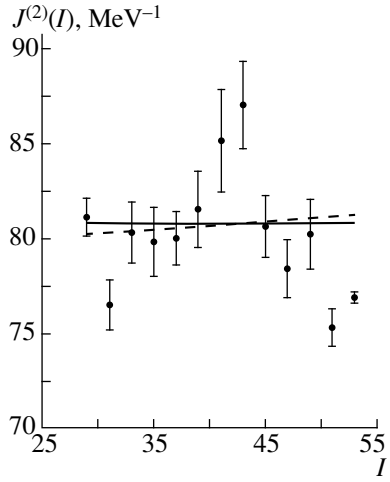

Fig. 3. Dynamical moment of inertia as a function of the nuclear spin for the ^{148}Gd(2) rotational band. The solid (dashed) curve corresponds to the best fit in terms of expression (14) [expression (16)] for the nonunitary (unitary) phase.

bands were described in two ways, in terms of expression (15) and in terms of expression (10). All such bands (there are 17 of these) were included in the third group, which is exemplified by the ^{148}Gd(2) rotational band. Either type of fit (on the basis of a unitary or a nonunitary phase) yields χ = 2.2 keV. The behavior of the dynamical moment of inertia for this case is illustrated in Fig. 3. The experimental values of the photon energies and the results obtained by fitting expressions (15) and (10) to them for the ^{194}Hg(2), ^{195}Pb(2), and ^{148}Gd(2) bands are quoted in Tables 3–5. For the last case, we present the results of fits based both on a unitary and on a nonunitary phase.

Table 3. Example of fitting the ^{194}Hg(2) band ($\delta E_\gamma = E_\gamma^{\text{theor}} - E_\gamma^{\text{expt}}$; energies are measured in keV; χ = 0.5 keV): unitary phase

I	$E_\gamma^{\text{expt (plain)}}$	$E_\gamma^{\text{theor (plain)}}$	δE_γ
8	200.79	201.20	0.41
10	242.25	242.55	0.30
12	283.14	283.35	0.21
14	323.45	323.54	0.09
16	363.12	363.06	−0.06
18	402.05	401.88	−0.17
20	440.31	439.97	−0.34
22	477.68	477.29	−0.39
24	514.23	513.83	−0.40
26	549.93	549.59	−0.34
28	584.82	584.56	−0.26
30	618.96	618.74	−0.22
32	652.02	652.16	0.14
34	684.57	684.81	0.24
36	716.20	716.72	0.52
38	746.89	747.90	1.01
40	777.73	778.37	0.64
42	807.78	808.16	0.38
44	837.48	837.27	−0.21
46	867.08	865.74	−1.34

The fitted values of the parameters J_0, I_0, and $I_{\min}$ for nonunitary bands and the fitted values of the parameters $E_{J0}(0)$, I_c^2, and $I_{\min}$ for unitary bands are given in Tables 6 and 7, respectively. These tables also display the values of the root-mean-square deviations χ and references to studies from which we borrowed experimental data. It should be emphasized that the quantity $I_{\min}$ for nonunitary rotational bands was determined by formulas (1) and (3) rather than fitted; therefore, its accuracy was one to two $\hbar$. The bands that could be described in two ways were included in both tables and were labeled with an asterisk.

Since we treat the phenomena of nuclear superdeformation and hyperdeformation as a feature peculiar to nuclear matter, the parameters of the bands are not expected to show a large scatter in the mass region being considered (they must become coincident upon taking into account effects associated with the finiteness of nuclear sizes). Within the model used here, the bands that can be described in two ways must therefore be treated in terms of the phase with which their parameters comply better. For example, the fits to the ^{152}Dy(6) band lead to χ = 1.0 and 1.3 keV for, respectively, the unitary and the nonunitary ansatz. The fitted values of the parameters of the unitary phase, $E_{J0}(0) = -1.5 \times 10^3$ MeV and $I_c^2 = 3.8 \times 10^4$, are two orders of magnitude greater than the analogous values for other unitary bands. The fitted value J_0 = 89 MeV^{-1} for the parameter of the nonunitary phase is close to the corresponding values for the nonunitary phases. On this basis, we interpret this band as that of the nonunitary phase.

In Tables 6 and 7, we also included three rotational bands of hyperdeformed nuclei, although the fitted values of their parameters differ strongly from the parameters of rotational bands of superdeformed nuclei. As was indicated in Section 2, nuclei can have rotational bands with weak signature splitting and spins differing by unity. In Tables 6 and 7, each pair of such bands is combined into one row (in all, there are 28 such pairs).

The results of our fit agree with the analogous results from [61, 64] for the same nuclei.

Finally, the fourth group comprises bands that do not meet the above criterion—that is, bands for which $\chi > 5$ keV. First, these are bands for which the dynamical moment of inertia is a decreasing function of the frequency of rotation. For example, this is so for ^{150}Gd(1). The experimental behavior of its dynamical

Table 4. Example of fitting the ^{195}Pb(2) band ($\delta E_\gamma = E_\gamma^{\text{theor}} - E_\gamma^{\text{expt}}$; energies are measured in keV; $\chi = 0.5$ keV): nonunitary phase

I	E_γ^{expt}	E_γ^{theor}	δE_γ
5.5	162.6	162.8	0.2
7.5	203.2	203.6	0.4
9.5	244.0	244.3	0.3
11.5	284.6	285.1	0.5
13.5	325.6	325.8	0.2
15.5	366.9	366.6	−0.3
17.5	408.0	407.4	−0.6
19.5	449.1	448.1	−1.0
21.5	489.7	488.9	−0.8
23.5	530.5	529.7	−0.8
25.5	570.3	570.4	0.1
27.5	610.8	611.2	0.4
29.5	650.6	652.0	1.4

Table 5. Example of fitting the ^{148}Gd(2) band ($\delta E_\gamma = E_\gamma^{\text{theor}} - E_\gamma^{\text{expt}}$; energies are measured in keV; $\chi_{\text{nonun}} = \chi_{\text{un}} = 2.2$ keV): unitary and nonunitary phases

I	E_γ^{expt}	E_γ^{nonun}	E_γ^{un}	$\delta E_\gamma^{\text{nonun}}$	$\delta E_\gamma^{\text{un}}$
30	787.8	789.2	788.2	1.4	0.4
32	837.1	838.7	838.0	1.6	0.9
34	889.4	888.2	887.8	−1.2	−1.6
36	939.2	937.7	937.6	−1.5	−1.6
38	989.3	987.2	987.3	−2.1	−2.0
40	1039.3	1036.7	1037.0	−2.6	−2.3
42	1088.4	1086.3	1086.6	−2.1	−1.8
44	1135.4	1135.8	1136.7	0.4	1.3
46	1181.4	1185.3	1185.7	3.9	4.3
48	1231.0	1234.8	1235.2	3.8	4.2
50	1282.0	1284.3	1284.6	2.3	2.6
52	1331.0	1333.8	1333.9	2.8	2.9
54	1385.0	1383.4	1383.3	−1.6	−1.7
56	1437.0	1432.9	1432.5	−4.1	−4.5

moment of inertia is illustrated in Fig. 4. Second, there are bands for which the dynamical moment of inertia is a nonmonotonic function of the frequency of rotation. This type of behavior is observed in ^{129}Ce and ^{133}Nd (see Fig. 5). It can be seen that, in the case of ^{129}Ce, the condition $J^{(2)} = \text{const} = 56$ MeV^{-1} is strongly violated only at one point, but this leads to $\chi = 16.3$ keV. Third, Fig. 6 displays the measured dynamical moments of inertia for the ^{193}Hg(1) and ^{193}Hg(4) bands as functions of the frequency of rotation. Gullen *et al.* [65] believe

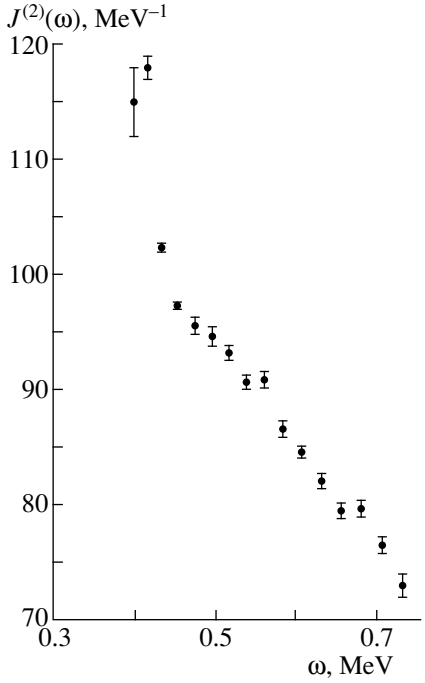

Fig. 4. Dynamical moment of inertia as a function of the frequency of rotation for the ^{150}Gd(1) rotational band.

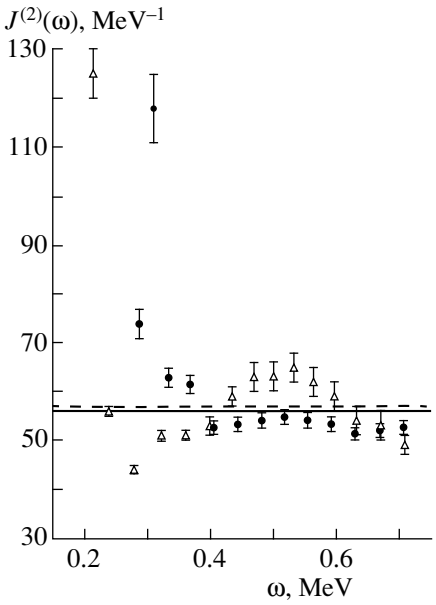

Fig. 5. Dynamical moment of inertia as a function of the frequency of rotation for the rotational bands in the (closed circles) ^{193}Hg(1) and (open triangles) ^{193}Hg nuclei. The solid and the dashed line represent fits assuming a nonunitary phase for ^{129}Ce and ^{133}Nd, respectively.

Table 6. Fitted parameters for nonunitary phases

Nucleus	I_{min}	$-I_0$	J_0, MeV^{-1}	Number of transitions	χ, keV	References
^{197}Bi(1)*	5.5	1.3	99	13	1.7	[3]
^{197}Pb(2)*	7.5	1.3	99	16	2.2	[4]
^{195}Pb(1)*	6.5	1.4	102	13	1.0	[5]
^{195}Pb(2)	5.5	1.0	98	13	0.5	[6]
^{193}Pb(1)*	11.5	1.1	101	10	0.7	[6]
^{193}Pb(2)	6.5	1.0	94	9	1.0	[6]
^{192}Tl(1)*	16	1.0	103	8	1.1	[11]
^{192}Tl(3)	17	1.3	106	8	0.5	[11]
^{192}Tl(4)	16	1.6	107	8	1.1	[11]
^{190}Hg(2)	27	1.0	123	8	0.9	[13]
^{153}Ho(2)	27.5	1.1	85	16	2.2	[19]
^{155}Dy	36.5	1.3	87	15	0.9	[20]
^{154}Dy	27	1.0	85	18	1.5	[21]
^{153}Dy(HD)*	82.5	1.7	138	11	1.7	[40]
^{153}Dy(1)	28.5	1.2	87	18	1.9	[22]
^{153}Dy(2)	25.5	1.3	84	18	2.9	[22]
^{153}Dy(3)	26.5	1.4	84	17	3.1	[22]
^{153}Dy(4)*	27.5	1.5	85	16	4.3	[22]
^{153}Dy(5)*	28.5	1.3	85	16	3.9	[22]
^{152}Dy(1)	22	1.7	85	21	3.1	[23]
^{152}Dy(6)*	31	1.4	89	16	1.3	[23]
^{151}Dy(2)	23.5	1.1	84	19	4.1	[24]
^{151}Dy(3)	26.5	1.4	82	16	3.4	[24]
^{151}Dy(4)	26.5	1.8	84	16	1.1	[24]
^{151}Dy(5)*	34.5	1.7	79	9	1.6	[24]
^{152}Tb(2)	31	1.1	85	13	4.8	[25]
^{151}Tb(2)	22.5	1.2	85	20	3.3	[26]
^{151}Tb(3)	24.5	1.7	82	18	2.6	[26]
^{151}Tb(4)*	29.5	1.1	84	16	0.8	[26]
^{151}Tb(5)	24.5	0.8	76	16	2.6	[25]
^{151}Tb(6)	25.5	1.0	76	15	3.2	[25]
^{151}Tb(7)	26.5	0.8	77	15	3.2	[25]
^{151}Tb(8)	27.5	0.9	77	12	2.4	[25]
^{150}Tb(1)	19	1.8	76	20	4.1	[27]
^{145}Tb*	18.5	1.7	69	14	1.8	[28]
^{150}Gd(5)*	34	1.3	81	14	4.9	[29]
^{149}Gd(3)	21.5	1.3	76	20	4.7	[37]
^{148}Gd(2)*	29	1.4	81	14	2.2	[30]
^{147}Gd(HD)(A)*	75.5	1.1	140	9	1.4	[41]
^{147}Gd(HD)(B)*	67.5	1.4	139	12	1.8	[41]
^{146}Gd(2)	26	0.9	71	15	4.1	[31]
^{145}Gd(3)	29.5	1.3	70	10	1.7	[32]
^{143}Eu	13.5	1.5	67	22	3.1	[33]
^{142}Eu*	20	1.8	66	15	2.0	[34]
^{142}Sm(1)	19	1.3	65	19	4.2	[35]
^{142}Sm(2)	22	1.8	70	16	1.8	[35]
^{132}Nd(2)	22	1.8	62	8	4.9	[43]
^{133}Pr(2)	20.5	1.8	55	10	3.6	[44]
^{133}Pr(4)	18.5	1.1	52	12	5.0	[44]

Note: Asterisks label bands that can be described in two ways.

Table 7. Fitted parameters for unitary phases

Nucleus	I_{min}	$-E_{j0}(0)$, MeV	$I_c^2 \times 10^{-2}$	Number of transitions	χ, keV	References
^{197}Bi(1)*	6.5	105.9	30.0	13	0.4	[3]
^{197}Bi(2)	7.5	47.4	13.4	10	0.5	[3]
^{198}Pb	12	36.4	9.5	16	0.8	[7]
^{197}Pb(1)	7.5	87.7	25.4	17	0.4	[4]
^{197}Pb(2)*	8.5	193	55.4	16	1.0	[4]
^{196}Pb	6	21.1	5.4	11	0.4	[7]
^{195}Pb(1)*	7.5	104	30.5	13	0.5	[5]
^{195}Pb(3)	7.5	24.0	6.6	14	1.6	[5]
^{195}Pb(4)	8.5	23.4	6.4	12	0.8	[5]
^{194}Pb(1)	6	18.1	4.7	12	0.4	[8]
^{194}Pb(2)	10	24.8	6.9	9	0.7	[9]
^{194}Pb(3)	11	25.2	7.0	9	0.4	[9]
^{193}Pb(1)*	11.5	48.6	13.5	10	0.7	[6]
^{193}Pb(3)	12.5	37.3	10.5	9	2.2	[6]
^{193}Pb(4)	13.5	24.6	6.8	9	0.3	[6]
^{193}Pb(5)	8.5	25.5	7.0	9	0.5	[6]
^{193}Pb(6)	9.5	24.2	6.7	10	0.6	[6]
^{192}Pb	10	14.0	3.6	11	0.6	[10]
^{195}Tl(1)	14.5	23.8	6.7	12	0.6	[10]
^{195}Tl(2)	15.5	31.5	8.8	10	0.6	[10]
^{194}Tl(1)	12	43.8	12.9	13	0.5	[10]
^{194}Tl(4)	9	43.2	12.8	14	0.2	[10]
^{194}Tl(2)	10	31.8	8.9	14	0.6	[10]
^{194}Tl(5)	9	32.7	9.3	14	0.9	[10]
^{194}Tl(3)	8	47.6	14.3	13	0.8	[10]
^{194}Tl(6)	9	53.5	16.1	12	0.8	[10]
^{193}Tl(1)	9.5	34.0	9.6	13	0.3	[10]
^{193}Tl(2)	10.5	27.6	7.8	13	0.5	[10]
^{192}Tl(1)*	16	71.3	20.4	8	0.6	[11]
^{192}Tl(2)	17	34.3	9.7	8	0.7	[11]
^{192}Tl(5)	15	13.3	3.2	8	0.5	[11]
^{192}Tl(6)	17	24.3	6.3	7	1.3	[11]
^{191}Tl(1)	13.5	27.4	7.5	10	0.6	[12]
^{191}Tl(2)	15.5	22.6	6.1	8	0.4	[12]
^{195}Hg(a)	12.5	21.6	6.0	19	1.4	[14]
^{195}Hg(b)	11.5	21.1	5.8	19	1.3	[14]
^{195}Hg(c)	10.5	18.1	4.5	17	4.4	[14]
^{195}Hg(d)	15.5	42.1	12.2	17	1.2	[14]
^{194}Hg(1)	10	19.1	5.1	20	2.2	[15]
^{194}Hg(2)	8	25.3	7.0	20	0.5	[15]
^{194}Hg(3)	11	26.9	7.5	19	0.7	[15]
^{193}Hg(2)	10.5	25.2	6.9	19	0.6	[16]
^{193}Hg(3)	9.5	24.8	6.9	19	0.6	[16]
^{193}Hg(5)	9.5	43.7	11.8	17	0.6	[16]
^{192}Hg	8	17.9	4.7	20	0.9	[10]
^{191}Hg(1)	14.5	24.0	6.4	12	0.6	[10]
^{191}Hg(2)	12.5	30.9	8.6	12	0.3	[10]
^{191}Hg(3)	13.5	26.4	7.4	12	0.3	[10]
^{190}Hg(1)	12	13.2	3.2	15	3.3	[13]
^{190}Hg(3)	12	33.2	9.4	11	0.5	[13]
^{189}Hg	14.5	19.5	4.9	10	0.7	[17]

Table 7. (Contd.)

Nucleus	I_{min}	$-E_{j0}(0)$, MeV	$I_c^2 \times 10^{-2}$	Number of transitions	χ, keV	References
^{191}Au(1)	6.5	19.8	5.2	20	3.5	[18]
^{191}Au(2)	17.5	22.6	6.1	11	0.7	[18]
^{191}Au(3)	16.5	20.4	5.5	13	0.5	[18]
^{153}Dy(HD)*	73.5	204.1	69.6	11	1.5	[40]
^{153}Dy(4)*	28.5	1592.0	394.5	16	2.7	[22]
^{153}Dy(5)*	29.5	3023.3	751.1	16	2.0	[22]
^{152}Dy(4)	24	319.2	71.5	15	1.0	[23]
^{152}Dy(5)	23	358.8	80.5	14	0.8	[23]
^{152}Dy(6)*	32	1464.3	381.3	16	1.0	[23]
^{151}Dy(1)	18.5	429.1	96.4	21	0.7	[24]
^{151}Dy(5)*	34.5	306.6	67.3	9	1.4	[24]
^{151}Tb(4)*	30.5	3694.0	909.8	16	0.8	[26]
^{150}Tb(2)	23	540.3	117.8	16	0.9	[27]
^{145}Tb*	18.5	427.9	84.5	16	1.5	[27]
^{150}Gd(5)*	35	4018.4	960.0	17	5.0	[29]
^{148}Gd(2)*	30	1634.1	386.3	14	2.2	[30]
^{147}Gd(HD)(A)*	74.5	1016.7	407.5	9	1.5	[41]
^{147}Gd(HD)(B)*	67.5	1316.1	526.9	12	1.8	[41]
^{147}Gd(1)	22.5	129.7	26.4	17	5.0	[30]
^{146}Gd(3)	27	34.6	5.6	9	2.9	[31]
^{142}Eu*	21	451.4	85.5	15	1.1	[34]
^{133}Pm(5)	5.5	25.0	3.0	8	1.1	[42]
^{133}Pm(6)	6.5	25.0	3.0	7	1.5	[42]
^{133}Pm(7)	3.5	1.6	0.1	6	2.9	[42]
^{81}Sr(2)	19.5	162.8	11.1	6	3.2	[49]
^{81}Sr(3)	19.5	179.6	11.6	7	4.6	[49]
^{81}Sr(4)	15.5	17.2	0.7	5	2.2	[49]

Note: Asterisks label bands that can be described in two ways.

that, in those cases, they observed the Landau–Zener effect—that is, band crossing. Although the resulting value of χ is less than 5 keV for these bands, they cannot be described within the present analysis, which takes no account of such effects.

From Tables 6 and 7, it can be seen that, in the mass region around $A \sim 190$, only 3 of 62 bands subjected to analysis elude description. At the same time, only 9 bands of 35 in the mass region around $A \sim 130$ can be described. In the mass region around $A \sim 150$, only 22 bands of 64 could not be described. In all probability, this is because the ground states of the nuclei in the mass region around $A \sim 190$ are not deformed; therefore, their rotational spectrum is completely determined by the phase transition to the superfluid state, whereby the nucleus appears to be in a superdeformed state. At the same time, the ground states of the nuclei in the mass regions around $A \sim 150$ and $A \sim 130$ are deformed.

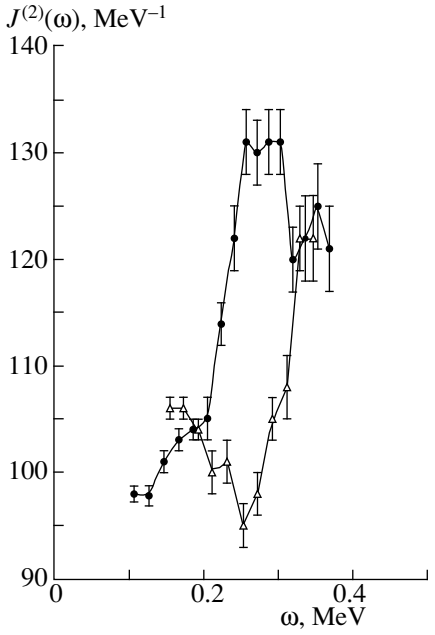

Fig. 6. Dynamical moment of inertia as a function of the frequency of rotation for the rotational bands in the (closed circles) ^{193}Hg(1) and (open triangles) ^{193}Hg(4) nuclei.

4. CONCLUSIONS

In the present study, the rotational states of superdeformed nuclei have been investigated on the basis of a model that admits triplet Cooper pairing in superfluid nuclear matter. One hundred and sixty-one rotational bands have been analyzed for nuclei from the mass regions around $A \sim 190$; 150; 130; and 80, 70.

Within our approach, we have successfully described 110 rotational bands. All these bands have the following special features:

(i) The parameters appearing in (10) and (15) are close within each mass region (this is illustrated by the data in Tables 6 and 7). If the finiteness of nuclear sizes has been taken into account correctly, these parameters must feature no dependence on the nuclear species, but they must appear to be characteristics of nuclear matter.

(ii) For nonunitary phases, the band must be terminated at spin values higher than the corresponding values for unitary phases. Tables 6 and 7 illustrate the correlation between the minimal spin of a band and the phase with which this band is associated.

(iii) Within the model used, there must occur pairs of bands showing weak signature splitting, corresponding to a single phase, and having spins that differ by unity. From the data in Tables 6 and 7, it follows that there are 28 such pairs.

Thus, the model of superfluid nuclear matter featuring triplet Cooper pairing is by and large consistent with available experimental data on the rotational states of superdeformed nuclei.

Despite obvious successes achieved in describing superdeformed nuclei, the theory presented here is unable to describe 51 rotational bands. For these bands, the behavior of the dynamical moment of inertia differs substantially from what is predicted by the theory. The disregard of boundary effects may be one of the reasons behind the aforementioned discrepancy.

ACKNOWLEDGMENTS

We are grateful to V.M. Kolybasov for stimulating discussions.

REFERENCES

1. P. J. Twin *et al.*, Phys. Rev. Lett. **57**, 811 (1986).
2. B. J. P. Gall *et al.*, Phys. Lett. B **345**, 124 (1995).
3. R. M. Clark *et al.*, Phys. Rev. C **51**, R1052 (1995).
4. R. Hibbert *et al.*, Phys. Rev. C **54**, 2253 (1996).
5. L. P. Farris *et al.*, Phys. Rev. C **51**, R2288 (1995).
6. J. R. Hughes *et al.*, Phys. Rev. C **51**, R447 (1995).
7. R. M. Clark *et al.*, Phys. Rev. C **50**, 1222 (1994).
8. K. Theine *et al.*, Z. Phys. A **336**, 113 (1990).
9. J. R. Hughes *et al.*, Phys. Rev. C **50**, R1265 (1994).
10. X.-L. Han and C.-L. Wu, At. Data Nucl. Data Tables **52**, 43 (1992).
11. Y. Liang *et al.*, Phys. Rev. C **46**, R2136 (1992).
12. S. Pilotte *et al.*, Phys. Rev. C **49**, 718 (1994).
13. A. N. Wilson *et al.*, Phys. Rev. C **54**, 559 (1996).
14. G. Hackman *et al.*, Phys. Rev. C **55**, 148 (1997).
15. R. Krücken *et al.*, Phys. Rev. C **54**, R2109 (1996).
16. M. J. Joyce *et al.*, Phys. Lett. B **340**, 150 (1994).
17. J. Bearden *et al.*, Z. Phys. A **341**, 491 (1992).
18. C. Schück *et al.*, Phys. Rev. C **56**, R1667 (1997).
19. D. E. Appelbe *et al.*, Phys. Rev. C **56**, 2490 (1997).
20. S. M. Fischer *et al.*, Phys. Rev. C **54**, R2806 (1996).
21. D. Nisius *et al.*, Phys. Rev. C **51**, R1061 (1995).
22. B. Cederwall *et al.*, Phys. Lett. B **346**, 244 (1995).
23. P. J. Dagnall *et al.*, Phys. Lett. B **335**, 313 (1994).
24. D. Nisius *et al.*, Phys. Lett. B **346**, 15 (1995).
25. G. de France *et al.*, Phys. Lett. B **331**, 290 (1994).
26. B. Kharraja *et al.*, Phys. Lett. B **341**, 268 (1995).
27. P. Fallon *et al.*, Phys. Rev. C **52**, 93 (1995).
28. S. M. Mullins *et al.*, Phys. Rev. C **50**, R2261 (1994).
29. P. Fallon *et al.*, Phys. Rev. Lett. **73**, 782 (1994).
30. B. Haas *et al.*, Nucl. Phys. A **561**, 251 (1993).
31. C. Schumacher, Phys. Rev. C **52**, 1302 (1995).
32. T. Rzaca-Urban, Phys. Lett. B **356**, 456 (1995).
33. A. Atac *et al.*, Phys. Rev. Lett. **70**, 1069 (1993).
34. S. M. Mullins *et al.*, Phys. Rev. C **52**, 99 (1995).
35. G. Hackman *et al.*, Phys. Rev. C **54**, R2293 (1996).
36. L. A. Bernstein *et al.*, Phys. Rev. C **52**, R1171 (1995).
37. S. Flibotte *et al.*, Nucl. Phys. A **584**, 373 (1995).
38. S. Lunardi *et al.*, Phys. Rev. Lett. **72**, 1427 (1994).
39. C. W. Beausang *et al.*, Phys. Rev. Lett. **71**, 1800 (1993).

40. A. Galindo-Uribarri *et al.*, Phys. Rev. Lett. **71**, 231 (1993).
41. D. R. La Fosse *et al.*, Phys. Rev. Lett. **74**, 5186 (1995).
42. A. Galindo-Uribarri *et al.*, Phys. Rev. C **54**, 1057 (1996).
43. D. T. Joss *et al.*, Phys. Rev. C **54**, R969 (1996).
44. J. N. Wilson *et al.*, Phys. Rev. Lett. **74**, 1950 (1995).
45. A. Galindo-Uribarri *et al.*, Phys. Rev. C **54**, R454 (1996).
46. A. T. Semple *et al.*, Phys. Rev. C **54**, 425 (1996).
47. D. Santos *et al.*, Phys. Rev. Lett. **74**, 1708 (1995).
48. M. A. Riley *et al.*, Phys. Rev. C **47**, R441 (1993).
49. F. Cristancho *et al.*, Phys. Lett. B **357**, 281 (1995).
50. D. R. LaFosse *et al.*, Phys. Rev. Lett. **78**, 614 (1997).
51. A. Bohr and B. R. Mottelson, Nucl. Phys. A **354**, 303 (1981).
52. R. V. F. Janssens and T. L. Khoo, Annu. Rev. Nucl. Part. Sci. **41**, 321 (1991).
53. V. I. Fal'ko and I. S. Shapiro, Zh. Éksp. Teor. Fiz. **91**, 1194 (1986) [Sov. Phys. JETP **64**, 706 (1986)].
54. I. S. Shapiro, Nucl. Phys. A **518**, 73 (1990).
55. A. Bohr, B. R. Mottelson, and D. Pines, Phys. Rev. **110**, 936 (1958).
56. S. T. Belyaev, K. Dan. Vidensk. Selsk. Mat. Fys. Medd. **31**, 11 (1959).
57. V. G. Soloviev, Nucl. Phys. **9**, 655 (1959).
58. V. P. Mineev, Usp. Fiz. Nauk **139**, 303 (1983) [Sov. Phys. Usp. **26**, 160 (1983)].
59. G. E. Volovik, Usp. Fiz. Nauk **143**, 73 (1984) [Sov. Phys. Usp. **27**, 363 (1984)].
60. G. E. Volovik, in *Exotic Properties of Superfluid ^{3}He* (World Sci., 1984).
61. R. Piepenbring and K. V. Protasov, Z. Phys. A **345**, 7 (1993).
62. V. A. Khangulyan and I. S. Shapiro, in *Proceedings of the International Conference on Nuclear Spectroscopy and Nuclear Structure, St. Petersburg, 1995.*
63. M. J. Joyce *et al.*, Phys. Rev. Lett. **71**, 2176 (1993).
64. R. Piepenbring and K. V. Protasov, Z. Phys. A **347**, 27 (1993).
65. D. M. Cullen *et al.*, Phys. Rev. Lett. **65**, 1547 (1990).

Translated by A. Isaakyan

Physics of Atomic Nuclei, Vol. 63, No. 9, 2000, pp. 1546–1561. Translated from Yadernaya Fizika, Vol. 63, No. 9, 2000, pp. 1631–1647.

NUCLEI
Theory

Effective Nucleon–Nucleon Forces and Interaction of Light Exotic Nuclei with Stable Nuclei at Low Energies

D. V. Bolotov, O. M. Knyazkov†, I. N. Kuchtina[1)], and S. A. Fayans[2)]

Institute of Physics, St. Petersburg State University, Universitetskaya nab. 7/9, St. Petersburg, 199164 Russia

Received April 15, 1999; in final form, August 2, 1999

Abstract—The effect of the density dependence of effective nucleon–nucleon forces on the folded potential of the interactions of the light exotic nuclei ^{6}He, ^{11}Li, ^{11}Be, and ^{8}B with the stable nucleus ^{12}C is studied, and the corresponding experimental data on the total reaction cross sections and on elastic scattering are analyzed. A semimicroscopic double-folding model featuring various density-dependent forces based on the M3Y interaction is used together with the nucleon densities as calculated within the density-functional method by using a unified set of parameters for all the above nuclei. It is shown that the angular distributions recently measured for elastic ^{6}He scattering on ^{12}C at an energy of 41.6 MeV per projectile nucleon and for elastic ^{11}Be scattering on ^{12}C at an energy of 49.3 MeV per projectile nucleon can be described satisfactorily if the real part of the optical folded potential is supplemented with a surface term mimicking the contribution of the dynamical polarization potential. *© 2000 MAIK "Nauka/Interperiodica".*

1. INTRODUCTION

The properties of exotic light nuclei lying far off the beta-stability line have been vigorously studied in recent years (for an overview, see [1–3] and references therein). Quasielastic scattering of exotic light nuclei on stable nuclei furnish information both about the potential of interaction between colliding nuclei and about the distribution of matter in them. The method based on the double-folding model underlies the most popular procedure for analyzing experimental angular distributions at low energies. Various versions of this model are surveyed in [3]. One of these versions was developed in [4] and used in [5] to analyze the quasielastic scattering of ^{11}Li nuclei on ^{28}Si nuclei at an energy of 29 MeV per projectile nucleon, of ^{11}Li nuclei on ^{12}C nuclei at an energy of 60 MeV per projectile nucleon, and of ^{7}Be and ^{8}B nuclei on ^{12}C nuclei at an energy of 40 MeV per projectile nucleon, as well as to study the energy dependence of the total reaction cross sections for the ^{11}Li + ^{12}C, ^{8}B + ^{12}C, and ^{8}B + ^{28}Si nuclear systems [6]. A reasonable description of experimental data was obtained in all of these cases.

In [4–6], the M3Y interaction [7], which does not depend on the density distribution in nuclear matter, was used to simulate effective forces between the nucleons of the colliding nuclei. An alternative version of the folding model employs effective nucleon–nucleon forces dependent on the density of nuclei. Originally, the DDM3Y effective interaction was introduced to analyze elastic alpha-particle scattering [8]; later on, it was applied to the case of heavy-ion scattering [9]. The effects of one-nucleon exchange were taken into account implicitly in those studies. Khoa and von Oertzen [10] employed density-dependent effective nucleon–nucleon forces and considered one-nucleon-exchange effects explicitly within the density-matrix formalism. These authors emphasized the important role of the density dependence of effective forces in describing the saturation of nuclear matter and indicated that angular distributions in heavy-ion scattering (for example, in the ^{16}O + ^{16}O system) are sensitive to the choice of the density-dependent factors. The set of density-dependent factors was later extended in [11].

In the present study, the approach developed in [4] is used to explore the effect of the density-dependent factor in effective nucleon–nucleon forces on the interactions between exotic light nuclei and stable nuclei and to analyze recent experimental data on the elastic scattering of such nuclei.

The ensuing exposition is organized as follows. In Section 2, we discuss various options of effective forces and schemes for computing double-folded potentials. In Section 3, we consider procedures for constructing nucleon densities for the ^{6}He, ^{11}Li, ^{11}Be, and ^{8}B nuclei and their integrated features. The potentials simulating the interaction of these nuclei with the target nucleus ^{12}C are deduced in Section 4. There, we also analyze the effect of the density-dependent factor on the properties of the double-folded potentials over a wide energy region. In Section 5, we present the results of the calculations performed within the proposed approach for the angular distributions in the elastic scattering of the nuclei being considered and for the corresponding total reaction cross sections. In Section 6, we

† Deceased.

1) Joint Institute for Nuclear Research, Dubna, Moscow oblast, 141980 Russia.

2) Russian Research Centre Kurchatov Institute, pl. Kurchatova 1, Moscow, 123182 Russia.

analyze experimental data on the elastic scattering of ^{6}He nuclei on ^{12}C nuclei at an energy of 41.6 MeV per projectile nucleon [12] and of ^{11}Be nuclei on ^{12}C nuclei at an energy of 49.3 MeV per projectile nucleon [13] and discuss the role of the dynamical polarization potential. In the Conclusions, we summarize the basic results of our study.

2. EFFECTIVE NUCLEON–NUCLEON FORCES AND SCHEME FOR CONSTRUCTING FOLDED POTENTIALS

2.1. Effective Nucleon–Nucleon Interaction

Our analysis will be performed within the popular approximation factorizing the coordinate and the density dependence of the effective forces [8]:

$$V^{D(E)}(s, \rho) = v^{D(E)}(s)F(\rho). \quad (1)$$

Here, s is the modulus of the radius vector between two nucleons from colliding nuclei, while the indices D and E label, respectively, the direct and the exchange component of effective forces. For the component of the effective forces that is independent of the matter-distribution density in nuclei, we take the total M3Y interaction [7], which is based on the G-matrix elements of the Reid and Elliott interactions. For the isoscalar components of these interactions, we have

$$v_0^D(s) = 7999\frac{\exp(-4s)}{4s} - 2134\frac{\exp(-2.5s)}{2.5s}, \quad (2)$$

$$v_0^E(s) = 4631\frac{\exp(-4s)}{4s} - 1787\frac{\exp(-2.5s)}{2.5s} - 7.847\frac{\exp(-0.7072s)}{0.7072s}. \quad (3)$$

For the isovector components, we also use the isovector part of the M3Y interaction:

$$v_1^D(s) = 4886\frac{\exp(-4s)}{4s} - 1176\frac{\exp(-2.5s)}{2.5s}, \quad (4)$$

$$v_1^E(s) = 1518\frac{\exp(-4s)}{4s} - 828.4\frac{\exp(-2.5s)}{2.5s} - 2.616\frac{\exp(-0.7072s)}{0.7072s}. \quad (5)$$

In the present study, we consider the target nucleus ^{12}C, for which $N = Z$, so that the role of the isovector components is insignificant for practical purposes.

The factor of the density dependence is chosen in the standard form

$$F_D(\rho) = C[1 + d\exp(-\gamma\rho)], \quad (6)$$

$$F_B(\rho) = C[1 + \alpha\rho^\beta]. \quad (7)$$

Here, $F_D(\rho)$ and $F_B(\rho)$ correspond to the DDM3Y interaction [8] and the BDM3Y interaction [10], respectively. In the ensuing analysis, we employ the M3Y interaction without density dependence (that is, the $C = 1$, $\alpha = 0$ version), one version of the DDM3Y interaction, and two versions of the BDM3Y interaction with the parameters specified in [10]. These parameters are quoted in Table 1.

Table 1. Parameters of effective nucleon–nucleon forces

Version of forces	C	d	γ, fm^3	α, fm^3	β, fm^3
M3Y	1	0	–	0	–
DDM3Y1	0.2845	3.6391	2.9605	–	–
BDM3Y1	1.2253	–	–	1.5124	1
BDM3Y2	1.0678	–	–	5.1069	2

It should be recalled that, in addition to the aforementioned factor of density dependence, yet another factor, that of energy dependence, is often introduced in (1) [8–11]. Since this energy dependence is much weaker than the energy dependence due to the explicit inclusion of one-nucleon-exchange effects, we disregard here the additional factor mentioned immediately above.

2.2. Double-Folded Potentials

Let us consider the interaction of two composite particles. In the first order in effective nucleon–nucleon forces, the interaction potential can be represented in the form

$$U(\mathbf{R}) = U^D(\mathbf{R}) + U^E(\mathbf{R}), \quad (8)$$

where $U^D(\mathbf{R})$ is the direct potential in the double-folding model [14]; it can be written as

$$U^D(\mathbf{R}) = \iint \rho^{(1)}(\mathbf{r}_1)V^D(\mathbf{s}, \rho)\rho^{(2)}(\mathbf{r}_2)d\mathbf{r}_1 d\mathbf{r}_2, \quad (9)$$

where $\rho^{(i)}(\mathbf{r}_i)$ are the densities of colliding nuclei ($i = 1, 2$). The leading contribution to the exchange potential $U^E(\mathbf{R})$ comes from one-nucleon-exchange effects, which can be described in the density-matrix formalism [15] as

$$U^E(\mathbf{R}) = \iint \rho^{(1)}(\mathbf{r}_1, \mathbf{r}_1 + \mathbf{s})V^E(\mathbf{s})\rho^{(2)}(\mathbf{r}_2, \mathbf{r}_2 - \mathbf{s}) \times \exp[i\mathbf{k}(\mathbf{R})\mathbf{s}/\eta]d\mathbf{r}_1 d\mathbf{r}_2. \quad (10)$$

This is the localized version of the exchange term. Here, $\rho^{(i)}(\mathbf{r}, \mathbf{r}')$ stands for the density matrices describing colliding nuclei; $\mathbf{s} = \mathbf{r}_2 - \mathbf{r}_1 + \mathbf{R}$; and $\mathbf{k}(\mathbf{R})$ is the local momentum, whose squared modulus is given by

$$k^2(\mathbf{R}) = (2m\eta/\hbar^2)[E - U(\mathbf{R}) - V_C(\mathbf{R})], \quad (11)$$

where E is the c.m. collision energy; $V_C(\mathbf{R})$ is the Coulomb potential; and η is the reduced mass number,

$$\eta = A_1A_2/(A_1 + A_2). \quad (12)$$

From the above relations, we can see that the calculation of the double-folded potential involves self-consistently solving a set of nonlinear equations, because the momentum $\mathbf{k}(\mathbf{R})$ depends on the sought potential. This problem is solved by means of an iterative procedure.

Expressions (9) and (10) coincide in form with the analogous formulas from [4], but a significant difference between these is that the former involve the density-dependent factor $F(\rho)$ in the effective forces. In the frozen-nucleon approximation, the expression for this factor in the region where the nuclei overlap can be represented as

$$F(\rho) = F\left[\rho_1\left(\mathbf{r}_1 + \frac{\mathbf{s}}{2}\right) + \rho_2\left(\mathbf{r}_1 - \frac{\mathbf{s}}{2}\right)\right]. \quad (13)$$

Thus, the density values are taken at the midpoint between the nucleons of colliding nuclei. The presence of the density-dependent factor $F(\rho)$ makes the relevant calculations cumbersome. By means of the same method as in [4], we can reduce, however, the integrals in (9) and (10) to radial integrals. By applying an iterative procedure to the exchange term $U^E(\mathbf{R})$, it is possible, in principle, to calculate the potentials exactly within the adopted approximation if we know the density matrices for colliding nuclei. A further considerable simplification of the calculations is achieved by employing the mixed coordinate–momentum representation and by going over from the density matrices to the nucleon densities with allowance for local correlations. In practice, this transition can be implemented to a high precision with the aid of the simple formula [16]

$$\rho(\mathbf{r}, \mathbf{r} + \mathbf{s}) = \rho(\mathbf{r} + \mathbf{s}/2) j_1[k_{\text{eff}}(\mathbf{r} + \mathbf{s}/2)s], \quad (14)$$

where $j_1(x) = 3(\sin x - x\cos x)/x^3$ is the exchange correlation function. For $s \longrightarrow 0$—that is, in the zero-range approximation for the interaction—we have $j_1(x) \longrightarrow 1$. The effective momentum k_{eff} takes into account boundary effects; in the case of semi-infinite nuclear matter, it coincides with the local Fermi momentum. The expression for k_{eff} can be found in [16].

3. NUCLEON DENSITIES

Thus, we have seen that, apart from effective nucleon–nucleon forces, the nucleon densities also appear to be an important ingredient of the scheme for computing the potentials being discussed. A distinctive feature of the present study is that the single-particle neutron and proton densities are calculated for all colliding nuclei—both projectiles and targets—rather than parametrized (as is often done in considering nuclear reactions on the basis of the double-folding model). This calculation is performed within the density-functional method [17–19] with a single set of parameters.

The density-functional method is based on the Hohenberg–Kohn theorem [20] and on the Kohn–Sham quasiparticle formalism admitting the introduction of a quasiparticle Hamiltonian featuring a free kinetic-energy operator where the effective nucleon mass m^* coincides with the vacuum mass m ($m^*/m = 1$). The nucleon density ρ is represented as a sum over single-(quasi)particle orbitals—that is, as a shell sum minimizing the energy of the system. The quasiparticle spectrum and the wave functions are calculated in a self-consistent mean field that is determined by the first functional derivative of the total energy with respect to the relevant density, while the effective interaction is determined by the second functional derivative. This approach can be considered as one of the versions of the self-consistent theory of finite Fermi systems [22–24], a version that has much in common with the Hartree–Fock–Bogolyubov method employing density-dependent effective forces [25]. A basic problem here lies in choosing that parametrization of the density functional which is appropriate for practical applications. One of the versions was proposed in [17], where the ρ dependence taking effectively into account many-body forces and complicated correlations was introduced via linear-fractional functions, while surface effects were included via finite-range forces also admitting the dependence on the density. The energy density is represented in the form

$$\varepsilon = \varepsilon_{\text{kin}} + \varepsilon_{\text{int}}, \quad (15)$$

where the first term is the kinetic-energy density given by

$$\varepsilon_{\text{kin}} = \sum_\lambda n_\lambda \int \varphi_\lambda^*(\mathbf{r}) \frac{\mathbf{p}^2}{2m} \varphi_\lambda(\mathbf{r}) d\mathbf{r}. \quad (16)$$

Here, n_λ is the number of particles at the level λ (if pairing is taken into account within the Bardeen–Cooper–Schrieffer scheme, we have $n_\lambda = (2j+1)\nu_\lambda^2$, where ν_λ^2 is the quasiparticle population factor), φ_λ is the corresponding single-particle wave function, and $\lambda = nljm\tau$ is a standard set of the single-particle quantum numbers. For spherical nuclei, we have

$$\varepsilon_{\text{kin}} = \frac{1}{4\pi}\sum_\lambda n_\lambda \frac{\hbar^2}{2m}\left[\left(\frac{dR_{nlj\tau}(r)}{dr}\right)^2 + \frac{l(l+1)}{r^2} R_{nlj\tau}^2(r)\right]. \quad (17)$$

The expression for the interaction-energy density involves a few terms,

$$\varepsilon_{\text{int}} = \varepsilon_{\text{main}} + \varepsilon_{\text{C}} + \varepsilon_{sl} + \varepsilon_{\text{pair}}, \quad (18)$$

where

$$\begin{aligned}\varepsilon_{\text{main}} = \frac{2}{3}\epsilon_{\text{F}}^0 \rho_0 [&a_+^v x_+^2 f_+^v + a_-^v x_-^2 f_-^v \\ &+ a_+^s x_+ f_+^s \widetilde{f_+^s x_+} + a_-^s x_- f_-^s \widetilde{f_-^s x_-}].\end{aligned} \quad (19)$$

Here, $x_\pm = (\rho_n \pm \rho_p)/2\rho_0$, ρ_n, ρ_p, and $2\rho_0$ being, respectively, the neutron density, the proton density, and the equilibrium density of symmetric nuclear matter ($N = Z$);

ϵ_F^0 is the Fermi energy in symmetric nuclear matter; and the density-dependent functions are given by

$$f_\pm^v = \frac{1 - h_{1\pm}^v x_+}{1 + h_{2\pm}^v x_+}, \quad f_\pm^s = \frac{1}{1 + h_\pm^s x_+}, \tag{20}$$

$$\widetilde{f_\pm^s x_\pm} = \int D(\mathbf{r} - \mathbf{r}') f_\pm^s(\mathbf{r}') x_\pm(\mathbf{r}') d\mathbf{r}', \tag{21}$$

where

$$D(\mathbf{r} - \mathbf{r}') = \delta(\mathbf{r} - \mathbf{r}') - V(|\mathbf{r} - \mathbf{r}'|)$$
$$= \delta(\mathbf{r} - \mathbf{r}') - \frac{1}{4\pi R^2 |\mathbf{r} - \mathbf{r}'|} \exp\left(-\frac{|\mathbf{r} - \mathbf{r}'|}{R}\right). \tag{22}$$

The second term in (22) is the Yukawa function normalized by the condition $\int d\mathbf{r} V(|\mathbf{r}|) = 1$. In the momentum representation, we have

$$D(q) = \frac{(q\mathbf{R})^2}{1 + (q\mathbf{R})^2}, \tag{23}$$

so that the last two terms in (19) correspond to the surface isoscalar and isovector interaction energy; in the case of infinite nuclear matter, they vanish. The Coulomb energy density ε_C is chosen in a conventional form with allowance for exchange in the Slater approximation:

$$\varepsilon_C = \frac{1}{2} e^2 \rho_p(r) \left(\frac{1}{r} \int_0^r \rho_p(r) r^2 dr + \int_r^\infty \rho_p(r) r dr \right) - \frac{3}{4} \left(\frac{3}{\pi}\right)^{1/3} e^2 \rho_p^{4/3}(r). \tag{24}$$

The term ε_{sl} in (18) corresponds to the contribution of *LS* spin–orbit interaction. For spherical nuclei, it can be expressed in terms of the spin–orbit densities as

$$\rho_{sl}^{n,p}(r) = \sum_\lambda n_\lambda \langle \boldsymbol{\sigma} \cdot \mathbf{l} \rangle_\lambda \left| \varphi_\lambda^{n,p}(\mathbf{r}) \right|^2, \tag{25}$$

where $\langle \boldsymbol{\sigma} \cdot \mathbf{l} \rangle_\lambda = j(j+1) - l(l+1) - 3/4$. With allowance for the spin-dependent first Fermi-liquid velocity harmonic proportional to $\hat{g}_1$, the *LS* interaction was chosen in the form

$$\hat{\mathcal{F}}_{sl} = C_0 r_0^2 \{ \hat{\kappa} [\nabla_1 \delta(\mathbf{r}_1 - \mathbf{r}_2)(\mathbf{p}_1 - \mathbf{p}_2)](\boldsymbol{\sigma}_1 + \boldsymbol{\sigma}_2) + \hat{g}_1 \delta(\mathbf{r}_1 - \mathbf{r}_2)(\boldsymbol{\sigma}_1 \cdot \boldsymbol{\sigma}_2)(\mathbf{p}_1 \cdot \mathbf{p}_2) \}, \tag{26}$$

where $C_0 = 2\epsilon_F^0 / 3\rho_0 = \pi^2 \hbar^3 / p_F^0 m$ is the inverse density of states at the Fermi surface in equilibrium nuclear matter; $\hat{\kappa} = \kappa + \kappa' \boldsymbol{\tau}_1 \cdot \boldsymbol{\tau}_2$; and $\hat{g}_1 = g_1 + g_1' \boldsymbol{\tau}_1 \cdot \boldsymbol{\tau}_2$, κ, κ', g_1, and g_1' being dimensionless strength constants. The contribution of these forces to the energy density takes the form

$$\varepsilon_{sl} = C_0 r_0^2 \sum_{i,k=n,p} \left(\frac{1}{r} \rho_{ls}^i \kappa^{ik} \frac{\partial \rho^k}{\partial r} + \frac{1}{4r^2} \rho_{ls}^i g_1^{ik} \rho_{ls}^k \right), \tag{27}$$

where $\kappa^{nn} = \kappa^{pp} = \kappa + \kappa'$, $\kappa^{pn} = \kappa^{np} = \kappa - \kappa'$, $g_1^{nn} = g_1^{pp} = g_1 + g_1'$, and $g_1^{pn} = g_1^{np} = g_1 - g_1'$.

The last term in (18) corresponds to the pairing-interaction-energy density

$$\varepsilon_{pair} = \frac{1}{2} \nu^\dagger \mathcal{F}^\xi \nu, \tag{28}$$

where ν is the anomalous (pairing) density and $\mathcal{F}^\xi$ is the effective interaction in the particle–particle channel. In the present study, this interaction was taken in the simplest form $\mathcal{F}^\xi = C_0 f^\xi \delta(\mathbf{r} - \mathbf{r}')$ with the same constant f^ξ for the neutrons and for the protons and was included in the calculation in a self-consistent way in terms of the basis of all bound single-particle states.

Below, we present the total set of parameters of the functional that is employed in the present study (see also [19]):

$$\left.\begin{aligned}
&a_+^v = -6.443, \quad h_{1+}^v = 0.162, \quad h_{2+}^v = 0.730,\\
&a_-^v = 5.473, \quad h_{1-}^v = h_{1+}^v, \quad h_{2-}^v = 2.5,\\
&a_+^s = 11.0, \quad h_+^s = 0.31,\\
&a_-^s = 5.0, \quad h_-^s = 0,\\
&\kappa^{pp} = \kappa^{pn} = 0.185, \quad g_1^{pp} = -g_1^{pn} = -0.10,\\
&f^\xi = -0.4,\\
&R = 0.35 \text{ fm}, \quad r_0 = 1.1462 \text{ fm}.
\end{aligned}\right\} \tag{29}$$

Some of the parameters are unambiguously related to basic features of nuclear matter. In particular, we have

$$\left.\begin{aligned}
a_+^v &= \alpha + (5\alpha + 6)/5\eta\\
h_{1+}^v &= 1 - \alpha/(a_+^v \eta)\\
h_{2+}^v &= 1/\eta - 1\\
a_-^v &= (3\beta^0/\epsilon_F^0 - 1)/f_-^v(x_+ = 1),
\end{aligned}\right\} \tag{30}$$

where

$$\alpha = 3\frac{\mu^0}{\epsilon_F^0} - \frac{9}{5}, \quad \eta = \frac{5K^0 + 6\epsilon_F^0}{18(\epsilon_F^0 - 5\mu^0)}. \tag{31}$$

Here, we have used the following notation: μ^0 is the chemical potential (binding energy per nucleon in equilibrium), K^0 is the compressibility modulus of nuclear matter, ϵ_F^0 is the Fermi energy, and β^0 is the parameter of the symmetry energy. The above parameter values

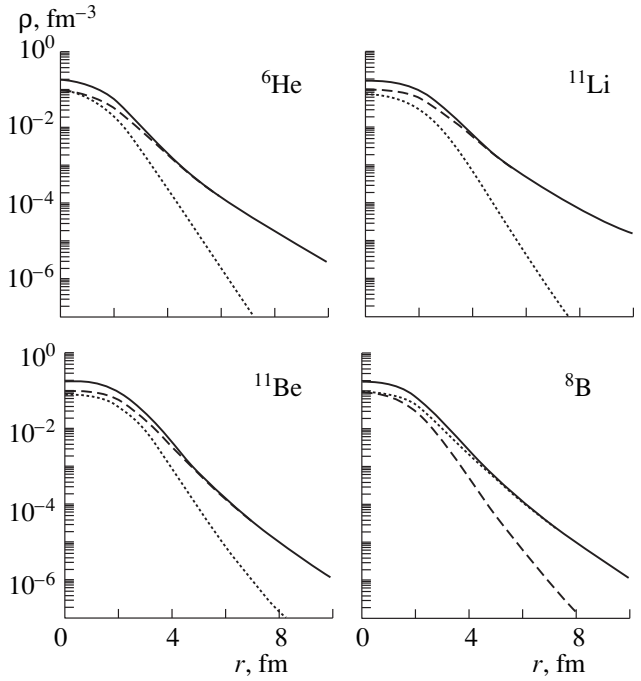

Fig. 1. Distributions of the (dashed curves) neutron, (dotted curves) proton, and (solid curves) matter densities in exotic light nuclei.

correspond to the following characteristics of equilibrium nuclear matter: $\mu^0 = -16.12$ MeV, $K^0 = 200$ MeV, $\epsilon_F^0 = (p_F^0)^2/2m = 36.62$ MeV, and $\beta^0 = 28.2$ MeV [$p_F^0/\hbar = (9\pi/8)^{1/3}/r_0 = 1.329$ fm^{-1}, $2\rho_0 = 3/4\pi r_0^3 = 0.1585$ fm^{-3}, and $C_0 = 308.0$ MeV fm^3].

The analysis reported here was performed for the ^{6}He + ^{12}C, ^{11}Li + ^{12}C, ^{11}Be + ^{12}C, and ^{8}B + ^{12}C systems. All projectiles that we chose belong to the class of so-called light exotic nuclei. They have a distinct nucleon halo—a neutron one in ^{6}He, ^{11}Li, and ^{11}Be and a proton one in ^{8}B (strictly speaking, it is preferable to use, in the last case, the concept of an extended proton tail rather than of a proton halo). For all chosen nuclear combinations, there are experimental data on angular distributions in quasielastic scattering. As was mentioned above, the quasielastic scattering of ^{11}Li and ^{8}B on ^{12}C was previously analyzed in [5] within the approach outlined above. As to experimental data on the angular distributions in the quasielastic scattering of ^{6}He and ^{11}Be on ^{12}C, they are analyzed in the present study.

Table 2. Root-mean-square radii (in fm) of the neutron (*n*), proton (*p*), and matter (*m*) distributions (also quoted are the values of the difference $\Delta r_{np} = \langle r_n^2\rangle^{1/2} - \langle r_p^2\rangle^{1/2}$)

Nucleus	$\langle r_n^2\rangle^{1/2}$	$\langle r_p^2\rangle^{1/2}$	$\langle r_m^2\rangle^{1/2}$	Δr_{np}
^{6}He	2.806 (3.213)	2.014 (2.026)	2.569 (2.872)	0.792 (1.187)
^{11}Li	3.255	2.235	3.012	1.020
^{11}Be	2.718	2.306	2.576	0.412
^{8}B	2.190	2.680	2.508	–0.490

Note: For ^{6}He, the first and the second row display the results of the calculations performed, respectively, with the parameters of the functional from [18] and the parameter values (29) of our study.

The pointlike neutron and proton densities computed according to the above scheme are depicted in Fig. 1, which also shows the matter-density distribution. The calculated root-mean-square radii of the neutron, proton, and matter distributions ($\langle r_n^2\rangle^{1/2}$, $\langle r_p^2\rangle^{1/2}$, and $\langle r_m^2\rangle^{1/2}$, respectively) in the ^{6}He, ^{11}Li, ^{11}Be, and ^{8}B nuclei are quoted in Table 2. Also given are the differences $\Delta r_{np} = \langle r_n^2\rangle^{1/2} - \langle r_p^2\rangle^{1/2}$, which characterize the spatial dimensions of the neutron—or proton for $\Delta r_{np} < 0$—halo (or the dimensions of the corresponding nucleon skin). As an illustration of the scatter of our results obtained with various parametrizations of the energy functional, quoted in Table 2 for the example of the ^{6}He nucleus are the integrated characteristics of the density distributions in two versions: the values presented parenthetically were calculated with the parameter set (29), while the values in the first row were found on the basis of the functional from [18]. The effect of this scatter on the angular distributions for elastic scattering is analyzed in Section 6. From data presented in Fig. 1 and in Table 2, it follows that, by and large, the results of the calculations are compatible with the concept that these are exotic nuclei featuring a distinct nucleon halo (nucleon skin).

4. FOLDED POTENTIALS AND THEIR INTEGRATED CHARACTERISTICS

By relying on the neutron and proton densities obtained within the density-functional method and presented in preceding section and on the four versions of effective nucleon–nucleon forces (their parameters are presented in Table 1) and by using the procedure described in Section 2, we have calculated the potentials of ^{6}He, ^{11}Li, ^{11}Be, and ^{8}B interaction with the target nucleus ^{12}C at energies between 20 and 60 MeV per projectile nucleon. The choice of the energy interval was motivated by the fact that, by now, it is the region where the angular distributions for the quasielastic scattering of the above exotic nuclei by ^{12}C target nuclei have been measured at several energy values (see [12, 13, 26, 27]). The radial dependence of the potentials that we obtained is illustrated in Figs. 2–5. Table 3 quotes the values of the volume integrals J_v, while Table 4 lists the values of the root-mean-square radii $\langle r_v^2\rangle^{1/2}$ of these potentials.

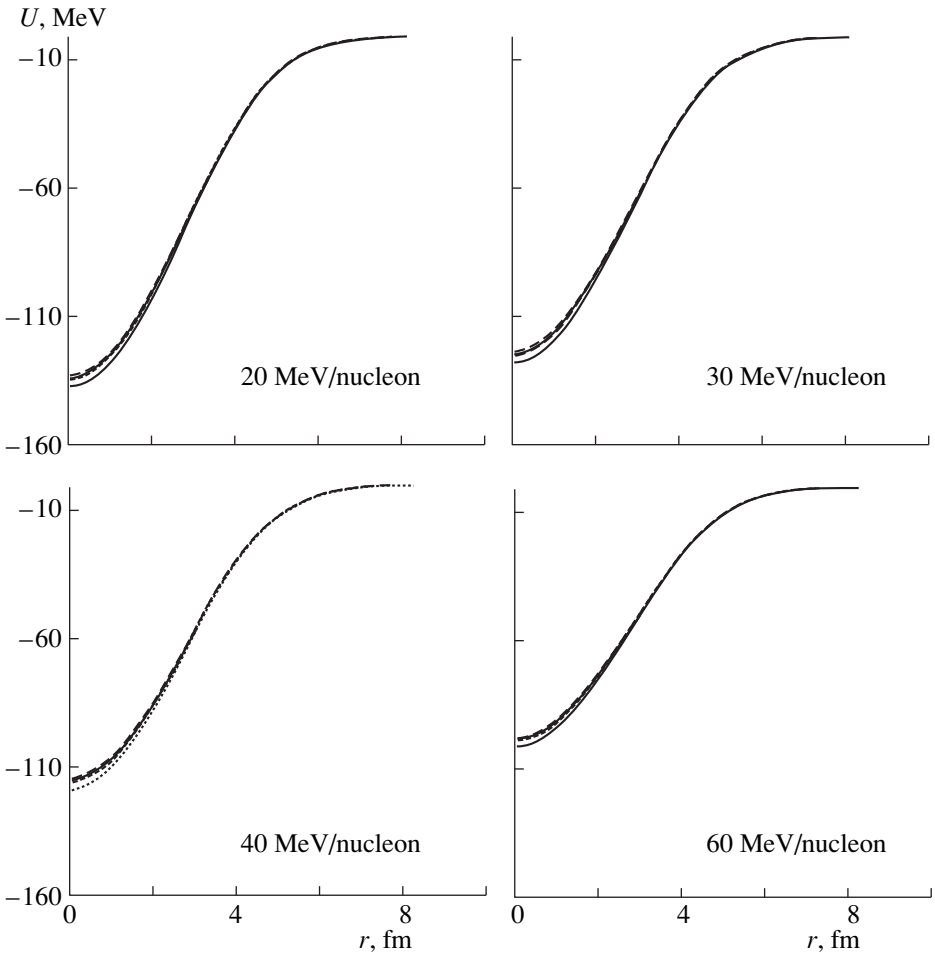

Fig. 2. Folded potentials for the ^{6}He + ^{12}C nuclear system at various energies. The results of the calculations with the M3Y, DDM3Y1, BDM3Y1, and BDM3Y2 interactions are shown by the solid curves, short dashes, dotted curves, and long dashes, respectively.

Let us now discuss the results that we obtained. From Fig. 2–5, we can easily see that, for the nuclear species being considered, the distinctions between the potentials due to the choice of the density dependence for effective forces are of importance at small values of the radius R—that is, in the region that can have but a

Table 3. Volume integrals of the folded potentials (in 10^3 MeV fm^3 units)

Version of forces	Energy, MeV/nucleon	Nuclear system				Version of forces	Energy, MeV/nucleon	Nuclear system			
		^{6}He + ^{12}C	^{11}Li + ^{12}C	^{11}Be + ^{12}C	^{8}B + ^{12}C			^{6}He + ^{12}C	^{11}Li + ^{12}C	^{11}Be + ^{12}C	^{8}B + ^{12}C
M3Y	20	–29.25	–52.68	–50.38	–37.85	BDM3Y1	20	–30.57	–54.91	–52.29	–39.43
	30	–27.23	–49.07	–47.11	–35.32		30	–28.35	–50.93	–48.64	–36.63
	40	–25.41	–45.82	–44.16	–33.04		40	–26.35	–47.34	–45.33	–34.10
	60	–22.30	–40.27	–39.06	–29.12		60	–22.93	–41.21	–39.63	–29.74
DDM3Y1	20	–30.39	–54.42	–51.50	–39.00	BDM3Y2	20	–29.57	–53.10	–50.47	–38.11
	30	–28.20	–50.50	–47.94	–36.25		30	–27.42	–49.23	–46.92	–35.38
	40	–26.22	–46.97	–44.72	–33.77		40	–25.48	–45.75	–43.71	–32.93
	60	–22.85	–40.96	–39.18	–29.51		60	–22.16	–39.80	–38.18	–28.70

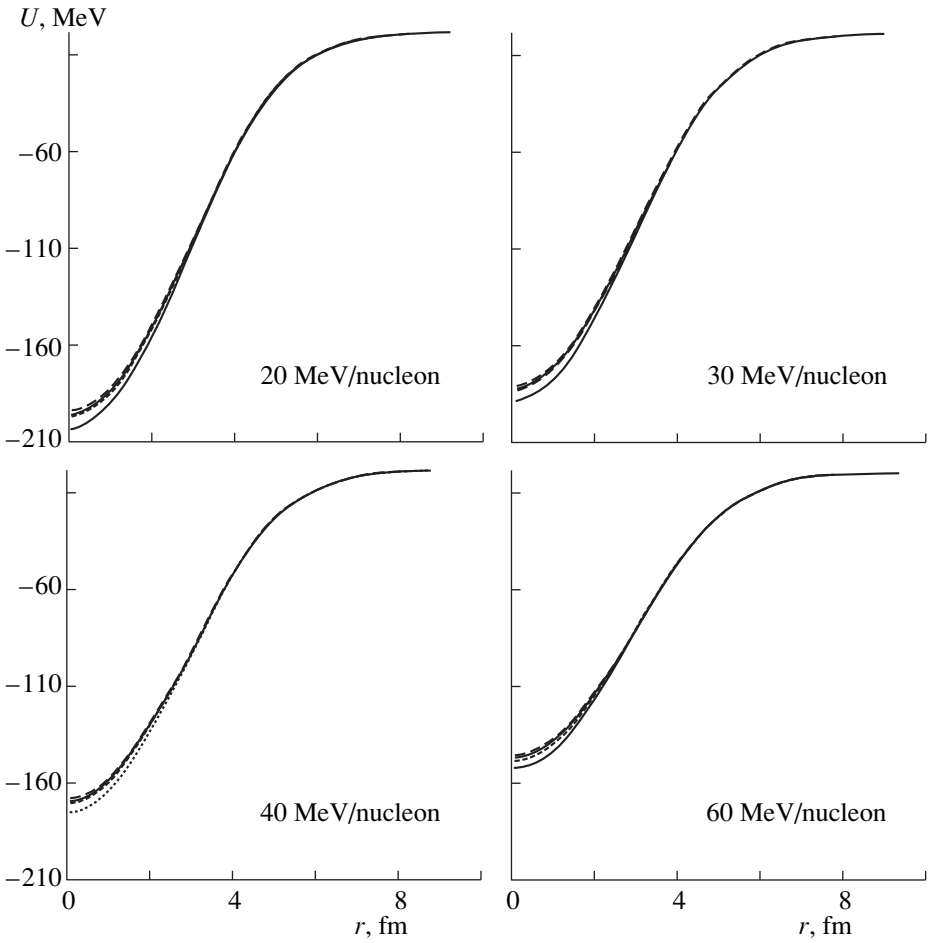

Fig. 3. As in Fig. 2, but for the ^{11}Li + ^{12}C nuclear system.

slight effect on the scattering cross section. In the surface region, which affects the scattering cross section at intermediate values of the angles, the distinctions between the potentials, albeit still present, are less pronounced. These regularities are independent of the projectile-nucleus species. The individual features of the projectile are manifested in that the potential depth at a fixed energy value increases with increasing mass number—that is, in going over from ^{6}He to ^{11}Li and ^{11}Be. The energy dependence of the potentials, which is asso-

Table 4. Root-mean-square radii of the potentials (in fm)

Version of forces	Energy, MeV/nucleon	Nuclear system				Version of forces	Energy, MeV/nucleon	Nuclear system			
		^{6}He + ^{12}C	^{11}Li + ^{12}C	^{11}Be + ^{12}C	^{8}B + ^{12}C			^{6}He + ^{12}C	^{11}Li + ^{12}C	^{11}Be + ^{12}C	^{8}B + ^{12}C
M3Y	20	4.04	4.35	4.07	4.01	BDM3Y1	20	4.07	4.39	4.10	4.04
	30	4.04	4.35	4.08	4.01		30	4.08	4.39	4.11	4.05
	40	4.05	4.36	4.09	4.02		40	4.09	4.39	4.12	4.06
	60	4.07	4.37	4.11	4.05		60	4.11	4.41	4.15	4.09
DDM3Y1	20	4.11	4.42	4.13	4.07	BDM3Y2	20	4.06	4.37	4.10	4.03
	30	4.11	4.42	4.14	4.08		30	4.06	4.38	4.11	4.04
	40	4.12	4.43	4.15	4.09		40	4.07	4.38	4.12	4.05
	60	4.14	4.45	4.17	4.11		60	4.10	4.40	4.14	4.08

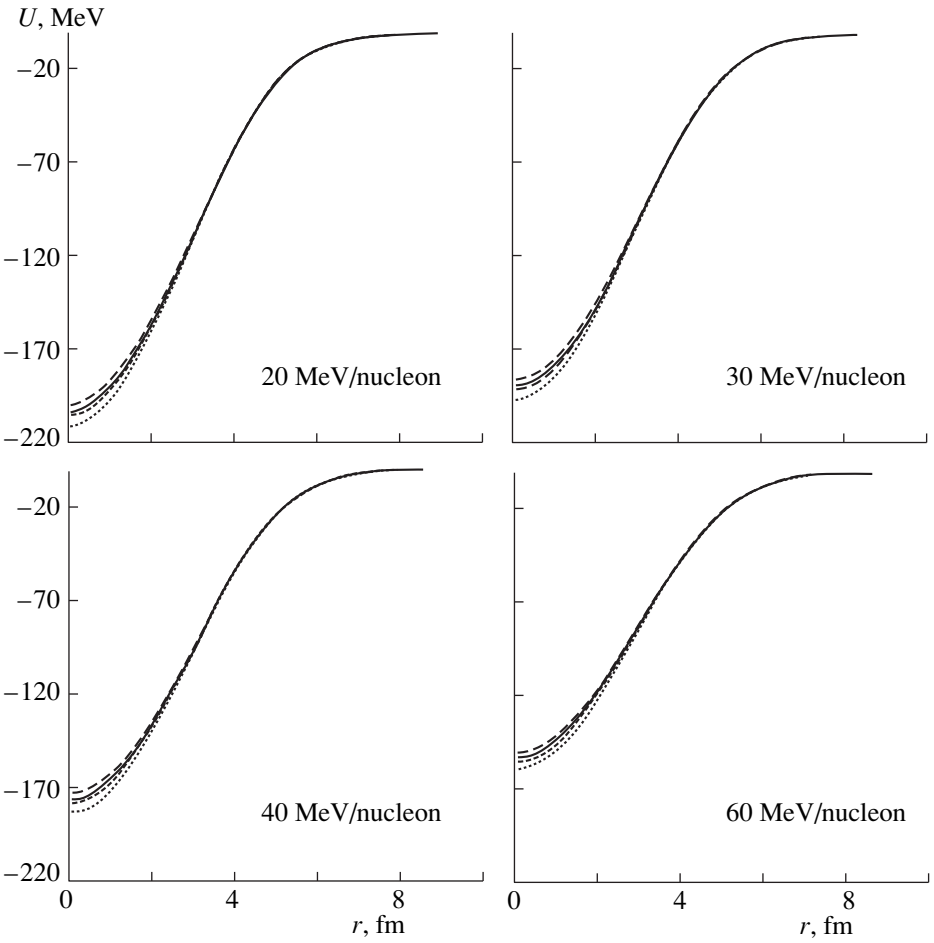

Fig. 4. As in Fig. 2, but for the ^{11}Be + ^{12}C nuclear system.

ciated primarily with one-nucleon-exchange effects, is sizable—in particular, the potential depth decreases by a factor of 1.5 as the energy is increased within the energy interval being considered.

A similar pattern is observed for the volume integrals J_v of the computed potentials (see Table 3). For all projectile-nucleus species, these integrals change within 4 to 5% in response to variations in the factor $F(\rho)$, the effect of $F(\rho)$ on J_v tending to become less pronounced with increasing mass number; at the same time, they decrease by 22–24% with increasing energy. For the root-mean-square radius of the potentials (see Table 4), the situation is reversed: changes in the absolute values are still smaller here, but $\langle r_v^2 \rangle^{1/2}$ is less affected by variations in energy than by variations in the factor of the density dependence of effective forces.

5. ANGULAR DISTRIBUTIONS AND TOTAL REACTION CROSS SECTIONS

We will make use of a semimicroscopic optical model and the coupled-channel method (in order to take into account the coupling of the elastic-scattering channel to inelastic channels) to calculate the angular distributions for elastic scattering and the total reaction cross sections. In accordance with [8], the total optical potential has the form

$$U_t(R) = U(R) + i\left[N_w U(R) - \alpha_w R\frac{dU(R)}{dR}\right], \quad (32)$$

where $U(R)$ is the double-folded potential (8) constructed without recourse to free parameters, while N_w and α_w are, respectively, the volume- and the surface-absorption parameter. These two free parameters must be determined by fitting the theoretical angular distributions and the total reaction cross sections to relevant experimental data. We note that, in the conventional semimicroscopic model employing the Woods–Saxon form factor, the absorption potential involves six free parameters. The choice of absorption potential in the form (32), with the radial dependence as determined by a combination of a real folded potential and its spatial gradient, can be considered as the simplest model of the total optical potential. It is rather difficult to perform a rigorous microscopic calculation of the imaginary part

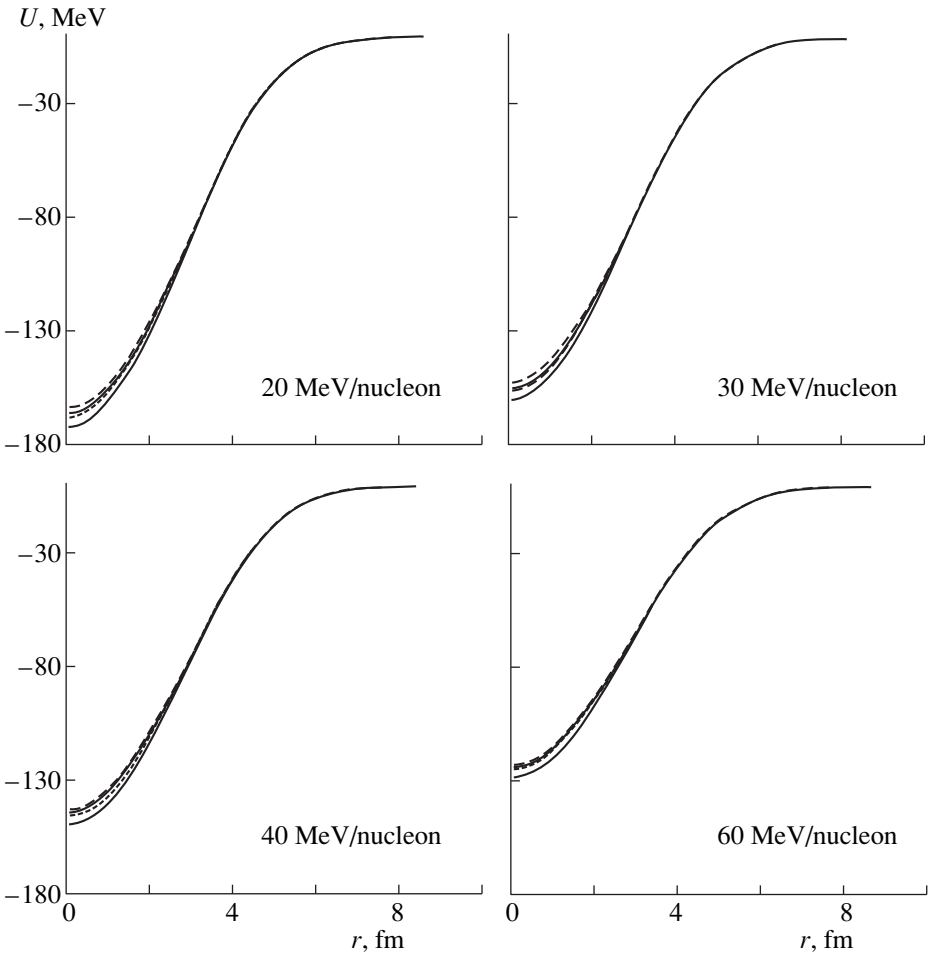

Fig. 5. As in Fig. 2, but for the $^{8}B + ^{12}C$ nuclear system.

of the optical potential, since this requires knowing microscopic transition densities and fine details of effective forces for a specific pair of colliding nuclei at a given energy value. No reliable method for such calculations has been developed so far. We only note that, in principle, the radial dependence of the imaginary part of the optical potential must differ, in accordance with the multichannel approach [28], from the radial dependence of the real part. This circumstance is taken into account in (32) with the aid of the parameter α_w. In this section, we present the results of methodological calculations with fixed values of the parameters N_w and α_w. For specific systems, their values correspond to an optimal description of experimental angular distributions (see the next section; see also the relevant analysis in [5]).

The results of the calculations are presented in Figs. 6–9 and in Table 5. It can easily be seen that, for all the systems being considered, the distinctions between the angular distributions for elastic scattering due to the density-dependent factor in effective forces manifest themselves at scattering angles $\theta_{c.m.}$ in excess of 15°–20°. These distinctions become more pronounced with increasing scattering angle, while the minimal scattering angle at which the density-dependent factor is operative decreases with increasing energy. At energies of 40 and 60 MeV per projectile nucleon and $\theta_{c.m.}$ values in excess of 40°, the effect of the choice of density dependence on the angular distributions is qualitatively similar to that which was observed in [10, 11] for the $^{16}O + ^{16}O$ nuclear system. Unfortunately, the scattering cross sections for exotic light nuclei decrease fast with increasing scattering angle; at present, experimental data cover only a small angular interval $\theta_{c.m.} < 20°$.

We note that, in a number of cases, the scattering pattern is of a rainbowlike character. For all systems being considered, with the exception of $^{6}He + ^{12}C$, rainbowlike effects manifest themselves at energies of 40 MeV per projectile nucleon and higher. They are the most spectacular for the $^{11}Li + ^{12}C$ nuclear system at an energy of 60 MeV per projectile nucleon. The integrated features of the reactions, such as σ_r, as well as the integrated features of the potentials, change insignificantly in response to variations in the density-dependent factor. As can be seen from Table 5, such

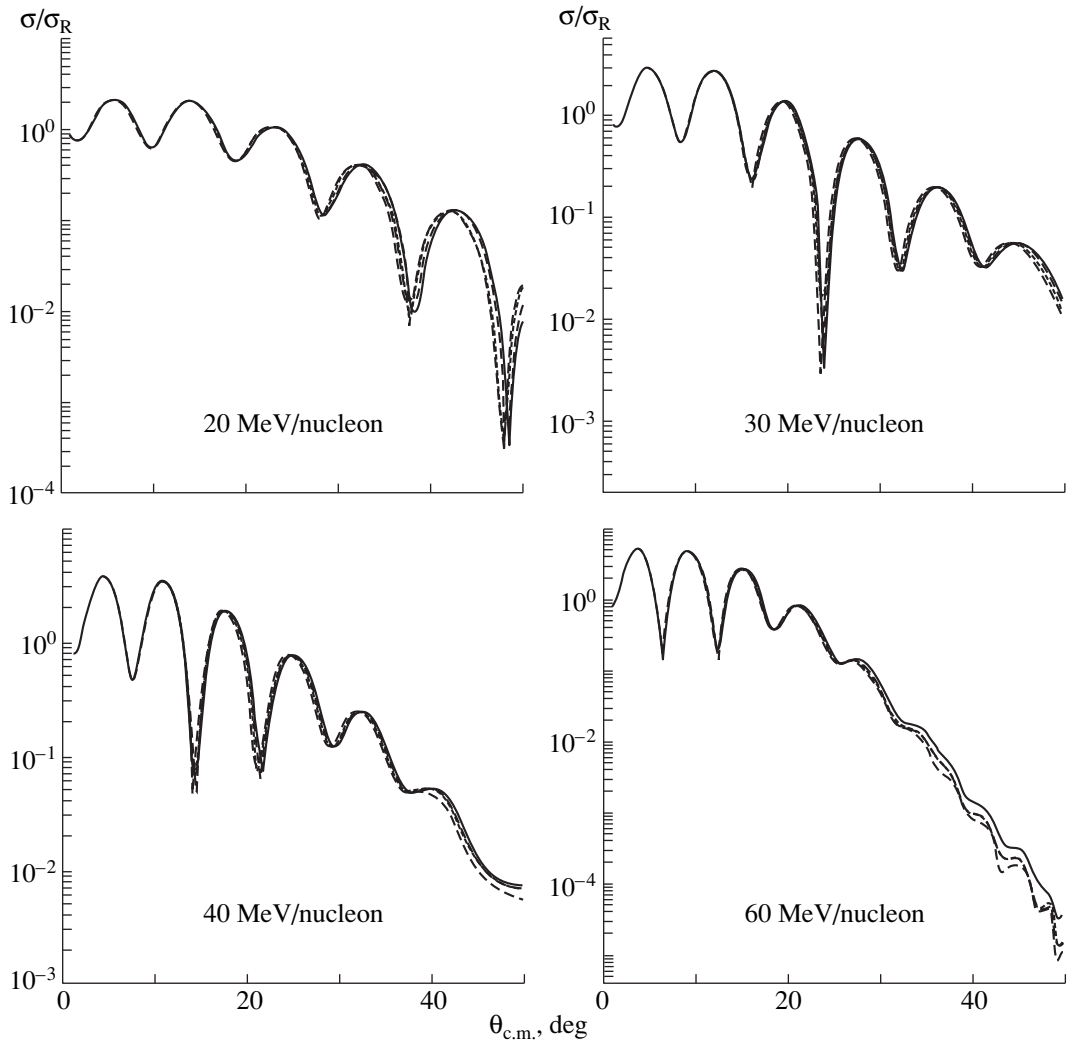

Fig. 6. Ratio of the angular distributions for the elastic scattering of ^{6}He nuclei on ^{12}C nuclei to the corresponding Rutherford cross section σ_R ($N_w = 0.5$, $\alpha_w = 0.03$). The notation for the curves is identical to that in Fig. 2.

changes in the total reaction cross section σ_r are within 3 to 4%; at the same time, an increase in the energy leads to a 17–21% decrease in σ_r. These changes are more pronounced for ^{11}Li than for other projectile species. The cross sections σ_r exhibit the greatest changes in the energy range between 20 and 40 MeV per projectile nucleon.

6. ANALYSIS OF EXPERIMENTAL DATA ON ELASTIC SCATTERING

In this section, the above semimicroscopic approach is used to analyze the angular distribution for the elastic scattering of ^{6}He nuclei on ^{12}C nuclei at an energy of 41.6 MeV per projectile nucleon and of ^{11}Be nuclei on ^{12}C nuclei at an energy of 49.3 MeV per projectile nucleon. In either case, experimental data were obtained with a high energy resolution at GANIL, where, in contrast to the previous experiments reported in [26, 27, 29, 30], the contribution of the inelastic excitation of the target nucleus ^{12}C was isolated in the scattering cross sections explicitly. In the case of the scattering of ^{11}Be projectiles, however, there is a contribution to the scattering cross section from the excitation of the first $(1/2)^-$ level in the ^{11}Be nucleus. Experimental data on ^{6}He scattering were obtained by Al-Khalili *et al.* [12], who simultaneously performed an analysis of these data within the eikonal four-body model. The first analysis of the experimental angular distributions for the elastic scattering of ^{11}Be nuclei on ^{12}C nuclei at an energy of 49.3 MeV per projectile nucleon was performed in [13]. These data were presented in the private communication of P. Roussel-Chomaz (GANIL, Caen, France).

Available experimental data cover a narrow interval of scattering angles ($\theta_{c.m.} < 13°$). For this reason, only one version of effective nucleon–nucleon interaction—namely, the M3Y version from Table 1—is used in the

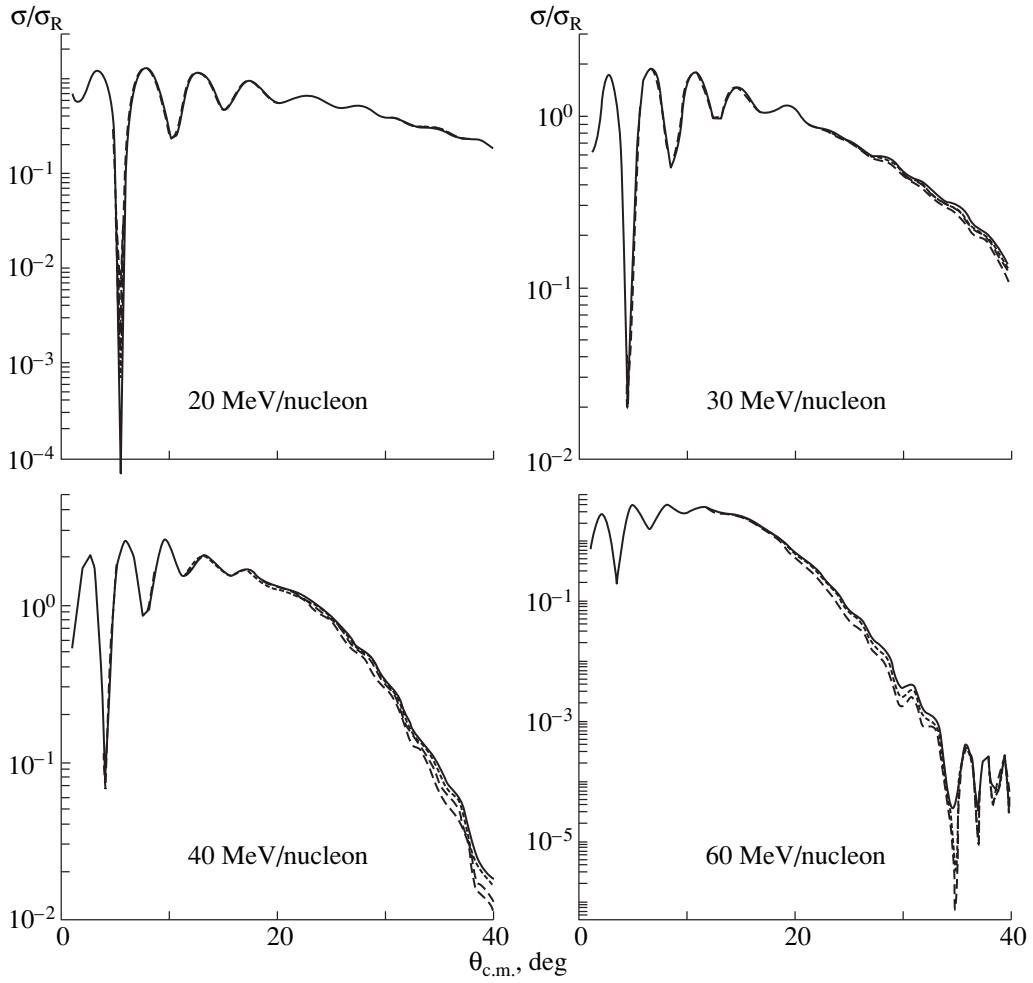

Fig. 7. Ratio of the angular distributions for the elastic scattering of ^{11}Li nuclei on ^{12}C nuclei to the corresponding Rutherford cross section σ_R (N_w = 0.3, α_w = 0.05). The notation for the curves is identical to that in Fig. 2.

present analysis. The scheme for constructing the cross sections is described in Section 5. The results that we obtained for this case are displayed in Fig. 10. We can see that, if the imaginary part of the optical potential is parametrized according to (32) in terms of only two parameters (N_w and α_w), oscillations in the computed

Table 5. Total reaction cross sections (in mb)

Version of forces	Energy, MeV/nucleon	Nuclear system				Version of forces	Energy, MeV/nucleon	Nuclear system			
		^{6}He + ^{12}C	^{11}Li + ^{12}C	^{11}Be + ^{12}C	^{8}B + ^{12}C			^{6}He + ^{12}C	^{11}Li + ^{12}C	^{11}Be + ^{12}C	^{8}B + ^{12}C
M3Y	20	1355	1839	1506	1437	BDM3Y1	20	1391	1884	1542	1474
	30	1269	1706	1428	1358		30	1303	1747	1461	1391
	40	1200	1604	1364	1292		40	1231	1642	1394	1322
	60	1089	1448	1260	1185		60	1116	1479	1285	1211
DDM3Y1	20	1404	1900	1553	1485	BDM3Y2	20	1367	1853	1520	1450
	30	1315	1761	1471	1402		30	1280	1719	1441	1370
	40	1242	1654	1403	1332		40	1210	1615	1374	1302
	60	1125	1490	1292	1219		60	1096	1455	1267	1192

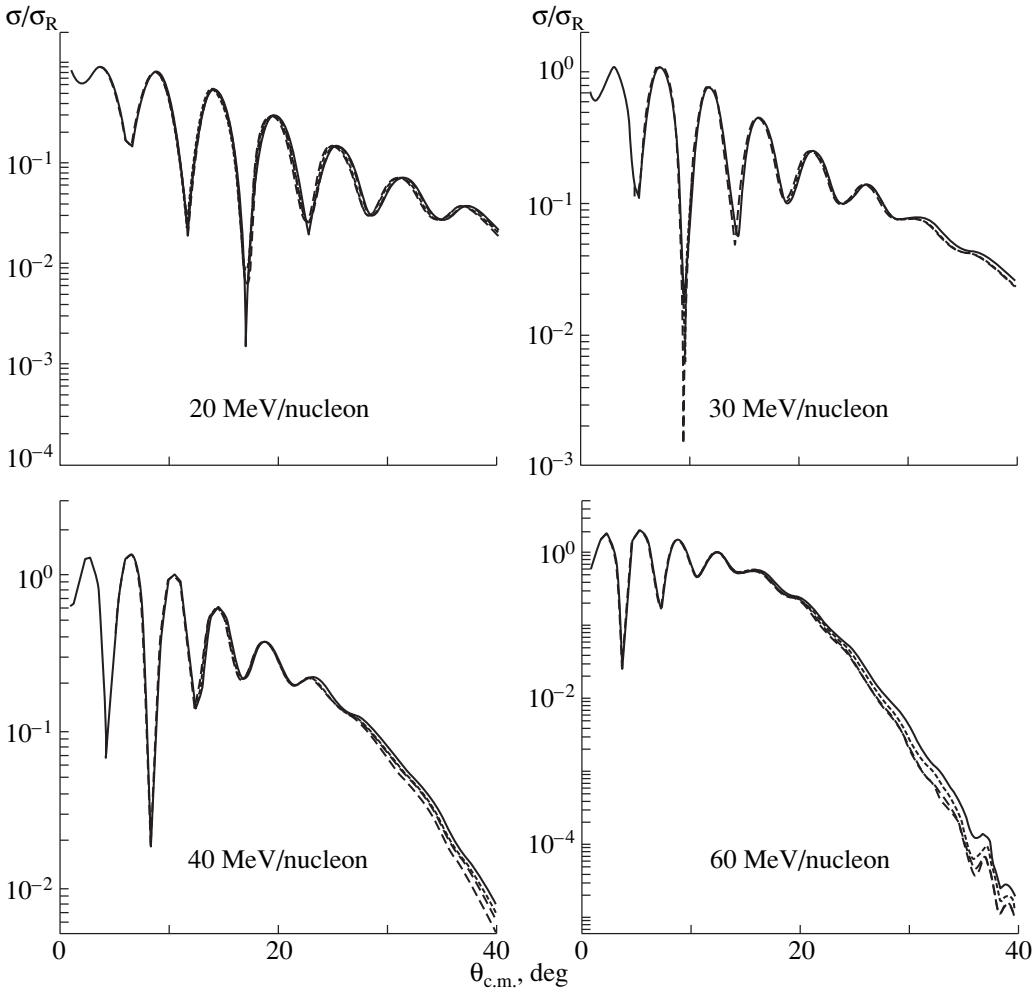

Fig. 8. Ratio of the angular distributions for the elastic scattering of ^{11}Be nuclei on ^{12}C nuclei to the corresponding Rutherford cross section σ_R (N_w = 0.4, α_w = 0.03). The notation for the curves is identical to that in Fig. 2.

angular distributions are shifted in phase with respect to experimental data. In the calculations, the parameters N_w and α_w were set to 0.5 and 0.03, respectively, for the ^{6}He nucleus and to 0.4 and 0.03, respectively, for the ^{11}Be nucleus. That the real part of the potential was supplemented with an additional surface term of the form $\alpha_v R\frac{dU(R)}{dR}$, which has the same structure as the surface term in the absorption potential, resulted in a satisfactory description of experimental data in both cases (solid curves).

The features of the potentials used in our analysis—specifically, their radial dependences, volume integrals, and root-mean-square radii—are displayed in Fig. 11 and in Table 6. In either case, the extra terms are of the same sign as the dominant potentials. For the ^{6}He nucleus, α_v = 0.15, the volume integral increases by 45%, and $\langle r_v^2\rangle^{1/2}$ increases by 10%. For the ^{11}Be nucleus, the contribution of the additional surface term is smaller: α_v = 0.07, the volume integral increases by 32%, and $\langle r_v^2\rangle^{1/2}$ increases by 8%. Usually, the introduction of the surface term in the real part of the optical potential is associated with the so-called dynamical polarization potential. This additional potential can be computed by the method of Green's functions within the multichannel theory of reactions [28]. Since this requires cumbersome computations, the dynamical polarization potential is introduced phenomenologically in the overwhelming majority of studies, in which

Table 6. Integrated characteristics of the potentials for the ^{6}He + ^{12}C and ^{11}Be + ^{12}C nuclear systems

System	^{6}He + ^{12}C		^{11}Be + ^{12}C	
α_v	0	0.15	0	0.07
J_v, 10^3 MeV fm^3	–25.14	–37.20	–41.67	–54.99
$\langle r_v^2\rangle^{1/2}$, fm	4.05	4.45	4.10	4.43

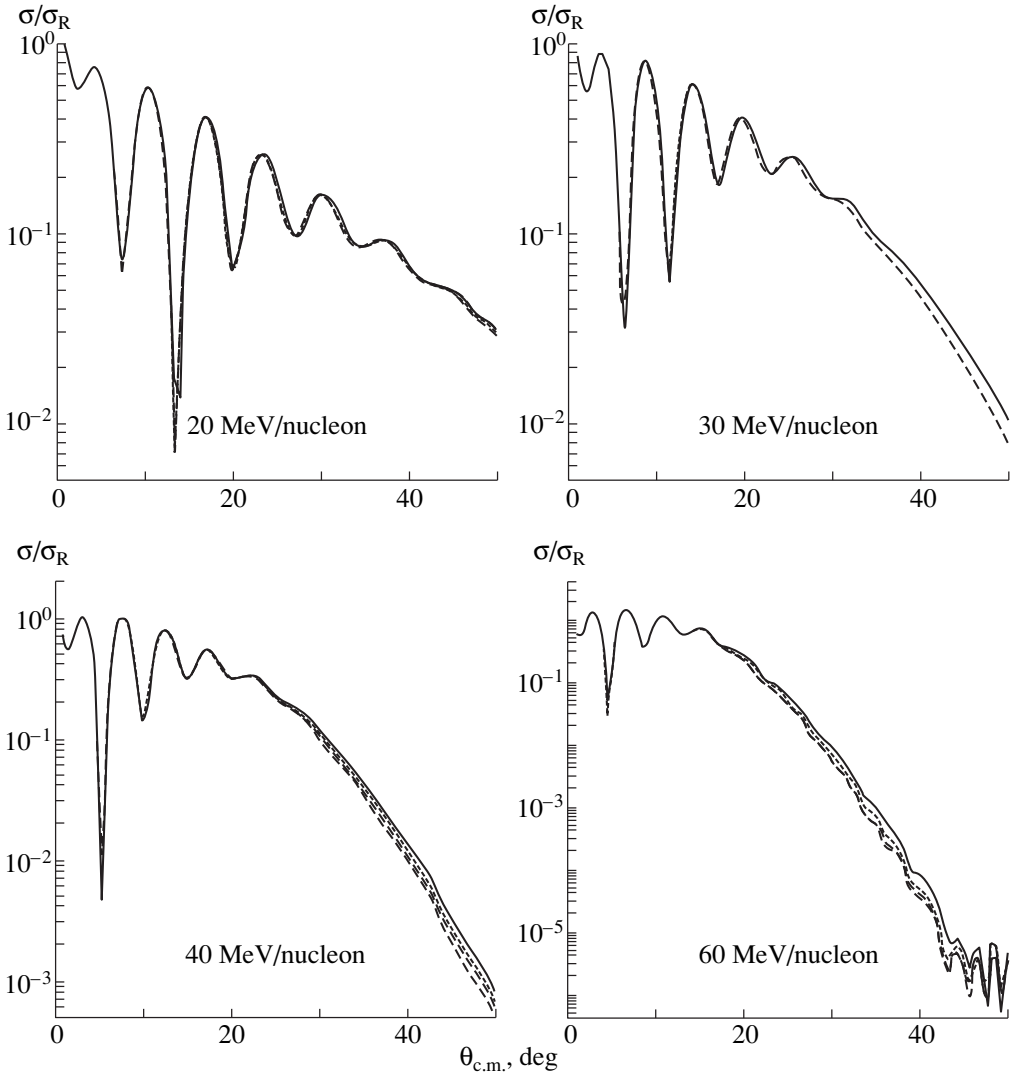

Fig. 9. Ratio of the angular distributions for the elastic scattering of ^{8}B nuclei on ^{12}C nuclei to the corresponding Rutherford cross section σ_R ($N_w = 0.5$, $\alpha_w = 0.03$). The notation for the curves is identical to that in Fig. 2.

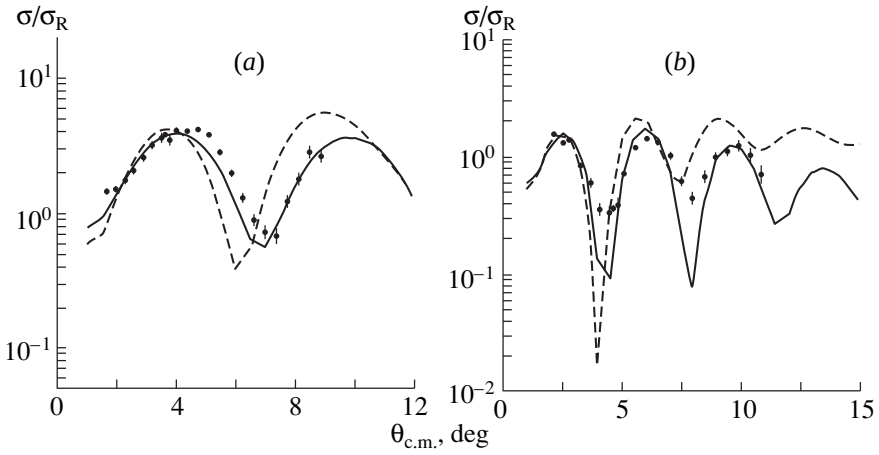

Fig. 10. (*a*) Ratio of the angular distributions for the elastic scattering of ^{6}He nuclei on ^{12}C nuclei at an energy of 41.6 MeV per projectile nucleon to the corresponding Rutherford cross section σ_R ($N_w = 0.5$, $\alpha_w = 0.03$): (dashed curve) results of the calculations with the folded potential and (solid curve) results of the calculations employing an additional surface term in the real part of the optical potential ($\alpha_V = 0.15$). (*b*) Results of similar calculations for the ^{11}Be + ^{12}C nuclear system at an energy of 49.3 MeV per projectile nucleon ($N_w = 0.5$, $\alpha_w = 0.03$, $\alpha_V = 0.07$).

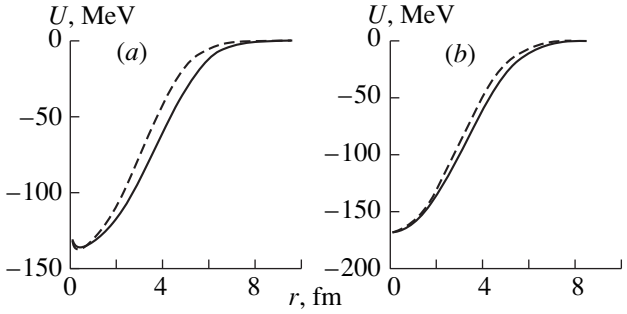

Fig. 11. Potentials of the interaction of the (*a*) ^{6}He and (*b*) ^{11}Be nuclei with the target nuclei ^{12}C at energies of, respectively, 41.6 and 49.3 MeV per projectile nucleon: (dashed curves) folded potentials and (solid curves) same folded potentials with the inclusion of a surface term (see the caption under Fig. 10).

case the sign of the dynamical polarization potential with respect to the sign of the leading real potential depends on its structure: it can either be opposite to it or coincide with it (see, for example, [30]). Moreover, the reversal of the sign of the dynamical polarization potential may occur in response to changes in the internuclear spacing [31].

In [13, 32], experimental data on the elastic scattering of ^{11}Be nuclei on ^{12}C nuclei at an energy of 49.3 MeV per projectile nucleon were analyzed by two methods: (i) within the Glauber approximation with allowance for noneikonal effects and (ii) on the basis of the adiabatic approach. The effect of the radius of the matter distribution in the ^{11}Be nucleus on the angular distributions was studied in either case. It was established that the optimal value of the matter radius is $\langle r_m^2 \rangle^{1/2}$ = 2.9 fm. We note that, in our approach, the proton and neutron densities for all colliding nuclear species were computed by the density-functional method independently of the procedure for the analysis of scattering. For the ^{11}Be nucleus, we obtained the value of $\langle r_m^2 \rangle^{1/2} \approx 2.6$ fm (see Table 2), which is less than that in [13, 32] by 11%. The use of the oscillator representation for the density in [33] in analyzing the cross sections for ^{11}Be interactions at an energy of 800 MeV per projectile nucleon yielded $\langle r_m^2 \rangle^{1/2} = 2.52 \pm 0.03$ fm. Thus, the greater value of $\langle r_m^2 \rangle^{1/2}$ for the ^{11}Be nucleus in [13, 32] may be explained by implicitly taking into account the effects of core polarization. This is consistent with the results of the analysis performed in the present study. To some extent, these considerations apply to the ^{6}He nucleus as well. At the same time, it should be noted that, within the folding model featuring no dynamical polarization potential, it is impossible to reproduce data on elastic scattering (measured thus far only at small values of the scattering angle) even by admitting wide density-distribution variations corresponding to strongly different values of $\langle r_m^2 \rangle^{1/2}$. This statement is illustrated in Fig. 12, which displays the nucleon-density distributions in the ^{6}He nucleus for two versions of the interaction (see Table 2) and the corresponding folded potentials and the angular distri-

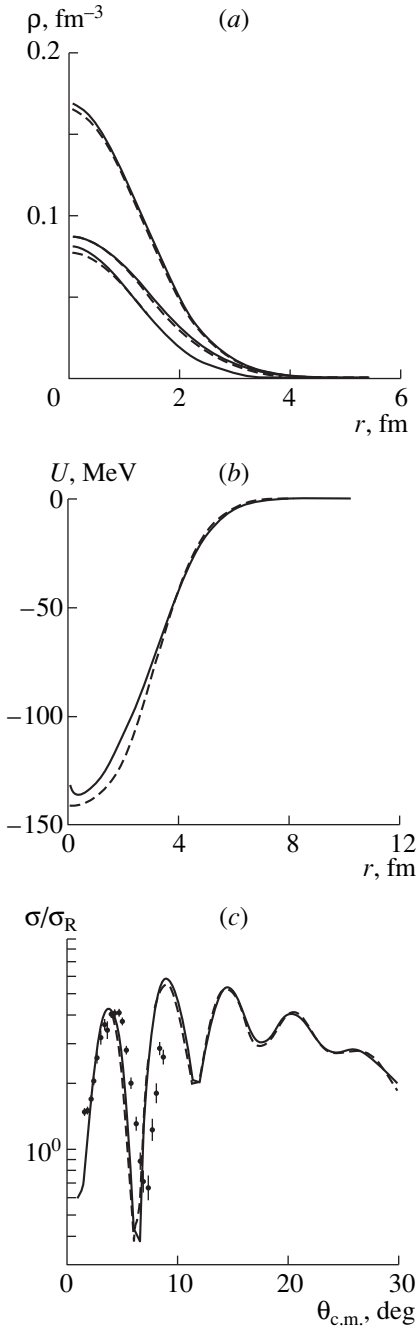

Fig. 12. (*a*) Matter-density distributions in the ^{6}He nucleus, (*b*) folded potentials, and (*c*) angular distributions for the elastic scattering of ^{6}He nuclei on ^{12}C nuclei at an energy of 41.6 MeV per projectile nucleon: (solid curves) results of the calculations with the parameter values specified in (29) (N_w = 0.5, α_w = 0.03) and (dashed curves) results of the calculations with the parameters of the functional from [18] (N_w = 0.5, α_w = 0.03).

butions for the elastic scattering of ^{6}He nuclei on ^{12}C nuclei at an energy of 41.6 MeV per projectile nucleon. It can be seen that, at small scattering angles, the angular distributions computed for the two versions in question differ insignificantly and that these versions show poor agreement with experimental data; the distinctions between the versions are pronounced beyond the measured region of angles.

The introduction of an additional surface attraction in the real part of the optical potential is not the only possibility for improving the description of the angular distributions in the case being considered: we can simulate successfully the role of the dynamical polarization potential by a combination of the volume and surface terms, relating the real part of the optical potential to its imaginary part through dispersion relations and introducing simplifying assumptions (for example, the approximation of separability in the spatial and energy variables [34]). However, this approach requires not only introducing additional parameters but also performing a global analysis of experimental data over a broad range of angles and, what is more important, over a maximally broad range of energies. This program was performed, in particular, for elastic ^{6}Li + ^{12}C scattering by Goncharov *et al.* [34], who obtained, among other things, evidence for anomalous dispersion—a sharp increase in the dispersive volume correction to the real part of the optical potential at energies of about 10–15 MeV per projectile nucleon. The total dispersive correction was found there to be positive at the surface and negative in the volume. More reliable conclusions on the magnitude and radial dependence of dispersive corrections to the real part of the optical potential in the scattering of exotic nuclei and on the role of the relationship between the surface and volume contributions to the imaginary potential—this relationship can sizably affect the angular distributions both in the region of small angles and in the region of rainbow scattering—can be drawn only after the appearance of new experimental data.

7. CONCLUSIONS

On the basis of the double-folding model, we have investigated the effect of various factors of density dependence in the M3Y effective forces on the real parts of the optical potentials, on the angular distributions in elastic scattering, and on the total cross sections for collisions of exotic light nuclei with stable ^{12}C nuclei at low energies. The effects of one-nucleon exchange are represented in a localized form within the density-matrix formalism by using spatial nucleon distributions as obtained for all nuclear species on the basis of the local-density approximation. For the unstable nuclei investigated here, these distributions have anomalously extended tails, which suggest the existence of nucleon halo in these nuclei. The imaginary part of the optical potential has been expressed in terms of its real part with the aid of two free parameters describing volume and surface absorption. The values of these parameters were fixed by fitting the results of the calculations to the measured angular distributions. The available body of experimental data cover limited angular and energy regions; for this reason, the conclusions that can be drawn from the present investigation are predominantly of a qualitative character. These conclusions are the following:

(i) The distinctions between the potentials due to different choices of the density-dependent factor $F(\rho)$ in effective forces take the greatest values at small distances. At a fixed energy value, the volume integrals of the potentials change only by a few percent in going over from one density-dependent factor to another, the root-mean-square radii of the potentials showing still smaller variations. The most pronounced energy dependence of the potentials is due to one-nucleon exchange: in the energy range 20–60 MeV, the potential depths decrease by a factor of 1.5 with increasing energy.

(ii) In response to variations in $F(\rho)$, the total reaction cross section σ_r changes only by 3 to 4%. At the same time, an increase in energy within the range being considered leads to a 17–21% decrease in σ_r. It is interesting to note that the changes in question are more pronounced for ^{11}Li than for the other nuclear species investigated here.

(iii) In the energy range being considered, the distinctions between the angular distributions in elastic scattering due to variations in $F(\rho)$ manifest themselves in the scattering-angle region $\theta_{c.m.} > 15°$–$20°$. These distinctions become more pronounced with increasing scattering angle and cover a wider angular region (that is, they appear at smaller angles) as the energy is increased. At energies in excess of 40 MeV per projectile nucleon, the scattering pattern may be of a rainbow-like character. The ^{11}Li + ^{12}C nuclear system at an energy of 60 MeV per projectile nucleon shows the most pronounced rainbow effects.

(iv) Experimental data on the angular distributions for the elastic scattering of ^{6}He nuclei on ^{12}C nuclei at an energy of 41.6 MeV per projectile nucleon and of ^{11}Be nuclei on ^{12}C nuclei at an energy of 49.3 MeV per projectile nucleon can be described satisfactorily by supplementing the real folded potential with an additional term, which is treated as that which takes effectively into account the dynamical polarization potential. The simplest choice, which improves considerably the agreement with available experimental data, consists in the inclusion of an extra surface term expressed in terms of the gradient of the optical potential. Additional experiments extending the angular and energy intervals of measurements are required for drawing more reliable conclusions on the role and the structure of the dynamical polarization potential in reactions involving exotic light nuclei.

ACKNOWLEDGMENTS

We are grateful to S.N. Ershov and S.A. Goncharov for stimulating discussions.

This work was supported in part by Deutsche Forschungs Gesellschaft and by the Russian Foundation for Basic Research (project nos. 98-02-16979 and 00-01-00617).

REFERENCES

1. C. A. Bertulani, L. F. Canto, and M. S. Hussein, Phys. Rep. **226**, 281 (1993).
2. I. Tanihata, J. Phys. G **22**, 157 (1996).
3. O. M. Knyaz'kov, I. N. Kukhtina, and S. A. Fayans, Fiz. Élem. Chastits At. Yadra **28**, 1061 (1997) [Phys. Part. Nucl. **28**, 418 (1997)].
4. O. M. Knyazkov, A. A. Kolozhvari, I. N. Kukhtina, and S. A. Fayans, Yad. Fiz. **59**, 466 (1996) [Phys. At. Nucl. **59**, 439 (1996)].
5. S. A. Fayans, O. M. Knyazkov, I. N. Kuchtina, *et al.*, Phys. Lett. B **357**, 509 (1995).
6. S. A. Fayans, O. M. Knyazkov, and I. N. Kuchtina, Nucl. Phys. A **626**, 263c (1997).
7. G. Bertsch, J. Borysowicz, H. McManus, *et al.*, Nucl. Phys. A **284**, 399 (1977).
8. A. M. Kobos, B. A. Brown, P. E. Hodgson, *et al.*, Nucl. Phys. A **384**, 65 (1982).
9. A. M. Kobos, B. A. Brown, R. Lindsay, *et al.*, Nucl. Phys. A **425**, 205 (1984).
10. D. T. Khoa and W. von Oertzen, Phys. Lett. B **304**, 8 (1993).
11. D. T. Khoa, G. R. Satchler, and W. von Oertzen, Phys. Rev. C **56**, 954 (1997).
12. J. S. Al-Khalili, M. B. Cortina-Gil, P. Roussel-Chomaz, *et al.*, Phys. Lett. B **378**, 45 (1996).
13. J. S. Al-Khalili, J. A. Tostevin, and J. M. Brooke, Phys. Rev. C **55**, R1018 (1997).
14. G. R. Satchler and W. G. Love, Phys. Rep. **55**, 183 (1979).
15. A. K. Chaudhuri and B. Sinha, Nucl. Phys. A **455**, 169 (1986).
16. X. Campi and A. Bouyssy, Phys. Lett. B **73**, 263 (1978).
17. A. V. Smirnov, S. V. Tolokonnikov, and S. A. Fayans, Yad. Fiz. **48**, 1661 (1988) [Sov. J. Nucl. Phys. **48**, 995 (1988)].
18. S. A. Fayans, A. P. Platonov, G. Graw, and D. Hofer, Nucl. Phys. A **577**, 557 (1994).
19. S. A. Fayans, S. V. Tolokonnikov, E. L. Tkykov, and D. Zawischa, Phys. Lett. B **338**, 1 (1994).
20. P. Hohenberg and W. Kohn, Phys. Rev. B **136**, 864 (1964).
21. W. Kohn and L. Sham, Phys. Rev. A **140**, 1133 (1965).
22. S. A. Fayans and V. A. Khodel', Pis'ma Zh. Éksp. Teor. Fiz. **17**, 633 (1973) [JETP Lett. **17**, 444 (1973)].
23. É. E. Sapershteĭn, S. A. Fayans, and V. A. Khodel', Fiz. Élem. Chastits At. Yadra **9**, 221 (1978) [Sov. J. Part. Nucl. **9**, 91 (1978)]; S. A. Fayans, E. E. Saperstein, and V. A. Khodel, Nucl. Phys. A **317**, 424 (1979); V. A. Khodel and E. E. Saperstein, Nucl. Phys. A **348**, 261 (1980).
24. V. A. Khodel and E. E. Saperstein, Phys. Rep. **92**, 185 (1982).
25. D. Vautherin and D. Brink, Phys. Rev. C **5**, 626 (1972).
26. J. J. Kolata, M. Zahar, R. Smith, *et al.*, Phys. Rev. Lett. **69**, 2631 (1992).
27. I. Pecina, R. Anne, D. Bazin, *et al.*, Phys. Rev. C **52**, 191 (1995).
28. H. Feshbach, Ann. Phys. (N.Y.) **5**, 357 (1958).
29. M. Lewitowicz, C. Borcea, F. Carstoiu, *et al.*, Nucl. Phys. A **562**, 301 (1993).
30. M. Zahar, M. Belbot, J. J. Kolata, *et al.*, Phys. Rev. C **49**, 1540 (1994).
31. S. A. Goncharov, O. M. Knyaz'kov, and A. A. Kolozhvari, Yad. Fiz. **59**, 666 (1996) [Phys. At. Nucl. **59**, 634 (1996)].
32. R. C. Johnson, J. S. Al-Khalili, and J. A. Tostevin, Phys. Rev. Lett. **79**, 2771 (1997).
33. I. Tanihata, I. Kobayashi, O. Yamakawa, *et al.*, Phys. Lett. B **206**, 592 (1988).
34. S. A. Goncharov, A. S. Dem'yanova, and A. A. Ogloblin, in *Proceedings of the Conference on Exotic Nuclei and Atomic Masses, ENAM-98, Bellaire, Michigan, 1998*, Ed. by B. M. Sherill, D. J. Morrissey, and C. N. Davids (Woodbury, New York, 1998); AIP Conf. Proc. **455**, 510 (1998).

Translated by A. Isaakyan

Physics of Atomic Nuclei, Vol. 63, No. 9, 2000, pp. 1562–1573. Translated from Yadernaya Fizika, Vol. 63, No. 9, 2000, pp. 1648–1659.

ELEMENTARY PARTICLES AND FIELDS
Experiment

Seeking and Investigating Isospin-Two Narrow Dibaryon Resonances in Neutron–Proton Interactions at $P_n = 5.20 \pm 0.13$ GeV/c

Yu. A. Troyan, V. N. Pechenov, E. B. Plekhanov, A. Yu. Troyan, S. G. Arakelyan[1)], V. I. Moroz, and A. P. Jerusalimov

Joint Institute for Nuclear Research, Dubna, Moscow oblast, 141980 Russia

Received December 9, 1998; in final form, April 28, 1999

Abstract—The results are presented that are obtained from searches for and an investigation of isospin-two narrow resonances in the effective-mass spectrum of $pp\pi^+$ combinations originating from the reaction $np \longrightarrow pp\pi^+\pi^-\pi^-$ induced by $P_n = 5.20 \pm 0.13$ GeV/c neutrons. Data subjected to our analysis come from the 1-m hydrogen bubble chamber installed at the Laboratory for High Energies, Joint Institute for Nuclear Research (Dubna), and exposed to a beam of quasimonochromatic neutrons. Narrow structures in the effective-mass spectrum of $pp\pi^+$ combinations are found at 2175, 2221, 2321, 2398, 2471, 2525, 2596, and 2709 MeV/c^2. The experimental widths of the resonances are determined primarily by the instrumental resolution. The branching fractions for various channels through which the 2596-MeV/c^2 resonance decays are determined to be (83 ± 23)% for the $\Delta_{33}^{++}p$ channel, (10 ± 3)% for the $(BB)_{2095}^{++}\pi^+$ channel, and (7_{-7}^{+15})% for the $pp\pi^+$ channel; here, $(BB)_{2095}^{++}$ is a dibaryon in the two-proton system with a mass around 2095 MeV/c^2. A qualitative analysis of the spins of the 2596- and 2709-MeV/c^2 resonances is performed. © *2000 MAIK "Nauka/Interperiodica".*

1. INTRODUCTION

The fact that quarks have color degrees of freedom underlies the prediction of a host of resonance states. For example, the formula from [1] for calculating dibaryon-resonance masses within the stretched-bag model predicts about 20 resonances in the $pp\pi^+$ system between 2 and 3 GeV/c^2. The values obtained on this basis for the resonance masses comply well with our data. Physically, it is clear that the widths of these new resonances must be at least one order of magnitude smaller than the widths of conventional resonances. We have already observed this property of exotic resonances in pp (see [2–12]; a survey of these results is given in [13]) and $\pi^-\pi^-$ (see [14]) systems. Some theoretical considerations relying on the fact that the systems being discussed have large dimensions were put forth in the study that was reported in [12] and which was devoted to an analysis of narrow pp resonances. An account of the approaches based on QCD sum rules was given in the studies of Bordes *et al.* [15] and Ellis and Lanik [16], who analyzed the properties of scalar glueballs. A general conclusion—presently, an intuitive one to a considerable extent—is that, in the case of narrow exotic resonances, we are dealing with nonperturbative effects generated by the large-distance structure of the QCD vacuum. A consistent theory of allied phenomena has yet to be developed.

The requirements on relevant experiments both in what is concerned with their statistical significance and in what is concerned with the purity of the data sample under study are quite high because the pursued objects are very intricate. The experiments at the Laboratory for High Energies, Joint Institute for Nuclear Research (JINR, Dubna), that were devoted to searches for exoticism in baryon resonances took advantage of a neutron beam from the synchrophasotron installed at this laboratory. By using unique properties of the beam (its relative momentum spread is $\Delta P_n/P_n \approx 2.5\%$; its angular divergence for angles close to zero is $\Delta\Omega \approx 10^{-7}$ sr; its initial momentum is readily controllable in the range 1.25–5.20 GeV/c; and the neutron flux is high in the chamber used) in conjunction with the potential of the domestic 1-m liquid-hydrogen bubble chamber (4π coverage and a high precision in the measurements of the track momenta and angles), it was possible to obtain data from an exclusive experiment that were sufficient for investigating some exotic phenomena—in particular, resonance states in the $pp\pi^+$ system that are discussed in the present article and which include a triply exotic baryon with isospin $I = 2$ and electric charge $Q = 3$.

In view of the aforementioned high requirements on the implementation of relevant experiments, the first sections of the article are devoted to various methodological issues. Further, we expose our physical results

[1)] Lebedev Institute of Physics, Russian Academy of Sciences, Leninskiĭ pr. 53, Moscow, 117924 Russia.

and draw a comparison with other available data, which are rather scanty at present. We do not aim at a detailed comparison of our results with theoretical predictions because the theoretical situation is very uncertain in this realm.

Preliminary results of these investigations were reported at the XII and XIII International Seminars on Problems in High-Energy Physics and published in [17–19].

2. PROCEDURES FOR ISOLATING REACTION CHANNELS

In the present study, we use five-prong events obtained in five experimental runs where the 1-m hydrogen bubble chamber was irradiated with quasimonochromatic neutrons originating from the stripping of deuterons on the internal target of the synchrophasotron [20]. The use of a neutron beam enabled us to increase the density of the primary-particle flux to the chamber by one order of magnitude in relation to irradiations with charged particles. The distributions of the relative errors in the measurements of the tracks are peaked, the corresponding FWHM value being $(2.0 \pm 0.8)\%$ for positively charged tracks and $(1.9 \pm 0.7)\%$ for negatively charged tracks; the analogous values are 0.0013 ± 0.0009 and 0.0023 ± 0.0014 for the errors in the tangents of the immersion angles ($\Delta\tan\alpha$) and 0.0008 ± 0.0005 and 0.0013 ± 0.0008 rad for the errors in the azimuthal angles β.

The data subjected to a physical analysis were selected by requiring that the results of measurements for a given group of events not deviate by more than 2.55σ from the mean value of the measured quantity over all groups of measurements, σ being the root-mean-square deviation of the relevant quantity over all groups of events.

Determination of Incident-Neutron-Beam Parameters

In each irradiation run, the absolute value of the momentum and the direction of the incident-neutron beam in the 1-m hydrogen bubble chamber were determined on the basis of the total-momentum distribution of charged particles for events that resulted in the production of only charged particles and which were singled out by means of an iterative procedure implemented as is described immediately below.

For each event, we calculated the total momentum of charged particles ($\mathbf{P}_s = \sum_{i=1}^{5} \mathbf{P}_i$) and the energy balance $F = \sqrt{P_s^2 + m_n^2} + m_p - E_s$, where m_n is the neutron mass, m_p is the target-proton mass, and $E_s = \sum_{i=1}^{5} E_i$ is the sum of the energies of charged secondaries. For events featuring no neutral final-state particles (this is so in the reaction $np \longrightarrow pp\pi^+\pi^-\pi^-$), the mean value of the energy balance ($\bar{F}$) must be equal to zero. Since it is unknown in advance which one of the three positively charged secondaries is a π^+ meson, the energy balance F was calculated for three hypotheses: $p_1p_2\pi_3^+$, $p_1\pi_2^+p_3$, and $\pi_1^+p_2p_3$ (here, a subscript indicates the number of a positive track). Of the three hypotheses, we chose that for which F had a value closest to zero. We further calculated the mean value $\bar{P}_s$ of the total momentum and its root-mean-square deviation σ_{P_s} and the analogous values for the energy balance ($\bar{F}$ and σ_F), for the azimuthal angles of the total momenta $\mathbf{P}_s$ ($\bar{\beta}$ and σ_β), and for the tangents of the immersion angle for the total momenta $\mathbf{P}_s$ ($\overline{\tan\alpha}$ and $\sigma_{\tan\alpha}$). From the initially selected group of events, we took those that satisfied the following four conditions simultaneously:

$$|P_s - \bar{P}_s| \le 3\sigma_{P_s},$$

$$|F - \bar{F}| \le 3\sigma_F,$$

$$|\beta - \bar{\beta}| \le 3\sigma_\beta,$$

$$|\tan\alpha - \overline{\tan\alpha}| \le 3\sigma_{\tan\alpha}.$$

This procedure was repeated until the next iterative step added or rejected no event. The distributions of the quantities P_s, F, β, and $\tan\alpha$ prior to and following iterations are shown in Fig. 1.

The values $\bar{P}_s$, $\bar{\beta}$, and $\overline{\tan\alpha}$ obtained after the completion of the iterative process were taken for the parameters of the incident neutron beam.

If the iterative process singled out a group of events that was characterized by a sizable deviation of the mean value of the energy balance from zero or by a distorted (asymmetric) distribution of the energy balance, it was assumed that either an incorrect value of the magnetic field was introduced in the code for geometric reconstruction or a disregarded spurious curvature was present. In such cases, the results were corrected for these quantities.

The corrections for the magnetic field in the chamber and for a spurious curvature were tested in various ways—for example, by checking the mass positions of the eta and omega mesons, which are clearly seen in the effective-mass spectrum of $\pi^+\pi^-\pi^0$ combinations originating from the reaction $np \longrightarrow pp\pi^+\pi^-\pi^0$, and by verifying fulfillment of isotopic symmetry in the reaction $np \longrightarrow p\pi^+\pi^+\pi^-\pi^-n$ (in this reaction, the momentum spectra of isotopically symmetric particles in the reaction c.m. frame must be coincident, while the particle emission angles θ^* must exhibit mirror symmetry). The parameters of the neutral particles π^0 and n were reconstructed by a kinematical-fit code as is described below. Figure 2 displays the effective-mass distribution of $\pi^+\pi^-\pi^0$ combinations originating from the reaction $np \longrightarrow pp\pi^+\pi^-\pi^0$ induced by $P_n \approx$

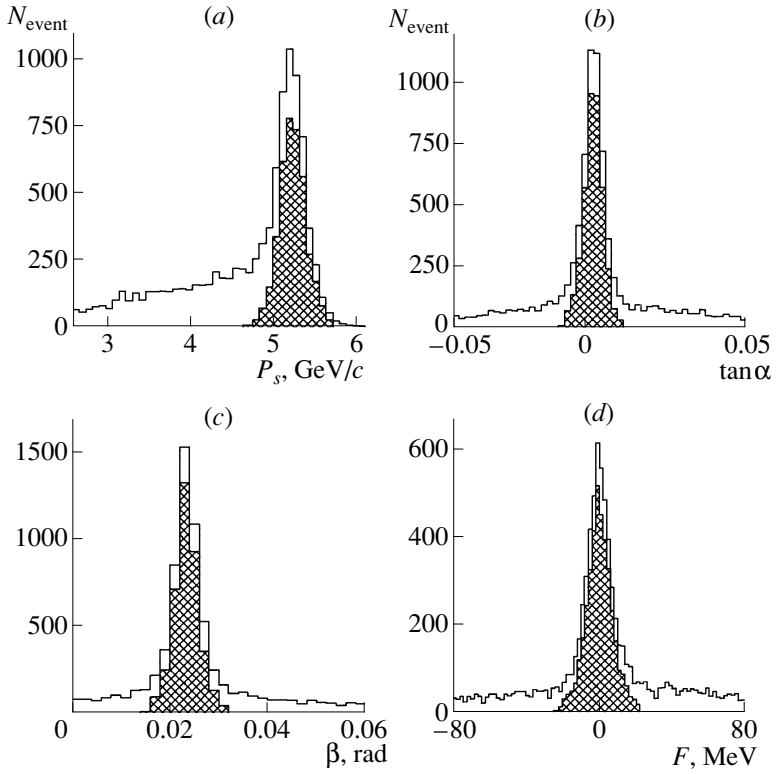

Fig. 1. Distribution of events with respect to (*a*) the total momentum P_s of charged particles, (*b*) the tangent tanα of the immersion angle for the total momentum, (*c*) the azimuthal angle β of the total-momentum direction, and (*d*) the energy balance *F* (unshaded histograms) prior to and (shaded histograms) after event selection by an iterative process (see main body of the text).

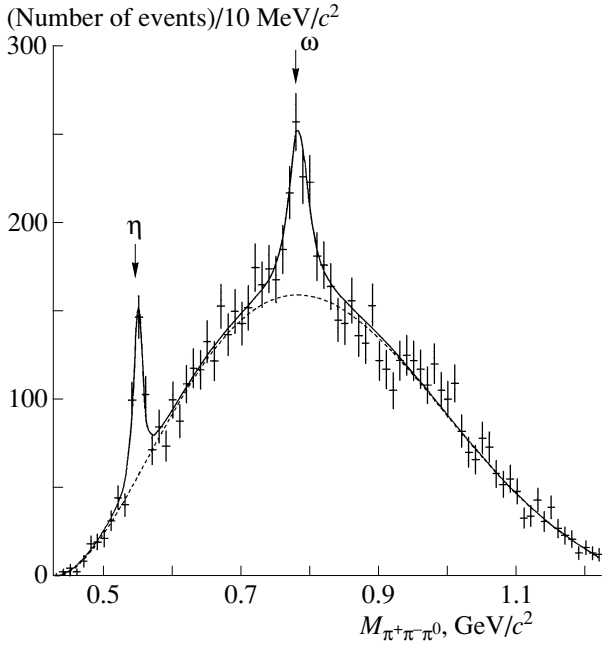

Fig. 2. Effective-mass distribution of $\pi^+\pi^-\pi^0$ combinations originating from the reaction $np \longrightarrow pp\pi^+\pi^-\pi^-\pi^0$ induced by $P_n \approx 5.2$ GeV/*c* neutrons. The solid curve represents two Breit–Wigner resonance peaks on top of a smooth background (their noncoherent sum). Arrows indicate the world-average values of the eta- and omega-meson masses.

5.2 GeV/*c* neutrons (summary data from all irradiation runs). The distribution in question was approximated by the noncoherent sum of the background curve represented as a superposition of Legendre polynomials of degrees not higher than five (the coefficients of the polynomials of higher degrees—if those are included—are insignificant) and two Breit–Wigner resonance peaks. The background fraction was 91.0%. Off the resonance regions, the above description of the background is characterized by the χ^2/NDF value of 1.03 ± 0.11, the square root of the variance of the χ^2 distribution being $\sqrt{D} = 1.47 \pm 0.08$; these values are close to those for a purely statistical distribution (χ^2/NDF = 1, $\sqrt{D} = 1.41$).

Our data on the eta and omega mesons are listed in Table 1, which displays (first column) the particle species; (second column) the world-average values of their masses; (third column) the experimental values of the resonance masses; (fourth columns) the experimental resonance widths; (fifth column) the cross sections for resonance production in the reaction $np \longrightarrow pp\pi^+\pi^-\pi^-\pi^0$, along with the uncertainties that include the errors in the determination of the cross section for this reaction (see [22]); and (sixth column) the number of standard deviations, which was calculated by the formula S.D. = $(N_{expt} - N_{backgr})/\sqrt{N_{backgr}}$, where N_{expt} is the number of

Table 1

Particle species	$M_t \pm \Delta M_t$, MeV/c^2	$M_e \pm \Delta M_e$, MeV/c^2	$\Gamma_e \pm \Delta\Gamma_e$, MeV/$c^2$	$\sigma \pm \Delta\sigma$, μb	S.D.
η	547.45 ± 0.19	548.6 ± 2.1	$11.2^{-3.1}_{+2.6}$	15.4 ± 2.1	13.4
ω	781.94 ± 0.12	783.1 ± 2.5	$32.8^{-6.6}_{+7.7}$	34.6 ± 5.0	10.7

events in a given experiment and N_{backgr} is the number of background events in the mass region being considered.

As can be seen from Table 1, the values found from our experiment for the eta- and omega-meson masses agree with the world-average values to within 1.5 MeV/c^2 (the maximal deviation is 0.3%).

The values that the different exposures of the hydrogen bubble chamber yield for the effective masses and the widths of eta and omega mesons and for their production cross sections are consistent within the experimental errors.

3. PARTITION OF EVENTS INTO REACTION CHANNELS

A kinematical fit of events was performed with the aid of a code developed specially for irradiations on the basis of the algorithm set forth in [23]. The neutron-momentum spread was taken to be 2.5% of the mean momentum value. This spread value was obtained from a theoretical calculation of the neutron spectrum in the stripping of deuterons [20], and it is in agreement with the value determined for this spread experimentally. Errors in the immersion angle and in the azimuthal angle of neutron-beam direction in the chamber were computed geometrically from the arrangement and dimensions of the aluminum target and of the second collimator. As a result, the same error value of 0.00033 rad was obtained for each of the two angles.

Five-prong events were assumed to be associated with one of the three reaction channels

$$np \longrightarrow pp\pi^+\pi^-\pi^- \text{ (0 channel; 4}C\text{ fit)},$$

$$np \longrightarrow pp\pi^+\pi^-\pi^-\pi^0 \text{ (π^0 channel; 1}C\text{ fit)},$$

$$np \longrightarrow p\pi^+\pi^+\pi^-\pi^- n \text{ (}N\text{ channel; 1}C\text{ fit)}.$$

Since it is not known in general which of the positively charged particles are protons and which are π^+ mesons, three hypotheses were tested in each channel; of these, we chose that which was characterized by the smallest value of χ^2. By estimating the fraction of events for which the choice of hypothesis was incorrect for one reaction channel, we have found that there are 1.1% of such events in the 0 channel, 2.9% of such events in the π^0 channel, and 2.2% of such events in the N channel.

In separating events into groups associated with the various reaction channels, we made use of the χ^2 criterion. Specifically, we selected events corresponding to $\chi^2 \leq \chi^2_{\text{bound}}$, with χ^2_{bound} being set to 12.5 for the 0 channel and to 6.5 for the reaction channels featuring the production of one neutral particle. These boundaries in χ^2 corresponded to an approximately 1% confidence level. If an event satisfied the criterion $\chi^2 \leq \chi^2_{\text{bound}}$ for the hypothesis of the 0 channel, it was assigned to this channel, irrespective of χ^2 values for the other channels (preference rule [24]). When the hypothesis of the π^0 channel and the hypothesis of the N channel both passed the above selection, we decided on the hypothesis for which χ^2 was smaller. According to our estimates, the admixtures of alien events in the individual channels did not exceed the following values: 3.2% π^0-channel events and 0.5% N-channel events in the 0 channel, 3.9% N-channel events in the π^0 channel, and 2.1% π^0-channel events in the N channel.

In selecting events in the various reaction channels, we additionally employed constraints on the error in the total momentum of all charged particles ($\Delta P_s/P_s \leq 3\%$) and on the missing mass ($M^2_{\min} < M^2_{\text{miss}} < M^2_{\max}$) for all reaction channels, on the cosine of the π^0 emission angle in the reaction c.m. frame (the condition requiring that the distribution in $\cos\theta^*_{\pi^0}$ be smooth) for the π^0 channel, and on the π^+ momentum in the laboratory frame [in order to take into account the requirement that $dN_{\pi^+}/dP_{\pi^+}(\text{lab}) = dN_{\pi^-}/dP_{\pi^-}(\text{antilab})$] for the N channel.

The reliability of our separation of events into groups associated with the various reaction channels is illustrated in Fig. 3, which demonstrates fulfillment of isotopic symmetry in the reaction $np \longrightarrow p\pi^+\pi^+\pi^-\pi^- n$, where the momentum distributions for isotopically conjugate particles must be identical in the reaction c.m. frame and where the angular distributions of such particles must be obtained by means of mirror reflections from each other. The histograms in Fig. 3 represent (*a*) the momentum distributions of the secondary proton and neutron in the reaction c.m. frame, (*b*) the distributions of events with respect to the squares of the transverse momenta of the secondary proton and neutron in the reaction c.m. frame, (*c*) the distributions of events with respect to the cosines of *p* and *n* emission angles measured from the reaction axis in the c.m. frame, (*d*) the momentum distributions of the product

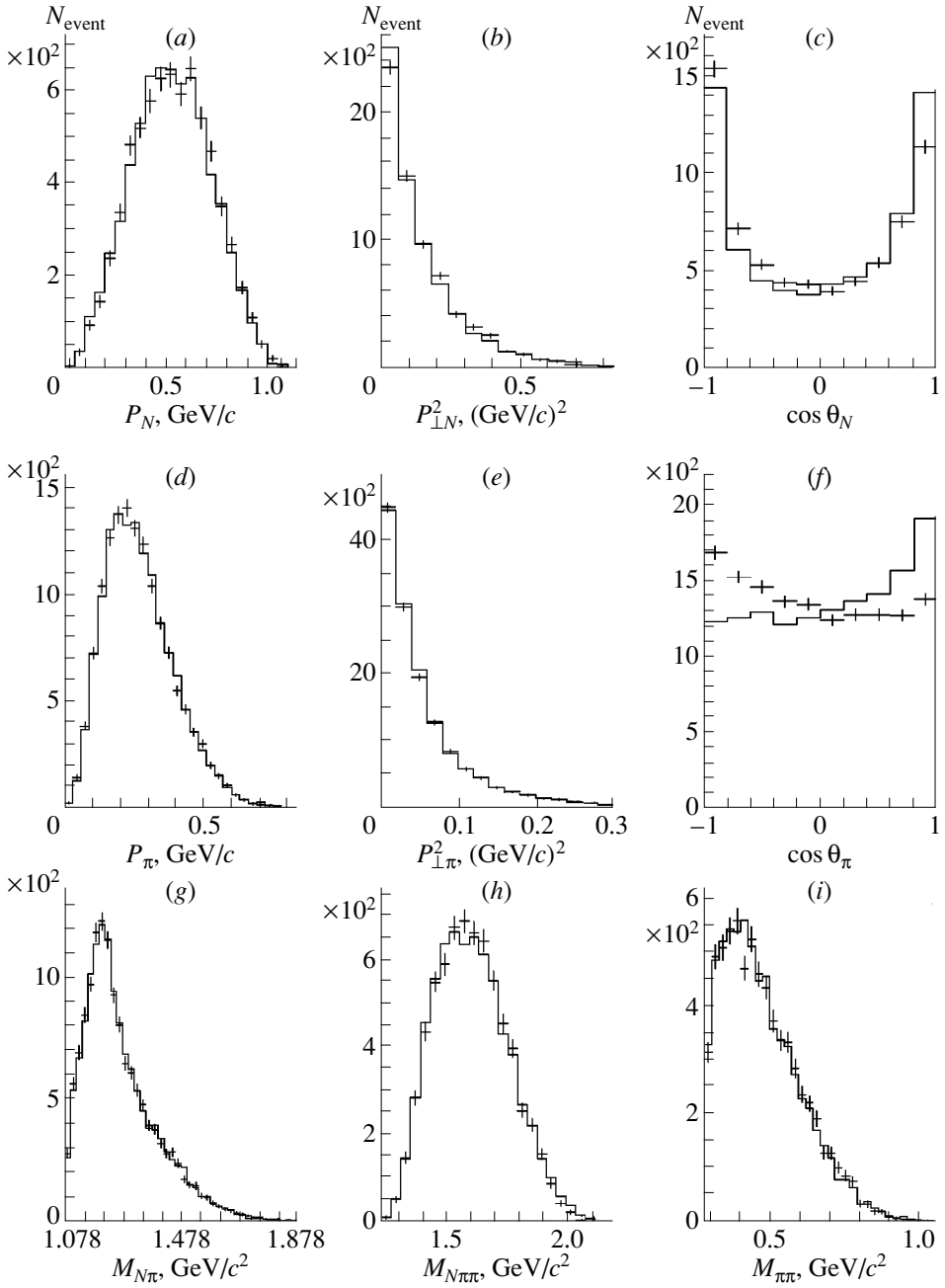

Fig. 3. Distributions demonstrating fulfillment of isotopic invariance in the reaction $np \longrightarrow p\pi^+\pi^+\pi^-\pi^-n$ (for a detailed description of the figure, see main body of the text).

π^+ and π^- mesons in the c.m. frame, (*e*) the distributions of events with respect to the squares of the π^+ and π^- transverse momenta in the c.m. frame, (*f*) the distributions of events with respect to the cosines of π^+ and π^- emission angles measured from the reaction axis in the c.m. frame, (*g*) the effective-mass distributions of $p\pi^+$ and $n\pi^-$ combinations, (*h*) the effective-mass distributions of $p\pi^+\pi^+$ and $n\pi^-\pi^-$ combinations, and (*i*) the effective-mass distributions of $\pi^+\pi^+$ and $\pi^-\pi^-$ combinations.

Table 2 displays the mean values of the above parameters and the square roots of the variances for the distributions depicted in Fig. 3. From this figure and from the table in question, it can be seen that the above distributions for isotopically symmetric particles agree fairly well. A modest distinction between the absolute values of mean angular distributions is due to a loss of a small number (a few percent) of particles that are very slow in the laboratory frame.

Upon the separation of the reaction channels and the application of additional selection criteria, there remain

Table 2

Parameter	Mean value	$\sqrt{D}$
P_p, MeV/c	532.6 ± 2.3	194.3 ± 1.7
P_n, MeV/c	527.1 ± 2.3	193.2 ± 1.6
$P^2_{\perp p}$, (GeV/c)^2	0.491 ± 0.0017	0.1419 ± 0.0012
$P^2_{\perp n}$, (GeV/c)^2	0.437 ± 0.0017	0.1411 ± 0.0012
$\cos\theta^*_p$	−0.0489 ± 0.0082	0.6827 ± 0.0058
$\cos\theta^*_n$	+0.0253 ± 0.0083	0.6933 ± 0.0059
P_{π^+}, MeV/c	268.6 ± 1.0	123.1 ± 0.7
P_{π^-}, MeV/c	270.3 ± 1.1	123.5 ± 0.7
$P^2_{\perp\pi^+}$, (GeV/c)^2	0.0534 ± 0.0005	0.0537 ± 0.0003
$P^2_{\perp\pi^-}$, (GeV/c)^2	0.0530 ± 0.0005	0.0530 ± 0.0003
$\cos\theta^*_{\pi^+}$	−0.0431 ± 0.005	0.5881 ± 0.0035
$\cos\theta^*_{\pi^-}$	+0.0685 ± 0.005	0.5896 ± 0.0035
$M_{p\pi^+}$, MeV/c^2	1268.4 ± 1.1	124.4 ± 0.7
$M_{n\pi^-}$, MeV/c^2	1270.3 ± 1.1	125.1 ± 0.8
$M_{p\pi^+\pi^+}$, MeV/c^2	1596.4 ± 1.8	149.1 ± 1.3
$M_{n\pi^-\pi^-}$, MeV/c^2	1597.4 ± 1.8	153.6 ± 1.3
$M_{\pi^+\pi^+}$, MeV/c^2	474.0 ± 1.6	130.6 ± 1.1
$M_{\pi^-\pi^-}$, MeV/c^2	471.4 ± 1.6	130.5 ± 1.1

8394 events of the reaction $np \longrightarrow pp\pi^+\pi^-\pi^-$, 3884 events of the reaction $np \longrightarrow pp\pi^+\pi^-\pi^-\pi^0$, and 6680 events of the reaction $np \longrightarrow p\pi^+\pi^+\pi^-\pi^- n$. This distribution of events among the reaction channels is consistent with the cross sections determined for these channels in [22].

4. INVESTIGATION OF $I = 2$ NARROW DIBARYON RESONANCES IN NEUTRON–PROTON INTERACTIONS

In seeking and investigating narrow resonances in the effective-mass spectra of $pp\pi^+$ combinations, we made use of the reactions

$$np \longrightarrow pp\pi^+\pi^-\pi^- \text{ at } P_n \approx 5.20 \text{ GeV}/c \text{ (8365 events)}, \quad (1)$$

$$np \longrightarrow pp\pi^+\pi^-\pi^-\pi^0 \text{ at } P_n \approx 5.20 \text{ GeV}/c \text{ (3822 events)}, \quad (2)$$

$$np \longrightarrow pp\pi^+\pi^-\pi^- \quad \text{at} \quad P_n = 4.43 \pm 0.11 \text{ GeV}/c \text{ (742 events)}, \quad (3)$$

$$np \longrightarrow pp\pi^+\pi^-\pi^-\pi^0 \quad \text{at} \quad P_n = 4.43 \pm 0.11 \text{ GeV}/c \text{ (215 events)}, \quad (4)$$

$$np \longrightarrow pp\pi^+\pi^-\pi^- \quad \text{at} \quad P_n = 3.88 \pm 0.10 \text{ GeV}/c \text{ (388 events)}, \quad (5)$$

$$np \longrightarrow pp\pi^+\pi^-\pi^-\pi^0 \quad \text{at} \quad P_n = 3.88 \pm 0.10 \text{ GeV}/c \text{ (65 events)}. \quad (6)$$

Figure 4 shows the effective-mass distribution of $pp\pi^+$ combinations originating from reaction (1). This distribution was approximated by the noncoherent sum of the background contribution represented by a superposition of Legendre polynomials of degrees not higher

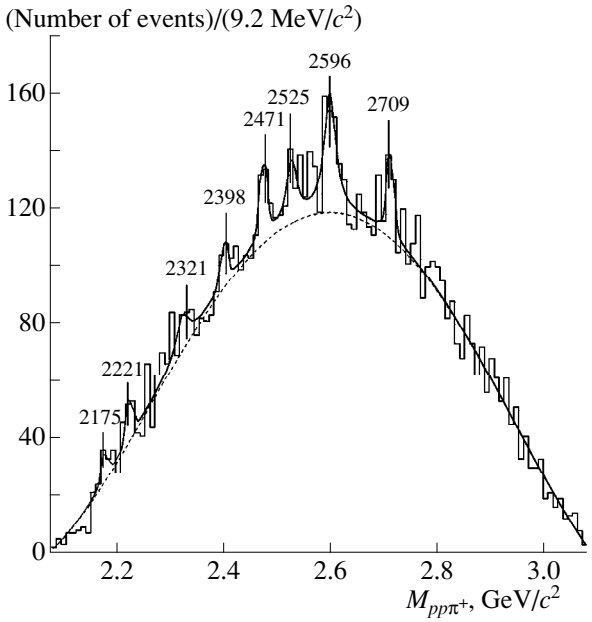

Fig. 4. Effective-mass distribution of $pp\pi^+$ combinations originating from the reaction $np \longrightarrow pp\pi^+\pi^-\pi^-$ induced by $P_n \approx 5.2$ GeV/c neutrons. The solid curve represents eight Breit–Wigner resonance peaks on top of a smooth background (see main body of the text). The dashed curve corresponds to the background contribution approximated by a Legendre polynomial of fourth degree.

than four (the inclusion of higher order Legendre polynomials is unnecessary since the fitted coefficients of these polynomials prove to be small) and eight Breit–Wigner resonance terms. The background fraction was 93.1%. Off the resonance regions, the description of the background was characterized by the χ^2/NDF value of 0.89 ± 0.12, the square root of the variance of the χ^2 distribution being $\sqrt{D} = 1.34 \pm 0.08$. These values are very close to those for a purely statistical distribution (χ^2/NDF = 1, $\sqrt{D}$ = 1.41). An attempt at describing the experimental distribution by the background curve normalized to the total number of events (which is taken to be 100%) resulted in χ^2/NDF = 1.14 ± 0.10 and $\sqrt{D}$ = 1.65 ± 0.07. We see that, in this case, the deviations from the theoretical values for a purely statistical distribution are much more pronounced.

The data that we obtained are compiled in Table 3, which displays (first column) the central values of the resonance masses; (second column) the experimental (apparent) resonance widths; (third column) the true resonance widths as obtained from the apparent ones by quadratically subtracting the relevant resolution with respect to the effective masses of $pp\pi^+$ combinations; (fourth column) the cross sections for resonance production in reaction (1), together with the uncertainties that include errors in the determination of the cross section for reaction (1) (see [22]); (fifth column) the number of standard deviations from the background; and (sixth column) the product of the probability that the structures being discussed are background fluctuations and the ratio of the number of bins in the whole distribution to the number of bins in the region around a given resonance.

The number of standard deviations was calculated by the formula S.D. = $(N_e - N_b)/\sqrt{N_b}$, which has already been used in connection with data quoted in Table 1 and which involves the same quantities as in that case.

The experimental resolution $\sigma_{res}(M)$ with respect to the effective masses of $pp\pi^+$ combinations is closely approximated by the formula $\sigma_{res} = 2.1[(M - M_0)/0.1] + 2.7$, where M is the effective resonance mass (in GeV/c^2) and M_0 is the rest mass (in GeV/c^2) of the system formed by two protons and a π^+ meson, the resolu-

Table 3

$M_e \pm \Delta M_e$, MeV/c^2	$\Gamma_e \pm \Delta\Gamma_e$, MeV/$c^2$	$\Gamma_{res} \pm \Delta\Gamma_{res}$, MeV/$c^2$	$\sigma \pm \Delta\sigma$, μb	S.D.	P
2175 ± 6	$17.6^{-5.5}_{+13.9}$	$12.8^{-5.5}_{+13.9}$	1.7 ± 0.7	2.8	7.4×10^{-2}
2221 ± 6	$18.5^{-5.3}_{+12.8}$	$12.1^{-5.3}_{+12.8}$	2.5 ± 0.8	3.5	9.2×10^{-3}
2321 ± 24	$35.1^{-15.5}_{+62.4}$	$30.0^{-15.5}_{+62.4}$	2.2 ± 1.1	3.2	1.0×10^{-2}
2398 ± 8	$19.7^{-6.6}_{+23.4}$	$0.0_{+23.4}$	2.9 ± 1.4	2.3	3.3×10^{-1}
2471 ± 5	$21.9^{-4.7}_{+9.6}$	$0.0_{+9.6}$	4.1 ± 1.3	3.4	1.1×10^{-2}
2525 ± 7	$28.6^{-10.7}_{+31.7}$	$10.1^{-10.1}_{+31.7}$	4.0 ± 1.4	3.2	2.6×10^{-2}
2596 ± 6	$31.5^{-9.1}_{+18.0}$	$10.3^{-9.1}_{+18.0}$	9.2 ± 1.9	5.6	1.9×10^{-7}
2709 ± 6	$19.2^{-5.8}_{+15.4}$	$0.0_{+15.4}$	4.9 ± 1.6	3.5	7.1×10^{-3}

tion σ_{res} being given in MeV/c^2. From this formula, it can be seen that the mass resolution grows linearly from 2.7 to 17 MeV/c^2 as the mass M is changed from M_0 to a value of about 2.7 GeV/c^2.

The resonances discovered in reaction (1) can manifest themselves in reaction (2) as well. Figure 5 shows the effective-mass distribution of $pp\pi^+$ combinations originating from reactions (1) and (2). In conformity with what was done for the distribution in Fig. 4, that in Fig. 5 was approximated by the noncoherent sum of the background contribution represented by a superposition of Legendre polynomials of degrees not higher than four (there is no need to include higher order polynomials, since the fitted coefficients of those proved to be insignificant) and eight Breit–Wigner resonance terms. The background fraction was 93.9%. Off the resonance regions, the description of the background yielded $\chi^2/\mathrm{NDF} = 0.89 \pm 0.12$ and $\sqrt{D} = 1.41 \pm 0.09$. Figure 5 also displays the effective-mass distribution of $pp\pi^+$ combinations produced in reaction (2) exclusively (lower histogram). The vertical dotted lines indicate the mass positions of the resonances. The results of the above fit are presented in Table 4, where we quote the values of the same parameters as in Table 3 (in the same columns).

From a comparison of the results listed in Tables 3 and 4, it can be seen that the growth of the statistical significances of the structures occurring in the $pp\pi^+$ mass region from 2200 to 2500 MeV/c^2 roughly complies with the increase in statistics in this mass region.

At the same time, the significances of the resonances at about 2184, 2602, and 2716 MeV/c^2 decreased. As can be seen from Fig. 5 (lower histogram), these resonances occur at the ends of the phase space of reaction (2). The effective-mass distribution of $pp\pi^+$ combinations originating from reaction (2) has edges going downward more steeply (below the mass of 2200 MeV/c^2 and above the mass of 2550 MeV/c^2). For this reason, the behavior of the background polynomial that describes the summary distribution for reactions (1) and (2) is determined, in these regions, primarily by reaction (1) with the result that the background is overestimated in the region of the above masses.

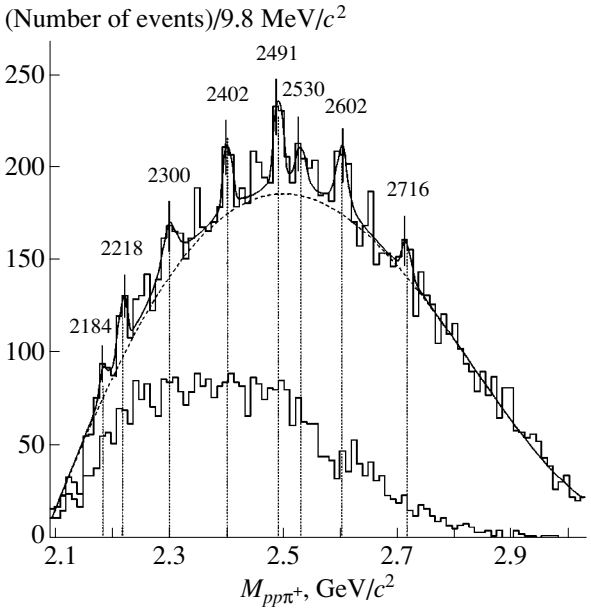

Fig. 5. Effective-mass distribution of $pp\pi^+$ combinations originating from reactions (1) and (2). The solid curve represents eight Breit–Wigner resonance peaks on top of a smooth background (see main body of the text). The dashed curve corresponds to the background contribution approximated by a Legendre polynomial of fourth degree. The lower histogram represents the distribution in question for reaction (2) exclusively. The vertical dotted lines indicate the fitted resonance masses.

Table 4

$M_e \pm \Delta M_e$, MeV/c^2	$\Gamma_e \pm \Delta\Gamma_e$, MeV/$c^2$	$\Gamma_{res} \pm \Delta\Gamma_{res}$, MeV/$c^2$	S.D.	P
2184 ± 7	$17.2^{-6.8}_{+21.7}$	$11.6^{-6.8}_{+21.7}$	2.5	2.3×10^{-1}
2218 ± 5	$21.0^{-5.5}_{+12.4}$	$15.8^{-5.5}_{+12.4}$	4.1	1.1×10^{-3}
2300 ± 8	$37.4^{-14.8}_{+45.2}$	$32.7^{-14.8}_{+45.2}$	3.7	2.5×10^{-3}
2402 ± 5	$21.3^{-5.5}_{+12.6}$	$0.0_{+12.6}$	3.6	8.3×10^{-3}
2491 ± 5	$23.8^{-4.0}_{+6.7}$	$0.0_{+6.7}$	4.8	3.0×10^{-5}
2530 ± 8	$29.5^{-8.2}_{+18.7}$	$10.6^{-8.2}_{+18.7}$	3.2	1.8×10^{-2}
2602 ± 7	$26.7^{-8.6}_{+20.6}$	$0.0_{+20.6}$	4.1	5.9×10^{-4}
2716 ± 6	$20.6^{-9.7}_{+6.9}$	$0.0_{+6.9}$	2.0	7.4×10^{-1}

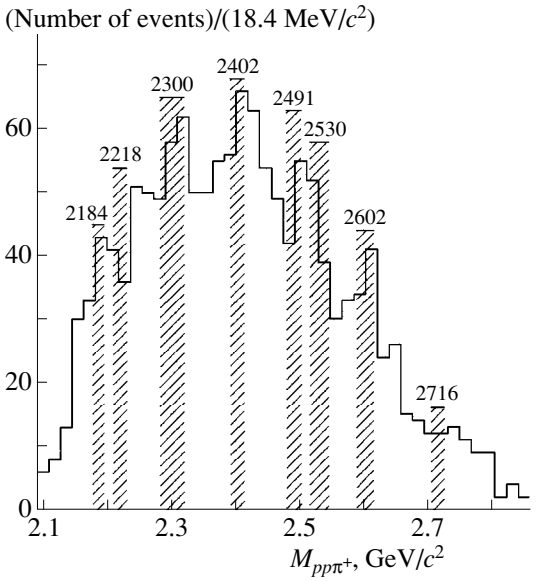

Fig. 6. Effective-mass distribution of $pp\pi^+$ combinations from reactions (3)–(6). Shaded regions correspond to the positions and apparent widths of the resonances found in reactions (1) and (2).

Figure 6 shows the effective-mass distribution of $pp\pi^+$ combinations originating from reactions (3)–(6). In this figure, the shaded regions correspond to the positions and the apparent widths of the resonances observed in reactions (1) and (2) (see Fig. 5 and Table 4). It can be seen that the features of these resonances comply well with the enhancements in the experimental effective-mass distributions in reactions (3)–(6).

These facts confirm the existence of the structures discovered in reaction (1).

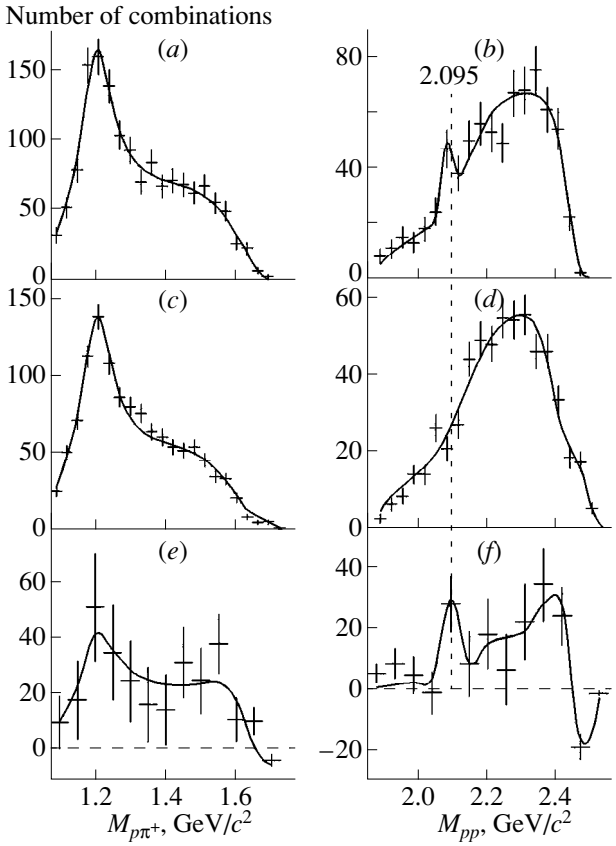

Fig. 7. (*a*, *b*) Effective-mass distributions of $p\pi^+$ and pp combinations from the region around the 2596-MeV/c^2 resonance; (*c*, *d*) background distributions in the resonance region that were obtained by means of a linear interpolation of the relevant distributions from the regions to the left and to the right of the resonance; and (*e*, *f*) difference of the distributions in the resonance region and the background distributions. The solid curves represent simulated distributions.

4.1. Determination of Decay Modes for the 2596-MeV/c^2 Resonance in the $pp\pi^+$ System

In a further analysis, we used only data for reaction (1).

In order to determine the relative weights of various modes of the decay of the 2596-MeV/c^2 resonance, we have analyzed the possible channels

$$(BB)^{+++}_{2596} \longrightarrow pp\pi^+,$$

$$(BB)^{+++}_{2596} \longrightarrow \Delta^{++}_{33}\, p,$$

$$(BB)^{+++}_{2596} \longrightarrow (BB)^{++}\, \pi^+,$$

where $(BB)^{++}$ is a resonance in the pp channel. Figures 7*a* and 7*b* display the effective-mass distributions of, respectively, $p\pi^+$ and pp combinations for events from the mass region around the 2596-MeV/c^2 resonance ($2582 < M_{pp\pi^+} < 2628$ MeV/c^2). The background distributions in Figs. 7*c* and 7*d* were obtained by means of a linear interpolation between the corresponding distributions in the regions to the left ($2536 < M_{pp\pi^+} < 2582$ MeV/c^2) and to the right ($2628 < M_{pp\pi^+} < 2683$ MeV/c^2) of the resonance. By subtracting the distributions in Figs. 7*c* and 7*d* from the distributions in Figs. 7*a* and 7*b*, respectively, we derived the mass spectra of $p\pi^+$ and pp combinations in the decay of the 2596-MeV/c^2 resonance (Figs. 7*e* and 7*f*, respectively). The mass spectrum of $p\pi^+$ combinations shows a Δ^{++}_{33} isobar, while the mass spectrum of pp combinations has a structure in the region around $M_{pp} \approx 2095$ MeV/c^2.

On the basis of the GENBOD code, we further simulated the decays of the $pp\pi^+$ system at the total energies set to the experimental values of the mass $M_{pp\pi^+}$. In doing this, we considered three possibilities (channels):

(i) the three-body phase space;

(ii) the production of a Δ^{++}_{33} isobar and a proton ($M_{\Delta^{++}_{33}} = 1204$ MeV/c^2, $\Gamma_{\Delta^{++}_{33}} = 101$ MeV/c^2);

(iii) the production of a $(BB)^{++}$ resonance and a π^+ meson ($M_{(BB)^{++}} = 2095$ MeV/c^2, $\Gamma_{(BB)^{++}} = 10$ MeV/c^2).

The Δ_{33}^{++} and $(BB)^{++}$ masses and widths were chosen by simultaneously fitting the effective-mass spectra of $p\pi^+$ and pp combinations. By approximating the experimental effective-mass distributions of $p\pi^+$ and pp combinations by the generated distributions, we then determined the contributions of the processes involving the production of a Δ_{33}^{++} isobar and of a $(BB)_{2095}^{++}$ resonance (in the regions to the right and to the left of the peak, there are no contributions from this resonance) for each of the three regions of the mass $M_{pp\pi^+}$. Solid curves in Fig. 7 represent the results of the above fit.

Knowing the contributions of the process involving Δ_{33}^{++} production in the regions of $M_{pp\pi^+}$ values to the right and to the left of the resonance, we were able to determine (by means of a linear interpolation) the fraction of this process in the background component within the resonance region. By subtracting this fraction from the Δ_{33}^{++} contribution to the whole region of the peak, we deduced the branching fraction for the resonance decay into Δ_{33}^{++} and p. It was straightforward to determine the probability of resonance decay into $(BB)_{2095}^{++}$ and π^+, since the $(BB)_{2095}^{++}$ resonance was not observed in the background regions (see Fig. 7*d*). As a result, we obtained the following values of the relevant branching fractions:

$$(83 \pm 23)\% \text{ for } (BB)_{2596}^{+++} \longrightarrow \Delta_{33}^{++} p,$$

$$(10 \pm 3)\% \text{ for } (BB)_{2596}^{+++} \longrightarrow (BB)_{2095}^{++} \pi^+,$$

$$(7_{-7}^{+15})\% \text{ for } (BB)_{2596}^{+++} \longrightarrow pp\pi^+.$$

4.2. Estimating the Spins of the 2596- and 2709-MeV/c^2 Resonances in the $pp\pi^+$ System

Figure 8 displays the results obtained from an analysis of the spins of the 2596- and 2709-MeV/c^2 resonances produced in reaction (1). It is well known that, in strong three-body resonance decays, the distributions of events with respect to the cosine $\cos\theta_{\mathbf{n},\widehat{\mathbf{P}}_{\text{res}}}$ of the angle between the normal $\mathbf{n}$ to the resonance-decay plane and the direction of the resonance momentum $\mathbf{P}_{\text{res}}$ in the reaction c.m. frame are described by a superposition of Legendre polynomials of even degrees not higher than $2J$, where J is the total spin [25]. Since available statistics are insufficient for unambiguously determining the resonance spins, the ensuing analysis is only qualitative.

For the 2596-MeV/c^2 resonance, Fig. 8*c* shows the background distribution with respect to $\cos\theta_{\mathbf{n},\widehat{\mathbf{P}}_{\text{res}}}$ as obtained by linearly interpolating, to the peak region, the distributions from the regions to the right and to the left of the resonance. Figure 8*d* displays the analogous distribution for the 2709-MeV/c^2 resonance. In these figures, the horizontal dashed lines correspond to the description of distributions in terms of the Legendre polynomial of zero degree (isotropic distribution), while the solid curves represent the results of a fit in terms of the Legendre polynomial of second degree. The corresponding confidence levels are given in the figures. Since polynomials of second degree provide the best description, we have taken them for the background distributions in the resonance regions. For events from the regions around the 2596- and 2709-MeV/c^2 resonances, the distributions with respect to $\cos\theta_{\mathbf{n},\widehat{\mathbf{P}}_{\text{res}}}$ as obtained upon background subtractions are presented in Figs. 8*a* and 8*b*, respectively. It can be seen that these distributions differ from the background ones, exhibiting a more complicated structure.

A further analysis consisted in the following. We constructed the distributions with respect to $\cos\theta_{\mathbf{n},\widehat{\mathbf{P}}_{\text{res}}}$ from 0 to 1 for events from the resonance region, employing partitions into 11, 12, …, 30 bins (in all, 20 histograms for each resonance). For each binning, the distributions were approximated by a set of Legendre polynomials of even degrees. The maximal degree of the polynomials was gradually increased in implementing this procedure. Upon each approximation, special attention was given to that coefficient of a Legendre polynomial (C_i, i being the degree of the corresponding polynomial) which was characterized by the largest relative error $\Delta C_i/C_i$. If this relative error was greater than 50%, the coefficient was set to zero, and the procedure was repeated. At the end of the iterative process, we were therefore left only with those degree of polynomials for which $\Delta C_i/C_i \le 50\%$. A large error in a given coefficient implies that the contribution of the relevant polynomial is insignificant and can be disregarded. After that, we chose polynomials of those degrees that passed reliably the selection $\Delta C_i/C_i \le 50\%$ in the majority of the cases for which we constructed approximations of the above type. By way of example, we indicate that, for the 2596-MeV/c^2 resonance, polynomials of second and sixth degree were always rejected by the above selection, whereas polynomials of fourth and eighth degree passed it in, respectively, 100 and 90% of the cases considered here. The results obtained by using approximations in terms of these polynomials are illustrated in Fig. 8*a*, where the dashed (horizontal) line, the dash-dotted curve, and the solid curve represent, respectively, the Legendre polynomial of zero degree; a superposition of the polynomials of zero and fourth degree; and a superposition of the polynomials of zero, fourth, and eighth degree. The polynomials that survived for the 2709-MeV/c^2 resonance processed in the same way are those of fourth and eighteenth degree (see Fig. 8*b*, where the dash-dotted and the solid curve represent, respectively, a superposition of the polyno-

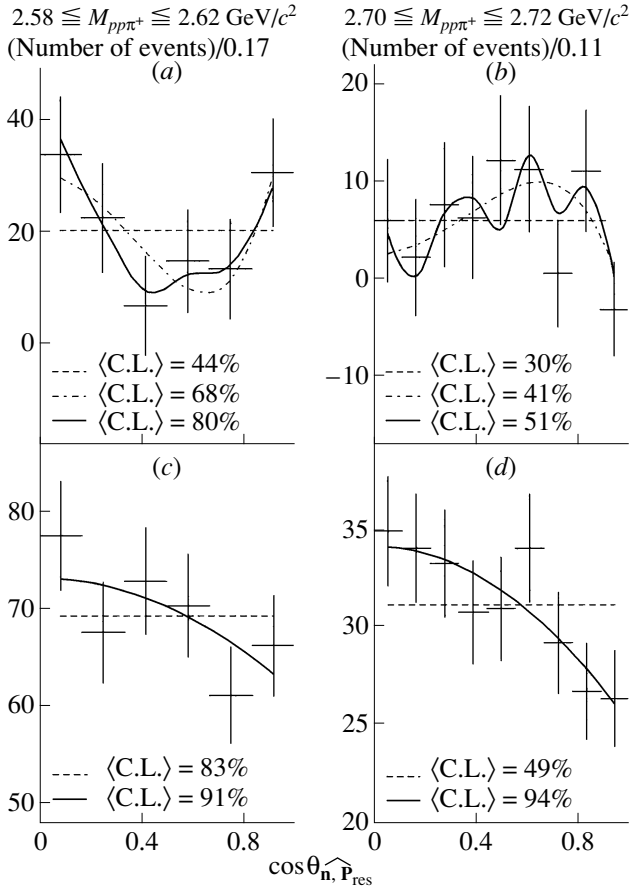

Fig. 8. Distributions of events from the regions around the (*a*) 2596- and (*b*) 2709-MeV/c^2 resonances with respect to $\cos\theta_{\mathbf{n},\widehat{\mathbf{P}}_{\mathrm{res}}}$ upon background subtractions (horizontal dashed lines represent the Legendre polynomial of zero degree, while the dash-dotted curves depict a superposition of Legendre polynomials of zero and fourth degree; the solid curve in Fig. 8*a* corresponds to a superposition of Legendre polynomials of zero, fourth, and eighth degree, while the solid curve in Fig. 8*b* corresponds to a superposition of Legendre polynomials of zero, fourth, and eighteenth degree) and background distributions with respect to $\cos\theta_{\mathbf{n},\widehat{\mathbf{P}}_{\mathrm{res}}}$ in the regions around the (*c*) 2596- and (*d*) 2709-MeV/c^2 resonances according to a linear interpolation of the distributions from the regions to the right and to the left of the resonances (the horizontal dashed lines and the solid curves represent fits to these background distributions in terms of Legendre polynomials of, respectively, zero and second degree).

mials of zero and fourth degree and a superposition of the polynomials of zero, fourth, and eighteenth degree). The same figures display the mean confidence levels for the descriptions of these distributions for versions employing 12 to 18 bins. It can be seen that, although we cannot exclude out of hand the possibility that the actual distribution is isotropic, the most probable spin values are $J \geq 4$ for the 2596-MeV/c^2 resonance and $J \geq 9$ for the 2709-MeV/c^2 resonance.

4.3. Survey of Experiments Devoted to Searches for I = 2 Dibaryon Resonances

So far, very few experimental studies have been aimed at pursuing and investigating resonances of the type being considered.

No statistically significant (above three standard deviations) structures were observed in [26, 27], but enhancements in the effective-mass spectrum of $pp\pi^+$ combinations at 2160 MeV/c^2 were discussed there. The analysis of Ermakov *et al.* [26] was performed on the basis of data obtained by irradiating ^{40}Ar nuclei (in a hybrid gas–liquid chamber) with $P_p \approx 1.7$ GeV/c protons, but the statistical significance was insufficient there. Combes-Comets *et al.* [27] investigated this structure in the reaction $p + p \longrightarrow \pi^- + X$ at T_p = 2.1 GeV (the product π^- mesons were recorded at an angle of 13.8°); its statistical significance in that study was 2.6σ. In the same reaction at T_p = 2.7 GeV, those authors also observed a narrow enhancement (2σ) in the mass region around 2460 MeV/c^2. Parker *et al.* [28] found no structures, but they explored either bound states in the $nn\pi^-$ system or the effective masses of this system in the region near the $NN\pi$ threshold.

Some studies (see, for example, [29] and references therein) were devoted to investigating the resonance yield of π^+ mesons from the interactions of $T \approx$ 350 MeV protons with various nuclei. The effect in question can be treated in terms of the production and subsequent decay of $I = 2$ resonances in proton–nucleus interactions, but there are explanations that do not invoke exotic resonances, but which are no less convincing than that discussed immediately above. A resonance-like structure was observed in reactions of π^- double charge exchange on various nuclei at meson energies less than the threshold for Δ_{33}-isobar formation (see references in the article of Brodowski *et al.* [30]). One of the possible explanations of the effect relies on the assumption that the $NN\pi$ system features a resonance—it was dubbed *d*'—having a mass of $M \approx$ 2.06 GeV/c^2, a width of $\Gamma_{NN\pi} \approx 0.5$ MeV/c^2, an even isospin, and a spin–parity of $J^P = 0^-$. In order to verify the hypothesis that this resonance exists, Brodowski *et al.* [30] studied the reaction $pp \longrightarrow pp\pi^-\pi^+$ at T_p = 750 MeV. They found an enhancement of four standard deviations in the effective-mass spectrum of the $pp\pi^-$ system around $M_{pp\pi^-} = 2.063$ GeV/c^2. These authors observed no such enhancement in the mass spectrum of the $pp\pi^+$ system, but they emphasized that the experimental mass resolution for $pp\pi^+$ is much poorer than that for $pp\pi^-$; therefore, the question of the isospin of the $M \approx$ 2.06 GeV/c^2 resonance remains open. The accumulation of statistics is being continued in a number of experiments. By the method of effective-mass spectra, Vorobyev *et al.* [31] studied $pp\pi^-$ and $pp\pi^+$ combinations in the reaction $pp \longrightarrow pp\pi^+\pi^-$ at T_p = 920 MeV. In

the $pp\pi^-$ system, they discovered an indication of a structure having a mass of 2.057 ± 0.002 GeV and a width of $\Gamma = 10.8 \pm 2.1$ MeV. No special features were found in the $pp\pi^+$ system.

It is worth noting that the aforementioned effects from [26–31] were observed in mass regions lying much lower than that which has been studied in our experiment.

5. BASIC CONCLUSIONS

For the first time, a set of narrow resonances in the $pp\pi^+$ system has been discovered in the reaction $np \longrightarrow pp\pi^+\pi^-\pi^-$ induced by $P_n \approx 5.2$ GeV/c neutrons. It has been shown that analogous structures are observed in the channel $np \longrightarrow pp\pi^+\pi^-\pi^-\pi^0$. These data comply well with the enhancements in the effective-mass spectra of the $pp\pi^+$ systems from the reaction $np \longrightarrow pp\pi^+\pi^-\pi^-$ and $np \longrightarrow pp\pi^+\pi^-\pi^-\pi^0$ that we have investigated at $P_n \approx 4.4$ and 3.9 GeV/c, respectively.

For the decay of the 2596-MeV/c^2 resonance in the $pp\pi^+$ system through various channels, we have found the following branching fractions: $(83 \pm 23)\%$ for the $\Delta_{33}^{++} p$ channel, $(10 \pm 3)\%$ for the $((BB)_{2095}^{++}\pi^+$ channel [here $(BB)_{2095}^{++}$ is a dibaryon in the two-proton system with a mass of about 2095 MeV/c^2], and $(7 \pm 15)\%$ for the $pp\pi^+$ channel.

A qualitative analysis of spin assignments has been performed for the 2596- and 2709-MeV/c^2 resonances.

ACKNOWLEDGMENTS

This work was supported in part by the Russian Foundation for Basic Research (project no. 97-02-16699).

REFERENCES

1. B. Tatischeff, IPNO-DRE, 94-19 (1994); P. J. Mulders *et al.*, Phys. Rev. D **21**, 2653 (1980); Phys. Rev. Lett. **40**, 1543 (1978); C. Besliu *et al.*, J. Phys. G **18**, 807 (1992).
2. C. Besliu *et al.*, Preprint No. D1-83-815, OIYaI (JINR, Dubna, 1983); in *Proceedings of the Symposium Nucleon–Nucleon and Hadron–Nucleus Interactions at Intermediate Energies*, Leningrad, 1984.
3. C. Besliu *et al.*, Preprint No. D1-85-433, OIYaI (JINR, Dubna, 1985).
4. Yu. A. Troyan *et al.*, Kratk. Soobshch. OIYaI, No. 13-85, 12 (1985).
5. Yu. A. Troyan *et al.*, in *Proceedings of the Symposium Nucleon–Nucleon and Hadron–Nucleus Interactions at Intermediate Energies*, Leningrad, 1986.
6. Yu. A. Troyan *et al.*, Preprint No. D1-88-329, OIYaI (JINR, Dubna, 1988); in *Proceedings of the IX International Seminar on Problems in High Energy Physics*, Dubna, 1988.
7. V. V. Avdeĭchikov *et al.*, Preprint No. R1-90-52, OIYaI (JINR, Dubna, 1990); Yad. Fiz. **54**, 111 (1991) [Sov. J. Nucl. Phys. **54**, 67 (1991)].
8. Yu. A. Troyan *et al.*, Preprint No. R1-90-78, OIYaI (JINR, Dubna, 1990).
9. Yu. A. Troyan *et al.*, Preprint No. R1-90-79, OIYaI (JINR, Dubna, 1990); Yad. Fiz. **54**, 1301 (1991) [Sov. J. Nucl. Phys. **54**, 792 (1991)].
10. Yu. A. Troyan *et al.*, in *Proceedings of the X International Seminar on High Energy Physics Problems, Dubna, 1990*, p. 149.
11. Yu. A. Troyan and V. N. Pechenov, Preprint No. R1-90-139, OIYaI (JINR, Dubna, 1990).
12. Yu. A. Troyan and V. N. Pechenov, Preprint No. R1-92-290, OIYaI (JINR, Dubna, 1992); Yu. A. Troyan *et al.*, in *Proceedings of the XI International Seminar on High Energy Physics Problems, Dubna*, 1992; Yu. A. Troyan and V. N. Pechenov, Yad. Fiz. **56** (4), 191 (1993) [Phys. At. Nucl. **56**, 528 (1993)].
13. Yu. A. Troyan, Fiz. Élem. Chastits At. Yadra **24**, 683 (1993) [Phys. Part. Nucl. **24**, 294 (1993)].
14. Yu. A. Troyan *et al.*, JINR Rapid Commun., No. 6[80]-96, 73 (1996).
15. Y. Bordes *et al.*, Phys. Lett. B **233**, 251 (1989).
16. Y. Ellis and J. Lanik, Phys. Lett. B **150**, 289 (1985).
17. Yu. A. Troyan *et al.*, in *Proceedings of the of Seminar on High Energy Physics Problems Related to Nuclear Physics and Quantum Chromodynamics*, Dubna, 1994.
18. Yu. A. Troyan *et al.*, JINR Rapid Commun., No. 4[67]-94, 67 (1994).
19. Yu. A. Troyan *et al.*, in *Proceedings of Seminar on High Energy Physics Problems Related to Nuclear Physics and Quantum Chromodynamics*, Dubna, 1996.
20. A. P. Gasparyan *et al.*, Prib. Tekh. Éksp., No. 2, 37 (1977); JINR Commun., No. 1-9111 (1975).
21. Particle Data Group, Phys. Rev. D **54**, 1 (1996).
22. C. Besliu *et al.*, Yad. Fiz. **43**, 888 (1986) [Sov. J. Nucl. Phys. **43**, 565 (1986)].
23. J. Peter Berge *et al.*, Rev. Sci. Instrum. **32**, 538 (1961).
24. A. Abdivaliev *et al.*, Preprint No. 1-10669, OIYaI (JINR, Dubna, 1977).
25. A. M. Baldin, V. I. Goldanskiĭ, and I. L. Rozental', *Kinematics of Nuclear Reactions* (Oxford Univ. Press, London, 1961, transl. of 1st Russ. ed.; Atomizdat, Moscow, 1968, 2nd ed.)
26. K. N. Ermakov *et al.*, Preprint No. 1158, LIYaF [Nuclear Physics Institute, USSR Academy of Sciences, Leningrad, 1986(7)].
27. M. P. Combes-Comets *et al.*, Phys. Rev. C **43**, 973 (1991).
28. B. Parker *et al.*, Phys. Rev. Lett. **63**, 1570 (1989).
29. J. Julien *et al.*, Z. Phys. A **347**, 181 (1994).
30. W. Brodowski *et al.*, Z. Phys. A **355**, 5 (1996).
31. L. V. Vorobyev *et al.*, Yad. Fiz. **61**, 855 (1998) [Phys. At. Nucl. **61**, 771 (1998)].

Translated by A. Isaakyan

Physics of Atomic Nuclei, Vol. 63, No. 9, 2000, pp. 1574–1583. From Yadernaya Fizika, Vol. 63, No. 9, 2000, pp. 1660–1669.

ELEMENTARY PARTICLES AND FIELDS
Experiment

Intranuclear Cascade in the Interactions of Neutrinos with Neon Nuclei*

E. S. Vataga[1)], V. S. Murzin[1)], M. Aderholz[2)], V. V. Ammosov[3)], A. S. Asratian[4)], M. Barth[5)], H. H. Bingham[†, 6)], E. B. Brucker[7)], R. A. Burnstein[8)], T. K. Chatterjee[9)], E. C. Clayton[10)], P. F. Ermolov[1)], I. N. Erofeeva[1)], P. J. W. Faulkner[11)], G. S. Gapienko[3)], J. Guy[12)], J. Hanlon[13)], G. Harigel[14)], A. A. Ivanilov[3)], V. Jain[15), #], G. T. Jones[11)], M. D. Jones[15)], T. Kafka[16)], V. S. Kaftanov[4)], M. Kalelkar[17)], J. M. Kohli[9)], V. A. Korablev[3)], M. A. Kubantsev[4)], M. Lauko[17)], O. Yu. Lukina[1)], J. Lys[6)], S. I. Lyutov[1)], P. Marage[5)], R. H. Milburn[16)], I. S. Mittra[9)], D. R. O. Morrison[14)], V. I. Moskalev[4)], G. Myatt[18)], R. Naon[8)], D. Passmore[16)], M. W. Peters[15)], H. Rubin[10)], J. Sacton[5)], J. Schneps[16)], J. B. Singh[9)], S. Singh[9)], W. Smart[17)], L. N. Smirnova[1)], P. Stamer[17)], K. E. Varvell[11), ##], W. Venus[12)], and S. Willocq[16), ###]
E632 Collaboration

Received March 3, 1999

Abstract—A method is developed for separating ν*N* interactions from interactions involving an intranuclear cascade in νNe scattering at a mean neutrino energy of 145 GeV. The fraction of events featuring a cascade is evaluated by using a sample of νNe charged-current interactions. It is found that the multiplicity of charged particles in the forward direction takes the same value for events with and without a cascade for $4 < W^2 < 550$ GeV^2. In the backward direction, cascade events have the charge multiplicity higher than the multiplicity for cascade-free events by 2.36 units. It is found that particles with momenta less than 2 GeV/*c* make a dominant contribution to the rescattering process. A depletion of the fastest particles for $W^2 < 50$ GeV^2 is observed, in accord with the formation-time concept. © *2000 MAIK "Nauka/Interperiodica".*

1. INTRODUCTION

Nuclei are common targets used in high-energy physics; hence, nuclear effects are an inevitable part of many experiments. For some, these may represent only a complication, but, for others, it offers a unique way to investigate various questions, such as the nature of hadron formation and the spacetime development of the hadronization process. The interaction of hadrons, immediately after their generation by string rupture, differs from ordinary hadron–nucleon interactions since product hadrons consist of valence quarks and do not have the full system of sea quarks, antiquarks, and gluons; therefore, they have a reduced probability for interaction [1–5].

Lepton–nucleus scattering is studied as a first step to understand better much more complicated hadron–nucleus or nucleus–nucleus collisions, where several strings interact with one another and with spectator nucleons. In the case of a lepton beam, only one color string is involved, and its direction is well known. But, as was indicated in [2], a virtual photon exhibits hadronic features in charged-lepton interaction at small values of x_B and can cause more than one projectile collision. Hence, neutrino interactions are thought to be particularly suitable for investigating hadron formation and intranuclear rescattering. However, only a few results from neutrino experiments have been published so far [6–11].

* This article was submitted by the authors in English.

† Deceased.
1) Moscow State University, Moscow, 119899 Russia.
2) Max-Planck-Institut für Physik, 80805 München, Germany.
3) Institute of High Energy Physics, Protvino, Moscow oblast, 142284 Russia.
4) Institute of Theoretical and Experimental Physics, Moscow, 117259 Russia.
5) Inter-University Institute for High Energies, USB-VUB, B-1050 Brussels, Belgium.
6) University of California, Berkley, California 94720, USA.
7) Stevens Institute of Technology, Hoboken, New Jersey 07030, USA.
8) Illinois Institute of Technology, Chicago, Illinois 60616, USA.
9) Panjab University, Chandigarch, 160014 India.
10) Imperial College of Science and Technology, London, SW7 2AZ United Kingdom.
11) University of Birmingham, Birmingham, B15 2TT United Kingdom.
12) Rutherford Appleton Laboratory, Chilton, Didcot, OX11 0QX, United Kingdom.
13) Fermilab, P.O. Box 500, Batavia, Illinois 60510, USA.
14) CERN, CH-1211 Geneva 23, Switzerland.
15) University of Hawaii, Honolulu, Hawaii 96822, USA.
16) Tufts University, Medford, Massachusetts 02155, USA.
17) Rutgers University, Piscataway, New Jersey, USA.
18) Department of Nuclear Physics, Oxford, OX1 3RH United Kingdom.
Present address: Vanderbilt University, Nashville, Tennessee 37235, USA.
Present address: ANSTO, Sydney, Menai NSW 2234, Australia.
Present address: University of Massachusetts, Amherst, Massachusetts 01003, USA.

1063-7788/00/6309-1574$20.00 © 2000 MAIK "Nauka/Interperiodica"

A basic way to study nuclear effects is to compare a hadron system in neutrino–nucleus interactions with that in neutrino–nucleon interactions. In the past, a painstaking comparison of two different experiments was necessary to achieve this goal [9]. It is therefore of interest to develop methods for extracting the desired results from only one experiment, as was proposed previously in [11] and, in a different context, in [12, 13]. We use this approach and compare the multiplicity and rapidity distributions for neutrino–nucleon (νN collision involving no cascade) and neutrino–nucleus interaction featuring a cascade. Several methods for classifying (anti)neutrino–nucleus interactions were proposed: by the presence or absence of "gray" protons with momenta below 600 MeV/c [13], by the presence of backward protons, by the final-state electric charge [14], or by means of some kinematical criteria [11]. In the present study, we examine criteria such as the target mass and the balance of longitudinal particle momenta in the hadron c.m. frame and consider a correlation between them.

This article is organized as follows. In Section 2, we present a summary of the data sample and the Monte Carlo model. In Section 3, we describe the method used to separate events with and without a cascade. Experimental results are given in Section 4: data on the multiplicity of charged hadrons in νNe and νN interactions are compared with the corresponding quantities for νp, νD, $\bar{\nu}$D , and μp scattering [15–17]; the excess multiplicity due to an intranuclear cascade as a function of W^2 is studied for forward and backward hemispheres; and the rapidity distributions are compared for two data samples and for different intervals of W^2. Our conclusions are summarized in Section 5.

2. EXPERIMENTAL PROCEDURE

2.1. Experiment and Data Sample

The Fermilab experiment E632 used a 15-foot bubble chamber (BC) both as a target and as a part of a detector system that also included the internal picket fence and the external muon identifier (EMI). The bubble chamber was exposed to a neutrino beam designed to obtain the highest neutrino energies. (Anti)neutrinos originated from the decays of charged mesons produced by 800-GeV/c protons from the Tevatron. Within the bubble chamber, neutrino and antineutrino interactions occurred in the ratio of 6 : 1 and had average energies of 145 and 110 GeV, respectively. Data were taken in two runs in 1985 and 1987. In the first (second) data run, the chamber was filled with a neon–hydrogen mixture containing 75% (63%) molar neon having a density of 0.71 g/cm^3 (0.54 g/cm^3). Events were recorded on film, scanned, and measured in the different laboratories of the collaborating institutions. Further experimental details are given in [18].

The present study is based on charged-current (CC) neutrino interactions:

$$\nu + N \longrightarrow \mu^- + X, \quad X \longrightarrow \text{hadrons}. \tag{1}$$

A muon candidate is required to have a momentum p in excess of 5 GeV/c and to be identified as a muon by EMI. The efficiency of identification for muons with such momenta is 91%. The background from hadron and muon decays and from accidental association does not exceed 0.7%. The total number of νNe CC events in our sample is 5567.

The range information is used to identify protons with momenta up to 1 GeV/c. All charged secondaries with momenta $p_{\text{lab}} > 1$ GeV/c are assigned a pion mass. (For Monte Carlo events, the fractions of protons and K^+ among possible particles with $p_{\text{lab}} > 1$ GeV/c are 20% and 8%, respectively.)

In an intranuclear cascade following a neutrino interaction, the product particles can knock protons and neutrons out of the residual nucleus and leave the nucleus in an excited state. This excitation energy is the basis for nuclear evaporation and fragmentation. All identified protons with momenta $p < 300$ MeV/c are considered to be evaporated and are excluded from further analysis. According to a Monte Carlo (MC) simulation, this cut removes, in addition to evaporated protons, 20–25% of the identified knock-on cascade protons. The probability for protons in cascade-free events to have momenta $p < 300$ MeV/c was less than 0.2%. In Section 3, we examine the effect of this cut on our final results.

The incident-neutrino energy E_ν is equal to the sum of the muon and hadron energies. The measured hadron energy is corrected for missing neutral particles by applying a factor based on transverse-momentum balance (Bonn method, [16]),

$$E_\nu = p_\parallel^\mu + \sum p_\parallel^h \left[1 + \frac{\left| \mathbf{p}_\perp^\mu + \mathbf{p}_\perp^h \right|}{\sum \left| \mathbf{p}_\perp^h \right|} \right], \tag{2}$$

where $p_\parallel$ ($p_\perp$) are components parallel (perpendicular) to the incoming-neutrino momentum. The average correction factor (bracketed expression) is equal to 1.4. Events characterized by a correction factor in excess of two (9% of the data sample) were excluded from our analysis. The root-mean-squared (RMS) error in the E_ν determination of Monte Carlo events is about 14%. Only events with 10 GeV $< E_\nu <$ 700 GeV were accepted for the analysis. In general, events characterized by low multiplicities have a larger value of the Bonn correction. Weights for the effects of the cut on the Bonn correction factor are applied to the multiplicity distribution and are shown in Table 1 ($n^\pm$ is the multiplicity in the hadron system, the muon from the primary interaction being excluded).

The cuts applied to select deep-inelastic-scattering (DIS) events are

$$Q^2 > 1 (\text{GeV}/c)^2, \quad W > 2 \text{ GeV}, \tag{3}$$

Table 1. Weights applied to correct the multiplicity distribution after a cut on the Bonn correction factor

$n^{\pm}$	W	$n^{\pm}$	W
1	1.35	10	1.07
2	1.28	11	1.06
3	1.22	12	1.05
4	1.17	13	1.04
5	1.14	14	1.03
6	1.11	15	1.02
7	1.10	16	1.01
8	1.09	>17	1.00
9	1.08		

Table 2. Fraction of events with and without intranuclear cascade and main characteristics of the two data samples

	Without cascade	With cascade
N_{ev}	2188	2288
f (stat. error)	0.49 ± 0.01	0.51 ± 0.01
f (after correction)	0.46 ± 0.05(syst.) ± 0.01(stat.)	0.54 ± 0.05(syst.) ± 0.01(stat.)
E_{ν_μ}, GeV	142 ± 2	145 ± 7
Q^2, $(\mathrm{GeV}/c)^2$	26.7 ± 0.8	28.5 ± 0.8
W, GeV	8.9 ± 0.2	8.8 ± 0.1
θ_h, deg	4.8 ± 0.1	5.0 ± 0.1
x_B	0.227 ± 0.003	0.238 ± 0.003
y_B	0.45 ± 0.2	0.45 ± 0.1
$\langle n^{\pm} \rangle$	5.26 ± 0.06	7.66 ± 0.07

where $Q^2 = -q^2$ is the 4-momentum transfer squared and W is the total energy of the hadronic system in its rest frame. These cuts leave 4476 νNe CC events.

Hadron production was analyzed in the hadronic c.m. frame, which is defined as

$$\mathbf{p}_\perp^h = -\mathbf{p}_\perp^\mu; \quad p_\parallel^h = \sum p_\parallel^{h(\mathrm{corr})};$$
$$W^2 = M_N^2 + 2M_N(E_\nu - E_\mu) - Q^2. \tag{4}$$

The properties of individual hadrons in the hadronic c.m. frame are measured by two longitudinal variables, the Feynman variable x_F and the rapidity y,

$$x_F = \frac{2p_\parallel^*}{W}, \quad y = \frac{1}{2}\ln\frac{E^* + p_\parallel^*}{E^* - p_\parallel^*}, \tag{5}$$

where E^* is the energy and $p_\parallel^*$ is the longitudinal momentum component (parallel to the current vector, **q**).

It should be noted that, in the case of a neon target, the final state is affected by intranuclear rescattering, where the direction of the particle momentum can be changed and where new particles can be created. But the c.m. frame of the overall hadron system is scarcely affected by a nuclear cascade since it is defined in terms of the neutrino and muon parameters. It can be seen from Table 2 that, within the statistical errors, E_ν, Q^2, W, θ_h (angle between the momentum of the hadron system and the beam axis), and y_B take the same values for cascade and cascade-free events.

2.2. Monte Carlo Model

Many theoretical effects of hadron fragmentation in nuclear matter are discussed in the literature. These include an increase in multiplicities, different production rates for negative or strange particles [6, 19], the energy loss of quarks before the formation of color-singlet objects (constituent-formation time) [9], and time evolution of color-singlet objects ("yo-yo" formation time) [4]. It is difficult to test the theoretical ideas without detailed model predictions. Unfortunately, there are only a few models incorporating lepton–nucleus interactions and rescattering occurring between product particles and target spectators. For our analysis, we have chosen the VENUS 4.10 code [20, 21], which describes rescattering processes in a rather simplified way.

In the VENUS package, the parton-fragmentation process is simulated by using the ideas of classical string theory embodied in the AMOR code (Artru Menessier Off-shell Resonances). Here, the initial string breaks up into substrings, and this process is continued until the mass of every string fragment becomes smaller than some cutoff. These fragments are then identified with resonances in accordance with their masses and quark content. After the corresponding lifetime, a resonance decays into two or more daughter particles. The VENUS package follows a complete spacetime evolution of the string and its decay products from the instant of string formation. This makes reinteractions possible at an early stage, before the string fragmentation is completed. Reinteractions occur mainly via fusion. Trajectories are assigned to all string fragments and spectator nucleons. Whenever trajectories of two objects (string fragments, decay products, clusters—results of previous fusions, spectator nucleons) come so close together that the distance between them is less than the sum of their sizes $r_i + r_j$, an interaction occurs. The scale of the distance of the closest approach is given by the meson and baryon radii, r_M and r_B, depending on the baryon number of the object. An interaction event results in cluster formation. The product cluster may interact again or may decay after an appropriate time interval. In addition to r_M and r_B, there is one more parameter describing rescattering, the reaction time—that is, the time (in the comoving frame) within which all interactions of a string (or a string fragment) are forbidden. It is assumed to be distributed exponentially with a mean value τ_r. This time affects most strongly whole strings, which would oth-

erwise interact immediately, and it is meant to be the time it takes to perform a color exchange.

To sum up, a lepton–nucleus interaction in the VENUS package is performed in the following way: after the first stage, an elementary lepton–nucleon interaction, the string fragments in a medium of target nucleons. Slow hadrons from string decay, which are close in momentum space to the spectator nucleons, interact with these nucleons, fuse into moderately excited resonances, and decay again into a baryon and one or two hadrons. In this way, the multiplicity is increased owing largely to additional nucleons. The default value of τ_r is 1.5 fm/c, and the meson and baryon radius are r_M = 0.35 fm and r_B = 0.65 fm; all these values are tuned to reproduce better experimental distributions. These parameters are not independent—for example, the effect of increasing τ_r is similar to the effect of decreasing r_M or r_B [21].

The inputs of our Monte Carlo calculations include the actual neutrino-beam energy spectrum, the experimental resolution, and the efficiencies of track measurements in the bubble chamber; we also take into account the Fermi motion of the nucleons in the nucleus. The LEPTO 6.3 [22] program was used to generate W, the total energy of the hadronic system in its rest frame ("string mass" in the VENUS model), and the flavor of the struck quark. Only the leading-order parton processes $W^{\pm}q \longrightarrow q'$ are generated. The VENUS program was used to simulate fragmentation and rescattering processes. Nuclear evaporation and breakup were not included in our model.

3. SEPARATION OF νN AND INTRANUCLEAR CASCADE SAMPLES

A collision between a neutrino and a neon nucleus can be considered as a two stage process: (i) the neutrino interacts with a single nucleon; (ii) particles produced in this elementary interaction have to move through the nucleus and can rescatter on spectator nucleons in the target nucleus, causing an intranuclear cascade. In the case where a primary collision involves a peripheral nucleon, product particles may leave the nucleus without any interaction. Such events are similar to νp or νn interactions, apart from the fact that the nucleon has a nonzero momentum due to the Fermi motion of the nucleons in the nucleus. It will be shown that these simple νN interactions can be separated by a number of criteria. Let us consider these criteria and their correlation in detail.

3.1. Target Mass

Taking into account the conservation of energy and momentum and considering that $E_\nu = p^\nu = \sum p_\parallel^i$, we find that the target mass M_t is given by

$$M_t = \sum E_i - E_\nu = \sum (E_i - p_\parallel^i). \qquad (6)$$

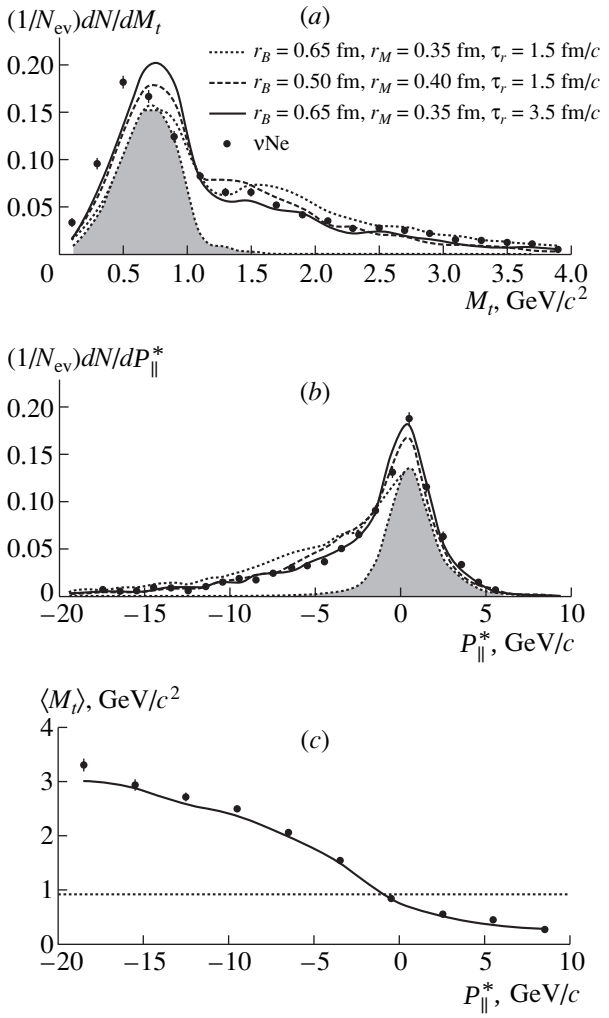

Fig. 1. Criteria used to separate νN interactions from interactions involving an intranuclear cascade: (*a*) target mass M_t; (*b*) the sum of the longitudinal momenta in the rest frame of the hadron system, $P_\parallel^*$; and (*c*) correlation between M_t and $P_\parallel^*$. The histograms in Figs. 1*a* and 1*b* are normalized to unity. The curves represent the results of Monte Carlo simulations using various rescattering parameters: the default values, the optimization from the study of the E665 collaboration, and the optimization used in the present analysis. The shaded area shows Monte Carlo events involving no intranuclear cascade. In Fig. 1*c*, all three sets of parameters give similar results; for this reason, we show only the results corresponding to the third set.

The experimental distribution of M_t normalized to unity is shown in Fig. 1*a*. In the case of νN interaction, $M_t = M_N$. Any additional interaction of product particles with a nucleon increases M_t by M_N. However, the distribution of M_t is smeared out because of undetected neutral particles and a wrong mass assignment of some charged particles. This smearing is simulated for events generated by the Monte Carlo method, and the results are shown by lines in Fig. 1*a*. The shaded area represents the fraction of Monte Carlo events without a cas-

cade. One can see that, in the absence of an intranuclear cascade, M_t lies in the region $0 < M_t < 1.5$ GeV/c^2 with a maximum at $M_t \approx 0.7$ GeV/c^2. Because of this smearing effect, the region $M_t < M_N$ is partly contaminated by cascade events.

3.2. Sum of Longitudinal Momenta in the Rest Frame of the Hadron System

In the c.m. frame of the hadron system, the total momentum of particles produced in a νN interaction,

$$P_\parallel^* = \sum p_\parallel^*, \tag{7}$$

is equal to zero. Our $P_\parallel^*$ distribution is displayed in Fig. 1*b*. The distribution is smeared for the above reasons. Moreover, according to our Monte Carlo simulation (shaded area for cascade-free events), the peak of this distribution is shifted to 0.7 GeV/c. In the case of a intranuclear cascade, particles produced in reinteractions move in the negative direction in the hadron c.m. frame; hence, the sum of the longitudinal momenta $P_\parallel^*$ for such events is also negative.

3.3. Total Charge of the Hadron System

The electric charge of the hadron system,

$$Q_{\text{tot}} = \sum q_i, \tag{8}$$

can also be used to separate events with an intranuclear cascade. If a neutrino interacts with a proton, the total charge of the hadron system is $Q_{\text{tot}} = 2$; if it interacts with a neutron, then $Q_{\text{tot}} = 1$. Any additional cascade interaction with a proton increases the value of Q_{tot} by one, while an interaction with a neutron does not change it. A problem associated with this method is that it relies on a charge determination: in our data sample, 36% of events have at least one track with $\Delta p/p > 0.7$, and the determination of the charge for such a track cannot be reliable. The mass of the target and the sum of the longitudinal momenta are not affected to so great an extent by tracks with large $\Delta p/p$.

3.4. Separation Criteria

Using these parameters, we have separated νN events from νNe events involving an intranuclear cascade. According to Monte Carlo calculations, the best separation is obtained for the cut

$$M_t < 0.9 \text{ GeV}/c^2. \tag{9}$$

The correlation between the first two criteria is depicted in Fig. 1*c*. The dotted line corresponds to $M_t = 0.9$ GeV/c^2. We notice that, for $P_\parallel^* > -1$, events have $\langle M_t \rangle < 0.9$ GeV/c^2.

The combination of cuts on M_t and $P_\parallel^*$ does not improve separation of the two samples. Hence, all events with $M_t < 0.9$ GeV/c^2 are assumed to be "pure" νN interactions, and the rest of the events are taken to involve an intranuclear cascade. This selection gives 2188 νN events and 2288 cascade events. Let us define the cascade fraction f as the ratio of the number of events featuring a cascade to the total number of events: $f = 0.51 \pm 0.01$ (stat.).

To be sure that our results are stable to slight variations in the separation criteria, all the above was repeated with other criteria (the fraction f of cascade events is shown in parentheses):

$$M_t < 1 \text{ GeV}/c^2 \ (f = 0.46),$$

$$|P_\parallel^* - 0.7| < 2 \text{ GeV}/c \ (f = 0.53),$$

$$M_t < 1 \text{ GeV}/c^2 \text{ and } |P_\parallel^* - 0.7| < 4 \text{ GeV}/c \ (f = 0.47).$$

In the present analysis, we use only protons with $p_{\text{lab}} > 300$ MeV/c. Meanwhile, slow protons make significant contribution to M_t because, for them, $E_i - p_\parallel^i \leq E_i - p^i \approx M_N$. As has already been noted in Subsection 2.1, this cut removes some of the protons that originated from an intranuclear cascade and has almost no effect on protons from primary interactions (<0.2%). Hence, there are two possible ways in which it can affect our analysis: (1) make cascade events mimic cascade-free events and reduce the fraction of cascade events and (2) decrease the multiplicity of positive particles in cascade events. If no cut is imposed on the proton momentum, f becomes 0.60.

In our Monte Carlo simulation, the fraction f is varied in a wide range, depending on cascade parameters. Since the default values in the VENUS model ($r_B = 0.65$ fm, $r_M = 0.35$ fm, $\tau_r = 1.5$ fm/c) overestimate the cascade fraction, we attempted to increase τ_r to fit better the experimental distributions. The dependence of the fraction f on τ_r is shown in Fig. 2. There, the solid line corresponds to the "actual" cascade fraction in simulated events, points represent the fractions derived by our method, and the area restricted by the dotted lines shows experimental data with the statistical error. The best agreement with the experimental data is achieved for $\tau_r = 3$–3.5 fm/c (which is about half the diameter of the Ne nucleus) and the default values of the meson and the baryon radius.

An optimization of rescattering parameters was performed for muon–xenon interactions in the E665 collaboration study [23]. They varied the meson and the baryon radius (to $r_M = 0.40$ fm and $r_B = 0.50$ fm) and obtained a similar result—a reduction in the fraction of cascade events in the Monte Carlo simulation. All three sets of parameters are shown in Figs. 1*a* and 1*b*.

3.5. Cascade Fraction

It can be seen from Fig. 2 that our method of separation underestimates the cascade fraction. This underestimation, which decreases with increasing τ_r, may be due to slow protons, as was discussed in the preceding subsection, as well as particle misidentification: a proton with $p_{\text{lab}} > 1$ GeV/c makes a smaller contribution to M_t when assigned a pion mass. Our experimental data corrected by using the data in Fig. 2 yield

$$f = 0.54 \pm 0.05(\text{syst.}) \pm 0.01(\text{stat.}). \quad (10)$$

All values are summarized in Table 2, which also quotes some characteristics of the two data samples.

Measurements of the rescattering fraction were performed for a deuteron in (anti)neutrino, pion, and proton beams (see [11] and references therein): $f_{\nu D} = 0.118 \pm 0.010$, $f_{\pi D} = 0.148 \pm 0.006$, and $f_{pD} = 0.189 \pm 0.010$. It was found that f is smaller at low values of energy transfer to the hadron system and becomes constant for higher values. At the energies of the present experiment, f is independent, within the statistical errors, of the mass of the hadron system or of energy transfer, as is shown in Table 3.

4. RESULTS

4.1. Charged-Hadron Multiplicities

Table 2 quotes mean charged-particle multiplicities for cascade and cascade-free events, the difference between them being 2.40 ± 0.09. In this section, we study charged-hadron multiplicities as functions of W^2 and determine the differences of the multiplicities of cascade and cascade-free events.

The mean charged-particle multiplicities for all νNe events and for the isolated νN events as functions of W^2 are plotted in Fig. 3. They are seen to follow straight lines parallel to each other up to $W^2 \approx 400$ GeV^2. The lines were fitted to

$$\langle n^{\pm} \rangle = A + B \ln W^2 \quad (11)$$

(solid lines), and the parameters of the fit are given in Table 4, along with the results of previous lepton–hadron experiments. It can be seen that νNe and νN events have the same slope and that these values are in agreement with other neutrino experiments. The fact that the total sample of νNe events and separated events involving no intranuclear cascade are characterized by the same slope indicates that there is an excess multiplicity due to the rescattering process and that this excess does not depend on W^2: $\langle n^{\pm} \rangle_{\nu\text{Ne}} - \langle n^{\pm} \rangle_{\nu N} = 1.18 \pm 0.06$. In [15], the difference between deuterium and hydrogen targets varied between 0.3 and 0.5 and was attributed to double-scattering effects.

Our νN data have a lower intercept A than ν_μD or $\nu_\mu p$. This may be due to the difference in the separation criteria (we excluded protons with $p_{\text{lab}} < 300$ MeV/c), the different fractions of interactions with protons and neutrons (in relation to νp data), and the method for separating cascade-free events. The multiplicities of Monte Carlo events tend to grow faster with W^2 and have a smaller difference between interactions on Ne and on a nucleon.

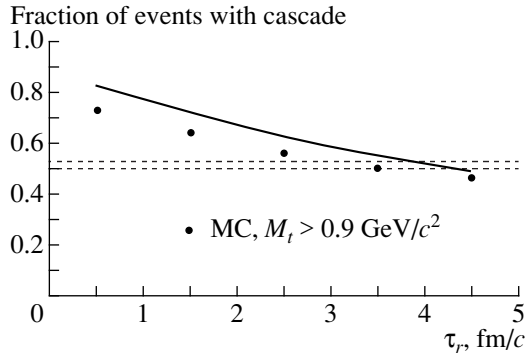

Fig. 2. Fraction of events featuring intranuclear rescattering versus the parameter τ_r in the Monte Carlo model. The solid line shows the true fraction of cascade events in the simulation, and points represent the fraction of events separated by our method. Dashed lines restrict the area of experimental data with a statistical error ($M_t > 0.9$ GeV/c^2).

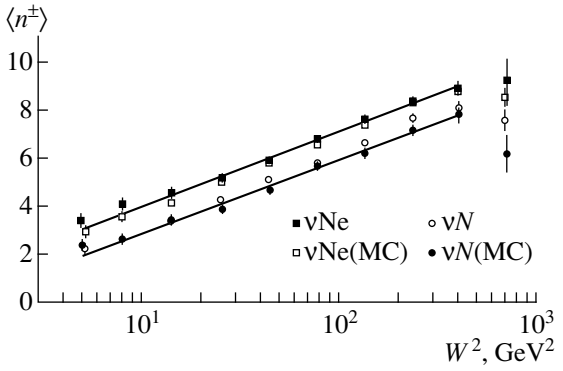

Fig. 3. Mean multiplicities of charged secondaries, $\langle n^{\pm} \rangle$, versus W^2. The solid lines represent linear fits to experimental data (the last points were not included in the fitting procedure).

4.2. Comparison of Forward and Backward Multiplicities for Cascade and Cascade-Free Events

The multiplicities of charged particles for lepton–nucleon interactions are different in the forward and in

Table 3. Rescattering fraction (only statistical errors are quoted) as a function of the mass of the hadron system, W (in GeV)

W	f	W	f
2–4	0.52 ± 0.02	10–12	0.53 ± 0.02
4–6	0.52 ± 0.02	12–16	0.48 ± 0.02
6–8	0.49 ± 0.02	16–20	0.54 ± 0.03
8–10	0.52 ± 0.02	20–30	0.46 ± 0.06

Table 4. Parameters of the linear fit $\langle n^{\pm}\rangle = A + B\ln W^2$

Reaction	Intercept A	Slope B	W^2 range, GeV^2	Target	References
ν_μNe	0.80 ± 0.18	1.38 ± 0.04	4–400	Ne	This experiment
$\nu_\mu N$	-0.30 ± 0.17	1.36 ± 0.04	4–400	Ne	This experiment
ν_μNe	0.37 ± 0.11	1.45 ± 0.03	4–400	Ne	Monte Carlo
$\nu_\mu N$	-0.49 ± 0.12	1.48 ± 0.03	4–400	Ne	Monte Carlo
ν_μD	0.05 ± 0.06	1.43 ± 0.02	4–140	D	E545(Fermilab) [15]
$\nu_\mu p$	0.37 ± 0.02	1.33 ± 0.02	4–350	H	WA21(BEBC) [26]
$\nu_\mu p$		1.35 ± 0.15	4–100	H	Fermilab [16]
$\bar{\nu}_\mu p$	0.02 ± 0.20	1.28 ± 0.08	6–140	D	WA25 (BEBC) [17]
$\bar{\nu}_\mu n$	0.80 ± 0.09	0.95 ± 0.04	2–140	D	WA25 (BEBC) [17]
$\nu_\mu N_F$	0.06 ± 0.11	0.76 ± 0.03	4–400	Ne	This experiment
$\nu_\mu N_B$	-0.22 ± 0.10	0.56 ± 0.03	4–400	Ne	This experiment
$\nu_\mu N_F^{\mathrm{casc}}$	-0.19 ± 0.11	0.81 ± 0.03	4–400	Ne	This experiment
$\nu_\mu N_B^{\mathrm{casc}}$	2.07 ± 0.19	0.59 ± 0.05	4–400	Ne	This experiment
$\bar{\nu}_\mu p_F$	0.22 ± 0.05	0.68 ± 0.02	4–140	D	WA25 (BEBC) [17]
$\bar{\nu}_\mu p_B$	0.56 ± 0.05	0.39 ± 0.03	4–140	D	WA25 (BEBC) [17]
$\bar{\nu}_\mu n_F$	0.22 ± 0.08	0.72 ± 0.03	4–140	D	WA25 (BEBC) [17]
$\bar{\nu}_\mu n_B$	0.80 ± 0.08	0.18 ± 0.04	4–140	D	WA25 (BEBC) [17]

the backward hemisphere because a single quark and a diquark fragment differently. In addition, particles produced in the forward hemisphere move faster relative to nucleons in a nucleus; therefore, their contribution to the intranuclear cascade must be different. For these reasons, we study the multiplicities of charged particles in the forward ($x_F > 0$) and in the backward ($x_F < 0$) hemisphere separately. Figure 4 shows the mean multiplicities $\langle n^{\pm}\rangle_{F,B}$ as functions of W^2 (*a*) for the total sample of νNe events, (*b*) for cascade events, and (*c*) for ν*N* events. As in the case of the overall multiplicities, each one satisfies a linear approximation in the form $\langle n^{\pm}\rangle_{F,B} = A + B\ln W^2$. For the complete event sample, $\langle n^{\pm}\rangle_F$ and $\langle n^{\pm}\rangle_B$ lie almost on one line; for the separated samples, however, they diverge considerably. In cascade events, the mean forward multiplicity $\langle n^{\pm}\rangle_F$ is smaller than the backward one, $\langle n^{\pm}\rangle_B$. On the other hand, the situation is opposite for "pure" ν*N* interactions: the mean forward multiplicity exceeds the mean backward multiplicity in the entire range of W^2 and shows a stronger increase with energy. The data in Fig. 4 thus demonstrate the difference in the fragmentation of diquarks and single quarks. The solid lines approximate the deuterium-target data from [15] and agree with our forward multiplicities, but they are systematically higher than our backward multiplicities. The parameters of the linear fit to $\nu_\mu N$ data with and without a cascade are given in Table 4.

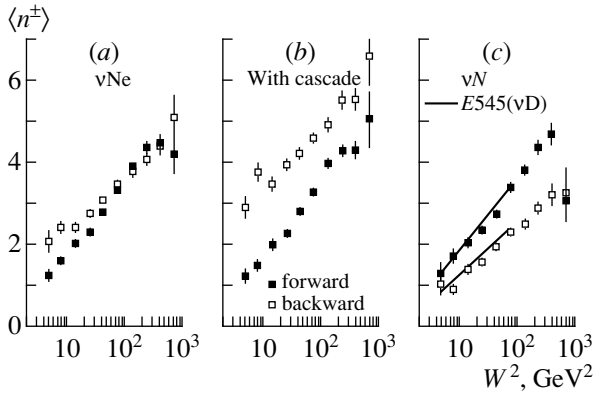

Fig. 4. Mean charged-hadron multiplicities versus W^2 in the forward ($x_F > 0$) and in the backward ($x_F < 0$) hemisphere for (*a*) the entire data sample and for selected events (*b*) with and (*c*) without a cascade. The solid lines in Fig. 1*c* are approximations of the deuterium-target data from [15].

To investigate the effect of intranuclear rescattering on the multiplicity as a function of W^2, we subtract $\langle n^{\pm}\rangle_{F,B}$ for ν*N* interactions from that of cascade events. It can be seen from Fig. 5 that, in the forward hemisphere, the multiplicities at all values of W^2 for cascade events are nearly identical to those for cascade-free events: $\langle n^{\pm}\rangle_F^{\mathrm{casc}} - \langle n^{\pm}\rangle_F^N = -0.06 \pm 0.04$. In the backward hemisphere, the multiplicity is higher by 2.36 ± 0.06 units

over a large region of W^2. The lines represent Monte Carlo predictions, which slightly underestimate the cascade multiplicity in the backward hemisphere. This underestimation persists for all values of τ_r from 1.5 to 4.5 fm/c.

The corresponding difference between the negative hadron multiplicities $\langle n^- \rangle^{\text{casc}}_{F,B} - \langle n^- \rangle^{N}_{F,B}$ has the same behavior: it is close to zero in the forward hemisphere and has an excess of 0.63 ± 0.03 units in the backward hemisphere. If we do not exclude protons with $p_{\text{lab}} <$ 300 MeV/c from our experimental-data sample or use other criteria for separating cascade and cascade-free events, the difference in the backward hemisphere varies slightly, but it is always around zero in the forward hemisphere.

In the separation of the forward and backward jets, we arbitrarily use the selections $x_F > 0$ and $x_F < 0$, the region of small x_F being contaminated by resonance-decay products, which may cross the hemisphere boundary. To eliminate complications due to resonances, we studied the difference of the multiplicities between cascade and cascade-free events, excluding the central region ($|x_F| < 0.05$). The multiplicity differences behave very similarly to those in Fig. 5, with the difference in the forward and in the backward hemisphere being close to zero and ranging from 2.0 to 2.8 units over the entire W^2 region, respectively.

We can conclude that charged-hadron multiplicities in the forward hemisphere take the same values for cascade and cascade-free events and that nuclear effects occur primarily in the backward hemisphere in the rest frame of the hadron system.

4.3. Rapidity Distributions of Cascade and Cascade-Free Events

Figure 6*a* shows normalized rapidity distributions of charged particles for νN and cascade events. The distributions are normalized to the total number of events for each data sample, so that the ordinate at any point represents the mean multiplicity of product particles per unit rapidity interval. We note that, for rapidity values of $y > 1$, the two distributions match very closely. For negative rapidities, cascade events have significantly larger multiplicities in the target-fragmentation region.

The shape of the rapidity distribution is affected by the mass misidentification of particles: the rapidities of kaons and especially protons assigned a pion mass increase by 0.5 to 2.0 units, this effect being more pronounced for faster particles. But this fact does not alter our analysis because, in the forward hemisphere, the rapidity distributions for cascade events change in the same way as the analogous distributions for cascade-free events. In the backward hemisphere, protons are rather slow, and the majority of these can be identified.

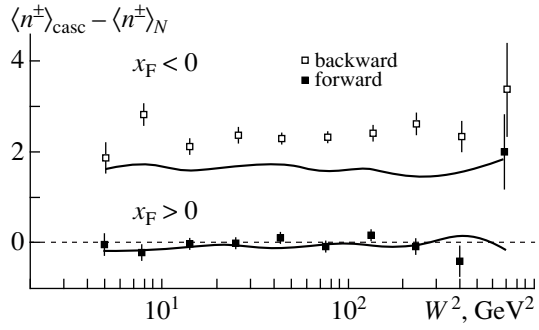

Fig. 5. Difference of the forward ($x_F > 0$) and backward ($x_F < 0$) multiplicities for the two data samples versus W^2. The lines represent Monte Carlo predictions.

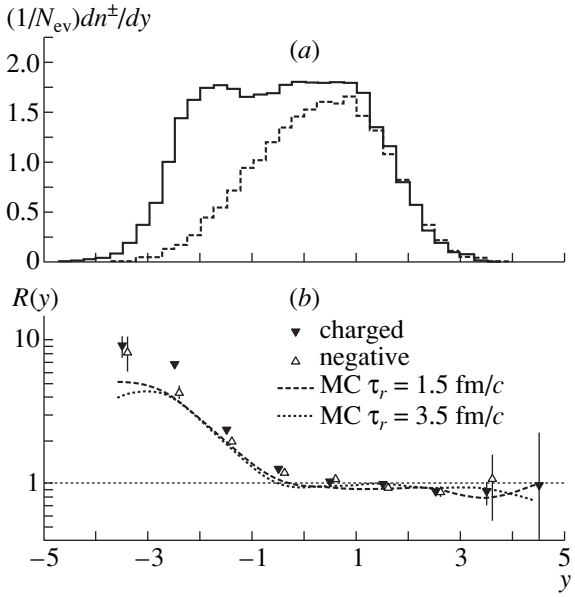

Fig. 6. (*a*) Rapidity distributions of charged particles for (solid line) cascade and (dashed line) cascade-free events (in each data sample, the distributions are normalized to the total number of events). (*b*) Ratio of the normalized rapidity distributions for events featuring an intranuclear cascade to those for cascade-free events. The results are depicted separately for all charged particles and only for negative particles. The lines represent the results of our Monte Carlo calculations.

In Fig. 6*b*, we show the ratio $R(y)$ of the normalized rapidity distributions for cascade events to that for νN interactions:

$$R(y) = \frac{[(1/N_{\text{ev}})dn^{\pm}/dy]_{\text{casc}}}{[(1/N_{\text{ev}})dn^{\pm}/dy]_N}. \qquad (12)$$

It can be seen from the figure that, in the target-fragmentation region, the ratio $R(y)$ increases to a value of ten. In the leading-quark-fragmentation region, this ratio flattens around unity within the experimental errors, showing equal mean multiplicities for cascade and cascade-free events.

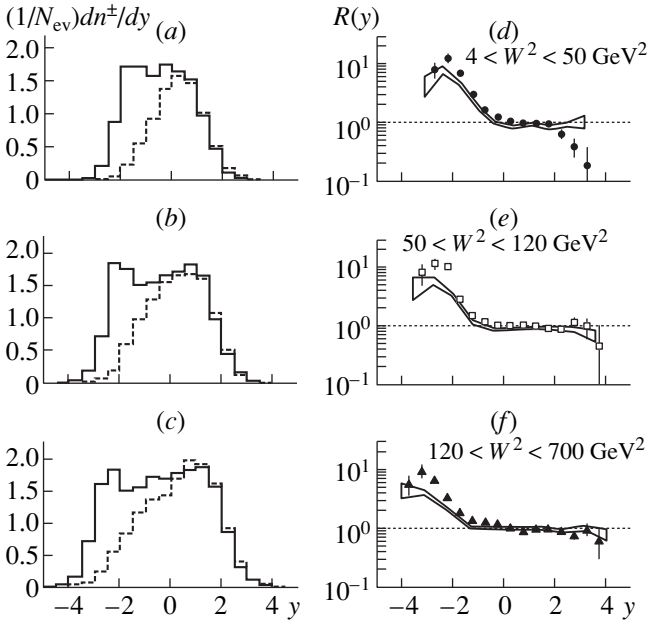

Fig. 7. (*a–c*) Normalized rapidity distributions for the two data samples and for three intervals of W^2. (*d–f*) Ratios of the normalized rapidity distributions for the various intervals of W^2. The areas between the lines correspond to Monte Carlo predictions with statistical errors.

To avoid effects due to proton contamination, we also show the rapidity ratio $R^-(y)$ for negative particles. It is very similar to $R(y)$, suggesting that our data are not significantly affected by misidentified protons. Figure 6*b* also shows Monte Carlo predictions for various values of τ_r. They are in reasonable agreement with the experimental data, although all of them underestimate the cascade multiplicity in the far backward region. Variations in τ_r change the distribution only slightly.

The same analysis was performed for the data sample with all protons included and with different criteria for separating νN and cascade events; the basic features of the distribution of the ratio $R(y)$ remain as before: it increases up to around ten in the region of negative rapidities and is around one in the quark-fragmentation region.

A similar analysis of rapidity distributions for hadron interactions on nuclear targets was performed at Fermilab [24] with $\pi^+/p/K^+$ beams of energy 200 GeV and at CERN [25] with π^+/K^+ beam of energy 250 GeV. The shape of the ratio $R(y)$ for hadron–nucleus interactions should be different from that for neutrino–nucleus interactions, since the absorption of the spectator quark(s) of a beam particle in nuclear matter can cause depletion of the fastest particles and produce a plateau at $R(y) > 1$ in the central rapidity region. Indeed, the ratio in the projectile-fragmentation region was found to be less than one, which in both experiments was interpreted in terms of the loss of the leading-particle energy in collisions within the nucleus. The Fermilab experiment [24] also observed a plateau in the region $(2 < y < 4)$ with a value of $R \approx 2$. In the target-fragmentation region, the authors of [24, 25] observed that the ratio for negative particles rises up to 10, in agreement with our results.

The rapidity distributions become wider with increasing W; for this reason, we separated W^2 into three intervals with more or less equal numbers of events and considered the ratio $R(y)$ for each of these intervals separately. It can be seen from Fig. 7 that, in the region $W^2 < 50$ GeV^2, this ratio is less than unity by more than one standard deviation for $y > 2$, $R(y) = 0.6 \pm 0.1$ (statistical error). At smaller y, $R(y)$ flattens around unity in the central region and peaks at $y \approx -2$. For $W^2 > 50$ GeV^2, $R(y) = 1$ within the statistical errors in the quark-fragmentation region and begins to grow between $y \approx -0.5$ and $y \approx -1$ in the target-fragmentation region. We also note that the point where the $R(y)$ distribution begins to grow moves toward smaller values of rapidity with increasing W^2, but this rapidity region always corresponds to the mean particle momentum in the laboratory frame about 1 to 2 GeV/c.

The Monte Carlo model [21] reproduces the general trend of the data, but it does not show the falloff in $R(y)$ at large y as seen for $W^2 < 50$ GeV^2. Also, in all three W^2 intervals, the model gives $R(y)$ values in the target-fragmentation region that are smaller than those that are observed.

The depletion of leading particles at low W^2 is due to interactions with target nucleons. With increasing W^2, this depletion disappears because leading particles become faster to such an extent that, at the instant of their eventual formation, they have already escaped from the nucleus. In an analysis of the $\nu/\bar{\nu}$Ne data from BEBC, Burkot *et al.* [9] considered two possible reasons for fast-hadron attenuation in nuclear matter: the hadron-formation time (or "yo–yo" time) and the constituent-formation time. The former, the time necessary for hadron formation, increases with increasing hadron energy owing to the Lorentz factor. Experimentally, this means that the absorption of the fastest particles in nuclear matter becomes less intense with increasing energy. The constituent-formation time is the time that elapses before the first hadron constituent appears via the rupture of the color string; this time tends to decrease with energy. If the cross section for single-quark interactions is different from zero, the attenuation of the fastest particle will not disappear at higher energies. We have an indication of the hadron-formation time, but no attenuation of fast hadrons at higher energies is observed within our statistics.

5. CONCLUSIONS

We have extracted two data samples for analysis: neutrino–neon interactions with and without an intranuclear cascade. The main results of our analysis are the following:

(i) A method for isolating νN interactions in νNe scattering has been developed. The fraction of events involving an intranuclear cascade is about 54% and is independent of the energy of the hadron system.

(ii) In the forward direction, the multiplicity of charged particles for νN events is approximately identical to that for events featuring an intranuclear cascade, this result being valid over a wide interval of W^2.

(iii) An intranuclear cascade adds 2.36 ± 0.06 units to the backward-hemisphere multiplicity in the region up to $W^2 \approx 400$ GeV^2.

(iv) The VENUS model [21] provides a reasonable description of νNe interactions in the backward hemisphere and, for $W^2 > 50$ GeV^2, in the forward hemisphere. Within this model, the observed fraction of events involving intranuclear rescattering suggests a reaction time in the range $\tau_r = 3.0$–3.5 fm/c.

ACKNOWLEDGMENTS

We are most grateful to the scanning and measuring staff of all participating institutions. We also thank Fermilab and the 15-foot bubble chamber crew for making the experiment possible. One of the authors, E.S. Vataga, wishes to thank Prof. G.M. Piacentino and the University of Cassino for support during the later stage of this work.

REFERENCES

1. L. Landau and I. Pomeranchuk, Dokl. Akad. Nauk SSSR **92**, 535 (1953).
2. N. N. Nikolaev, Z. Phys. C **5**, 291 (1980).
3. A. Bialas and T. Chmaj, Phys. Lett. B **133**, 241 (1983).
4. A. Bialas and M. Gyulassy, Nucl. Phys. B **291**, 793 (1987).
5. A. Ferrari *et al.*, Z. Phys. C **70**, 413 (1996).
6. BEBC WA21/WA59 Collab. (D. R. O. Morrison), in *Proceedings of the International Europhysics Conference, Brighton, 1983*, p. 164.
7. SKAT Bubble Chamber Collab. (D. S. Baranov *et al.*), Yad. Fiz. **40**, 1454 (1984) [Sov. J. Nucl. Phys. **40**, 923 (1984)].
8. A. El-Naghy and S. M. Eliseev, J. Phys. G **16**, 39 (1990).
9. BEBC WA21/WA59 Collab. (W. Burkot *et al.*), Z. Phys. C **70**, 47 (1996).
10. European Muon Collab. (J. Ashman *et al.*), Z. Phys. C **52**, 1 (1991).
11. BEBC WA25 Collab. (A. G. Tenner and N. N. Nikolaev), Nuovo Cimento A **105**, 1001 (1992).
12. T. Kitagaki *et al.*, Phys. Lett. B **214**, 281 (1988).
13. BEBC WA21/WA25/WA59 Collab. (J. Guy *et al.*), Phys. Lett. B **229**, 421 (1989).
14. Fermilab 15-ft Bubble Chamber Antineutrino Collab. (V. I. Efremenko *et al.*), Phys. Lett. B **84**, 511 (1979).
15. Fermilab E545 Collab. (D. Zieminska *et al.*), Phys. Rev. D **27**, 47 (1983).
16. J. Bell *et al.*, Phys. Rev. D **19**, 1 (1979).
17. BEBC WA25 Collab. (S. Barlag *et al.*), Z. Phys. C **11**, 283 (1982).
18. Fermilab E632 Collab. (D. De Prospo *et al.*), Phys. Rev. D **50**, 6691 (1994).
19. N. N. Nikolaev, Z. Phys. C **44**, 645 (1989).
20. K. Werner and P. Koch, Z. Phys. C **47**, 255 (1990).
21. K. Werner, Phys. Rep. **232**, 87 (1993).
22. G. Ingelman *et al*., *DESY HERA Workshop, 1991*, p. 1366.
23. Fermilab E665 Collab. (M. R. Adams *et al.*), Z. Phys. C **65**, 225 (1995).
24. D. H. Brick *et al.*, Phys. Rev. D **41**, 765 (1990).
25. N. M. Agababyan *et al.*, Z. Phys. C **50**, 361 (1991).
26. BEBC WA21 Collab. (P. Allen *et al.*), Nucl. Phys. B **181**, 385 (1981).

Physics of Atomic Nuclei, Vol. 63, No. 9, 2000, pp. 1584–1588. Translated from Yadernaya Fizika, Vol. 63, No. 9, 2000, pp. 1670–1674.

ELEMENTARY PARTICLES AND FIELDS
Experiment

Analysis of the Inclusive Spectra of π^- Mesons from Nucleus–Nucleus Collisions in Terms of Light-Front Variables

L. T. Akhobadze, V. R. Garsevanishvili, M. A. Dasaeva†, T. R. Djalagania, G. O. Kuratashvili, T. G. Kuratashvili, Yu. V. Tevzadze*, and Sh. M. Esakia

High Energy Physics Institute, Tbilisi State University, Universitetskaya ul. 9, GE-380086 Tbilisi, Republic of Georgia

Received March 19, 1999

Abstract—The spectra of π^- mesons originating from *p*C, HeC, CC, and CTa collisions are analyzed in terms of the light-front variables ξ and ζ. The angular and momentum distributions of π^- mesons are studied in various regions of the variables $\xi^\pm$ and $\zeta^\pm$. These distributions in the regions $\xi^+ < \tilde{\xi}^+$ and $\xi^+ > \tilde{\xi}^+$ do not admit a unified description. In the region $\xi^+ < \tilde{\xi}^+$, the distributions in question are consistent with predictions of the statistical model. The temperature parameter *T* decreases almost linearly with increasing product of the mass numbers of colliding nuclei (that is, with increasing number of interacting nucleons). The distributions in the region $\xi^+ > \tilde{\xi}^+$ are fitted to semiempirical forms. © *2000 MAIK "Nauka/Interperiodica".*

An appropriate choice of kinematical variables for studying observables is of great importance for clarifying the properties of hadron–hadron interactions. By studying $\pi^- p$ collisions at 5 and 40 GeV/*c* and $\bar{p}p$ collisions at 22.4 GeV/*c* in terms of light-front variables, it was found in [1–3] from an analysis of differential invariant cross sections that the angular and momentum distributions of secondary π^- mesons have some special features. In particular, these distributions proved to be very different in two regions of the phase space that were selected in terms of light-front variables.

In this connection, it is of interest to analyze the inclusive spectra of π^- mesons from relativistic nucleus–nucleus collisions in terms of light-front variables. Here, we perform such an analysis, paying special attention to the dependences of these spectra on the mass numbers of the incident and target nuclei (A_i and A_t, respectively).

The experimental data used here were collected with the 2-m propane bubble chamber (PPK-500) installed at the Laboratory for High Energies, Joint Institute for Nuclear Research (JINR, Dubna), [4]. The chamber, which housed tantalum targets of thickness about 1 mm, was irradiated with protons and deuterons and by relativistic He, C, F, and Mg nuclei of incident momenta that varied between 2 and 10 GeV/*c* per projectile nucleon. Here, we analyzed π^- mesons emitted in *p*C, HeC, CC, and CTa collisions at an incident momentum of 4.2 GeV/*c* per nucleon. Methodological questions associated with processing and analyzing data collected with the PPK-500 chamber are discussed in [4, 5].

Let us consider an arbitrary 4-vector $p_\mu = (p_0, \mathbf{p})$ and introduce the corresponding light-front variables $p_\pm = p_0 \pm p_3$ [6], which are convenient in studying relativistic composite systems (see [7–13] and references therein). For a generic reaction $A + B \longrightarrow C + X$, we define the scale-invariant quantities

$$\xi^\pm = \pm\frac{p_\pm^C}{p_\pm^A + p_\pm^B}, \tag{1}$$

where $p_\pm = p_0 \pm p_z$ are the aforementioned light-front variables for the particles *A*, *B*, and *C* (the *z* axis is aligned with the collision axis, $p_z = p_3$). The variables $\xi^\pm$ are seen to be invariant under Lorentz boosts along the collision axis. In the c.m. frame of an *NN* collision, we have

$$\xi^\pm = \pm\frac{E^C \pm p_z^C}{\sqrt{s}}, \tag{2}$$

where $\sqrt{s}$ is the c.m. energy of such a collision; by convention, the upper (lower) sign refers to particles traveling in the forward (backward) hemisphere—that is, to $p_z > 0$ ($p_z < 0$).

The invariant cross section in terms of the variables $(\xi^\pm, \mathbf{p}_\perp)$ can be written as

$$E^C\frac{d\sigma}{d^3\mathbf{p}^C} = \frac{\xi^\pm}{\pi}\frac{d\sigma}{d\xi^\pm d(p_\perp^C)^2}. \tag{3}$$

† Deceased.

* e-mail: tevza@sun20.hepi.edu.ge

The variables $\xi^{\pm}$ differ from the Feynman variable $x_F = 2p_z/\sqrt{s}$ in that the region $|\xi^{\pm}| \le m_C/\sqrt{s}$ (near the point $\xi^{\pm} = 0$) is kinematically forbidden (the differential cross section vanishes there) and in that $\xi^{\pm}$ distributions of secondary particles show maxima at relatively small values of $\xi^{\pm}$ that are denoted by $\tilde{\xi}^{\pm}$ [1, 2].

In order to clarify the origin of these enhancements, the angular and $p_\perp^2$ distributions of secondary π^- mesons were separately plotted in [1, 2] for the regions $|\xi^{\pm}| < |\tilde{\xi}^{\pm}|$ and $|\xi^{\pm}| > |\tilde{\xi}^{\pm}|$. The angular distributions proved to be very anisotropic in the region $|\xi^{\pm}| > |\tilde{\xi}^{\pm}|$ and nearly isotropic in the region $|\xi^{\pm}| < |\tilde{\xi}^{\pm}|$. In addition, the $p_\perp^2$ distributions for the two regions showed very different slopes. These observations suggest that pions populating two parts of the phase space that are separated by the surfaces

$$p_z^C = ((p_\perp^C)^2 + m_C^2 - (\tilde{\xi}^{\pm})^2 s)/(-2\tilde{\xi}^{\pm}\sqrt{s}) \qquad (4)$$

have very different characteristics.

We note that, in the large-p_z limit (according to the commonly adopted terminology, $|p_z^C| \gg p_\perp^C$ singles out the fragmentation region), the variables $\xi^{\pm}$ reduce to the well-known scale-invariant Feynman variable x_F and that, in the large-$p_\perp$ limit ($p_\perp^C \gg |p_z^C|$), these variables go over to $x_\perp = 2p_\perp/\sqrt{s}$.

For a further analysis of inclusive reactions in terms of light-front variables, it is convenient to define [1, 2]

$$\zeta^{\pm} = \mp \ln|\xi^{\pm}|, \qquad (5)$$

where the upper and the lower sign again refer to secondaries, respectively, with $p_z > 0$ and $p_z < 0$ in the c.m. frame.

Within the approach outlined above, the reactions $p + C \longrightarrow \pi^- + X$, $He + C \longrightarrow \pi^- + X$, $C + C \longrightarrow \pi^- + X$, and $C + Ta \longrightarrow \pi^- + X$ at 4.2 GeV/c per nucleon are analyzed here in terms of the light-front variables. The data on the reaction $\bar{p} + p \longrightarrow \pi^{\pm} + X$ at 22.4 GeV/c [2] are also quoted in Tables 1 and 2 for the sake of comparison.

The measured invariant differential spectra $(\xi^{\pm}/\pi)(dN/d\xi^{\pm})$ and $(1/\pi)(dN/d\zeta^+)$ are illustrated in Figs. 1 and 2, respectively. For all spectra of either type, the positions of the maxima are seen to be virtually coincident (Table 1), these positions being denoted by $\tilde{\xi}^{\pm}$ and $\tilde{\zeta}^{\pm}$ for the former and the latter spectra, respectively. For a further, more detailed, analysis and comparison with theoretical hypotheses, we choose the reaction $C + C \longrightarrow \pi^- + X$. Since this reaction is symmetric, it is sufficient to consider one hemisphere—in particular, the right-hand one. For π^- mesons emitted in the regions $\xi^+ < \tilde{\xi}^+$ and $\xi^+ > \tilde{\xi}^+$, the squared-transverse-momentum distribution $dN/dp_\perp^2$ and the distribution $dN/d\cos\vartheta$ with respect to the cosine of the emission angle in the c.m. frame are plotted in Figs. 3 and 4, respectively. Secondary π^- mesons emitted into the region $\xi^+ < \tilde{\xi}^+$ show a more anisotropic angular distribution and a steeper squared-transverse-momentum distribution than those emitted into the region $\xi^+ > \tilde{\xi}^+$.

The inclusive spectra of π^- mesons emitted into the region $|\xi^{\pm}| < |\tilde{\xi}^{\pm}|$ were then fitted in terms of the Boltzmann distribution

$$f(E) \sim e^{-E/T}. \qquad (6)$$

In this region, the distributions $(1/\pi)(dN/d\zeta)$,

Table 1. Results of fitting the distributions $(1/\pi)(dN/d\zeta^+)$, $dN/dp_\perp^2$, and $dN/d\cos\vartheta$ of secondary pions in the region $\xi^+ < \tilde{\xi}^+$ on the basis of expressions (7)–(9)

Reaction	$\tilde{\zeta}^{\pm}$	Temperature T, MeV		
		$\frac{1}{\pi}\frac{dN}{d\zeta^+}$	$\frac{dN}{d\cos\vartheta}$	$\frac{dN}{dp_\perp^2}$
$\bar{p}p \longrightarrow \pi^{\pm} + X$	2.0	119 ± 3	105 ± 1	86 ± 3
$pC \longrightarrow \pi^- + X$	2.0	107 ± 15	89 ± 20	75 ± 7
$HeC \longrightarrow \pi^- + X$	1.8	100 ± 4	99 ± 10	87 ± 3
$CC \longrightarrow \pi^- + X$	1.9	93 ± 3	60 ± 4	72 ± 2
$CTa \longrightarrow \pi^- + X$	2.0	71 ± 5	68 ± 10	64 ± 4

Table 2. Results of fitting the distributions $dN/dp_\perp^2$ and $(1/\pi)(dN/d\zeta^+)$ of secondary pions in the region $\xi^+ > \tilde{\xi}^+$ on the basis of expressions (13) and (14)

Reaction	$\frac{dN}{dp_\perp^2}$			$\frac{1}{\pi}\frac{dN}{d\zeta^+}$
	α	β_1, $(\text{GeV}/c)^{-2}$	β_2, $(\text{GeV}/c)^{-2}$	n
$\bar{p}p \longrightarrow \pi^{\pm} + X$	0.8 ± 0.3	6.0 ± 0.1	2.8 ± 0.3	3.7 ± 0.1
$pC \longrightarrow \pi^- + X$	0.9 ± 0.1	11.3 ± 2.4	3.0 ± 1.5	3.8 ± 0.2
$HeC \longrightarrow \pi^- + X$	0.9 ± 0.1	7.8 ± 1.1	0	3.8 ± 0.2
$CC \longrightarrow \pi^- + X$	0.66 ± 0.04	24.0 ± 3.1	6.7 ± 0.4	3.8 ± 0.2
$CTa \longrightarrow \pi^- + X$	0.8 ± 0.3	11.9 ± 3.0	4.9 ± 3.0	4.4 ± 0.3

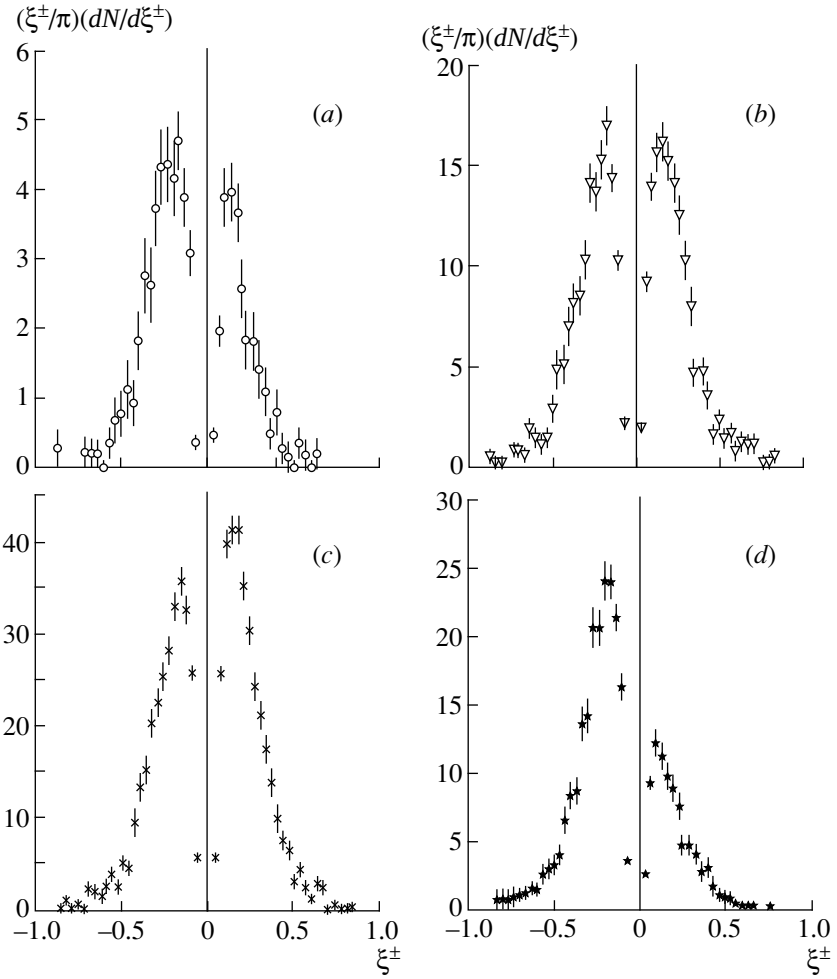

Fig. 1. Distributions $(\xi^{\pm}/\pi)(dN/d\xi^{\pm})$ for the reactions (*a*) $p + C \longrightarrow \pi^- + X$, (*b*) $He + C \longrightarrow \pi^- + X$, (*c*) $C + C \longrightarrow \pi^- + X$, and (*d*) $C + Ta \longrightarrow \pi^- + X$.

$dN/dp_\perp^2$, and $dN/d\cos\vartheta$ can then be represented as

$$\frac{1}{\pi}\frac{dN}{d\zeta} \sim \int_0^{(p_\perp^2)^{\max}} Ef(E)dp_\perp^2, \tag{7}$$

$$\frac{dN}{dp_\perp^2} \sim \int_0^{p_z^{\max}} f(E)dp_z, \tag{8}$$

$$\frac{dN}{d\cos\vartheta} \sim \int_0^{p^{\max}} p^2 f(E)dp, \tag{9}$$

where

$$(p_\perp^2)^{\max} = (\tilde{\xi}^+\sqrt{s})^2 - m_\pi^2, \tag{10}$$

$$p_z^{\max} = \frac{p_\perp^2 + m_\pi^2 - (\tilde{\xi}\sqrt{s})^2}{-2\tilde{\xi}^+\sqrt{s}}, \tag{11}$$

$$p^{\max} = \frac{-\tilde{\xi}^+\sqrt{s}\cos\vartheta + \sqrt{(\tilde{\xi}^+\sqrt{s})^2 - m_\pi^2\sin^2\vartheta}}{\sin^2\vartheta}. \tag{12}$$

In the region $\xi^+ < \tilde{\xi}^+$, the distributions $(1/\pi)(dN/d\zeta)$, $dN/dp_\perp^2$, and $dN/d\cos\vartheta$, were approximated by expressions (7), (8), and (9), respectively. The results of this approximation are presented in Figs. 2–4 and in Table 1.

In the region $\xi^+ > \tilde{\xi}^+$, the above parametrizations lead to unsatisfactory results. There, the distributions dN/dp^2 and $(1/\pi)(dN/d\zeta)$ were approximated as

$$\frac{dN}{dp^2} \sim \alpha e^{\beta_1 p^2} + (1-\alpha)e^{\beta_2 p^2}, \tag{13}$$

$$\frac{1}{\pi}\frac{dN}{d\zeta} \sim (1-\xi^+)^n = (1-e^{|\zeta^+|})^n. \tag{14}$$

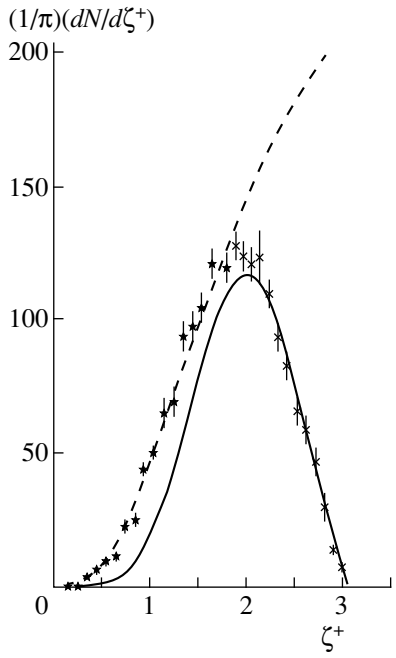

Fig. 2. Distributions $(1/\pi)(dN/d\zeta^+)$ for the reaction C + C $\longrightarrow \pi^- + X$ in the regions (×) $\xi^+ < \tilde{\xi}^+$ and (★) $\xi^+ > \tilde{\xi}^+$. The solid and the dashed curve represent fits on the basis of, respectively, expression (7) for $\xi^+ < \tilde{\xi}^+$ and expression (14) for $\xi^+ > \tilde{\xi}^+$.

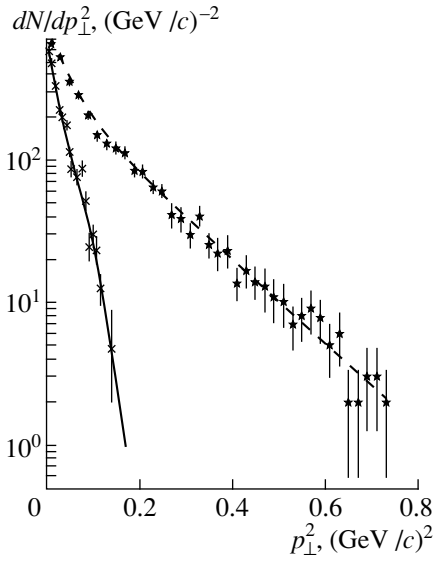

Fig. 3. Distributions $dN/d\,p_\perp^2$ for the reaction C + C $\longrightarrow \pi^- + X$ in the regions (×) $\xi^+ < \tilde{\xi}^+$ and (★) $\xi^+ > \tilde{\xi}^+$. The solid and the dashed curve represent fits on the basis of, respectively, expression (8) for $\xi^+ < \tilde{\xi}^+$ and expression (13) for $\xi^+ > \tilde{\xi}^+$.

(We note that these parametrizations fail in the region $\xi^+ < \tilde{\xi}^+$.) In the limit $\xi^+ \longrightarrow 1$, the last parametrization corresponds to the well-known x_F distribution predicted by the quark–parton model in the form of $(1 - x)^n$, where $x = 2p_z/\sqrt{s}$. The fitted values of the parameters α, β_1, β_2, and n are listed in Table 2, and the corresponding fits are depicted by dashed curves in Figs. 2 and 3.

In the region $\xi^+ < \tilde{\xi}^+$, the fits to the observed distributions $(1/\pi)(dN/d\zeta)$, $dN/d\,p_\perp^2$, and $dN/d\cos\vartheta$ on the basis of expressions (7)–(9) predicted by the statistical model show (see Table 1) that the temperature T decreases with increasing number of nucleons involved in the reaction $A + B \longrightarrow \pi^- + X$. To illustrate this, the T values deduced from the above fit to the distribution $(1/\pi)(dN/d\zeta)$ is plotted in Fig. 5 as a function of $(A_iA_t)^{1/2}$. In all probability, the reduction of the temperature with increasing number of interacting nucleons is due to the growth of mean multiplicity, in which case a secondary receives a smaller fraction of primary energy.

In the future, it would be of interest to analyze and compare the characteristic temperatures for various nucleus–nucleus, nucleon–nucleus, and lepton–nucleon collisions at various energies.

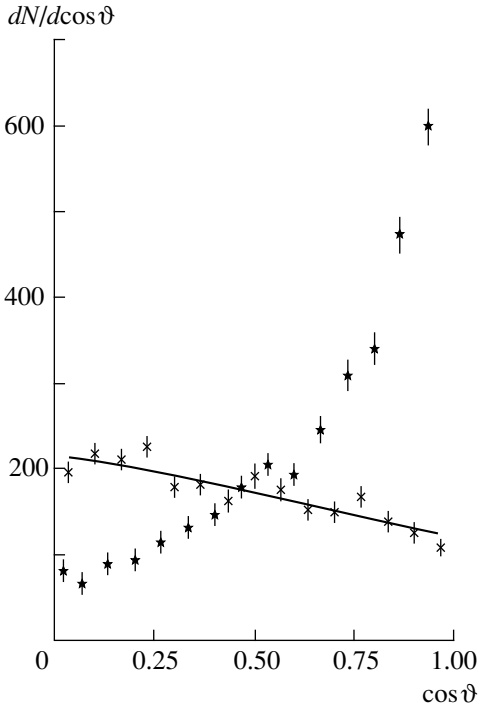

Fig. 4. Distributions $dN/d\cos\vartheta$ for the reaction C + C $\longrightarrow \pi^- + X$ in the regions (×) $\xi^+ < \tilde{\xi}^+$ and (★) $\xi^+ > \tilde{\xi}^+$. The solid curve represents a fit on the basis of expression (9).

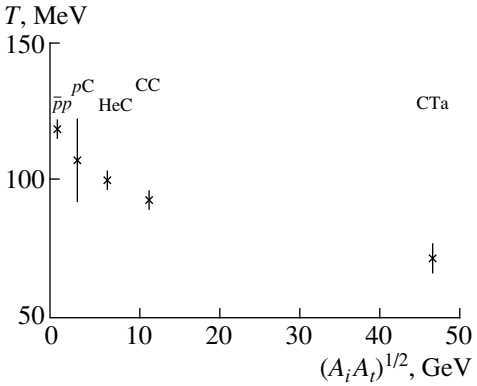

Fig. 5. Temperature T as estimated by fitting the distribution $(1/\pi)(dN/d\zeta)$ in the region $\xi^+ < \tilde{\xi}^+$ on the basis of expression (7) versus $(A_iA_t)^{1/2}$, where A_i and A_t are the mass numbers of, respectively, the incident and the target nucleus.

We may conclude that, for nucleus–nucleus collisions, in just the same way as for hadron–hadron collisions [1, 2], an analysis of inclusive spectra of π^- mesons in terms of the light-front variables $(\xi^\pm, \zeta^\pm)$ reveals that the angular and transverse-momentum distributions of secondary pions are very different in the kinematical regions $|\xi^\pm| < |\tilde{\xi}^\pm|$ and $|\xi^\pm| > |\tilde{\xi}^\pm|$. That the maxima in the distributions with respect to the variables $\xi^\pm$ and $\zeta^\pm$ single out two regions where secondaries behave so differently may suggest that the production mechanisms are different in these two regions.

ACKNOWLEDGMENTS

We are grateful to the physicists running the 2-m propane bubble chamber at JINR for their kind permission to analyze their data. We are also indebted to A.A. Kuznetsov, Z.V. Metreveli, and N.S. Grigalashvili for assistance and stimulating discussions.

REFERENCES

1. L. N. Abesalashvili *et al.*, Pis'ma Zh. Éksp. Teor. Fiz. **30**, 448 (1979) [JETP Lett. **30**, 419 (1979)].
2. N. S. Amaglobeli *et al.*, Preprint IC/82/191 (Trieste, 1982).
3. N. S. Amaglobeli *et al.*, Tr. Tbilis. Univ., Fiz. **14**, 53 (1982).
4. N. S. Grigalashvili *et al.*, Yad. Fiz. **48**, 476 (1988) [Sov. J. Nucl. Phys. **48**, 301 (1988)].
5. G. N. Agakishiev *et al.*, Yad. Fiz. **45**, 1373 (1987) [Sov. J. Nucl. Phys. **45**, 852 (1987)].
6. P. A. M. Dirac, Rev. Mod. Phys. **21**, 392 (1949).
7. V. R. Garsevanishvili, V. G. Kadyshevskiĭ, R. M. Mir-Kasimov, and N. B. Skachkov, Teor. Mat. Fiz. **7**, 203 (1971).
8. V. R. Garsevanishvili, A. N. Kvinikhidze, V. A. Matveev, *et al.*, Teor. Mat. Fiz. **23**, 310 (1975).
9. S. J. Chang, R. G. Root, and T. M. Yan, Phys. Rev. D **7**, 1133 (1973).
10. H. Leutwyler, Nucl. Phys. B **76**, 413 (1974).
11. S. J. Brodsky and H. C. Pauli, in *Recent Aspects of Quantum Fields*, Ed. by H. Miller and H. Gausterer (Springer-Verlag, Berlin, 1991).
12. V. R. Garsevanishvili and Z. R. Menteshashvili, *Relativistic Nuclear Physics in the Light Front Formalism* (Nova Sci., New York, 1993); B. Desplanques, V. A. Kazmanov, and J. P. Mathiot, Nucl. Phys. A **589**, 697 (1995).
13. V. R. Garsevanishvili, G. R. Jibuti, and Sh. M. Ésakiya, Yad. Fiz. **55**, 2768 (1992) [Sov. J. Nucl. Phys. **55**, 1548 (1992)].

Translated by A. Asratyan

Physics of Atomic Nuclei, Vol. 63, No. 9, 2000, pp. 1589–1594. Translated from Yadernaya Fizika, Vol. 63, No. 9, 2000, pp. 1675–1681.

ELEMENTARY PARTICLES AND FIELDS
Theory

Exact Calculation of $O(\alpha)$ QED Corrections for $f_1\bar{f}_1 \to f_2\bar{f}_2$ Processes Induced by Polarized Incident Particles

V. G. Khotilovich[1)] and N. M. Shumeiko

National Scientific and Educational Center, Particle and High Energy Physics, Belarus State University, ul. Bogdanovicha 153, 240040 Minsk, Belarus

Received May 19, 1999

Abstract—For $f_1\bar{f}_1 \to f_2\bar{f}_2(\gamma)$ processes induced by polarized incident particles, exact covariant expressions for the energy spectrum of one of the emitted fermions, for the total cross section, and for the polarization asymmetry are obtained in the α^3 order of QED. © *2000 MAIK "Nauka/Interperiodica".*

1. INTRODUCTION

A correct interpretation of observables in modern elementary-particle physics requires taking into account radiative corrections. In this respect, fermion–antifermion annihilation into two other fermions,

$$f_1 + \bar{f}_1 \to f_2 + \bar{f}_2, \tag{1}$$

has received the most detailed study both in the Standard Model and beyond it [1]. But even for this simple process and even at the QED level, an analytic calculation of radiative corrections is very cumbersome. The problem is pressing, however, since, the inclusion of QED corrections as a background to finer physical effects is of prime importance. In the case being considered, the main difficulty is presented by hard-photon bremsstrahlung (*R* contribution)

$$\begin{aligned} &f_1(p_1, \xi_-) + \bar{f}_1(p_2, \xi_+) \\ &\to f_2(p_5) + \bar{f}_2(p_3) + \gamma(p_4), \end{aligned} \tag{2}$$

where p_i ($i = 1, \ldots, 5$) are the particle momenta, and $\xi_\pm$ are the incident-fermion polarization vectors. We now know only one study, that reported in [2], where the authors were able to calculate analytically the corrections under discussion, retaining nonzero particle masses, but they disregarded polarizations.

In recent years, plans for constructing linear e^+e^- and $\mu^+\mu^-$ colliders have been widely discussed in the literature [3, 4], where a great deal of attention has been given to the possibility of creating polarized beams. With an eye to this possibility, we calculate here, following the same lines as in [2], the energy spectrum of one of the fermions emitted in $f_1\bar{f}_1 \to f_2\bar{f}_2(\gamma)$ processes and the total cross section for such processes, taking into account arbitrary polarizations of incident particles. The resulting expressions prove to be much more cumbersome in this case, and additional difficulties arise in relevant integrations. The calculation would hardly be possible without invoking systems for analytic computer transformations. Thus, the problem of automating the calculations of radiative corrections becomes very acute (see, for example, the review article of Harlander and Steinhauser [5]). We have introduced some refinements in the method of tensor integration (see [6]), obtained a convenient representation for the polarization vectors, and developed a REDUCE code that performs a major part of the calculations.

Corrections associated with the exchange of an additional virtual photon (*V* contribution) are known exactly (see, for example, [7]). We only note that they factorize in front of the Born cross section and that all contributions to them, with the exception of the anomalous-magnetic-moment and two-photon-exchange contributions are independent of polarizations. However, the total cross section for $f_1\bar{f}_1 \to f_2\bar{f}_2(\gamma)$ QED processes is a *C*-even quantity; therefore, the two-photon-exchange diagrams and the interference of the diagrams describing bremsstrahlung from the initial and from the final particles do not contribute (see [2, 7]). We tested our calculations by requiring that these contributions vanish. We eliminated an infrared divergence by the Bardin–Shumeiko covariant method [8] (see also [9]).

The ensuing exposition is organized as follows. In Section 2, we introduce the required notation and representations for the polarization vectors. In Section 3, we describe an improved technique of tensor integration. In Section 4, we present exact expressions to order α^3 for the polarization parts of the fermion energy spectrum and of the total cross section for $f_1\bar{f}_1 \to f_2\bar{f}_2(\gamma)$ QED processes.

[1)] Belarus State University, Minsk, Belarus.

1063-7788/00/6309-1589$20.00 © 2000 MAIK "Nauka/Interperiodica"

2. KINEMATICS AND NOTATION

We begin by introducing the notation

$$\begin{aligned} q &= p_1 + p_2, \quad S = q^2, \quad Q = (p_5 + p_3)^2, \\ X &= 2p_3q, \quad t = 2p_1p_3, \quad S_X = S - X = 2p_5p_4, \\ v &= 2p_3p_4, \quad z = 2p_1p_4, \quad \bar{z} = 2p_2p_4, \\ X_t &= X - t, \quad S_t = S - t, \quad \tau = S_X + M^2, \\ \lambda_S &= S^2 - 4m^2S, \quad \lambda_X = X^2 - 4M^2S. \end{aligned} \tag{3}$$

In the c.m. frame, we have

$$t = \frac{X}{2} - \frac{\sqrt{\lambda_S\lambda_X}}{2S}\cos\widehat{p_1p_3}, \quad X = 2\sqrt{S}p_{30}.$$

In performing tensor integration and in obtaining exact expressions for the polarization vectors, we use Gram determinants [10] and more general notation for them that is based on the generalized Kronecker symbols [11]. We restrict our consideration to the interesting case of four-dimensional space and set $\varepsilon^{0123} = -\varepsilon_{0123} = 1$ for the sake of definiteness. By way of example, we indicate that the nonsymmetric fourth-order Gram determinant constructed from the vectors p_i and some 4-vectors q_i ($i = 1, \ldots, 4$) can be represented as (here, we use a convenient notation for contractions of vectors)

$$\begin{aligned} G\begin{pmatrix} p_1 & p_2 & p_3 & p_4 \\ q_1 & q_2 & q_3 & q_4 \end{pmatrix} \\ = -\varepsilon^{\alpha_1\alpha_2\alpha_3\alpha_4}\varepsilon_{\beta_1\beta_2\beta_3\beta_4}p_{\alpha_1}p_{\alpha_2}p_{\alpha_3}p_{\alpha_4}q^{\beta_1}q^{\beta_2}q^{\beta_3}q^{\beta_4} \\ = -\varepsilon^{p_1p_2p_3p_4}\varepsilon_{q_1q_2q_3q_4} = \delta^{p_1p_2p_3p_4}_{q_1q_2q_3q_4}. \end{aligned}$$

If a generalized Kronecker symbol involves less than four momenta, then

$$\delta^{p_1\ldots p_m}_{q_1\ldots q_m} = -\varepsilon^{p_1\ldots p_m\alpha_{m+1}\ldots\alpha_4}\varepsilon_{q_1\ldots q_m\alpha_{m+1}\ldots\alpha_4}/\Gamma(5-m).$$

A more detailed discussion for the case of n dimensions can be found in [11]. Below, we will need a condensed notation for the following Gram determinants:

$$\begin{aligned} \Delta_2 &= \delta^{p_1p_2}_{p_1p_2} = -\lambda_S/4, \ \Delta_3 = \delta^{p_1p_2p_3}_{p_1p_2p_3}, \ \Delta_4 = \delta^{p_1p_2p_3p_4}_{p_1p_2p_3p_4}, \\ \Delta_v &= \delta^{qp_3p_4}_{qp_3p_4}, \ \Delta_k = \delta^{p_1p_2p_4}_{p_1p_2p_4}, \ \Delta_{pk} = \delta^{p_1p_2p_4}_{p_1p_2p_3}. \end{aligned} \tag{4}$$

Let us express the phase space of reaction (2) in terms of four independent invariant variables as

$$\int d\Gamma = \frac{\pi}{4\sqrt{\lambda_S}}\int_{2M\sqrt{S}}^{S} dX \int_{t_{\min}}^{t_{\max}} dt \int_{Q_{\min}}^{Q_{\max}} dQ \int_{z_{\min}}^{z_{\max}} \frac{dz}{4\sqrt{-\Delta_4}}, \tag{5}$$

where the limits of integration are given by

$$\begin{aligned} t_{\min(\max)} &= \frac{X}{2} \mp \frac{\sqrt{\lambda_S\lambda_X}}{2S}, \\ Q_{\min(\max)} &= \frac{M^2S}{\tau} + \frac{S_X}{2\tau}(X \mp \sqrt{\lambda_X}), \\ z_{\min(\max)} &= \frac{4}{\lambda_X}((Q-S)\delta^{p_3q}_{p_3p_1} + (X-Q)\delta^{qp_3}_{qp_1} \mp 2\sqrt{\Delta_3\Delta_v}). \end{aligned} \tag{6}$$

For the polarization vectors, we introduce the representation

$$\xi^\mu_\pm = \pm P^\pm_L\frac{\delta^{p_{2(1)}\mu}_{p_{2(1)}p_{1(2)}}}{m\sqrt{-\Delta_2}} - P^\pm_T\frac{\delta^{p_1p_2\mu}_{p_1p_2p_3}}{\sqrt{-\Delta_2\Delta_3}} + P^\pm_\perp\frac{\varepsilon^{p_1p_2p_3\mu}}{\sqrt{\Delta_3}}, \tag{7}$$

which is similar to that which was used in [12] and which relied on an expansion of the polarization vectors in a specially chosen basis in four-dimensional space. The quantities $P^\pm_L$, $P^\pm_T$, and $P^\pm_\perp$ are the degrees of various particle polarizations (longitudinal, transverse, and orthogonal, respectively) defined with respect to the plane of $\overline{f}_2$ emission as the following projections of the particle polarization vectors: P_L is the projection onto the z axis aligned with the f_1-beam direction; P_T is the projection onto the x axis lying in the plane determined by the z axis and the direction of $\overline{f}_2$ emission; and $P_\perp$ is the projection onto the y axis. Often, the degrees of transverse polarization ($P^\pm_{\mathrm{tr}}$), one of the azimuthal angles of the polarization vectors ($\varphi^\pm$), and their difference ($\Delta\varphi$) are used instead of the variables $P^\pm_T$ and $P^\pm_\perp$, which are expressed as

$$P^\pm_T = P^\pm_{\mathrm{tr}}\cos\varphi^\pm, \ P^\pm_\perp = P^\pm_{\mathrm{tr}}\sin\varphi^\pm, \ \varphi^- = \varphi^+ + \Delta\varphi. \tag{8}$$

As is obvious from (5), integration with respect to the azimuthal angle φ (which can be identified with one of the angles $\varphi^\pm$) has already been performed (this integration yielded the factor 2π) because, upon the substitution of the expansions for the tensor integrals (see Section 3) into the integrand, we arrive at an expression where the degree of transverse polarization appears only in the combination

$$\begin{aligned} \delta^{p_1p_2\xi_+}_{p_1p_2\xi_-} &= \xi_+\xi_-\Delta_2 + \frac{S-2m^2}{2}p_1\xi_+p_2\xi_- \\ &= -\Delta_2P^+_{\mathrm{tr}}P^-_{\mathrm{tr}}\cos\Delta\varphi, \end{aligned} \tag{9}$$

which is independent of φ. Here, we have used representation (7) and taken into account Eq. (8).

3. TECHNIQUE OF COVARIANT INTEGRATION

In order to calculate the total cross section, it is necessary to perform integration over the phase space of

the emitted photon and antifermion. Expressions involving the scalar products $p_3\xi_\pm$ and $p_4\xi_\pm$ lead to the vector and tensor integrals (which are later contracted with the vectors $\xi_\pm^\mu$)

$$([p_3^\mu], [p_4^\mu], [p_3^\mu p_3^\nu], [p_4^\mu p_4^\nu], [p_3^\mu p_4^\nu]) = \int d\Gamma A(X, t, Q, z)(p_3^\mu, p_4^\mu, p_3^\mu p_3^\nu, p_4^\mu p_4^\nu, p_3^\mu p_4^\nu), \quad (10)$$

where A is a relevant function of invariant variables.

We applied a refined technique of tensor integration using the basic ideas of the algorithm proposed in [11] for reducing one-loop tensor integrals.

Let us consider the determinant

$$\delta^{p_1p_2\mu}_{p_1p_2p_3} = p_3^\mu\Delta_2 - p_1^\mu\delta^{p_1p_2}_{p_3p_2} - p_2^\mu\delta^{p_1p_2}_{p_3p_1}.$$

For p_3^μ, we then have

$$p_3^\mu = P_3^\mu + \delta^{p_1p_2\mu}_{p_1p_2p_3}/\Delta_2, \quad (11)$$

where

$$P_3^\mu = \frac{1}{\Delta_2}(p_1^\mu\delta^{p_1p_2}_{p_3p_2} + p_2^\mu\delta^{p_1p_2}_{p_3p_1}). \quad (12)$$

If we substitute (11) into the vector integral $[p_3^\mu]$, the term that involves $\delta^{p_1p_2\mu}_{p_1p_2p_3}$ does not contribute, because $[p_3^\mu]$ is expressed in terms of a linear combination of the remaining free vectors p_1 and p_2 and because $\delta^{p_1p_2\mu}_{p_1p_2p_3}$ is orthogonal to either of these. Similarly, we can consider the vector p_4^μ (it is only necessary to replace the subscript 3 by 4). For the vector integrals, we therefore arrive at

$$[p_3^\mu] = [P_3^\mu], \quad [p_4^\mu] = [P_4^\mu]. \quad (13)$$

Let us consider the product

$$p_3^\mu p_3^\nu = P_3^\mu P_3^\nu + (P_3^\mu\delta^{p_1p_2\nu}_{p_1p_2p_3} + P_3^\nu\delta^{p_1p_2\mu}_{p_1p_2p_3})/\Delta_2 + \delta^{p_1p_2\mu}_{p_1p_2p_3}\delta^{p_1p_2\nu}_{p_1p_2p_3}/\Delta_2^2.$$

Since the integral $[p_3^\mu p_3^\nu]$ can eventually be represented as the sum of terms proportional to $p_i^\mu p_j^\nu$ $(i, j = 1, 2)$ and $g^{\mu\nu}$, we again conclude that terms linear in δ make zero contribution. As to the integral $[\delta^{p_1p_2\mu}_{p_1p_2p_3}\delta^{p_1p_2\nu}_{p_1p_2p_3}]$, it can be proportional only to the projection operator $\delta^{p_1p_2\mu}_{p_1p_2\alpha}g^{\alpha\nu}$. The proportionality factor is easily calculable. By considering $[p_4^\mu p_4^\nu]$ and $[p_3^\mu p_4^\nu]$, we similarly arrive at

$$[p_3^\mu p_3^\nu] = [P_3^\mu P_3^\nu] + \frac{[\Delta_3]}{2\Delta_2^2}\delta^{p_1p_2\mu}_{p_1p_2\alpha}g^{\alpha\nu},$$
$$[p_4^\mu p_4^\nu] = [P_4^\mu P_4^\nu] + \frac{[\Delta_k]}{2\Delta_2^2}\delta^{p_1p_2\mu}_{p_1p_2\alpha}g^{\alpha\nu}, \quad (14)$$
$$[p_3^\mu p_4^\nu] = [P_3^\mu P_4^\nu] + \frac{[\Delta_{pk}]}{2\Delta_2^2}\delta^{p_1p_2\mu}_{p_1p_2\alpha}g^{\alpha\nu}.$$

The calculation of the squared matrix element and four analytic integrations were performed by using a code based on the REDUCE system for analytic transformations. Instead of calculating the form in (10) for each individual function A, we substituted (13) and (14) into the general expression for the squared matrix element and contracted it with the polarization vectors (7). The ensuing calculation of the resulting scalar integrals was performed in a conventional way by substituting the table of z, Q, t, and X integrals. The majority of the integrals were calculated in [13], but a few new integrals have appeared owing to the inclusion of polarization in our consideration.

The expressions for the energy spectrum are obtained as an intermediate result upon performing integration with respect to z, Q, and t.

In order to calculate the total cross section for $f_1\bar{f}_1 \longrightarrow f_2\bar{f}_2(\gamma)$ processes to order α^3, it is necessary, in addition to performing integration with respect to X in the finite part of the R contribution, to take into account the V contribution and the soft-photon-emission contribution, which we consider on the basis of the covariant method developed in [8]. The code performs integration of all contributions to the total cross section, producing a result free from infrared divergences.

4. RESULTS OF THE CALCULATIONS

The final expression for the energy spectrum of one of the final fermions has the form

$$\frac{1}{\sigma_0}\frac{d\sigma}{dx} = \frac{\alpha}{\pi}\frac{1}{\beta}\Big\{(Q_i^2S_I(x) + Q_f^2S_F(x)(1+2\rho)) \times\Big[1 + P_L^+P_L^-\frac{1-2\rho}{1+2\rho} + P_{tr}^+P_{tr}^-\cos\Delta\varphi\frac{2\rho}{1+2\rho}\Big] + Q_i^2(P_L^+P_L^-\Delta S_L(x) + P_{tr}^+P_{tr}^-\cos\Delta\varphi\rho\Delta S_{tr}(x))\Big\}, \quad (15)$$

where

$$\sigma_0 = \frac{4\pi\alpha^2}{3S}Q_i^2Q_f^2;$$

$$\Delta S_L(x) = \frac{1}{\beta^2(1+2\rho)}\Big\{-2x\beta_x\Big[1+6\rho+14\rho^2 - \rho(1+30\rho-28\rho^2)\frac{L(\beta)}{\beta}\Big] + 2x^2\beta_x\Big[1+9\rho+20\rho^2 - \rho(1+42\rho-40\rho^2)\frac{L(\beta)}{\beta}\Big] - L(\beta_x)\Big[(1+2\rho)(1+2\rho+12\rho\rho_f) - 2\rho(1+2\rho+4\rho(1-\rho)(1+6\rho_f))\frac{L(\beta)}{\beta}\Big] + x(1-x)L(\beta_x)\Big[1+2\rho+12\rho^2-24\rho^2(1-\rho)\frac{L(\beta)}{\beta}\Big] + L(x,\beta_x)\Big[1+6\rho-4\rho^2-4\rho(1+2\rho^2)\frac{L(\beta)}{\beta}\Big]\Big\}, \quad (16)$$

$$\Delta S_{\rm tr}(x) = \frac{1}{\beta^2(1+2\rho)}\Big\{x\beta_x\Big[8+22\rho - (3+26\rho-44\rho^2)\frac{L(\beta)}{\beta}\Big] - 2x^2\beta_x\Big[11+28\rho - (3+38\rho-56\rho^2)\frac{L(\beta)}{\beta}\Big] + L(\beta_x)[3(1+2\rho)(1+2\rho_f) - 2(1-4\rho+6\rho(1-\rho)(1+2\rho_f))\frac{L(\beta)}{\beta}\Big] - x(1-x)L(\beta_x)\Big[2+10\rho-(1+10\rho(1-2\rho))\frac{L(\beta)}{\beta}\Big] - L(x,\beta_x)\Big[4+2\rho-(3-2\rho-4\rho^2)\frac{L(\beta)}{\beta}\Big]\Big\}; \quad (17)$$

Q_i (Q_f) are the charges of the initial (final) fermions in the positron-charge units; and

$$x = \frac{X}{S} = \frac{p_{30}}{E} \in \Big[\frac{M}{E}, 1\Big], \quad \rho = \frac{m^2}{S}, \quad \rho_f = \frac{M^2}{S},$$

$$\beta = \sqrt{1-4\rho} = \sqrt{\lambda_S}/S, \quad \beta_x = \sqrt{1-4\rho_f/x^2} = \sqrt{\lambda_X}/X,$$

$$\beta_f = \beta_x|_{x=1} = \sqrt{1-4\rho_f}, \quad L(\beta) = \ln\frac{1+\beta}{1-\beta},$$

$$L(x,\beta_x) = \frac{1}{2}\Big[L(\beta_x) + \ln\frac{2-x(1-\beta_x)}{2-x(1+\beta_x)}\Big].$$

Here, x and β_x are, respectively, the c.m. energy in units of E (energy of colliding particles) and the c.m. velocity of one of the final fermions; β_f is its maximum velocity; and β is the velocity of colliding particles. Exact expressions for the functions $S_I(x)$ and $S_F(x)$ can be found in [2] [Eqs. (6) and (7)].

We can see that the part generated by the transverse polarization is proportional to the mass of the incident particles, and we include it here merely to demonstrate the feasibility of an exact calculation. The polarization structure of radiation from the final state is very simple—it is completely described by the bracketed factor in expression (15). The functions $\Delta S_L(x)$ and $\Delta S_{\rm tr}(x)$ represent a new result. They characterize the deviation from the aforementioned proportionality for radiation from the initial state. These functions do not contribute to the infrared divergence for $x \longrightarrow 1$. In the ultrarelativistic approximation (ρ, $\rho_f \ll 1$), $\Delta S_L(x)$ assumes the form

$$\Delta S_L(x) = 6[x(1-x)(L(\beta_x) - 2\beta_x) - L(\beta_x) + L(x,\beta_x)]. \quad (18)$$

It can be seen from Fig. 1*a* that the difference between the exact and approximate results for $\Delta S_L(x)$ is insignificant.

Following [6], we can introduce yet another observable—the asymmetry in the spin flip of one of the initial particles (this asymmetry determines the polarized part with respect to the unpolarized one),

$$A(x,\rho,\rho_f) = \frac{1}{P_L^+P_L^-}\Big(\frac{d\sigma^{\uparrow\uparrow}}{dx} - \frac{d\sigma^{\uparrow\downarrow}}{dx}\Big)\Big/\Big(\frac{d\sigma^{\uparrow\uparrow}}{dx} + \frac{d\sigma^{\uparrow\downarrow}}{dx}\Big), \quad (19)$$

where

$$\frac{d\sigma^{\uparrow\downarrow}}{dx} = \frac{d\sigma(-P_L^-, P_L^+)}{dx}, \quad \frac{d\sigma^{\uparrow\uparrow}}{dx} = \frac{d\sigma(P_L^-, P_L^+)}{dx}.$$

Substituting (15) into (19) and neglecting the transverse polarization, we arrive at

$$A(x,\rho,\rho_f) = A_0 + \frac{Q_i^2\Delta S_L(x)}{Q_i^2 S_I(x) + Q_f^2 S_F(x)(1+2\rho)}, \quad (20)$$

where

$$A_0 = \frac{1-2\rho}{1+2\rho}. \quad (21)$$

In other words, radiation from the initial state—more precisely, the function $\Delta S_L(x)$—determines primarily the difference of the asymmetry and A_0 at high energies. Figure 1*b* displays a typical x dependence of the asymmetry and the difference of the exact and the approximate expressions. The asymmetry is seen to tend to unity for $x \longrightarrow 1$; this is due to the infrared

divergence of the functions $S_I(x)$ and $S_F(x)$ in the denominator on the right-hand side of (20). The curve slowly approaches unity with increasing energy {in the high-energy limit, doubly logarithmic terms vanish in $\Delta S_L(x)$ [see (18)]}.

To order α^3, the total QED cross section for $f_1\bar{f}_1 \longrightarrow f_2\bar{f}_2(\gamma)$ processes induced by polarized particles has the form

$$\begin{aligned}\sigma &= \sigma_a + P_L^+P_L^-\sigma_p + P_{\rm tr}^+P_{\rm tr}^-\cos\Delta\varphi\sigma_{\rm tr}\\ &= \sigma_a^0(1+\delta_a) + P_L^+P_L^-\sigma_p^0(1+\delta_p)\\ &\quad + P_{\rm tr}^+P_{\rm tr}^-\cos\Delta\varphi\sigma_{\rm tr}^0(1+\delta_{\rm tr})\\ &= (\sigma_a^0 + P_L^+P_L^-\sigma_p^0 + P_{\rm tr}^+P_{\rm tr}^-\cos\Delta\varphi\sigma_{\rm tr}^0)(1+\delta_a)\\ &\quad + P_L^+P_L^-\sigma_p^0\Delta\delta_p + P_{\rm tr}^+P_{\rm tr}^-\cos\Delta\varphi\sigma_{\rm tr}^0\Delta\delta_{\rm tr},\end{aligned} \tag{22}$$

where

$$\sigma_a^0 = \sigma_0\frac{\beta_f}{\beta}(1+2\rho)(1+2\rho_f)$$

is the unpolarized part of the Born cross section, while

$$\sigma_p^0 = \sigma_0\frac{\beta_f}{\beta}(1-2\rho)(1+2\rho_f),\quad \sigma_{\rm tr}^0 = \sigma_0\frac{\beta_f}{\beta}\rho(1+2\rho_f)$$

are the parts of the Born cross section that are generated by, respectively, the longitudinal and the transverse part of incident-particle polarization.

The corrections δ_a, δ_p, and $\delta_{\rm tr}$ are given by

$$\begin{aligned}&\delta_a = \delta_I + \delta_F + \delta_{VP},\quad \delta_p = \delta_a + \Delta\delta_p,\\ &\delta_{\rm tr} = \delta_a + \Delta\delta_{\rm tr},\end{aligned} \tag{23}$$

where

$$\begin{aligned}\delta_I &= \frac{\alpha}{\pi}Q_i^2\left\{\frac{1}{2}\left[\frac{1+\beta^2}{\beta}L(\beta)-2\right]\ln\frac{\beta_f^4}{\rho_f^2\rho}\right.\\ &\quad -\frac{4L(\beta_f)[\beta L(\beta)-1]}{\beta_f(3-\beta^2)(3-\beta_f^2)}\\ &\quad +\frac{1+\beta^2}{\beta}\left[{\rm Li}_2\left(\frac{2\beta}{\beta-1}\right)-{\rm Li}_2\left(\frac{2\beta}{\beta+1}\right)+\frac{\pi^2}{2}\right]\\ &\quad +\frac{2}{3}\left[1+2\left(\frac{1-\beta^2}{3-\beta^2}\right)\left(\frac{3-2\beta_f^2}{3-\beta_f^2}\right)\right]\\ &\quad \left.-\frac{L(\beta)}{3\beta(3-\beta^2)}\left[1+\frac{(1-\beta^2)}{(3-\beta_f^2)}(24+9\beta^2-2\beta_f^2-5\beta^2\beta_f^2)\right]\right\},\end{aligned} \tag{24}$$

$$\begin{aligned}\Delta\delta_p &= \frac{\alpha}{\pi}Q_i^2\frac{1}{\beta^2(1+\beta^2)}\left\{\frac{3}{2}\frac{L(\beta)}{\beta}\right.\\ &\quad \times\left[\frac{8-8\beta^2+\beta^4-3\beta^6}{3-\beta^2}-2\frac{8-8\beta^2-\beta^4}{3-\beta_f^2}\right]\\ &\quad -\frac{2L(\beta_f)}{\beta_f(3-\beta^2)(3-\beta_f^2)}\left[2(9-8\beta^2+3\beta^4)\right.\\ &\quad \left.-3\frac{L(\beta)}{\beta}(3+\beta^2)(1-\beta^2)^2\right]\\ &\quad \left.-\frac{8}{3(3-\beta^2)}\left[9-2\beta^2-3\beta^4-6\frac{9-5\beta^2}{3-\beta_f^2}\right]\right\},\end{aligned} \tag{25}$$

$$\begin{aligned}\Delta\delta_{\rm tr} &= \frac{\alpha}{\pi}Q_i^2\frac{1}{\beta^2}\left\{-\frac{L(\beta)}{3\beta}\left[\frac{18+12\beta^2+5\beta^4}{3-\beta^2}-12\frac{3+2\beta^2}{3-\beta_f^2}\right]\right.\\ &\quad +\frac{L(\beta_f)}{\beta_f(3-\beta^2)(3-\beta_f^2)}\left[2(9-5\beta^2)-\frac{L(\beta)}{\beta}(9-5\beta^4)\right]\\ &\quad \left.+\frac{4}{3(3-\beta^2)}\left[9+\beta^2-6\frac{9-2\beta^2}{3-\beta_f}\right]\right\},\end{aligned} \tag{26}$$

and ${\rm Li}_2(x) = -\int_0^x\frac{\ln(1-t)}{t}dt$.

The correction δ_a (23) corresponds to the absence of polarization. It includes the quantities δ_I (δ_F) appearing

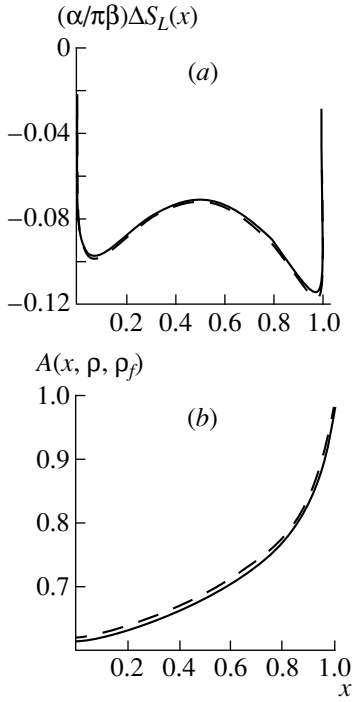

Fig. 1. (*a*) Function $\Delta S_L(x)$ and (*b*) asymmetry $A(x, \rho, \rho_f)$ for the process $p\bar{p} \longrightarrow e^+e^-\gamma$ at $E = 16$ GeV versus x according to the (solid curves) exact and (dashed curves) approximate calculations.

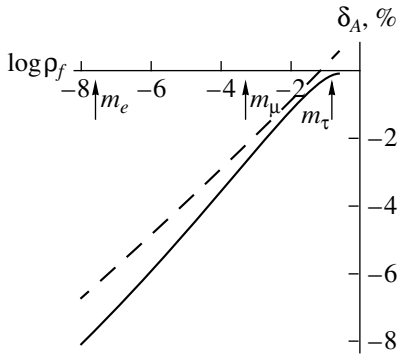

Fig. 2. Radiative correction δ_A as function of the final-fermion mass for $p\bar{p} \longrightarrow f\bar{f}(\gamma)$ processes at $E = 2$ GeV. The dashed curve represents the approximate value of δ_A.

to be the sum of the factorized parts of the R contribution, the contributions of the vertex functions for the initial (final) particles (see [2]), and the vacuum-polarization contribution δ_{VP} (see, for example, [7]). The corrections δ_I and δ_F were obtained in [2] [Eqs. (12) and (13)]. Our expression for δ_I differs slightly from eq. (12) presented in [2]: our denominator of the last term in (24) contains $3 - \beta_f^2$ instead of $2(3 - \beta_f^2)$. Among new results, we can indicate deviations of the polarization corrections from δ_a as represented by the expressions for $\Delta\delta_p$ and $\Delta\delta_{\rm tr}$. Like the energy spectra, they are generated by the radiation from the initial state exclusively. In the ultrarelativistic approximation, we have

$$\Delta\delta_p = \frac{\alpha}{\pi}\left(-2L_M + \frac{16}{3}\right), \tag{27}$$

$$\Delta\delta_{\rm tr} = \frac{\alpha}{\pi}\left(-L_m L_M + \frac{25}{6}L_m + 2L_M - \frac{22}{3}\right), \tag{28}$$

where $L_m = \ln\dfrac{S}{m^2}$ and $L_M = \ln\dfrac{S}{M^2}$. As in the cases of $\dfrac{d\sigma}{dX}$, the part associated with the transverse polarization is of merely theoretical interest because of the smallness of $\sigma_{\rm tr}^0$. The spin-flip asymmetry can be introduced for the longitudinal polarization as well:

$$A(\rho, \rho_f) = \frac{1}{P_L^+ P_L^-}\frac{\sigma^{\uparrow\uparrow} - \sigma^{\uparrow\downarrow}}{\sigma^{\uparrow\uparrow} + \sigma^{\uparrow\downarrow}} = \frac{\sigma_p}{\sigma_a} = A_0\frac{1+\delta_p}{1+\delta_a} = A_0(1+\delta_A). \tag{29}$$

Here, the Born asymmetry A_0 and the correction to it, δ_A, are given by

$$A_0 = \frac{\sigma_p^0}{\sigma_a^0}, \quad \delta_A = \frac{\Delta\delta_p}{1+\delta_a}. \tag{30}$$

Figure 2 displays the difference of the exact and the approximate values of δ_A. The difference is noticeable only near the threshold.

5. CONCLUSION

Thus, we have obtained exact QED expressions to order α^3 for the energy spectrum of one of the final fermions in $f_1\bar{f}_1 \longrightarrow f_2\bar{f}_2(\gamma)$ processes involving massive fermions, as well as for their total cross sections and the corresponding polarization asymmetries. Our calculations extend the results obtained in [2] to the case of arbitrarily polarized incident particles, an improved method for tensor integration and the use of computer systems for analytic transformations playing a key role in our derivation.

REFERENCES

1. D. Bardin *et al.*, Nucl. Phys. B **351**, 1 (1991); W. Hollik and C. Schappacher, Nucl. Phys. B **545**, 98 (1999).
2. A. A. Akhundov, D. Yu. Bardin, T. Riemann, and O. M. Fedorenko, Yad. Fiz. **42**, 1204 (1985) [Sov. J. Nucl. Phys. **42**, 762 (1985)].
3. ECFA/DESY LC Physics Working Group Collab. (E. Accomando *et al.*), Phys. Rep. **299**, 1 (1997); D. J. Miller, hep-ex/9901039.
4. V. Barger, hep-ph/9803480.
5. R. Harlander and M. Steinhauser, hep-ph/9812357.
6. T. V. Kukhto and N. M. Shumeiko, Nucl. Phys. B **219**, 412 (1983).
7. F. A. Berends, K. J. Gaemer, and R. Gastmans, Nucl. Phys. B **57**, 381 (1973).
8. D. Y. Bardin and N. M. Shumeiko, Nucl. Phys. B **127**, 242 (1977).
9. O. M. Fedorenko and T. Riemann, Acta Phys. Pol. B **18**, 761 (1987).
10. E. Byckling and K. Kajantie, *Particle Kinematics* (Wiley, New York, 1973; Mir, Moscow, 1975).
11. G. J. van Oldenborgh and J. A. Vermaseren, Z. Phys. C **46**, 425 (1990).
12. I. V. Akushevich and N. M. Shumeiko, J. Phys. G **20**, 513 (1994).
13. A. A. Akhundov, D. Y. Bardin, O. M. Fedorenko, and T. Riemann, Preprint No. E2-84-777 (JINR, Dubna, 1984).

Translated by M. Kobrinsky

Physics of Atomic Nuclei, Vol. 63, No. 9, 2000, pp. 1595–1602. Translated from Yadernaya Fizika, Vol. 63, No. 9, 2000, pp. 1682–1689.

ELEMENTARY PARTICLES AND FIELDS
Theory

Charm Photo- and Electroproduction at High Energies

A. V. Berezhnoy[1)], V. V. Kiselev*, and A. K. Likhoded

Institute for High Energy Physics, Protvino, Moscow oblast, 142284 Russia

Received May 19, 1999; in final form, September 27, 1999

Abstract—The differential and total cross sections for the photoproduction of vector D^* mesons and for their production in deep-inelastic interactions at the HERA collider are estimated on the basis of a model motivated by perturbative calculations within QCD. The proposed model makes it possible to take into account higher twists in the meson transverse momentum at $p_T \sim m_c$ and to reproduce correctly the dominance of c-quark fragmentation for $p_T \gg m_c$. The possibility of the hadronization of an octet $c\bar{q}$ state into a meson is considered, whereby good agreement with experimental data is obtained both for the case of D^*-meson photoproduction and for the case of D^*-meson formation in a deep-inelastic process. © *2000 MAIK "Nauka/Interperiodica".*

1. INTRODUCTION

In connection with the emergence of new data on charm photo- and electroproduction that were obtained by the ZEUS ([1]) and H1 ([2]) collaborations from experiments at the HERA collider, there arises the question of interpreting these data within perturbative QCD (pQCD). This point is of importance because, along with a confirmation of qualitative pQCD predictions, glaring quantitative discrepancies between the measured cross sections and their theoretical estimates are observed in some kinematical domains—in particular, discrepancies in the shapes of the D^*-meson spectra.

The use of perturbation theory in such processes is firmly justified by the high D^*-meson transverse momenta involved, $p_T \geq m_c$. At the same time, nonperturbative effects cannot be eliminated from the calculations completely, and the hadronization of c quarks formed in a hard collision of initial partons is described in terms of the fragmentation function $D(z, \mu)$, where the parameter μ specifies the factorization scale for the perturbative subprocess and the scale of the quark binding energy in a hadron, this binding energy being determined by the dynamics of confinement.[2)] Information about the nonperturbative fragmentation function is extracted from data on charm production in e^+e^- annihilation [3, 4]. The μ dependence of the fragmentation function is determined by the leading-logarithm approximation in QCD (leading order abbreviated as LO) and by corrections to it in the next-to-leading order (NLO) and in the order next to the NLO (NNLO) [4]. In calculating the cross section for heavy-quark production to $O(\alpha\alpha_s^2)$ terms, some authors disregard the dependence of $D(z, \mu)$ on $\mu \sim p_T$ in the hadronization process [5]. In other studies, this additional dependence in the fragmentation function was taken into account in the NNLO [6]. The input fragmentation function at $\mu = \mu_0 \sim 1$ GeV was taken either in the form of ansätze based on the reciprocity relation [7] or in the form proposed for the fragmentation function by Peterson *et al.* [8].

At present, two approaches are used in pQCD to calculate the cross section for $c\bar{c}$-pair production to $O(\alpha\alpha_s^2)$ terms. In one of these, it is assumed that only light quarks and gluons are present in the photon or in the proton as partons and that c quarks are produced as the result of light-parton interactions. The finite c-quark mass is taken into account in this approach [5].

In the other approach, a c quark appears to be an extra active flavor. There, the c quark is assumed to be massless, and the c-quark component of initial particles is taken into account in the form of relevant structure functions [6, 9].

In either case, the hadronization of c quarks is described within the fragmentation model in terms of the convolution of the perturbative distribution of c quarks and the fragmentation function; that is,

$$\frac{d\sigma_{D^*}}{dp_T} = \int\limits_{2p_T/\sqrt{\hat{s}}}^{1} \frac{d\hat{\sigma}_{c\bar{c}}(k_T, \mu)}{dk_T}\bigg|_{k_T = \frac{p_T}{z}} \frac{D_{c\to D^*}(z, \mu)}{z} dz, \quad (1)$$

where $D_{c\to D^*}(z, \mu)$ is the fragmentation function normalized to the probability of the c-quark transition into a D^* meson {this probability, $w(c \longrightarrow D^*) = 0.22 \pm 0.014 \pm 0.014$, was determined from data on e^+e^- annihilation [3]} and μ is the factorization scale for the perturbative parton cross section $d\hat{\sigma}_{c\bar{c}}/dk_T$.

[1)] Institute of Nuclear Physics, Moscow State University, Vorob'evy gory, Moscow, 119899 Russia.

[2)] Although the evolution of parton distributions in response to variations in the factorization scale for structure functions can be considered within pQCD, a description of these distributions in the initial state appears to be yet another realm where it is necessary to invoke phenomenological parametrizations because of a nonperturbative character of interactions.

* e-mail: kiselev@mx.ihep.su

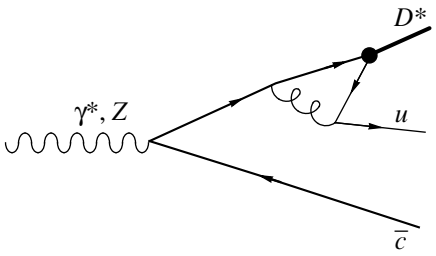

Fig. 1. Leading-order diagram for D^*-meson production in the reaction $e^+e^- \longrightarrow \gamma^*, Z \longrightarrow D^* + X$.

The condition $p_T \gg m_c$ or $m_{c\bar{c}} \gg m_D$, which leads to a jet character of events, plays a key role in the ideology of the fragmentation of a heavy c quark. However, a dominant contribution to the total number of events comes from the region around $p_T \sim m_c$, where the model specified by equation (1) is inapplicable.

In our model, which is based on pQCD, we describe the formation of a $c\bar{q}$ state, which reproduces, according to the assumption of semilocal duality [10], the hadron distribution, apart from a factor dependent on the $c\bar{q}$ and hadron quantum numbers. For this purpose, we consider the total set of Feynman diagrams corresponding to the formation of a $c\bar{q}$ system in the leading order in α and α_s. Not only does this procedure enable us to describe correctly the formation of D mesons at $p_T \sim m_c$, but it also reproduces faithfully the results that arise in the fragmentation model for $p_T \gg m_c$.

2. FRAGMENTATION FUNCTION

One of the known parametrizations of the fragmentation function (it was introduced within the model proposed by Peterson *et al.* [8]) has the form

$$D(z) = \frac{N}{z\left(1 - \frac{1}{z} - \frac{\epsilon}{(1-z)}\right)^2}, \qquad (2)$$

where N is a normalization factor and ϵ is a free phenomenological parameter; it can be assumed that this parameter is dependent on μ. This fragmentation function describes fairly well experimental data on B- and D-meson production in e^+e^- annihilation at high energies, in which case the fragmentation mechanism is dominant.

According to the argument presented by the authors of the parametrization in (2), the z dependence in this expression is determined primarily by the propagator for the heavy c quark. We will discuss this point in some detail. We denote by P_{D^*} the momentum of the product D^* meson and by P_{jet} the momentum of the jet accompanying it. The denominator of the perturbative propagator can then be written as

$$m_c^2 - (P_{D^*} + P_{\text{jet}})^2.$$

By expanding this expression in powers of the small parameters m_{D^*}/E_{D^*} and $m_{\text{jet}}/E_{\text{jet}}$ and considering that $z = E_{D^*}/(E_{D^*} + E_{\text{jet}})$, we obtain

$$m_c^2 - (P_{D^*} + P_{\text{jet}})^2 \approx m_c^2 - \frac{m_{D^*}^2}{z} - \frac{m_{\text{jet}}^2}{1-z}$$

$$\approx m_c^2 - \frac{m_c^2}{z} - \frac{m_{\text{jet}}^2}{1-z} \sim 1 - \frac{1}{z} - \frac{m_{\text{jet}}^2}{m_c^2}\frac{1}{1-z}.$$

Although N and ϵ appear in (2) as phenomenological parameters, it is clear that ϵ has the meaning of the square of the ratio of the jet mass to the quark mass and that this ratio increases logarithmically with increasing energy of an e^+e^- collision.

By consistently analyzing heavy-quark fragmentation with allowance for the quantum numbers of final-state mesons and for the QCD structure of the vertices of the diagram in Fig. 1, the authors of [11] obtained the analytic expression

$$D_{\bar{c}\to D^*}(z) = \frac{8\alpha_s^2\langle O_{(1)}\rangle}{27m_q^3}\frac{rz(1-z)^2}{[1-(1-r)z]^6}[2 - 2(3-2r)z + 3(3-2r+4r^2)z^2 - 2(1-r)(4-r+2r^2)z^3 + (1-r)^2(3-2r+2r^2)z^4], \qquad (3)$$

where $r = m_q/(m_q + m_c)$ and

$$\langle O_{(1)}\rangle = \frac{1}{12M}\left(-g^{\mu\nu} + \frac{p^\mu p^\nu}{M^2}\right) \times \langle D^*(p)|(\bar{c}\gamma_\mu q)(\bar{q}\gamma_\nu c)|D^*(p)\rangle.$$

In the nonrelativistic potential model, the last expression reduces to the square of the wave function at the origin for two heavy quarks: $\langle O_{(1)}\rangle|_{\text{NR}} = |\Psi(0)|^2$. The effective mass of the light quark, m_q, determines both the form and the normalization of the fragmentation function; that is,

$$w(c \longrightarrow D^*) = \int_0^1 D_{c\to D^*}(z)dz = \frac{\alpha_s^2(\mu_R)\langle O_{(1)}(\mu_R)\rangle}{m_q^3} I(r), \qquad (4)$$

where

$$I(r) = \frac{8}{27}\left[\frac{24 + 109r - 126r^2 - 174r^3 - 89r^4}{15(1-r)^5} + \frac{r(7 - 4r - 3r^2 + 10r^3 + 2r^4)}{(1-r)^6}\ln r\right]. \qquad (5)$$

In our model, we assume that the fragmentation probability $w(c \longrightarrow D^*)$ is independent of the scale μ_R, so that this probability w can be treated as a strictly fixed quantity, which is determined from experimental data (see above).

In the fragmentation model being considered, the heavy-quark virtuality is given by

$$m_c^2 - (P_{D^*} + P_{\text{jet}})^2 \approx m_{D^*}^2\left[(1-r)^2 - \frac{1}{z} - \frac{r^2}{1-z}\right]$$

$$= -\frac{m_{D^*}^2}{z(1-z)}[1-(1-r)z]^2,$$

so that $r^2 \approx \epsilon$. By choosing appropriately the parameters m_q and m_c, we can ensure that the behavior of the fragmentation function in (3) becomes similar to the behavior of the fragmentation function in (2). The aforementioned logarithmic dependence of the parameter ϵ in the near-threshold region, where $\ln(p_T/m_c) \sim 1$, can be disregarded.

3. $c\bar{c}$ PHOTO- AND ELECTROPRODUCTION

It was shown above that, in the case of e^+e^- annihilation, it is possible to obtain a reliable description of the inclusive cross section for charm production by using perturbative calculations with nonzero light-quark mass. Here, all calculations amount to evaluating the contribution of one diagram in the special axial gauge (see Fig. 1) [11]. The number of diagrams contributing to other reactions is much greater. The full set of $O(\alpha\alpha_s^3)$ diagrams for the process $g\gamma^* \longrightarrow D^*$ is displayed in Fig. 2. In this set (here, the initial photon is real in the case of photoproduction and virtual in the case of deep-inelastic interaction), there are diagrams (for example, diagrams *16* and *19*) in which $c\bar{c}$ production to order $\alpha\alpha_s$ is followed by heavy-quark fragmentation to order α_s^2. The contribution of these diagrams is dominant in the kinematical region $p_T \gg m_c$, where they reproduce the predictions of the fragmentation model specified by equation (1).

In order to demonstrate this, we consider sufficiently high energies of the $g\gamma^*$ subprocess and compare the asymptotic expression for the full set of diagrams[3)] in the high-p_T limit with the predictions of the fragmentation model specified by equation (1), where $d\hat{\sigma}_{c\bar{c}}/dk$ is the cross section for the production of a $c\bar{c}$ pair in the Born approximation (that is, in order $\alpha\alpha_s$). From Fig. 3, it can be seen that, at $p_T \simeq 12$ GeV, the factorization hypothesis is valid, so that the differential cross section can be represented in the form (1). For $p_T < 12$ GeV, the fragmentation model is inapplicable since this region is dominated by the contribution of diagrams that are different from the fragmentation diagrams and which involve the independent production of $c\bar{c}$ and $q\bar{q}$ pairs—we will refer to such diagrams as recombination diagrams (these include diagrams *5*, *6*, and *7* in Fig. 2). In the region $p_T \gg m_c$, the contribution of these diagrams to $d\sigma/dp_T^2$ decreases in proportion to $\sim 1/p_T^6$, in contrast to the contribution of the fragmentation diagrams showing the $1/p_T^4$ behavior. Thus, the

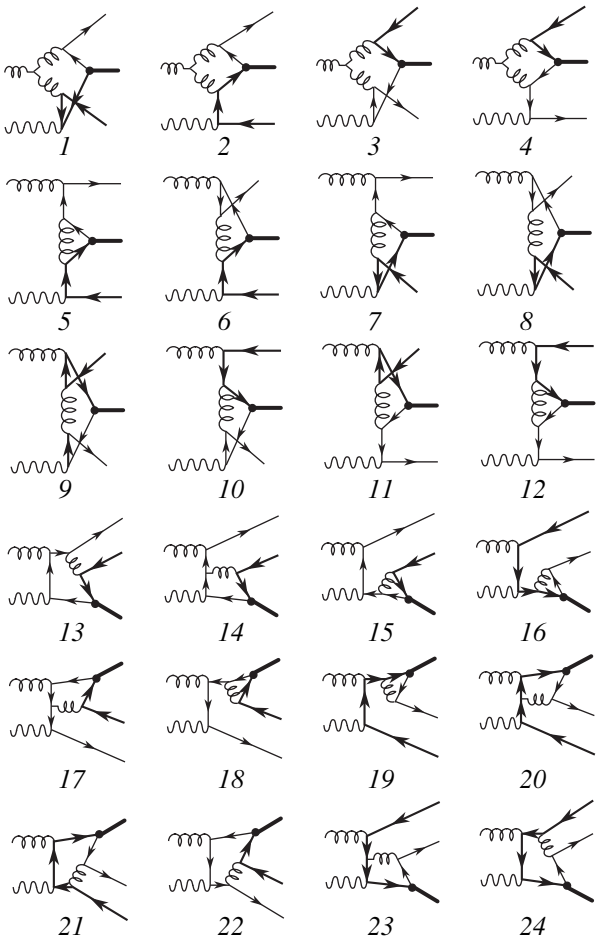

Fig. 2. Leading-order QCD diagrams for the production of a $c\bar{q}$ state in $g\gamma^*$ interactions.

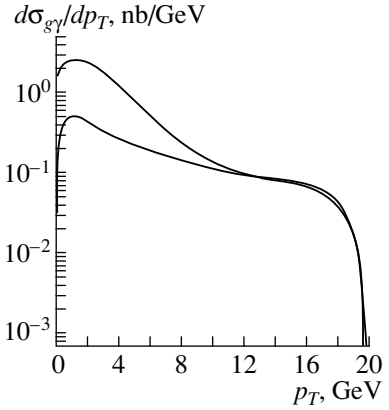

Fig. 3. Transverse-momentum distribution of the cross section for D^*-meson production in $g\gamma$ interactions at 40 GeV (upper curve) along with the relevant prediction of the fragmentation model (lower curve).

[3)] A technique that can be used to evaluate numerically such diagrams within pQCD is described in [12].

inclusion of the recombination diagrams enables us to take into account the contribution of higher twists in the transverse momentum.

It should be emphasized that perturbative calculations for the production of $c\bar{q}$ systems can describe the region around $p_T \sim m_c$, provided that the effective mass of the light quark, m_q, is chosen appropriately. In our calculations, we set $m_q = 0.3$ GeV $\sim m_\rho/2$. Since the gluon virtualities exceed $|k_g^2| \sim p_T^2 + m_\rho^2$ in this case, we can use pQCD, not caring about the region of infrared divergence.

It should be recalled that, in the region $p_T > 12$ GeV, we normalize the absolute cross-section value on the basis of relation (4), assuming that the fragmentation probability is independent of the scale.

Further, we note that, in addition to the formation of the color-singlet $c\bar{q}$ state, it is necessary to take into account the formation of the color-octet $c\bar{q}$ state, which is then converted into a hadron (D^* meson). For mesons consisting of two heavy quarks, it is well known that the octet contribution to the production process is suppressed, the suppression factor being proportional to the third power of the relative velocity v of the quarks in the meson [13]. In our case, this velocity is not small, so that the octet contribution can be commensurate with the singlet contribution. Because of the special features of the color amplitude, the relationship between the production of the color-singlet $c\bar{q}$ state and the production of the color-octet $c\bar{q}$ state in e^+e^- annihilation is such that, when the octet contribution is taken into account, the quantity $\langle O_{(1)}\rangle$ in expressions (3) and (4) for the fragmentation process must be replaced by $\langle O^{\text{eff}}\rangle$,

$$\langle O^{\text{eff}}\rangle = \langle O_{(1)}\rangle + \frac{1}{8}\langle O_{(8)}\rangle, \tag{6}$$

where

$$\langle O_{(8)}\rangle = \frac{1}{8M}\left(-g^{\mu\nu} + \frac{p^\mu p^\nu}{M^2}\right)$$
$$\times \langle D^*(p)\left|(\bar{c}\gamma_\mu\lambda^a q)(\bar{q}\gamma_\nu\lambda^b c)\right|D^*(p)\rangle\frac{\delta^{ab}}{8}.$$

For mesons containing a light relativistic quark, we can expect that $\langle O_{(8)}\rangle/\langle O_{(1)}\rangle \sim 1$ since $v \sim 1$; from (6), it then follows that color-singlet production is dominant in e^+e^- annihilation. Within the fragmentation model, the differential cross section has the same form for the singlet and for the octet mechanism, so that it is impossible to separate the singlet and the octet contributions to D^*-meson production in e^+e^- interactions. The situation is totally different for the photoproduction process—and this case is not unique in this sense, because analogous conclusions are valid for the electroproduction process—where our calculations have led to very dissimilar relationships between the fragmentation and the recombination contributions for the octet and for the singlet mechanism. If $\langle O_{(8)}\rangle/\langle O_{(1)}\rangle \sim 1$, the contribution of recombination diagrams to octet production proves to be commensurate with their contribution to singlet production. It follows that, at $p_T \sim m_c$—these are transverse-momentum values at which recombination is dominant—the cross section for octet production is commensurate with the cross section for singlet production, while, for $p_T \gg m_c$—this is the region dominated by the fragmentation process—octet production is suppressed in proportion to 1/8, in accordance with Eq. (6).

It should be emphasized that the inclusion of the octet contribution induces virtually no changes in the cross section for D^*-meson production at transverse-momentum values much higher than the charmed-quark mass, but this generates an additional contribution in the region where the transverse momentum is on the same order of magnitude as this mass.

4. DESCRIPTION OF ZEUS DATA ON D^*-MESON PHOTOPRODUCTION

Provided that the specific values of the parameters μ_R, m_q, and m_c are chosen in one way or another and that the condition in (4) is imposed, the fixed value of $w(c \longrightarrow D^*) = 0.22$, which was extracted from data on D^*-meson production in e^+e^- annihilation at LEP, determines unambiguously the expectation value $\langle O^{\text{eff}}(\mu_R)\rangle$. If, for example,

$$\begin{aligned} \mu_R &= m_{D^*}, \\ m_q &= 0.3\ \text{GeV}, \\ m_c &= 1.5\ \text{GeV}, \\ w(c \longrightarrow D^*) &= 0.22, \end{aligned} \tag{7}$$

then we have

$$\langle O^{\text{eff}}(m_{D^*})\rangle = 0.25\ \text{GeV}^3.$$

This choice has enabled us to describe data on D^*-meson photoproduction. The calculated cross sections for D^*-meson photoproduction are displayed in Fig. 4, along with ZEUS data from [1], which were obtained in the kinematical region specified by the inequalities $p_T > 2$ GeV, $-1.5 < \eta < 1.5$, $130 < W < 280$ GeV, and $Q^2 < 1$ GeV^2, where W is the total energy of γp interaction, Q^2 is the photon virtuality squared, and η is the D^*-meson pseudorapidity.

From Fig. 4, it can be seen that the experimental value of the cross section for D^*-meson production is not saturated by the color-singlet contribution within our model. The relative value of the color-octet contribution, $\langle O_{(8)}\rangle/\langle O_{(1)}\rangle = 1.3$, enables us to describe well the D^*-meson spectrum. It is worth noting once again that the transverse-momentum distributions behave very differently for the octet and for the singlet mecha-

nism. At the above expectation values of the relevant operators, the octet contribution is commensurate with the singlet contribution at $p_T \sim m_c$ and is much less than it in the region $p_T \gg m_c$.

For the gluon structure function in the proton, the factorization scale was fixed at $\mu_F = 2m_{D^*}$. In calculating the differential cross section, we have chosen two factorization-scale values for the matrix elements $\langle O_{(1,8)}\rangle$ of the relevant quark operators: $\mu_R = m_{D^*}$ (upper curve) and $\mu_R = 2m_{D^*}$ (lower curve). It can be seen that HERA data on D^*-meson photoproduction are best reproduced by our model at $\mu_F = 2m_{D^*}$ and $\mu_R = m_{D^*}$.

Figure 5 illustrates the predictions for D^*-meson photoproduction in a different kinematical region studied by the ZEUS collaboration [14], that which is specified by the inequalities $p_T > 2$ GeV, $-1.0 < \eta < 1.5$, $80 < W < 120$ GeV, and $Q^2 < 0.01$ GeV^2. In the relevant calculations, we have employed the same expectation values $\langle O_{(1)}\rangle$ and $\langle O_{(8)}\rangle$ as in the preceding case.

Unfortunately, available experimental data are insufficient for establishing the value of $\langle O_{(8)}\rangle$. Taking into account the variations in the factorization scale [15], we can only assume that

$$\langle O_{(8)}\rangle \approx 0.33\text{–}0.49 \text{ GeV}^3.$$

It is obvious that, by varying $\langle O_{(1)}\rangle/\langle O_{(8)}\rangle$, we can enhance or reduce the contributions of higher twists in the region of small p_T. In our calculations, we can also disregard the difference of the spectra of vector and pseudoscalar octet states, whose contributions are effectively summed in the relevant operator. No account is taken here of the possible effect of P-wave octet states either, since our experience gained from previous calculations suggests that the production of these states is suppressed in relation to the S-wave contributions.

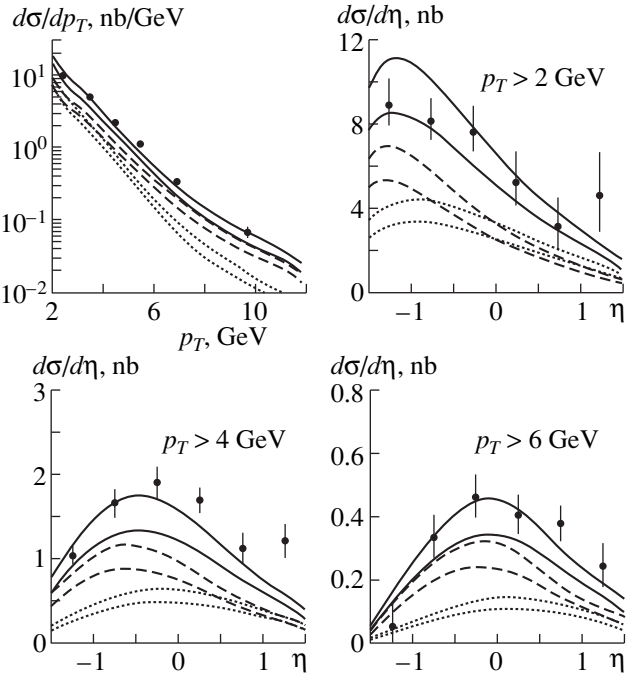

Fig. 4. Calculated transverse-momentum (p_T) and pseudorapidity (η) distributions of the cross section for D^*-meson photoproduction (curves) along with data obtained by the ZEUS collaboration in the region specified by the inequalities $130 < W < 280$ GeV and $Q^2 < 1$ GeV^2 (points): (dashed curves) contribution of the color-singlet state, (dotted curve) contribution of the color-octet state, and (solid curves) sum of these two contributions. The upper and lower curves of the same type correspond to two factorization scales for the matrix elements of the quark operators (see main body of the text).

5. DESCRIPTION OF ZEUS DATA ON D_s- AND D_s^*-MESON PHOTOPRODUCTION

Within our model, we also predict the cross sections for the production of D_s and D_s^* mesons. According to approximate $SU(3)$ symmetry, the expectation values $\langle O_{(1)}\rangle_s$ and $\langle O_{(8)}\rangle_s$ of the color-singlet and color-octet operators in D_s^*-meson production satisfy the relations

$$\begin{aligned}\langle O_{(1)}\rangle_s &\approx \langle O_{(1)}\rangle,\\ \langle O_{(8)}\rangle_s &\approx \langle O_{(8)}\rangle.\end{aligned} \tag{8}$$

In addition, we assume that the expectation values of the relevant operators for the production of a pseudoscalar D_s meson are approximately equal to the corresponding expectation values for the production of a vector D_s^* meson.

By making use of these two assumptions and by replacing $m_q = 0.3$ GeV by $m_s = 0.5$ GeV in our calcu-

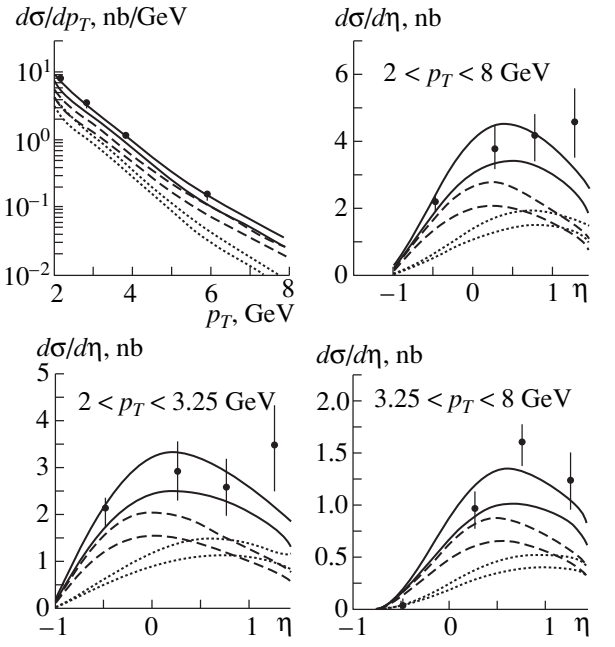

Fig. 5. Differential distributions of the cross section for D^*-meson photoproduction in the region specified by the inequalities $80 < W < 120$ GeV and $Q^2 < 0.01$ GeV^2. The notation is identical to that in Fig. 4.

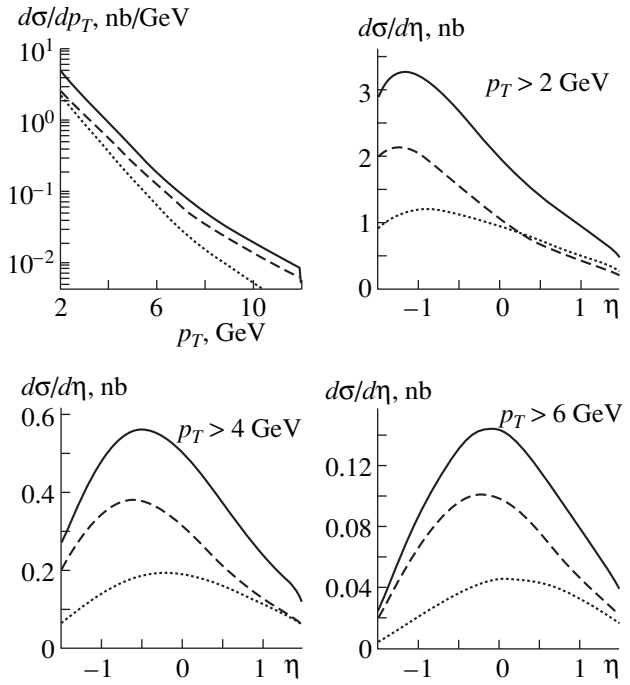

Fig. 6. Differential distributions of the cross section for D_s- and D_s^*-meson photoproduction in the region specified by the inequalities $130 < W < 280$ GeV and $Q^2 < 1$ GeV^2. The notation is identical to that in Fig. 4.

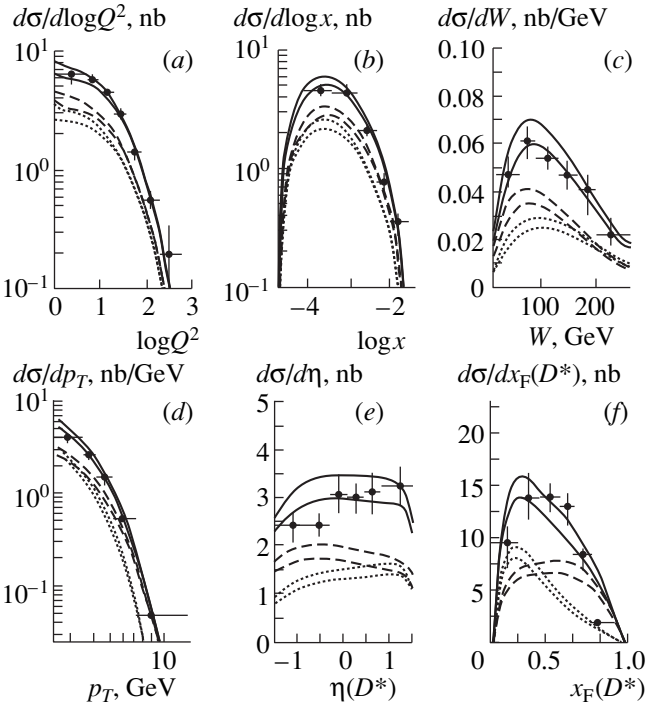

Fig. 7. Differential cross sections for D^*-meson production with respect to (*a*) the photon virtuality Q (in GeV), (*b*) the Bjorken variable x, (*c*) the invariant mass of final-state hadrons, (*d*) the transverse momentum, (*e*) the pseudorapidity, and (*f*) the Feynman variable x_F in deep-inelastic e^+p interactions along with data obtained by the ZEUS collaboration. The notation is identical to that in Fig. 4.

lations, we were able to predict the total differential cross section for the production of D_s and D_s^* mesons, a quantity that is most appropriate for data analysis, since it is difficult to separate experimentally D_s and D_s^* events (the point is that the detection of the dominant decay mode $D_s^* \longrightarrow D_s\gamma$ requires recording a soft photon, but this is hardly possible, as a rule). The results of the relevant calculations are displayed in Fig. 6.

It should be recalled that a preliminary investigation of this process was reported in [16], but the experimental constraints at the operating facilities were disregarded there.

6. D^*-MESON ELECTROPRODUCTION

The computational procedure used here also makes it possible to obtain the cross sections for D^*-meson production in the case where the virtuality of the initial photon is sizable. For this purpose, the matrix element for photoproduction, M_i, where the subscript i indicates photon polarization, is squared and contracted with the spin-averaged square of the electron current according to the formula

$$|A|^2 = \sum_{ij} \frac{k_1^i k_2^j + k_1^j k_2^i - (Q^2/2)g^{ij}}{Q^4} M_i M_j^*, \qquad (9)$$

where $|A|^2$ is the square of the amplitude for D^*-meson electroproduction; k_1 and k_2 are, respectively, the initial and the final positron momentum; and $Q^2 = -(k_1 - k_2)^2$.

The results of the calculations for D^*-meson production in a deep-inelastic e^+p collision are presented in Fig. 7, along with the experimental data of the ZEUS collaboration [17] for the kinematical domain specified by the inequalities $1 < Q^2 < 600$ GeV^2, $-1.5 < \eta < 1.5$, $1.5 < p_T < 15$ GeV, and $0.02 < y < 0.7$, where $y = W^2/s$.

In the calculations of the matrix element, the running coupling constant for strong interaction was taken at the scale $\mu_R = \sqrt{m_{D^*}^2 + Q^2}$ (upper curve) or at the scale $\mu_R = \sqrt{4m_{D^*}^2 + Q^2}$ (lower curve); for the gluon structure function in the proton, the scale was set to $\mu_F = \sqrt{4m_{D^*}^2 + Q^2}$. This option makes it possible to describe electroproduction, on one hand, and to go over at $Q^2 = 0$ to the scale values that we used in the case of photoproduction.

The ratio $\langle O_{(1)}\rangle/\langle O_{(8)}\rangle$ was chosen to be identical to that in the case of photoproduction, an option that makes it possible to describe experimental data fairly well.

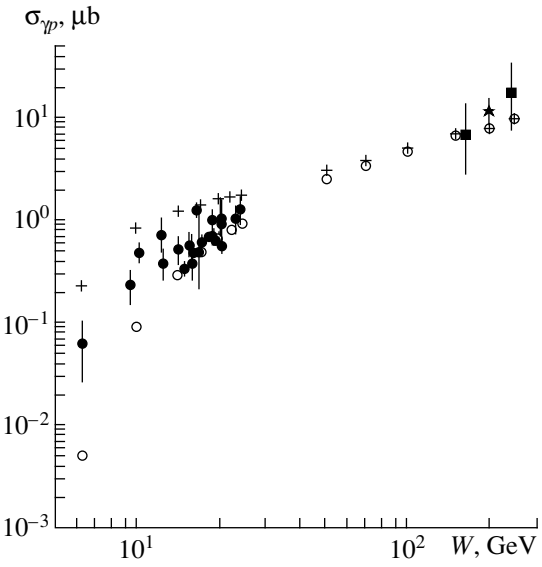

Fig. 8. Charm-photoproduction cross section as a function of the γp-interaction energy W. Closed symbols represent experimental data borrowed from (■) [1], (★) [2], and (●) [18]. The results of the calculations performed without and with allowance for the valence-quark contribution are shown by open circles and crosses, respectively.

7. TOTAL CROSS SECTION FOR CHARM PHOTOPRODUCTION

Since the model being considered describes better data on charm photoproduction at $p_T \sim m_c$, it is interesting to verify its predictions for the total charm-photoproduction cross section over a wide energy region [18]. We have estimated the cross section for charmed-particle production at γp-interaction energies ranging from 20 to 300 GeV (see Fig. 8).

In order to assess the cross section for charm production in the $g\gamma$ subprocess, we divided the cross section for D^{*+} and D^{*-} production by 0.44, the charm-production fraction saturated by these particles according to the results deduced from the investigation of e^+e^- annihilation. Moreover, the additional contribution from diagrams associated with D^*-meson formation on valence quarks in the subprocess $\gamma q_v \longrightarrow (\bar{c}q) + c \longrightarrow D^{*-} + X$ must be taken into account for low-energy data. This contribution can be considered without introducing additional parameters, since the normalization of the cross section is again determined by the factor $\langle O^{\text{eff}} \rangle$. In contrast to the contribution of the subprocess $g\gamma \longrightarrow (\bar{c}q) + c + \bar{q}$, the contribution of the subprocess $\gamma q_v \longrightarrow (\bar{c}q) + c$ is weakly dependent on the light-quark mass m_q. In view of the subsidiary condition (4), which relates m_q and $\langle O^{\text{eff}} \rangle$, there is, however, an implicit m_q dependence of the cross section for charm production on a valence quark. By way of example, we indicate that, when the light-quark mass is reduced from 0.3 to 0.26 GeV, the contribution of this subprocess decreases by a factor of about 1.5, all the remaining contributions suffering no changes.

By varying the mass m_q, we can therefore modify the contribution of the subprocess $\gamma q_v \longrightarrow (\bar{c}q) + c \longrightarrow D^{*-} + X$ owing to the normalization factor $\langle O^{\text{eff}} \rangle$; in this way, a slight excess of the results of our calculations over the experimental data from [18] can be remedied by means of a modest correction of m_q.

At HERA collider energies, the contribution of valence quarks is as small as a few percent; therefore, it does not seem reasonable to discuss this contribution here.

8. CONCLUSION

We have presented a model for describing the production of charmed mesons. That the degrees of freedom of both heavy and light quarks are taken there into account within pQCD in the transverse-momentum region $p_T \geq m_c$ is an important element of the model. Within this model, the hadronization process is described at the level of matrix elements via the factorization of a hard parton subprocess and nonperturbative quark operators corresponding to quark transitions into hadrons. According to semilocal quark–hadron duality, the differential characteristics of a quark pair reproduce the characteristics of hadron distributions in the region where pQCD is applicable ($p_T \geq m_c$). In the region of high transverse momenta ($p_T \gg m_c$), the production cross section is represented, as might have been expected on the basis of the theorem of factorization of hard subprocesses in the form of the convolution of the cross section for heavy-quark production and the fragmentation function.

The region around $p_T \sim m_c$ is described by contributions differing from the fragmentation contribution and having a $1/p_T^6$ asymptotic behavior. In addition, we have increased the cross section for charm production in the region being considered by taking into account the contribution of the octet $c\bar{q}$ state.

Within the uncertainties, we have been able to describe, on the basis of our model, data on D^*-meson photo- and electroproduction at HERA collider energies and data on the total cross section for charm photoproduction on a fixed target.

Of prime importance is that the proposed approach has enabled us to take into account interference and higher twists in the transverse momentum.

It is obvious that the scheme proposed here for calculating additional contributions to heavy-meson production can be extended to the case of hadroproduction. In this connection, it would be interesting to perform a comparison with data on B-meson yields at the TEVATRON. We are going to do this in the near future.

ACKNOWLEDGMENTS

We are grateful to L.K. Gladilin for help in our investigations and for stimulating discussions. We are also indebted to S.S. Gershtein and G. Kramer for enlightening comments and discussions.

This work was supported in part by the Russian Foundation for Basic Research (project nos. 99-02-16558 and 96-15-96575).

REFERENCES

1. ZEUS Collab. (J. Breitweg *et al.*), Eur. Phys. J. C **6**, 67 (1999).
2. H1 Collab. (C. Adloff *et al.*), Preprint No. 98-204 (DESY, Hamburg, 1998); hep-ex/9812023.
3. OPAL Collab. (K. Akerstaff *et al.*), Eur. Phys. J. C **1**, 439 (1998).
4. P. Nason and C. Oleari, Phys. Lett. B **447**, 327 (1999).
5. S. Frixione, M. L. Mangano, P. Nason, and G. Ridolfi, Phys. Lett. B **348**, 633 (1995); S. Frixione, P. Nason, and G. Ridolfi, Nucl. Phys. B **454**, 3 (1995).
6. B. A. Kniehl, G. Kramer, and M. Spira, Z. Phys. C **76**, 689 (1997); J. Binnewies, B. A. Kniehl, and G. Kramer, Z. Phys. C **76**, 677 (1997); Phys. Rev. D **58**, 014014 (1998).
7. V. G. Kartvelishvili, A. K. Likhoded, and V. A. Petrov, Phys. Lett. B **78**, 615 (1978).
8. C. Peterson *et al.*, Phys. Rev. D **27**, 105 (1983).
9. M. Cacciari and M. Greco, Z. Phys. C **69**, 459 (1996); M. Cacciari, M. Greco, S. Rolli, and A. Tanzini, Phys. Rev. D **55**, 2736 (1997); M. Cacciari and M. Greco, Phys. Rev. D **55**, 7134 (1997).
10. Yu. L. Dokshitzer, V. A. Khoze, and S. I. Troyan, J. Phys. G **17**, 1585 (1991); Phys. Rev. D **53**, 89 (1996).
11. C.-H. Chang and Y.-Q. Chen, Phys. Rev. D **46**, 3845 (1992); Erratum: Phys. Rev. D **50**, 6013 (1994); E. Braaten, K. Cheung, and T. C. Yuan, Phys. Rev. D **48**, 4230 (1993); V. V. Kiselev, A. K. Likhoded, and M. V. Shevlyagin, Z. Phys. C **63**, 77 (1994); T. C. Yuan, Phys. Rev. D **50**, 5664 (1994); K. Cheung and T. C. Yuan, Phys. Rev. D **53**, 3591 (1996).
12. A. V. Berezhnoy, V. V. Kiselev, and A. K. Likhoded, Z. Phys. A **356**, 79, 89 (1996).
13. G. T. Bodwin, E. Braaten, and G. P. Lepage, Phys. Rev. D **51**, 1125 (1995); T. Mannel and G. A. Schuller, Z. Phys. C **67**, 159 (1995); E. Braaten, S. Fleming, and T. C. Yuan, Annu. Rev. Nucl. Part. Sci. **46**, 197 (1996).
14. ZEUS Collab. (Y. Eisenberg), hep-ex/9905008.
15. A. V. Berezhnoy, V. V. Kiselev, and A. K. Likhoded, hep-ph/9901333.
16. A. V. Berezhnoy, V. V. Kiselev, and A. K. Likhoded, Yad. Fiz. **61**, 302 (1998) [Phys. At. Nucl. **61**, 252 (1998)].
17. ZEUS Collab., Report at XXIX International Conference on High Energy Physics, Vancouver, 1998.
18. CIF Collab. (M. S. Atiya *et al.*), Phys. Rev. Lett. **43**, 414 (1979); BFP Collab. (A. R. Clark *et al.*), Phys. Rev. Lett. **45**, 682 (1980); SLAC HFP Collab. (K. Abe *et al.*), Phys. Rev. D **30**, 1 (1984); EMC Collab. (M. Arneodo *et al.*), Z. Phys. C **35**, 1 (1987); PEC Collab. (M. Adamovich *et al.*), Phys. Lett. B **187**, 437 (1987); E691 Collab. (J. C. Anjos *et al.*), Phys. Rev. Lett. **65**, 2503 (1990); NA-14 Collab. (M. P. Álvarez *et al.*), Z. Phys. C **60**, 53 (1993).

Translated by A. Isaakyan

Physics of Atomic Nuclei, Vol. 63, No. 9, 2000, pp. 1603–1611. Translated from Yadernaya Fizika, Vol. 63, No. 9, 2000, pp. 1690–1698.

ELEMENTARY PARTICLES AND FIELDS
Theory

Direct Production of Muon Pairs by High-Energy Muons

S. R. Kel'ner, R. P. Kokoulin, and A. A. Petrukhin

Moscow State Engineering Physics Institute (Technical University), Kashirskoe sh. 31, Moscow, 115409 Russia

Received May 26, 1999

Abstract—For ultrarelativistic muons, the cross section for the process $\mu + Z \longrightarrow \mu + Z + \mu^+ + \mu^-$ is calculated with allowance for the nuclear and atomic form factors. It is shown that the nuclear form factor affects significantly the cross-section value. The transverse-momentum distribution of muons is calculated. An approximate formula determining the total cross section to within 2 to 3% is derived. The fluxes of groups of cosmic-ray muons generated by the above process are estimated at various depths. It is shown that calculations performed earlier overestimate significantly the fluxes of such groups. *© 2000 MAIK "Nauka/Interperiodica".*

1. INTRODUCTION

The cross section for the direct production of muon pairs in muon–nucleus collisions,

$$\mu + Z \longrightarrow \mu + Z + \mu^+ + \mu^-, \qquad (1)$$

is much smaller than the cross section for the bremsstrahlung process and for the production of electron–positron pairs. Since the cross-sections ratio $\sigma(\mu \longrightarrow \mu\mu^+\mu^-)/\sigma(\mu \longrightarrow \mu e^+e^-)$ is on the order of 10^{-4}, the effect of process (1) on the formation of the cosmic-ray-muon spectra is negligible. Nevertheless, this process can lead to observable events when a group of three or two[1)] muons separated by small distances traverses the detecting array. In the following, such events will be referred to as triples and couples.

The first estimates of the fluxes of triples and couples and a comparison of the results of calculations with experimental data were presented in [1, 2]. The estimates in question were based on the cross section that was derived from the results obtained in [3] and which describes muon-pair production by a muon on a screened Coulomb center to a logarithmic accuracy only in the limiting case of full screening. This cross section, which is quoted in [4] [expression (1.51)], has been used thus far as a basis for calculating the features of triples and couples. In particular, it underlay the analysis of Kudryavtsev and Ryazhskaya [5, 6], who performed a Monte Carlo simulation of the generation of triples and couples and their propagation to depths of 3000 and 10000 mwe. They showed that couples and triples originating from the direct production of muon pairs contribute noticeably to the number of events characterized by low multiplicities and small distances between the particles involved. The same cross section was also employed by Battistoni and Scapparone [7] in simulating muon groups.

However, the Coulomb center and full-screening approximations within which expression (1.51) from [4] is valid are incorrect in the case being considered for the following reasons:

(i) The characteristic momentum transfer to the nucleus involved in the process under investigation is about muon mass—that is, it is on the same order of magnitude as the inverse radius of the nucleus. It follows that, here—in just the same way as in the case of bremsstrahlung from muons [8]—the nucleus cannot be treated as a Coulomb center. As will be shown below, the replacement of an actual nucleus by a point-like object leads to an overestimation of the cross section.

(ii) In calculating the fluxes of triples and couples, it is more correct to disregard screening, since the screening of nuclei by atomic electrons is operative only in the muon-energy region $E \gg 183Z^{-1/3}\mu^2/m \approx 4Z^{-1/3}$ TeV, where m and μ are, respectively, the electron and the muon mass. Within a logarithmic accuracy, the total cross section for pair production on an unscreened Coulomb center has the form (see, for example, [9])

$$\sigma_c = \frac{28}{27\pi}(Z\alpha r_\mu)^2 \ln^3(\kappa \times 2E/\mu). \qquad (2)$$

In the limit of full screening, we have

$$\sigma_s = \frac{28}{9\pi}(Z\alpha r_\mu)^2 \ln^2(\kappa' \times 2E/\mu) \times \ln(\kappa' \times 183Z^{-1/3}\mu/m), \qquad (3)$$

where κ and κ' are undetermined factors emerging in the calculation to a logarithmic accuracy and r_μ is the classical radius of the muon. Expressions (2) and (3) are commensurate only at $E \sim (183Z^{-1/3}\mu/m)^3\mu \sim 10^{11}$ GeV (at $Z = 11$). At energies close to $E \sim 10^3$ GeV, which are characteristic of the production of triples and couples (see below), a transition to the full-screening limit considerably overestimates the cross section.

[1)] A third muon can be moderated by a medium or miss the array used.

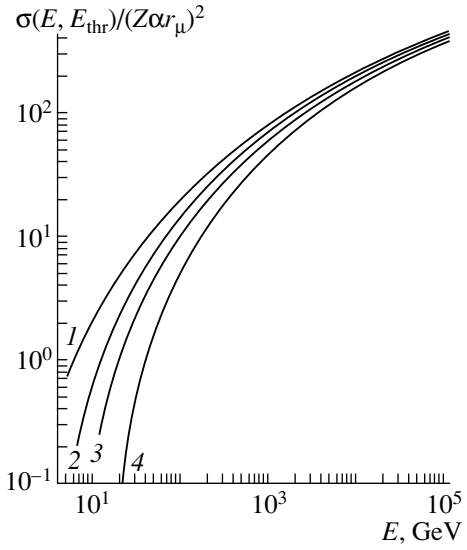

Fig. 1. Total cross section for muon-pair production by a muon in standard rock at the threshold energy values of E_{thr} = (*1*) μ, (*2*) 1, (*3*) 2, and (*4*) 5 GeV.

It should be noted that, for pair production by a particle (in contrast to pair production by a photon or bremsstrahlung), the use of the logarithmic approximation can lead to a large error in the cross section. For scattering on a Coulomb center, an exact expression for the cross section can be obtained with the aid of formula (71) from [10]. Having calculated the numerical coefficients in that formula, we obtain

$$\sigma_c = (Z\alpha r_\mu)^2 \times (0.3301 l_0^3 - 2.098 l_0^2 + 0.8669 l_0 + 13.160), \quad (4)$$

where $l_0 = \ln(2E/\mu)$. The coefficient of l_0^2 is large in relation to the coefficient of l_0^3 and is of opposite sign. If we retain only the leading logarithmic term in this formula [this is equivalent to setting $\kappa = 1$ in (2)], then the cross section at $E = 100$ GeV (we take this value by way of example) is enhanced by a factor of 3. A reasonable choice of κ in (2) is possible only if we know the cross section exactly. In the case being considered, the coefficient κ is much smaller than unity. If we set $\kappa = 1/12$, the distinction between expressions (2) and (4) in the region $E > 20$ GeV will not exceed 3%.

Thus, we see that the formula from [4] overestimates the cross section for muon-pair production, thereby leading to excessive fluxes of muon groups. In this study, we obtain a more precise expression for the cross section and use it to estimate the fluxes of couples and triples formed via reaction (1).

2. REACTION CROSS SECTION

In calculating the total and differential cross sections, we use the results reported by one of the present authors (S.R.K.) in [3], where he analyzed the production of electron–positron pairs by a muon. In a collision of a muon with a Coulomb center, the distribution of particles forming the product pair with respect to the energies $E_\pm$ and the momentum transfer q to the target can be represented as

$$d\sigma = (Z\alpha r_\mu)^2 \times [f_a(E, E_+, E_-, q) + f_b(E, E_+, E_-, q)] dE_+ dE_- dq, \quad (5)$$

where E is the incident-muon energy, and f_a and f_b are the contributions of, respectively, diagrams *a* and *b* from [3] (or the γγ and γ diagrams in the notation adopted in [11]). The explicit expressions for the functions f_a and f_b involve double integrals and are very cumbersome. If the masses of the particles forming the product pair are set to the muon mass, then expression (5) will describe the cross section for the process under investigation but without the interference between the direct and exchange diagrams.

The interference term σ_{int} can be estimated on the basis of the following considerations. The cross section for the production of an electron–positron pair by muons on atomic electrons ($\mu + e^- \longrightarrow \mu + e^- + e^+ + e^-$) was calculated in [12] with allowance for exchange diagrams. Since the muon mass differs significantly from the electron mass and since the total cross section is invariant, the results presented in [12] also describe the production of an electron–positron pair by an electron on a Coulomb center. By replacing the electron mass by the muon mass, we obtain the cross section for the production of a muon pair by a muon. By using the results from [12], we find that σ_{int} reduces the total cross section by about 5% at the muon energy of $E = 10$ GeV and by 3% at $E = 30$ GeV; for $E > 100$ GeV, the contribution of σ_{int} is less than 1%. Therefore, the quantity σ_{int} can be disregarded at high muon energies.

In order to take into account the screening of a nucleus by electrons and the finiteness of nuclear sizes, we must multiply expression (5) by the factor $[F_n(q) - F_a(q)]^2$, where $F_n(q)$ and $F_a(q)$ are, respectively, the nuclear and the atomic elastic form factor. The atomic form factor was determined on the basis of the Thomas–Fermi model; for the nuclear form factor, use was made of the Fermi charge distribution in a nucleus with the parameters from [13]. The total and the differential (with respect to E_+ and E_-) cross section were calculated numerically.

The total cross section for the production of muon pairs by muons in standard rock ($Z = 11$, $A = 22$) is plotted in Fig. 1 for several values of the threshold energy E_{thr} (it is assumed that the total energy of each of the three final muons exceeds E_{thr}). As the muon energy increases, the E_{thr} dependence of the cross section becomes weaker.

Figure 2 illustrates the effect of the atomic and the nuclear form factor on the total reaction cross section. The elastic nuclear form factor changes significantly

the cross section at any energy value. By way of example, we indicate that, at $E = 100$ GeV, the cross section for the process on a finite nucleus is nearly one-half as large as the cross section for the process on a Coulomb center. At the same time, the screening of a nucleus by atomic electrons is operative only for $E \gg 10^4$ GeV. At $E = 5 \times 10^5$ GeV, the atomic form factor diminishes the cross section only by 5%. Curve *3* in Fig. 2 represents the ratio of the cross section calculated by formula (1.51) from [4] to the cross section for the process on a Coulomb center. In the energy range $E = 10^3$–10^4 GeV, the values corresponding to curve *3* are three to four times as great as those of the precise cross section calculated with allowance for the nuclear form factor and depicted by curve *1*.

Muon pairs can also be produced in collisions of muons with atomic electrons,

$$\mu + e \longrightarrow \mu + e + \mu^+ + \mu^-, \tag{6}$$

provided that the incident-muon energy exceeds the threshold energy $E'_{\text{thr}} = \mu(4\mu + 3m)/m = 87.7$ GeV. Numerical calculations reveal that the cross section σ_e for this process[2)] is much smaller than σ_c/Z^2. The reason behind this smallness can be clarified in the following way. To a logarithmic accuracy, the cross section for process (6) is given by

$$\sigma_e = \frac{28}{27\pi}(\alpha r_\mu)^2 l_e^3, \tag{7}$$

where $l_e = \ln(Em/4\mu^2)$. The factor of 1/4 in the argument of the logarithmic function was chosen on the basis of a fit to the results of numerical calculations, the accuracy of the formula in (7) being approximately 20%. The cross section σ_c depends on E/μ, while σ_e depends on mE/μ^2. Therefore, the graph of the function $\sigma_e(E)$ is shifted with respect to the graph of the function $\sigma_c(E)$ by two orders of magnitude in energy toward higher values of E.

The correction to the total cross section from the process in (6) can be taken into account by replacing the factor Z^2 in (5) by $Z(Z + \zeta)$. The quantity ζ grows with increasing muon energy, but it is much smaller than unity for all reasonable energy values (for example, $\zeta = 0.1$ at $E = 10$ TeV and $\zeta = 0.2$ at $E = 100$ TeV). In calculating the fluxes of triples and couples in standard rock without taking into account muon-pair production on atomic electrons, this will lead to an error not exceeding 1%.

Let us consider the correction to the cross section from the excitation of the nucleus in the process of muon-pair production. In order to calculate this correction, we must know the nuclear inelastic electromagnetic form factor $F_n^{\text{in}}(q)$. Andreev *et al.* [14] suggest a simple model that makes it possible to express the nuclear inelastic form factor in terms of the elastic one as

$$F_n^{\text{in}}(q) = 1 - (F_n(q))^2. \tag{8}$$

This equality is obtained in the approximation where the wave function of the nucleus is described by a nonantisymmetrized product of the wave functions of individual protons. The cross section for the process involving the excitation of the nucleus can be written in the form $d\sigma' = F_n^{\text{in}}(q)d\sigma/Z$. From (8), it follows that, within this model, the correction associated with the nuclear inelastic form factor can be estimated as

$$d\sigma' = (d\sigma_{\text{Coul}} - d\sigma_{\text{el}})/Z, \tag{9}$$

where $d\sigma_{\text{Coul}}$ is the differential cross section for the process on a Coulomb center and $d\sigma_{\text{el}}$ is the cross section calculated with allowance for the nuclear elastic form factor. For standard rock, correction (9) to the total cross section is approximately 6% at $E = 100$ GeV and 3% at $E = 10$ TeV.

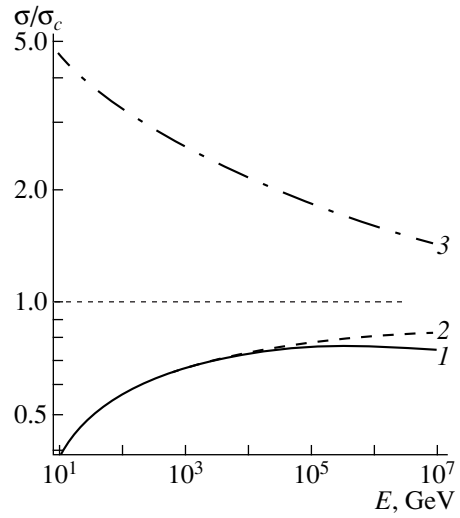

Fig. 2. Ratios of the cross section taking into account (curve *1*) the atomic and nuclear form factors or (curve *2*) only the nuclear factor to the cross section σ_{Coul} for the production process on the Coulomb center. Curve *3* represents the ratio of the cross section from [4] to σ_{Coul}. All curves were calculated for standard rock, the threshold energy being set to 1 GeV.

3. TRANSVERSE-MOMENTUM DISTRIBUTION

The distances between the muons in triple- and couple-type events are determined by the initial transverse momenta of the particles forming a pair and by the transverse momentum of the parent particle, as well as by multiple scattering. For the muon groups produced near the detection point, the initial transverse momentum can have a strong effect on the spatial distribution of particles.

[2)] In order to determine σ_e, it is sufficient to interchange the muon and the electron mass in the code used in [12] to calculate numerically the cross section for the process $e + \mu \longrightarrow e + \mu + e^+ + e^-$.

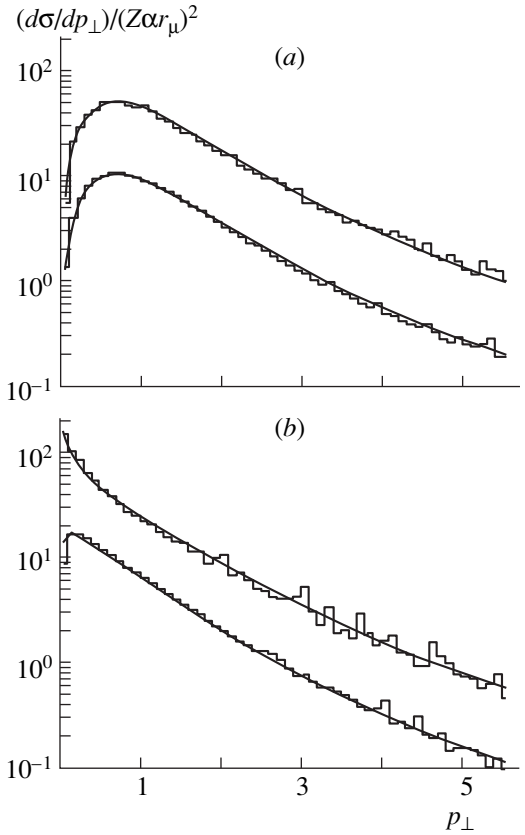

Fig. 3. Transverse-momentum distributions of (*a*) the particles forming a product pair and (*b*) the parent particle for two initial muon energies at the threshold energy of 1 GeV (the results presented in this figure are normalized to the total cross section): (histograms) results of numerical calculations and (curves) results based on approximate formulas (10) and (11). The lower and upper curves correspond to energies of 100 and 1000 GeV, respectively. The transverse momentum are measured in μc units.

Since the interference term makes but a small contribution to the total cross section, the transverse-momentum distribution was calculated without taking into account the interference between the direct and exchange diagrams. In interpreting the results, we can therefore disregard the presence of two identical particles in the final state. We denote by $f(p_\perp)dp_\perp$ the probability that the transverse momentum $p_\perp$ of a particle from the pair lies within the interval $(p_\perp, p_\perp + dp_\perp)$ and by $g(p_\perp)dp_\perp$ the analogous probability for the parent particle.

The functions $f(p_\perp)$ and $g(p_\perp)$ were obtained by numerically integrating the precise fully differential cross section $d\sigma$ determined on the basis of Feynman diagrams. Analytic calculations were computerized by using the Maple code, while numerical calculations were performed by the Monte Carlo method. We determined the total cross section for pair production by evaluating a sevenfold integral and simultaneously constructed histograms characterizing transverse-momentum distributions. The nuclear elastic form factor was taken in accordance with the model of a uniformly charged sphere, the screening of the nucleus by electrons being disregarded.

Our numerical calculations revealed that the functions $f(p_\perp)$ and $g(p_\perp)$ depend only slightly on the incident-muon energy and on the radius R of the nucleus. At the detection threshold E_{thr} of 1 GeV and at incident-muon energy E in excess of 100 GeV, the mean transverse momentum of the particles from a pair is $\langle p_\perp \rangle = 1.5\mu$, while the mean transverse momentum of the parent particle is $\langle p_\perp \rangle = 1.0\mu$. These estimates are valid to a precision higher than 10% for all substances from helium to lead. Under the same conditions, the functions $f(p_\perp)$ and $g(p_\perp)$ can be approximated by the simple expressions

$$f(p_\perp)dp_\perp \sim \frac{p_\perp dp_\perp}{(1 + p_\perp^2/p_f^2)^{9/4}}, \quad p_f = 1.3\mu, \tag{10}$$

$$g(p_\perp)dp_\perp \sim \ln^2\left(1 + \frac{Ep_\perp}{3\mu E_{\text{thr}}}\right)\frac{dp_\perp}{p_\perp(1 + p_\perp^2/p_g^2)^{3/2}}, \tag{11}$$

$$p_g = \mu(\ln(E/4E_{\text{thr}}))^{1/2}.$$

In the transverse-momentum region $\mu E_{\text{thr}}/E \ll p_\perp \ll \mu$, formula (11) complies with the expression $g(p_\perp) \sim \ln^2(Ep_\perp/\mu E_{\text{thr}})/p_\perp$, which can easily be obtained analytically to a logarithmic accuracy by using the results from [11].

The curves calculated numerically and those obtained on the basis of (10) and (11) are compared in Fig. 3.

That the shape of the $p_\perp$ distribution depends weakly on the radius R of a nucleus can be explained in the following way. Let us write the differential (with respect to the transverse momentum $p_\perp$ and the momentum transfer q to the nucleus) cross section as

$$d\sigma = \Phi(p_\perp, q)|F_n(q)|^2\frac{dq}{q}dp_\perp. \tag{12}$$

In order to obtain the $p_\perp$ distribution, we must integrate expression (12) over the region $q > q_{\min}$, where

$$q_{\min} = \frac{1}{2E}\left[\left(\sqrt{p_\perp^2 + 4\mu^2} + \sqrt{p_\perp^2 + \mu^2}\right)^2 - \mu^2\right] \tag{13}$$

is the minimum momentum transfer at a given value of $p_\perp$. A calculation to a logarithmic accuracy yields

$$d\sigma = \Phi(p_\perp, 0)\ln(1/q_{\min}R)\,dp_\perp. \tag{14}$$

To the same accuracy, we can set $\ln(1/q_{\min}R) \approx \ln(E/4\mu^2R)$, so that the dependence of the cross section on R factorizes.

4. APPROXIMATE FORMULA

For practical purposes—for example, in calculating the fluxes of triples and couples or in simulating events by the Monte Carlo method—expression (5) is not convenient because the integrals involved are multidimensional and because the relevant integrands are cumbersome. To perform calculations, it is therefore desirable to have simpler analytic formulas. Approximate formulas describing the cross section for the production of electron–positron pairs by a muon were constructed in [15] with allowance for the screening of a nucleus by electrons and the finiteness of nuclear sizes. Following [15], we can approximate the double-differential cross section for the process under investigation as

$$\sigma(E, \nu, \rho)d\nu d\rho = \frac{2}{3\pi}(Z\alpha r_\mu)^2\frac{1-\nu}{\nu}\Phi(\nu, \rho)\ln X d\nu d\rho. \quad (15)$$

Here, $\nu = (E - E')/E = (E_+ + E_-)/E$ is the energy fraction transferred to the particles of a pair, where E and E' are, respectively, the initial and the final energy of the parent particle and E_+ and E_- are the energies of the product particles, and $\rho = (E_+ - E_-)/(E_+ + E_-)$ is the asymmetry parameter. The energies of the final particles are expressed in terms of the quantities ν and ρ as

$$E' = E(1-\nu), \quad E_\pm = \frac{1}{2}E\nu(1 \pm \rho). \quad (16)$$

The kinematical region of the variables ν and ρ is determined by the inequalities

$$\frac{2\mu}{E} \le \nu \le 1 - \frac{\mu}{E}, \quad |\rho| \le \rho_{\max} \equiv 1 - \frac{2\mu}{\nu E}. \quad (17)$$

The function Φ has the form

$$\Phi(\nu, \rho) = [(2+\rho^2)(1+\beta) + \xi(3+\rho^2)]\ln\left(1+\frac{1}{\xi}\right) + \left[(1+\rho^2)\left(1+\frac{3}{2}\beta\right) - \frac{1}{\xi}(1+2\beta)(1-\rho^2)\right] \times \ln(1+\xi) - 1 - 3\rho^2 + \beta(1-2\rho^2), \quad (18)$$

where

$$\xi = \frac{\nu^2(1-\rho^2)}{4(1-\nu)}, \quad \beta = \frac{\nu^2}{2(1-\nu)}. \quad (19)$$

The argument X of the logarithmic function in (15) is determined as follows. We denote by $U(E, \nu, \rho)$ the function

$$U(E, \nu, \rho) = \frac{0.65A^{-0.27}BZ^{-1/3}\mu/m}{1 + \dfrac{2\sqrt{e}\mu^2 BZ^{-1/3}(1+\xi)(1+Y)}{mE\nu(1-\rho^2)}}, \quad (20)$$

where $B = 183$, $e = 2.718\ldots$, A is the atomic weight, and

$$Y = 12\sqrt{\mu/E}. \quad (21)$$

We then have

$$X = 1 + U(E, \nu, \rho) - U(E, \nu, \rho_{\max}), \quad (22)$$

where $\rho_{\max}$ is defined in (17). The function U is chosen in such a way that, in the limiting cases of the absence of screening and full screening, formula (15) reproduces the leading logarithmic term in the cross section. The factor $0.65A^{-0.27}$ in (20), which takes into account the finiteness of nuclear sizes, was borrowed from [16], where it was shown that, for light nuclei, this factor leads to a cross-section value more accurate than that containing the factor $(2/3)Z^{-1/3}$ normally used [8]. The function Y and the numerical constants were chosen in such a way that the approximate formula guarantees a more accurate value of the total cross section. It should be noted that the cross section $\sigma(E, \nu, \rho)$ is nonnegative over the entire kinematically accessible region (17) and vanishes on the lines $\rho = \pm\rho_{\max}$, as it must.

For primary-muon energies in the region $E > 10$ GeV and secondary-particle energies satisfying the conditions E', E_+, $E_- > 1$ GeV, the discrepancy between the precise differential cross section and its approximated form (15) does not exceed 10%. The total cross section calculated by the approximate formula is smaller than the cross section obtained by numerically integrating precise formulas from [3] by about 5% in the energy range $10 < E < 30$ GeV and by 2 to 3% for energies in the region $E > 30$ GeV.

The formula for the cross section $\sigma(E, \nu, \rho)$ takes into account the finiteness of nuclear sizes and the screening of a nucleus by electrons. In the limiting case of no screening [$E \ll \mu^2 BZ^{-1/3}(1+\xi)/m\nu(1-\rho^2)$], the function U is simplified considerably to become

$$U(E, \nu, \rho) = \frac{0.197A^{-0.27}E\nu(1-\rho^2)}{\mu(1+\xi)(1+Y)}. \quad (23)$$

This function describes pair production on a finite (nonpointlike) nucleus. In the opposite case of full screening, we have

$$X \approx U(E, \nu, \rho) = 0.65BZ^{-1/3}A^{-0.27}\mu/m. \quad (24)$$

The cross section from [4] can be represented as

$$\sigma(E, \nu, \rho)d\nu d\rho = \frac{2}{3\pi}Z(Z+1)(\alpha r_\mu)^2\frac{1-\nu}{\nu} \times \Phi(\nu, \rho)\ln(BZ^{-1/3}\mu/m)d\nu d\rho. \quad (25)$$

This expression differs from (15) in that the arguments of the logarithmic function are different and in that the product $Z(Z+1)$ occurs in the former instead of Z^2. In Fig. 4, the differential cross sections as calculated by formulas (15) and (25) are shown as functions of ρ. Since the cross section is an even function of ρ, only half of the graph is displayed in the figure. We can see that formula (25) overestimates strongly the cross section over the entire kinematical region of variables and even distorts the qualitative dependences, since it does

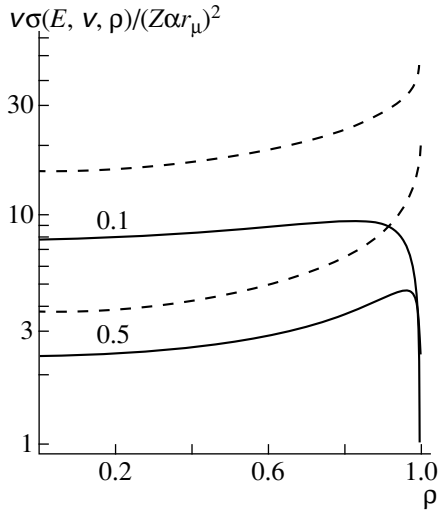

Fig. 4. Cross sections calculated by formulas (solid curves) (15) and (dashed curves) (25) as functions of the parameter ρ. The values of ν are indicated on the curves. All calculations were performed for standard rock at a primary-muon energy of 1 TeV.

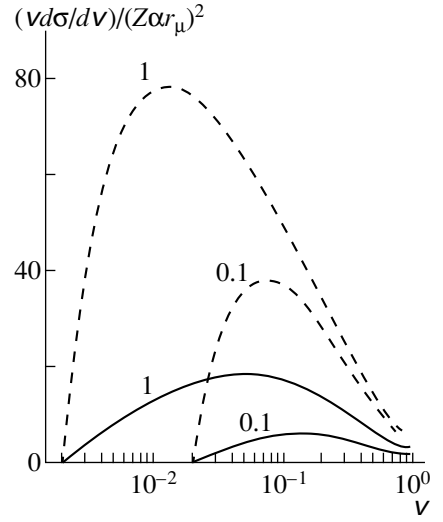

Fig. 5. Distributions with respect to the energy fraction ν transferred to a pair. The solid and dashed curves represent the results of the calculations by formulas (15) and (25), respectively. The muon-energy values (in TeV) are indicated on the curves. All calculations were performed for standard rock and the threshold energy of 1 GeV.

not take into account the vanishing of the cross section at the points $\rho = \pm\rho_{max}$.

For the cross sections (15) and (25), the distribution with respect to the energy fraction ν transferred to the product pair is plotted in Fig. 5 for two energy values. Although the energy E does not enter into expression (25), the E dependence of $d\sigma/d\nu$ emerges upon integration with respect to ρ, since the domain of integration depends on the initial muon energy. A noticeable distinction between the curves is due primarily to an excessive contribution of asymmetric pairs ($\rho \sim 1$) to the cross section (25).

Expressions (15)–(22) describe the distribution of final particles with respect to ν and ρ. The distribution with respect to the energies E_+ and E_- of the particles forming a product pair is given by

$$\sigma(E, E_+, E_-)dE_+dE_- = \sigma(E, \nu, \rho)d\nu d\rho, \qquad (26)$$

whence it follows that

$$\sigma(E, E_+, E_-) = \frac{2}{E^2\nu}\sigma(E, \nu, \rho). \qquad (27)$$

In order to take into account the correction associated with the excitation of the nucleus involved, it is sufficient to substitute the quantity $(0.65A^{-0.27})^{(1-1/Z)}$ for the factor $0.65A^{-0.27}$ in the definition (20) of the function $U(E, \nu, \rho)$. This substitution approximately corresponds to taking into account the nuclear inelastic form factor in the form (8).

5. EQUILIBRIUM FLUXES OF TRIPLES AND COUPLES

As was indicated above, muon-pair production by a muon generates events in which three or two muons traverse simultaneously the detecting array used. We will estimate the frequency of such events for a vertical muon flux, disregarding fluctuations in energy lost by secondaries; that is, we assume that, at depths h' and h, the energies of final muons $E_{h'}$ and E_h are related by the equation

$$E_{h'} = \left(E_h + \frac{a}{b}\right)\exp[b(h-h')] - \frac{a}{b}, \qquad (28)$$

where a and b are coefficients determining the mean energy losses: $\langle dE/dx\rangle = -(a + bE)$. The integrated flux of triples and couples can then be represented in the form

$$J(>E_h, h) = \frac{N_A}{A}\int_0^h dh' \int_{E_{min}}^{\infty} dE N_\mu(E, h')\tilde{\sigma}(E, E_{h'}), \quad (29)$$

where N_A is Avogadro's number, $N_\mu(E, h')$ is the differential spectrum of single muons at a depth h', and $\tilde{\sigma}(E, E_{h'})$ is the muon-pair-production cross section integrated with respect to the final-particle energies. It should be recalled that, in the case of triples, the energy of each of the three particles must exceed $E_{h'}$; in the case of couples, the energy of the two final particles must exceed $E_{h'}$, while the energy of the third particle must be less than this. The lower limit of integration with respect to energy is $E_{min} = 3E_{h'}$ for the triples and $E_{min} = 2E_{h'} + \mu$ for couples.

We emphasize that, by couples, we mean here only those events where one of the three final muons is stopped in a medium. Analysis of events where one of

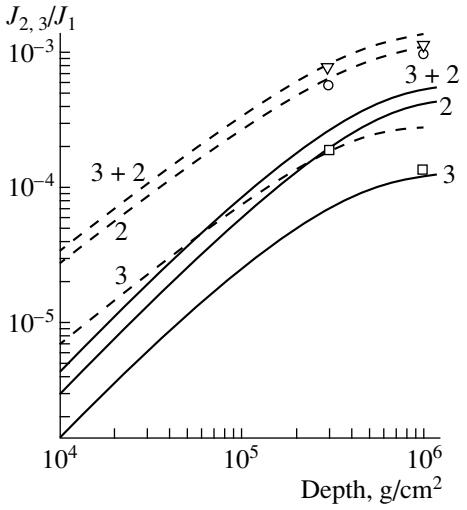

Fig. 6. Ratios of the integrated fluxes of (3) triples and (2) couples and of (3 + 2) their total flux to the integrated flux of single muons as functions of the depth of observation. The solid and dashed curves were calculated with the aid of the cross sections (15) and (25), respectively. Points represent data from [6].

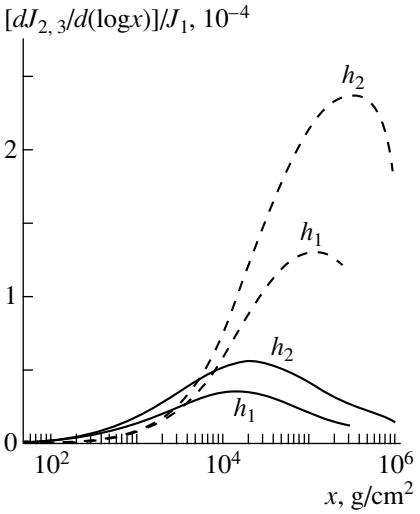

Fig. 7. Distributions of (solid curves) triples and (dashed curves) couples with respect to the distance x from the production vertex to the detection point in standard rock at the depths of $h_1 = 3 \times 10^5$ g/cm^2 and $h_2 = 10^6$ g/cm^2.

the particles misses the array requires calculating muon transport with allowance for the angular distribution of the product particles and their multiple scattering. Such calculations must be performed for a specific array and are beyond the scope of this article.

The differential spectrum of a vertical muon flux at the surface was specified in the form (see, for example, [17])

$$N_\mu(E, 0) = \frac{\text{const}}{E^\gamma}\left(\frac{0.71}{E + B_\pi} + \frac{0.29}{E + B_K}\right), \qquad (30)$$

where $\gamma = 2.7$, $B_\pi = 105$ GeV, and $B_K = 770$ GeV. The integrated spectrum of primary muons at a depth h was determined by the formula

$$J_\mu(>E_h, h) = J_\mu(>E_0, 0)\exp[-\gamma h(b_{\text{ef}} - b'_{\text{ef}})], \quad (31)$$

where

$$E_h = \left(E_0 + \frac{a}{b'_{\text{ef}}}\right)\exp(-b'_{\text{ef}}h) - \frac{a}{b'_{\text{ef}}}. \qquad (32)$$

The parameters b_{ef}, $b'_{\text{ef}} \neq b$ take into account the effect of fluctuations of energy losses on the spectrum of primary muons at large depths (for details, see [18]) Our numerical calculations by formula (29) were performed at the following parameter values: $a = 2.2 \times 10^{-3}$ GeV cm^2/g, $b = 4.5 \times 10^{-6}$ cm^2/g, $b_{\text{ef}} = 3.8 \times 10^{-6}$ cm^2/g, and $b'_{\text{ef}} = b_{\text{ef}} - (b - b_{\text{ef}})/(\gamma - 1)$.

Figure 6 displays the ratios of the integrated fluxes of triples and couples and their sum to the integrated flux of single muons as functions of the depth of observation according to the calculations with the aid of the cross sections (15) and (25). The calculations were performed for standard rock, with the threshold for muon detection being set to 1 GeV. As can be seen from the figure, the calculation with (25) overestimates the fluxes of triples and couples by a factor of about 3. Figure 6 also displays the results obtained in [6] at depths of 3000 and 10000 mwe. The calculations from [6] were performed by using the cross section (25); therefore, the computed points should fall on the dashed curves. For a depth of 3000 mwe, the results from [6] agree with ours, provided that the cross section (25) is used, while, for a depth of 10000 mwe, the values from [6] appear to be noticeably smaller, especially for the flux of triples. The discrepancy is partly due to the fact that only one (first) interaction producing a muon triple was taken into account in [6]. As a result, a sizable part of muons (10–15% at 10000 mwe) ceased to produce triples prior to achieving the observation level. Another reason for the discrepancy may be associated with low statistics accumulated in simulating triples by the Monte Carlo method (only 53 events were obtained in [6] at a depth of 10000 mwe).

Muon pairs are formed within all layers of substance above the array. It is interesting to determine the contributions from different layers to the total flux of triples and couples at a given depth. For this, it is necessary to perform integration in (29) only with respect to the primary-muon energy. The distribution of triples and couples with respect to the distance $x = h - h'$ from the production vertex to the detection point is plotted in Fig. 7 for two depths ($x = 0$ corresponds to the detection point). As can be seen from this figure, the relative contribution of events featuring pair production near the detection point appears to be much greater for triples than for couples. In the case of triples, “close” events

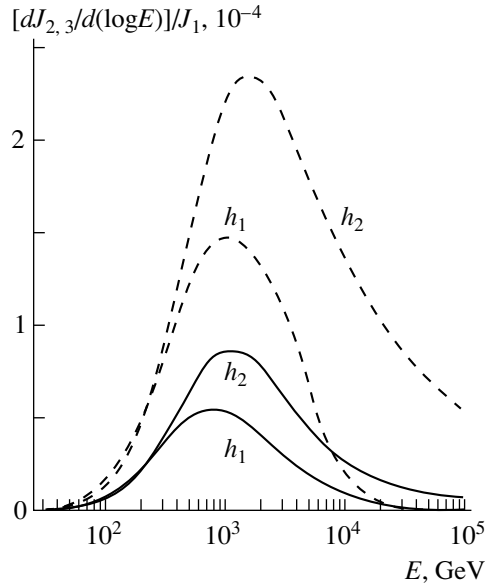

Fig. 8. Distribution of (solid curves) triples and (dashed curves) couples with respect to the parent-particle energy in standard rock at the depths of $h_1 = 3 \times 10^5$ g/cm^2 and $h_2 = 10^6$ g/cm^2.

contribute considerably to the integrated flux. From Fig. 7, it is also obvious that, if muon-pair production occurs at distances smaller than 5×10^3 g/cm^2, such an event will be detected as a triple with a high probability.

Let us denote by x_* a characteristic distance such that, for $x \ll x_*$, the spatial divergence of the particles forming a product pair is determined by the initial opening angle and that, for $x \gg x_*$, it is determined by multiple scattering. On the basis of the results presented in Section 3, this characteristic distance can be estimated at $x_* \approx 5000$ g/cm^2. As can be seen from Fig. 7, approximately 30% of triples are produced at distances from the detection point that do not exceed x_*; therefore, the inclusion of the initial transverse momenta is necessary in analyzing the spatial distribution of particles forming triples.

The parent-particle-energy distribution of events contributing to the fluxes of triples and couples is displayed in Fig. 8 for two depths of observation. These results were obtained from expression (29) by performing integration only with respect to the depth h'. As follows from this figure, the characteristic energies of primary muons making the main contribution to the fluxes of triples and couples at large depths appear to be on the order of 10^3 GeV.

6. CONCLUSION

The above analysis of muon-pair production by a muon has revealed that the effect of the nuclear form factor on the cross section for the process is significant at all muon energies; at the same time, the atomic form factor becomes operative only in the energy region $E \gg 4Z^{-1/3}$ TeV (Fig. 2). Formula (1.51) from [4] [it is equivalent to our expression (25)], which is usually used to estimate the reaction cross section, corresponds to the case of full screening and takes no account of the nuclear form factor. This formula significantly overestimates the cross section at energies E in the region around 1 TeV, which makes the main contribution to the equilibrium fluxes of muon triples and couples in rock.

The approximate formula (15) derived here describes the differential cross section for the direct production of muon pairs by a muon with allowance for the atomic and the nuclear elastic form factor and makes it possible to calculate the total cross section to within 2 to 3%. We have also obtained the simple approximate formulas (10) and (11) describing the transverse-momentum distribution of particles. For muon groups produced at distances $x < 5000$ g/cm^2 from the array, the initial divergence of particles affects the distances between the tracks.

The previous estimates of the observed fluxes of triples and couples obtained on the basis of the cross section (25) must be revised. Relevant quantitative calculations must be performed for a particular experimental array with allowance for the angular and energy distributions of product muons and for their multiple scattering.

ACKNOWLEDGMENTS

This work was supported in part by the Russian Foundation for Basic Research (project no. 97-02-17450).

REFERENCES

1. S. R. Kel'ner, Yu. D. Kotov, and V. M. Logunov, Acta Phys. Acad. Sci. Hung. **29**, Suppl. 4, 299 (1970).
2. S. R. Kel'ner, Yu. D. Kotov, and V. M. Logunov, Yad. Fiz. **21**, 763 (1975) [Sov. J. Nucl. Phys. **21**, 394 (1975)].
3. S. R. Kel'ner, Yad. Fiz. **5**, 1092 (1967) [Sov. J. Nucl. Phys. **5**, 778 (1967)].
4. É. V. Bugaev, Yu. D. Kotov, and I. L. Rozental', *Cosmic Muons and Neutrinos* (Atomizdat, Moscow, 1970).
5. V. A. Kudryavtsev and O. G. Ryazhskaya, in *Proceedings of the 25th International Cosmic Ray Conference, Durban, 1997*, Vol. 6, p. 405.
6. V. A. Kudryavtsev and O. G. Ryazhskaya, Nuovo Cimento C **21**, 171 (1998).
7. G. Battistoni and E. Scapparone, Nucl. Phys. B (Proc. Suppl.) **75A**, 394 (1999).
8. A. A. Petrukhin and V. V. Shestakov, Can. J. Phys. **46**, S377 (1968).
9. V. B. Berestetskiĭ, E. M. Lifshitz, and L. P. Pitaevskiĭ, *Quantum Electrodynamics* (Nauka, Moscow, 1980; Pergamon, Oxford, 1982).
10. G. Racah, Nuovo Cimento **14**, 93 (1937).

11. A. I. Nikishov and N. V. Pichkurov, Tr. Fiz. Inst. Akad. Nauk SSSR **168**, 200 (1986).
12. S. R. Kel'ner, Yad. Fiz. **61**, 511 (1998) [Phys. At. Nucl. **61**, 448 (1998)].
13. L. R. B. Elton, *Nuclear Sizes* (Oxford Univ. Press, Oxford, 1961; Inostrannaya Literatura, Moscow, 1962).
14. Yu. M. Andreev, L. B. Bezrukov, and É. V. Bugaev, Yad. Fiz. **57**, 2146 (1994) [Phys. At. Nucl. **57**, 2066 (1994)].
15. R. P. Kokoulin and A. A. Petrukhin, in *Proceedings of the 12th International Cosmic Ray Conference, Hobart, 1971*, Vol. 6, p. 2436.
16. S. R. Kelner, R. P. Kokoulin, and A. A. Petrukhin, Preprint No. 024-95, MEPhI (Moscow Engineering Physics Institute, 1995).
17. T. K. Gaisser, *Cosmic Rays and Particle Physics* (Cambridge Univ. Press, Cambridge, 1990).
18. R. P. Kokoulin, Nucl. Phys. B (Proc. Suppl.) **70**, 475 (1999).

Translated by A. Isaakyan

Physics of Atomic Nuclei, Vol. 63, No. 9, 2000, pp. 1612–1622. Translated from Yadernaya Fizika, Vol. 63, No. 9, 2000, pp. 1699–1709.

ELEMENTARY PARTICLES AND FIELDS
Theory

Determination of the ππ Scattering Lengths from Data on $\pi N \longrightarrow \pi\pi N$ Reactions by the Method of Roy Equations

V. N. Mayorov, O. O. Patarakin, and V. N. Tikhonov

Russian Research Centre Kurchatov Institute, pl. Kurchatova 1, Moscow, 123182 Russia

Received June 16, 1999; in final form, August 31, 1999

Abstract—Fitted phase-shift curves from the threshold to the dipion mass, which is equal to 1 GeV, are constructed on the basis of all available experimental values of the *S*- and *P*-wave phase shifts for five charged channels of pion–pion scattering. The resulting phase-shift curves are introduced in the Roy equations in order to obtain the subtraction constants $\lambda_l^I(s)$. By using these subtraction-constant values as functions of the dipion mass, the S_0- and S_2-wave pion–pion scattering lengths are found to be $a_0^0 = (0.240 \pm 0.023)m_\pi^{-1}$ and $a_0^2 = (-0.034 \pm 0.013)m_\pi^{-1}$. A strong correlation of the *S*-wave scattering lengths is demonstrated. © *2000 MAIK "Nauka/Interperiodica".*

1. INTRODUCTION

Although pion–pion interaction has been studied for more than 40 years, investigations into these realms are being actively developed even nowadays. That it is of paramount importance to know the parameters of pion–pion interaction and that it is difficult to deduce these parameters reliably continue furnishing a sufficient motivation for this. Presently, a special role is played by the investigation of the near-threshold parameters of pion–pion interaction—especially of scattering lengths. This is associated with evolving QCD models in the region of low energies and models featuring the breakdown of chiral symmetry. By way of example, we indicate that models based on chiral perturbation theory [1–3] and on generalized chiral perturbation theory [4–7] have been actively developed at present. These models predict light-quark masses of about 1 GeV in the first version and small values for these masses in the second version, the value of the quark condensate, and the pion–pion scattering lengths ($a_0^0 = 0.21$ in the first version and $a_0^0 = 0.27$ in the second version[1)]). Thus, a reliable determination of the pion–pion scattering lengths would make it possible to estimate the amount of chiral-symmetry violation and to choose thereby an adequate version of theory. The current accuracy of the scattering lengths for pion–pion interaction is rather poor. The main reason for this is that it is impossible to obtain direct information about pion–pion interaction—only indirect methods can be used. Despite many attempts at harnessing various processes to extract required information, investigation of processes like $\pi N \longrightarrow \pi\pi N$ (or $\pi N \longrightarrow \pi\pi\Delta$) that is followed by an extrapolation of the parameters of pion–pion scattering to the pion pole remains the source of the most important data of relevance. In implementing this program, it is assumed that experimentalists are able to isolate the one-pion exchange (OPE) diagram.

Of course, the procedure being discussed depends, to a considerable extent, on the presence of other diagrams and on the methods for their inclusion. It is usually assumed (for an overview, see, for example, [8, 9]) that, at an incident-pion momentum of a few GeV/*c* units, we can hope for the dominance of the OPE diagram and, accordingly, for a reliable determination of the parameters of pion–pion scattering. Although data on the *S*- and *P*-wave phase shifts from different experiments show considerable scatter, their general behavior is thought to be well established.

The use of the general principles of unitarity, analyticity, and crossing symmetry is one of the seminal approaches to studying pion–pion interaction. The integral equations derived with the aid of dispersion relations and known as the Roy equations [10, 11] proved to be very useful on this path. These equations determine the real parts of the partial-wave amplitudes in the region $-4 < s < 60$, which includes the unphysical region $-4 < s < 4$, in terms of relevant quantities in the physical region $4 < s < \infty$.[2)] Once the Roy equations had been derived, it became possible to compensate for the absence of reliable experimental data in the region of low energies by constructing an analytic continuation that satisfies the Roy equations and the unitarity condi-

[1)]The *S*-wave scattering lengths a_0^0 and a_0^2 are given in m_π^{-1} units, while the *P*-wave scattering lengths a_1^1 are given in m_π^{-3} units.

[2)]Here and below, *s* is the Mandelstam variable defined as $s = m_{\pi\pi}^2/m_\pi^2$.

tion. This computational method, which relies both on theoretical principles and on relevant experimental information, was used, for example, in [12, 13] to determine the *S*- and *P*-wave scattering lengths.

When calculations of this type are based on a single specific set of experimental data, it is necessary to invoke, as a rule, iterative processes, but this impairs the reliability and accuracy of results. An attempt was made in [14] to employ the entire body of data on pion–pion scattering phases as inputs for the calculations on the basis of the Roy equations. At present, vast arrays of experimental information have been accumulated over the entire dipion-mass range of our interest. This makes it possible to construct solutions to the set of Roy equations without recourse to iterative processes. Thereby, questions concerning the convergence of such solutions are lifted, and there arises the possibility of seeking solutions more consistently and more correctly without harnessing ad hoc assumptions.

In the present study, we invoke all available experimental values of the *S*- and *P*-wave pion–pion phase shifts as obtained from an analysis of five charged channels in the region from the threshold to 1 GeV. The exposition is organized as follows. In Section 2, we perform fitting for each phase shift and obtain a smooth curve adequately describing experimental data. The resulting phase-shift curves are introduced in the Roy equations in order to determine the subtraction constants $\lambda_l^I(s)$. It is shown that these subtraction constants are described, as they must in accordance with the Roy equations, by a linear function of the dipion mass; that is, the present procedure for utilizing the Roy equations is self-consistent. Sections 3 and 4 are devoted to describing this procedure and the computational methods used. In Section 5, the dependences $\lambda_l^I(s)$ derived within the proposed procedure are used to determine the *S*-wave pion–pion scattering lengths for which the partial-wave amplitudes satisfy the requirements of analiticity, unitarity, and crossing symmetry and fit well experimental data in terms of the χ^2 criterion. In Section 6, we describe a method for deducing the *P*-wave scattering length a_1^1. In Section 7, we present basic conclusions and discuss our results.

The results of the calculations for the features of pion–pion interaction (such as scattering cross sections and angular distributions), which are important for practical applications, will be presented in a separate publication.

2. FITTING THE *S*- AND *P*-WAVE PHASE SHIFTS

This study, as well as that reported in [14], is based on the assumption that experimentalists extract correctly the values of the pion–pion phase shifts from data on $\pi N \longrightarrow \pi\pi N$ and $\pi N \longrightarrow \pi\pi\Delta$ processes. In order to apply the Roy equations, it is necessary to have at our disposal smoothed curves for the *S*- and *P*-wave phase shifts in the region from the threshold to 1 GeV. Such smoothed curves are obtained here on the basis of the experimental values of the phase shifts in five charged channels of pion–pion scattering. The basic data set used in [14] is supplemented here with experimental data from [15], which are characterized by vast statistics. Of four possible versions reported in [15], we use here only the values from the down-flat set. In the region being studied, the down-steep set coincides with the down-flat solution, whereas the up-flat and up-steep versions cannot be described by a smooth phase-shift curve and are strongly different from the other data used.

2.1. S_0-Wave Phase Shift

Data from [15–20] enabled us to obtain a smoothed curve for the phase shift $\delta_0^0(s)$ over the entire region being considered. In order to arrive at this description, we approximated the phase shift by a polynomial in odd powers of the pion momentum q; that is, we relied on the expansion usually used near the threshold:

$$\delta_0^0(s) = \frac{2}{\sqrt{s}}(a_1 q + a_2 q^3 + a_3 q^5 + a_4 q^7). \qquad (1)$$

The coefficients a_i are treated as adjustable parameters, their optimal values being

$$a_1 = 0.236 \pm 0.037, \quad a_2 = 0.323 \pm 0.027,$$
$$a_3 = -0.033 \pm 0.006, \quad a_4 = 0.0018 \pm 0.0004.$$

A further increase in the number of terms in the series does not improve the accuracy of description in terms of the χ^2 criterion, nor does this lead to significant changes in the values of the coefficients a_i. Thus, we conclude that the proposed polynomial description is stable. The experimental values of the phase shift $\delta_0^0(s)$ are presented in Fig. 1, along with the fitting curve. This description corresponds to the value of $\chi^2 = 127$ for 98 degrees of freedom. This demonstrates that the present fit to the data used is of reasonably good quality. The question of whether there are (or there are no) possible scalar resonances (see, for example, [15, 21, 22]) has not been considered in the present approach.

2.2. S_2-Wave Phase Shift

It should be emphasized that, until recently, there were no experimental values of the phase shift $\delta_0^2(s)$ near the threshold. Because of this, it was necessary to construct a fitting curve by relying only on the data for the dipion mass in excess of 500 MeV. At the same time, it was shown in [23] that it is the near-threshold behavior that is crucial for finding solutions to the Roy equations; therefore, the absence of reference points

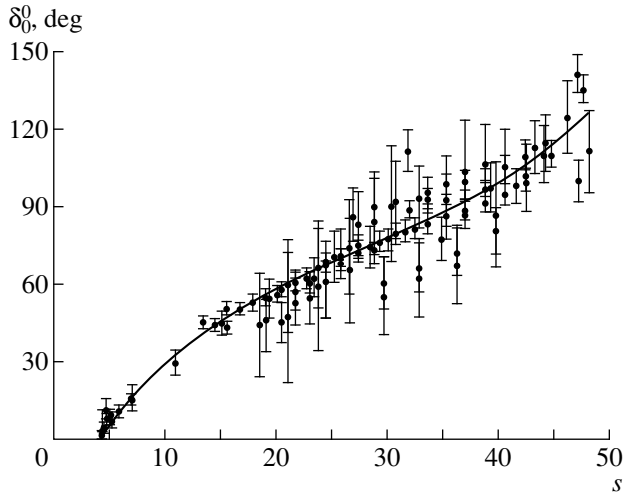

Fig. 1. S_0-wave phase shift. The solid curve represents the result of fitting in terms of expression (1).

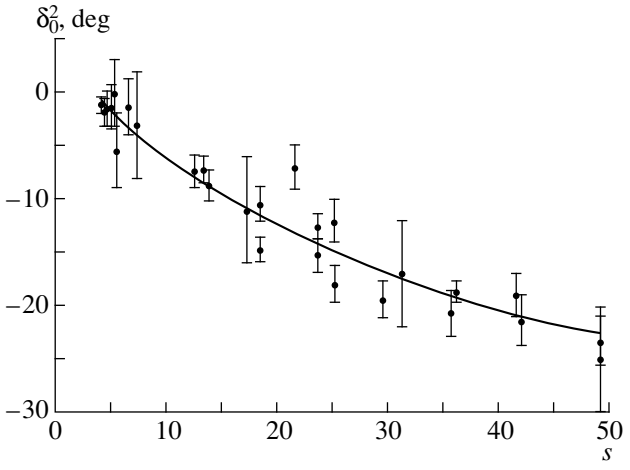

Fig. 2. S_2-wave phase shift. The solid curve represents the result of fitting in terms of expression (2).

near the threshold impairs drastically the accuracy of the results obtained in this way.

Precise values of the cross sections $\sigma_{\pi^+\pi^-}(s)$ near the threshold were obtained in [24]. This permitted estimating the phase shift $\delta_0^2(s)$ under the assumption that the phase shift $\delta_0^0(s)$ is known. By using the values of $\delta_0^0(s)$ from [14], we have calculated the phase shift $\delta_0^2(s)$ and the error in it, $\sigma(\delta_0^2)$, on the basis of the cross section $\sigma_{\pi^+\pi^-}(s)$. The resulting values are displayed in the table.

Thus, reference experimental data near the threshold have appeared, which made it possible to obtain a more reliable description of the S_2-wave phase shift without ad hoc assumptions. It should be noted that the $\delta_0^0(s)$ values that have been taken for calculating $\delta_0^2(s)$ comply well with the values presented in [24]. The $\delta_0^2(s)$ values computed in the near-threshold region were added to the basic set of data from [18–20, 23–31].

Table

s	E, MeV	δ_0^2, deg	$\sigma(\delta_0^2)$, deg
4.15	284.3	−1.14	0.71
4.45	294.3	−1.89	1.00
4.75	304.2	−1.50	1.13
5.05	313.7	−1.37	1.25
5.35	322.8	0.025	2.34
5.65	331.8	−5.38	2.46

At this step, the data were also fitted in terms of the threshold expansion

$$\delta_0^2(s) = \frac{2}{\sqrt{s}}(a_1 q + a_2 q^3 + a_3 q^5 + a_4 q^7). \qquad (2)$$

The coefficients in (2) were again treated as adjustable parameters, their optimal values being

$$a_1 = -0.058 \pm 0.031, \quad a_2 = -0.053 \pm 0.019,$$

$$a_3 = 0.022 \pm 0.035, \quad a_4 = -0.00002 \pm 0.00018.$$

The experimental data used and the fitting curve that we obtained are displayed in Fig. 2. The resulting description corresponds to the value of $\chi^2 = 34$ for 24 degrees of freedom.

Data from the electron experiment reported in [26] were processed separately, because it was shown earlier (see [14]) that the results obtained upon taking those data into account differ considerably from the results of the calculations disregarding them. For the data of the electron experiment, we obtained a description characterized by the value of $\chi^2 = 9$ for four degrees of freedom. Thus, we can see that the smoothing procedure is correct in either case, although the values of the coefficients a_i exhibit a considerable scatter between the two cases. The results obtained by processing the electron experiment are presented in Fig. 3. In the following, we will revisit the two possible descriptions of the S_2-wave phase shift.

2.3. P Wave

In the present study, we assume that, in the energy range being considered, the P wave is determined by the ρ resonance almost completely. In order to smooth the dependence $\delta_1^1(s)$, it is therefore natural to employ the relation

$$\delta_1^1(s) = \arctan\left[\frac{m_\rho \Gamma_\rho}{m_\rho^2 - E^2}\left(\frac{q}{q_\rho}\right)^3\right], \qquad (3)$$

where m_ρ and Γ_ρ are, respectively, the mass and width of the ρ resonance; $q = \frac{1}{2}\sqrt{E^2 - 4m_\pi^2}$ is the c.m. pion momentum; $q_\rho = \frac{1}{2}\sqrt{m_\rho^2 - 4m_\pi^2}$; and E is the total energy in the dipion c.m. frame. Here, we treat m_ρ and Γ_ρ as adjustable parameters. Relation (3) represents a particular case of a more general, so-called relativistic, relation that is obtained upon introducing the Durr–Pilkuhn form factor [31]:

$$\delta_1^1(s) = \arctan\left[\frac{m_\rho\Gamma_\rho}{m_\rho^2 - E^2}\left(\frac{q}{q_\rho}\right)^3\left(\frac{1 + q^2A}{1 + q_\rho^2A}\right)\right]. \qquad (4)$$

Here, $A = R^2$, where R is a parameter that characterizes the dimensions of the spatial interaction region. It is obvious that, according to the physical meaning of the parameter R, it is nonnegative. At $A = 0$, expression (4) reduces to expression (3). It should be noted that the fitting of the P wave involves some serious problems. First, the fitting of the experimental dependence $\delta_1^1(s)$ in terms of either (3) or (4) leads to an overly great value of χ^2. Second, nonpositive values of the parameter A were obtained upon fitting in terms of (4)—that is, R^2 takes negative values.

The experimental values of the phase shift $\delta_1^1(s)$ that are used here are shown in Fig. 4, along with the optimal dependences chosen on the basis of (3) and (4). It should be noted that, in either case, we are dealing with large values of χ^2, although the description of the dependence $\delta_1^1(s)$ visually seems correct, especially in the case of expression (4). Let us consider this situation in greater detail.

We obtain the value of $\chi^2 = 1117$ for 79 degrees of freedom in the case of fitting in terms of (3) and $\chi^2 = 376$ for 78 degrees of freedom in the case of fitting in terms of (4). Thus, the introduction of the additional parameter A reduces the value of χ^2 by 741—that is, nearly by a factor of 3. This is direct evidence for the significance of this parameter. At the same time, the value of $\chi^2/N_s \approx 5$ (N_s is the number of degrees of freedom) is still overly high, although the dependence given by (4) describes smoothly experimental points (see Fig. 4). We assume that this situation arises as the result of the concerted effect of several factors. The right-hand sides of equations (3) and (4) feature a singularity at $E = m_\rho$; since the fitting function changes very fast in the vicinity of this point, the behavior of the phase shift in this region is very sensitive to errors in determining the energy E. That such errors do indeed exist is proven by means of a simple analysis. We performed fitting on the basis of expression (4) and calculated χ^2 for individual groups of experimental data in overall statistics. As a result, the sum of χ_i^2 taken over all groups turned out to be $\sum\chi_i^2 = 222$. In fitting the entire array of data borrowed from different experiments and treated as a whole, we obtained $\chi^2 = 376$ (see above)—that is, χ^2 is nearly doubled in relation to the case of processing separately individual groups of data. This confirms the conjecture that, between the results coming from different experiments, there is some methodological bias, which is most likely due to errors in determining the energy E. This in turn affects the χ^2 value that results from fitting. In other words, this implies that, the authors of some studies underestimated errors in phase shifts because of the disregard of methodological uncertainties in determining the energy E.

Thus, we deem that the problem of regularly smoothing data on the P wave can be solved quite reliably on the basis of expression (4). At the same time, it should be borne in mind that, in describing the P-wave phase shift in terms of the relativistic formula (4),

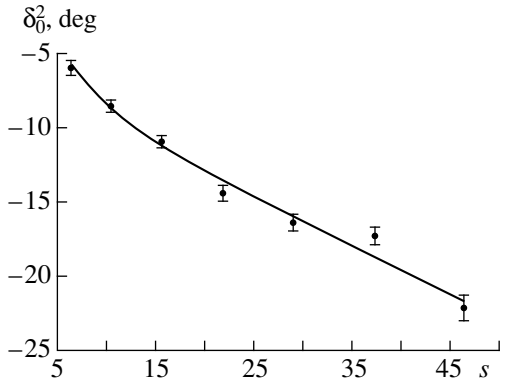

Fig. 3. S_2-wave phase shift. Data from the electron experiment are presented here. The solid curve represents the result of fitting in terms of expression (2).

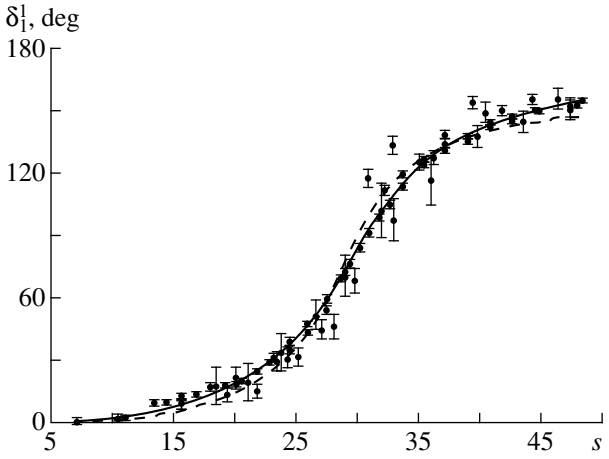

Fig. 4. P-wave phase shift. The dashed and the solid curve represent the results of fitting in terms of expressions (3) and (4), respectively.

which involves the Durr–Pilkuhn form factor, the parameter characterizing the dimensions of the interaction region proves to be negative:

$$R^2 = -2.81 \pm 0.06 \text{ GeV}^{-2}.$$

We were unable to find any explanation for this fact. At the same time, the dependence in (4) serves our present purposes quite well, since we now address the problem of regularly smoothing the experimental dependence $\delta_1^1(s)$ in order to use it subsequently in integrating the Roy equations. Nonetheless, the problem of negative R^2 is of considerable interest in itself, and it calls for a further study.

The optimal values of the remaining parameters m_ρ and Γ_ρ as obtained from a fit in terms of expression (4) are

$$m_\rho = 770.5 \pm 0.6 \text{ MeV},$$
$$\Gamma_\rho = 154.7 \pm 1.4 \text{ MeV},$$

which are very close to the world-average values [21]

$$m_\rho = 770.0 \pm 0.8 \text{ MeV},$$
$$\Gamma_\rho = 150.7 \pm 1.1 \text{ MeV}.$$

3. ROY EQUATIONS

The Roy equations represent a set of nonlinear integral equations relating the real parts of the partial-wave amplitudes to integrals over the physical region that involve combinations of the imaginary parts of the partial-wave amplitudes. In the derivation of these equations, use is made of the dispersion relations with a double subtraction at fixed t[3)] and of the properties of analyticity and crossing symmetry of the scattering amplitude.

Here, we restrict our consideration to *S* and *P* waves (so-called *S–P* analysis). For the case of charged pions, the Roy equations are given by

$$\operatorname{Re} f_l^I(s) = \lambda_l^I(s) + \frac{1}{\pi}\int_4^{51} \Psi_l^I(x,s)\,dx + \varphi_l^I(s), \qquad (5)$$

where $\Psi_l^I(x,s) = \operatorname{Im} f_0^0(x)\,{}_1K_l^I(x,s) + \operatorname{Im} f_0^2(x)\,{}_2K_l^I(x,s) + \operatorname{Im} f_0^2(x)\,{}_3K_l^I(x,s)$.

Explicit expressions for the kernels ${}_jK_l^I(x,s)$ of the integral equations (5) are presented in the Appendix. The corrections $\varphi_l^I(s)$ standing for the estimated contributions from higher waves ($l \geq 2$) and from the region of large masses were borrowed from [12] in the form

$$\varphi_0^0 = (13 \pm 5) \times 10^{-5}(s^2 - 16),$$
$$\varphi_0^2 = (13 \pm 6) \times 10^{-5} s(s-4), \qquad (6)$$
$$\varphi_1^1 = (3.0 \pm 1.5) \times 10^{-5} s(s-4).$$

In accordance with the theory being considered, the subtraction constants $\lambda_l^I(s)$ are given by

$$\lambda_0^0(s) = a_0^0 + \frac{s-4}{12}(2a_0^0 - 5a_0^2), \qquad (7)$$

$$\lambda_0^2(s) = a_0^2 - \frac{s-4}{24}(2a_0^0 - 5a_0^2), \qquad (8)$$

$$\lambda_1^1(s) = \frac{s-4}{72}(2a_0^0 - 5a_0^2). \qquad (9)$$

The real and the imaginary part of the $\pi\pi$-scattering amplitude are expressed in terms of the phase shift in a standard way by taking into account the unitarity condition:

$$\operatorname{Re} f_l^I(s) = \frac{1}{2}\sqrt{\frac{s}{s-4}}\sin\delta_l^I(s),$$
$$\operatorname{Im} f_l^I(s) = \frac{1}{2}\sqrt{\frac{s}{s-4}}(1 - \cos\delta_l^I(s)). \qquad (10)$$

4. DETERMINATION OF THE SUBTRACTION CONSTANTS

Our objective is to solve equations (5) for the subtraction constants—that is, to obtain the experimental dependences $\lambda_l^I(s)$—and, after that, to estimate, with the aid of equations (7)–(9), the scattering lengths a_0^0 and a_0^2. It is natural that, on the basis of the dependence $\lambda_1^1(s)$, we can estimate only the parameter $(2a_0^0 - 5a_0^2)$, which characterizes the so-called universal curve. In order to integrate the singular equations (5), it is necessary to smooth, for each set of the phase-shift curves, the experimental dependences with the aid of some analytic function by using the χ^2 criterion of consistency.

Solving the Roy equations for the subtraction constants $\lambda_l^I(s)$ reduces to integrating these equations for each set of $\delta_l^I(s)$. The integration was performed to precision higher than 1%. The values of $\operatorname{Re} f_l^I(s_i)$ were taken at each experimental point s_i where the phase shift $\delta_l^I(s_i)$ was measured. By solving the Roy equations for each value of s_i, we obtained, for the first time,

[3)] The quantity t is defined as the 4-momentum transfer in the $\pi\pi$ c.m. frame.

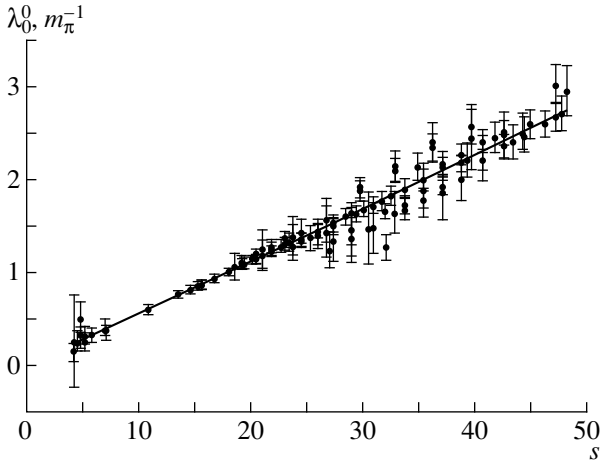

Fig. 5. Subtraction constant $\lambda_0^0(s)$ as obtained from the Roy equations (5). The straight line represents the result of fitting in terms of expression (7).

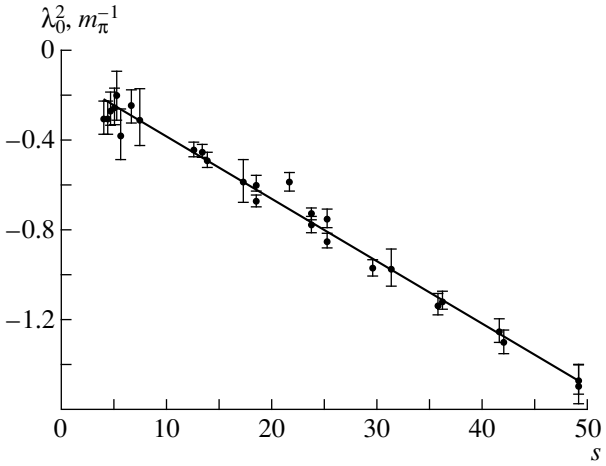

Fig. 6. Subtraction constant $\lambda_0^2(s)$ as obtained from the Roy equations (5). The straight line represents the result of fitting in terms of expression (8).

the values of the subtraction constants $\lambda_l^I(s_i)$ from the experimental data on the phase shifts for pion–pion scattering. These values, together with the theoretical approximations described by formulas (7)–(9), are depicted in Figs. 5–8. It should be noted that the error bars presented in the figures are purely statistical—that is, they are eventually determined by the errors in the measured phase shifts $\delta_l^I(s)$. For the variance D_λ of the quantity $\lambda_l^I(s)$, we use the sum of the variances,

$$D_\lambda = D_{\mathrm{Re}} + D_I. \tag{11}$$

Here, D_{Re} is determined by the error in the quantity $\mathrm{Re}\, f_l^I(s_i)$, while D_I is the variance of the integral $I = \frac{1}{\pi}\int_4^{51} \psi_l^I(x, s)dx$ in formula (5) due both to the errors in determining the smoothing parameters a_i in formulas (1), (2), and (4) and to the correlation between these parameters. The explicit expression for this variance is

$$D_I = \sum_i \sum_k K_{ij}\left(\frac{\partial I}{\partial a_i}\right)\left(\frac{\partial I}{\partial a_j}\right), \tag{12}$$

where K_{ij} are the correlation moments of the quantities a_i and a_j. It should be emphasized that the expression for the variance D_λ does not contain the theoretical errors $\Delta\varphi_l^I(s_i)$ in the quantities $\varphi_l^I(s_i)$, since they are not, generally speaking, statistical: they change the behavior of the function simultaneously for all s [see equation (6)]. Because of this, the theoretical error in $\varphi_l^I(s)$ behaves as a random function with respect to $\Delta\varphi_l^I(s_i)$. Therefore, a dedicated consideration is required for taking into account the effect of the theoretical error $\Delta\varphi_l^I(s_i)$ on the calculation of uncertainties in the scattering lengths a_0^0 and a_0^2. It will be conducted below.

5. EXTRACTING THE VALUES OF a_0^0 AND a_0^2 FROM THE DEPENDENCE $\lambda_l^I(s)$

We have calculated the scattering lengths a_0^0 and a_0^2 and the correlation factor r separately for each dependence $\lambda_l^I(s_i)$ by fitting this dependence with the aid of linear functions by formulas (7)–(9). Let us consider each dependence $\lambda_l^I(s)$ separately.

(a) $\lambda_0^0(s)$. By fitting the constructed dependence $\lambda_0^0(s)$ (see Fig. 5) in terms of expression (7), we obtained

$$\begin{aligned} a_0^0 &= 0.238 \pm 0.016, \quad r = 0.994, \\ a_0^2 &= -0.039 \pm 0.009, \quad N_s = 100, \quad \chi^2 = 90. \end{aligned} \tag{13}$$

These values, together with their errors and the correlation factor, determine the statistical ellipse of scatter (due to the statistical uncertainties in the experiment) for the parameters a_0^0 and a_0^2. This result is depicted in Fig. 9. Further, we consider the effect of the theoretical error $\Delta\varphi_0^0$ on the uncertainties in determining a_0^0 and a_0^2. In solving the Roy equations, the substitution of $\Delta\varphi_0^0$ for the theoretical function $\varphi_0^0(s)$ in (6) modifies the subtraction constants $\lambda_0^0(s)$ and, accordingly, the

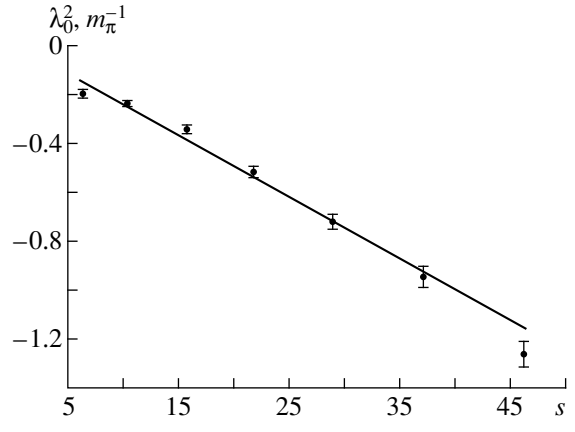

Fig. 7. Subtraction constant $\lambda_0^2(s)$ as obtained from the Roy equations (5) according to data from the electron experiment. The straight line represents the result of fitting in terms of expression (8).

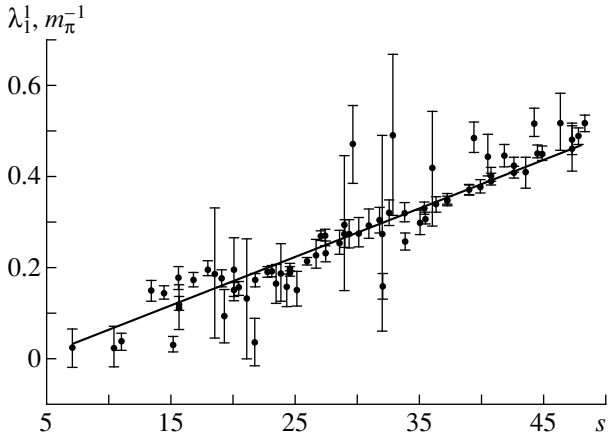

Fig. 8. Subtraction constant $\lambda_1^1(s)$ as obtained from the Roy equations (5). The straight line represents the result of fitting in terms of expression (9).

sought scattering lengths a_0^0 and a_0^2. Thus, the theoretical error translates into the errors in the values of a_0^0 and a_0^2. The errors determine the degenerate ellipse of scatter with the parameters

$$a_0^0 = 0.238 \pm 0.016, \quad r = 1, \qquad a_0^2 = -0.039 \pm 0.012. \tag{14}$$

It is also depicted in Fig. 9. Since the statistical experimental errors and the theoretical error $\Delta\varphi_0^0$ do not depend on each other, the resulting ellipse of scatter due to both the experimental errors and the theoretical error $\Delta\varphi_0^0$ (that is, to the concerted effect of these two factors) is formed by combining the above two ellipses of scatter. For the set of $\lambda_0^0(s)$, we eventually obtain

$$a_0^0 = 0.238 \pm 0.023, \quad r = 0.987, \qquad a_0^2 = -0.039 \pm 0.015. \tag{15}$$

The resulting ellipse of scatter is displayed in Fig. 9.

(b) $\lambda_0^2(s)$. Following the same line of reasoning and fitting the dependence $\lambda_0^2(s)$ (Fig. 6) on the basis of expression (8), we obtain the parameters of the statistical ellipse of scatter. Explicitly, the results are

$$a_0^0 = 0.285 \pm 0.051, \quad r = 0.995, \qquad a_0^2 = -0.020 \pm 0.017, \quad N_s = 25, \quad \chi^2 = 25. \tag{16}$$

The theoretical uncertainty $\Delta\varphi_0^2$ forms a degenerate ellipse of scatter with the following parameter values:

$$a_0^0 = 0.285 \pm 0.083, \quad r = 1, \qquad a_0^2 = -0.020 \pm 0.020. \tag{17}$$

Combining the two ellipses, we eventually obtain the following values for the set $\lambda_0^2(s)$:

$$a_0^0 = 0.285 \pm 0.097, \quad r = 0.986, \qquad a_0^2 = -0.020 \pm 0.026. \tag{18}$$

All these results are presented in Fig. 9.

(c) $\lambda_0^0(s) + \lambda_0^2(s)$. For the scattering lengths a_0^0 and a_0^2, we have obtained the ellipses of scatter on the basis of each set $\lambda_0^0(s)$ and $\lambda_0^2(s)$ individually (these sets were in turn deduced from solutions to the Roy equations). Since these results were derived independently, it is legitimate to perform averaging in order to determine the weighted means of a_0^0 and a_0^2 for the sets $\lambda_0^0(s)$ and $\lambda_0^2(s)$ with allowance for statistical weights. On the basis of the entire array of $\lambda_0^0(s_i)$ and $\lambda_0^2(s_i)$ values, we eventually obtain the following parameter values:

$$a_0^0 = 0.240 \pm 0.023, \quad r = 0.945, \qquad a_0^2 = -0.034 \pm 0.013, \qquad (2a_0^0 - 5a_0^2) = 0.650 \pm 0.022. \tag{19}$$

The resulting ellipse of scatter and the corridor for the universal curve are displayed in Fig. 10.

(d) $\lambda_0^2(s)$, electron experiment. As was indicated above, data on the phase shifts $\delta_0^2(s)$ from the electron experiment [26] were processed here separately, because it was indicated previously that the scattering lengths a_0^0 and a_0^2 as deduced from data of this electron experiment differ considerably from the results obtained by processing the rest of the data array for the phase shifts $\delta_0^2(s)$. The subtraction constants $\lambda_0^2(s_i)$ determined in solving the Roy equations for the present case are displayed in Fig. 7, along with the fitting function that corresponds to expression (8). The statistical ellipse of scatter has the following parameters:

$$a_0^0 = 0.080 \pm 0.031, \quad r = 0.983,$$
$$a_0^2 = -0.090 \pm 0.010, \quad N_s = 5, \quad \chi^2 = 19. \tag{20}$$

On the basis of these results, we can conclude that the data from the electron experiment are described by the theoretical dependence (8) much more poorly (in terms of the χ^2 criterion) than the main array of data on the S_2 wave. The errors in a_0^0 and a_0^2 due to the theoretical uncertainty specify the ellipse of scatter with the parameters

$$a_0^0 = 0.080 \pm 0.056, \quad r = 1,$$
$$a_0^2 = -0.090 \pm 0.010. \tag{21}$$

Performing summation, we eventually find the following parameter values as determined from a set of $\lambda_0^2(s_i)$ values coming from the electron experiment:

$$a_0^0 = 0.080 \pm 0.064, \quad r = 0.955,$$
$$a_0^2 = -0.090 \pm 0.014. \tag{22}$$

The resulting ellipse of scatter is presented in Fig. 10. In summary, we can state that the a_0^0 and a_0^2 values as obtained from the data coming from the electron experiment lie far off the values deduced from the remaining array of data on λ_0^0 and λ_0^2 (this is clearly seen in Fig. 10), as well as far off the region of the a_0^0 and a_0^2 values quoted in the majority of studies. Thus, we can conclude that, although the overall statistics of events of pion–pion scattering is much vaster in the electron experiment than the entire body of remaining data on the S_2 wave, so that it could be considered as a basic experiment, it appears unfortunately that the presence of some methodological errors distorted the results for the phase shifts $\delta_0^2(s)$. This conclusion is confirmed both by the fact that the subtraction constants $\lambda_0^2(s_i)$ are poorly reproduced by the theoretical function in (8) and by the extremal values obtained for the scattering lengths a_0^0 and a_0^2.

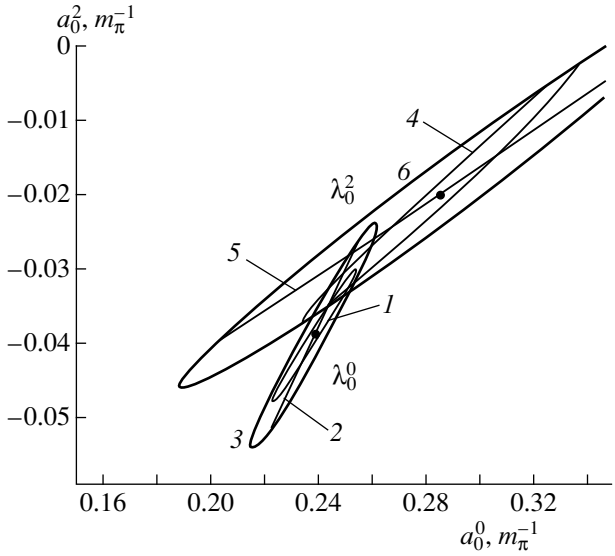

Fig. 9. (*1*) Statistical ellipse of scatter on the basis of data on $\lambda_0^0(s)$, (*2*) degenerate ellipse of scatter on the basis of data on $\lambda_0^0(s)$ that are associated with the theoretical error $\Delta\varphi_0^0$, (*3*) resulting ellipse of scatter on the basis of data on $\lambda_0^0(s)$, (*4*) statistical ellipse of scatter on the basis of data on $\lambda_0^2(s)$, (*5*) degenerate ellipse of scatter on the basis of data on $\lambda_0^2(s)$ that are associated with the theoretical error $\Delta\varphi_0^2$, and (*6*) resulting ellipse of scatter on the basis of data on $\lambda_0^2(s)$.

(e) $\lambda_1^1(s)$. In order to deduce the parameter $(2a_0^0 - 5a_0^2)$, we fitted the constructed dependence $\lambda_1^1(s)$ in terms of expression (9). From our fit, we excluded three points characterized by individual χ_i^2 values in excess of 50, assuming that such points correspond to extremely large fluctuations. After that, we obtained $\chi^2 = 218$ for 74 degrees of freedom. As was indicated in Subsection 2.3, there still remains the problem of large χ^2 values in smoothing data on the phase shifts $\delta_1^1(s)$. Naturally, this problem is present in fitting the dependence $\lambda_1^1(s)$ as well. The resulting data with allowance for the theoretical error $\Delta\varphi_1^1$ are the following:

$$(2a_0^0 - 5a_0^2) = 0.76 \pm 0.04. \tag{23}$$

Taking into account all that was said in Subsection 2.3, we can state that there arise problems in analyzing the phase shifts $\delta_1^1(s)$; therefore, we present the

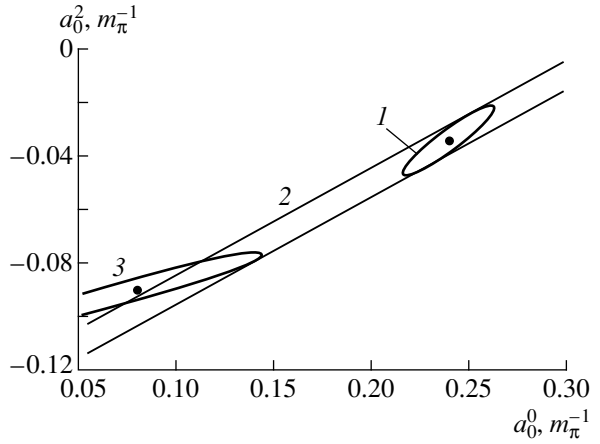

Fig. 10. (*1*) Resulting ellipse of scatter on the basis of data on $\lambda_0^0(s) + \lambda_0^2(s)$; (*2*) corridor for the universal curve, $(2a_0^0 - 5a_0^2)$; and (*3*) ellipse of scatter on the basis of data on $\lambda_0^2(s)$ from the electron experiment.

results in (23) as an illustration that calls for a further refinement, but we do not use these data in eventually determining the scattering lengths a_0^0 and a_0^2. The dependence $\lambda_1^1(s_i)$ is shown in Fig. 8, along with the theoretical straight line optimally chosen on the basis of expression (9).

To conclude this section, we would like to highlight the following circumstance. In analyzing the structure of the ellipses of scatter in Fig. 9 for the sets of λ_0^0 and λ_0^2, one can notice that the contribution to the final result from the uncertainties due to the statistical experimental errors is commensurate with theoretical uncertainties. Therefore, the problem of reducing uncertainties in the scattering lengths a_0^0 and a_0^2 cannot be solved by increasing statistics and improving experimental accuracies. Theoretical efforts at reducing the theoretical uncertainty $\Delta\varphi_l^I$ are also necessary.

6. EVALUATION OF a_1^1

The *P*-wave scattering length a_1^1 does not appear in the Roy equations, but it can be obtained from the Gribov–Froissart integral representation

$$a_1^1 = \frac{4}{3\pi}\int_4^{51}\frac{ds}{s^2}\left[\frac{1}{3}\mathrm{Im}\,f_0^0(s) + \frac{3(s+4)}{2(s-4)}\mathrm{Im}\,f_1^1(s) - \frac{5}{6}\mathrm{Im}\,f_0^2(s)\right] + \eta_1^1, \qquad (24)$$

$$\eta_1^1 = (1.31 \pm 0.16)\times 10^{-2}.$$

By using the same smoothed dependences of the pion–pion phase shifts as in solving the Roy equations, we obtain

$$a_1^1 = 0.0356 \pm 0.0017. \qquad (25)$$

It should be noted that the error in the scattering length a_1^1 is determined completely by the theoretical uncertainty $\Delta\eta_1^1$ in equation (24).

In order to draw a comparison with a solution obtained from the Roy equations, we further calculated the parameter $(2a_0^0 - 5a_0^2)$ by using the Wanders transformation

$$(2a_0^0 - 5a_0^2) = 18a_1^1 + \frac{16}{\pi}\int_4^{51}\frac{ds}{s^2(s-4)}\left[2\mathrm{Im}\,f_0^0(s) - 9\frac{3s-4}{s-4}\mathrm{Im}\,f_1^1(s) - 5\mathrm{Im}\,f_0^2(s)\right] - (8.6 \pm 4.3)\times 10^{-3}. \qquad (26)$$

Performing integration in (26) and substituting the value of a_1^1 from (25), we arrive at

$$(2a_0^0 - 5a_0^2) = 0.622 \pm 0.035. \qquad (27)$$

This result is quite consistent with the value in (19), which was obtained from the Roy equations. Yet another special feature is worthy of note. We make use of the definition of a_1^1 as a limit and assume that the near-threshold behavior of the phase shift is completely determined by the ρ resonance. By definition, we have

$$a_1^1 = \lim_{q\to 0}\left(\frac{\tan\delta_1^1(s)}{q^3}\right). \qquad (28)$$

By using expression (28) with the optimal parameter values presented in Subsection 2.3, we arrive at

$$(a_1^1)_{\mathrm{lim}} = 0.0136 \pm 0.0002. \qquad (29)$$

In all probability, the distinction between the values a_1^1 and $(a_1^1)_{\mathrm{lim}}$ should be treated as a manifestation of the fact that, near the threshold, the phase shift $\delta_1^1(s)$ is not exhausted by the contribution of the ρ resonance. However, this issue requires a dedicated consideration.

7. CONCLUSIONS

(i) By using data on pion–pion phase shifts for charged pions from the threshold to the dipion mass of 1 GeV, we have obtained the *S*- and *P*-wave subtraction constants $\lambda_l^I(s)$ (which appear to be solutions to the Roy equations) satisfying the conditions of analyticity, unitarity, and crossing symmetry. It has been shown that the solutions that we obtained are described well

by linear dependences, in accord with theoretical considerations.

(ii) On the basis of the resulting solutions $\lambda_0^0(s)$ and $\lambda_0^2(s)$, we have calculated the scattering lengths:

$$a_0^0 = (0.240 \pm 0.023)m_\pi^{-1},$$
$$a_0^2 = (-0.034 \pm 0.013)m_\pi^{-1}.$$

The relevant correlation coefficient proved to be $r = 0.945$. For the universal curve, the corresponding result is

$$(2a_0^0 - 5a_0^2) = (0.650 \pm 0.022)m_\pi^{-1}.$$

For the sake of comparison, we have calculated the parameters of the universal curve from the Wanders relation. The result is

$$(2a_0^0 - 5a_0^2) = (0.622 \pm 0.035)m_\pi^{-1}.$$

That the above solutions are close demonstrates the reliability of the approach used.

(iii) The effect of the statistical experimental errors on the uncertainties in the scattering length and the analogous effect of the theoretical uncertainties $\Delta\varphi_l^I$ have been taken into account separately. It has been shown that the contributions to the final results from these two sources of error are commensurate.

(iv) We would like to emphasize that, in describing the *P*-wave phase shift $\delta_1^1(s)$ by the relativistic formula involving the Durr–Pilkuhn form factor, the parameter characterizing the dimensions of the interaction region proved to be negative: $R^2 = -2.81 \pm 0.06$ GeV^{-2}. The remaining ρ-resonance parameters obtained in this way, $m_\rho = 770.5 \pm 0.6$ MeV and $\Gamma_\rho = 154.7 \pm 1.4$ MeV, are virtually coincident with the corresponding world-average values.

(v) The *P*-wave scattering length a_1^1 obtained from the Gribov–Froissart relation is

$$a_1^1 = (0.0356 \pm 0.0017)m_\pi^{-3}.$$

In calculating a_1^1 as the limit of δ_1^1/q^3 near the threshold, we have arrived at the value

$$(a_1^1)_{\lim} = (0.0136 \pm 0.0002)m_\pi^{-3}.$$

This suggests that, near the threshold, the *P* wave receives some contributions other than those from the ρ resonance.

ACKNOWLEDGMENTS

We are grateful to K.N. Mukhin, M.Zh. Shmatikov, V.V. Vereshchagin, G. Smith, and D. Pochanich for numerous stimulating discussions.

This work was supported in part by the Russian Foundation for Basic Research (project no. 97-02-16647).

APPENDIX

$$ {}_1K_0^0 = \frac{s-4}{(x-s)(x-4)} + \frac{2}{3x}\left[\frac{x}{s-4}\ln\left(\frac{x+s-4}{x}\right)-1\right] - \frac{2(s-4)}{3x(x-4)},$$

$$ {}_2K_0^0 = \frac{3}{x}\left\{2\left(1+\frac{2s}{x-4}\right)\times\left[\frac{x}{s-4}\ln\left(\frac{x+s-4}{x}\right)-1\right]+\frac{s-4}{x-4}\right\},$$

$$ {}_3K_0^0 = \frac{5}{3x}\left\{\left(2\left[\frac{x}{s-4}\ln\left(\frac{x+s-4}{x}\right)-1\right]+\frac{s-4}{x-4}\right\},$$

$$ {}_1K_1^1 = \frac{1}{3}\left\{\frac{4}{s-4}\left[\left(\frac{1}{2}+\frac{x}{s-4}\right)\times\ln\left(\frac{x+s-4}{x}\right)-1\right]-\frac{s-4}{3x(x-4)}\right\},$$

$$ {}_2K_1^1 = \frac{s-4}{(x-s)(x-4)} + \frac{6}{s-4}\left(1+\frac{2s}{x-4}\right)\times\left[\left(\frac{1}{2}+\frac{x}{s-4}\right)\ln\left(\frac{x+s-4}{x}\right)-1\right]-\frac{3(s-4)}{2x(x-4)},$$

$$ {}_3K_1^1 = -\frac{5}{3}\left\{\frac{2}{s-4}\left[\left(\frac{1}{2}+\frac{x}{s-4}\right)\times\ln\left(\frac{x+s-4}{x}\right)-1\right]-\frac{s-4}{6x(x-4)}\right\},$$

$$ {}_1K_0^2 = \frac{1}{3x}\left\{\left(2\left[\frac{x}{s-4}\ln\left(\frac{x+s-4}{x}\right)-1\right]-\frac{s-4}{x-4}\right\},$$

$$ {}_2K_0^2 = -\frac{3}{x}\left\{\left(1+\frac{2s}{x-4}\right)\times\left[\frac{x}{s-4}\ln\left(\frac{x+s-4}{x}\right)-1\right]-\frac{s-4}{2(x-4)}\right\},$$

$$
{}_3K_0^2 = \frac{s-4}{(x-s)(x-4)}
$$

$$
+\frac{1}{3x}\left[\frac{x}{s-4}\ln\left(\frac{x+s-4}{x}\right)-1\right]-\frac{5(s-4)}{6x(x-4)}.
$$

REFERENCES

1. J. Gasser and H. Leutwyler, Phys. Lett. B **125**, 321, 325 (1983).
2. J. Gasser and H. Leutwyler, Ann. Phys. (N.Y.) **158**, 142 (1984).
3. J. Gasser and H. Leutwyler, Nucl. Phys. B **250**, 465, 517, 539 (1985).
4. N. H. Fuchs, H. Sazdjian, and J. Stern, Phys. Lett. B **238**, 380 (1990).
5. J. Stern, H. Sazdjian, and N. H. Fuchs, Phys. Rev. D **47**, 3814 (1993).
6. M. Knecht, B. Moussallam, J. Stern, and N. H. Fuchs, Nucl. Phys. B **457**, 513 (1995).
7. M. Knecht, B. Moussallam, J. Stern, and N. H. Fuchs, Nucl. Phys. B **471**, 445 (1996).
8. B. R. Martin, D. Morgan, and G. Shaw, *Pion–Pion Interaction in Particle Physics* (New York, 1976).
9. K. N. Mukhin and O. O. Patarakin, Usp. Fiz. Nauk **133**, 377 (1981) [Sov. Phys. Usp. **24**, 161 (1981)].
10. S. M. Roy, Phys. Lett. B **36**, 353 (1971).
11. J. L. Basdevant, C. D. Frogatt, and J. L. Petersen, Phys. Lett. B **41**, 178 (1972).
12. M. R. Pennington and S. D. Protopopescu, Phys. Rev. D **7**, 1429 (1973).
13. E. A. Alekseeva, K. N. Mukhin, and O. O. Patarakin, Yad. Fiz. **35**, 917 (1982) [Sov. J. Nucl. Phys. **35**, 533 (1982)].
14. O. O. Patarakin, K. N. Mukhin, and V. N. Tikhonov, Nucl. Phys. A **598**, 335 (1996).
15. R. Kaminski *et al.*, Z. Phys. C **74**, 79 (1997).
16. L. Rosselet *et al.*, Phys. Rev. D **15**, 574 (1977).
17. S. D. Protopopescu *et al.*, Phys. Rev. D **7**, 1279 (1973).
18. E. A. Alekseeva *et al.*, Zh. Éksp. Teor. Fiz. **82**, 1007 (1982) [Sov. Phys. JETP **55**, 591 (1982)].
19. J. Carroll *et al.*, Phys. Rev. D **10**, 1430 (1974).
20. E. A. Estabrooks and A. D. Martin, Nucl. Phys. B **79**, 301 (1974).
21. Review of Particle Physics, Eur. Phys. J. C **3**, 1 (1998).
22. M. Svec, Phys. Rev. D **55**, 5727 (1997).
23. O. O. Patarakin and V. N. Tikhonov, Preprint No. 5629/2, IAÉ (Kurchatov Institute of Atomic Energy, Moscow, 1993).
24. M. Kermani, O. Patarakin, G. R. Smith, *et al.*, Phys. Rev. C **58**, 3431 (1998).
25. C. N. Kennedy *et al.*, Nucl. Phys. B **59**, 367 (1973).
26. W. Hoogland *et al.*, Nucl. Phys. B **126**, 109 (1977).
27. J. Losty *et al.*, Nucl. Phys. B **69**, 185 (1974).
28. E. Colton *et al.*, Phys. Rev. D **3**, 2028 (1971).
29. G. V. Beketov *et al.*, Yad. Fiz. **19**, 1032 (1974) [Sov. J. Nucl. Phys. **19**, 528 (1974)].
30. N. B. Durusoy *et al.*, Phys. Lett. B **45**, 517 (1973).
31. H. Durr and H. Pilkuhn, Nuovo Cimento A **40**, 899 (1965).

Translated by A. Isaakyan

Physics of Atomic Nuclei, Vol. 63, No. 9, 2000, pp. 1623–1628. From Yadernaya Fizika, Vol. 63, No. 9, 2000, pp. 1710–1715.

ELEMENTARY PARTICLES AND FIELDS
Theory

Hamiltonian Approach to the Bound-State Problem in QCD_2*

Yu. S. Kalashnikova, A. V. Nefediev***, and A. V. Volodin******

Institute of Theoretical and Experimental Physics, Bol'shaya Cheremushkinskaya ul. 25, Moscow, 117259 Russia

Received August 12, 1999

Abstract—Bosonization of two-dimensional QCD in the large-N_C limit is performed within the Hamiltonian approach in the Coulomb gauge. A generalized Bogolyubov transformation is applied to diagonalize the Hamiltonian in the bosonic sector of the theory, and the composite operators creating (annihilating) bosons are obtained in terms of dressed quark operators. The bound-state equation is reconstructed as the result of the generalized Bogolyubov transformation, and the form of its massless solution, a chiral pion, is found explicitly. The chiral properties of the theory are discussed. © *2000 MAIK "Nauka/Interperiodica".*

Two-dimensional quantum chromodynamics (QCD_2) in the large-N_C limit was first considered many years ago [1], but it still remains popular in studies of various aspects of strong interactions. The reason for this is twofold. There are no transverse gluons in two dimensions, so that the theory is relatively simple; moreover, in the large-N_C limit, only planar graphs are to be summed, and a simple diagrammatic approach can be developed. On the other hand, this theory does have a nontrivial content, exhibiting both confinement and chiral-symmetry breaking.

The majority of the studies in QCD_2 were performed in the light-cone gauge, which considerably simplifies the spectrum calculations, but which yields a perturbative vacuum. An alternative approach based on the Coulomb gauge $A_1 = 0$ is more technically involved [2], and it is not a straightforward exercise to demonstrate the equivalence of the two formulations. In particular, it appears that the vacuum is nontrivial in the Coulomb gauge version, and a nonzero quark condensate exists for massless quarks [3]. The latter feature is confirmed by the sum-rule approach [4] in the light-cone gauge. The confused situation was resolved to a large extent in the formulation on finite intervals [5], and the equivalence was demonstrated.

In the present paper, we study the Hamiltonian formulation of QCD_2 in the Coulomb gauge. In contrast to [5], the theory is quantized on the ordinary time hypersurface. Our main purpose is to investigate some special properties of meson wave functions. It will be shown that the Bogolyubov–Valatin approach offers the most natural setting for such studies. Finally, we perform a generalized Bogolyubov transformation and reformulate the theory in terms of the effective mesonic degrees of freedom. The proposed approach allows straightforward calculations of any matrix elements of quark operators, and we exemplify this property by evaluating the pion decay constant.

The Lagrangian of QCD_2 has the form

$$L(x) = -\frac{1}{4}F^a_{\mu\nu}(x)F^a_{\mu\nu}(x) + \bar{q}(x)(i\hat{D} - m)q(x), \quad (1)$$

where $\hat{D} = (\partial_\mu - igA^a_\mu t^a)\gamma_\mu$, and our convention for γ matrices is $\gamma_0 = \sigma_3$, $\gamma_1 = i\sigma_2$, and $\gamma_5 = \gamma_0\gamma_1$. The large-$N_C$ limit implies that g^2N_C remains finite.

The gluon propagator in the Coulomb gauge $A_1 = 0$ takes the form $D_{00}(k_0, k) = -1/k^2$, and the infrared singularity is regularized by the principal-value prescription yielding linear confinement:

$$D^{ab}_{00}(x_0 - y_0, x - y) = -\frac{i}{2}\delta^{ab}|x - y|\delta(x_0 - y_0). \quad (2)$$

The Hamiltonian can be obtained by standard methods and reads

$$H = \int dx q^+(x)\left(-i\gamma_5\frac{\partial}{\partial x} + m\gamma_0\right)q(x) - \frac{g^2}{2}\int dxdy q^+(x)t^a q(x)q^+(y)t^a q(y)\frac{|x-y|}{2}, \quad (3)$$

where the quark and antiquark fields are defined by

$$q_i(x_0, x) = \int\frac{dk}{2\pi}[u(k)b_i(x_0, k) + v(-k)d_i(x_0, -k)]e^{ikx}, \quad (4)$$

$$b_i(k)|0\rangle = d_i(-k)|0\rangle = 0 \quad (5)$$

with

$$u(k) = T(k)\begin{pmatrix}1\\0\end{pmatrix}, \quad v(-k) = T(k)\begin{pmatrix}0\\1\end{pmatrix}, \quad T(k) = e^{-\frac{1}{2}\theta(k)\gamma_1}. \quad (6)$$

The parameter $\theta(k)$ has the meaning of the Bogolyubov–Valatin angle describing a rotation from the bare to the dressed quarks. As in [2], the Hamiltonian in (3)

* This article was submitted by the authors in English.

** e-mail: yulia@vxitep.itep.ru
*** e-mail: nefediev@vxitep.itep.ru
**** e-mail: volodin@vxitep.itep.ru

can be normally ordered in the basis of the fermion operators (5):

$$H = LN_C\mathcal{E}_v + :H_2: + :H_4:. \tag{7}$$

Here, $\mathcal{E}_v$ is the vacuum-energy density (L being the one-dimensional volume of the space):

$$\mathcal{E}_v = \int\frac{dp}{2\pi}\mathrm{tr}\{(\gamma_5 p + m\gamma_0)\Lambda_-(p)\} + \frac{\gamma}{4\pi}\int\frac{dpdk}{(p-k)^2}\mathrm{tr}\{\Lambda_+(k)\Lambda_-(p)\}, \tag{8}$$

$$\gamma = \frac{g^2}{4\pi}\left(N_C - \frac{1}{N_C}\right) \xrightarrow[N_C\to\infty]{} \frac{g^2 N_C}{4\pi}.$$

The part $:H_2:$ is bilinear in quark fields,

$$:H_2: = \int dx : q_i^+(x)\left(-i\gamma_5\frac{\partial}{\partial x} + m\gamma_0\right)q_i(x) : - \frac{\gamma}{2}\int dxdy\frac{|x-y|}{2}\int dk : q_i^+(x)[\Lambda_+(k) - \Lambda_-(k)] \times q_i(y) : e^{ik(x-y)}, \tag{9}$$

and the projection operators $\Lambda_\pm$ are introduced as

$$\Lambda_\pm = T(k)\frac{1\pm\gamma_0}{2}T^+(k). \tag{10}$$

The angle $\theta(k)$ is defined from the condition of diagonalizing the bilinear in the quark-field part of the Hamiltonian $:H_2:$. This condition gives a system of integral equations for $\theta(p)$ and quark dispersion $E(p)$,

$$E(p)\cos\theta(p) = m + \frac{\gamma}{2}\int\frac{dk}{(p-k)^2}\cos\theta(k),$$
$$E(p)\sin\theta(p) = p + \frac{\gamma}{2}\int\frac{dk}{(p-k)^2}\sin\theta(k), \tag{11}$$

which leads to a gap equation for the angle $\theta(p)$,

$$p\cos\theta(p) - m\sin\theta(p) = \frac{\gamma}{2}\int\frac{dk}{(p-k)^2}\sin[\theta(p) - \theta(k)]. \tag{12}$$

Note that, once the "dressed" quarks, (4) and (5), define excitations over the true quark vacuum $|0\rangle$, then gap equation (12) could be reconstructed as the extremum condition

$$\frac{\delta\mathcal{E}_v[\theta]}{\delta\theta(p)} = 0, \tag{13}$$

which ensures that the vacuum energy is minimal.

Thus, the diagonalized Hamiltonian $:H_2:$ takes the form

$$:H_2: = \int\frac{dk}{2\pi}E(k)\{b_i^+(k)b_i(k) + d_i^+(-k)d_i(-k)\}. \tag{14}$$

The obvious properties of all solutions to the set of equations (11) are $\theta(k) = -\theta(-k)$, $E(k) = E(-k)$, and $\theta(k) \longrightarrow \pi/2$ when $k \longrightarrow \infty$.

Alternatively, equation (12) could be found as a solution to the Schwinger–Dyson equations for the quark propagator:

$$S(p_0, p) = \frac{1}{\hat{p} - m - \Sigma(p)}, \tag{15}$$

$$\Sigma(p) = -i\frac{\gamma}{2\pi}\int\frac{dk_0 dk}{(p-k)^2}\gamma_0 S(k_0, k)\gamma_0 = [E(p)\cos\theta(p) - m] + \gamma_1[E(p)\sin\theta(p) - p]. \tag{16}$$

The gap equation (12) contains the entire body of information about the one-fermion sector of the theory, but not about the interaction between fermions, because the $:H_4:$ part of the Hamiltonian was not involved so far. To proceed further, we introduce, as in [5], the color-singlet bilinear operators

$$B(p, p') = \frac{1}{\sqrt{N_C}}b_i^+(p)b_i(p'),$$
$$D(p, p') = \frac{1}{\sqrt{N_C}}d_i^+(-p)d_i(-p'),$$
$$M(p, p') = \frac{1}{\sqrt{N_C}}d_i(-p)b_i(p'), \tag{17}$$
$$M^+(p, p') = \frac{1}{\sqrt{N_C}}b_i^+(p')d_i^+(-p)$$

with the commutation relations

$$[M(p, p')M^+(q, q')] = -\frac{2\pi}{\sqrt{N_C}}\{D(q, p)\delta(p'-q') + B(q', p')\delta(p-q)\} + (2\pi)^2\delta(p'-q')\delta(p-q) \xrightarrow[N_C\to\infty]{} (2\pi)^2\delta(p'-q')\delta(p-q), \tag{18}$$

$$[B(p, p')B(q, q')] = \frac{2\pi}{\sqrt{N_C}}(B(p, q')\delta(p'-q) - B(q, p')\delta(p-q')) \xrightarrow[N_C\to\infty]{} 0,$$

$$[D(p, p')D(q, q')] = \frac{2\pi}{\sqrt{N_C}}(D(p, q')\delta(p'-q) - D(q, p')\delta(p-q')) \xrightarrow[N_C\to\infty]{} 0,$$

$$[B(p, p')M(q, q')] = -\frac{2\pi}{\sqrt{N_C}}M(q, p')\delta(p-q') \xrightarrow[N_C\to\infty]{} 0,$$

$$[B(p, p')M^+(q, q')] = \frac{2\pi}{\sqrt{N_C}}M^+(q, p)\delta(p'-q') \xrightarrow[N_C\to\infty]{} 0, \tag{19}$$

$$[D(p, p')M(q, q')] = -\frac{2\pi}{\sqrt{N_C}}M(p', q')\delta(p-q) \xrightarrow[N_C\to\infty]{} 0,$$

$$[D(p, p')M^+(q, q')]$$
$$= \frac{2\pi}{\sqrt{N_C}} M^+(p, q')\delta(p' - q) \xrightarrow[N_C \to \infty]{} 0.$$

In terms of these operators, the Hamiltonian in (3) can be represented as

$$H = LN_C\mathscr{E}_v + \sqrt{N_C}\int\frac{dk}{2\pi}E(k)\{B(k, k) + D(k, k)\}$$
$$-\frac{\gamma}{2}\int\frac{dpdkdQ}{(2\pi)^2(p-k)^2}\left\{2\cos\frac{\theta(p)-\theta(k)}{2}\right.$$
$$\times\sin\frac{\theta(Q-p)-\theta(Q-k)}{2}[M^+(p, p-Q)D(k-Q, k)$$
$$+M^+(p-Q, p)B(k-Q, k) - B(p, p-Q)M(k-Q, k)$$
$$-D(p, p-Q)M(k, k-Q)] + \cos\frac{\theta(p)-\theta(k)}{2}$$
$$\times\cos\frac{\theta(Q-p)-\theta(Q-k)}{2}[B(p-Q, p)B(k, k-Q) \quad (20)$$
$$+D(p, p-Q)D(k-Q, k)+M^+(p-Q, p)M(k-Q, k)$$
$$+M^+(p, p-Q)M(k, k-Q)] + \sin\frac{\theta(p)-\theta(k)}{2}$$
$$\times\sin\frac{\theta(Q-p)-\theta(Q-k)}{2}[B(p, p-Q)D(k, k-Q)$$
$$+B(p-Q, p)D(k-Q, k) + M(p, p-Q)M(k-Q, k)$$
$$\left.+M^+(p-Q, p)M^+(k, k-Q)]\right\}.$$

It can be easily verified that the ansatz [5]

$$B(p, p') = \frac{1}{\sqrt{N_C}}\int\frac{dq''}{2\pi}M^+(q'', p)M(q'', p'),$$
$$D(p, p') = \frac{1}{\sqrt{N_C}}\int\frac{dq''}{2\pi}M^+(p, q'')M(p', q'') \quad (21)$$

satisfies the commutation relations (19), so that, in the leading order in N_C, the Hamiltonian in (20) can be rewritten as

$$H = LN_C\mathscr{E}_v + \int\frac{dQdp}{(2\pi)^2}$$
$$\times\{(E(p) + E(Q-p))M^+(p-Q, p)M(p-Q, p)$$
$$-\frac{\gamma}{2}\int\frac{dk}{(p-k)^2}[2C(p, k, Q)M^+(p-Q, p)M(k-Q, k) \quad (22)$$
$$+S(p, k, Q)(M(p, p-Q)M(k-Q, k)$$
$$+M^+(p, p-Q)M^+(k-Q, k))]\},$$

where

$$C(p, k, Q) = \cos\frac{\theta(p)-\theta(k)}{2}\cos\frac{\theta(Q-p)-\theta(Q-k)}{2},$$
$$S(p, k, Q) = \sin\frac{\theta(p)-\theta(k)}{2}\sin\frac{\theta(Q-p)-\theta(Q-k)}{2}. \quad (23)$$

We are now to perform a second Bogolyubov transformation that should diagonalize this Hamiltonian. Let us define the new operators as

$$m_n^+(Q) = \int\frac{dq}{2\pi}\{M^+(q-Q, q)\varphi_+^n(q, Q)$$
$$+M(q, q-Q)\varphi_-^n(q, Q)\},$$
$$m_n(Q) = \int\frac{dq}{2\pi}\{M(q-Q, q)\varphi_+^n(q, Q) \quad (24)$$
$$+M^+(q, q-Q)\varphi_-^n(q, Q)\},$$

where the functions φ_+^n and φ_-^n parametrize this transformation and obey a Bogolyubov-type normalization and completeness conditions ($m, n > 0$):

$$\int\frac{dp}{2\pi}(\varphi_+^n(p, Q)\varphi_+^m(p, Q) - \varphi_-^n(p, Q)\varphi_-^m(p, Q)) = \delta_{nm},$$
$$\int\frac{dp}{2\pi}(\varphi_+^n(p, Q)\varphi_-^m(p, Q) - \varphi_-^n(p, Q)\varphi_+^m(p, Q)) = 0; \quad (25)$$

$$\sum_{n=0}^{\infty}(\varphi_+^n(p, Q)\varphi_+^n(k, Q) - \varphi_-^n(p, Q)\varphi_-^n(k, Q))$$
$$= 2\pi\delta(p-k), \quad (26)$$

$$\sum_{n=0}^{\infty}(\varphi_+^n(p, Q)\varphi_-^n(k, Q) - \varphi_-^n(p, Q)\varphi_+^n(k, Q)) = 0.$$

By using these conditions, it can easily be shown that, in the limit $N_C \longrightarrow \infty$, the new operators $m(Q)$ and $m^+(Q)$ obey the standard boson commutation relations

$$[m_n(Q)m_m^+(Q')] = 2\pi\delta(Q-Q')\delta_{nm},$$
$$[m_n(Q)m_m(Q')] = [m_n^+(Q)m_m^+(Q')] = 0. \quad (27)$$

A straightforward, but tedious, calculation shows that the transformation in (24) diagonalizes the Hamiltonian in (22) if the functions φ_+^n and φ_-^n are solutions to the set of equations

$$[E(p) + E(Q-p) - Q_0]\varphi_+(p, Q)$$
$$= \gamma\int\frac{dk}{(p-k)^2}[C(p, k, Q)\varphi_+(k, Q) - S(p, k, Q)\varphi_-(k, Q)],$$
$$[E(p) + E(Q-p) + Q_0]\varphi_-(p, Q) \quad (28)$$
$$= \gamma\int\frac{dk}{(p-k)^2}[C(p, k, Q)\varphi_-(k, Q) - S(p, k, Q)\varphi_+(k, Q)].$$

The resulting Hamiltonian takes the form

$$H = LN_C\mathscr{E}'_v + \frac{1}{2}\sum_{n=0}^{+\infty}\int\frac{dQ}{2\pi}Q_n^0(Q) \times\{m_n^+(Q)m_n(Q) + m_n(Q)m_n^+(Q)\}, \tag{29}$$

where $Q_n^0(Q)$ is the nth positive eigenvalue of the set of equations (28). The Hamiltonian in (29), together with boson operators (20), comprises our procedure of bosonization. Note that, here, the vacuum-energy density $\mathscr{E}'_v$ contains an $O(1/N_C)$ extra contribution that comes from the mesonic-operator ordering.

Equations (28) are nothing but those that were obtained by Bars and Green in [2] for the Bethe–Salpeter wave function

$$\Phi(p, Q) = T(p)\left(\frac{1+\gamma_0}{2}\gamma_5\varphi_+(p, Q) + \frac{1-\gamma_0}{2}\gamma_5\varphi_-(p, Q)\right)T^+(Q-p). \tag{30}$$

There is a very important point concerning Bars–Green equations (28). While equations (25) and (26) represent quite natural conditions imposed on the parameters of Bogolyubov–Valatin transformations, it is apparently unacceptable to assume such normalization and completeness conditions for solutions to bound-state equations. In fact, the problem is rooted in the properties of Bars–Green equations (28). It can easily be verified that, if the set of equations (28) is rewritten in the form of the matrix integral Schrödinger-like equation

$$Q_0^n\begin{pmatrix}\varphi_+^n\\ \varphi_-^n\end{pmatrix} = \hat{K}\begin{pmatrix}\varphi_+^n\\ \varphi_-^n\end{pmatrix}, \tag{31}$$

then the integral operator $\hat{K}$ is not Hermitian. Fortunately, this does not cause a disaster since the eigenvalues are real: integrating both sides of (28) with respect to p, doing the same for the complex-conjugate equations, and taking the appropriate linear combination, one arrives at

$$\sum_{n=-\infty}^{+\infty}(Q_n^0 - Q_m^{0*})\int\frac{dp}{2\pi}(\varphi_+^n(p, Q)\varphi_+^{m*}(p, Q) - \varphi_-^n(p, Q)\varphi_-^{m*}(p, Q)) = 0, \tag{32}$$

which yields

$$Q_0^n = Q_0^{n*} \tag{33}$$

together with the orthonormality condition

$$\int\frac{dp}{2\pi}(\varphi_+^n(p, Q)\varphi_+^m(p, Q) - \varphi_-^n(p, Q)\varphi_-^m(p, Q)) = \delta_{nm},$$
$$\int\frac{dp}{2\pi}(\varphi_+^n(p, Q)\varphi_-^m(p, Q) - \varphi_-^n(p, Q)\varphi_+^m(p, Q)) = 0. \tag{34}$$

Solutions to the set of equations (28) come in pairs: for each eigenvalue Q_0^n with the eigenfunction $(\varphi_+^n, \varphi_-^n)$, there exists another eigenvalue $-Q_0^n$ with eigenfunction $(\varphi_-^n, \varphi_+^n)$. With this symmetry, equation (34) can be rewritten in the form (25), which involves only positive eigenvalues. Similarly, the completeness conditions (26) can be derived in an attempt at constructing the Green's function for the set of equations (28).

From the point of view of the Bethe–Salpeter equation, the reason for such an unusual norm is the following. The matrix equation for the function Φ contains the projection operators (10), so that Φ is subject to the constraint

$$\Lambda_+(p)\Phi(p, Q)\Lambda_+(Q-p) = \Lambda_-(p)\Phi(p, Q)\Lambda_-(Q-p) = 0, \tag{35}$$

as is clear from (30). Thus, both the norm and the completeness conditions are defined in the truncated space (35).

It is well known that not only does the Bogolyubov–Valatin transformation change the operators, it also transforms the ground state. Indeed, the boson-annihilation operator $m_n(Q)$ does not annihilate the vacuum state $|0\rangle$ defined by equation (5). The explicit expression relating bosonic ($|\Omega\rangle$) and fermionic ($|0\rangle$) vacua is rather complicated, but the matrix elements of quark bilinears calculated in the old and in the new vacua fortunately coincide in the large-N_C limit. For example, the chiral condensate

$$\langle\bar{q}q\rangle = \langle\Omega|\bar{q}_i(x)q^i(x)|\Omega\rangle \xrightarrow[N_C\to\infty]{} \langle 0|\bar{q}_i(x)q^i(x)|0\rangle = N_C\int\frac{dk}{2\pi}\mathrm{tr}\{\gamma^0\Lambda_-(k)\} = -\frac{N_C}{2\pi}\int_{-\infty}^{+\infty}dk\cos\theta(k) \tag{36}$$

coincides with that which was found in [3].

The form (24) of the operator $m_n^+(Q)$ suggests the obvious particle–hole interpretation: the wave function of a meson moving forward in time contains two pieces, that of a quark–antiquark pair moving forward in time with the amplitude φ_+ and that of a pair moving backward with the amplitude φ_-. No such effect could ever occur in potential quark models.

What can be said about the relative magnitude of the two amplitudes φ_+ and φ_-? The set of equations (28) was solved numerically in [6], and it was shown that the component φ_- is small (i) if the quark mass is large and (ii) for higher excited states. In these two cases, the potential quark model with a local linear confinement serves as a good approximation.

In addition, the component φ_- dies out with increasing total meson momentum Q: in the infinite-momentum frame ($Q \longrightarrow \infty$), it is zero, whereas the equation

for φ_+ goes over to the 't Hooft equation [1] after appropriate rescaling, as was shown in [2].

In conclusion, let us briefly consider the state that suffers from the effect of backward motion in the most dramatic way. It is the two-dimensional pion. It was shown in [3] that the gap equation has a nontrivial solution in the chiral limit $m = 0$ and that the chiral condensate (36) does not vanish with this solution. Therefore, the Goldstone mode must exist in the spectrum. Indeed, the set of functions

$$\varphi^{\pi}_{\pm}(p, Q) = N_{\pi}^{-1}\left(\cos\frac{\theta(Q-p)-\theta(p)}{2} \pm \sin\frac{\theta(Q-p)+\theta(p)}{2}\right) \quad (37)$$

is a solution to the set of equations (28) for $Q_0 = \sqrt{Q^2}$ and $Q > 0$ (for $Q < 0$, $\varphi_{\pm} \longleftrightarrow \varphi_{\mp}$!). Here, N_π is the pion norm defined according to the general form (34),

$$\int_{-\infty}^{+\infty}\frac{dp}{2\pi}[(\varphi^{\pi}_{+}(p, Q))^2 - (\varphi^{\pi}_{-}(p, Q))^2] = 1, \quad (38)$$

or, with solution (37) substituted, one arrives at

$$N^2_{\pi}(Q) = \int_{-\infty}^{+\infty}\frac{dp}{\pi}[\sin\theta(p) + \sin\theta(Q-p)] = \frac{2}{\pi}Q. \quad (39)$$

For $Q = 0$, we have $\varphi_+(p, 0) = \varphi_-(p, 0) \sim \cos\theta(p)$; the pion spends half of the time in the backward motion of the pair, and, as follows from equation (39), such a function has zero norm, as this should be for a massless particle at rest. In the opposite limiting case of $Q \longrightarrow \infty$, the backward-motion part dies out, so that

$$\varphi^{\pi}_{+}(p, Q) \xrightarrow[Q\to\infty]{} \sqrt{\frac{2\pi}{Q}}, \quad 0 \le p \le Q, \quad (40)$$

which coincides with the Goldstone mode of the 't Hooft equation. Nevertheless, this does not mean that pion physics is exhausted by the simple picture of a linear confinement in the infinite-momentum frame. The nontrivial content of the wave function (37) is concentrated entirely in the boundary regions $x \longrightarrow 0$ and $x \longrightarrow 1$, $x = p/Q$. The same is true of course for the QCD_2 quantized at the light-cone [4], where quantities like chiral condensate do not come out trivially, and one is forced to employ the sum-rule approach to arrive at a reliable answer.

With the above Hamiltonian approach, it is straightforward to calculate any matrix element of currents between mesonic states. By way of example, we indicate that, in order to evaluate the pion decay constant f_π defined in the standard way as

$$\langle\Omega|J^5_{\mu}(x)|\pi(Q)\rangle = f_{\pi}Q_{\mu}\frac{e^{-iQx}}{\sqrt{2Q_0}}, \quad (41)$$

we can express the axial-vector current $J^5_\mu(x) = \bar{\psi}(x)\gamma_\mu\gamma_5\psi(x)$ in terms of meson creation–annihilation operators m^+_n and m_n. This allows us to calculate the matrix element on the left-hand side explicitly. The resulting expression for f_π is

$$f_{\pi} = \sqrt{\frac{N_C}{\pi}}. \quad (42)$$

It is instructive to note that, for any mesonic state $\mathcal{M}_n(Q)$, the analogous matrix element $\langle\Omega|J^5_\mu(x)|\mathcal{M}_n(Q)\rangle$ contains this meson wave function integrated with the pion wave function, which obviously vanishes for any mesonic state but the pion, in which case there appears the pion norm (39). Thus, the matrix element (41) is the only nontrivial one, and the corresponding decay constants for higher excitations of mesonic states vanish.

We can now slightly relax the chiral limit and find the pion mass in the limit of a small, but nonzero, quark mass m. To this end, we rewrite the set of equations (28) as a single equation for the matrix function $\Phi(p, Q)$ in the form

$$\begin{aligned} Q_0\Phi(p, Q) &= (\gamma_5 p + \gamma_0 m)\Phi(p, Q) \\ &- \Phi(p, Q)(\gamma_5(Q-p) + \gamma_0 m) \\ &+ \gamma\int\frac{dk}{(p-k)^2}\{\Lambda_+(k)\Phi(p, Q)\Lambda_-(Q-k) \\ &- \Lambda_+(p)\Phi(k, Q)\Lambda_-(Q-p) - \Lambda_-(k)\Phi(p, Q)\Lambda_+(Q-k) \\ &+ \Lambda_-(p)\Phi(k, Q)\Lambda_+(Q-p)\}. \end{aligned} \quad (43)$$

Multiplying equation (43) by $\gamma_0\gamma_5$, taking the trace over spinor indices, and integrating the result with respect to the momentum p, one can arrive at

$$\begin{aligned} Q_0\int\frac{dp}{2\pi}\mathrm{tr}[\gamma_0\gamma_5\Phi(p, Q)] - Q\int\frac{dp}{2\pi}\mathrm{tr}[\gamma_0\Phi(p, Q)] \\ = -2m\int\frac{dp}{2\pi}\mathrm{tr}[\gamma_5\Phi(p, Q)]. \end{aligned} \quad (44)$$

By substituting the pion wave function (37) and using the definition in (30), we can recast the last equation into the well-known relation [7]

$$f^2_{\pi}M^2_{\pi} = -2m\langle\bar{q}q\rangle. \quad (45)$$

For the pion mass, we then have the expression

$$M^2_{\pi} = 2m\int_0^{\infty}dp\cos\theta(p) \sim m\sqrt{\gamma}, \quad (46)$$

which vanishes in the exact chiral limit.

The last concluding remark concerning the Hamiltonian in (29) is in order here. As could have been anticipated from the outset, this Hamiltonian describes free noninteracting mesons, whereas the interaction sup-

pressed by powers of N_C is hidden in the terms that are present in (20), but which are omitted in (29). These terms define three- and four-meson vertices, so that recovering them gives quite a natural way to consider strong meson decays and scattering amplitudes. This investigation is of special interest in view of the fact that the pion wave function is found explicitly; hence, the "mysterious" influence of $q\bar{q}$-pair backward motion in time upon excited-meson decay into pions can easily be resolved. This work is in progress and will be reported elsewhere.

ACKNOWLEDGMENTS

We would like to thank A.A. Abrikosov, Jr., for stimulating discussions.

This work was supported by the Russian Foundation for Basic Research (project nos. 97-02-16404 and 96-15-96740).

REFERENCES

1. G. 't Hooft, Nucl. Phys. B **75**, 461 (1974).
2. I. Bars and M. B. Green, Phys. Rev. D **17**, 537 (1978).
3. Ming Li, Phys. Rev. D **34**, 3888 (1986).
4. A. R. Zhitnitskiĭ, Yad. Fiz. **43**, 1553 (1986) [Sov. J. Nucl. Phys. **43**, 999 (1986)]; Yad. Fiz. **44**, 220 (1986) [Sov. J. Nucl. Phys. **44**, 139 (1986)].
5. F. Lenz and M. Thies, Ann. Phys. (N.Y.) **208**, 1 (1991).
6. Ming Li, L. Wilets, and M. C. Birse, J. Phys. G **13**, 915 (1987).
7. M. Gell-Mann, R. J. Oakes, and B. Renner, Phys. Rev. **175**, 2195 (1968).

Physics of Atomic Nuclei, Vol. 63, No. 9, 2000, pp. 1629–1634. Translated from Yadernaya Fizika, Vol. 63, No. 9, 2000, pp. 1716–1721.

ELEMENTARY PARTICLES AND FIELDS
Theory

Fragmentation Production of Ω_{ccc} Baryons at LHC Energies

V. A. Saleev

Samara State University, ul. Akademika Pavlova 1, Samara, 443011 Russia

Received May 20, 1999; in final form, August 26, 1999

Abstract—Within the nonrelativistic quark–diquark model for heavy baryons, the fragmentation functions for the transitions of a c-quark and a doubly charmed vector diquark into an Ω_{ccc} baryon are calculated in the leading order of perturbative QCD. The cross section for Ω_{ccc} production in high-energy hadron interactions is estimated. It is assumed that Ω_{ccc} baryons are formed via the fragmentation of a c quark or a vector (cc) diquark produced in the partonic subprocesses $gg \longrightarrow c\bar{c}$, $q\bar{q} \longrightarrow c\bar{c}$, $gg \longrightarrow (cc) + \bar{c} + \bar{c}$, and $q\bar{q} \longrightarrow (cc) + \bar{c} + \bar{c}$. *© 2000 MAIK "Nauka/Interperiodica".*

1. INTRODUCTION

Interest in the physics of baryons containing heavy quarks has quickened considerably in recent years [1]. This is due primarily to the emergence of new experimental data on the masses and decay widths of charmed and beauty baryons and on the cross sections for their production [2]. Advances in experimental studies has stimulated theoretical work aimed at predicting production rates for doubly heavy baryons in the *ep* and *pp* interactions at high energies [3–6]. It is probable that the Ξ'_{cc} and Ξ^*_{cc} baryons containing two charmed quarks each can be detected at the Tevatron energies ($\sqrt{s}$ = 1.8 TeV). At the LHC energies ($\sqrt{s}$ = 14 TeV), the production rate for doubly charmed baryons is expected to be greater than that at the Tevatron energies by four orders of magnitude [7]. The predicted production rates for *bc* and *bb* baryons at LHC amount to, respectively, 1/3 and 1/100 of that for the *cc* baryons [8].

In the present study, an attempt is made to estimate the cross sections for the production of triply heavy baryons Ω_{ccc} in *pp* collisions at the Tevatron and LHC energies. It is assumed that triply heavy baryons are formed in the fragmentation of heavy quarks or doubly heavy diquarks produced in the hard subprocesses $gg \longrightarrow c\bar{c}$, $q\bar{q} \longrightarrow c\bar{c}$, $gg \longrightarrow (cc) + \bar{c} + \bar{c}$, and $q\bar{q} \longrightarrow (cc) + \bar{c} + \bar{c}$. In contrast to the production of heavy and doubly heavy baryons, the production of baryons involving three heavy quarks can be self-consistently calculated within perturbative QCD and the nonrelativistic quark model for hadrons, which is successfully employed to describe the production of heavy-quarkonia [9].

The form factor for the transition of a virtual gluon into a pair consisting of a cc diquark and a $(\bar{c}\bar{c})$ antidiquark, $g^* \longrightarrow (cc) + (\bar{c}\bar{c})$, can be calculated rigorously in the leading order in α_s and $(v/c)^2$. This form factor can be expressed in terms of the diquark wave function at the origin, $\Psi_{cc}(0)$. Owing to this, the fragmentation functions for c-quark and cc-diquark transitions into a Ω_{ccc} baryon can be related to the parameters of the diquark form factor and the baryon wave function at the origin, $\Psi_{\Omega_{ccc}}(0)$ in the quark–diquark approximation [6, 10].

2. FORM FACTOR FOR THE VECTOR cc DIQUARK

In the process $g^* \longrightarrow (cc) + (\bar{c}\bar{c})$, where (cc) is a doubly heavy vector diquark, the gluon virtuality satisfies the relation $k^2 > 4m_{cc}^2 = 16m_c^2 \gg \Lambda^2_{\mathrm{QCD}}$, where m_c is the c-quark mass and m_{cc} is the diquark mass. Owing to this condition, the diquark elastic form factor $F_D(k^2)$ for the transition $g^* \longrightarrow (cc) + (\bar{c}\bar{c})$ can be calculated within perturbative QCD. In the leading order in the coupling constant α_s, four diagrams in Fig. 1 contribute to the form factor in question.

In the nonrelativistic approximation, the diquark is assumed to be the system consisting of two quarks with equal 4-momenta and occurring in the spin-1 color-antitriplet state. From an analysis of the diagrams in Fig. 1, it can be deduced that the vertex for the transition $g^* \longrightarrow (cc) + (\bar{c}\bar{c})$ can be parametrized as

$$\begin{aligned}(-ig_s)T^a F_D((p_1+p_2)^2)V_{\alpha\mu\beta}(p_1,p_2),\\ V^a_{\alpha\mu\beta}(p_1,p_2) = -g_{\alpha\beta}(p_1-p_2)_\mu\\ - g_{\beta\mu}(3p_2+2p_1)_\alpha + g_{\mu\alpha}(3p_1+2p_2)_\beta.\end{aligned} \tag{1}$$

Here, $g_s = \sqrt{4\pi\alpha_s}$; $T^a = \lambda^a/2$ are the Gell-Mann matrices; p_1 is the diquark 4-momentum, p_2 is the antidiquark 4-momentum; and

$$F_D(k^2) = F_{D0}\left(\frac{m_{cc}^2}{k^2}\right)^2, \tag{2}$$

1063-7788/00/6309-1629$20.00

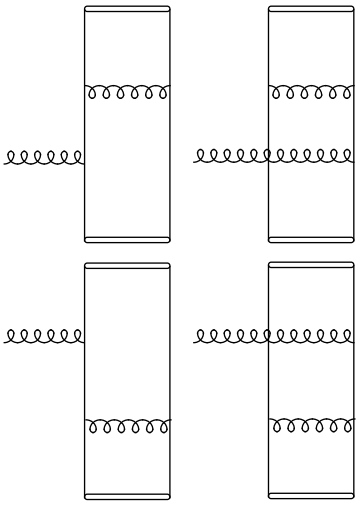

Fig. 1. Diagrams describing the diquark form factor for the transition $g^* \longrightarrow (cc) + (\bar{c}\bar{c})$ in the leading order in α_s (wavy lines, solid lines, and ovals represent, respectively, gluons, quarks, and diquarks and antidiquarks).

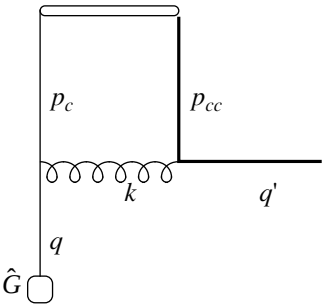

Fig. 2. Diagram making the leading contribution to *c*-quark fragmentation function for Ω_{ccc}-baryon production.

where

$$F_{D0} = 128\pi\alpha_s \frac{|\Psi_{cc}(0)|^2}{m_{cc}^3}.$$

3. *c*-QUARK FRAGMENTATION FUNCTION FOR THE TRANSITION INTO A Ω_{ccc} BARYON

Heavy-quark fragmentation into heavy quarkonia was considered in the study of Braaten *et al.* [11], who proposed a method for calculating the relevant fragmentation functions on the basis of perturbative QCD and the nonrelativistic quark model. This method was then used to compute the analogous functions for heavy-quark fragmentation into a doubly heavy diquark, $D_{Q\to(QQ)}(z, \mu)$ [3], and into a doubly heavy baryon, $D_{Q\to(QQq)}(z, \mu)$ [6]. In the latter case, the calculation treated a doubly heavy baryon as a two-particle system consisting of a heavy quark Q and a light–heavy diquark (qQ) and employed phenomenological (qQ)-diquark form factors, which are poorly known.

Below, *c*-quark fragmentation into a Ω_{ccc} baryon is considered in a similar manner, but the well-defined expression (2) is used here for the diquark form factor.

The *c*-quark fragmentation function for Ω_{ccc}-baryon production is given by [11]

$$D_{c\to\Omega_{ccc}}(z, \mu_0) = \frac{1}{16\pi^2}\int_{s_{\min}}^{\infty} ds \lim_{q_0\to\infty}\frac{|\mathcal{M}|^2}{|\mathcal{M}_0|^2}, \qquad (3)$$

where $\mathcal{M}$ is the amplitude for the production of an Ω_{ccc} baryon of mass M and an antidiquark $\bar{c}\bar{c}$ of mass $m_{cc} = 2m_c$ and total 4-momentum $q = (q_0, 0, 0, q_3)$, $s = q^2$ is the invariant mass of the antidiquark, and $\mathcal{M}_0$ is the on-mass-shell amplitude for the production of a *c* quark of momentum $\mathbf{q}$. In the limit $q_0 \longrightarrow \infty$, we obtain

$$s_{\min} = \frac{M^2}{z} + \frac{m_{cc}^2}{1-z} \quad \text{and} \quad z = \frac{p_0 + p_3}{q_0 + q_3}.$$

We use the axial gauge, where the gluon propagator is given by

$$d_{\mu\nu} = -g_{\mu\nu} + \frac{k_\mu n_\nu + k_\nu n_\mu}{(kn)},$$

with $n = (1, 0, 0, -1)$. In this gauge, the dominant contribution to the amplitude $\mathcal{M}$ in the leading order in α_s comes from the diagram in Fig. 2. The corresponding expression is

$$\mathcal{M} = \frac{|\Psi_{\Omega_{ccc}}(0)|}{\sqrt{2m_{cc}}}\frac{4\delta^{ij}}{3\sqrt{3}}(4\pi\alpha_s)^2\frac{F_D(k^2)}{k^2(s-m_c^2)}$$

$$\times\,\bar{\Psi}^\beta(p)\gamma^\nu(\hat{q}+m_c)\hat{G}\left(-g_{\mu\nu}+\frac{k_\mu n_\nu + k_\nu n_\mu}{(kn)}\right) \qquad (4)$$

$$\times\, V_{\alpha\mu\beta}(q, p_c)\varepsilon_\alpha^*(q'),$$

where the factor $\hat{G}$ describes the production of a *c* quark of 4-momentum $q = p + q'$, $4\delta^{ij}/3\sqrt{3}$ is the color factor of the diagram, $F_D(k^2)$ is the vector-diquark form factor in the diquark–gluon–diquark vertex, $\bar{\Psi}^\beta(p)$ is the spin vector describing the spin-3/2 baryon of 4-momentum p, and $\varepsilon_\alpha^*(q')$ is the polarization vector of the antidiquark. In the nonrelativistic approximation, we have $p_{(cc)} = (1-r)p$ and $p_c = rp$, where $r = m_c/M$. The scalar products of the 4-vectors k, p, and q are expressed in terms of the invariant mass s of the *c* quark as follows:

$$k^2 = (1-r)(s-m_c^2), \quad 2(qk) = (2-r)(s-m_c^2),$$

$$2(kp) = s-m_c^2, \quad 2(pq) = s-m_c^2+2rM^2.$$

The sum over the polarizations of the spin-3/2 baryon is computed by making use of the projection operator:

$$\sum_{\text{spin}}\Psi_\mu(p)\bar{\Psi}_\nu(p) = (\hat{p}+M)\left(-g_{\mu\nu}+\frac{1}{3}\gamma_\mu\gamma_\nu+\frac{2}{3}\frac{p_\mu p_\nu}{M^2}+\frac{p_\nu\gamma_\mu-p_\mu\gamma_\nu}{3M}\right). \quad (5)$$

However, we consider that, in the nonrelativistic limit, the quark and the vector diquark in the baryon are free particles. In this case, summation over baryon polarization is equivalent to summation over the polarizations of the quark and the vector diquark:

$$\sum_{\text{spin}}\Psi_\mu(p)\bar{\Psi}_\nu(p) = \frac{2}{3}\sum_{\text{spin}}U(p)\bar{U}(p)\sum_{\text{spin}}\varepsilon_\mu(p)\varepsilon_\nu^*(p). \quad (6)$$

Upon evaluating the ratio $|\mathcal{M}|^2/|\mathcal{M}_0|^2$ and performing a trivial integration with respect to s in the limit $q_0 \longrightarrow \infty$, we arrive at

$$D_{c\to\Omega_{ccc}}(z,\mu_0) = \frac{|\Psi_{\Omega_{ccc}}(0)|^2}{M^3}\alpha_s^2(\mu_0)F_{D0}^2\Phi_c(z), \quad (7)$$

where

$$\Phi_c(z) = \frac{36z^4(1-z)^3}{35(z-3)^{14}}(113519z^8-1303182z^7+8764206z^6-26818758z^5+52452396z^4-73464138z^3+66215394z^2-32322402z+6506325).$$

The fragmentation function $D_{c\to\Omega_{ccc}}(z,\mu)$ for $\mu > \mu_0 = 4m_c$ can be determined by solving the evolution equation

$$\mu\frac{\partial D}{\partial\mu}(z,\mu) = \int_z^1\frac{dy}{y}\mathcal{P}_{c\to c}\left(\frac{z}{y},\mu\right)D(y,\mu), \quad (8)$$

where $\mathcal{P}_{c\to c}(x,\mu)$ is the splitting function in the leading order in α_s,

$$\mathcal{P}_{c\to c}(x,\mu) = \frac{4\alpha_s(\mu)}{3\pi}\left(\frac{1+x^2}{1-x}\right)_+, \quad (9)$$

where

$$f(x)_+ = f(x)-\delta(1-x)\int_0^1 f(x')dx'.$$

The fragmentation function $D_{c\to\Omega_{ccc}}(z,\mu)$ normalized to unity is shown in Fig. 3 for $\mu=\mu_0$ (curve *1*) and μ = 45 GeV (curve *2*). The corresponding mean values of z are $\langle z\rangle_{\mu_0} = 0.61$ and $\langle z\rangle_{45} = 0.42$. By virtue of the condition

$$\int_0^1\mathcal{P}_{c\to c}(x,\mu)dx = 0,$$

the probability $P_{c\to\Omega_{ccc}}$ of quark fragmentation into a baryon does not depend on the parameter μ appearing in the fragmentation function. Specifically, we have

$$P_{c\to\Omega_{ccc}} = \int_0^1 D_{c\to\Omega_{ccc}}(z,\mu_0)dz = A_c\alpha_s^2(\mu_0)F_{D0}^2\frac{|\Psi_{\Omega_{ccc}}(0)|^2}{M^3}, \quad (10)$$

where

$$A_c = \frac{263585448}{5}\ln\left(\frac{3}{2}\right)-\frac{1100381933317}{51480}\approx 4.19\times10^{-3}.$$

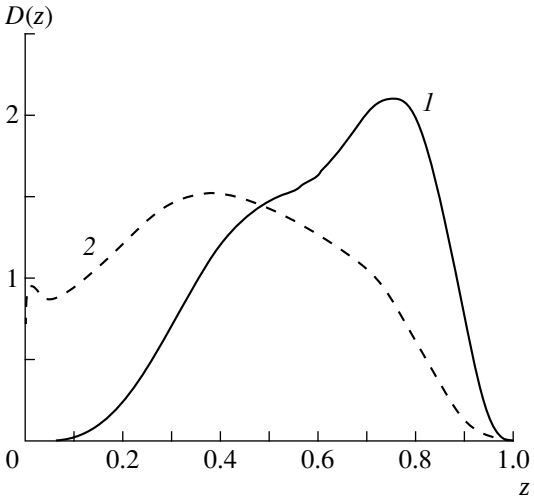

Fig. 3. Fragmentation function $D_{c\to\Omega_{ccc}}(z,\mu)$ at (curve *1*) $\mu=\mu_0$ and (curve *2*) μ = 45 GeV.

4. (cc)-DIQUARK FRAGMENTATION FUNCTION FOR Ω_{ccc}-BARYON PRODUCTION

Alternatively, Ω_{ccc} baryons can be produced in a two-stage process where c-quark fragmentation into a (cc) diquark is followed by the hadronization of the product diquark into an Ω_{ccc} baryon. The c-quark fragmentation function for Ω_{ccc}-baryon production can then

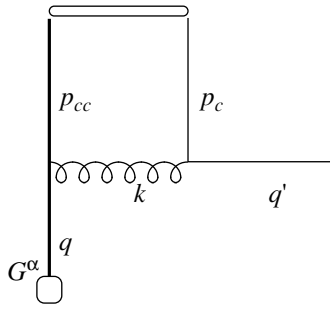

Fig. 4. Diagram making the leading contribution to the (cc)-diquark fragmentation function for Ω_{ccc}-baryon production.

be represented as the convolution of the fragmentation functions $D_{c\to(cc)}(z,\mu)$ and $D_{(cc)\to\Omega_{ccc}}(z,\mu)$; that is,

$$D_{c\to\Omega_{ccc}}(z,\mu) = \int dx \int dy D_{c\to(cc)}(x,\mu) \times D_{(cc)\to\Omega_{ccc}}(y,\mu)\delta(z-xy). \quad (11)$$

The $c \longrightarrow (cc)$ fragmentation function has the form [3]

$$D_{c\to(cc)}(z,\mu) = \frac{16}{9}\alpha_s(\mu_0)^2\frac{|\Psi_{cc}(0)|^2}{m_c^3}\frac{z(1-z)^2}{(2-z)^6} \times (16-32z+72z^2-32z^3+5z^4). \quad (12)$$

The corresponding fragmentation probability is given by

$$P_{c\to(cc)} = \frac{16}{9}\alpha_s(\mu_0)^2\frac{|\Psi_{cc}(0)|^2}{m_c^3}\left(\frac{1189}{30}-57\ln(2)\right). \quad (13)$$

The fragmentation function $D_{(cc)\to\Omega_{ccc}}(z,\mu)$ is determined by expression (3), where the following notation is used: $\mathcal{M}$ is the amplitude for the production of an Ω_{ccc} baryon of mass M and c-antiquark of mass m_c with a 4-momentum $q = (q_0, 0, 0, q_3)$, and an invariant mass $s = q^2$, while $\mathcal{M}_0$ is the on-mass-shell amplitude for the production of a vector (cc) diquark of momentum $\mathbf{q}$. In the limit $q_0 \longrightarrow \infty$, we obtain

$$s_{\min} = \frac{M^2}{z}+\frac{m_c^2}{1-z}, \quad z = \frac{p_0+p_3}{q_0+q_3}.$$

In the axial gauge, the amplitude $\mathcal{M}$ is determined by the diagram in Fig. 4. The resulting expression is

$$\mathcal{M} = \frac{|\Psi_B(0)|}{\sqrt{2M}}\frac{4\delta^{ij}}{3\sqrt{3}}(4\pi\alpha_s)^2\frac{F_V(k^2)}{k^2(q^2-m_{cc}^2)} \times \bar{\Psi}^\beta(p)\gamma^\nu V(q')\left(-g_{\mu\nu}+\frac{k_\mu n_\nu + k_\nu n_\mu}{(kn)}\right)V_{\alpha\mu\beta}(q,p_{cc})G^\alpha, \quad (14)$$

where the factor G^α describes the production of a vector diquark of 4-momentum $q = p + q'$. The rest of the notation is similar to that in (4).

It is convenient to compute the square of the absolute value of the amplitude, $|\mathcal{M}|^2$, for the longitudinal and transverse components of the diquark polarization separately. Transversely polarized states are described by the 4-vectors

$$\varepsilon_{\perp 1} = (0,0,1,0), \quad \varepsilon_{\perp 2} = (0,1,0,0),$$

which satisfy the orthogonality conditions

$$(\varepsilon_{\perp 1}q) = (\varepsilon_{\perp 2}q) = 0, \quad (\varepsilon_{\perp 1}k) = (\varepsilon_{\perp 2}k) = 0.$$

A longitudinal polarization of the diquark is described by the 4-vector

$$\varepsilon_L^\mu = \frac{p^\mu}{M}-\frac{Mn^\mu}{(np)},$$

which satisfies the relations

$$(\varepsilon_L q) = \frac{(qp)}{M}-\frac{M}{z}, \quad (\varepsilon_L k) = \frac{(np)}{M}.$$

The scalar products of the relevant 4-vectors can be expressed in terms of the invariant s as

$$k^2 = r(s-m_{cc}^2), \quad 2(pk) = s-m_{cc}^2,$$
$$2(qk) = (1+r)(s-m_{cc}^2),$$
$$2(pq) = s-m_{cc}^2+2r(1-r)M^2.$$

Upon integrating the ratio $|\mathcal{M}|^2/|\mathcal{M}_0|^2$ with respect to s in the limit $q_0 \longrightarrow \infty$, we obtain

$$D_{(cc)\to\Omega_{ccc}}(z,\mu_0) = \frac{1327104}{5}\frac{|\Psi_{\Omega_{ccc}}(0)|^2}{M^3} \times \alpha_s^2(\mu_0)F_{D0}^2\frac{z^6(1-z)^6}{(3-2z)^{14}}(369-372z+164z^2). \quad (15)$$

The probability of (cc)-diquark fragmentation into an Ω_{ccc} baryon is given by

$$P_{(cc)\to\Omega_{ccc}} = A_{cc}F_{D0}^2\alpha_s^2(\mu_0)\frac{|\Psi_{\Omega_{ccc}}(0)|^2}{M^3}, \quad (16)$$

where

$$A_{cc} = \frac{25110174688}{675675}-\frac{169128}{5}\ln(3).$$

Using the "schroe" package [12] and simulating the quark–quark interaction by the Martin potential [13]

$$V_{Q\bar{Q}}(r) = -A+B(r\cdot 1\ \text{GeV})^n, \quad V_{QQ} = \frac{1}{2}V_{Q\bar{Q}},$$

where $A = -8.064$ GeV, $B = 6.898$ GeV, and $n = 0.1$, we obtain the following values for the masses of the vector (cc) diquark and the Ω_{ccc} baryon and for their wave functions at the origin: $m_{cc} = 3.48$ GeV, $M = 4.70$ GeV, $|\Psi_{cc}(0)|^2 = 0.03$ GeV^3, and $|\Psi_{\Omega_{ccc}}(0)|^2 = 0.115$ GeV^3.

Let us compare the probability of c-quark fragmentation immediately into an Ω_{ccc} baryon and the probability of c-quark fragmentation into an Ω_{ccc} baryon via the production of a (cc) diquark in the intermediate state. At the effective QCD coupling constant of $\alpha_s(\mu_0) = 0.2$, we obtain

$$P_{c\to(cc)} = 6.8\times10^{-5} \text{ and } P_{(cc)\to\Omega_{ccc}} = 1.2\times10^{-6}. \tag{17}$$

For the latter case, the fragmentation probability is

$$P_{c\to(cc)\to\Omega_{ccc}} = 8.2\times10^{-11}. \tag{18}$$

If the c quark fragments immediately into an Ω_{ccc} baryon, picking up a (cc) diquark, the probability of the process is

$$P_{c\to\Omega_{ccc}} = 1.15\times10^{-9}. \tag{19}$$

5. Ω_{ccc} PRODUCTION IN HADRON INTERACTIONS

It was shown in [7] that the fragmentation production of hadrons containing heavy quarks (B_c, Ξ_{cc}, …) in partonic subprocesses is dominant only at sufficiently high transverse momenta ($p_\perp > 30$ GeV/c at $\sqrt{\hat{s}} = 100$ GeV). For this reason, the fragmentation mechanism saturates only a small fraction of the total cross section for the production of these baryons. An accurate description of the production of triply heavy baryons presents a problem on two counts: first, the number of Feynman diagrams is an order of magnitude greater than that for the production of doubly heavy baryons; second, it is necessary to take into account a direct hadronization of three heavy quarks into a baryon—that is, a hadronization process skipping the formation of a doubly heavy diquark in the intermediate state.

Although the fragmentation mechanism is well justified only at high $p_\perp$, the heavy-hadron spectra obtained as convolutions with the parton distributions in colliding hadrons agree by and large with the results of precise calculations even in the transverse-momentum region $p_\perp > 5$ GeV/c [7, 14].

Within the fragmentation mechanism, we estimate below the cross section for Ω_{ccc} production at the Tevatron and LHC energies for $p_\perp > 5$ GeV/c and $|y| < 1$.

From the factorization hypothesis, it follows that, in the fragmentation region, the transverse-momentum spectrum of Ω_{ccc} baryons is related to the transverse-momentum spectrum of charmed quarks by the equations

$$\frac{d\sigma}{dp_\perp}(p\bar{p}\longrightarrow\Omega_{ccc}X) = \int_0^1 D_{c\to\Omega_{ccc}}(z,\mu) \times\frac{d\sigma}{dp_{\perp c}}\left(p\bar{p}\longrightarrow cX,\ p_{\perp c} = \frac{p_\perp}{z}\right)dz, \tag{20}$$

$$\frac{d\sigma}{dp_\perp}(p\bar{p}\longrightarrow cX) = 2p_\perp K\int_{y_{\min}}^{y_{\max}}dy\int_{x_{1,\min}}^{1}dx_1\frac{x_1x_2s}{x_1s+u-m_c^2} \times\sum_{i,j}F_i^p(x_1,\mu)F_j^{\bar{p}}(x_2,\mu)\frac{d\hat{\sigma}}{d\hat{t}}(ij-c\bar{c}), \tag{21}$$

where $F_i^p(x_{1,2},\mu)$ and $F_i^{\bar{p}}(x_{1,2},\mu)$ are the quark or gluon distributions, in respectively, the proton and the antiproton, (in the calculations, we use the CTEQ5 parametrization [15]), while K is a phenomenological factor, which is approximately equal to three and which takes effectively into account the contributions of higher order perturbative corrections in α_s. The value of this factor is determined by comparing the results of the calculations in the leading order of perturbation theory with data on b-quark production in $p\bar{p}$ interactions at $\sqrt{s} = 1.8$ TeV.

In the leading order in α_s, the cross sections for the partonic subprocesses are given by

$$\frac{d\hat{\sigma}}{d\hat{t}}(q\bar{q}\longrightarrow c\bar{c}) = \frac{4\pi\alpha_s^2}{9\hat{s}^2}\frac{\hat{t}^2+\hat{u}^2+2m_c^2(2\hat{s}-m_c^2)}{\hat{s}^2}, \tag{22}$$

$$\frac{d\hat{\sigma}}{d\hat{t}}(gg\longrightarrow c\bar{c}) = \frac{\pi\alpha_s^2}{16\hat{s}^2}\Phi_0\left(\frac{8}{3}-6\Phi_1\right), \tag{23}$$

where

$$\Phi_0 = \frac{m_c^2-\hat{t}}{m_c^2-\hat{u}}+\frac{m_c^2-\hat{u}}{m_c^2-\hat{t}} + 4\left(\frac{m_c^2}{m_c^2-\hat{u}}+\frac{m_c^2}{m_c^2-\hat{u}}\right)-4\left(\frac{m_c^2}{m_c^2-\hat{u}}+\frac{m_c^2}{m_c^2-\hat{u}}\right)^2,$$

$$\Phi_1 = \frac{(m_c^2-\hat{t})(m_c^2-\hat{u})}{\hat{s}^2}.$$

By performing a numerical integration on the right-hand side of Eq. (20) for $p_\perp > 5$ GeV/c and $|y| < 1$, we arrive at

$$\sigma(p\bar{p}\longrightarrow\Omega_{ccc},\sqrt{s} = 1.8\text{ TeV}) = 3.6\times10^{-3}\text{ pb}, \tag{24}$$

$$\sigma(p\bar{p}\longrightarrow\Omega_{ccc},\sqrt{s} = 14\text{ TeV}) = 3.45\times10^{-2}\text{ pb}. \tag{25}$$

At integrated luminosities of the Tevatron and LHC about 10^2 and 10^5 pb^{-1}, respectively, we expect less than one event of Ω_{ccc} production per year at the Teva-

tron and some 3.5×10^3 such events per year at the LHC.

In conclusion, we note that the above results have been obtained by using the elastic form factor for the transition $g^* \longrightarrow (cc) + (\bar{c}\bar{c})$. It is obvious that the contribution of the inelastic form factor for $g^* \longrightarrow (cc) + \bar{c} + \bar{c}$ to the production of a single Ω_{ccc} baryon is considerably greater than the contribution of the above elastic form factor. If we assume that the probability of $(\bar{c}\bar{c})$-antidiquark hadronization into a doubly charmed antibaryon is equal to unity, our results actually describe the associated production of a $\Omega_{ccc} + \bar{\Xi}_{cc}$ baryon pair. Roughly, the cross section obtained with the (cc)-diquark inelastic form factor must involve the extra factor

$$\frac{m_c^3}{|\Psi_{cc}|^2} \approx 10^2.$$

Thus, we can conjecture that the cross section for the Ω_{ccc} production is two orders of magnitude larger than the values in (24) and (25). In this case, the number of Ω_{ccc}-production events per year will amount to a few tens at the Tevatron and about 10^5 at the LHC.

Since the present estimate is no more than a lower bound on the event rate for Ω_{ccc} production—more accurate calculations can only increase it—it is highly feasible that Ω_{ccc} production will be observed at the LHC.

ACKNOWLEDGMENTS

I am grateful to A.K. Likhoded and A.P. Martynenko for interest in this study and an enlightening discussion on the problems of heavy-baryon physics.

This work was supported in part by the Russian Foundation for Basic Research (project no. 98-15-96040) and by the Ministry for Higher Education of the Russian Federation (project no. 98-0-6.2-53).

REFERENCES

1. J. G. Korner, D. Pirjol, and M. Kramer, Prog. Part. Nucl. Phys. **33**, 787 (1994).
2. Particle Data Group, Phys. Rev. D **54**, 1 (1996).
3. A. F. Falk, M. Luke, M. Savage, and M. Wise, Phys. Rev. D **49**, 555 (1994).
4. V. V. Kiselev *et al.*, Phys. Lett. B **332**, 411 (1994).
5. S. P. Baranov, Phys. Rev. D **54**, 3228 (1996).
6. A. P. Martynenko and V. A. Saleev, Phys. Lett. B **385**, 297 (1996); Yad. Fiz. **60**, 517 (1997) [Phys. At. Nucl. **60**, 443 (1997)].
7. A. V. Berezhnoy, V. V. Kiselev, A. K. Likhoded, and A. I. Onishchenko, Phys. Rev. D **57**, 4385 (1998).
8. S. P. Baranov, Phys. Rev. D **56**, 3046 (1997).
9. M. Beneke, M. Kramer, and M. Vanttinen, Preprint CERN-TH/97-235 (1997); G. A. Schuler, Preprint CERN-TH 7179/94 (1994).
10. V. A. Saleev, Phys. Lett. B **426**, 384 (1998); Izv. Vyssh. Uchebn. Zaved., Fiz. **42**, 66 (1999).
11. E. Braaten, K. Cheung, and T. C. Yan, Phys. Rev. D **48**, 4230 (1993).
12. W. Lucha and F. F. Schoberl, Preprint HEPHY-Pub 703/98 (1998); hep-ph/9811453.
13. A. Martin, Phys. Lett. B **93**, 338 (1980).
14. M. A. Doncheski, J. Steegborn, and M. L. Stong, Preprint OCIP/C-95-8; hep-ph/9507220.
15. CTEQ Collab., hep-ph/9903282.

Translated by R. Rogalyov

Physics of Atomic Nuclei, Vol. 63, No. 9, 2000, pp. 1635–1639. From Yadernaya Fizika, Vol. 63, No. 9, 2000, pp. 1722–1727.

ELEMENTARY PARTICLES AND FIELDS
Theory

Fine-Structure Splittings of Excited *P*- and *D*-Wave States in Charmonium*

A. M. Badalian, V. L. Morgunov, and B. L. G. Bakker[1)]

Institute of Theoretical and Experimental Physics, Bol'shaya Cheremushkinskaya ul. 25, Moscow, 117259 Russia

Received December 16, 1999

Abstract—It is shown that, in the relativistic case, the fine-structure splittings of the excited 2^3P_J and 3^3P_J states in charmonium are as large as those of the 1^3P_J state if the same value of $\alpha_s(\mu) \approx 0.36$ is used. The predicted mass of $M(2^3P_0) = 3.84$ GeV appears to be 120 MeV lower than the center of gravity of the 2^3P_J multiplet and lies below the $D\bar{D}^*$ threshold. Our value of $M(2^3P_0)$ is nearly 80 MeV lower than that from the Godfrey and Isgur article [Phys. Rev. D **32**, 189 (1985)], while the differences in other masses are not greater than 20 MeV. © *2000 MAIK "Nauka/Interperiodica".*

1. INTRODUCTION

At present, only the 1^3D_1 and 2^3D_1 states lying above the $D\bar{D}$ threshold have been identified with the experimentally observed $c\bar{c}$ mesons, $\psi(3770)$ and $\psi(4160)$. Still, a large number of other excited *P*- and *D*-wave states above the flavor threshold were predicted. Their masses and fine-structure splittings were calculated by Godfrey and Isgur in 1985 within the relativistic approach [1]. Also, the properties of *P*- and *D*-wave levels in charmonium and bottomonium were intensively studied in the nonrelativistic approximation [2, 3]. There is the point of view that one or more charmonium $2P_J$ states can be sufficiently narrow to have a substantial branching ratio for the $\gamma + \psi(2S)$ channel [4, 5] and could play a role in the hadronic production of $\psi(2S)$ mesons. In particular, 2*P* states can be related to the enhancement observed in the $J/\psi\pi^+\pi^-$ system near $M = 3.84$ GeV in [6] (but not confirmed by another group, [7]). Therefore, precise knowledge of their masses is especially important.

A precise description of the charmonium spectrum and of the fine-structure splittings of the 1*P* level was presented in [8, 9], where the relativistic kinematics was taken into account, as in [1], by means of the spinless Salpeter equation. As was shown in [9], relativistic corrections to the matrix elements, like $\langle r^{-3}\rangle$, defining the spin structure, are on the order of 40%; therefore, the nonrelativistic approach cannot be considered as an appropriate one in investigating the spin structure.

We will show here that, in the relativistic approach, spin–orbit and tensor splittings are sufficiently large for *P*-wave states, both for the ground state and for excited levels. This result depends weakly on the choice of the strong-coupling constant $\alpha_s(\mu)$. Here, the value of $\alpha_s(\mu) \approx 0.36$ ($\mu = 0.92$ GeV) will be used for all states, but the splittings remain virtually unchanged if one takes $\alpha_s(\mu) = 0.30$ ($\mu = m = 1.48$ GeV).

The fine-structure splittings predicted here appear to be larger than those in [1], especially for the 2*P* and 3*P* states. (The reasons for this will be discussed in Section 3.) As a result, the 2^3P_0 mass, $M(2^3P_0) = 3.84$ GeV, in our case is nearly 80 MeV smaller than that in [1], and this level lies below $D\bar{D}^*$ threshold. The $2^3P_{1,2}$ levels have mass values close to the Godfrey–Isgur predictions, and so do n^3D_J states. For the first time, we also predict large fine-structure splittings for the 3*P* states.

2. SPIN-AVERAGED SPECTRUM

The relativistic effects in charmonium are not expected to be small, especially for the wave functions and matrix elements in which we are mostly interested here. In order to find the spin-averaged spectrum, the spinless Salpeter equation will therefore be solved as was already done in several studies [1, 10, 11]:

$$[2\sqrt{p^2 + m^2} + V_0(r)]\psi_{nl}(r) = M_{nl}\psi_{nl}(r). \qquad (1)$$

The static interaction $V_0(r)$ will be taken in the form of the Cornell potential

$$V_0(r) = -\frac{4}{3}\frac{\tilde{\alpha}}{r} + \sigma r + C_0, \qquad (2)$$

and the values of $\tilde{\alpha} \equiv \alpha_V(\mu)$, the string tension σ, and the pole mass of the *c* quark will be taken as in [8] in a fit to the fine structure of the 1*P* charmonium state,

$$m = 1.48 \text{ GeV}, \ \sigma = 0.18 \text{ GeV}^2, \ \tilde{\alpha} = 0.42. \qquad (3)$$

On the basis of a fit to the spin-averaged mass of 1*S* state, $\bar{M}(1S) = 3067.6$ MeV [12], the constant C_0 in (2)

* This article was submitted by the authors in English.
[1)] Free University, Amsterdam, The Netherlands.

Table 1. Spin-average masses $\bar{M}(nL)$ (in MeV) in charmonium for two sets of parameters

$\bar{M}(nL)$	Godfrey, Isgur [1]	This paper	Experiment
	m = 1.628 GeV, σ = 0.18 GeV^2, α_{cr} = 0.6 (running $\alpha(r)$), C_0 = –253 MeV	m = 1.48 GeV, σ = 0.18 GeV^2, $\tilde{\alpha}$ = 0.42, C_0 = –140 MeV	
$\psi(1S)$	3067.5	3067.6	3067.0 ± 0.6
$\psi(2S)$	3665	3659*	3663 ± 1.3
$\psi(3S)$	4090	4077**	4040 ± 10
$\psi(4S)$	4450	4425	4415 ± 6
$\psi(5S)$		4732	
$\chi_c(1P)$	3520	3528	3525.5 ± 0.4
$\chi_c(2P)$	3960	3962	
$\chi_c(3P)$		4320	
$M(1D)$	3840	3822	3768.9 ± 2.5
$M(2D)$	4210	4194	4159 ± 20
$M(3D)$	4520	4519.5	

* Mixing of 2*S*- and 1*D*-wave states is not taken into account.

** Mixing of 3*S*- and 2*D*-wave states is not taken into account.

was fixed at C_0 = –140.2 MeV. In our approach, the strong-coupling constant $\tilde{\alpha}$ in the potential (2) was taken to be invariable, while, in general, it depends on the distance r. In perturbation theory, valid at small distances, the static potential in coordinate space was calculated in the one-loop approximation some years ago [13] and was recently deduced in the two-loop approximation in momentum and coordinate spaces [14, 15]. These perturbative expressions for $\alpha_s(r)$ can be used if $r \ll \Lambda_R^{-1} \approx 0.3$ fm, whereas the sizes of nP and nD states in charmonium are significantly larger; for example, their root-mean-square radii $R(nL) = \sqrt{\langle r^2 \rangle_{nL}}$ are the following:

$$R(1P) \cong 0.65 \text{ fm}, \; R(2P) \cong 1.0 \text{ fm}, \; R(3P) \cong 1.3 \text{ fm},$$

$$R(1D) \cong 0.85 \text{ fm}, \; R(2D) \cong 1.2 \text{ fm}.$$

It was indicated in [8] that, at such large distances, the influence of vacuum background fields must be taken into account and that the strong-coupling constant in background-field theory, denoted as $\alpha_B(r)$, is modified. At distances $r \gtrsim 0.4$ fm, $\alpha_B(r)$ approaches the constant or the freezing value $\alpha_B(r \longrightarrow \infty)$. The estimates in [8] yield $\alpha_B(\infty) \approx 0.40$–$0.45$, and, as soon as the point r = 0.6 fm is achieved, the difference $\delta\alpha_B(r)$,

$$\alpha_B(r) = \tilde{\alpha} + \delta\alpha_B(r), \quad \tilde{\alpha} = \text{const}, \qquad \delta\alpha_B(r) = \alpha_B(r) - \tilde{\alpha}, \tag{4}$$

appears to be less than 3%. To a high precision, the effective constant can therefore be taken to be $\tilde{\alpha} \approx 0.40$–$0.45$.

The parameters chosen as in (3) can be compared with the parameters from [1], where m = 1.628 GeV, while σ = 0.18 GeV^2 coincides with σ in (3). For α, Godfrey and Isgur used the running coupling constant whose critical value of $\alpha_{cr} = \alpha(r = 0) = 0.60$ is greater than the constant $\tilde{\alpha}$ = 0.42 in our case. Also, C_0 = –253 MeV in [1], whereas C_0 = –140 MeV in our calculations.

Nevertheless, the calculated spin-averaged masses for the two parameter sets are close to each other: the differences are less than 10 MeV for *P*-wave states and less than 20 MeV for *D*-wave states (see Table 1).

In many studies, charmonium excited states were analyzed in the nonrelativistic approximation [16], which works quite well for the spectrum. It was shown in [8, 9], however, that relativistic corrections to matrix elements like $\langle r^{-3} \rangle$ and $\langle r^{-3} \ln(mr) \rangle$, which determine fine-structure splittings, are sufficiently large, about 30–40%. That is why only relativistic calculations of fine-structure splittings of charmonium excited states will be considered in this article.

3. FINE-STRUCTURE PARAMETERS OF *P*-WAVE LEVELS

Although the spin-averaged masses in our calculations are very close to those in [1], we expect that spin–orbit and tensor splittings of *P*-wave states will be larger in our case. There are two reasons for this. First, the second-order α_s corrections will be taken into account here. Second, our calculations of various matrix elements have shown that, for excited *P*-wave states, the matrix element $\langle r^{-3} \rangle$, which determines splittings, does not decrease. For the parameter set in (3), it was found that, in the relativistic case, $\langle r^{-3} \rangle_{1P} = 0.142$,

$\langle r^{-3}\rangle_{2P} = 0.157$, and $\langle r^{-3}\rangle_{3P} = 0.167$ GeV^3—that is, $\langle r^{-3}\rangle_{nP}$ even increase for $2P$ and $3P$ states. This result is peculiar to the Salpeter equation; in the nonrelativistic case, the matrix elements $\langle r^{-3}\rangle$ for excited states decrease—for example, $\langle r^{-3}\rangle_{1P} = 0.101$, $\langle r^{-3}\rangle_{2P} = 0.093$, and $\langle r^{-3}\rangle_{3P} = 0.089$ GeV^3. The accuracy of our calculations was checked to be $(1–2)\times 10^{-4}$.

The fine-structure parameters are defined as the matrix elements of the spin–orbit and tensor interactions,

$$a = \langle \tilde{V}_{LS}(r)\rangle, \quad c = \langle \tilde{V}_T(r)\rangle, \tag{5}$$

where the scalar functions $\tilde{V}_{LS}(r)$ and $\tilde{V}_T(r)$ are introduced as

$$\hat{V}_{LS}(r) = \tilde{V}_{LS}(r)\mathbf{L}\cdot\mathbf{S},$$
$$\hat{V}_T(r) = \tilde{V}_T(r)\hat{S}_{12}, \quad \hat{S}_{12} = 3(\mathbf{s}_1\cdot\mathbf{n})(\mathbf{s}_2\cdot\mathbf{n}) - \mathbf{s}_1\mathbf{s}_2, \tag{6}$$
$$\mathbf{n} = \frac{\mathbf{r}}{r}.$$

Here, the spin–orbit parameter a is defined in the same manner as in other studies, whereas the definition of the tensor parameter c differs from that in [1], where the tensor parameter is $T = (1/2)c$, and from that in [2], where $b = 4c$.

In our calculations, we assume that the P-wave hyperfine splitting is small, as is the case for the $h_c(1P)$ meson, for which the hyperfine shift relative to the center of gravity of the ^3P_J multiplet, $\overline{M}(1^3P_J)$, is less than 1 MeV. When hyperfine splitting is neglected, the mass of the $S = 0$ states coincides with the center of gravity of the ^3L_J multiplet denoted as $\overline{M}_L$. Their values, taken from Table 1, are

$$M(1^1P_1) = 3528 \text{ MeV}, \quad M(2^1P_1) = 3962 \text{ MeV},$$
$$M(1^1D_2) = 3822 \text{ MeV}, \quad M(2^1D_2) = 4194 \text{ MeV}, \tag{7}$$

which are by about 20 MeV lower than in [1] for D- and some S-wave states.

For $S = 1$, $L \neq 0$ states, the mass of a state can be represented as

$$M(^3P_J) = \overline{M}_L + a\langle \mathbf{L}\cdot\mathbf{S}\rangle + c\langle \hat{S}_{12}\rangle, \tag{8}$$

where the operator $\hat{S}_{12}$ is defined as in (6). For P-wave states, this yields

$$M(^3P_2) = \overline{M}_1 + a - 0.1c,$$
$$M(^3P_1) = \overline{M}_1 - a + 0.5c, \tag{9}$$
$$M(^3P_0) = \overline{M}_1 - 2a - c.$$

Godfrey and Isgur [1] took into account only first-order terms in α_s and, for a and c, obtained the values

$$a(1P) = 28 \text{ MeV}, \; c(1P) = 26 \text{ MeV}, \tag{10}$$

$$a(2P) \approx 17 \text{ MeV}, \; c(2P) \approx 8 \text{ MeV}. \tag{11}$$

These are about 20% and 30% less than the currently existing experimental values for the $1P$ state [8, 12]:

$$a_{\exp}(1P) = 34.56 \pm 0.19 \text{ MeV},$$
$$c_{\exp}(1P) = 39.12 \pm 0.62 \text{ MeV}. \tag{12}$$

In our approach, we will take into account second-order terms in α_s and represent the total values of a and c as

$$a_{\text{tot}} = a_{\text{P}}^{(1)} + a_{\text{P}}^{(2)} + a_{\text{NP}},$$
$$c_{\text{tot}} = c_{\text{P}}^{(1)} + c_{\text{P}}^{(2)} + c_{\text{NP}}, \tag{13}$$

where the nonperturbative contribution to spin–orbit splitting coming from linear confining potential is

$$a_{\text{NP}} = -\frac{\sigma}{2m^2}\langle r^{-1}\rangle. \tag{14}$$

In the tensor splitting (13), the small nonperturbative term c_{NP} will be neglected (see the discussion in [9]). In order to consider perturbative contributions, Godfrey and Isgur [1] introduced some smearing of short-range potentials at small distances, but this generates additional unknown parameters. Here, we consider spin-effects as a perturbation using explicit analytic expressions for spin–orbit and tensor potentials in coordinate space within the $\overline{MS}$ renormalization scheme from [13]. The first-order terms in α_s, $a_{\text{P}}^{(1)}$ and $c_{\text{P}}^{(1)}$, are

$$a_{\text{P}}^{(1)} = \frac{2\alpha_s(\mu)}{m^2}\langle r^{-3}\rangle, \quad c_{\text{P}}^{(1)} = \frac{4}{3}\frac{\alpha_s(\mu)}{m^2}, \tag{15}$$

while the second-order perturbative corrections are

$$a_{\text{P}}^{(2)} = \frac{2\alpha_s^2(\mu)}{\pi m^2}\left\{4.5\ln\frac{\mu}{m}\langle r^{-3}\rangle + 2.5\langle r^{-3}\ln(mr)\rangle + 1.582\langle r^{-3}\rangle\right\}, \tag{16}$$

$$c_{\text{P}}^{(2)} = \frac{4\alpha_s^2(\mu)}{3\pi m^2}\left\{4.5\ln\frac{\mu}{m}\langle r^{-3}\rangle + 1.5\langle r^{-3}\ln(mr)\rangle + 3.449\langle r^{-3}\rangle\right\}. \tag{17}$$

The second-order expressions are given here for $n_f = 3$, where n_f is the number of flavors. Our calculations have shown that, at $n_f = 4$, the values of a and c remained virtually unchanged (the differences are less than 0.5 MeV); therefore, only the $n_f = 3$ case will be presented here.

With the solutions to the Salpeter equation (1), all matrix elements defined by (14)–(17) can be calculated, and the only uncertainty comes from the choice

Table 2. Spin–orbit and tensor splittings a and c (in MeV) for P and D levels

	Godfrey, Isgur*	This paper $\alpha_s(\mu) = 0.365$	Experiment
$a(1P)$	28	34.56	34.56 ± 0.19
$c(1P)$	26	39.12	39.12 ± 0.62
$a(2P)$	17	38.7	
$c(2P)$	8	41.5	
$a(3P)$		42.3	
$c(3P)$		44.0	
$a(1D)$	≈ 5	3.64	
$c(1D)$	≈ 10	10.94	
$a(2D)$	≈ 5	5.43	
$c(2D)$	≈ 10	11.37	

* The values of a, c for $2P$ and D states are extracted from the masses $M(^3D_J)$ and $M(2^3P_J)$ given in [1].

Table 3. Masses of n^3P_J and n^3D_J states (in MeV) in charmonium

	Godfrey, Isgur*	This paper $\alpha_s(\mu) = 0.365$	Experiment
2^3P_0	3920	3843	
2^3P_1	3950	3944	
2^3P_2	3980	3996	
3^3P_0		4192	
3^3P_1		4300	
3^3P_2		4358	
1^3D_1	3820	3800*	3768.9 ± 2.5
1^3D_2	3840	3823	
1^3D_3	3850	3827	
2^3D_1	4190	4167**	4159 ± 20
2^3D_2	4210	4195	
2^3D_3	4220	4204	

* Mixing of $2S$- and $1D$-wave states is not taken into account.
** Mixing of $3S$- and $2D$-wave states is not taken into account.

of the strong-coupling constant $\alpha_s(\mu)$ and the value of renormalization scale μ. In [9], it was found that, for the charmonium $1P$ state, the value

$$\alpha_s(\mu) = 0.365 \ (\mu = 0.92 \text{ GeV}) \tag{18}$$

gives a precise description of spin splittings. For excited $2P$ and $3P$ states, where there are no experimental data, we will also use the same value in (18) for $\alpha_s(\mu)$. The main argument in favor of this choice can be taken from a fine-structure analysis in bottomonium, where the values of $\alpha_s(\mu)$ for $1P$ and $2P$ states differ by only about 20% [17].

With $\alpha_s(\mu) = 0.365$ for the $1P$ state in [8], it was found that

$$\begin{aligned} a_{\rm P}^{(1)}(1P) &= 47.6 \text{ MeV}, \quad a_{\rm P}^{(2)}(1P) = 3.6 \text{ MeV}, \\ a_{\rm NP}(1P) &= -16.6 \text{ MeV}, \quad c_{\rm P}^{(1)}(1P) = 31.7 \text{ MeV}, \\ c_{\rm P}^{(2)}(1P) &= 7.4 \text{ MeV}, \end{aligned} \tag{19}$$

so that $a_{\rm tot}(1P)$ and $c_{\rm tot}(1P)$ just agree with their experimental values in (12).

For the excited $2P$ state, the spin–orbit and tensor parameters are as large as those for the $1P$ state, because the matrix element $\langle r^{-3}\rangle_{2P}$ is even about 10% larger than $\langle r^{-3}\rangle_{1P}$ for the $1P$ state. Here, we face the difference between the relativistic approach and the nonrelativistic one for which matrix elements like $\langle r^{-3}\rangle_{nP}$ decrease with increasing $n = n_r + 1$. For the $2P$ state, our calculations yield

$$\begin{aligned} a_{\rm P}^{(1)}(2P) &= 52.5 \text{ MeV}, \quad a_{\rm P}^{(2)}(2P) = -0.4 \text{ MeV}, \\ a_{\rm NP}(2P) &= -13.4 \text{ MeV}, \quad c_{\rm P}^{(1)}(2P) = 35.0 \text{ MeV}, \\ c_{\rm P}^{(2)}(2P) &= 6.5 \text{ MeV}, \end{aligned} \tag{20}$$

so that

$$a_{\rm tot}(2P) = 38.7 \text{ MeV}, \ c_{\rm tot}(2P) = 41.5 \text{ MeV} \tag{21}$$

are even slightly greater than the corresponding values for the $1P$ state.

Comparing the values obtained for $a(2P)$ and $c(2P)$ with those in (11) from [1], one can see that a and c in our calculations are, respectively, twice and fivefold as great as the corresponding Godfrey–Isgur values (see also Table 2). This discrepancy is partly due to the inclusion of the second-order radiative corrections, which are not large. But even with only first-order perturbative terms, our values of $a(2P)$ and $c(2P)$ are much greater than the values in (11).

With the values of a and c from (21) and with $\overline{M}_1(2P) = 3962$ MeV from Table 1, the masses of the 2^3P_J states can be calculated to be

$$\begin{aligned} M(2^3P_0) &= 3843 \text{ MeV}, \\ M(2^3P_1) &= 3944 \text{ MeV}, \\ M(2^3P_2) &= 3997 \text{ MeV}. \end{aligned} \tag{22}$$

Our predicted mass of the 2^3P_0 state, $M(2^3P_0) = 3.84$ GeV, appeared to be about 80 MeV less than that in [1]; for the other two states, 2^3P_1 and 2^3P_2, the predicted masses only slightly differ from the Godfrey–Isgur values (see Table 3) owing to the cancellation of terms having opposite signs.

It is important that, in our calculations, the 2^3P_0 level lies below the $D\overline{D}^*$ threshold [$M_{\rm thr}(D\overline{D}^*) \approx 3.87$ GeV] but higher than $M_{\rm thr}(D\overline{D}) = 3.73$ GeV. This fact can affect the 2^3P_0-state decay rates.

For the $3P$ state, we again use $\alpha_s(\mu) = 0.365$ and $\mu = 0.92$ GeV (as for the $1P$ state); from (14)–(17), we can then obtain

$$a_P^{(1)}(3P) = 56.7 \text{ MeV}, \quad a_P^{(2)}(3P) = -3.6 \text{ MeV},$$
$$a_{NP}(3P) = -11.8 \text{ MeV}, \quad c_P^{(1)}(3P) = 37.8 \text{ MeV}, \tag{23}$$
$$c_P^{(2)}(3P) = 6.2 \text{ MeV} \quad (c_{NP} = 0),$$

so that

$$a_{tot}(3P) = 42.3 \text{ MeV}, \; c_{tot}(3P) = 44.0 \text{ MeV}. \tag{24}$$

With these values of a and c and the spin-averaged mass $\overline{M}_1(3P) = 4320$ MeV, it follows that

$$M(3^3P_1) = 4300 \text{ MeV}, \quad M(3^3P_2) = 4358 \text{ MeV}, \tag{25}$$
$$M(3^3P_0) = 4192 \text{ MeV}.$$

The level 3^3P_0 lies 128 MeV lower than the center of gravity of the 3^3P_J multiplet. It is of interest that the difference $M(n^3P_2) - M(n^3P_0) \equiv \Delta(nP) = 3a + 0.9c$ is large in all cases, slightly increasing for excited states,

$$\Delta(1P) = 138.9 \text{ MeV}, \quad \Delta(2P) = 143 \text{ MeV}, \tag{26}$$
$$\Delta(3P) = 166 \text{ MeV}.$$

We have checked the sensitivity of the predicted values of a and c to the choice of the renormalization scale μ and of $\alpha_s(\mu)$. To this end, we considered the commonly used value of $\mu = m$, which leads to $\alpha_s(\mu = m = 1.48 \text{ GeV}) = 0.29$. We then obtain $a_{tot}(2P) = 36.5$ MeV and $c_{tot}(2P) = 37.5$ MeV for the $2P$ state and $a_{tot}(3P) = 40.5$ MeV and $c_{tot}(3P) = 39.8$ MeV for the $3P$ state. These results are very close to the values in (20), (21), (23), and (24) with $\mu_0 = 0.92$ GeV and $\alpha_s(\mu_0) = 0.365$, which were found in [8] from a fit to the fine-structure splittings of the $1P$ states.

4. FINE-STRUCTURE SPLITTINGS OF D-WAVE LEVELS

For D-wave states, the expressions for the masses $M(n^3D_J)$ in terms of the parameters a and c can be found in [2]:

$$M(^3D_1) = \overline{M}_2 - 3a - 0.5c,$$
$$M(^3D_2) = \overline{M}_2 - a + 0.5c, \tag{27}$$
$$M(^3D_3) = \overline{M}_2 + 2a - \frac{1}{7}c.$$

For the spin-averaged masses $\overline{M}(nD)$, our calculations with the parameters from (3) yield

$$\overline{M}_2(1D) = 3822 \text{ MeV}, \; \overline{M}_2(2D) = 4194 \text{ MeV}. \tag{28}$$

All fine-structure parameters, a and c, for D-wave levels are given in Table 2, along with their values from [1]. As can be seen from Table 2, the values of a and c virtually coincide in the two cases. Still, our predicted masses for the 1^3D_J and 2^3D_J states appear to be about 20 MeV lower than those in [1] because of the smaller value of the spin-averaged masses.

5. CONCLUSIONS

Our analysis has led to the following conclusions:

(i) In the relativistic case, the fine-structure splittings of charmonium $S = 1$ P-wave states are much larger than those in the nonrelativistic case.

(ii) For the excited $2P$ states, the fine-structure parameters are even slightly larger than those for the ground 1^3P_J state.

(iii) The mass of the n^3P_0 state ($n = 1, 2, 3$) appears to be about 130 MeV lower than the center of gravity of the n^3P_J multiplet. This fact can be important for explaining decays of charmonium excited states.

Our predicted value of $M(2^3P_0) = 3.84$ GeV is about 80 MeV lower than that in [1]. This state lies below the $D\overline{D}^*$ threshold and only about 100 MeV higher than the $D\overline{D}$ threshold. There exists the point of view that this state could be very broad because it lies above the $D\overline{D}$ threshold and should therefore have a large hadronic width [18]. On the other hand, this state lies relatively close to the $D\overline{D}$ threshold, and the phase space could be suppressed. Therefore, this state could play a role in the production of $\psi(2S)$ charmonium mesons as was discussed in [5, 6].

REFERENCES

1. S. Godfrey and N. Isgur, Phys. Rev. D **32**, 189 (1985).
2. W. Kwong and J. L. Rosner, Phys. Rev. D **38**, 279 (1988).
3. A. K. Grant *et al.*, Phys. Rev. D **53**, 2742 (1996).
4. F. E. Close, Phys. Lett. B **342**, 369 (1995).
5. P. Cho, M. B. Wise, and S. P. Trivedi, Phys. Rev. D **51**, 2039 (1995).
6. L. Antoniazzi *et al.*, Phys. Rev. D **50**, 4258 (1994).
7. A. Gribushin *et al.*, Phys. Rev. D **53**, 4723 (1996).
8. A. M. Badalian and V. L. Morgunov, Phys. Rev. D **60**, 116008 (1999); hep-ph/9901430.
9. A. M. Badalian and V. L. Morgunov, Yad. Fiz. **62**, 1086 (1999) [Phys. At. Nucl. **62**, 1019 (1999)].
10. S. Jacobs, M. G. Olsson, and C. Suchyta, Phys. Rev. D **33**, 3338 (1986).
11. L. P. Fulcher, Phys. Rev. D **44**, 2079 (1991); **50**, 447 (1994).
12. Particle Data Group, Eur. Phys. J. C **3** (1998).
13. J. Pantaleone, S.-H. H. Tye, and Y. J. Ng, Phys. Rev. D **33**, 777 (1986).
14. M. Peter, Phys. Rev. Lett. **78**, 602 (1997); Y. Schröder, Phys. Lett. B **447**, 321 (1999).
15. M. Melles, hep-ph/0001295.
16. F. Halzen *et al.*, Phys. Rev. D **47**, 3013 (1993).
17. A. M. Badalian and B. L. G. Bakker, hep-ph/0004021.
18. H.-W. Huang and K.-T. Chao, Phys. Rev. D **54**, 6850 (1996).

Physics of Atomic Nuclei, Vol. 63, No. 9, 2000, pp. 1640–1645. Translated from Yadernaya Fizika, Vol. 63, No. 9, 2000, pp. 1728–1733.

ELEMENTARY PARTICLES AND FIELDS
Theory

Perturbative Fragmentation of a Vector Color Particle into Bound States Involving a Heavy Antiquark

V. V. Kiselev* and A. E. Kovalsky[1)]

Institute for High Energy Physics, Protvino, Moscow oblast, 142284 Russia

Received May 19, 1999

Abstract—Vector-particle fragmentation into possible *S*-wave bound states involving a heavy antiquark is considered for high-energy processes at high transverse momenta, and the relevant fragmentation function is calculated in the leading order of perturbative QCD for various patterns of the anomalous magnetic moment. One-loop equations describing the q^2 evolution of the fragmentation-function moments that is caused by hard-gluon emission from the vector particle are derived. The integrated probabilities of fragmentation are obtained. The distribution of the bound state in the transverse momentum defined with respect to the fragmentation axis is calculated in the scaling limit. © *2000 MAIK "Nauka/Interperiodica".*

1. INTRODUCTION

Investigation of the production of hadrons containing leptoquarks [1]—that is, scalar and vector particles appearing in various Grand Unified Theories in the form of color triplets if their total width is less than the QCD confinement scale, $\Gamma_{LQ} \ll \Lambda_{\mathrm{QCD}}$—is of interest in connection with inquiries into the properties inherent in interactions beyond the Standard Model. In [2], the production of $(\bar{q}LQ)$ baryons is discussed for the scalar-leptoquark case.

In the present article, we study the production of baryons involving a vector leptoquark. Within QCD, the leptoquark represents a local triplet vector field; therefore, our results can be used to calculate vector-diquark fragmentation into baryons. For the sake of convenience, a local triplet vector field will be referred to below as a leptoquark.

Here, we have to solve the new problem of choosing the Lagrangian for the interaction of a vector color particle with a gluon field. For this, the Lagrangian obtained by extending the derivatives in the free-vector-field Lagrangian $-1/2H_{\mu\nu}\bar{H}^{\mu\nu}$, where $H_{\mu\nu} = \partial_\mu U_\nu - \partial_\nu U_\mu$, U_μ being a complex vector field, can be supplemented with a gauge-invariant term proportional to $S^{\alpha\beta}_{\mu\nu} G^{\mu\nu} U_\beta \bar{U}_\alpha$, where $S^{\alpha\beta}_{\mu\nu} = 1/2(\delta^\alpha_\mu\delta^\beta_\nu - \delta^\alpha_\nu\delta^\beta_\mu)$ is the spin tensor, and $G^{\mu\nu}$ is the gluon-field strength tensor. This leads to a certain parameter (anomalous magnetic moment—see Section 2) in the leptoquark–gluon interaction vertex. In the present study, we consider the effect of this parameter on the high-energy production of a spin-1/2 bound state involving a heavy vector particle.

At high transverse momenta, the production of heavy-leptoquarkonium bound states is dominated by leptoquark fragmentation, which can be calculated within perturbative QCD [3] upon isolating the factor of soft bound-state production as obtained within nonrelativistic potential models [4, 5]. The relevant fragmentation function appears to be universal for any high-energy process resulting in direct leptoquarkonium production.

In the leading order in α_s, the fragmentation function has a scaling form, which provides the initial condition for perturbative QCD evolution caused by hard-gluon emission from the leptoquark prior to hadronization. The relevant splitting function differs from that for a heavy quark because of the spin structure of gluon coupling to the leptoquark, which is a color-triplet vector particle.

This article is organized as follows. In Section 2, the scaling fragmentation function is calculated in the leading order of perturbation theory for two different types of behavior of the anomalous magnetic moment. The limit of an infinitely heavy leptoquark, $m_{LQ} \longrightarrow \infty$, is obtained from a QCD analysis of fragmentation. In Section 3, the distribution of the heavy quarkonium in the transverse momentum defined with respect to the fragmentation axis is calculated in the leading order of perturbative QCD. In Section 4, we derive the splitting kernel within Dokshitzer–Gribov–Lipatov–Altarelli–Parisi (DGLAP) evolution and obtain and solve one-loop renormalization-group equations for the fragmentation-function moments. These equations appear to be universal since they do not depend on whether the leptoquark occurs in a free or a bound state in the low-virtuality region, where the perturbative-evolution regime ceases to be valid. In Section 5, we determine the integrated probabilities of leptoquark fragmentation into

* e-mail: kiselev@mx.ihep.su

[1)] Moscow Institute of Physics and Technology, Institutskiĭ proezd 9, Dolgoprudnyĭ, Moscow oblast, 141700 Russia.

heavy leptoquarkonia. The results of this study are summarized in the Conclusion.

2. FRAGMENTATION FUNCTION IN THE LEADING ORDER

The fragmentation contribution to direct heavy-leptoquarkonium production is given by

$$d\sigma[l_H(p)] = \int_0^1 dz d\hat{\sigma}[LQ(p/z), \mu] D_{LQ\to l_H}(z, \mu),$$

where $d\sigma$ and $d\hat{\sigma}$ are the differential cross sections for, respectively, the production of a quarkonium of 4-momentum p and the hard production of a leptoquark of 4-momentum p/z, while $D(z)$ is the fragmentation function dependent on the momentum fraction z carried away by the bound state. The quantity μ specifies the factorization scale. According to the general pattern of DGLAP evolution, the μ-dependent fragmentation function satisfies the equation

$$\frac{\partial D_{LQ\to l_H}(z,\mu)}{\partial \ln \mu} = \int_z^1 \frac{dy}{y} P_{LQ\to LQ}(z/y, \mu) D_{LQ\to l_H}(y, \mu), \quad (1)$$

where P is a kernel that is controlled by hard-gluon emission from the leptoquark until a heavy-quark pair is formed. Therefore, the initial form of the fragmentation function is determined by the diagram in Fig. 1, so that the relevant initial factorization scale is $\mu = 2m_Q$. Moreover, this function can be obtained within an expansion in $\alpha_s(2m_Q)$. The leading-order contribution is calculated in this section.

We now consider the fragmentation diagram in the reference frame where the initial-quark momentum is $q = (q_0, 0, 0, q_3)$ and where the initial leptoquarkonium momentum is p, so that

$$q^2 = s, \quad p^2 = M^2.$$

Within the static approximation, the masses of the heavy quark and of the leptoquark in their bound state satisfy the relations $m_Q = rM$ and $m = (1 - r)M = \bar{r}M$. The vertex for vector-leptoquark interaction with a gluon is given by

$$T^{VVg}_{\alpha\mu\nu} = -ig_s t^a [g_{\mu\nu}(q + \bar{r}p)_\alpha - g_{\mu\alpha}((1+\kappa)\bar{r}p - \kappa q)_\nu - g_{\nu\alpha}((1+\kappa)q - \kappa\bar{r}p)_\mu], \quad (2)$$

where κ is the anomalous magnetic moment and t^a is the generator of the QCD group in the fundamental representation.

The sum over the polarizations of the vector leptoquark of momentum q ($q^2 = s$) depends on the choice of gauge in the free-field Lagrangian (this can be, for example, the Stückelberg gauge), but the physical quantity under calculation (the fragmentation function) is independent of the gauge parameter, which affects the form of the contribution of the longitudinal field components. Without loss of generality, the sum over polarizations can then be chosen in the form

$$P(q)_{\mu\nu} = -g_{\mu\nu} + \frac{q_\mu q_\nu}{s}.$$

The matrix element for fragmentation into a spin-1/2 state has the form

$$\mathcal{M} = -\frac{2\sqrt{2\pi}\alpha_s}{9\sqrt{M^3}} \frac{R(0)}{r\bar{r}(s-m^2)^2} P(q)_{\nu\delta} P(\bar{r}p)_{\mu\eta} \times T^{VVg}_{\alpha\mu\nu} \rho_{\alpha\beta} \bar{q}\gamma^\beta (\hat{p} - M)\gamma^\eta \gamma^5 l_H \mathcal{M}_0^\delta, \quad (3)$$

where the sum over gluon polarizations is written in the axial gauge with $n = (1, 0, 0, -1)$,

$$\rho_{\mu\nu}(k) = -g_{\mu\nu} + \frac{k_\mu n_\nu + k_\nu n_\mu}{kn},$$

and $k = q - (1 - r)p$. The spinors l_H and $\bar{q}$ correspond, respectively, to the leptoquarkonium and to the heavy quark accompanying fragmentation. The quantity $\mathcal{M}_0$ stands for the matrix element for high-energy hard leptoquark production, while $R(0)$ is the value of the radial wave function at the origin. Upon squaring the matrix elements and performing summation over the helicities of the final particles, we arrive at

$$|\overline{M}|^2 = W_{\mu\nu} M_0^\mu M_0^\nu.$$

In the high-energy limit $qn \longrightarrow \infty$, $W_{\mu\nu}$ assumes the form

$$W_{\mu\nu} = -g_{\mu\nu} W + R_{\mu\nu}, \quad (4)$$

where $R_{\mu\nu}$ can depend on the gauge parameters. Upon an expansion in the Lorentz structures, R leads to scalar quantities that are much smaller than W. We define

$$z = \frac{pn}{qn}.$$

The fragmentation function has the form [6]

$$D(z) = \frac{1}{16\pi^2} \int ds \theta\left(s - \frac{M^2}{z} - \frac{m_Q^2}{1-z}\right) W,$$

where W is given by (4). At a constant anomalous magnetic moment not equal to –1, the integral appearing in the expression for the fragmentation function diverges logarithmically. Here, we consider two types of behavior of the anomalous magnetic moment. The first is $\kappa = -1$, in which case the resulting fragmentation function

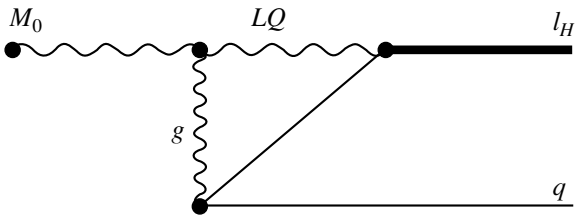

Fig. 1. Diagram for leptoquark fragmentation into a heavy leptoquarkonium.

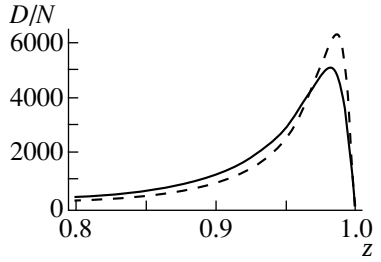

Fig. 2. Leptoquark fragmentation function for heavy-leptoquarkonium production: (dashed curve) $\kappa = -1$ and (solid curve) $1 + \kappa = 3M^2/(s - m_{LQ}^2)$. The factor N is given by the expression $N = \dfrac{8\alpha_s^2}{243\pi}\dfrac{|R(0)|^2}{M^3 r^2 (1-r)^2}$ ($r = 0.02$).

coincides, apart from a spin factor of 1/3, with that for the scalar leptoquark;[2)] that is,

$$D(z) = \frac{8\alpha_s^2}{243\pi}\frac{|R(0)|^2}{M^3 r^2 \bar{r}^2}\frac{z^2(1-z)^2}{[1-\bar{r}z]^6} \times \{3 + 3r^2 - (6 - 10r + 2r^2 + 2r^3)z + (3 - 10r + 14r^2 - 10r^3 + 3r^4)z^2\}. \quad (5)$$

For $r \longrightarrow 0$ and $y = (1 - (1 - r)z)/(rz)$, expression (5) tends to

$$\tilde{D}(y) = \frac{8\alpha_s^2}{243\pi y^6}\frac{|R(0)|^2}{m_Q^3}\frac{(y-1)^2}{r}\{8 + 4y + 3y^2\}. \quad (6)$$

The limiting form $\tilde{D}(y)$ is obtained in accordance with the general consideration of an $1/m$ expansion for the fragmentation function [7], where

$$\tilde{D}(y) = \frac{1}{r}a(y) + b(y).$$

It should be noted that the resulting y dependence is identical to that for heavy-quark fragmentation into a quarkonium [6].

[2)] An incorrect sign appeared in [2] because of an arithmetic error, but this error affects the final result insignificantly in the small-r region considered there.

In the other case under consideration, κ behaves as $-1 + AM^2/(s - m_{LQ}^2)$. The resulting fragmentation function is given by

$$D(z) = \frac{8\alpha_s^2}{243\pi}\frac{|R(0)|^2}{16M^3 r^2 \bar{r}^2}\frac{z^2(1-z)^2}{[1-\bar{r}z]^6} \times \{16(3 + 3r^2 - 6z + 10rz - 2r^2 z - 2r^3 z + 3z^2 - 10z^2 r + 14z^2 r^2 - 10z^2 r^3 + 3z^2 r^4) + A(3A + 24r - 6zA - 2rzA - 32rz - 16r^2 z + 3z^2 A + 2z^2 rA + 8z^2 r + 3z^2 r^2 A - 32z^2 r^2 + 24z^2 r^3)\}. \quad (7)$$

For $r \longrightarrow 0$ and $y = (1 - (1 - r)z)/(rz)$, it tends to

$$\tilde{D}(y) = \frac{8\alpha_s^2}{243\pi 16y^6}\frac{|R(0)|^2}{m_Q^3}\frac{(y-1)^2}{r}\{16(8 + 4y + 3y^2) + A(8A - 8yA + 3y^2 A - 64 + 16y)\}. \quad (8)$$

The perturbative fragmentation functions calculated in the leading order in α_s are displayed in Fig. 2 at $r = 0.02$. They represent rather hard distributions, which become softer upon taking into account evolution (see [2]).

3. TRANSVERSE MOMENTUM OF THE LEPTOQUARKONIUM

In the reference frame where the momentum of the fragmenting leptoquark is infinitely high, its invariant mass can be expressed in terms of the leptoquarkonium longitudinal-momentum fraction z and the transverse momentum p_T with respect to the fragmentation axis. In this way, we arrive at (see Fig. 1)

$$s = m^2 + \frac{M^2}{z(1-z)}[(1 - (1-r)z)^2 + t^2],$$

where $t = p_T/M$. Evaluation of the diagram in Fig. 1 yields the double distribution for the fragmentation probability in the form

$$\frac{d^2P}{dsdz} = \mathcal{D}(z, s),$$

where $\mathcal{D}$ is written as

$$\mathcal{D}(z, s) = \frac{256\alpha_s^2}{81\pi}\frac{|R(0)|^2}{r^2\bar{r}^2}\frac{M^3}{[1-\bar{r}z]^2(s-m^2)^4} \times \left\{r\bar{r}^2 + \bar{r}(1 + r - z(1 + 4r - r^2)) \times \frac{s-m^2}{M^2} - z(1-z)\left(\frac{s-m^2}{M^2}\right)^2\right\} \quad (9)$$

in the case of $\kappa = -1$ and as

$$\mathcal{D}(z,s) = \frac{8\alpha_s^2}{81\pi}\frac{|R(0)|^2}{r^2\bar{r}^2}\frac{M^3}{[1-\bar{r}z]^2(s-m^2)^4}$$
$$\times\Big\{8r(A-4+4r)^2(1-z+rz)^2$$
$$+2(-A-4-4r+zA+4z-rzA+16rz-4r^2z)\times(1-z+rz)(A-4+4r)\frac{s-m^2}{M^2}$$
$$-32(1-z)z\left(\frac{s-m^2}{M^2}\right)^2\Big\} \quad (10)$$

in the case of $\kappa = -1 + AM^2/(s - m_{LQ}^2)$.

It can then be easily seen that the transverse-momentum distribution can be obtained by means of integration with respect to z:

$$D(t) = \int_0^1 dz\mathcal{D}(z,s)\frac{2M^2t}{z(1-z)}.$$

For the first case, this yields

$$D(t) = \frac{64\alpha_s^2}{81\pi}\frac{|R(0)|^2}{3(1-r)^5M^3}\frac{1}{t^6}$$
$$\times\Big\{t\Big(30r^3-30r^4-61t^2r+45r^2t^2+33r^3t^2$$
$$-17r^4t^2+3t^4-9rt^4+15r^2t^4-9r^3t^4)$$
$$-(30r^4-99r^2t^2-54r^3t^2+27r^4t^2+9t^4$$
$$+18rt^4-6r^2t^4+18r^3t^4+3r^4t^4+3t^6$$
$$-6rt^6+9r^2t^6)\arctan\left(\frac{(1-r)t}{r+t^2}\right)$$
$$+24(2r^3t+rt^3+r^2t^3)\ln\left(\frac{r^2(1+t^2)}{r^2+t^2}\right)\Big\}. \quad (11)$$

The distribution for the second case at $A = 3$ is presented in the Appendix. A typical shape of the distributions of leptoquarkonia in the transverse momentum as defined with respect to the leptoquark-fragmentation axis is illustrated in Fig. 3.

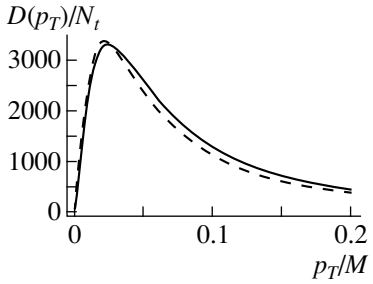

Fig. 3. Distribution of leptoquarkonia in the transverse momentum defined with respect to the axis of leptoquark-fragmentation into a heavy leptoquarkonium for the $(\bar{b}LQ)$ state with $r = 0.02$: (dashed curve) $\kappa = -1$ and (solid curve) $\kappa = -1 + 3M^2/(s - m_{LQ}^2)$. The factor N_t is given by the expression $N_t = \frac{8\alpha_s^2}{81\pi}\frac{|R(0)|^2}{M^4r^2(1-r)^7}$.

4. HARD-GLUON EMISSION

The one-loop contribution of hard-gluon emission can be calculated by the same method as that described in the preceding sections. This contribution depends only on that part of the leptoquark–gluon interaction vertex which is independent of the anomalous magnetic moment. Hence, the splitting kernel for a vector leptoquark coincides with that for a scalar leptoquark and has the form

$$P_{LQ\to LQ}(x,\mu) = \frac{4\alpha_s(\mu)}{3\pi}\left[\frac{2x}{1-x}\right]_+, \quad (12)$$

where the plus symbol denotes the following standard operation: $\int_0^1 dx f_+(x)g(x) = \int_0^1 dx f(x)[g(x) - g(1)]$. The splitting function can be compared with the analogous function for a heavy quark,

$$P_{Q\to Q}(x,\mu) = \frac{4\alpha_s(\mu)}{3\pi}\left[\frac{1+x^2}{1-x}\right]_+,$$

which has the same normalization factor for $x \longrightarrow 1$.

By multiplying the evolution equation by z^n and integrating the result with respect to z, we can find from (1), within the renormalization-group method, that, in the one-loop approximation, the μ dependence of the fragmentation-function moments $a_{(n)}$ is governed by the equation

$$\frac{\partial a_{(n)}}{\partial \ln\mu} = -\frac{8\alpha_s(\mu)}{3\pi}\left[\frac{1}{2}+\ldots+\frac{1}{n+1}\right]a_{(n)}, \quad n \geq 1. \quad (13)$$

At $n = 0$, the right-hand side of (13) is equal to zero. This implies that the integrated probability of leptoquark fragmentation into a heavy leptoquarkonium does not change in the course of evolution, being specified by the initial fragmentation function calculated above within perturbative QCD [2].

A solution to (13) has the form

$$a_{(n)}(\mu) = a_{(n)}(\mu_0)\left[\frac{\alpha_s(\mu)}{\alpha_s(\mu_0)}\right]^{\frac{16}{3\beta_0}\left[\frac{1}{2}+\ldots+\frac{1}{n+1}\right]}, \quad (14)$$

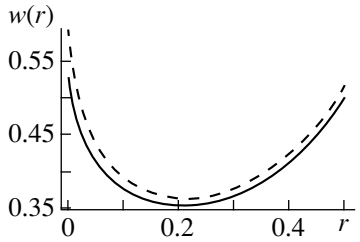

Fig. 4. Function w for vector-leptoquark fragmentation into a heavy leptoquarkonium as a function of the ratio $r = m_Q/M$: (dashed curve) $\kappa = -1$ and (solid curve) $\kappa = -1 + 3M^2/(s - m_{LQ}^2)$.

where we have used the one-loop expression

$$\alpha_s(\mu) = \frac{2\pi}{\beta_0 \ln(\mu/\Lambda_{\mathrm{QCD}})}$$

for the QCD coupling constant with $\beta_0 = 11 - 2n_f/3$, n_f being the number of flavors of quarks with mass values $m_q < \mu < m_{LQ}$.

The relation in (14) is universal since it does not depend on whether the leptoquark is free or bound at virtuality values less than μ_0. In the present study, we take into account evolution in fragmentation into a heavy leptoquarkonium. The leptoquark can lose up to about 20% of its momentum before undergoing hadronization [2].

5. INTEGRATED FRAGMENTATION PROBABILITIES

As was indicated above, the integrated fragmentation probability remains unchanged throughout the evolution process and admits an explicit evaluation. The result is

$$\int dz D(z) = \frac{8\alpha_s^2}{81\pi} \frac{|R(0)|^2}{16m_Q^3} w(r). \tag{15}$$

For the first of the cases considered above, we obtain

$$w(r) = \frac{16[(8 + 15r - 60r^2 + 100r^3 - 60r^4 - 3r^5) + 30r(1 - r + r^2 + r^3)\ln r]}{15(1-r)^7}. \tag{16}$$

For the second case at $A = 3$, we arrive at

$$w(r) = \{(143 + 701r - 1882r^2 + 3250r^3 - 3245r^4 + 2017r^5 - 936r^6 - 48r^7) + 30r(25 - 21r + 43r^2 + r^3 + 8r^4 + 16r^5)\ln r\}\frac{1}{15(1-r)^9}. \tag{17}$$

The functions $w(r)$ for small r values are displayed in Fig. 4.

6. CONCLUSION

We have studied the production of spin-1/2 bound states of a local color vector field (referred to by convention as a leptoquark) with a heavy antiquark in high-energy processes at high transverse momenta, in which case fragmentation appears to be a dominant production mechanism. In doing this, we have considered two types of behavior of the anomalous magnetic moment. The first is that of $\kappa = -1$ (at any other constant value of the anomalous magnetic moment, the integral appearing in the expression for the fragmentation function diverges). In this case, the fragmentation function coincides, apart from a factor, with that for scalar-color-particle fragmentation into a bound state involving a heavy quark and has the form

$$D(z) = \frac{8\alpha_s^2}{243\pi} \frac{|R(0)|^2}{M^3 r^2 \bar{r}^2} \frac{z^2(1-z)^2}{[1-\bar{r}z]^6} \times \{3 + 3r^2 - (6 - 10r + 2r^2 + 2r^3)z + (3 - 10r + 14r^2 - 10r^3 + 3r^4)z^2\},$$

where r is the ratio of the quark mass to the bound-state mass. In the limit of an infinitely heavy leptoquark, $D(z)$ takes a form consistent with what is expected from a general consideration of the $1/m$ expansion of the fragmentation function. In the second case, $\kappa = -1 + AM^2/(s - m_{LQ}^2)$, the fragmentation function assumes the different form

$$D(z) = \frac{8\alpha_s^2}{243\pi} \frac{|R(0)|^2}{16M^3 r^2 \bar{r}^2} \frac{z^2(1-z)^2}{[1-\bar{r}z]^6} \times \{16(3 + 3r^2 - 6z + 10rz - 2r^2z - 2r^3z + 3z^2 - 10z^2r + 14z^2r^2 - 10z^2r^3 + 3z^2r^4) + A(3A + 24r - 6zA - 2rzA - 32rz - 16r^2z + 3z^2A + 2z^2rA + 8z^2r + 3z^2r^2A - 32z^2r^2 + 24z^2r^3)\}.$$

This distribution function will be employed in the subsequent study to calculate the heavy-quark fragmentation function for baryon production. The distribution of leptoquarkonia in the transverse momentum defined with respect to the leptoquark-fragmentation axis has also been calculated in the leading order of perturbative QCD. The relative distributions are given by (11) and by the corresponding expression from the Appendix for the first and the second case, respectively. Hard-gluon corrections caused by vector-leptoquark

splitting can be taken into account perturbatively. The evolution kernel then assumes the form

$$P_{LQ\to LQ}(x,\mu) = \frac{4\alpha_s(\mu)}{3\pi}\left[\frac{2x}{1-x}\right]_+,$$

which leads to the corresponding one-loop equation for the fragmentation-function moments [see equations (13) and (14)].

According to numerical estimates, the probability of fragmentation into the bound states of a heavy vector leptoquark of mass about 300 GeV with c and b quarks, amounts to 10^{-4}–10^{-3}. In view of this suppression, it is rather hard to observe the above states experimentally. Nevertheless, we can employ perturbative expressions as models for fragmentation into hadrons involving light and strange quarks, in which case the bound-state-formation probabilities are as large as a few tens of percent. In this sense, it is of interest to consider the production of doubly heavy baryons via the fragmentation of heavy diquarks consisting of two heavy quarks, but this will be the subject of our further studies.

ACKNOWLEDGMENTS

The work was supported in part by the Russian Foundation for Basic Research (project nos. 99-02-16558 and 96-15-96575).

APPENDIX

For the case of $\kappa = -1 + 3M^2/(s - m_{LQ}^2)$, the transverse-momentum distribution of leptoquarkonia is given by

$$D(t) = \frac{8\alpha_s^2}{81\pi}\frac{|R(0)|^2}{3(1-r)^7M^3t^6}$$

$$\times\left\{30r^3t - 270r^4t + 720r^5t - 480r^6t - 727t^3r\right.$$

$$+ 2441r^2t^3 - 2041r^3t^3 - 65r^4t^3 + 664r^5t^3$$

$$- 272r^6t^3 + 129t^5 - 285t^5r$$

$$+ 477r^2t^5 - 489r^3t^5 + 312r^4t^5 - 144r^5t^5$$

$$- [30r^4 - 240r^5 + 480r^6 + t^2(-909r^2 + 2412r^3$$

$$- 45r^4 - 1080r^5 + 432r^6) + t^4(171 + 288r$$

$$- 492r^2 + 696r^3 - 165r^4 + 264r^5 + 48r^6)$$

$$+ t^6(129 - 156r + 321r^2 - 168r^3 + 144r^4)]$$

$$\times \arctan\left(\frac{(1-r)t}{r+t^2}\right) + 192tr(1-r)$$

$$\left.\times[-2t^2(1-r^2) + (1-4r)r^2]\ln\left(\frac{r^2(1+t^2)}{r^2+t^2}\right)\right\}.$$

REFERENCES

1. W. Buchmüller, R. Rückl, and D. Wyler, Phys. Lett. B **191**, 442 (1987).
2. V. V. Kiselev, Phys. Rev. D **58**, 054008 (1998); V. V. Kiselev, Yad. Fiz. **62**, 335 (1999) [Phys. At. Nucl. **62**, 300 (1999)].
3. E. Braaten, S. Fleming, and T. C. Yuan, Annu. Rev. Nucl. Part. Sci. **46**, 197 (1997).
4. A. Martin, Phys. Lett. B **93**, 338 (1980).
5. W. Buchmüller and S. H. H. Tye, Phys. Rev. D **24**, 132 (1981).
6. E. Braaten and T. C. Yuan, Phys. Rev. Lett. **71**, 1673 (1993); E. Braaten, K. Cheung, and T. C. Yuan, Phys. Rev. D **48**, 4230, 5049 (1993).
7. R. L. Jaffe and L. Randall, Nucl. Phys. B **415**, 79 (1994).

Translated by O. Chernavskaya

Physics of Atomic Nuclei, Vol. 63, No. 9, 2000, pp. 1646–1649. From Yadernaya Fizika, Vol. 63, No. 9, 2000, pp. 1734–1737.

ELEMENTARY PARTICLES AND FIELDS
Theory

Two-Loop Corrections to the Correlation Function for Tensor Currents in Gluodynamics*

A. A. Pivovarov

Institute for Nuclear Research, Russian Academy of Sciences, pr. Shestidesyatiletiya Oktyabrya 7a, Moscow, 117312 Russia

Received June 18, 1999; in final form, September 17, 1999

Abstract—The results of evaluating the leading-order α_s corrections to the correlation function for tensor currents in pure gluodynamics are presented. These corrections to the parton result for the correlation function are not large numerically, which allows one to use perturbation theory to analyze the resonance spectrum within the sum-rule method. © *2000 MAIK "Nauka/Interperiodica".*

Gluonia—hadronic resonances strongly coupled to gauge-invariant operators built from gluon fields—represent a very spectacular manifestation of the color structure of strong interactions. The experimental discovery of these particles would decisively confirm the validity of QCD as a theory of hadrons (see, for example, [1]). Theoretically, information about the properties of gluonia can be obtained (apart from numerical simulations on a lattice) from an analysis based on the sum-rule technique, which requires computing various correlation functions for corresponding gluonic interpolating currents within an operator-product expansion (OPE). An extensive review of gluonia properties is presented in [2], while Borel sum rules and finite-energy sum rules (FESR) were analyzed for the first time in [3–5] (see also [6–10]).

One of the most striking features of perturbation theory used so far to analyze gluonic-current correlation functions within the sum-rule approach is a large scale of higher order corrections. In the case of scalar and pseudoscalar gluonic currents, the next-to-leading-order corrections are too large in the standard $\overline{MS}$ scheme of renormalization and are entirely out of control [11]. In view of this, the applicability of a complete analysis based on OPE is questionable. Perturbation-theory corrections to correlation functions for gluonic currents with other quantum numbers have not been available yet. In the present study, we fill this gap and report on the results for the leading-order correction to the correlation function for tensor gluonic currents in pure gluodynamics [12]. Tensor mesons in full QCD were considered in [13–15].

As to the origin of large corrections in the scalar and pseudoscalar channels, there are serious arguments, based on a consideration of instanton contributions possible in both these channels, that perturbation theory (and OPE) breaks down even at a very large scale. This conclusion was drawn from an analysis of the magnitude of power-law corrections to the gluonic-current correlation functions in the leading-order of perturbation theory [3, 4]. Perturbation-theory corrections are also large in both channels [11]. On the other hand, the interaction of instantons with tensor gluonic currents is thought to be much weaker (no direct instanton contribution to the correlation function is possible because of the unsuitable quantum numbers $J^{PC} = 2^{++}$), and one expects that perturbation-theory corrections are not too large and that OPE is still applicable at momenta considerably smaller than those for the (pseudo)scalar case. The results of the present study strictly confirm this expectation: the computation shows that perturbation-theory corrections to the correlation function for tensor gluonic currents are not large and that the expansion is valid at smaller scales than in the case of the scalar and pseudoscalar gluonic currents.

To analyze the resonance spectrum in the channel of tensor gluonic mesons, one considers a two-point correlation function for gluonic operators that have a nonzero projection onto the $J^{PC} = 2^{++}$ hadronic state. The gauge-invariant interpolating current for the tensor gluonium, $j_{\mu\nu}$, is chosen in the explicit form

$$j_{\mu\nu} = G^a_{\mu\alpha}G^a_{\alpha\nu} + \frac{1}{4}g_{\mu\nu}G^2, \quad a = 1, \ldots, N_c^2 - 1, \quad (1)$$

where

$$G_{\mu\nu} = [D_\mu, D_\nu] = G^a_{\mu\nu}t^a, \quad D_\mu = \partial_\mu - ig_sA_\mu,$$
$$A_\mu = A^a_\mu t^a.$$

Here, $G_{\mu\nu}$ is the gluon-field strength, A_μ is the gluon field, D_μ is the covariant derivative, and t^a are the generators of the color gauge symmetry group $SU(N_c)$ that are normalized by the relation

$$\mathrm{tr}(t^at^b) = \frac{1}{2}\delta^{ab},$$

where G^2 is the condensed notation for $G^a_{\mu\nu}G^a_{\mu\nu}$. The current $j_{\mu\nu}$ coincides with the energy–momentum ten-

* This article was submitted by the author in English.

sor for pure gluodynamics. It is symmetric and traceless at the tree level and is conserved owing to the equations of motion for the gluon fields. These properties lead to some linear constraints on the components of the tensor $j_{\mu\nu}$. These constraints effectively kill the superfluous components of the general two-index tensor in four-dimensional spacetime and preserve just the necessary number of components to describe five polarization states of a massive spin-2 meson in four-dimensional spacetime. Radiative corrections are known to destroy this perfect picture and lead to the trace anomaly of the form [16–19]

$$j^{\mu}_{\mu} = \frac{\beta(\alpha_s)}{2\alpha_s}G^2, \tag{2}$$

where $\beta(\alpha_s)$ is the standard renormalization-group beta function describing the evolution of the running coupling constant. While a rigorous proof of the relation for the trace anomaly requires more delicate definitions of the quantities entering into (2), there is a simple mnemonic rule to recover the proper normalization of the right-hand side of it. In D-dimensional spacetime (with $D = 4 - 2\varepsilon$), one finds formally from (1) with $g^{\mu}_{\mu} = D$ that

$$j^{\mu}_{\mu} = \frac{D-4}{4}G^2 = -\frac{\varepsilon}{2}G^2. \tag{3}$$

Recalling that the D-dimensional β_ε function is given by the expression $\beta_\varepsilon(\alpha_s) = -\varepsilon\alpha_s + O(\alpha_s^2)$ and substituting $\varepsilon = -\beta_\varepsilon(\alpha_s)/\alpha_s$ into the expression on the right-hand side of (3), one reproduces the correctly normalized form on the right-hand side of (2) upon noticing that $\lim_{\varepsilon\to 0}\beta_\varepsilon(\alpha_s) = \beta(\alpha_s)$.

The emergence of a nonzero trace of the gluonic operator in (1) means that the operator has a nonvanishing projection onto scalar hadronic states as well.

In terms of Green's functions, this means that the correlation function

$$T_{\mu\nu,\alpha\beta}(q) = i\int dx e^{iqx}\langle Tj_{\mu\nu}(x)j_{\alpha\beta}(0)\rangle \tag{4}$$

receives contributions not only from the $J^{PC} = 2^{++}$ tensor mesons but also from the $J^{PC} = 0^{++}$ states (scalar gluonium). Therefore, the correlation function (4) is not described by a single scalar function when radiative corrections are included. The most general tensor decomposition of the correlation function (4) has the form

$$T_{\mu\nu,\alpha\beta}(q) = \eta_{\mu\nu,\alpha\beta}(q)T(q^2) + f_{\mu\nu,\alpha\beta}(q)T_S(q^2), \tag{5}$$

where the tensor object $\eta_{\mu\nu,\alpha\beta}(q)$ is defined in terms of the elementary transverse tensors

$$\eta_{\mu\nu} = q_\mu q_\nu - q^2 g_{\mu\nu}$$

by the expression

$$\eta_{\mu\nu,\alpha\beta}(q) = \eta_{\mu\alpha}\eta_{\nu\beta} + \eta_{\mu\beta}\eta_{\nu\alpha} - \frac{2}{3}\eta_{\mu\nu}\eta_{\alpha\beta}. \tag{6}$$

The quantity $\eta_{\mu\nu,\alpha\beta}(q)$ is the density (polarization) matrix for a spin-2 particle, which determines the structure of its propagator in the momentum space. It possesses the inherent properties

$$\begin{aligned} q^{\mu}\eta_{\mu\nu,\alpha\beta}(q) = 0, \quad q^{\alpha}\eta_{\mu\nu,\alpha\beta}(q) = 0, \\ \eta_{\mu\mu,\alpha\beta}(q) = 0, \quad \eta_{\mu\nu,\alpha\alpha}(q) = 0. \end{aligned} \tag{7}$$

Note that the last two relations in (7) are valid only in four-dimensional spacetime. The proper tensor in D-dimensional spacetime, necessary for computations within dimensional regularization, reads

$$\eta^{D}_{\mu\nu,\alpha\beta}(q) = \eta_{\mu\alpha}\eta_{\nu\beta} + \eta_{\mu\beta}\eta_{\nu\alpha} - \frac{2}{D-1}\eta_{\mu\nu}\eta_{\alpha\beta}. \tag{8}$$

It has zero trace and is orthogonal to the quantity $f_{\mu\nu,\alpha\beta}(q)$. However, these two are equivalent to the perturbation-theory order that we use here, and the difference between (6) and (8) is of no importance. The quantity $\eta_{\mu\nu,\alpha\beta}(q)$ is symmetric in both pairs of subscripts $(\mu\nu)$ and $(\alpha\beta)$. The second tensor object entering into (5),

$$f_{\mu\nu,\alpha\beta}(q) = \eta_{\mu\nu}\eta_{\alpha\beta},$$

is the tensor structure related to the contribution of scalar particles. In a more general D-dimensional spacetime, the tensors $f_{\mu\nu,\alpha\beta}(q)$ and $\eta_{\mu\nu,\alpha\beta}(q)$ are not orthogonal to each other. The perturbation-theory expansion of the function $T_S(q^2)$ begins from α_s^2 terms (nonvanishing imaginary part) and is negligible in the (next-to-leading) order in α_s to which we limit ourselves in the present study. The nonvanishing term of this tensor structure emerges because of the trace anomaly. Thus, we conclude that, up to $O(\alpha_s^2)$ terms, the correlation function (4) is determined by the single scalar function $T(q^2)$ related only to the contribution of tensor gluonia. The anomalous dimension of the current $j_{\mu\nu}$ vanishes, which renders the function $T(q^2)$ invariant under renormalization-group transformations.

The results of direct computations of the function $T(q^2)$ are as follows. The leading-order contribution to the function $T(q^2)$ is well known [4]. Within a dimensional regularization, where $D = 4 - 2\varepsilon$ is the spacetime dimensionality, it has the form

$$\frac{N_c^2-1}{(4\pi)^2}\frac{1}{10\varepsilon}\left(\frac{\mu^2}{Q^2}\right)^{\varepsilon}G(\varepsilon), \quad Q^2 = -q^2. \tag{9}$$

Here, the quantity $G(\varepsilon)$ is related to the specific definition of the integration measure in the D-dimensional momentum spacetime and has the series expansion $G(\varepsilon) = 1 + O(\varepsilon)$ at small ε [20], while μ is the 't Hooft mass of dimensional regularization. The factor $N_c^2 - 1$

counts the number of gluons (or partons at this level of computation within perturbation theory) of the color group $SU(N_c)$ that propagate in the single loop to which the correlation function reduces in this order of perturbation theory.

For the amplitude $T(Q^2)$, with allowance for the two-loop perturbation-theory corrections, one finds

$$T(Q^2) = \frac{N_c^2-1}{10(4\pi)^2}\frac{1}{\varepsilon}\left(\frac{\mu^2}{Q^2}\right)^{\varepsilon} G(\varepsilon) \times\left[1+\frac{\alpha_s}{4\pi}N_c\left(-\frac{10}{9}\right)\left(\frac{\mu^2}{Q^2}\right)^{\varepsilon} G(\varepsilon)\right]. \quad (10)$$

This expression represents the main result of the present study. The coefficient of the leading-order correction to the correlation function was first computed in [12] and later confirmed by the independent computation from [21]. The basic method of the computation was described in detail by Kataev *et al.* [11], who considered the scalar and pseudoscalar cases. Relevant diagrams are identical to those in the tensor case. The explicit expressions for vertices and the results for individual diagrams can be found in [12]. The only complication in the present case is associated with the tensor structure of the diagrams. There are several different tensor projection operators that can reduce the necessary expressions to the scalar form. Some relevant integrals can be found in the study of Pivovarov and Popov [22], who considered the correlation function for quark currents with spin *n*. Poles of order ε^2 that are possible at the two-loop level (in α_s order) and which are actually present in the expressions for particular diagrams, cancel in expression (10), as they must because of renormalization-group invariance of the current $j_{\mu\nu}$. For the corresponding *D* function [a derivative of the amplitude $T(Q^2)$], which is multiplicatively renormalized, one has

$$D_T(Q^2) = -Q^2\frac{d}{dQ^2}T(Q^2) = \frac{N_c^2-1}{160\pi^2}\left(1-\frac{\alpha_s}{4\pi}N_c\frac{20}{9}\right). \quad (11)$$

The coefficient of α_s in the last expression is independent of the renormalization scheme used to calculate the amplitude $T(Q^2)$; this can also be seen from the fact that it is not necessary to fix a precise definition of the integration measure: the quantity $G(\varepsilon)$ enters into the final answer only as the factor $G(0) = 1$. Evaluating this coefficient is the actual content of the two-loop calculation of the correlation function (4) and the amplitude $T(q^2)$ in (5), in particular.

For the standard gauge group with $N_c = 3$, we numerically obtain

$$D_T(Q^2) = \frac{1}{20\pi^2}\left[1-\frac{5}{3}\frac{\alpha_s(Q^2)}{\pi}\right]. \quad (12)$$

Thus, the next-to-leading-order correction to the correlation function for tensor gluonic currents is not large, and the perturbation-theory expansion is quite well convergent numerically even at $\alpha_s \approx 0.3$, which corresponds to the scale of ordinary hadrons. A remarkable feature of this correction is its sign. In the majority of cases, α_s corrections are positive, while, for the tensor correlation function for currents (1), it is negative. The inclusion of fermions has a twofold effect: loop corrections through the gluon propagator and mixing with fermionic operators at the tree level. The former effect is trivial (explicit results can be found in [12]), while the latter was discussed in the literature.

The small value of the first-order correction to observables that are renormalization-group-invariant at the parton level is a general feature of hadron phenomenology. The most famous example is the total cross section for e^+e^- annihilation into hadrons, where perturbative corrections in the $\overline{MS}$ scheme are not large, with the leading-order correction being explicitly given by

$$\sigma_{\text{tot}}(e^+e^- \longrightarrow \text{hadrons}) \sim 1 + \frac{\alpha_s}{\pi} + \ldots.$$

However, they can be rather large in the $\overline{MS}$ scheme if corrections depend on the definition of the coupling constant in the channels being considered (as in the case of scalar or pseudoscalar gluonia). In particular, the result for the pseudoscalar gluonium with the interpolating operator

$$j_{PS} = \alpha_s G\tilde{G} = \alpha_s\frac{1}{2}\varepsilon^{\mu\nu\alpha\beta}G^a_{\mu\nu}G^a_{\alpha\beta}$$

is [11]

$$D_{PS}(Q^2) = \frac{2\alpha_s^2(Q^2)}{\pi^2}\left[1+\frac{97}{4}\frac{\alpha_s(Q^2)}{\pi}\right]. \quad (13)$$

The correction of order α_s in (13) is much larger than that in (12), violating the applicability of perturbation theory at momenta close to hadron-resonance masses.

It is worth noting that the functions *D* are defined in Euclidean domain, while the physical spectrum requires the correlation functions to be evaluated on the physical cut. For two-point correlation functions, the analytic properties are well established, and the analytic continuation can be performed in all orders in α_s (see, for example, [23]), which can, however, change the effective numerical value of the total correction in specific applications.

The question of whether the value of corrections reflects the physical situation—the contribution of instantons and an early breakdown of perturbation theory—is still open, urgently requiring a further investigation.

ACKNOWLEDGMENTS

I am grateful to K.G. Chetyrkin for discussions, encouragement, and correspondence.

This work was supported in part by the Volkswagen Foundation (contract no. I/73611) and by the Russian Foundation for Basic Research (project nos. 97-02-17065 and 99-01-00091).

REFERENCES

1. K. Hagiwara, Nucl. Phys. B **137**, 164 (1978).
2. S. Narison, Nucl. Phys. B **509**, 312 (1998); Nucl. Phys. B (Proc. Suppl.) **64**, 210 (1998).
3. V. A. Novikov, M. A. Shifman, A. I. Vainshtein, and V. I. Zakharov, Phys. Lett. B **86**, 347 (1979); Pis'ma Zh. Éksp. Teor. Fiz. **29**, 649 (1979) [JETP Lett. **29**, 594 (1979)]; Nucl. Phys. B **165**, 67 (1980); Acta Phys. Pol. B **12**, 399 (1981).
4. V. A. Novikov, M. A. Shifman, A. I. Vainshtein, and V. I. Zakharov, Nucl. Phys. B **191**, 301 (1981); Fiz. Élem. Chastits At. Yadra **13**, 542 (1982) [Sov. J. Part. Nucl. **13**, 224 (1982)].
5. N. V. Krasnikov, A. A. Pivovarov, and N. N. Tavkhelidze, Z. Phys. C **19**, 301 (1983).
6. C. A. Domínguez and N. Paver, Z. Phys. C **32**, 391 (1986).
7. E. E. Boos, Phys. Lett. B **193**, 301 (1987).
8. F. E. Close, Rep. Prog. Phys. **51**, 833 (1988).
9. E. E. Boos and A. U. Daineka, Phys. Lett. B **283**, 113 (1992).
10. D. Asner, R. B. Mann, J. L. Murison, and T. G. Steele, Phys. Lett. B **296**, 171 (1992).
11. A. L. Kataev, N. V. Krasnikov, and A. A. Pivovarov, Phys. Lett. B **107**, 115 (1981); Nucl. Phys. B **198**, 508 (1982); Erratum: Nucl. Phys. B **490**, 505 (1997).
12. A. A. Pivovarov, PhD Thesis, Moscow, 1985 (unpublished).
13. T. M. Aliev and M. A. Shifman, Yad. Fiz. **36**, 1532 (1982) [Sov. J. Nucl. Phys. **36**, 891 (1982)]; Phys. Lett. B **112**, 401 (1982).
14. E. Bagan, A. Bramon, and S. Narison, Phys. Lett. B **196**, 203 (1987).
15. E. Bagan and S. Narison, Phys. Lett. B **214**, 451 (1988).
16. R. Crewther, Phys. Rev. Lett. **28**, 1421 (1972).
17. M. Chanowitz and J. Ellis, Phys. Lett. B **40**, 397 (1972); Phys. Rev. D **7**, 2490 (1973).
18. S. L. Adler, J. C. Collins, and A. Duncan, Phys. Rev. D **15**, 1712 (1977).
19. J. C. Collins, A. Duncan, and S. D. Joglekar, Phys. Rev. D **16**, 438 (1977).
20. K. G. Chetyrkin, A. L. Kataev, and F. V. Tkachev, Nucl. Phys. B **174**, 345 (1980).
21. K. G. Chetyrkin, private communication.
22. A. A. Pivovarov and E. N. Popov, in *Proceedings of Quarks-84, Tbilisi, 1984*, Vol. 2, p. 135; Phys. Lett. B **205**, 79 (1988).
23. A. A. Pivovarov, Z. Phys. C **53**, 461 (1992); Nuovo Cimento A **105**, 813 (1992).

Physics of Atomic Nuclei, Vol. 63, No. 9, 2000, pp. 1650–1656. From Yadernaya Fizika, Vol. 63, No. 9, 2000, pp. 1738–1744.

ELEMENTARY PARTICLES AND FIELDS
Theory

Restrictions on Exact Current Correlation Functions and Reliability of Sum-Rule Results*

A. A. Pivovarov and A. S. Zubov

Institute for Nuclear Research, Russian Academy of Sciences, pr. Shestidesyatiletiya Oktyabrya 7a, Moscow, 117312 Russia

Received June 18, 1999; in final form, September 17, 1999

Abstract—Criteria of reliability are studied for results obtained within the sum-rule approach in QCD and in some toy models. The criterion of validity of the approximation for current correlation functions based on operator-product expansion within Borel sum rules, suggested previously in the literature, is critically reexamined. A new criterion of validity of a perturbative approximation that makes use of the Källen–Lehmann representation and finite-energy sum rules is proposed. The stability of criteria against small variations in expansion coefficients is investigated in an exactly solvable model and in QCD. © *2000 MAIK "Nauka/Interperiodica".*

1. INTRODUCTION

Quantum chromodynamics (QCD), being a consistent theory of strong interactions and quite successful in describing the properties of hadrons in the high-energy domain within perturbation theory, is not directly applicable in the low-energy region, where resonances are formed. In contrast to electroweak interactions, where the small value of the coupling constant allows one to perform perturbative calculations in good agreement with experimental data, one encounters serious difficulties in computing low-energy processes with hadrons as strongly interacting particles. The QCD coupling constant grows with increasing distances, and perturbation theory is applicable only at high energies, where quarks become asymptotically free owing to small values of the coupling constant. Nonperturbative methods have to be used to study the infrared, or low-energy, region. These include an approach based on dispersion sum rules combining the high-energy behavior of Green's functions described within perturbation theory with the behavior in the low-energy resonance region (see, for example, [1–4]). Although the sum-rule method has proved to be a useful tool for studying various problems arising in elementary-particle physics, the question of its predictive power and of the reliability of the results that it yields has not been ultimately solved. There is no strict quantitative criterion that could allow one to accept or reject definitively a model spectrum that is usually obtained from the sum-rule analysis. In some well-known cases, sum rules lead either to a deeper theoretical understanding of the situation in question or to a better quantitative accuracy than other methods, but the validity of sum-rule results is uncertain to a considerable extent if the qualitative structure of the spectrum in the channel being considered is unknown a priori. The absence of such an estimator for the applicability of the sum-rule method based on the inherent properties of the procedure itself rather than on invoking additional phenomenological information reduces the predictive power of the approach and restricts its applicability in new channels where there is a deficit of experimental data. The difficulty of introducing an estimator that satisfies the natural requirements of reliability lies in the nature of the problem: theoretical simulations of the spectrum from theoretical calculations in the asymptotic region is a nonuniversal procedure. For instance, the method of analytic continuation, which can be used for this purpose, is known to be an ill-posed problem. Various aspects of the reliability problem have been considered since the technique was developed both in realistic cases [5] and in exactly solvable models (see, for example, [6]). In recent years, interest in this problem has been rekindled in connection with more stringent requirements on the accuracy of the predictions and on the reliability of estimates within new physics [7–9].

The present article is devoted to an analysis of a criterion that guarantees the validity of results obtained through the sum-rule method. While there exist a great number of implementations of the general sum-rule idea, we will consider here only finite-energy sum rules (FESR) [3, 10, 11] and Borel sum rules [4] as the most popular techniques for practical applications.

The basic object for analysis within the sum-rule technique is the vacuum expectation value of the chronological product of two hadronic currents,

$$\begin{aligned}\Pi_{\mu\nu}(q) &= (q_\mu q_\nu - q_{\mu\nu}q^2)\Pi(q^2)\\ &= i\int\langle 0|Tj_\mu(0)j_\nu(x)|0\rangle e^{iqx}dx.\end{aligned} \tag{1}$$

In this equation, we have chosen a conserved vector current that leads to the transverse correlation function $\Pi_{\mu\nu}(q)$. The invariant scalar function $\Pi(q^2)$ admits the

* This article was submitted by the authors in English.

standard Källen–Lehmann representation

$$\Pi(q^2) = \int_0^\infty \frac{\rho(s)}{s - q^2} ds, \quad (2)$$

where

$$\rho(s) = [\Pi(s + i\varepsilon) - \Pi(s - i\varepsilon)]/2\pi i$$

is the spectral density. From this representation, it is possible to infer analytic properties of the polarization function $\Pi(z)$: it is an analytic function in the entire complex plane, with the exception of the positive part of the real axis, where a cut is chosen. Equation (2) is an ill-posed problem when considered as an integral equation for the unknown spectral density $\rho(s)$ with the function $\Pi(q^2)$ on the left-hand side. Small variations in the function $\Pi(q^2)$ can lead to arbitrarily large variations of the depending quantity $\rho(s)$.

The sum-rule method provides a way to extract any information about the physical spectrum $\rho(s)$ from the calculation of the polarization function $\Pi(q^2)$. As has been mentioned before, this is not the most correct way because of an unstable solution to the integral equation. Finite-energy sum rules appear after integrating the product $\Pi(z)z^k$ along the contour shown in Fig. 1. The factors z^k have no singularities at positive integral values of k in the entire complex plane, whence it follows that the analytic properties of the product $\Pi(z)z^k$ are identical to those of the polarization operator itself. The basic relation has the form

$$\frac{1}{2\pi i}\int_0^{s_1} \rho(s)s^k ds = -\oint_C \Pi(z)z^k dz. \quad (3)$$

The function $\Pi(z)$ can be computed for large values of the complex variable z that lie sufficiently far from the positive part of the real axis. For a theoretical evaluation, the operator-product expansion in the deep Euclidean region and perturbation theory are used. We denote by $\Pi^{\text{theor}}(z)$ this approximation for $\Pi(z)$. By substituting $\Pi^{\text{theor}}(z)$ for $\Pi(z)$ in (3), we arrive at finite-energy sum rules in the form

$$\int_0^{s_1} \rho(s)\varphi(s)ds = \int_0^{s_1} \rho_{\text{theor}}(s)\varphi(s)ds, \quad (4)$$
$$\varphi(s) = s^k, \quad k = 1, 2, \ldots,$$

where

$$\rho_{\text{theor}}(s) = \frac{1}{2\pi i}[\Pi^{\text{theor}}(s + i\varepsilon) - \Pi^{\text{theor}}(s - i\varepsilon)].$$

Note that, in the massless-quark limit (which is a good approximation for the light-quark sector), the averaging-interval length s_1 is the only dimensional parameter in (4). It determines the scale of the process for a perturbative analysis and enters as a scale into the running coupling constant of strong interactions. Therefore, the simplest (necessary) criterion of validity for the sum rules (4) is the natural inequality $s_1 \gg \Lambda_{\text{QCD}}$ for perturbation theory to converge.

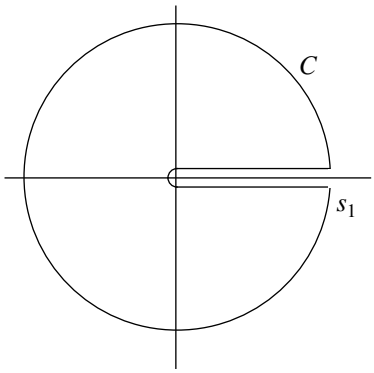

Fig. 1. Contour of integration in the complex plane of the variable q^2.

The shape of the exact spectral density $\rho(s)$ is extracted from experimental data. The hadronic spectrum is usually seen as a set of resonances plus some continuum contribution, and there is some energy gap between these two parts. Therefore, the solution for the spectral density $\rho(s)$ can be sought in the general form

$$\rho(s) = \sum_{i=1}^{n} F_i \delta(s - m_i^2) + \theta(s - s_0),$$

where delta functions represent the resonance contributions and $\theta(s - s_0)$ is the continuum part. Substituting the right-hand side of this expression into (4), one obtains a set of equations for the resonance masses m_i and the coefficients F_i related to the constants of resonances coupling to the interpolating quark–gluon currents. The general criterion for the validity of the results obtained is the existence of well-pronounced resonances closely coupled to the current, as well as the wide energy gap between resonances and the continuum, which begins from the energy s_0; the difference $(s_0 - m_n^2)$ has to be sufficiently large. The FESR method is supplied with a semiphenomenological inclusion of the complex vacuum structure that introduces terms containing nonzero quark and gluon condensates, $\langle \bar{q}q \rangle$ and $\langle \alpha_s G_{\mu\nu}^2 \rangle$, in the expansion of the polarization function $\Pi(q^2)$ [4]. This allows us to deduce useful information about the most important dynamical properties of hadrons [3, 10]. It should also be noted that, because averaging is performed only along a part of the spectrum, these sum rules reflect the local duality between quarks and hadrons. The concept of local duality is different from the pointwise analysis of the spectral density, the latter being the least reliable way to analyze the spectrum theoretically.

It is worth emphasizing that, by choosing the special averaging interval $s_1 = \infty$ and the particular weight function $\varphi(s) = e^{-s/M^2}$ in (4), one can transform the FESR into the Borel sum rules [4]. The introduction of the exponential cutoff suppresses contributions of high states; therefore, the Borel sum rules are applicable only to studying the ground state of the resonance spectrum. To do this, it is necessary to use the criterion of stability of results against variations in the Borel variable M^2 within some proper interval. The Borel sum rules can also be obtained by means of the Borel transformation

$$\hat{B} = \lim_{\substack{n, Q^2 \to \infty, \\ Q^2/n = M^2}} \frac{Q^{2n}}{(n-1)!}\left(\frac{d}{dQ^2}\right)^n \qquad (5)$$

applied to the polarization function $\Pi(Q^2)$ ($Q^2 = -q^2$ is an Euclidean momentum). Because averaging runs through the whole spectrum in this case (at least formally, since the weight function does not vanish everywhere on the real positive semiaxis), this setting reflects the global duality between quarks and hadrons.

2. PREDICTIVE POWER OF SUM RULES AND UNIQUENESS OF THE SOLUTION

The sum-rule method has demonstrated its efficiency for a quantitative improvement of accuracy for some known channels quite successfully. Still, the uniqueness of solutions and the reliability of the results related to prediction of new states remain an important question. There is the question of whether the agreement of a trial resonance spectral density with the asymptotic behavior of the polarization function is a sufficient criterion for the existence of particles with corresponding quantum numbers in nature. This question is definitely an exaggerated quest; still, to some extent, it is the way that sum rules are used. The answer to this question is negative because the solution to the relation

$$\Pi(Q^2) = \int_0^\infty \frac{\rho(s)}{s + Q^2} ds,$$

considered as an integral equation for unknown function $\rho(s)$, is unstable when $\Pi(Q^2)$ is defined only within the interval $Q \in [s_1, \infty]$. This means that some small variations in the function $\Pi(Q^2)$ can induce a noticeable change in the spectral density $\rho(s)$. Because the exact function $\Pi(Q^2)$ is unknown, one should not conclude that a resonance occurs in the real world. Despite these imperfections, the sum rules remain one of a few theoretical tools that is based on the first principles of QCD and which is nearly model-independent. In this respect, it is more similar to the lattice approximation, which is, however, purely numerical. Therefore, the predictive power of the sum-rule method is still of great interest. A situation can emerge where two different spectral densities approximate the same correlation function rather well, although their shapes are not close to each other. This paradox was discovered in the toy model based on the ladder approximation for the correlation functions in four-dimensional spacetime [7]. The paradox is quite straightforward: the phenomenological resonance solution, being in good agreement with the sum rules, is different from the exact one given by the ladder approximation. This is an explicit failure of the sum-rule method to detect the true structure of the spectrum, while the formal requirements of stability for a phenomenological solution are satisfied. Therefore, it would be desirable to have some criterion enabling one to reject the solution given by sum rules or showing that a particular approximation used for the correlation function is wrong. Such criteria are usually based on some general properties of quantum field theory—for instance, positivity of the scalar product or of the state-vector length. A criterion for the Borel sum-rule analysis was considered in [8, 9]. In the present study, we critically reexamine the efficiency of this criterion and propose a new criterion for an FESR analysis.

3. BOREL SUM-RULE CRITERION

The Borel transformation (5) applied to the correlation function (1) with the truncated spectrum from (2) determines the function

$$\begin{aligned} R_k(\tau, s_0) &= \frac{1}{\tau}\hat{B}[(-Q^2)^k \Pi(Q^2)] - \text{continuum} \\ &= \frac{1}{\tau}\hat{B}\left[(-Q^2)^k \int_0^{s_0} \frac{\rho(s)}{s + Q^2} ds\right] = \int_0^{s_0} t^k e^{-t\tau} \rho(t) dt, \end{aligned} \qquad (6)$$

where $\tau = 1/M^2$. In the standard approach based on the stability analysis, the ratio R_1/R_0 gives the mass of the lowest resonance in the simple resonance-plus-continuum model for the spectral density $\rho(s)$. However, the functions $R_k(\tau, s_0)$ are subject to some restrictions following immediately from the general properties of positivity of the spectral density and the functional form of dispersion relations. To formulate the restrictions, we introduce the concept of Hölder's inequality, which, for integrals over the measure $d\mu$, is given by

$$\left|\int_{t_1}^{t_2} f(t) g(t) d\mu\right| \le \left(\int_{t_1}^{t_2} |f(t)|^p d\mu\right)^{1/p} \left(\int_{t_1}^{t_2} |g(t)|^q d\mu\right)^{1/q}, \qquad (7)$$

where

$$\frac{1}{p} + \frac{1}{q} = 1, \quad p, q \ge 1.$$

At $p = q = 2$, the Hölder's inequality reduces to the well-known Schwarz's inequality. The spectral density in (2) is positive (the spectrality condition), which leads to a positive measure of integration and to the applicability of Hölder's inequalities. By choosing

$$\rho(t) dt = d\mu, \quad f(t) = t^\alpha e^{-at\tau}, \quad g(t) = t^\beta e^{-bt\tau}$$

in (6) and applying Hölder's inequality, we find the following restrictions on the physical correlation function:

$$R_{\alpha+\beta}(\tau, s_0) \le R^{1/p}_{\alpha p}(ap\tau, s_0) R^{1/q}_{\beta q}(bq\tau, s_0), \quad a + b = 1. \tag{8}$$

The function $R_k(\tau, s_0)$ on the left-hand side of (6) is well defined only within that area of the (τ, s_0) parameter space where the stability analysis is carried out. Therefore, we can introduce the variable

$$\omega = \frac{\tau_{\max} - \tau}{\delta\tau}, \quad 0 \le \omega \le 1$$

within the interval $[\tau_{\min}, \tau_{\max}]$. Assuming that

$$a = \frac{\tau_{\min}}{\tau}\frac{\tau_{\max} - \tau}{\delta\tau} = \frac{\omega\tau_{\min}}{\omega\tau_{\min} + (1-\omega)\tau_{\max}}$$

and considering that the parameters $k = \alpha + \beta$, α/ω, and $\beta/(1-\omega)$ must take integral values, we obtain the following results at $k = 0, 1$:

$$R_0(\omega\tau_{\min} + (1-\omega)\tau_{\max}, s_0) \le R^{\omega}_0(\tau_{\min}, s_0) R^{1-\omega}_0(\tau_{\max}, s_0), \tag{9}$$

$$R_1(\omega\tau_{\min} + (1-\omega)\tau_{\max}, s_0) \le R^{\omega}_1(\tau_{\min}, s_0) R^{1-\omega}_1(\tau_{\max}, s_0), \tag{10}$$

$$R_0\left(\frac{\tau_{\min} + \tau_{\max}}{2}, s_0\right) \le R^{1/2}_0(\tau_{\min}, s_0) R^{1/2}_2(\tau_{\max}, s_0), \tag{11}$$

$$R_1\left(\frac{\tau_{\min} + \tau_{\max}}{2}, s_0\right) \le R^{1/2}_2(\tau_{\min}, s_0) R^{1/2}_0(\tau_{\max}, s_0), \tag{12}$$

$$0 \le \omega \le 1, \quad \tau_{\min} \le \tau_{\max}.$$

Similar inequalities can be written for $k \ge 2$ as well. However, we restrict ourselves to studying (9) and (10) because, for small $\delta\tau \equiv \tau_{\max} - \tau_{\min}$ (in realistic examples from QCD, $\delta\tau \approx 0.1$ GeV^{-2}), (11) and (12) are generally kept in the first two inequalities. Other relations furnish no additional information of use.

For these Borel sum rules to give reliable and consistent results, it is proposed using them only in that region of the (τ, s_0) parameter space where the following fundamental restrictions are valid:

$$r_0(\omega, s_0) \equiv \frac{R_0(\omega\tau_{\min} + (1-\omega)\tau_{\max}, s_0)}{R^{\omega}_0(\tau_{\min}, s_0) R^{1-\omega}_0(\tau_{\max}, s_0)} \le 1, \quad \forall 0 \le \omega \le 1, \tag{13}$$

$$r_1(\omega, s_0) \equiv \frac{R_1(\omega\tau_{\min} + (1-\omega)\tau_{\max}, s_0)}{R^{\omega}_1(\tau_{\min}, s_0) R^{1-\omega}_1(\tau_{\max}, s_0)} \le 1, \quad \forall 0 \le \omega \le 1. \tag{14}$$

It is worth noting that, for the one-resonance spectral density, the identity $r_0 \equiv r_1 \equiv 1$ holds. Let us apply this criterion to the toy model from [7], where

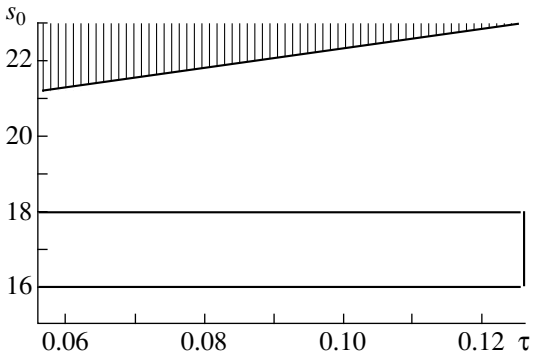

Fig. 2. Toy model. The inequalities are satisfied within the shaded region. The boxed region is the area of stability where we perform a common analysis on the basis of Borel sum rules.

$$R_0(\tau, s_0) = \frac{1 - e^{-s_0\tau}}{\tau} - 6\zeta(3) + 20\zeta(5)\tau - 35\zeta(7)\tau^2 + 42\zeta(9)\tau^3 + \ldots, \tag{15}$$

$$R_1(\tau, s_0) = \frac{1 - (1 + s_0\tau)e^{-s_0\tau}}{\tau^2} - 20\zeta(5) + 70\zeta(7)\tau - 129\zeta(9)\tau^2 + \ldots. \tag{16}$$

Here, $\zeta(n)$ are Riemann zeta functions. The inequalities in (13) and (14) are violated in some area of the (τ, s_0) parameter space. This suggests that the exact spectral density of the model,

$$\rho(s) = 1 + \Delta\rho(s) = 1 - \sum_{N=0}^{\infty} \frac{ns\sqrt{s}}{\sqrt{\frac{4}{n^2} - s}}\theta\left(\frac{4}{n^2} - s\right)\theta(s), \tag{17}$$

is negative within some interval on the positive part of the real axis. The region where $r_0(\omega, s_0) \le 1$ and $r_1(\omega, s_0) \le 1$ is shown in Fig. 2. [In this case, (13) contains (14); $\tau_{\min} = 0.05$, $\tau_{\max} = 0.125$, and, respectively, $\delta\tau = 0.075$ GeV^{-2}.) As one can see, this region does not overlap the area of stability; hence, the analysis employing Borel sum rules is not justified according to our criterion. Thus, there does not arise the paradox of two quite different spectral densities [9].

On the other hand, one has the following (simplified) expressions for the polarization function in the realistic case of the ρ meson:

$$\Pi_{\text{theor}}(Q^2) = -\ln\frac{Q^2}{\mu^2} + \frac{4\pi^2(m_u + m_d)\langle\bar{q}q\rangle}{Q^4} + \frac{\pi^2}{3Q^4}\left\langle\frac{\alpha_s}{\pi}G^2\right\rangle - \frac{896\pi^3}{81Q^6}\langle\sqrt{\alpha_s}\bar{q}q\rangle^2. \tag{18}$$

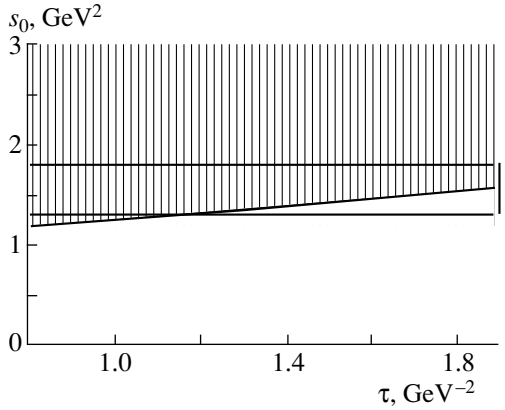

Fig. 3. Region where the inequalities hold for the ρ meson.

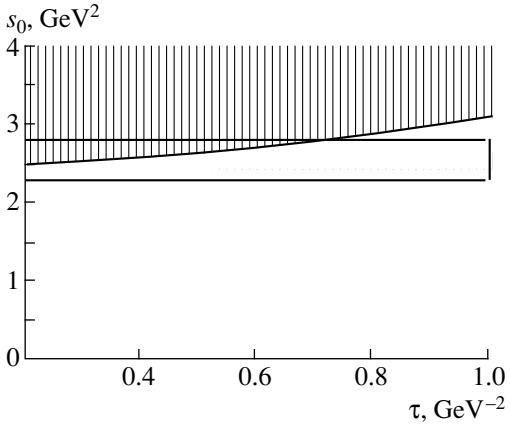

Fig. 4. Region where the inequalities hold for the A_1 meson.

The corresponding results for the quantities $R_0(\tau, s_0)$ and $R_1(\tau, s_0)$ are

$$R_0(\tau, s_0) = \frac{1-e^{-s_0\tau}}{\tau} + \left(8\pi^2 m_u\langle\bar{q}q\rangle + \frac{\pi^2\left\langle\frac{\alpha_s}{\pi}G^2\right\rangle}{3}\right)\tau - \frac{448\pi^3}{81}\langle\sqrt{\alpha_s}\bar{q}q\rangle^2\tau^2, \quad (19)$$

$$R_1 = \frac{1-(1+s_0\tau)e^{-s_0\tau}}{\tau^2} + \left(8\pi^2 m_u\langle\bar{q}q\rangle + \frac{\pi^2\left\langle\frac{\alpha_s}{\pi}G^2\right\rangle}{3}\right) - \frac{896\pi^3}{81}\langle\sqrt{\alpha_s}\bar{q}q\rangle^2\tau. \quad (20)$$

In our model analysis, we use the standard numerical values for the vacuum condensates, $\left\langle\frac{\alpha_s}{\pi}G^2\right\rangle = 0.012$ GeV^4 and $\langle\sqrt{\alpha_s}\bar{q}q\rangle = (-0.25\ \text{GeV})^3$.

In this case (see Fig. 3), the inequalities are valid within some stability region; therefore, the criterion allows one to use Borel sum rules to analyze the system in question [9].

Yet another example familiar from QCD is that of the A_1 meson (axial-vector channel with the ground-state resonance mass of $m = 1.23$ GeV). In this case, the criterion being discussed is also satisfied, and the use of sum rules giving a good agreement with experimental data is justified. The polarization function for the A_1 meson,

$$\Pi_{\text{theor}}(Q^2) = -\ln\frac{Q^2}{\mu^2} - \frac{4\pi^2(m_u+m_d)\langle\bar{q}q\rangle}{Q^4} + \frac{\pi^2}{3Q^4}\left\langle\frac{\alpha_s}{\pi}G^2\right\rangle + 44\pi^3\frac{32}{81Q^6}\langle\sqrt{\alpha_s}\bar{q}q\rangle^2. \quad (21)$$

is well approximated by the two-resonance (π and A_1-mesons) spectral density

$$\rho^{\text{expt}}(s) = 8\pi^2\left[f_\pi^2\delta(s) + \frac{m_{A_1}^2}{f_{A_1}^2}\delta(s-m_{A_1}^2)\right] + \theta(s-s_0),$$

where $4\pi/f_{A_1}^2 = 0.16$, $m_{A_1} = 1.27$ GeV, and $f_\pi = 93$ MeV and f_{A_1} are the coupling constants [$\langle 0|j_\mu^{(A_1)}(0)|\pi(p)\rangle = if_\pi p_\mu$ and $\langle 0|j_\mu^{(A_1)}(0)|A_1(\lambda, p)\rangle = \frac{m_{A_1}^2}{f_{A_1}}\varepsilon_\mu(\lambda, p)$, $\varepsilon_\mu(\lambda, p)$ being A_1-meson polarization]. One can see from Fig. 4 that, in this case, the criterion allows a sum-rule analysis. As is obvious from the examples given above, this criterion allows one to apply the Borel sum rules when the spectral density does contain a resonance and prevents the use of the Borel sum rules in the toy model where there is no resonance.

4. STABILITY OF THE CRITERION AGAINST SMALL VARIATIONS

Let us discuss this criterion in more detail. One of the main properties of this criterion is the stability against small variations in $\Pi_{\text{theor}}(Q^2)$. This is so because the coefficients at powers Q^{-2n} in the theoretical expansion of a correlation function are not known exactly. For instance, only ladder diagrams are taken into account in the toy model, while the numerical values of the quark and gluon condensates in QCD are known only within some uncertainty as well. For example, the most important four-quark correction in correlation functions for ρ- and A_1 mesons is calculated within the factorization hypothesis [4] $\langle\alpha_s\bar{q}^2q^2\rangle \approx \langle\sqrt{\alpha_s}\bar{q}q\rangle^2$ (the use of this relation may result in more than twofold deviations from true values), which brings about a large uncertainty. The criterion mentioned above is unstable. In the toy model, the surface $[x = 1 - r_0(\omega, s_0)]$ is close

to zero; therefore, the area where $r_0(\omega, s_0) \le 1$ depends sizably on the coefficients of $\Pi_{\text{theor}}(Q^2)$. For the criteria to be satisfied everywhere within the stability region, it is therefore sufficient to vary independently the coefficients by some amounts: specifically, changes of –3%, 4%, and –12% in the coefficients at, respectively, the first, the second, and the third power of $1/Q^2$ will suffice. On the other hand, the inequalities become invalid over the whole stability area upon increasing the numerical value of the quark condensate $\langle \alpha_s \bar{q}^2 q^2 \rangle$ for the ρ and the A_1 mesons by 40 and 20%, respectively; hence, the results appear to be inconsistent according to the criterion, but the shape of the spectrum does not change drastically—the resonances do not vanish. Moreover, the agreement with experimental data becomes even better. The variation procedure for the condensate values in the ρ-meson correlation function seems to be quite large, but it is worth emphasizing that the uncertainty in the parameter s_0 (width of the stability rectangle) from [9] is large (25%) as well. Thus, this criterion is not valid from the viewpoint of stability.

5. VALIDITY CRITERION FOR FESR

Let us now consider the FESR method. The criterion of reliability has not yet been formulated in the literature. In this study, we propose one such criterion based on the spectral properties of two correlation functions for vector and axial currents. It is useful to define the function

$$F(Q^2, Q_0^2, s) = [\Pi_s(Q^2) - \Pi_s(Q_0^2)]/(Q_0^2 - Q^2), \quad (22)$$

where

$$\Pi_s(Q^2) = \int_0^s \frac{\rho(s')}{s' + Q^2} ds' = \Pi(Q^2) - \int_s^\infty \frac{\rho(s') ds'}{s' + Q^2} \quad (23)$$

is the correlation function related to the truncated spectral density. By means of the Källen–Lehmann representation, formula (22) can be written as

$$F(Q^2, Q_0^2, s) = \int_0^s \frac{\rho(s')}{(s' + Q^2)(s' + Q_0^2)} ds'.$$

Considering the right-hand side of this relation as an integral of the product of two functions $((s' + Q^2)^{-1}$ and $((s' + Q_0^2)^{-1}$ with the measure $d\mu = \rho(s')ds'$ and using Schwarz's integral inequality, we find that the exact correlation function is constrained as

$$F(Q^2, Q_0^2, s) \le \sqrt{\int_0^s \frac{\rho(s') ds'}{(s' + Q^2)^2} \int_0^s \frac{\rho(s') ds'}{(s' + Q_0^2)^2}} \quad (24)$$

$$= \sqrt{\Pi_s'(Q^2)\Pi_s'(Q_0^2)}$$

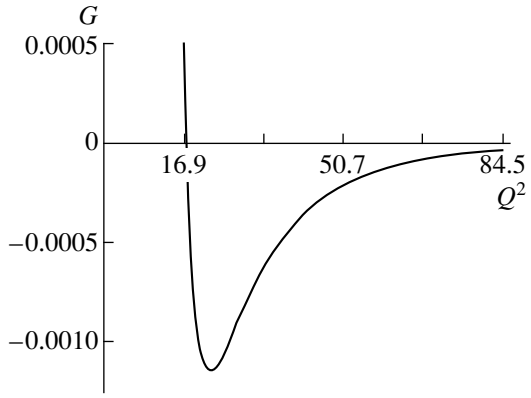

Fig. 5. Function $G(Q^2, 10s_0, s_0)$ in a toy model. The general picture is independent of $Q_0^2 > Q^2$ and s.

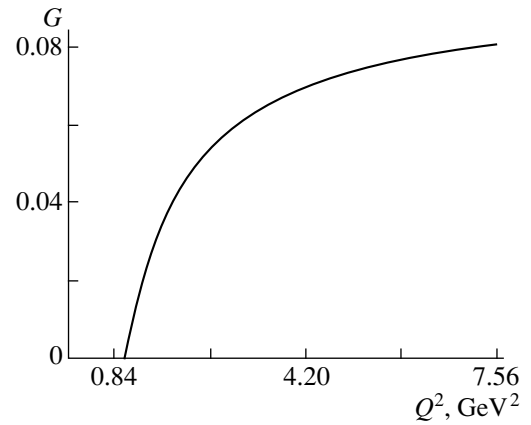

Fig. 6. Function $G(Q^2, 10s_0, s_0)$ for the ρ meson.

with $\Pi_s'(Q^2) = d\Pi_s(Q^2)/dQ^2$. Therefore, this inequality should be satisfied if we calculate the correlation function $\Pi^{\text{theor}}(z)$ within perturbation theory and believe that it is a good approximation to the realistic one in some internal region of momenta. Let us apply this criterion to the FESR. In deriving the sum rules, it is assumed that $\Pi^{\text{theor}}(z)$ is close to $\Pi(z)$ when $|z| > s_1$ [see (3)]; hence, the inequality

$$G(Q^2, Q_0^2, s) = 1 - \frac{\Pi_s^{\text{theor}}(Q^2) - \Pi_s^{\text{theor}}(Q_0^2)}{(Q_0^2 - Q^2)\sqrt{\dfrac{d\Pi_s^{\text{theor}}}{dQ^2}(Q^2)\dfrac{d\Pi_s^{\text{theor}}}{dQ^2}(Q_0^2)}} \ge 0 \quad (25)$$

should be valid in this area. If, however, this inequality is not valid in this region, the sum rules are not applicable. It is worth noting that s_1 must be sufficiently small in order that the continuous part of the spectrum not suppress the resonance contribution, but it must not be overly small in order that we could calculate $\Pi_s(Q^2)$ as the left-hand side of (23). It is reasonable to take it to be

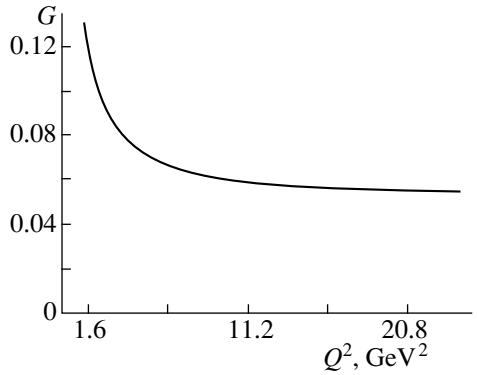

Fig. 7. Function $G(Q^2, 16s_0, s_0)$ for the A_1 meson.

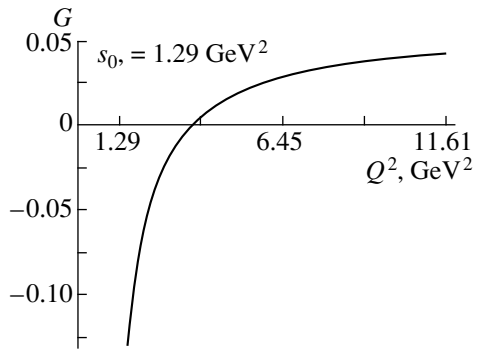

Fig. 8. Function $G(Q^2, 16s_0, s_0)$ for the ρ meson with a quark condensate scaled by a factor of three.

close to s_0. The function $G(Q^2, Q_0^2, s)$ of the toy model of the ρ and A_1 mesons is shown in Figs. 5–7 (the variation of the parameters Q_0^2 and s does not modify the general picture).

One can see that, in contrast to the last two cases, the function $G(Q^2, Q_0^2, s_0)$ in the toy model is negative; that is, $G(Q^2, Q_0^2, s_0) < 0$. This means that the ladder diagrams poorly approximate the true correlation function and that sum rules are not applicable here. For the ρ and A_1 mesons, the above criterion is satisfied and is stable: this is so for the A_1 meson in a wide range of varied coefficients and for the ρ meson (see Fig. 8) up to the threefold greater value of the quark condensate $\langle \alpha_s \bar{q}^2 q^2 \rangle$. As the numerical value of the condensate is increased further, the area where our inequality is valid is displaced rightward, with the continuum beginning to suppress the resonance contribution.

In the toy model, however, stability against small variations in the coefficients does not appear, and the inequality in (25) becomes valid in two cases: (i) if $s = s_0$ with the same variation in the coefficients as in the Borel sum-rule criteria and (ii) if $s = s_0/2$ with separate variations in the coefficients (by –5%, 8%, and –46% at, respectively, the first, the second, and the third power of $1/Q^2$).

This suggests that one can find a truncation of the whole series that does not change the general shape of the spectrum, but which satisfies the criterion of applicability.

6. CONCLUSION

To summarize, we have studied the reliability of results given by sum rules in QCD. We have verified the criterion of the Borel sum-rule reliability and have shown that it is unsatisfactory from the viewpoint of stability against small variations in the correlation-function coefficients. The criterion of applicability for the FESR method has also been proposed, and its application to the same problems has been considered. This criterion imposes more stringent constraints on the correlation function and is stable against small variations in the operator-product-expansion coefficients for the correlation functions. Thus, we have constructed a powerful method for estimating the accuracy of theoretical calculations.

REFERENCES

1. E. Poggio, H. Queen, and S. Weinberg, Phys. Rev. D **13**, 1958 (1976).
2. R. Shankar, Phys. Rev. D **15**, 755 (1977).
3. K. G. Chetyrkin, N. V. Krasnikov, and A. N. Tavkhelidze, Phys. Lett. B **76**, 83 (1978).
4. M. A. Shifman, A. I. Vainshtein, and V. I. Zakharov, Nucl. Phys. B **147**, 385, 448, 519 (1979).
5. V. A. Novikov *et al.*, Nucl. Phys. B **237**, 525 (1984).
6. A. A. Pivovarov, A. N. Tavkhelidze, and V. F. Tokarev, Phys. Lett. B **132**, 402 (1983).
7. A. A. Penin and A. A. Pivovarov, Phys. Lett. B **357**, 427 (1995).
8. M. Benmerrouche, G. Orlandini, and T. G. Steele, Phys. Lett. B **366**, 354 (1996).
9. T. G. Steele, S. Alavian, and J. Kwan, Phys. Lett. B **392**, 189 (1997).
10. N. V. Krasnikov, A. A. Pivovarov, and N. N. Tavkhelidze, Z. Phys. C **19**, 301 (1983).
11. N. V. Krasnikov and A. A. Pivovarov, Phys. Lett. B **112**, 397 (1982).

Physics of Atomic Nuclei, Vol. 63, No. 9, 2000, pp. 1657–1670. Translated from Yadernaya Fizika, Vol. 63, No. 9, 2000, pp. 1745–1758.

ELEMENTARY PARTICLES AND FIELDS
Theory

Superfield Effective Action within the General Chiral Superfield Model

I. L. Buchbinder and A. Yu. Petrov
Tomsk State Pedagogical University, Tomsk, 634068 Russia
Received April 20, 1999; in final form, October 21, 1999

Abstract—The chiral superfield model associated with the low-energy limit of superstring theory and characterized by the Kähler and the chiral potential [$K(\Phi, \bar{\Phi})$ and $W(\Phi)$, respectively] is analyzed. An approach to solving a general problem is developed, and quantum loop corrections at arbitrary $K(\Phi, \bar{\Phi})$ and $W(\Phi)$ are found. Various aspects of a supergraph technique that are associated with calculating perturbative contributions to the superfield effective action are analyzed. Explicit expressions for the one- and two-loop corrections to the Kähler potential are calculated. The leading two-loop correction to the chiral potential is obtained, and it is shown that, irrespective of the form of $K(\Phi, \bar{\Phi})$ and $W(\Phi)$, counterterms are not needed for deducing this correction. © *2000 MAIK "Nauka/Interperiodica".*

1. INTRODUCTION

From the viewpoint of superstring theory, low-energy models of elementary particles are effective theories where integration with respect to massive string modes is performed and where a ten-dimensional background manifold has the structure $M^4 \times K$; here, M^4 and K are, respectively, four-dimensional Minkowski space and a suitable six-dimensional compact manifold, and a reduction to M^4 is accomplished. It turns out [1] that the resulting effective theories comprise, as an ingredient, $N = 1$ chiral superfields Φ^i governed by the action functional

$$S[\Phi, \bar{\Phi}] = \int d^8 z K(\bar{\Phi}^i, \Phi^i) + \left(\int d^6 z W(\Phi^i) + \text{h.c.}\right). \quad (1)$$

Here, $d^8 z = d^4 x d^2\theta d^2\bar{\theta}$ and $\Phi^i = \Phi^i(z)$, where $z^A \equiv (x^a, \theta_\alpha, \bar{\theta}_{\dot{\alpha}})$ with $a = 0, 1, 2, 3$ and $\alpha = 1, 2$ ($\dot{\alpha} = \dot{1}, \dot{2}$). The real-valued function $K(\bar{\Phi}^i, \Phi^i)$ is referred to as a Kähler potential, while a holomorphic function $W(\Phi^i)$ is known as a chiral potential [2]. Expression (1) represents the most general action functional for a chiral superfield without higher derivatives at the component level [2]. The theory specified by the action functional (1) will be referred to as the model of a general chiral superfield. In the particular case where $K(\bar{\Phi}^i, \Phi^i) = \Phi\bar{\Phi}$ and $W(\Phi^i) \sim \Phi^3$, we arrive at the well-known Wess–Zumino model. At $W(\Phi^i) = 0$, the theory represents the $N = 1$ supersymmetric sigma model [2]. In accordance with the procedure for deriving expression (1) for the action functional from superstring theory, this expression must be interpreted as a classical action functional specifying a theory used to describe phenomena whose characteristic energies are much less than the Planck energy. The general chiral-superfield model considered here is extensively used to study possible phenomenological implications of superstring theory (see [3, 4] and references therein).

The present study is devoted to calculating the low-energy effective action within the theory governed by the classical action functional (1). We will consider the case of a one-component chiral superfield. A transition to the case of a multicomponent field appears to be quite straightforward in the matrix notation.

It should be emphasized from the outset that, at arbitrary $K(\bar{\Phi}^i, \Phi^i)$ and $W(\Phi^i)$, the theory specified by equation (1) is unrenormalizable in the index; in order to eliminate divergences, one needs an infinite number of counterterms, which cannot be generated by a finite number of renormalization constants. It should be borne in mind, however, that the theory under investigation is essentially an effective one; therefore, it is characterized by some energy scale, which plays the role of a natural cutoff. The relevant dimensional parameters arise in the model specified by Eq. (1) in deriving this model from superstring theory and are expressed in terms of the string tension and the characteristic size of the compact manifold K.

Our objective here is to calculate lower order loop contributions to the effective action dependent on superfields without going over to components at any stage of the calculations. In this way, we ensure manifest supersymmetry at intermediate stages and in the final result. In just the same way as in the nonsupersymmetric case, the low-energy effective action for the model specified by Eq. (1) is described by effective potentials that are now dependent on superfields.

Below, it will be shown, however, that, if $W''(\Phi)|_{\Phi=0} \neq 0$, corrections to the Kähler potential $K(\bar{\Phi}, \Phi)$ are the only admissible corrections beginning from the one-loop approximation. At $W''(\Phi)|_{\Phi=0} = 0$, the chiral potential $W(\Phi)$ also develops quantum corrections, the first of these emerging in the two-loop approximation. It should be noted that the concept of a superfield effective potential was introduced in [5, 6] and that the superfield technique for calculating quantum corrections to the chiral potential was developed in [7, 8]. The method of a superfield effective potential was further refined in [4, 9, 10]. Previously, all these investigations were performed within the Wess–Zumino model. Here, we evolve a general approach to determining the effective potentials in the theory that is specified by equation (1) and which involves arbitrary functions $K(\Phi, \bar{\Phi})$ and $W(\Phi)$.

The ensuing exposition is organized as follows. In Section 2, we describe the classical action functional, Green's functions, and the general structure of the effective action. Section 3 is devoted to calculating the one-loop Kähler effective potential. Further, we calculate the two-loop chiral effective potential in Sections 4 and 5 and the two-loop Kähler effective potential in Section 6. It is interesting to note that, despite unrenormalizability of the model in the general case, the chiral effective potential does not require renormalization and does not depend on normalization conditions; therefore, it is automatically finite. The results that we obtained are summarized in the Conclusion. Throughout this study, we heavily rely on the technique of Feynman diagrams in superspace—that is, the supergraph technique (see, for example, [2]).

2. STRUCTURE OF THE EFFECTIVE ACTION

Let us consider the theory of a chiral and an antichiral superfield [$\Phi(z)$ and $\bar{\Phi}(z)$, respectively] governed by the action functional (1). It should be recalled that all fields entering into this action functional are taken to be one-component. As usual, the effective action $\Gamma[\Phi, \bar{\Phi}]$ is determined with the aid of the Legendre transformation of the generating functional $W[J, \bar{J}]$ for connected Green's functions; that is,

$$\exp\left(\frac{i}{\hbar}W[J, \bar{J}]\right) = \int \mathcal{D}\varphi \mathcal{D}\bar{\varphi} \exp\left(\frac{i}{\hbar}(S[\varphi, \bar{\varphi}] + (\int d^6 z J\varphi + \text{h.c.}))\right), \quad (2)$$

$$\Gamma[\Phi, \bar{\Phi}] = W[J, \bar{J}] - (\int d^6 z J\Phi + \text{h.c.}).$$

In order to perform loop calculations, it is convenient to make a shift in the functional integral (2) according to the rule $\Phi \longrightarrow \Phi + \sqrt{\hbar}\phi$ and $\bar{\Phi} \longrightarrow \bar{\Phi} + \sqrt{\hbar}\bar{\phi}$ and to recast relation (2) into the form

$$\exp\left(\frac{i}{\hbar}\Gamma[\Phi, \bar{\Phi}]\right) = \int \mathcal{D}\phi \mathcal{D}\bar{\phi} \exp\left(\frac{i}{\hbar}S[\Phi + \sqrt{\hbar}\phi, \bar{\Phi} + \sqrt{\hbar}\bar{\phi}]\right. \quad (3)$$
$$\left. - \left(\int d^6 z \frac{\delta\Gamma[\Phi, \bar{\Phi}]}{\delta\Phi(z)}\phi(z) + \text{h.c.}\right)\right)$$

(for details, see [2, 11]). Let us represent the effective action as $\Gamma[\Phi, \bar{\Phi}] = S[\Phi, \bar{\Phi}] + \tilde{\Gamma}[\Phi, \bar{\Phi}]$, where $\tilde{\Gamma}[\Phi, \bar{\Phi}]$ is a quantum correction to the classical action functional. From (3), we then obtain

$$\tilde{\Gamma}[\Phi, \bar{\Phi}] = \sum_{n=1}^{\infty} \hbar^n \Gamma^{(n)}[\Phi, \bar{\Phi}]. \quad (4)$$

Each loop correction $\Gamma^{(n)}[\Phi, \bar{\Phi}]$ can be expressed in terms of functional integrals. In particular, the one-loop correction has the form

$$\exp(i\Gamma^{(1)}[\Phi, \bar{\Phi}]) = \int \mathcal{D}\phi \mathcal{D}\bar{\phi} \exp(iS_2[\Phi, \bar{\Phi}; \phi, \bar{\phi}]), \quad (5)$$

where $S_2[\Phi, \bar{\Phi}; \phi, \bar{\phi}]$ is the second-order part of the classical action functional $\frac{1}{\hbar}S[\Phi + \sqrt{\hbar}\phi, \bar{\Phi} + \sqrt{\hbar}\bar{\phi}]$ in quantum superfields. It can be represented as

$$S_2 = \frac{1}{2}\int d^8 z (\phi\ \bar{\phi}) \begin{pmatrix} K_{\Phi\Phi} & K_{\Phi\bar{\Phi}} \\ K_{\Phi\bar{\Phi}} & K_{\bar{\Phi}\bar{\Phi}} \end{pmatrix} \begin{pmatrix} \phi \\ \bar{\phi} \end{pmatrix} + \left[\int d^6 z \frac{1}{2} W''\phi^2 + \text{h.c.}\right], \quad (6)$$

where $K_{\Phi\bar{\Phi}} = \partial^2 K(\Phi, \bar{\Phi})/\partial\Phi\partial\bar{\Phi}$, $K_{\Phi\Phi} = \partial^2 K(\Phi, \bar{\Phi})/\partial\Phi^2$, etc., and where $W'' = d^2W/d\Phi^2$. We assume that the effective action functional $\Gamma[\Phi, \bar{\Phi}]$ can be expanded in terms of the supercovariant derivatives $D_A = (\partial_a, D_\alpha, \bar{D}_{\dot{\alpha}})$ as (below, we use the notation adopted in [2])

$$\Gamma[\Phi, \bar{\Phi}] = \int d^8 z \mathcal{L}_{\text{eff}}(\Phi, D_A\Phi, D_A D_B\Phi; \bar{\Phi}, D_A\bar{\Phi}, D_A D_B\bar{\Phi}) + (\int d^6 z \mathcal{L}^{(c)}_{\text{eff}}(\Phi) + \text{h.c.}) + \dots, \quad (7)$$

where $\mathcal{L}_{\text{eff}}$ is the general effective Lagrangian, while $\mathcal{L}^{(c)}_{\text{eff}}$ is the chiral effective Lagrangian. Each of these Lagrangians can be expanded in powers of the deriva-

tives $D_A\Phi$, $D_AD_B\Phi$, $D_A\bar{\Phi}$, $D_AD_B\bar{\Phi}$, …, so that we have

$$\begin{aligned}\mathcal{L}_{\text{eff}} &= K_{\text{eff}}(\Phi, \bar{\Phi}) + \ldots \\ &= K(\Phi, \bar{\Phi}) + \sum_{n=1}^{\infty} K^{(n)}(\Phi, \bar{\Phi}) + \ldots, \\ \mathcal{L}^{(c)}_{\text{eff}} &= W_{\text{eff}}(\Phi) + \ldots = W(\Phi) + \sum_{n=1}^{\infty} W^{(n)}(\Phi) + \ldots,\end{aligned} \tag{8}$$

where ellipses stand for terms dependent on the covariant derivatives D_A of the superfields Φ and $\bar{\Phi}$. Here, $K_{\text{eff}}(\Phi, \bar{\Phi})$ and $W_{\text{eff}}(\Phi)$ are referred to, respectively, as a Kähler effective potential and as a chiral effective potential; $K^{(n)}$ is the n-loop correction to the Kähler potential K; and $W^{(n)}$ is the n-loop correction to the chiral potential W. The objective of our study is to calculate the one- and two-loop expressions for $K_{\text{eff}}(\Phi, \bar{\Phi})$ and $W_{\text{eff}}(\Phi)$ within the theory specified by the action functional (1).

Let us consider the theory of superfields ϕ and $\bar{\phi}$ in the background fields Φ and $\bar{\Phi}$ that is specified by the action functional $S_2[\Phi, \bar{\Phi}, \phi, \bar{\phi}]$ (6). This theory is characterized by the matrix superpropagator

$$G(z_1, z_2) = \begin{pmatrix} G_{++}(z_1, z_2) & G_{+-}(z_1, z_2) \\ G_{-+}(z_1, z_2) & G_{--}(z_1, z_2) \end{pmatrix}, \tag{9}$$

which satisfies the equation

$$\begin{pmatrix} W'' - \frac{1}{4}\bar{D}^2 K_{\Phi\Phi} & -\frac{1}{4}\overrightarrow{\bar{D}^2} K_{\Phi\bar{\Phi}} \\ -\frac{1}{4}\overrightarrow{D^2} K_{\Phi\bar{\Phi}} & \bar{W}'' - \frac{1}{4}D^2 K_{\bar{\Phi}\bar{\Phi}} \end{pmatrix} \begin{pmatrix} G_{++} & G_{+-} \\ G_{-+} & G_{--} \end{pmatrix} = -\begin{pmatrix} \delta_+ & 0 \\ 0 & \delta_- \end{pmatrix}. \tag{10}$$

Here, an arrow over an operator means that this operator acts on all functions on the right of it; $\delta_+ = -\frac{1}{4}\bar{D}^2\delta^8(z_1 - z_2)$ and $\delta_- = -\frac{1}{4}D^2\delta^8(z_1 - z_2)$ are, respectively, a chiral and an antichiral delta function; and the plus (minus) sign in the matrix elements of the superpropagator $G(z_1, z_2)$ indicates that they are chiral (antichiral) in the corresponding argument. It is obvious that superpropagator (9) depends on the background superfields Φ and $\bar{\Phi}$.

We now note that, as soon as the covariant derivatives are applied to $K_{\Phi\Phi}$, $K_{\Phi\bar{\Phi}}$, and $K_{\bar{\Phi}\bar{\Phi}}$ in Eq. (10), we inevitably arrive at terms involving $D^\alpha\Phi$, $\bar{D}_{\dot{\alpha}}\bar{\Phi}$, $D^2\Phi$, and $\bar{D}^2\bar{\Phi}$. If superpropagator (9) is used in calculating the effective action, the above terms cannot contribute to the quantity $K_{\Phi\bar{\Phi}}$, because it is independent of derivatives. In calculating $K_{\Phi\bar{\Phi}}$, we can therefore omit all such terms in Eq. (10) and assume that the matrix superpropagator $G(z_1, z_2)$ satisfies the equation

$$\begin{pmatrix} W'' & -\frac{1}{4}K_{\Phi\bar{\Phi}}\bar{D}^2 \\ -K_{\Phi\bar{\Phi}}\frac{1}{4}D^2 & \bar{W}'' \end{pmatrix} \begin{pmatrix} G_{++} & G_{+-} \\ G_{-+} & G_{--} \end{pmatrix} = -\begin{pmatrix} \delta_+ & 0 \\ 0 & \delta_- \end{pmatrix}. \tag{11}$$

This equation can be solved explicitly for the background superfields that contribute to the effective potentials $K_{\text{eff}}(\Phi, \bar{\Phi})$ and $W_{\text{eff}}(\Phi)$. The resulting solution is written as

$$G = \frac{1}{K^2_{\Phi\bar{\Phi}}\Box - W''\bar{W}''} \begin{pmatrix} \bar{W}'' & K_{\Phi\bar{\Phi}}\frac{1}{4}\bar{D}^2 \\ K_{\Phi\bar{\Phi}}\frac{1}{4}D^2 & W'' \end{pmatrix} \times \begin{pmatrix} \delta_+ & 0 \\ 0 & \delta_- \end{pmatrix}. \tag{12}$$

It is this propagator that will be used in the following to derive the one- and two-loop contributions to the Kähler effective potential $K_{\text{eff}}(\Phi, \bar{\Phi})$. The problem of the chiral effective potential $W_{\text{eff}}(\Phi)$ will be investigated in Sections 4 and 5.

3. ONE-LOOP KÄHLER EFFECTIVE POTENTIAL

According to relations (5), the one-loop contribution to the effective action has the form

$$\Gamma^{(1)} = -\frac{i}{2}\text{tr}\ln G, \tag{13}$$

where G is the matrix superpropagator (12). In order to calculate the functional $\Gamma^{(1)}$, we will use the supergraph technique (see, for example, [2]). Since we aim here at finding K_{eff}, we will assume that the quantities $K_{\Phi\bar{\Phi}}$, $K_{\bar{\Phi}\bar{\Phi}}$, $K_{\Phi\Phi}$, W'', and $\bar{W}''$ are constants.

Let us represent the action functional $S_2 = S_2[\Phi, \bar{\Phi}; \phi, \bar{\phi}]$ (6) in the form

$$\begin{aligned}S_2 &= S_0 + S_{\text{int}}, \\ S_0 &= \int d^8z K_{\Phi\bar{\Phi}}\phi\bar{\phi},\end{aligned} \tag{14}$$

$$S_{\rm int} = \frac{1}{2}\int d^8z(K_{\Phi\Phi}\phi^2 + K_{\bar\Phi\bar\Phi}\bar\phi^2) \qquad (15)$$
$$+\int d^6z W''\phi^2 + \int d^6\bar z \bar W''\bar\phi^2.$$

In order to find $K_{\rm eff}$, we sum the contributions to $\Gamma^{(1)}$ from all one-loop supergraphs generated by the action functional S_2 (14).

Let us proceed to describe the supergraph technique for the case under consideration. The superpropagator G_0 associated with the action functional S_0 is obtained from the general expression (12) at $W'' = \bar W''$. By virtue of the definitions of the chiral and antichiral delta functions, the result has the form

$$G = \frac{1}{K_{\Phi\bar\Phi}\Box}$$
$$\times\begin{pmatrix} 0 & -\frac{1}{16}\bar D_1^2 D_2^2\delta^8(z_1-z_2) \\ -\frac{1}{16}D_1^2\bar D_2^2\delta^8(z_1-z_2) & 0\end{pmatrix}. \qquad (16)$$

In constructing the required diagram technique, each vertex of the form $\int d^6z_2\frac{1}{2}W''(z_2)\phi^2(z_2)$ in the expression for the relevant diagram will be associated with the structure

$$\int d^6z_2\frac{1}{2}W''(z_2)\frac{1}{K^2_{\Phi\bar\Phi}(z_2)\Box^2}\frac{1}{16}\bar D_1^2 D_2^2\delta^8(z_1-z_2)$$
$$\times\frac{1}{16}D_2^2\bar D_3^2\delta^8(z_2-z_3) = -\int d^8z_2\frac{1}{2}W''(z_2) \qquad (17)$$
$$\times\frac{1}{K^2_{\Phi\bar\Phi}(z_2)\Box^2}\frac{1}{4}D_1^2\delta^8(z_1-z_2)\frac{1}{16}\bar D_2^2 D_3^2\delta^8(z_2-z_3).$$

Thus, each vertex proportional to $W''(z_i)$ will be associated with the factor $-\frac{1}{4}\bar D_i^2$. By virtue of this, it is natural to include the factors $-\bar D^2/4$ and $-D^2/4$ entering into (16) in vertices and to assume that the propagator corresponding to the second-order action in (14) has the form

$$G(z_1,z_2) = -\frac{1}{K_{\Phi\bar\Phi}\Box}\delta^8(z_1-z_2). \qquad (18)$$

(For the Wess–Zumino model, the details are described in [2].) As a result, the factor $-\bar D^2/4$ ($-D^2/4$) is associated with each vertex involving W'' ($\bar W''$). As to vertices of the $K_{\Phi\Phi}\phi^2$ and $K_{\bar\Phi\bar\Phi}\bar\phi^2$ types, we can say that, if there is, for example, the vertex $K_{\Phi\Phi}\phi^2$ in a diagram, the contribution of this diagram develops the term

$$\int d^8z_2\frac{1}{2}K_{\Phi\Phi}(z_2)\frac{1}{K^2_{\Phi\bar\Phi}(z_2)\Box^2}\frac{1}{16}\bar D_1^2 D_2^2\delta^8(z_1-z_2)$$
$$\times\frac{1}{16}D_2^2\bar D_3^2\delta^8(z_2-z_3) = \int d^8z_2\frac{1}{8}(D_2^2K_{\Phi\Phi}(z_2))$$
$$\times\frac{1}{K^2_{\Phi\bar\Phi}(z_2)\Box^2}\frac{1}{4}D_1^2\delta^8(z_1-z_2)\frac{1}{16}\bar D_2^2 D_3^2\delta^8(z_2-z_3);$$

that is, there arises the expression $D^2K_{\Phi\Phi}$, which inevitably generates terms featuring $D^\alpha\Phi$, $\bar D_{\dot\alpha}\bar\Phi$, $D^2\Phi$, and $\bar D^2\bar\Phi$ when D^2 is applied to $K_{\Phi\Phi}$. In a similar way, we can show that the presence of the vertex $K_{\bar\Phi\bar\Phi}\bar\phi^2$ again leads to the emergence of contributions in the effective action that are dependent on the derivatives of superfields. Because of this, diagrams involving such vertices do not contribute to the Kähler effective potential.

Thus, possible diagrams that lead to the one-loop Kähler effective potential can involve only vertices that are proportional to W'' and $\bar W''$. We note that the same number of the vertices W'' and $\bar W''$ must be contained in each such diagram. In order to demonstrate this explicitly, we recall that, by virtue of the well-known property of the variational derivatives of chiral superfields [2], the factor $\bar D^2$ (D^2) corresponds to each vertex W'' ($\bar W''$). Upon transformations of the D algebra, the equal numbers of the factors D^2 and $\bar D^2$ are converted into momenta according to the rules $\bar D^2D^2\bar D^2 = -16k^2\bar D^2$ and $D^2\bar D^2D^2 = -16k^2D^2$. The contraction of a loop into a point in θ space according to the rule $\delta_{12}\bar D_1^2D_1^2\delta_{12} = \delta_{12}$ also requires one factor D^2 and one factor $\bar D^2$. If the contribution of some diagram contains unequal numbers of the factors D^2 and $\bar D^2$, the extra factors D^2 ($\bar D^2$) can act only on external lines, so that such diagrams do not contribute to the Kähler effective potential. It should be emphasized that vertices proportional to W'' and $\bar W''$ must alternate—otherwise, at least one of the two factors D^2 (or $\bar D^2$) occurring at the neighboring $\bar W''$ (W'') vertices can be transferred to only an external superfield upon the transformations of the D algebra, whereby it is proven that such diagrams make no contribution to the Kähler effective potential. The structure of possible diagrams is illustrated in Fig. 1. There, double external lines correspond to alternating W'' and $\bar W''$ vertices; lines between the vertices ($\langle\phi\bar\phi\rangle$) represent propagators of the form (18); and the factor

$-\bar{D}^2/4$ ($-D^2/4$) is associated with each vertex proportional to W'' ($\bar{W}''$). A diagram that has the above structure and which features $2n$ external legs appears to be an n-link ring of the type shown in Fig. 2.

The contribution of each such link is given by

$$R = W''\bar{W}''\frac{1}{(K_{\Phi\bar{\Phi}}k^2)^2}\frac{D_{l-1}^2}{4}\delta_{l-1,l}\frac{\bar{D}_l^2}{4}\delta_{l,l+1}. \quad (19)$$

According to the definition of a Kähler effective potential, the superfields W'' and $\bar{W}''$ are taken here to be constant in spacetime, and the external momenta are equal to zero.

The contribution of such a diagram with $2n$ external legs has the form

$$I_{2n} = \frac{1}{2n}\int\prod_{k=1}^{2n}d^4\theta_1\ldots d^4\theta_{2n}\int\frac{d^4k}{(2\pi)^4}R^n$$
$$= \frac{1}{2n}\int\prod_{k=1}^{2n}d^4\theta_1\ldots d^4\theta_{2n}\int\frac{d^4k}{(2\pi)^4}(W''\bar{W}'')^n\frac{1}{(K_{\Phi\bar{\Phi}}k^2)^{2n}} \quad (20)$$
$$\times\frac{D_1^2}{4}\delta_{12}\frac{\bar{D}_2^2}{4}\delta_{23}\ldots\frac{D_{2n-1}^2}{4}\delta_{2n-1,2n}\frac{\bar{D}_{2n}^2}{4}\delta_{2n,1},$$

where $2n$ is a symmetry factor (see, for example, [9]). Considering that supercovariant derivatives obey the relation $D^2\bar{D}^2D^2 = -16k^2D^2$, we can show that

$$I_{2n} = \int d^4\theta\int\frac{d^4k}{(2\pi)^4k^2}\frac{1}{2n}\left(-\frac{W''\bar{W}''}{K_{\Phi\bar{\Phi}}^2k^2}\right)^n. \quad (21)$$

In the momentum representation, the total contribution from all diagrams having the above structure is determined by the sum of all I_{2n}; that is, we have

$$K^{(1)} = \sum_{n=1}^{\infty}I_{2n}$$
$$= \int d^4\theta\int\frac{d^4k}{(2\pi)^4k^2}\sum_{n=1}^{\infty}\frac{1}{2n}\left(-\frac{W''\bar{W}''}{K_{\Phi\bar{\Phi}}^2k^2}\right)^n. \quad (22)$$

By using the well-known relation

$$\sum_{n=1}^{\infty}\frac{1}{2n}(-a)^n = -\ln(1+a),$$

we further reduce $K^{(1)}$ to the form

$$K^{(1)} = \sum_{n=1}^{\infty}I_{2n} = -\int d^4\theta\int\frac{d^4k}{(2\pi)^4k^2}\ln\left(1+\frac{W''\bar{W}''}{K_{\Phi\bar{\Phi}}^2k^2}\right). \quad (23)$$

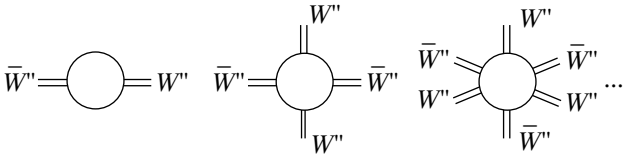

Fig. 1. Diagrams contributing to the one-loop Kähler potential.

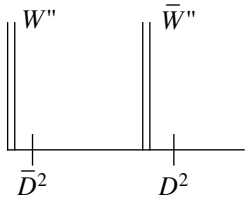

Fig. 2. Element of the one-loop diagram contributing in the Kähler potential.

Via a Wick rotation and subsequent integration with respect to angular variables, we now go over from d^4k to $\pi^2k^2dk^2$. Since the integral with respect to k^2 is divergent, it is necessary to introduce some regularization at this stage. We will rely on a dimensional regularization, making the substitution $\pi^2k^2dk^2 \longrightarrow \pi^2k^{2(1+\epsilon/2)}dk^2$, where ϵ is a regularization parameter. As a result, the expression for the one-loop Kähler effective potential takes the form

$$K^{(1)} = -\mu^{-\epsilon}\int d^4\theta\frac{dk^2(k^2)^{\epsilon/2}}{32\pi^2}\ln\left(1+\frac{W''\bar{W}''}{K_{\Phi\bar{\Phi}}^2k^2}\right), \quad (24)$$

where μ is an arbitrary parameter of mass dimension. Further, it can easily be shown that

$$-\mu^{-\epsilon}\int_0^{\infty}dk^2(k^2)^{\epsilon/2}\ln\left(1+\frac{A}{k^2}\right) = -A^{1+\epsilon}\Gamma(-1-\epsilon/2)$$
$$= \left(-\frac{2}{\epsilon}+\gamma-1\right)A - A\ln\frac{A}{\mu^2} + O(\epsilon),$$

where γ is the Euler constant. Therefore, the one-loop correction to the Kähler potential can be represented as

$$K^{(1)} = -\frac{1}{32\pi^2}\int d^4\theta\frac{W''\bar{W}''}{K_{\Phi\bar{\Phi}}^2}\left\{\frac{2}{\epsilon}-\gamma+1+\ln\frac{W''\bar{W}''}{\mu^2K_{\Phi\bar{\Phi}}^2}\right\}. \quad (25)$$

Relation (25) explicitly demonstrates that the theory being considered is not multiplicatively renormalizable at arbitrary $K(\Phi, \bar{\Phi})$ and $W(\Phi)$. We will illustrate this statement by considering the example of $W(\Phi) \sim \Phi^4$ and $K(\Phi, \bar{\Phi}) = \Phi\bar{\Phi}$. In this case, the divergent part has the form $K_{\rm div}^{(1)} \sim \frac{1}{\epsilon}(\Phi\bar{\Phi})^4$. In order to remove divergences

and ensure that the renormalization was multiplicative, it is necessary to assume that the input function is $K(\Phi, \bar{\Phi}) \sim \Phi\bar{\Phi} + (\Phi\bar{\Phi})^4$. According to (25), however, the divergent part $K^{(1)}_{\rm div}$ will appear to be an infinite power series in terms of $\Phi\bar{\Phi}$. In performing renormalizations, multiplicativity requires that the input function $K(\Phi, \bar{\Phi})$ also be an infinite power series in terms of $\Phi\bar{\Phi}$ with an infinite set of coefficients, which must be interpreted as an infinite set of coupling constants. But now, elimination of divergences requires introducing an infinite number of counterterm types. The only choice of $K(\Phi, \bar{\Phi})$ and $W(\Phi)$ leading to a finite number of counterterm types corresponds to the Wess–Zumino model, in which case we have $K(\Phi, \bar{\Phi}) = \Phi\bar{\Phi}$ and $W(\Phi) \sim \Phi^3$. As a result, we arrive at the conclusion that the model being discussed must be interpreted as an effective theory whose applicability range is bounded by some energy scale chosen on the basis of phenomenological considerations. Presently, (multiplicatively unrenormalizable) effective theories are being widely used in quantum field theories and its applications (for example, four-dimensional Gross–Neveu model, Nambu–Jona-Lasinio model, and quantum gravity). From this point of view, the chiral-superfield model is not unique.

In order to obtain a finite one-loop correction to the Kähler potential, we will merely assume that the Lagrangian is supplemented with the one-loop counterterm

$$S^{(1)}_{\rm ct} = \frac{1}{(4\pi)^2\epsilon}\frac{|W''|^2}{K^2_{\Phi\bar{\Phi}}}. \qquad (26)$$

As a result, we obtain a finite one-loop correction $K^{(1)}_R$ in the form

$$K^{(1)}_R = -\frac{1}{32\pi^2}\frac{|W''|^2}{K^2_{\Phi\bar{\Phi}}}\left(1 - \gamma + \ln\frac{|W''|^2}{\mu^2 K^2_{\Phi\bar{\Phi}}}\right). \qquad (27)$$

Expression (27) represents the eventual form of the one-loop quantum contribution to the Kähler potential. At $K = \Phi\bar{\Phi}$ and $W(\Phi) \sim \Phi^3$, it reduces to the well-known result for the one-loop Kähler potential in the Wess–Zumino model [5, 6].

4. PROCEDURE FOR CALCULATING THE CHIRAL EFFECTIVE POTENTIAL

Let us now consider a chiral effective potential. By definition, it depends only on the chiral superfield but not on its derivatives. The reason behind the emergence of chiral corrections is the following. According to the nonrenormalization theorem (see, for example, [2]), all corrections to the effective action can be represented in the form of an integral over the full superspace; that is,

$$\int d^4\theta f(\Phi, \bar{\Phi}), \qquad (28)$$

where $f(\Phi, \bar{\Phi})$ is a function of superfields. Naively, it can be thought that the nonrenormalization theorem forbids the emergence of corrections proportional to an integral over the chiral subspace, but this is not so in fact. As was indicated in [12] (see also [7]), the emergence of finite corrections of the form

$$\int d^8 z f(\Phi)\left(-\frac{D^2}{4\Box}\right)g(\Phi) \qquad (29)$$

in the effective action does not contradict this theorem. Upon going over to an integral over chiral superspace according to the rule $\int d^8 z F(\Phi, \bar{\Phi}) = \int d^6 z\,(-\bar{D}^2/4)F(\Phi, \bar{\Phi})$, expression (29) takes the form

$$\int d^6 z f(\Phi) g(\Phi), \qquad (30)$$

where $f(\Phi)$ and $g(\Phi)$ are functions of the chiral superfield Φ. In the above transformations, it is important that the superfields Φ and $\bar{\Phi}$ are not constants, because expression (29) depends substantially on the derivatives of the superfields.

Let us now show that, at a nonzero mass, the effective action does not develop chiral corrections. We begin by indicating that the factor $\Box^{-1}$ in (29) may originate only from the propagators of massless superfields. Indeed, the propagators in massive theories are proportional to $(\Box - m^2)^{-1}$. Instead of a structure of the type in (29), we will then obtain the expression

$$\int d^8 z f(\Phi)\left(-\frac{D^2}{4(\Box - m^2)}\right)g(\Phi). \qquad (31)$$

Going over to integration over chiral subspace, we obtain

$$\int d^6 z f(\Phi)\left(\frac{\Box}{\Box - m^2}\right)g(\Phi). \qquad (32)$$

In the momentum representation, this corresponds to the expression

$$\int \frac{d^4 p}{(2\pi)^4} f(\Phi)\left(\frac{p^2}{p^2 + m^2}\right)g(\Phi), \qquad (33)$$

which obviously disappears in the limit of slowly varying fields, $p^2 \longrightarrow 0$, if $m \neq 0$. Hence, a nontrivial chiral effective potential may arise only in a massless theory.

In order to derive chiral corrections to the effective action, it is sufficient to set $\bar{\Phi} = 0$. Here and in the next section, we will therefore consider all the derivatives of K and W at $\bar{\Phi} = 0$. It can then be established that the

action functional dependent only on chiral background fields has the form

$$S_2 = \frac{1}{2}\int d^8z(\phi\ \bar{\phi})\begin{pmatrix} K_{\Phi\Phi} & K_{\Phi\bar{\Phi}} \\ K_{\Phi\bar{\Phi}} & K_{\bar{\Phi}\bar{\Phi}} \end{pmatrix}\begin{pmatrix}\phi \\ \bar{\phi}\end{pmatrix} + \int d^6z\frac{1}{2}W''\phi^2 + \ldots, \tag{34}$$

since $\overline{W}''|_{\Phi=0} = 0$. In expression (34), the ellipsis stands for vertices of third and higher orders in quantum fields. In order to construct perturbation theory, we single out the free term and interaction vertices in this action functional. For the free term, it is convenient to choose the expression

$$S_0 = \int d^8z\phi\bar{\phi}$$

with the standard superpropagator

$$G(z_1, z_2) = -\frac{D_1^2\overline{D}_2^2}{16\Box}\delta^8(z_1 - z_2), \tag{35}$$

all the remaining terms in (34) being associated with interaction. Thus, we must refer all factors D to propagators rather than to vertices. In constructing a diagram technique, it should be borne in mind, however, that, for vertices of the $W''\phi^2$ and $W'''\phi^3$ types and for other vertices proportional to an integral over chiral (antichiral) subspace, one of the factors $\overline{D}^2$ (D^2) contained in the propagators is used to go over to integration over a full superspace in the corresponding vertex function. Therefore, one of the propagators associated with one of such vertices has one factor $\overline{D}^2$ (D^2) less.

The one- and two-loop corrections receive contributions from the vertices

$$K_{\Phi\Phi}\phi^2, \quad (K_{\Phi\bar{\Phi}} - 1)\phi\bar{\phi}, \quad \frac{1}{2}W''\phi^2,$$
$$W_{\Phi\Phi\Phi}\phi^3, \quad W_{\Phi\Phi\Phi\Phi}\phi^4, \quad K_{\Phi\Phi\bar{\Phi}}\phi^2\bar{\phi}, \tag{36}$$
$$K_{\Phi\Phi\bar{\Phi}\bar{\Phi}}\phi^2\bar{\phi}^2, \quad K_{\Phi\Phi\Phi\bar{\Phi}}\phi^3\bar{\phi}$$

and from the vertices conjugate to those in (36). The first three vertices from (36) can be present in one-loop diagrams, while the remaining ones appear only from the two-loop approximation.

We further perform a dimensional analysis of diagrams that contribute to the chiral effective Lagrangian in the one- and the two-loop approximation.

Each loop yields a contribution of 2 to the dimensionality. This can be explained as follows: (i) Each loop includes momentum integration, which yields 4. (ii) Each contraction of a loop into a point according to the rule $\delta_{12}D_1^2\overline{D}_1^2\delta_{12} = 16\delta_{12}$ reduces the number of the factors D and $\overline{D}$ capable of transforming into momenta by 4; hence, the possible dimension is reduced by 2, so that the eventual contribution to the dimensionality from each loop is equal to the value indicated above.

Zero contribution comes from each propagator, since the propagators are given by (35) (in performing a dimensional analysis, it is more convenient to include the factors D in propagators, as was done in Section 3, rather than in vertices). Formally, two factors $\overline{D}^2$ are associated with each vertex proportional to W''. Of these two, one factor $\overline{D}^2$ is used to go over to an eight-dimensional integral with respect to z. Therefore, each such vertex reduces the dimensionality by one. In just the same way, each vertex that is independent of W'', but which is proportional to an integral over chiral subspace—that is, vertices of the forms $W'''\phi^3$ and $W''''\phi^4$, as well as those that are conjugate to them—also reduces the dimensionality by one. One of the factors D^2 does not contribute to the total dimensionality since it is converted into the square of the total momentum in transforming expressions of the type (29) into an integral over chiral subspace [integral of the form (30)]. Further, an additional square of the total momentum arises upon going over from (29) to (30). Therefore, the dimensionality of the contribution from each diagram is $2L + 1 - n_{W''} - n_{V_c}$, where L is the number of loops, $n_{W''}$ is the number of external lines W'', and n_{V_c} is the number of vertices of the types $W'''\phi^3$ and $W''''\phi^4$ and those that are conjugate to them. By definition, the effective potential represents the effective Lagrangian in the limit $p^2 \longrightarrow 0$. Therefore, a nontrivial contribution to the effective potential is possible only at

$$2L + 1 - n_{W''} - n_{V_c} = 0. \tag{37}$$

The contribution of a diagram that does not satisfy this condition either vanishes in the infrared limit or has a singularity in this limit. We note that vertices proportional to the derivatives of $K(\Phi, \bar{\Phi})$ do not contribute to dimensionalities.

For a given contribution to be chiral, it must include one extra factor D^2 in relation to the number of factors $\overline{D}^2$, once all the vertices have been represented in terms of four-dimensional integrals with respect to θ. This is necessary because, after the conversion of each pair $\overline{D}^2D^2$ into the square of the internal momentum, there remains one more factor D^2, which is transformed into the square of the external momentum in going over from a four-dimensional to a two-dimensional integral with respect to θ [see Eqs. (29) and (30)].

By literally repeating the proof from the preceding section, it can be shown that one of the two factors $\overline{D}^2$ appearing in the vertex function proportional to $K_{\Phi\Phi}$

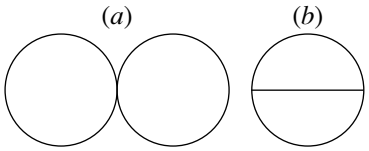

Fig. 3. Possible two-loop diagrams.

can be transferred only to an external leg. Since all the derivatives of K and W are considered at $\bar{\Phi} = 0$, the action of $\bar{D}^2$ on the external leg $K_{\Phi\Phi}$ yields zero result. In calculating the chiral effective potential, we can therefore set $K_{\Phi\Phi} = 0$.

Let us now consider possible one- and two-loop diagrams. By virtue of (37), the relation $n_{W''} + n_{V_c} = 3$ is fulfilled in one loop. Since n_{V_c} is equal to zero for one-loop diagrams, we have $n_{W''} = 3$. For the contribution of a given diagram to include one factor D^2 more in relation to the number of the factors $\bar{D}^2$, two vertices proportional to $K_{\bar{\Phi}\bar{\Phi}}$ must be present because $\bar{D}^2$ corresponds to each of the three external lines W''. A direct construction reveals, however, that a one-loop diagram of this type involves a line proportional to $(\bar{D}_1^2\bar{D}_2^2/16)\delta_{12} = 0$. Therefore, the contribution of this diagram as a whole is zero—that is, the one-loop correction to the chiral potential vanishes, $W^{(1)}(\Phi) = 0$.

From (37), it follows that two-loop diagrams satisfy the condition $n_{W''} + n_{V_c} = 5$. Since the number of purely chiral and antichiral vertices independent of W'' can be 0, 1, or 2 in two-loop diagrams, the number of external lines W'' is equal to 3, 4, or 5, respectively.

It is well known that there exist two types of single-particle-irreducible two-loop diagrams (see Fig. 3).

In order to evaluate the contributions of these diagrams, it should be borne in mind, however, that each of these may include all vertices listed in (36). It was shown above that (i) one factor $\bar{D}^2$ corresponds to each vertex proportional to W'', (ii) $n-1$ factors $\bar{D}^2$ (D^2) correspond to a chiral (antichiral) vertex proportional to ϕ^n ($\bar{\phi}^n$),[1)] and m factors $\bar{D}^2$ and n factors D^2 correspond to a vertex proportional to $\phi^m\bar{\phi}^n$. It is worth noting that the propagator $\langle\phi\bar{\phi}\rangle$ is the only Green's function in the theory being considered. In all possible supergraphs, the vertices must therefore be chosen in such a way as to ensure equality of the total numbers of quantum chiral superfields ϕ and antichiral superfields $\bar{\phi}$ corresponding to all vertices. Moreover, it was indicated above that the contribution to the chiral effective potential from any diagram is nontrivial if—and only if—this contribution involves one extra factor D^2 in relation to the number of factors $\bar{D}^2$.

Let us first consider diagrams of the type in Fig. 3*a*. The only fourth-order vertex in quantum superfields has the form $\phi^l\bar{\phi}^{4-l}$, where l is an integer that can vary from 0 to 4. Two fields ϕ ($\bar{\phi}$) are associated with each vertex proportional to W'' ($K_{\bar{\Phi}\bar{\Phi}}$). Finally, one field ϕ and one field $\bar{\phi}$ correspond to each vertex proportional to $K_{\Phi\bar{\Phi}} - 1$. Thus, the total number of the fields ϕ at the vertices leading to such a diagram is $l + 2n_{W''} + n_{K_{\bar{\Phi}\bar{\Phi}}}$, while the number of the fields $\bar{\phi}$ is accordingly $4 - l + 2n_{K_{\bar{\Phi}\bar{\Phi}}} + n_{K_{\Phi\bar{\Phi}}}$, where $n_{W''}$, $n_{K_{\Phi\bar{\Phi}}}$, and $n_{K_{\bar{\Phi}\bar{\Phi}}}$ are the numbers of vertices proportional to W'', $K_{\Phi\bar{\Phi}} - 1$, and $K_{\bar{\Phi}\bar{\Phi}}$, respectively. Thus, the condition requiring that the numbers of the fields ϕ and $\bar{\phi}$ be equal has the form $l + 2n_{W''} = 4 - l + 2n_{K_{\bar{\Phi}\bar{\Phi}}}$, whence it follows that $n_{K_{\bar{\Phi}\bar{\Phi}}} = n_{W''} + l - 2$.

Let us consider the question of the factors D^2 and $\bar{D}^2$ in this diagram. We begin by indicating that l factors $\bar{D}^2$ and $4 - l$ factors D^2 correspond to a vertex proportional to $\phi^l\bar{\phi}^{4-l}$. If, however, $l = 0$ ($l = 4$), the number of the factors D^2 ($\bar{D}^2$) must be reduced by unity since a transition from integration over chiral (antichiral) subspace to integration over the entire superspace decreases by unity the number of the factors $\bar{D}^2$ (D^2) present in the diagrams in question. Therefore, $l - N_V$ factors $\bar{D}^2$ and $4 - l - N_{\bar{V}}$ factors D^2, where N_V and $N_{\bar{V}}$ are the numbers of, respectively, chiral and antichiral vertices of third and higher orders in quantum fields (in the case being considered, N_V and $N_{\bar{V}}$ can take values of 0 and 1), correspond to a fourth-order vertex in quantum fields. Moreover, two factors D^2 (one factor $\bar{D}^2$) correspond (corresponds) to a vertex proportional to $K_{\bar{\Phi}\bar{\Phi}}$ (W''). As a result, the total number of the factors D^2 is $2n_{K_{\bar{\Phi}\bar{\Phi}}} + 4 - l - N_{\bar{V}} + n_{K_{\Phi\bar{\Phi}}}$, while the total number of the factors $\bar{D}^2$ is $n_{W''} + l - N_V + n_{K_{\Phi\bar{\Phi}}}$. The corresponding contribution to the chiral effective

[1)] We recall that each such vertex is associated with a six-dimensional integral with respect to z ($\bar{z}$). Here, each field ϕ ($\bar{\phi}$) generates one factor $\bar{D}^2$ (D^2). Therefore, n factors $\bar{D}^2$ (D^2) are associated with a vertex proportional to ϕ^n ($\bar{\phi}^n$). Of these, one factor is used to go over to an eight-dimensional integral with respect to z.

potential is nonzero if the total number of the factors D^2 is greater by one than the total number of the factors $\bar{D}^2$. Taking into account the condition $n_{K_{\bar{\Phi}\Phi}} = n_{W''} + l - 2$ (see above), we can show that this relationship between the numbers of the factors D^2 and $\bar{D}^2$ is fulfilled if $n_{W''} + N_V - N_{\bar{V}} = 1$. Previously, it was shown, however, that the two-loop chiral effective potential is nonzero if $n_{W''} \geq 3$. Since the numbers N_V and $N_{\bar{V}}$ take only the values of 0 and 1, the relation $n_{W''} - N_V + N_{\bar{V}} = 1$ cannot be satisfied. Therefore, diagrams of the type being considered do not contribute to the chiral effective potential.

Let us now consider diagrams of the type in Fig. 3*b*. Such diagrams involve two third-order vertices in quantum fields. These are proportional to either $\phi^{l_1}\bar{\phi}^{3-l_1}$ or $\phi^{l_2}\bar{\phi}^{3-l_2}$, where l_1 and l_2 can take integral values from 0 to 3. By analogy with the preceding case, we can show that the total number of the fields ϕ leading to a diagram of this type is $l_1 + l_2 + 2n_{W''} + n_{K_{\Phi\bar{\Phi}}}$, while the total number of the fields $\bar{\phi}$ is accordingly $4 - l + 2n_{K_{\bar{\Phi}\bar{\Phi}}} + n_{K_{\Phi\bar{\Phi}}}$. The condition requiring that their numbers be equal leads to the relation $n_{K_{\bar{\Phi}\bar{\Phi}}} = n_{W''} + l_1 + l_2 - 3$. Further, the number of the factors D^2 is $2n_{K_{\bar{\Phi}\bar{\Phi}}} + 6 - l_1 - l_2 - N_{\bar{V}} + n_{K_{\Phi\bar{\Phi}}}$, while the number of the factors $\bar{D}^2$ is $n_{W''} + l_1 + l_2 - N_V + n_{K_{\Phi\bar{\Phi}}}$. As before, the number of the factors D^2 must be greater by one than the number of the factors $\bar{D}^2$. Taking into account the relation $n_{K_{\bar{\Phi}\bar{\Phi}}} = n_{W''} + l_1 + l_2 - 3$, we arrive at the conclusion that a nontrivial contribution to the chiral effective potential arises at $n_{W''} + N_V - N_{\bar{V}} = 1$. This condition is satisfied only in the case where $n_{W''} = 3$, $N_V = 0$, and $N_{\bar{V}} = 2$. Thus, either third-order vertex in quantum fields has the form $\bar{W}'''\bar{\phi}^3$; hence, $n_{K_{\bar{\Phi}\bar{\Phi}}} = 0$. We note that no restrictions on the number of vertices proportional to $K_{\Phi\bar{\Phi}} - 1$ arise. A possible diagram that obeys all these requirements contains three external legs W'' and two antichiral vertices of the $\bar{W}'''\bar{\phi}^3$ type. There is only one such diagram (see Fig. 5 below). Its contribution will be considered in the next section.

5. TWO-LOOP CORRECTION TO THE CHIRAL EFFECTIVE POTENTIAL

Let us now proceed to evaluate directly the two-loop contributions to the chiral effective potential. As was

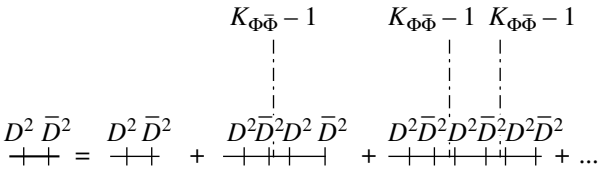

Fig. 4. Superpropagator $\langle\phi\bar{\phi}\rangle$.

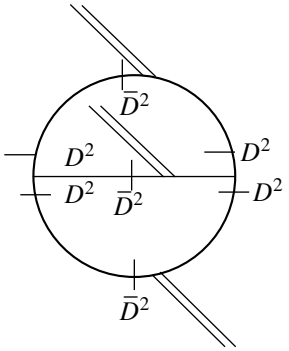

Fig. 5. Diagram determining the two-loop chiral potential.

shown in the preceding section, possible supergraphs can contain only vertices proportional to W'', $\bar{W}'''$, and $K_{\Phi\bar{\Phi}} - 1$. This implies that the relevant diagram technique can be constructed on the basis of the following action functional for quantum fields [compare with Eq. (34)]:

$$S = \int d^8z K_{\Phi\bar{\Phi}}\phi\bar{\phi} + \int d^6z \frac{1}{2}W''\phi^2 + \int d^6\bar{z}\frac{1}{3!}\bar{W}'''\bar{\phi}^3. \quad (38)$$

Let us establish the form of the propagator for the quantum field ϕ whose dynamics is governed by the action functional $S_0 = \int d^8z K_{\Phi\bar{\Phi}}\phi\bar{\phi}$. It is convenient to represent this propagator as an expansion in terms of the vertices $K_{\Phi\bar{\Phi}} - 1$. In this expansion as illustrated in Fig. 4, thick and thin lines depict, respectively, the propagator corresponding to the quadratic part of the action functional in Eq. (38) and the standard superpropagator (35); dash-dotted lines represent the external field $K_{\Phi\bar{\Phi}} - 1$.

Summing the chain of diagrams depicted in Fig. 4, we find the required propagator in the form

$$\langle\phi\bar{\phi}\rangle = -\bar{D}_1^2 D_2^2 \frac{\delta^8(z_1 - z_2)}{16K_{\Phi\bar{\Phi}}(z_1)\Box}. \quad (39)$$

We note that, in general, the superfield $K_{\Phi\bar{\Phi}}(z_1)$ is not constant.

The analysis performed in the preceding section revealed that, in order to determine the two-loop chiral correction to the effective potential, it is sufficient to con-

sider the only diagram shown in Fig. 5. In this diagram, double external lines represent the superfields W''.

The contribution of the diagram in Fig. 5 is given by

$$I = \int\frac{d^4p_1d^4p_2}{(2\pi)^8}\frac{d^4kd^4l}{(2\pi)^8}\int d^4\theta_1 d^4\theta_2 d^4\theta_3 d^4\theta_4 d^4\theta_5$$
$$\times\frac{W''(-p_1,\theta_3)}{K^2_{\Phi\bar\Phi}(-p_1,\theta_3)}\frac{W''(-p_2,\theta_4)}{K^2_{\Phi\bar\Phi}(-p_2,\theta_4)}\frac{W''(p_1+p_2,\theta_5)}{K^2_{\Phi\bar\Phi}(p_1+p_2,\theta_5)}\overline{W}''^2 \quad (40)$$
$$\times\frac{1}{k^2l^2(k+p_1)^2(l+p_2)^2(l+k)^2(l+k+p_1+p_2)^2}$$
$$\times\delta_{13}\frac{\overline{D}_3^2}{4}\delta_{32}\frac{D_1^2\overline{D}_4^2}{16}\delta_{14}\delta_{42}\frac{D_1^2\overline{D}_5^2}{16}\delta_{15}\delta_{52}.$$

Upon the transformations of the D algebra, this expression assumes the form

$$I = \int\frac{d^4p_1d^4p_2}{(2\pi)^8}\frac{d^4kd^4l}{(2\pi)^8}\int d^2\theta\overline{W}''^2W''(-p_1,\theta)$$
$$\times W''(-p_2,\theta)W''(p_1+p_2,\theta)K^{-6}_{\Phi\bar\Phi} \quad (41)$$
$$\times\frac{k^2p_1^2+l^2p_2^2+2(k_1k_2)(p_1p_2)}{k^2l^2(k+p_1)^2(l+p_2)^2(l+k)^2(l+k+p_1+p_2)^2}.$$

Let us consider expression (41) in some detail. According to the definition in (8), the effective potential is equivalent to the effective Lagrangian in the limit of superfields that change slowly in spacetime. In the following, we therefore assume that, upon integration with respect to internal momenta, expression (41), which represents the sought contribution to the effective action, becomes

$$\int d^2\theta\int\frac{d^4p_1\ldots d^4p_n}{(2\pi)^n}W''(-p_1,\theta)\ldots W''(-p_2,\theta) \quad (42)$$
$$\times W''(p_1+p_2,\theta)S(p_1,p_2),$$

where p_1 and p_2 are external momenta. In the case being considered, the function $S(p_1, p_2)$ is equal to

$$\frac{k^2p_1^2+l^2p_2^2+2(k_1k_2)(p_1p_2)}{k^2l^2(k+p_1)^2(l+p_2)^2(l+k)^2(l+k+p_1+p_2)^2}.$$

Upon going over to the coordinate representation, expression (42) takes the form

$$\int d^2\theta\int d^4x_1\ldots d^4x_{n+1}\frac{d^4p_1\ldots d^4p_n}{(2\pi)^n}W(x_1,\theta)W(x_2,\theta)$$
$$\times W(x_3,\theta)\exp[i(-p_1x_1-p_2x_2+(p_1+p_2)x_3)] \quad (43)$$
$$\times S(p_1,p_2).$$

Since the superfields change slowly in spacetime, we can set $W(x_1, \theta)W(x_2, \theta)W(x_3, \theta) \simeq W^3(x_1, \theta)$, which leads to the expression

$$\int d^2\theta\int d^4x_1\ldots d^4x_{n+1}\frac{d^4p_1\ldots d^4p_n}{(2\pi)^n}W^3(x_1,\theta) \quad (44)$$
$$\times\exp[i(-p_1x_1-p_2x_2+(p_1+p_2)x_3)]S(p_1,p_2).$$

Four-dimensional integrations with respect to x_2 and x_3 yield delta functions forming the combination $\delta(p_2)\delta(p_1 + p_2)$; as a result, expression (43) assumes the form

$$\int d^2\theta\int d^4x_1W^3(x_1)S(p_1,p_2)\big|_{p_1,\ldots,p_n=0}. \quad (45)$$

Upon the above transformations, the quantity I in (40) becomes

$$I = \frac{6}{(16\pi^2)^2}\zeta(3)\int d^6z\overline{W}''^2\left\{\frac{W''(z)}{K^2_{\Phi\bar\Phi}(z)}\right\}^3,$$

where we have considered that [8]

$$\int\frac{d^4kd^4l}{(2\pi)^8}\frac{k^2p_1^2+l^2p_2^2+2(k_1k_2)(p_1p_2)}{k^2l^2(k+p_1)^2(l+p_2)^2(l+k)^2(l+k+p_1+p_2)^2}\bigg|_{p_1=p_2=0} = \frac{6}{(4\pi)^4}\zeta(3).$$

Therefore, the eventual result for the two-loop correction to the chiral potential has the form

$$W^{(2)} = \frac{6}{(16\pi^2)^2}\zeta(3)\overline{W}''^2\left\{\frac{W''(z)}{K^2_{\Phi\bar\Phi}(z)}\right\}^3. \quad (46)$$

We note that the two-loop chiral correction (46) is generally finite, requiring no renormalization. In the case of $W = \frac{\lambda}{3!}\Phi^3$ and $K = \Phi\bar\Phi$, the above expressions reproduce the result known within the Wess–Zumino model [7, 8].

6. TWO-LOOP KÄHLER EFFECTIVE POTENTIAL

Let us now proceed to calculate the two-loop Kähler effective potential. In order to determine it, we can make use of the background-superfield-dependent matrix superpropagator in the form (12). The possible vertices, which are also dependent on background superfields, are presented in (36). We further note that, by definition, the Kähler potential depends only on the

superfields Φ and $\bar{\Phi}$, but that it is independent of their derivatives. Upon representing all vertices in the form of four-dimensional integrals with respect to θ, the contributions to the Kähler effective potential must therefore include equal numbers of the factors D^2 and $\bar{D}^2$. This is necessary for ensuring fulfillment of the requirement that the eventual contribution obtained upon transforming the spinor supercovariant derivatives into momenta according to the rules $\bar{D}^2 D^2 \bar{D}^2 = -16p^2\bar{D}^2$ and $D^2\bar{D}^2 D^2 = -16p^2 D^2$ and upon contracting loops in θ space into a point according to the rule $\delta_{12}\bar{D}_1^2 D_2^2 \delta_{12} = \delta_{12}$ not depend on the derivatives of the superfields.

The components of the matrix superpropagator (12) are given by

$$
\begin{aligned}
G_{++} &= \frac{\bar{W}''}{K_{\Phi\bar{\Phi}}\Box + |W''|^2}\frac{\bar{D}_1^2}{4}\delta_{12},\\
G_{+-} &= \frac{1}{K_{\Phi\bar{\Phi}}\Box + |W''|^2}\frac{\bar{D}_1^2 D_2^2}{16}\delta_{12},\\
G_{-+} &= \frac{1}{K_{\Phi\bar{\Phi}}\Box + |W''|^2}\frac{D_1^2\bar{D}_2^2}{16}\delta_{12},\\
G_{--} &= \frac{W''}{K_{\Phi\bar{\Phi}}\Box + |W''|^2}\frac{D_1^2}{4}\delta_{12}.
\end{aligned}
\tag{47}
$$

It is obvious that equal numbers of the factors D^2 and $\bar{D}^2$ are possible in the following cases (see Fig. 6):

(i) A diagram involves only the G_{+-} and G_{-+} lines and a single vertex, proportional to a four-dimensional integral with respect to θ (Fig. 6*a*).

(ii) A diagram contains only the G_{+-} and G_{-+} lines and two vertices proportional to a four-dimensional integral with respect to θ (Fig. 6*b*).

(iii) A diagram contains only the G_{+-} and G_{-+} lines, one vertex proportional to a two-dimensional integral with respect to θ, and the second vertex proportional to a two-dimensional integral with respect to $\bar{\theta}$ (Fig. 6*c*).

(iv) A diagram contains equal numbers of the G_{--} and G_{++} lines, a G_{+-} line, and two vertices proportional to a four-dimensional integral with respect to θ (Fig. 6*d*).

(v) A diagram contains two G_{+-} lines, one G_{--} line, one vertex proportional to a two-dimensional integral with respect to $\bar{\theta}$, and the second vertex proportional to a four-dimensional integral with respect to θ (Fig. 6*e*).

(vi) A diagram contain two G_{+-} lines, one G_{++} line, one vertex proportional to a two-dimensional integral with respect to θ, and the second vertex proportional to a four-dimensional integral with respect to θ (Fig. 6*f*).

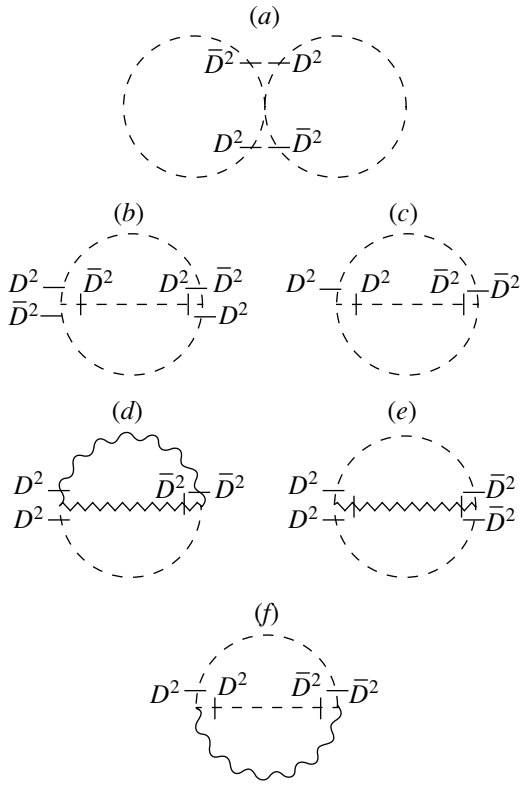

Fig. 6. Diagrams contributing to the two-loop Kähler potential.

In the diagrams presented in Fig. 6, we use the following notation:

$$
\text{- - -} = \frac{1}{K_{\Phi\bar{\Phi}}\Box + |W''|^2}, \qquad \sim\sim = \frac{W''}{K_{\Phi\bar{\Phi}}\Box + |W''|^2},
$$

$$
\sim\sim = \frac{\bar{W}''}{K_{\Phi\bar{\Phi}}\Box + |W''|^2}.
$$

We denote by J_1, J_2, etc., the contributions of the diagrams in Figs. 6*a*, 6*b*, etc. These contributions are given by

$$
\begin{aligned}
J_1 &= \frac{1}{2}\int d^4\theta_1 d^4\theta_2 K_{\Phi\bar{\Phi}}^2 K_{\Phi\Phi\bar{\Phi}\bar{\Phi}}\frac{\bar{D}_1^2 D_1^2}{16}\delta_{11}\frac{\bar{D}_1^2 D_1^2}{16}\delta_{11}\\
&\times\int\frac{d^4k d^4l}{(2\pi)^8}\frac{1}{(K_{\Phi\bar{\Phi}}k^2 + |W''|^2)(K_{\Phi\bar{\Phi}}l^2 + |W''|^2)},\\
J_2 &= \frac{J}{2}\int d^4\theta_1 d^4\theta_2 K_{\Phi\bar{\Phi}}^2 K_{\Phi\Phi\bar{\Phi}} K_{\Phi\bar{\Phi}\bar{\Phi}}\\
&\times\frac{\bar{D}_1^2 D_2^2}{16}\delta_{12}\frac{\bar{D}_1^2 D_2^2}{16}\delta_{12}\frac{D_1^2\bar{D}_2^2}{16}\delta_{12},
\end{aligned}
$$

$$J_3 = \frac{J}{6}\int d^4\theta_1 d^4\theta_2 K_{\Phi\bar\Phi}^3 |W'''|^2 \frac{\bar D_1^2 D_2^2}{16}\delta_{12}\frac{\bar D_1^2 D_2^2}{16}\delta_{12}\delta_{12},$$

$$J_4 = \frac{J}{6}\int d^4\theta_1 d^4\theta_2 W''\bar W'' K_{\Phi\bar\Phi}K_{\Phi\Phi\bar\Phi}K_{\Phi\bar\Phi\bar\Phi} \quad (48)$$
$$\times \frac{D_1^2\bar D_2^2}{16}\delta_{12}\frac{\bar D_2^2}{4}\delta_{12}\frac{D_1^2}{4}\delta_{12},$$

$$J_5 = \frac{J}{6}\int d^4\theta_1 d^4\theta_2 \bar W'' W''' K_{\Phi\bar\Phi}^2 K_{\Phi\Phi\bar\Phi}$$
$$\times \frac{D_1^2\bar D_2^2}{16}\delta_{12}\frac{D_1^2\bar D_2^2}{16}\delta_{12}\delta_{12},$$

$$J_6 = \frac{J}{6}\int d^4\theta_1 d^4\theta_2 \bar W''' W'' K_{\Phi\bar\Phi}^2 K_{\Phi\bar\Phi\bar\Phi}$$
$$\times \frac{D_1^2\bar D_2^2}{16}\delta_{12}\frac{D_1^2\bar D_2^2}{16}\delta_{12}\delta_{12},$$

where

$$J = \int \frac{d^4k d^4l}{(2\pi)^8}\frac{1}{(K_{\Phi\bar\Phi}k^2 + |W''|^2)(K_{\Phi\bar\Phi}l^2 + |W''|^2)(K_{\Phi\bar\Phi}(k-l)^2 + |W''|^2)}.$$

In the expression for J_1, the factor $(\bar D_1^2 D_1^2/16)\delta_{11}$ should be treated as $(\bar D_1^2 D_1^2/16)\delta_{12}$ if $\theta_1 = \theta_2$—that is, $(\bar D_1^2 D_1^2/16)\delta_{11} = 1$. The two-loop Kähler effective potential $K^{(2)}$ represents the sum of all these contributions; after the transformations of the D algebra, it assumes the form

$$K^{(2)} = \int \frac{d^4k d^4l}{(2\pi)^8}\frac{1}{(K_{\Phi\bar\Phi}k^2 + |W''|^2)(K_{\Phi\bar\Phi}l^2 + |W''|^2)(K_{\Phi\bar\Phi}(k-l)^2 + |W''|^2)}\left(\frac{1}{6}K_{\Phi\bar\Phi}^3|W'''|^2 + \frac{1}{6}(\bar W'' W''' K_{\Phi\bar\Phi}^2 K_{\Phi\Phi\bar\Phi} + \text{h.c.})\right.$$
$$\left. + \frac{1}{6}W''\bar W'' K_{\Phi\bar\Phi}K_{\Phi\Phi\bar\Phi}K_{\Phi\bar\Phi\bar\Phi} + \frac{1}{2}K_{\Phi\bar\Phi}^2|W''|^2 K_{\Phi\Phi\bar\Phi}K_{\Phi\bar\Phi\bar\Phi}\right) + \frac{1}{2}\int \frac{d^4k d^4l}{(2\pi)^8}\frac{1}{(K_{\Phi\bar\Phi}k^2 + |W''|^2)(K_{\Phi\bar\Phi}l^2 + |W''|^2)} \quad (49)$$
$$\times (K_{\Phi\bar\Phi}^2 K_{\Phi\Phi\bar\Phi}K_{\Phi\bar\Phi\bar\Phi} + K_{\Phi\bar\Phi}^2 K_{\Phi\Phi\bar\Phi\bar\Phi}).$$

It is obvious from (49) that $K^{(2)}$ involves two terms. The first is determined by the integral

$$\int \frac{d^4k d^4l}{(2\pi)^8}\frac{1}{K_{\Phi\bar\Phi}^3}\frac{1}{(k^2 + |W''|^2/K_{\Phi\bar\Phi})(l^2 + |W''|^2/K_{\Phi\bar\Phi})((k-l)^2 + |W''|^2/K_{\Phi\bar\Phi})};$$

upon a dimensional regularization, it can be represented as (for details, see [8])

$$-\frac{1}{(4\pi)^4}\frac{1}{K_{\Phi\bar\Phi}^3}\left(\frac{6|W''|^2}{K_{\Phi\bar\Phi}\epsilon^2} + \frac{3|W''|^2}{K_{\Phi\bar\Phi}\epsilon}\left(3 - 2\gamma - 2\ln\frac{|W''|^2}{K_{\Phi\bar\Phi}\mu^2}\right)\right.$$
$$+ 3\frac{|W''|^2}{K_{\Phi\bar\Phi}}\left(\ln^2\frac{|W''|^2}{K_{\Phi\bar\Phi}\mu^2} - (3-2\gamma)\ln\frac{|W''|^2}{K_{\Phi\bar\Phi}\mu^2}\right) \quad (50)$$
$$\left. + 9\frac{|W''|^2}{K_{\Phi\bar\Phi}}(1-\gamma)\right).$$

The second term is determined by the integral

$$\int \frac{d^4k d^4l}{(2\pi)^8}\frac{1}{K_{\Phi\bar\Phi}^2(k^2 + |W''|^2/K_{\Phi\bar\Phi})(l^2 + |W''|^2/K_{\Phi\bar\Phi})}$$
$$= \frac{|W''|^2}{(4\pi)^4 K_{\Phi\bar\Phi}^4}\left(\frac{2}{\epsilon} - \gamma + 1 - \ln\frac{|W''|^2}{K_{\Phi\bar\Phi}\mu^2}\right)^2.$$

The renormalization of the resulting contribution is performed by subtracting the one- and two-loop divergences according to the standard scheme. For this, we supplement the Lagrangian with the one-loop counterterm (26) and the two-loop counterterm

$$S_{\rm ct}^{(2)} = -\frac{1}{(4\pi)^4}\left(\frac{1}{\epsilon^2} - \frac{3}{2\epsilon}\right)\frac{|W''|^2}{K_{\Phi\bar\Phi}^4}. \quad (51)$$

In implementing this procedure, it is necessary to subtract both the one-loop and the two-loop divergences in order to renormalize the first term. The renormalization of the second term reduces to subtracting only the one-loop divergence with the aid of the counterterm in (26).

The resulting renormalized correction to the two-loop Kähler effective potential has the form

$$K^{(2)} = \frac{1}{(16\pi^2)^2}\frac{|W''|^2}{K^4_{\Phi\bar\Phi}}\Biggl\{-\frac{1}{4}\ln^2\frac{|W''|^2}{\mu^2 K_{\Phi\bar\Phi}} + \frac{3-\gamma}{2}\ln\frac{|W''|^2}{\mu^2 K_{\Phi\bar\Phi}} + \frac{3}{2}(\gamma-1) + \frac{1}{4}(\gamma^2+\zeta(2))\Biggr\}$$
$$\times\Biggl\{\frac{1}{6}(K^3_{\Phi\bar\Phi}|W'''|^2 + (\bar W''' W''' K^2_{\Phi\bar\Phi}K_{\Phi\Phi\bar\Phi} + \text{h.c.}) + W''\bar W'' K_{\Phi\bar\Phi}K_{\Phi\Phi\bar\Phi}K_{\Phi\bar\Phi\bar\Phi} + K^2_{\Phi\bar\Phi}|W''|^2|K_{\Phi\Phi\bar\Phi}|^2) + \frac{1}{2}K^2_{\Phi\bar\Phi}|W''|^2 K_{\Phi\Phi\bar\Phi}K_{\Phi\bar\Phi\bar\Phi}\Biggr\} + \frac{1}{(16\pi^2)^2}\frac{|W''|^4}{K^4_{\Phi\bar\Phi}}$$
$$\times\left(\gamma - 1 + \ln\frac{|W''|^2}{\mu^2 K_{\Phi\bar\Phi}}\right)^2(K^2_{\Phi\bar\Phi}K_{\Phi\Phi\bar\Phi}K_{\Phi\bar\Phi\bar\Phi} + K^2_{\Phi\bar\Phi}K_{\Phi\Phi\bar\Phi\bar\Phi}). \quad (52)$$

Relation (52) is the eventual result. The normalization point μ can be fixed by means of an appropriate normalization condition. In the case of $W = (\lambda/3!)\Phi^3$ and $K = \Phi\bar\Phi$, we arrive at the well-known result for the Wess–Zumino model [7, 8].

7. CONCLUSION

We have considered the general chiral-superfield model that is specified by Eq. (1) and which involves an arbitrary Kähler potential $K(\Phi, \bar\Phi)$ and an arbitrary chiral potential $W(\Phi)$ and have investigated the problem of determining the superfield effective action without fixing the explicit form of the functions $K(\Phi, \bar\Phi)$ and $W(\Phi)$. It is this problem that arises naturally in exploring the possible phenomenological implications of superstring theory.

It has been shown that a supergraph technique making it possible to preserve manifest supersymmetry at all stages of loop calculations can be formulated and used efficiently to determine quantum corrections to arbitrary classical potentials $K(\Phi, \bar\Phi)$ and $W(\Phi)$. We have calculated the one- and two-loop quantum corrections to the Kähler potential [expressions (27) and (52), respectively] and the leading two-loop corrections to the chiral potential [expression (46).] It turned out that, although the model specified by Eq. (1) is unrenormalizable at arbitrary $K(\Phi, \bar\Phi)$ and $W(\Phi)$, the chiral potential is always finite. In the particular case of $K(\Phi, \bar\Phi) = \Phi\bar\Phi$ and $W(\Phi) \sim \Phi^3$, the situation corresponds to the Wess–Zumino model—our results given by Eqs. (27), (46), and (52) then reduce to well-known results obtained previously (see [5–8, 12].

The approach developed in the present study admits a natural generalization to models involving multicomponent chiral superfields, which play an important role in phenomenological applications of superstring theory (see, for example, [3]). In our study performed together with Cvetic (see [4]), it was shown that the inclusion of the one-loop quantum corrections within the model of the two-component scalar superfield associated with the low-energy limit of superstring theory leads to the new aspects of the decoupling of massive states and can change some phenomenological predictions that had been obtained without taking into account quantum effects. In this connection, investigation of general models involving a few chiral superfields seems very promising. Another important possibility for a further development of the approach described in this study is associated with taking into account the interaction with a gauge superfield that is naturally present in models obtained in the low-energy limit of superstring theory.

ACKNOWLEDGMENTS

The authors are grateful to S.M. Kuzenko for numerous discussions and M. Cvetic for a discussion on the possible phenomenological applications of the model investigated here.

This work was supported in part within project no. INTAS-96-0308 of the International Association for the Promotion of Cooperation with Scientists from the Independent States of the Former Soviet Union, the joint project no. 96-02-00180 of the Russian Foundation for Basic Research and Deutsche Forschungs Gesellschaft, project no. 99-02-16617 of the Russian Foundation for Basic Research, and project no. 97-6.2-34 of the Contest Center for Fundamental Natural Sciences at the Ministry of Higher Education of the Russian Federation.

REFERENCES

1. M. Green, J. H. Schwarz, and E. Witten, *Superstring Theory* (Cambridge Univ. Press, Cambridge, 1987; Mir, Moscow, 1990), Vol. 2.
2. I. L. Buchbinder and S. M. Kuzenko, *Ideas and Methods of Supersymmetry and Supergravity or a Walk Through Superspace* (IoP Publ., Bristol, 1995; revised ed. 1998).
3. G. Cleaver, M. Cvetic, J. R. Espinosa, *et al.*, Nucl. Phys. B **525**, 3 (1998); hep-th/9805133; M. Cvetic, L. Everett, and J. Wang, Nucl. Phys. B **538**, 52 (1999); M. Cvetic, J. R. Espinosa, L. Everett, *et al.*, hep-ph/9807479; hep-ph/9811355.
4. I. L. Buchbinder, M. Cvetic, and A. Yu. Petrov, hep-th/9903243.
5. I. L. Bukhbinder, S. M. Kuzenko, and Zh. V. Yarevskaya, Yad. Fiz. **56** (5), 202 (1993) [Phys. At. Nucl. **56**, 680 (1993)].

6. I. L. Buchbinder, S. M. Kuzenko, and J. V. Yarevskaya, Nucl. Phys. B **411**, 665 (1994).
7. I. L. Buchbinder, S. M. Kuzenko, and A. Yu. Petrov, Phys. Lett. B **321**, 372 (1994).
8. I. L. Bukhbinder, S. M. Kuzenko, and A. Yu. Petrov, Yad. Fiz. **59**, 157 (1996) [Phys. At. Nucl. **59**, 148 (1996)].
9. M. T. Grisaru, M. Rocek, and R. von Unge, Phys. Lett. B **383**, 415 (1996); A. Pickering and P. West, Phys. Lett. B **383**, 54 (1996).
10. B. DeWitt, M. T. Grisaru, and M. Rocek, Phys. Lett. B **374**, 297 (1996); P. McArthur and T. D. Gargett, Nucl. Phys. B **497**, 525 (1997); N. G. Pletnev and A. T. Banin, hep-th/9811031.
11. I. L. Buchbinder, S. D. Odintsov, and I. L. Shapiro, *Effective Action in Quantum Gravity* (IoP Publ., Bristol, 1992).
12. P. West, Phys. Lett. B **261**, 396 (1991); I. Jack, D. R. T. Jones, and P. West, Phys. Lett. B **258**, 382 (1991).

Translated by A. Isaakyan

Physics of Atomic Nuclei, Vol. 63, No. 9, 2000, pp. 1671–1672. From Yadernaya Fizika, Vol. 63, No. 9, 2000, pp. 1759–1760.

LETTERS TO THE EDITOR

Left–Right Asymmetry of the Angular Distribution of Long-Range Alpha Particles from Ternary ^{235}U Fission Induced by Cold Polarized Neutrons*

G. V. Danilyan[1)], A. M. Fedorov[1)], A. M. Gagarski[2)], F. Goennenwein[3)], P. Jesinger[3)], J. von Kalben[4)], A. Koetzle[3)], Ye. I. Korobkina[5)], I. T. Krasnoshchekova[2)], M. Mutterer[4)], V. V. Nesvizhevsky[6)], S. R. Neumaier[4)], Yu. B. Novozhilov[1)], V. S. Pavlov[1)], G. A. Petrov[2)], V. I. Petrova[2)], S. M. Solovyev[7)], W. H. Trzaska[8)], and O. Zimmer[6)]

Received December 22, 1999

In our previous publication [1], we announced the discovery of a *T*-odd angular correlation in ternary ^{233}U fission induced by cold polarized neutrons. The observed angular distribution of long-range alpha particles can be described as

$$W = \text{const} \times (1 + D \times \mathbf{S} \cdot [\mathbf{P}_{\text{LF}} \times \mathbf{P}_{\alpha}]), \qquad (1)$$

where D is the correlation coefficient; $\mathbf{S}$ is a unit vector in the direction of neutron polarization; and $\mathbf{P}_{\text{LF}}$ and $\mathbf{P}_{\alpha}$ are unit vectors in the directions of, respectively, the light-fragment and the alpha-particle momentum. The measured value of D was found to be equal to $(-2.34 \pm 0.7) \times 10^{-3}$. This correlation seems to be odd under time reversal, but theory predicts that this can be due to strong or electromagnetic interaction of particles in the final state. It should be noted that the contribution to the measured asymmetry from trivial *s*- and *p*-wave interference effect in the entrance reaction channel, which leads to left–right asymmetry of the resulting distribution of fragments relative to the plane spanned by the vectors of neutron polarization, $\mathbf{S}$, and momentum, $\mathbf{P}_n$, should be excluded because, for binary ^{233}U fission induced by cold polarized neutrons, it is one order of magnitude less [2] than the observed correlation. Moreover, our experiment was performed in a longitudinally polarized neutron beam, for which the *sp*-interference effect should vanish.

Actually, **I**—the unit vector in the direction of fissile-nucleus polarization—should be substituted for $\mathbf{S}$ in expression (1); therefore, the measured coefficient D should be corrected by taking into account the average degree of nuclear polarization, P. The last depends on the spin value of the compound nucleus in the following way:

$$P = (+P_n/3)[1 + 2/(2J + 1)] \quad \text{for} \quad I = J + 1/2,$$
$$P = (-P_n/3) \quad \text{for} \quad I = J - 1/2. \qquad (2)$$

Here, P_n is the degree of neutron-beam polarization and J is the spin value of the target nucleus. The negative sign of polarization means that the direction of fissile-nucleus polarization is opposite to the direction of the neutron-beam polarization.

Actually, both spin states contribute to the fission cross section at any neutron-energy value. In order to calculate the average degree of fissile-nucleus polarization, it is therefore necessary to know the spin-dependent fission cross section. Unfortunately, such data are available only for ^{235}U [3]. Using these data, we can easily find that the average degree of the polarization of ^{235}U nuclei at thermal neutron energies is $0.14P_n$. The degree of neutron-beam polarization was measured many times during both experiments, and it is equal to 0.95. Thus, we have $P \approx 0.13$.

To measure the correlation coefficient D for ^{235}U, the same experimental setup was used with one exception: we employed thicker PIN diodes in detecting ternary charged particles to provide sufficient depletion depths to stop at least the alpha particles.

As in the previous experiment, two types of detection of coincidences between pulses from PIN diodes and from MWPCs (fragment detector) were used: on-line (with the aid of counters) and off-line (evaluation from accumulated data). The results of the former on-line measurement for ^{233}U was $D(^{233}\text{U}) = (-2.76 \pm 0.06) \times 10^{-3}$, whereas the result of the off-line evalua-

* This article was submitted by the authors in English.

1) Institute of Theoretical and Experimental Physics, Bol'shaya Cheremushkinskaya ul. 25, Moscow, 117259 Russia.
2) Petersburg Nuclear Physics Institute, Russian Academy of Science, Gatchina, 188350 Russia.
3) Physikalisches Institut, Tübingen, Germany.
4) Institut fur Kernphysik, Darmstadt, Germany.
5) Russian Research Centre Kurchatov Institute, pl. Kurchatova 1, Moscow, 123182 Russia.
6) Institute Laue–Langevin, Grenoble, France.
7) Research and Production Association Khlopin Radium Institute, St. Petersburg, 194021 Russia.
8) Department of Physics, University of Jyväskylä, PO Box 35, FIN 40351 Jyväskylä, Finland.

tion was found to be $D = (-2.34 \pm 0.07) \times 10^{-3}$. This difference of the results was due to the use of different electronics in the on-line and in the off-line method. Afterward, it was found that the asymmetry coefficient D depends on the amplitude of PIN diode pulses [4]. Physically, this can be explained as the dependence of D on the kinetic energy of ternary alpha particles: the modulus of D increases with alpha-particle energy. But it is impossible to rule out the existence of some physical background that contributes to the low-energy part of the amplitude spectrum from PIN diodes. A more detailed handling of the accumulated data will give the final results. In order to compare now the values of D for ^{233}U and ^{235}U, we will use the results of the on-line measurements.

The on line measurement of D with counters gave $D_{on}(^{235}\text{U}) = (0.76 \pm 0.09) \times 10^{-3}$. Because the opposite sign and the lower value of D were obtained for ^{235}U, the measurements for ^{233}U target were repeated at the same threshold. The result is $D_{on}(^{233}\text{U}) = (-1.90 \pm 0.11) \times 10^{-3}$.

Thus, the asymmetry coefficient for ^{235}U is approximately 2.5 times less than that for ^{233}U and has an opposite sign. It is easy to explain these differences if we assume that, at the neutron energy of $E_n = 0.0017$ eV (20 K), the 2^+ neutron resonances mainly contribute to the cross section for ^{233}U fission. Under this assumption, the left–right asymmetry will be universal (that is, it does not depend on the fissile nucleus), and its absolute value is equal approximately to 7×10^{-3}. It is then possible to predict the magnitude and the sign of the left–right asymmetry coefficient for the ternary fission of ^{239}Pu because, in the region of thermal neutrons, only one of the two possible spin states, 0^+ and 1^+, may contribute to the correlation under investigation in *s*-wave neutron capture. Considering that the well-known resonance at a neutron energy of 0.3 eV is responsible for 51% of the fission cross section at thermal neutron energies and using expression (2), we can estimate the mean degree of nucleus polarization at 0.38. Therefore, the expected experimental value of the asymmetry coefficient is

$$D(^{239}\text{Pu}) \geq +2 \times 10^{-3}.$$

The measurement of D for ^{239}Pu in the near future will test the validity of our assumption.

ACKNOWLEDGMENTS

We are grateful to the technical services of ILL for support of the present experiment.

This work forms a part of the PhD thesis of P. Jesinger and was supported in part by BMBF under contract no. 06 TU 669 and by the Russian State Program Fundamental Nuclear Physics (project no. 134-06).

REFERENCES

1. P. Jesinger *et al.*, Yad. Fiz. **62**, 1723 (1999) [Phys. At. Nucl. **62**, 1608 (1999)].
2. V. P. Alfimenkov *et al.*, Yad. Fiz. **58**, 799 (1995) [Phys. At. Nucl. **58**, 737 (1995)].
3. W. I. Furman *et al.*, in *Nuclear Fission and Fission-Product Spectroscopy: Second International Workshop*, Ed. by G. Fioni *et al.* (1998), p. 356.
4. P. Jesinger *et al.*, in *Nuclear Fission and Fission-Product Spectroscopy: Second International Workshop*, Ed. by G. Fioni *et al.* (1998), p. 395.